APSYM 2006

PROCEEDINGS OF APSYM 2006

National Symposium on

ANTENNAS & PROPAGATION

DECEMBER 14-16, 2006

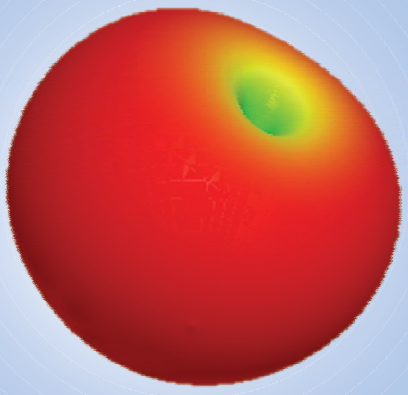

DEPARTMENT OF ELECTRONICS

COCHIN UNIVERSITY OF

SCIENCE AND TECHNOLOGY

KOCHI – 682 022

Co-sponsored by:

University Grants Commission

All India Council of Technical Education

Department of Science & Technology (Govt. of India)

Council of Scientific and Industrial Research

Kerala State Council for Science Technology and Environment (Govt. of Kerala)

IEEE Student Branch, Cochin

PROCEEDINGS OF

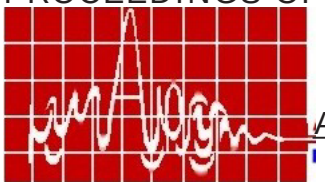

APSYM 2006

Tenth National Symposium on

ANTENNAS AND PROPAGATION

December 14- 16 2006

Centre for Research in ElectroMagnetics and Antennas (CREMA)
Department of Electronics
Cochin University of Science and Technology
Kochi, India
Phone: 91 484 2576418
Fax : 91 484 2575800
URL : www.doe.cusat.edu

Proceedings of APSYM 2006
December 14-16, 2006

Organised by,
Centre for Research in ElectroMagnetics and Antennas (CREMA)
Department of Electronics
Cochin University of Science and Technology
Kochi, India
Phone: 91 484 2576418
Fax : 91 484 2575800
URL : www.doe.cusat.edu

Editors:

Prof. K.G. Nair
Prof. K.G. Balakrishnan
Prof. P.R.S. Pillai
Prof. K. Vasudevan
Prof. K.T. Mathew
Prof. P. Mohanan
Dr. C.K. Aanandan

Co-sponsored by

University Grants Commission (UGC).
All India Council of Technical Education (AICTE).
Department of Science & Technology , DST(Govt. of India).
Council of Scientific and Industrial Research(CSIR).
Kerala State Council for Science Technology and Environment(Govt. of Kerala).
IEEE Student Branch, Kochi.

Copyright © 2006, CREMA, Department of Electronics, Cochin University of Science And Technology, Kochi, India.

All rights reserved. No part of this publication may be reproduced, stored in a retrieval system or transmitted in any form or by any means, electronic, mechanical, photocopying and recording or otherwise without the prior permission of the publisher.

This book has been published from Camera ready copy/softcopy provided by the contributors.

Published by CREMA, Department of Electronics, Cochin University of Science And Technology, Cochin – 682022 India and printed at Maptho Printers, South Kalamassery, India.

Proceedings of APSYM2006, Dec. 14-16., Dept. of Electronics, CUSAT, India.

Chairman Welcomes you

Dear friend,

It is nice that you are planning to attend the Antennas and Propagation Symposium ***(APSYM 2006)*** *at Cochin University of Science and Technology - Department of Electronics. I welcome you warmly to this important event.*

"APSYM 2006" is the 10th one in the series, which we started in 1988. A chronological listing of the earlier APSYMs is given below.

Sixty four papers are scheduled to be presented during APSYM 2006. The APSYM 2006 organising committee has planned an excellent technical programme with fifteen invited talks by eminent scientists in the field from India and abroad. This time a special European ACE session has been planned, in which Scientists from different parts of Europe will be talking on the latest developments in the field of Microwaves.

In order to provide online access, the information about the advance programme is also available in the website www.doe.cusat.edu/apsym.

Chronology of APSYMs

Sl.No.	Symposium	Dates of Symposium	Number of papers	Number of invited talks
1	APSYM-88	Dec. 15- 17- 1988	42	2
2	APSYM-90	Nov. 28-30- 1990	51	10
3	APSYM-92	Dec. 29-31-1992	91	2
4	APSYM-94	Nov.17-19-1994	75	6
5	APSYM-96	Nov.01-02-1996	42	2
6	APSYM-98	Dec.15-16-1998	57	1
7	APSYM-2000	Dec.06-08-2000	71	3
8	APSYM-2002	Dec.09-11-2002	84	10
9	APSYM-2004	Dec.21-23-2004	55	4
10	APSYM-2006	Dec.14-16-2006	64	16
11	APSYM-2008	Dec.10-12-2008	Scheduled	

Proceedings of the earlier symposia are available with Organisers of APSYM 2006 and those who are interested may please contact the Organisers.

Wishing you all a warm welcome once again and hoping very fruitful discussions in the sessions.

Cochin - 22
December 01, 2006

Prof. K.G. Nair

OUR TRIBUTES TO THE GREAT PIONEERS

JAMES CLERK MAXWELL

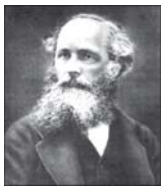

The founder of Electromagnetic theory of Radiation. His theoretical prediction of the existence of Electric and Magnetic fields associated with wave propagation carrying energy of Electromagnetic nature was a break-through in the history of Science. A new era of Electromagnetism was thus opened by this great scientist.

HEINRICH HERTZ

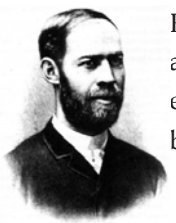

Experimentally demonstrated the generation, propagation and detection of electromagnetic waves. Thus he gave a firm experimental support for the theoretical conclusions drawn by James Clerk Maxwell.

JAGADISH CHANDRA BOSE

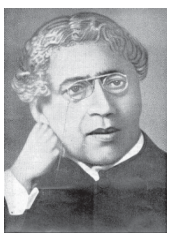

The First Indian Scientist who marked his footprints in the world of Electromagnetics. In fact, Bose generated millimeter waves using a circuit developed in his laboratory and used these waves for communication, much earlier than the western scientists. He also developed microwave antennas (horns) which are still considered to be ideal feeds.

Proceedings of APSYM2006, Dec. 14-16., Dept. of Electronics, CUSAT, India.

ORGANISING COMMITTEE

Chairman
Prof. K.G. Nair
Emeritus Professor

Director
Prof. K. Vasudevan

Vice-chairman
Prof. K.G. Balakrishnan

Publications
Prof. P.R.S.Pillai

Registration
Prof. K.T. Mathew

Technical Programme
Prof. P. Mohanan

Local Arrangements
Dr. C. K. Aanandan

Members

Dr. Tessamma Thomas	Mr. James Kurien
Dr. D. Rajaveerappa	Mrs. Supriya M.H.
Mr. Gijo Augustin	Ms. Bybi P.C
Mr. Rohith K Raj	Dr. Jaimon Yohannan
Ms. Nimisha C.S.	Ms. Jitha B.
Ms. M.N. Suma	Mr. Anupam R Chandran
Mr. Manoj Joseph	Ms. Sreedevi K Menon
Mrs. Deepthi Das	Mr. Gopi Krishanan
Mr. Deepu V	Mr. A.V. Praveen Kumar
Mr. V.P. Dinesh	Mr. Robin Augustin
Mr. Anil Lonappan	Mr. Vinu Thomas
Dr. S. Mridula	Dr. Binu Paul
Mr. Jinto George	Mr. Prajas John
Mr. Shaheer Kankalathil	Mr. Mahendran M.G
Mr. Anantha Krishnan	Mr. S. Maheshwaran
Mr. Gopakumar C.	Mrs. Shameena V.A

Board of Referees

1. Prof. Bharathi Bhat, IIT Delhi.
2. Prof. Ramesh Garg, IIT Kharagpur.
3. Dr. S. Pal, ISRO Bangalore.
4. Prof. S.N. Sinha, IIT Roorkee.
5. Dr. Lakshmeesha V.K., ISRO Bangalore.
6. Dr. Raj Kumar, IAT Pune.
7. Prof. V.M. Pandharipande, Osmania University, Hyderabad.
8. Prof. M.C. Chandramouly, MIC Colleage of Technology, Vijayavada.
9. Prof. K.J. Vinoy, IIC Bangalore.
10. Mr. K.K. Sood, SAC Ahemmedabad.
11. Prof. C.S. Sridhar,SBMS Institute of Technology Bangalore.
12. Dr. P.A. Praveenkumar, NPOL, Cochin.
13. Dr. K.P. Ray, SAMEER, Mumbai.
14. Dr. R. Ratheesh, C-MET Trichur
15. Prof.K.G. Nair, Cochin University, Kochi.
16. Prof. K. Vasudevan, Cochin University, Kochi.
17. Prof. K.T. Mathew, Cochin University, Kochi.
18. Prof. P Mohanan, Cochin University, Kochi.
19. Dr. C.K. Aanandan, Cochin University, Kochi.

MILESTONES IN THE HISTORY OF ELECTROMAGNETICS

1747	Benjamin Franklin	Types of Electricity
1773	Henri Cavendish	Inverse square law
1785	Coulomb	Law of electric force
1813	Gauss	Divergence theorem
1820	Ampere	Ampere's experiment
1826	Ohm	Ohm's law
1831	Faraday	Electromagnetic Induction
1844	Morse	Telegraphy
1855	Sir William Thomson	Transmission lines theory
1864	Lord Rayleigh	Theory of Sound Propagation
1865	James Clerk Maxwell	Electromagnetic field equations
1873	James Clerk Maxwell	Unified theory of Electricity and Magnetism
1876	Graham Bell & Gray	Telephone
1883	Thomas Alva Edison	Electron Emission from Heated Filament
1885	Heinrich Hertz	Electromagnetic Wave Propagation
1887	Heinrich Hertz	Spark plug experiment
1888	Heinrich Hertz	Half-wave dipole antenna
1890	Ernst Lecher	Lecher wire
1893	Heinrich Hertz	Spark Gap Generator
1893	Thomson	Waveguide theory
1894	Marconi	Wireless Telegraphy
1895	Jagadish Chandra Bose	5-6mm wavelength Signal Transmission
1897	Lord Rayleigh	Boundary values and modes in Metallic cylinders
	Jagadish Chandra Bose	Horn antenna and Millimeter wave source
1898	Lodge	Tuned Transmitters and Receivers
1900	Marconi	TransAtlantic Communication
1902	Weber	Propagation in Hollow Tube
	Fleming	Vaccum Tube
1903	Hulsmeyer	Radar
1906	Fessenden	Rotating Alternator and audio modulation
	Thomas et.al	Crystal Detector
	Fessenden	Radio broadcasting
	Dunwoody	Crystal detectors
1907	DeFroest	Triode
1912	Eccles	Ionospheric propagation
1914	AT & T	170 kHz Radio
1915	Carson	Single side-band transmission
1918	Watson	Ground wave propagation
1919	Southworth	Lecher line circuit
	Heinrich Barkhausen & Kurz	Triode electron tube at 1.5 GHz
1920	Hull	Magmetron
1921	Hull	Smooth bore Magnetron
1922	Affel	Directional Coupler
	Marconi	Shortwaves for detection of objects
	Brillouin	Acoustoopic Effect
1923	HH Beverage	Beverage Antenna
1925	Van Boetzelean	Short Wave Radio
	Yagi and Uda	Yagi-Uda antenna
	Appleton	Ionospheric Layer
1927	Okabe	Split Anode Magnetron
1929	Clavier	Microwave Communication
1930	Hansen	Resonant Cavity
	Karl G Jansky	Bruce Curtain Antenna
	Barrow L	

1931	Marconi	Circular Waveguide
	Andre G	propagation
	Clavier	600 MHz radio link in Italy
		Microwave Radio
1932	Southworth	transmission across English
	Marconi	Channel
		Circular Waveguide
	Claud Cleton	57cm Radio telephone and
1933	Barrow	teleprinter service
		Microwave spectroscopy
		Circular Waveguide Propagation
	Armstrong	Frequency modulation
	US Naval Research Lab	Detection of Aircraft with a 3 MHz wave
1934	Schdlkunoff	TE01 mode in Circular Waveguide
	Watson-Watt	Experimental Radar Station
1935	Oscar Heil	Velocity modulation
	Watson watt	RADAR
1936	Southworth and	Microwave propagation in
	Barrow	Circular Waveguide,Horn
		Antenna for aircraft landing
	G.H. Brown	Turnstile antenna
1937	Varian Brothers	Klystron
	Janskey	Radio Astronomy
	Manson	Waveguide Filter
	Russel & Varian Bros	
	A,H. Boot, JT. Randall	Klystron
	M.L. Oliphant	Magnetron
	Pollard	Radar aiming Anti-aircraft guns
1938	J.D. Kraus	Corner reflector
	British Air_defence	25 MHz Radar
1939	Barrow	Magic Tee
	Peterson et.al	Diode Mixer
	P.H. Smith	Smith impedance
	Boot & Randall	Cavity Magnetron
	Peterson Llewellyn	Vacum tube diode mixer
1940	Hansen	Leakywave Antenna
	Quakenbush	UHF coaxial Connector
	Bowen, Dummer et.al	P.P.I Scope
1941	MIT Radiation Laboratory	K-band Radar
1942	Wheeler	Stripline Technology
	Neill	N-type connector
	Herold	Broad band UHF Receiver
1943	AT & T Lab	4.5 GHz Multichannel PPM digitally modulated microwave Radio.
		Microwave Radar 3 GHz and X band frequencies
1944	Meyers et.al	Reflectometers
	Mumford	Multihole Directional Coupler
	MIT Radiation Laboratory	Electronic Scanning array
1945	Kompfner	TWT
1946	Clarke	Forecasts geosynchrous Satellite
	J.D. Kraus	Helical antenna
	Percy Spencer	Microwave oven
1947	AT & T Lab	3.7-4.2 LOS link
	Cohn	Ridge Waveguide

1948	Van der Ziel	Non-linear capacitors
1950	C.L. Dolph	Dolph-Tchebyscheff array
	Goubau	Goubau line
1951	Coleman	Dielectric WG at mm and sub mm wave length
1952	Assadourian et.al	Microstrip transmission Line
1953	Townes	Ammonia Maser
	Deschamps	Microstrip antenna
1954	Towns	Maser
1955	Page	Monopulse Radar
1956	Esaki	Tunnel Diode
	Bloembergen	Three level Maser
1957	Kroemer	Hetrojunction Transistor
	Bakanowski et al	Varactor
	Hines et.al	Parametric Amplifier
	V.H. Rumsey	Frequency independent antenna
	Weiss	Parametric amplifier
1958	Bloembergen	Solid state Maser
	John D Dyson	Spiral antenna
	Read	Read diode
		Satellite launching
		Space Communication
	Maiman	Ruby Laser
	L.Lewin	Strip line radiator
	DeGrasse et.al.	Solid State Maser Amplifier
1959	D.Wigst Isbell	Log periodic antenna
1963	J.B. Gunn	Gunn diode
1964	White	p-i-n diode
	Anderson Dennison	Microwave Network Analyzer
	A.F.Kay	Scalar feed
	Arno Penzias & Big	
	R.Wilson	Big Bang theory Proved by microwave Antenna expts.
1965	Hakki and Irvin	Gunn diode oscillators and Amplifiers
	R.C. Johnston	
	Cohen, DeLloach	IMPATT diode
1968	Victor Veselago	Predicted DNG Materials
1969	Wen	Coplanar Line
1970	Silvester	FEM
	Byron	Microstrip array
1971	Itoh and Mittra	Wave Analysis of Microstrip
1975	Bekati	Relativistic cavity Magnetron
1980	Mimura	HEMT
1986	Didenko et.al	Advance relativistic Magnetron
1988	S.K. Khamas	High Tc Super conducting dipole
1992	Victor Trip, Johnson	
	Wang	Paste-on antenna
1993	Te-Kao Wu et al	Multiple Diachronic Surface
		Cassegrain Reflector
1996	Clorfeine & Delohh	TRAPATT diode
1996	John W Mc Carkle	Microstrip DC to GHz Field Stacking Balun
2000	Zhores I Alferov	
	Herbert Kroemer	Fast opto and microelectronic Semiconductor heterostructures
2002	George V Eleftheriades	Planar Negative LC loaded Refractive media
2004	Thomas purr et al	Miniaturized Directional Antenna
2006	John c Mather &	Cosology and Cosmic
	George F. Smoot	Microwave Background 2006 (CMB) Cosmic Microwave Background Radiation

Proceedings of APSYM2006, Dec. 14-16., Dept. of Electronics, CUSAT, India.

CONTENTS

Proceedings of APSYM2006, Dec. 14-16., Dept. of Electronics, CUSAT, India.

RESEARCH SESSION I

MICROSTRIP ANTENNAS I

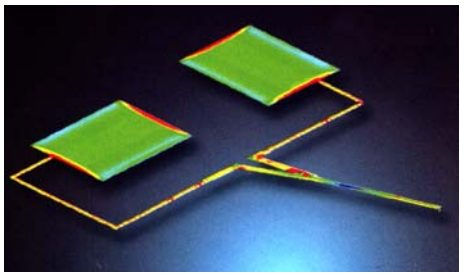

December 14, Thursday
(2.00 p.m. - 3.00 p.m.)

RESEARCH SESSION I

MICROSTRIP ANTENNAS I

Chair: Dr. S. N. Joshi
CEERI, Pilani.

Proceedings of APSYM2006, Dec. 14-16., Dept. of Electronics, CUSAT, India.

Design of an Elliptic CPW Ultra-Wideband Antenna

R. K. Arya, Ramesh Garg, *FIEEE*

Department of Electronics and Electrical Communication Engineering

Indian Institute of Technology Kharagpur, Kharagpur- 721302, India

Tel: +91-(3222)-283522, Fax: +91-(3222)-255303, E-mail: garg@ece.iitkgp.ernet.in

***Abstract* — In this paper, we propose a CPW fed ultra-wideband (UWB) antenna. It consists of an elliptic disc embedded in an elliptic slot. The antenna design procedure and simulation results are presented.**

***Index Terms* — Ultra-wideband antenna, elliptic CPW antenna, CPW feed.**

I. Introduction

In UWB communications systems, antenna is the most important component. Low power consumption dictates the antenna to have good return loss within 3.1 to 10.6 GHz. The major work in UWB antenna had started with three dimensional antennas (such as horn antenna, bow-tie, log-periodic, volcano smoke and biconical antenna) and later on turned to planar antennas due to ease of manufacturing and compatibility with ICs. While many antennas for UWB applications have been reported, the design methodology is still not clear although there are some attempts [1].

Our design methodology starts with the investigation of an optimized UWB antenna reported in [2]. First we have tried to understand the functioning of given antenna and with the insight of this antenna, we designed an antenna with FR4 substrate and the new design verifies the design approach.

The optimized antenna consists of an elliptic disc embedded in an elliptic slot with $2b$=11mm and $2a$=17mm for the disc. It is fed by a 50 ohm microstrip line. The ground plane underneath the disc is etched with an elliptic slot of semi major and minor axis A=13mm and B=12.3 mm, respectively. The slot and the patch are separated by a substrate with $\varepsilon_r = 7.8$, h=1mm and tanδ=0.002. The centres of the disc and the slot are displaced with respect to each other by 3.9 mm.

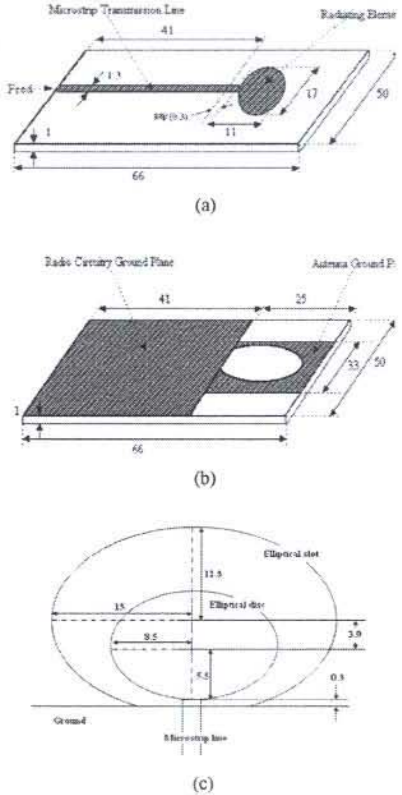

Fig. 1 Configuration of planar UWB antenna (units in mm) [1] (a) top layer and (b) bottom layer (c) top view of the disc and slot (not to scale).

II. ANALYSIS OF OPTIMIZED ANTENNA

The principal reason behind the use of elliptic resonator is the existence and excitation of various modes in the UWB. For this, analytical expressions for cut-off frequencies of various modes in an elliptic hollow waveguide are available [3]. These are used to determine the cut-off frequencies for resonant modes in the elliptic disc and slot. These values are compared with direct simulations in Table 1. The discrepancy between the two sets may be due to the effect of fringing fields and the effective dielectric constant being different for different modes and from ε_r of the substrate. However, the number of modes provided by the two analyses are comparable. It is due to this large number of modes generated by the disc and slot that the geometry is wideband.

This optimized antenna was simulated with CST Microwave Studio. The simulated return loss and radiation patterns matched with those reported in [2]. The simulations were also carried out by varying the feed gap and the *A* value of slot. It was found that 0.3mm gap between the ground plane and the disc was optimum for return loss greater than 10dB over the bandwidth. The value of *A* was adjusted so that the lower edge frequency matched with 3.1GHz. It was observed that 2*b* was nearly equal to $\lambda_1/4$ and 2*A* should be nearly equal to $\lambda_1/2$, where λ_1 corresponds to the wavelength in the substrate at the lower edge frequency.

III. CPW ANTENNA

With the optimized dimensions known for an UWB antenna, we designed our own antenna on FR4 substrate with $\varepsilon_r = 4.3$, *h*=1.58mm and tanδ=0.02. For this, we scaled the dimensions as follows

$$a' = a\sqrt{\frac{7.8}{4.3}} \text{ and } B' = B\sqrt{\frac{7.8}{4.3}} \qquad (1)$$

where primed values correspond to the CPW antenna and unprimed for the antenna described earlier. The ellipticities were optimized for designed return loss and found to be 0.71 for the disc and 0.55 for the slot.

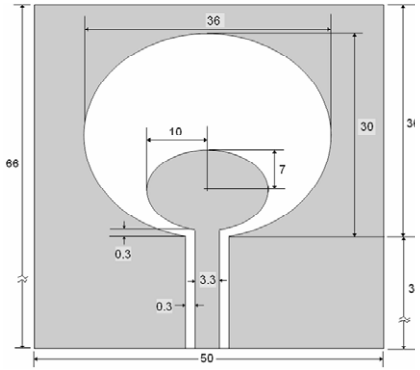

Fig. 2 Configuration of planar CPW fed UWB antenna (units in mm)

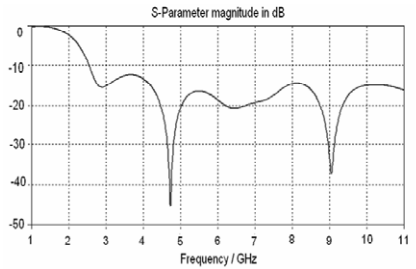

Fig. 3 Return loss versus frequency for CPW fed UWB antenna of Fig. 2.

The feed position of the UWB antenna is very critical for the desired return loss. We have selected a CPW feed and the slot width at the feed point corresponds to 100ohm impedance, and in this case the slot width is 0.3mm as shown in Fig. 2. This slot width fixed the off-centering of the disc from the slot by ($B'-b'$– slot width).

Fig.3 shows the simulated return loss versus frequency. It is seen that the antenna has more than 10 dB return loss from 2.5 to 11 GHz. Fig. 4 shows the simulated radiation patterns for this antenna at 3, 6 and 9GHz. We observe that at lower frequency the antenna behaves like a monopole antenna. This antenna has nearly omni-directional pattern as required for UWB applications.

Proceedings of APSYM2006, Dec. 14-16., Dept. of Electronics, CUSAT, India.

VI. CONCLUSION

In this paper, an optimized UWB antenna is investigated and the effect of various parameters is studied for better design. We have presented a general methodology for designing the antenna, which could be useful for the CPW UWB antenna. The simulated return loss and the radiation patterns are reported with nearly omni-directional radiation patterns over 3.1-10.6 GHz.

REFERENCES

[1] A. M. Abbosh, M. E. et. al., "Investigations into an LTCC based ultra wideband antenna", *2005 APMC Proceedings,* vol. 3, Dec. 2005.

[2] Chen Ying; Zhang, Y.P. "A planar antenna in LTCC for single-package ultrawide-band radio", *IEEE Transactions on Antennas and Propagation,* pp. 3089- 3093, Vol. 53, Issue 9 Sept. 2005

[3] J. G. Kretzschmar, "Wave propagation in hollow conducting elliptical waveguides", *IEEE Trans Microwave Theory Tech.*, vol. MTT-18, pp. 547-554, Sept. 1970.

Table 1

RESONANT FREQUENCIES FOR VARIOUS MODES IN ELLIPTIC DISC AND SLOT

Mode	Computed resonant frequencies for unloaded elliptic disc (*a*=8.5mm, *b*=5.5mm, ε_r=7.8) (GHz)	Simulated resonant frequencies in UWB Band (GHZ)	Mode	Computed resonant frequencies for unloaded elliptic slot (*a*=13mm, *b*=12.3mm, ε_r=7.8) (GHz)	Simulated resonant frequencies in UWB Band (GHz)
TM_{c11}	3.75	3.14 3.61 4.00 4.45 5.00 5.58 6.12 6.65 7.13 7.65 8.2 8.78 9.33 9.88 10.3	TE_{c21}	4.01	3.78 5.26 6.64 8.01 9.41
TM_{c21}	6.77				
TM_{c01}	10.75		TE_{c01}	5.33	
TM_{s11}	5.6				
TM_{s21}	7.88		TE_{s21}	6.26	
TE_{c01}	6.28		TM_{c01}	3.48	
TE_{c11}	8.91		TM_{c11}	5.44	
TE_{s11}	10.97		TM_{s11}	5.36	

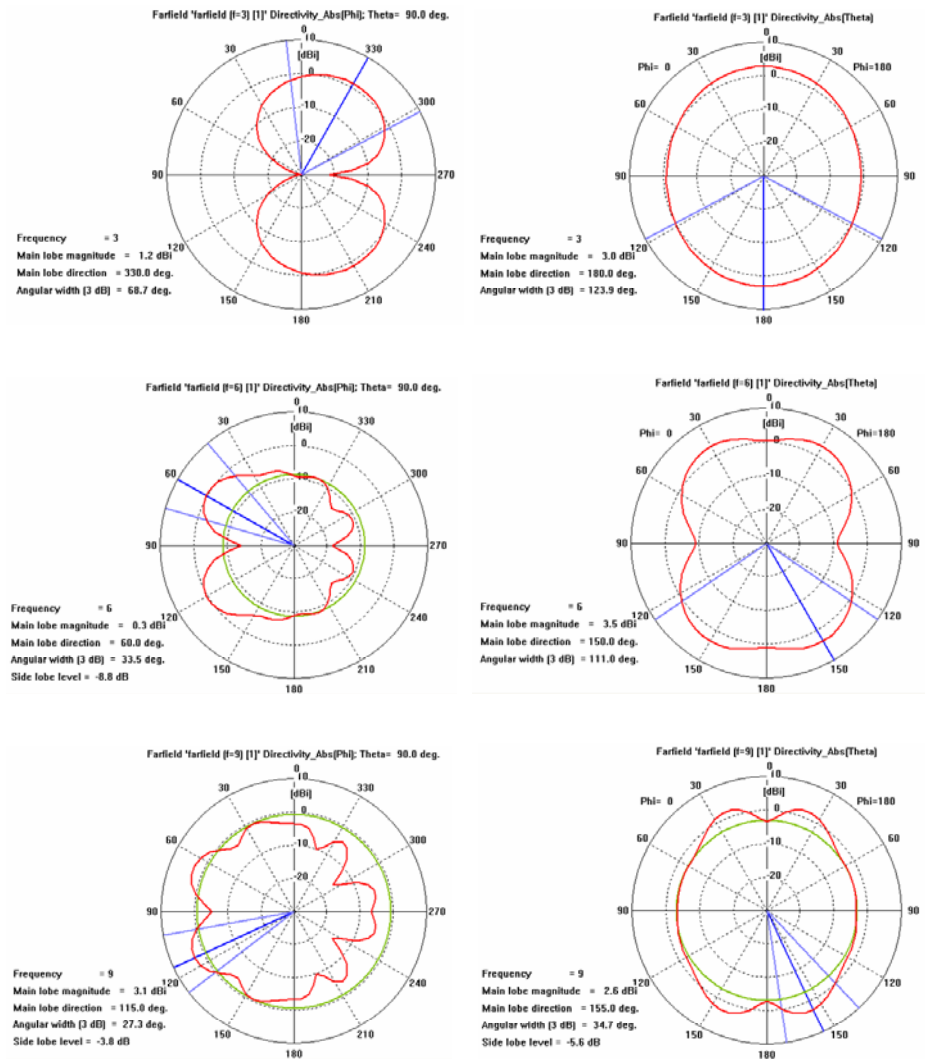

Fig. 4: Simulated radiation patterns for the antenna of Fig. 2

Proceedings of APSYM2006, Dec. 14-16., Dept. of Electronics, CUSAT, India.

Vertex Truncated Ultra Wideband Printed Triangular Monopole Antenna

K. P. Ray [*(1)] *and Y. Ranga*[(1)]
(1) SAMEER, IIT Campus, Powai, Mumbai, India, 400076, E.mail: kpray@rediffmail.com

Abstract: *A microstrip-fed printed monopole configuration of vertex truncated equilateral triangular patch has been studied, which gives ultra wide impedance bandwidth ratio of 12.4:1 for voltage standing wave ratio of 2 and over 23:1 for voltage standing wave ratio equal to 2.7. Experiments have been carried out to measure bandwidth and radiation patterns of this ultra wideband printed monopole antenna, which tally well with simulated results.*

Introduction: The demand for printed monopole antennas are increasing for ultra wideband (UWB) technology because of their compactness, low cost and simplicity to integrate them with printed circuit configurations. Various shapes of these antennas have been reported, which yield ultra wide bandwidth. A printed circular monopole antenna (PCMA) has been reported to yield large bandwidth from 2.78 to 9.78 GHz for voltage standing wave ratio VSWR $\leq$ 2 [1]. A printed inverted cone antenna is also reported to yield ultra wide bandwidth performance of over 10:1 for VSWR$\leq$ 2 with improved omni-directional radiation pattern [2]. Among the different triangular monopole antenna (TMA) configurations, a strip line fed printed equilateral TMA (PETMA) is reported to give 2.1 to 3.0 times bandwidth as compared to that of a simple strip monopole with reduction in height of 0.63 times [3]. Similarly, a coplanar wave-guide fed TMA has been reported for ultra-wideband operation [4]. Another printed triangular monopole antenna, which is fed by microstrip line, has been reported to give large bandwidth from 4 to 10 GHz for the VSWR $\leq$ 3, with almost omni directional radiation pattern in H plane [5]. Very recently, a small size PTMA topology has been reported, wherein wide bandwidth has been obtained by adding slots in the antenna structure [6].

In this paper, a simple compact configuration of vertex truncated PETMA has been proposed for very large bandwidth. The theoretical study of this configuration has been carried out using HP high frequency structure simulator (HP HFSS) three-dimensional electromagnetic simulator [7]. Very wide bandwidth obtained using proposed configuration completely covers wide communication channels like DCS1800 (1.71-1.88 GHz), DCS1900 (1.85-1.99 GHz), WiBro (2.3-2.39 GHz), GSM (900-1800MHz), UMTS (1885-2200 MHz), WCDMA (1.92-2.17 GHz), DMB (2.605-2.655 GHz) and UWB (3.1-10.6 GHz) [8].

Vertex truncated printed equilateral triangular monopole antenna: Normal vertex fed PETMA, is investigated first. The height of the PETMA is estimated from the formulation given for planar monopole antennas equating its surface area with that of a same height equivalent cylindrical monopole antenna, to cover the lower band edge frequency of 900 MHz [9, 10]. The bandwidth of 1607 MHz for VSWR $\leq$ 2 is obtained for vertex fed PETMA when designed on glass epoxy substrate with dimension 9.0 cm x 9.0 cm, ε_r = 4.4, h = 0.159 cm and $tan\delta$ = 0.02. It has been noted that for vertex fed PETMA, multiple loops are formed in the input impedance plot but the impedance variation is very large swinging from very

high impedance to low impedance in the Smith chart resulting in not very large bandwidth. It is similar to an equilateral triangular microstrip antenna, where the impedance at the vertex is very high at the resonance frequency corresponding to fundamental mode [10].

When it is fed at vertex, there will be large impedance variation between various modes of the equilateral triangular microstrip antenna. So, it is expected that if the sharp vertex of the PETMA is truncated off partially, the input impedance of the antenna will reduce and the loops will be formed in the lower impedance region in the Smith chart, leading to less variation of input impedance at various modes yielding wide bandwidth. The modified (vertex truncated) PETMA fed with a microstrip line is shown in Figure.1 (a). The effect of shifting the feed-point *x* away from the center of the truncated width on the bandwidth is investigated. The feed point is moved away from center in the step of 1.0 mm and bandwidth of the configuration is noted. Input impedance loci in the Smith chart for two values of x; 0 and 4.0 mm are shown in Figure 1(b). It is observed that when feed point is moved away from center, loop size reduces and smaller loops in the impedance loci are formed. This is because for the off-centered feed, the impedance variation amongst higher order modes is reduced. It is observed from Figure. 1 (b) that for x = 4.0 mm, the complete input impedance loci, starting from lower frequency of 0.80 GHz to 5.0 GHz is inside VSWR $\leq$ 2 circle yielding very large bandwidth. This modified PETMA was fabricated using FR4 substrate, as mentioned above and measurements were carried out for input VSWR and radiation patterns. The measured and simulated input VSWR of optimized vertex truncated PETMA configuration in the frequency range of 0.50 to 20.00 GHz is compared in Figure. 2.

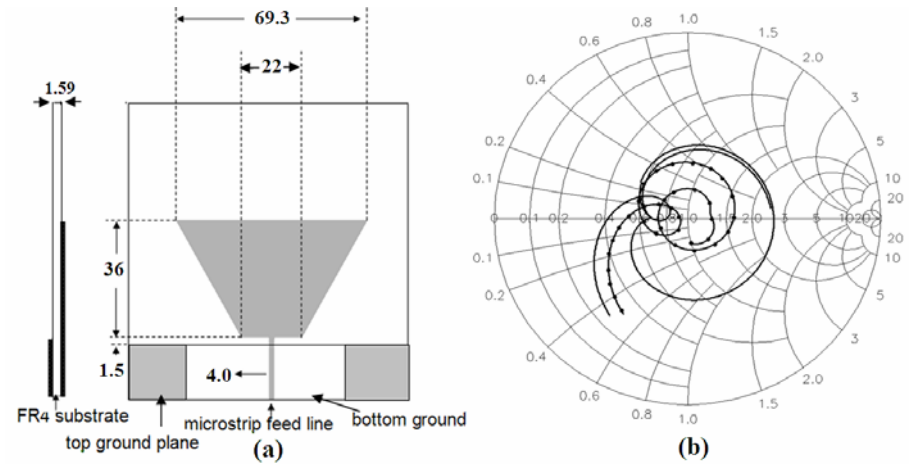

Figure. 1 (a) Vertex truncated printed triangular monopole antenna, (all dimensions are in mm), (b) Impedance variation of a vertex truncated printed triangular monopole antenna for microstrip feed at the ——— x=0 and ◆◆◆◆◆◆ x=4.0 mm

The measured and theoretical plots of VSWR are in good agreement. This configuration yields ultra wide bandwidth. The measured bandwidth for the VSWR $\leq$ 2 is from 0.86 to 10.70 GHz against the theoretical values of 0.800 GHz to 9.86 GHz. Both measured and theoretical bandwidth extends up to 20 GHz if the input VSWR up to 2.7 is tolerated. This leads to very large band width ratio of measured value of 12.4:1 in comparison with the simulated value of 12.3:1 for VSWR $\leq$ 2, the corresponding frequency ratios are 23.9:1 and 25:1 respectively for VSWR $\leq$ 2.7. The radiation pattern of the proposed vertex truncated

PETMA was simulated up to 12 GHz. Measurements of radiation patterns in both the planes are carried out at two frequencies; 1 GHz and 5 GHz and are compared with simulated radiation patterns in Figure. 3. Figure. 3 (a) and (c) compare the elevation radiation patterns, whereas Figure. 3 (b) and (d) compare the azimuthal radiation patterns

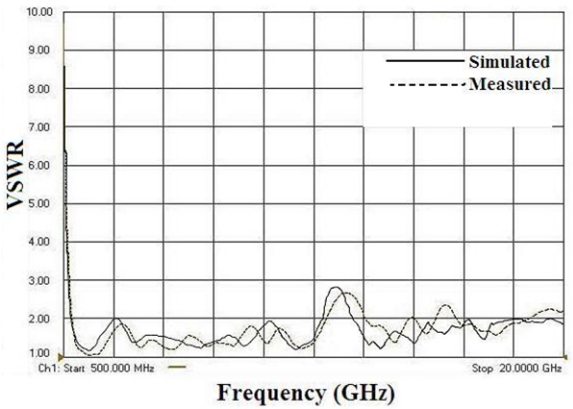

Figure. 2 Simulated and measured VSWR plots of vertex truncated printed equilateral triangular monopole antenna

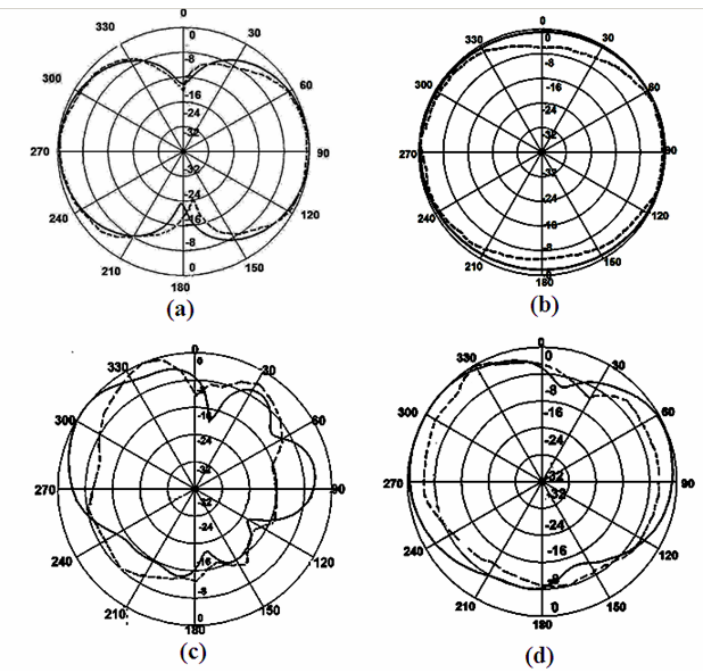

Figure.3 Radiation Pattern at (a) 1 GHz elevation pattern (b) 1 GHz azimuthal pattern (c)

5 GHz elevation pattern (d) 5 GHz azimuthal pattern ——— simulated - - - measured. There is agreement between the measured and simulated radiation patterns. Minor deviations between two are because of reflections from near by objects in the laboratory. At lower frequencies upto 3 GHz, azimuthal radiation patterns are close to omni directional, whereas in elevation it is figure of eight because of very small ground plane. At higher frequencies, radiation patterns in both the planes remain similar to those at lower frequencies with more variations in elevation plane. In the azimuthal plane maximum dip is about 16 dB in higher frequency range. Cross-polar levels are 15 dB down as compared to corresponding co polar levels upto 5 GHz, which becomes only 4 dB down at 12 GHz.

Conclusions: Study of printed vertex truncated equilateral triangular monopole antenna that gives larger bandwidth than any other reported printed monopole antenna configurations has been investigated for UWB applications. The measured bandwidth ratio of the proposed configuration is 12.7:1 for VSWR $\leq$ 2 and 23.9:1 for VSWR $\leq$ 2.6, which tally well with the simulated results. The radiation patterns of this antenna are similar to that of a corresponding cylindrical monopole antenna. Vertex truncated PETMA yield larger bandwidth and completely covers all the communication channels like DCS1800, DCS1900, WiBro, DMB, GSM, UMTS, WCDMA and UWB.

Reference:

[1] J. Liang, C. C Chiau, X. Chen, and C. G. Parini, "Printed circular disc monopole antenna for ultra wideband applications", Electron. Lett. , Vol.40, No.20, pp. 1246- 1248, 2004.

[2] S. Y. Sub, W. L. Stutzman, and W. A. Davis, "A new wideband printed monopole antenna: the planar inverted cone antenna (PICA)", IEEE Tans. Antennas Propag., Vol.52, No.5, pp. 1361-1365, 2005.

[3] Lu. K. Wong and F.Y. Lin, "Stripline-fed printed triangular monopole", Electron. Lett., Vol.33, No.17, pp. 1428-1429, 1997.

[4] W. Chung and C. KaoP, "CPW-fed triangular monopole antenna for ultra-wideband Operation", Microwave Optical Technol. Lett, Vol.47, pp. 580-582, 2005.

[5] C. C. Lin, C. Y. Kan, C. L. Kuo and R. H. Chuang, "A planar triangular monopole antenna for UWB communication", IEEE Microwave and Wireless Components Lett., Vol.15, No.10, pp. 624-626, 2005.

[6] J. R. Verbiest and G. A. E. Vandenbosch, "Small-size planar triangular monopole antenna for UWB WBAN applications", Electron. Lett., Vol.42, No. 17, pp. 566-567, 2006.

[7] HP High Frequency Structure Simulator HPHFSS, version 5.4.

[8] http:// en.wikipedia.org/wiki/Main_page.

[9] N. P. Agrawall, G. Kumar and K. P. Ray, "Wideband planar monopole antennas", IEEE Tans. Antennas Propag., Vol. 46, No. 2, pp. 294-295,1998.

[10] G. Kumar, and K. P. Ray, "Broad band microstrip antennas", Artech House, Boston and London, 2003.

A Capacitive Feed Technique for Microstrip Patch Antennas with Ultrawide Bandwidth

*Dibyant S. Upadhyay, Veeresh G Kasabegoudar, and K. J. Vinoy**

Microwave Laboratory, ECE Dept., Indian Institute of Science, Bangalore, 560 012

*Email: kjvinoy@ece.iisc.ernet.in

Abstract: *A new feeding technique is proposed here for wideband operation of rectangular microstrip patch antennas. This method is based on capacitively coupling the radiator with a very small feed patch. We have demonstrated nearly 43% impedance bandwidth for antennas on stacked air-dielectric substrate with only one metal layer above the ground. This method is equally useful for other patch geometries.*

Introduction: Microstrip patch antennas have several advantages such as low cost, low profile, light weight, and are easy to fabricate. In addition, these antennas are conformal and hence can be easily incorporated into any mobile system. Based on these characteristics microstrip antennas are increasingly preferred for wireless personal communications applications. In this context, as newer wireless standards become popular, the demands on antennas are also bound to increase.

It is widely known that the use of microstrip antennas is often limited by its low radiation efficiency and small bandwidth. Several schemes have been suggested to improve the bandwidth of these antennas, including the use of (i) stacked dielectric arrangement, usually with multiple metal layers; (ii) slots of various shapes on the patch [1]; (iii) meandered probe feed [2], or (iv) capacitively-coupled feed [3, 4]. While some of these were indeed easy to fabricate, they do not offer enough bandwidth required in several applications, and/or result is large size for the patch. Stacked arrangements with multiple metal layers often require a laborious precise assembly. The meandered probe, on the other hand would be extremely difficult to fabricate by standard procedure. Adding capacitive patches along radiating edges of the patch result in a larger footprint for the antenna.

Narrow bandwidth has been a major disadvantage of microstrip antennas in practical applications. Several modifications of microstrip antennas have been employed for the present-day wireless communication systems, where the required operating bandwidths for antennas are about 7.6% for a global system for mobile communication, 9.5% for a digital communication system, 7.3% for a personal communication system. One such bandwidth enhancement technique uses coplanar directly coupled and gap-coupled parasitic patches [5]. This antenna has a compact configuration such that the antenna size is minimized. Experimental results show that, with the use of an inexpensive FR4 substrate such an antenna can have an impedance bandwidth of about 12.7% [5], which is far higher than that of a direct-driven antenna. In another work [6], a novel and broadband semi-disc MSA has been designed. Using new bandwidth enhancement and size miniaturization methods, this small antenna is shown to have a broad impedance bandwidth of 32.4% (1.86-2.58GHz), which is used to provide the antenna with multiple frequency band operation. In yet another MSA design by Guo et al. [7], several other techniques including the use of high dielectric substrate, short circuit and shorting pin are used to miniaturize the antenna. In this case, two antenna patches were used to provide dual band operation.

Compared to these bands of operation, the WiMAX is a new radio technology that supports high-speed data transfers and enables the personal area networking industry to greater quality of service. As this standard evolves, signals may be transmitted between 3.1 GHz and 10.6 GHz at power levels up to –41 dBm/MHz. The data rate over UWB can range from 110 Mbps at a distance of 10 meters up to 480 Mbps at a distance of 2 meters in realistic multi path environments, while consuming very little power and silicon area. However these links do not use the entire 7.5 GHz band to transmit information, but a specific minimum bandwidth of 500 MHz at a -10 dB level. Yet, for antennas to be used in this application, it is preferred that they operate in as much of the bandwidth as possible. This therefore calls for ultra wideband antenna designs. Antennas with fractional bandwidth greater than 0.25 are typically considered ultrawide band.

The proposed antenna configuration on the other hand has a very small feed patch (strip) which is in the same plane as the radiator patch, and is coupled capacitively to it. An airgap is provided between the substrate and the ground plane for enhanced bandwidth. A similar feed arrangement has been proposed earlier for an annular ring antenna [8] and rectangular patch [9]. However the length of the feed strip was comparable with the radius of the radiating ring, and the bandwidth was only about 20% in the first case [8]. In the second case this was about 26% [9] even with an air gap of 15mm. In the proposed configuration the bandwidth is above 40% for the patch geometries studied. The asymmetry in radiation characteristic caused by the presence of the feed patch is marginal at most frequencies of interest. Preliminary experimental results show good agreement with numerical simulations.

Antenna Configuration: The geometry of the proposed antenna with a capacitive feed and stacked dielectric is shown in Fig.1. This antenna consists of two patches. The larger patch works as the radiator and the smaller patch serves as a feed patch which couples the energy to the radiator by capacitive means. The radiator patch has dimensions of length (L_1=15.5mm) and width (W_1=16.4mm). The feed patch has been optimized for dimensions length (L_2=1.158mm) and width (W_2=3.72mm) and a distance (d=0.5mm) between the patches. These patches are on a microwave laminate from Rogers Corp. USA (dielectric constant = 3., loss tangent = 0.0013, thickness h_1= 1.56mm.) The dielectric is placed at a height h_2 = 6mm above the ground plane (dimensions 150 x 150mm^2). The pin of the SMA connector is extended to reach the feed patch and is soldered there.

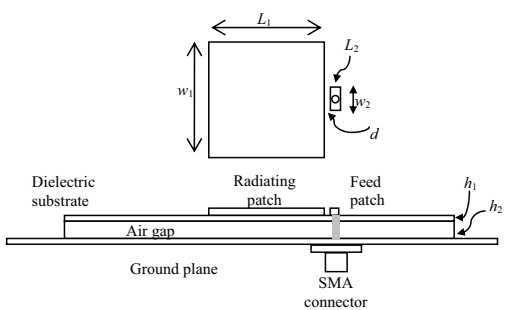

Fig.1 Geometry of a rectangular patch antenna with a new capacitive feed arrangement.

Experimental Results: The performance of the proposed antenna configuration was simulated and optimized using IE3D (version 11.15). A prototype was fabricated and tested

for S_{11} using Agilent PNA (N5230A) and radiation pattern in an in-house microwave anechoic chamber. As shown in Fig. 2, the measured S_{11} is better than 10dB (VSWR<2) for frequencies in the range 4.34 to 6.74GHz. This corresponds to a percentage bandwidth of 43%. The slight difference between the simulated and measured results may be attributed to the infinite ground plane assumption in the simulations and fabrication inaccuracies. The antenna gain is above 5dBi in the frequency band mentioned above. The measured radiation patterns of the proposed antenna are plotted at several indicative spot frequencies within this band and are shown in Fig. 3. The cross polarization level at the boresight is very low, but degrades at other angles. The E-plane radiation patterns of the antenna are symmetrical at all frequencies, but there is a small asymmetry in the H-plane patterns, particularly at higher frequencies within the region. The backlobe radiations are less than -20dB within the frequencies. Similar performance has also been obtained for other patch configurations such as triangular and semi-elliptical patches where the feed patch is located parallel to the straight edge.

Conclusions: We have presented a feed arrangement for an ultra wideband microstrip patch antenna configuration that is simple to construct and easy to adapt for various patch geometries. Simulated and measured results indicate that the proposed antenna has a wide impedance bandwidth of 43% (S11<-10dB) and has low backlobe radiation. The antenna gain is better than 5dBi in the band of interest. Radiation patterns at all frequencies within the band are similar, but the cross polarization level needs further investigation. Further experimental characterizations of the antennas are presently going on to extend the bandwidth even further. With these, the antenna can be used for emerging ultra wideband (UWB) applications. Investigations are going on with other patch geometries including fractals. We are also working on an analytical model for this type of feed mechanism to better understand the antenna performance.

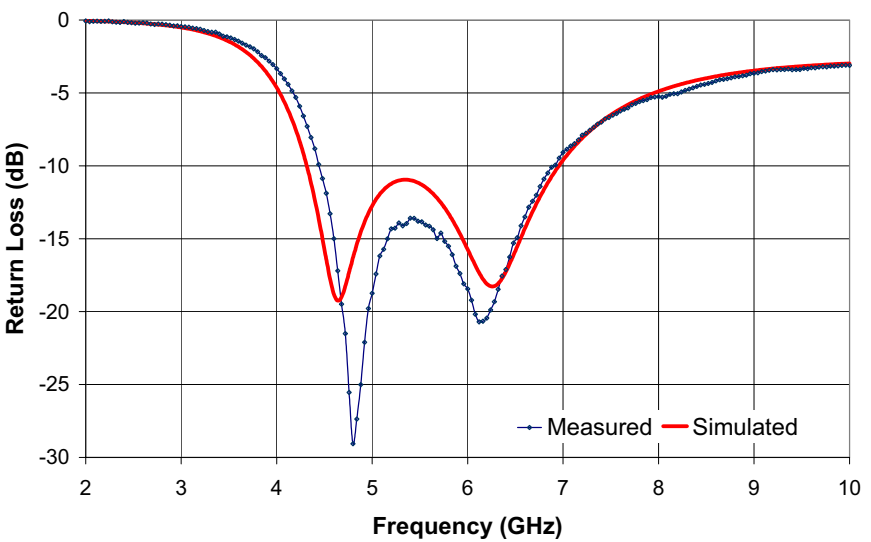

Fig.2 Experimental validation of the wideband characteristics of the antenna.

References

[1] G. Kumar and K.P. Ray, *Broadband Microstrip Antennas*. Artech House, 2003.

[2] H.W. Lai and K.M. Luk, "Wideband stacked patch antenna fed by meandering probe," *Electronics Letters*, vol.41, 2005.

[3] Y.X.Guo, K.M.Luk and K.F. Lee, "L-probe proximity fed short circuited patch antennas," *Electronics Letters*, vol.35, pp.2069-2070, 1999.

[4] J.-S. Row and S.-H. Chen, "Wideband monopolar square- ring patch antenna", *IEEE Trans. Antennas Propagation*, vol.54, pp.1335-1339, 2006.

[5] C. K. Wu and K. L. Wong, "Broadband microstrip antenna with directly coupled and gap-coupled parasitic patches," *Microwave Opt. Technol. Lett.* vol. 22, 348–349, 1999.

[6] Y.J. Wang, Y.B. Gan, and C. K. Lee, "A broadband and compact microstrip antenna for IMT-2000, DECT and Bluetooth Integrated Handsets," *Microwave Opt. Technol. Lett.*, Vol.32, No.3, 2002.

[7] Y.X. Guo, K.M. Luk, K.F. Lee, and R. Chair, "A quarterwave U-shaped patch antenna with two unequal arms for wideband and dual frequency operation," 2001 IEEE Antennas and Propagation Society International Symposium, Vol.4, pp.54-57, 2001.

[8] G. Mayhew-Ridgers, J.W. Odondaal and J. Joubert, "New feeding mechanism for annular-ring microstrip antenna", *Electronics Letters*, vol.36, pp.605-606, 2000.

[9] G. Mayhew-Ridgers, J.W. Odondaal and J. Joubert, "Single-layer capacitive feed for wideband probe-fed microstrip antenna elements," *IEEE Trans. Antennas Propagation*, vol. 51, pp. 1405-1407, 2003.

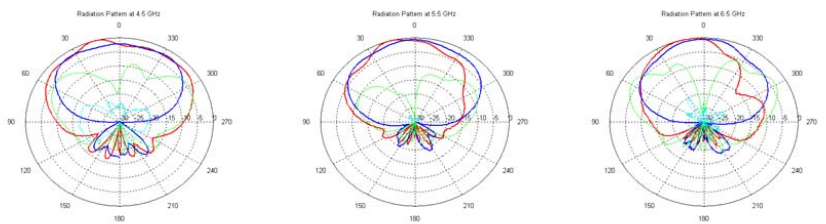

Fig.3 Normalized radiation pattern (measured) of the ultra wideband antenna at selected frequency points. . H-plane co-pol., E-plane co-pol., E-plane cross pol., H-plane Cross pol.

Proceedings of APSYM2006, Dec. 14-16., Dept. of Electronics, CUSAT, India.

Conformal Mapping Analysis of Microstrip with Finite Strip Thickness

C. B. Ashesh and R. Garg
Department of Electronics and Electrical Communication Engineering,
IIT Kharagpur, West Bengal, 721302.
Email: {ashesh, garg}@ece.iitkgp.ernet.in

Abstract *Conformal mapping method (CMM) is used here for the analysis of microstrip line with finite strip thickness. CMM is a simple technique and can yield closed-form design equations. CMM results are compared with the results based on boundary element method.*

Introduction: Planar transmission lines, like the microstrip and CPW, form the basic building blocks of many microwave hybrid and monolithic integrated circuits (MICs) [1]. Both these transmission lines have been studied using various approaches over the years [1-3]. In most of these studies, the metallization thickness is considered to be infinitesimally small to reduce the complexity in determining the characteristics of the line. Full-wave analysis [2-3] have also been used, but are often complex and do not give the electrical parameters in a CAD-friendly closed form. Wheeler [4] and Goano et. al., [5] have presented the finite metallization thickness effect on planar lines using CMM, but some of the details are not available in the work.

In this paper, we focus on presenting the details of the CMM procedure to take into account the finite strip thickness of microstrip line. The geometry under consideration is shown in Fig. 1.

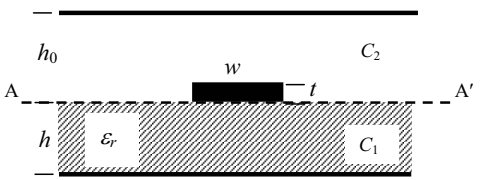

Fig. 1. Microstrip geometry under consideration.

Theory: The conformal mapping procedure involves the transformation from one plane to another. When used with regard to planar transmission lines, it can transform a complex geometry into a simpler geometry, from which the characteristic impedance and effective dielectric constants can be determined easily. In the CMM, the microstrip geometry is divided along the dashed line AA′. The total capacitance of the geometry consists of partial capacitances contributed by the air and dielectric regions, i.e., $C_{\varepsilon_r} = C_1 + C_2$, where C_1 is the capacitance of the dielectric region and C_2 is the capacitance due to the air region. The strip thickness is included in the air region. For determining the characteristics of line, another capacitance C_{air} is also computed, where C_{air} represents the capacitance per unit length with dielectric replaced by air. Using these capacitances, the characteristic impedance and effective dielectric constants can be obtained as follows

$$\varepsilon_{re} = \frac{C_{\varepsilon_r}}{C_{air}} \quad \text{and} \quad Z_0 = \frac{1}{(3x10^8 m/\sec)\sqrt{C_{\varepsilon_r} C_{air}}} \tag{1}$$

The conformal mapping procedure for C_1 is well documented and is given by [6]

$$C_1 = 2\varepsilon_0 \varepsilon_r \frac{K(k_1)}{K'(k_1)} \tag{2}$$

where, $K'(k) = K(k')$, $k_1 = \tanh(\pi a/(2h))$ and $k_1' = \sqrt{1-k_1^2}$. In this paper we lay emphasis on the conformal transformation of the air-region of microstrip geometry.

The air region and the corresponding mappings to obtain a parallel plate capacitor are depicted in Fig. 2. Symmetry in the geometry is considered and hence only one-half of the air-filled region is used.

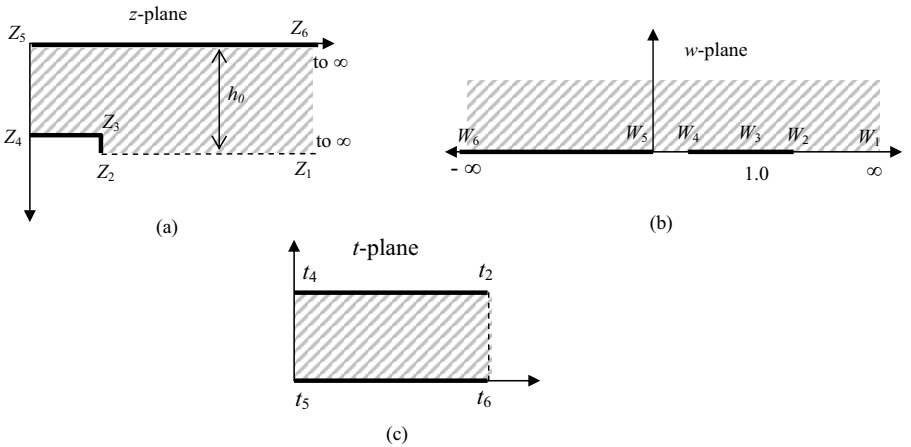

Fig. 2. Mapping of the dielectric and air-regions into a parallel plate capacitor.

The polygon in Fig. 2(a) is mapped on to the real axis and the upper-half of the *w*-plane as shown in Fig. 2(b). This transformation is done using the following mapping:

$$z = A\int_0^w \sqrt{\frac{(w-w_3)}{(w-w_2)(w-w_4)(w-w_5)}}\,dw + B \tag{3}$$

where, A and B are constants. Here, $B = 0$, as $z_5 = 0$ is mapped into $w_5 = 0$. Conformal mapping procedure allows us to choose three nodes [7]. We use $w_3 = 1$, $w_1 = \infty$ and $w_6 = -\infty$, (Fig. 2(b)). Thus, eq. (3) can be rewritten as:

$$z = A\int_0^w \sqrt{\frac{(w-1)}{(w-w_2)(w-w_4)(w)}}\,dw = A\int_0^w F(w)\,dw \tag{4}$$

This expression is applied to the various dimensions of the air region, i.e.,

$$\begin{aligned} -jh_0 &= A\int_0^{w_4} F(w)\,dw \\ a &= A\int_{w_4}^{w_3} F(w)\,dw \\ -jt &= A\int_{w_3}^{w_2} F(w)\,dw \end{aligned} \tag{5}$$

Eliminating A from these equations gives

$$\begin{aligned} \frac{a}{-jh_0}\int_0^{w_4} F(w)dw - \int_{w_4}^{1} F(w)dw = 0 \\ \frac{t}{h_0}\int_0^{w_4} F(w)dw - \int_1^{w_2} F(w)dw = 0 \end{aligned} \tag{6}$$

Eqs. (6) are non-linear equations, and are solved to determine w_2 and w_4 numerically. For this we used Newton-Raphson method [8] and Gauss-quadrature integration, with the initial guess such that $w_2 > 1$ and $0 < w_4 < 1$.

Having determined values of all the mapped points in *w*-plane, we do the final transformation from the *w*-plane to the *t*-plane as shown in Fig. 2(c). The transformation used is

$$t = \int_0^w \sqrt{\frac{1}{(w-w_2)(w-w_4)(w)}}\,dw \tag{7}$$

which maps the upper half of the *w*-plane and the real axis to the interior of t_2-t_4-t_5-t_6-t_2. The capacitance for this region can now be expressed as

$$C_2 = 2\varepsilon_0 \frac{K(k_2)}{K'(k_2)} \tag{8}$$

where, $k_2 = \sqrt{1-w_4/w_2}$.

Thus, the total capacitances are given by:

$$C_{\varepsilon_r} = C_1(\varepsilon_r) + C_2 \text{ and } C_{air} = C_1(\varepsilon_r = 1) + C_2 \tag{9}$$

Results: Table 1 compares the characteristic impedance of microstrip line obtained using CMM, and boundary element method (BEM) [9]. It may be observed that there exists some

difference in the final values. This can be due to the assumption of magnetic wall boundary condition at the air-dielectric interface, which may not hold good in the true sense especially when $h \neq h_0$. Further, the present study was conducted for microstrip with no lateral shielding and that in [9] is based on shielded microstrip line.

Table1: Comparison of Z_0 obtained using CMM and BEM [9] (h = 1 mm, $h_0 = 1.5h$, t = 0.05 mm).

a/h	$\varepsilon_r = 2.65$		$\varepsilon_r = 9.6$	
	Z_0 [9]	Z_0 [CMM]	Z_0 [9]	Z_0 [CMM]
0.25	103.5	105.8	61.5	61.8
0.50	76.0	78.2	44.5	45.3
1.0	50.5	52.3	29.0	30.1
1.5	38.5	39.3	22.0	22.6
2.0	28.5	31.3	16.5	17.9

Conclusions:

A detailed procedure for implementing conformal mapping for microstrip line with finite metallization thickness is presented. The results obtained match closely with those available in literature. Further study is needed to characterize shielded microstrip and other planar structures like coplanar waveguide and coplanar strip geometries.

References:

[1]. G. A. Kouzaev, et al., "An approximate parallel-plate waveguide model of a lossy multilayered microstrip line," Microwave and Optical Technology Letters, Vol. 45, No. 1, pp. 23-26, April 2005.

[2]. Shih-Yoan Lin, Chin C. Lee, "A full wave analysis of microstrips by the boundary element method," IEEE Microwave Theory and Techniques, Vol. 44, No. 11, pp. 1977-1983, November 1996.

[3]. J. –Y – Ke, and C. H. Chen, "Modified spectral-domain approach for microstrip lines with finite metallization thickness and conductivity," IEE. Proc.-Microw. Antennas Propag., Vol. 142, No. 4, pp. 357-363. August 1995.

[4]. H. A. Wheeler, "Transmission-line Properties of a strip on a dielectric sheet on a plane," IEEE Microwave Theory and Techniques, Vol. 25, No. 8, pp. 631-647, August 1977.

[5]. M. Goano, et. al., "A general conformal-mapping approach to the optimum electrode design of coplanar waveguide with arbitrary cross section," IEEE Microwave Theory and Techniques, Vol. 49, No. 9, pp. 1573-1580, September 2001.

[6]. C. Nguyen, Analysis methods of RF, Microwave, and millimeter-wave planar transmission line structures, John Wiley Sons, 2000.

[7]. R. V. Churchill, and J. W. Brown, Complex Variables and Applications, Mc Graw Hill. 1989.

[8]. W. H. Press, et. al., Numerical recipes in C, Cambridge University Press, 2nd ed. 1992.

[9]. T-N. Chang and C-H. Tan, "Analysis of a shielded microstrip line with finite metallization thickness by the boundary element method," IEEE Microwave Theory and Techniques, Vol 38, No. 8, pp. 1130-1132, August 1990.

Proceedings of APSYM2006, Dec. 14-16., Dept. of Electronics, CUSAT, India.

A New Feed Technique for Microstrip Ring Antennas and its Application in Multi-Ring Multi-band Antennas

Arpan Pal, Subhrakantha Behera and K.J. Vinoy[*],
Microwave Laboratory, ECE Dept., Indian Institute of Science, Bangalore 560 012
*Email: kjvinoy@ece.iisc.ernet.in

Abstract: *In this work we propose a new feed scheme for microstrip ring antennas that enables a systematic approach for the design of multi-band antennas. Discontinuities in a feeding transmission line have been designed to make it couple the energy to the ring at the resonant frequency. To validate the concept, an antenna with three rings have been fabricated and characterized. It has been observed that, by this approach, the combination of three ring antennas operate in the same three bands as the individual rings (if these were to operate separately). The antenna showed reasonable bandwidth in each of the bands, good cross polarization rejection and has a gain of about 5.5 dBi at all the bands of interest. Furthermore, the harmonics of the lower resonant rings are filtered out by the nature of the feed arrangement.*

Introduction: With the wide proliferation of wireless systems and the trend to incorporate multiple functions into a single terminal, the design of multi-functional mobile terminals has come to the forefront of research and development. This requirement of increased functionality within a confined volume places a greater burden in today's transmit-receive systems. Antennas that operate in several frequency bands and that can be integrated on a package for mass-production are high in demand. Many of these applications are for personal communication systems and hence have the additional requirement that the antennas be small and conformal. The microstrip antenna is widely accepted as one of the best suited to fulfill these demands.

In the present work, we investigated ring antennas as these have the potential of being extended toward multi-band operation as several concentric rings could be used in an antenna. Indeed Song et al have reported one such configuration of multi-ring monopole antenna [1]. However this configuration is not conformal. Ring antennas are usually excited either with capacitive strip for wideband operation [2] or with patches or rings in other layers of a stack [3]. Neither of these feed configurations can excite multiple concentric rings simultaneously. It may be recalled that popular feed schemes in (solid) patch antennas are not preferred for ring antennas [4, 5].

A tri-band antenna consisting of ring-slot and a coplanar waveguide feed has been reported in [6]. But slot antennas usually require larger real estate. In yet another study, using concentric annular rings for dual band microstrip antenna, the second ring was placed within the first ring, each ring operating in the TM_{12} mode.

In contrast we propose here an out-of-plane capacitive feed arrangement for the ring type microstrip antenna. By adjusting the dimensions of the capacitive strip on the open circuited microstrip transmission line in layer beneath the radiating patch optimum coupling

to the radiator can be achieved. An air layer is provided between the dielectric layers with the microstrip line and the radiating ring to improve the bandwidth and the coupling. In this work we demonstrate the usefulness of this feed scheme to design square ring antennas. However it must be pointed out that this scheme can be extended easily for rings of any other shape, including fractals.

Proposed Feed Structure and its Optimization: The proposed antenna structure has three layers: two dielectric layers of RO 3003 (ε_r = 3, tanδ = 0.0013, thickness = 1.56mm) and an air gap between them, suitably adjusted to maximize the antenna performance. The dielectric layer at the bottom has a microstrip transmission line patterned on one side of this (with copper ground on the other side). The antenna configuration is shown in Figure 1. The feed microstrip line has a discontinuity introduced purposely to affect line characteristics as well as couple energy to the radiating ring. We used a rectangular strip as the discontinuity.

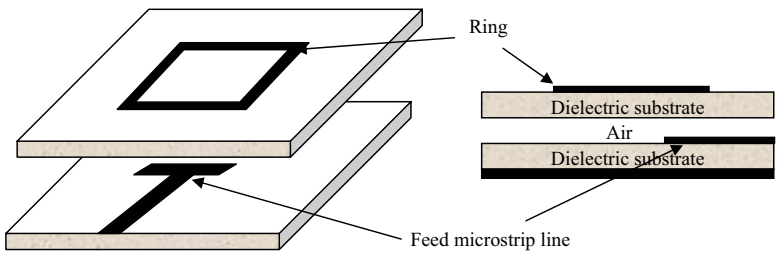

Figure 1. Schematic of the new feed scheme for the ring antenna

For operation as a single band antenna at 3.5GHz, the outer dimension of the square ring (width = 1mm) is found to be 16.8 mm. The feed microstrip line has a rectangular patch at its end, having dimensions width = 1.6mm, length = 7.6 mm. An air gap of 0.5mm between the dielectric slabs has been found to give the best results.

Application of the New Feed Scheme for Multi-band Antennas: Based on the algorithm described in Section II, we have redesigned single band antennas for 2.4 GHz and 5.78 GHz. For consistency we have taken uniform air gap of 0.5 mm and ring width of 1 mm at all bands. Other geometrical parameters are compared in Table I. We now combined the above designs to form a single tri-band antenna. The ring dimensions are kept as is, but to account for the mutual interaction, the dimensions of the feed strip are adjusted using IE3D simulations. The proposed tri-band antenna configuration is shown in Figure 2.

Results & Discussion: EM simulations show that the resonant frequencies of these antennas do not change when these antennas are combined (Figure 3). Furthermore, resonances due to the excitation of higher order modes in the single band antennas have disappeared in the multi-band design. Therefore we can conclude that this antenna configuration ensures dominant mode excitations in all resonance bands. This is further verified using the radiation patterns, which are also unaltered while combining the rings. The antenna also showed reasonable gain characteristics. The values of boresight gain at the resonant frequencies of the antenna are listed in Table II.

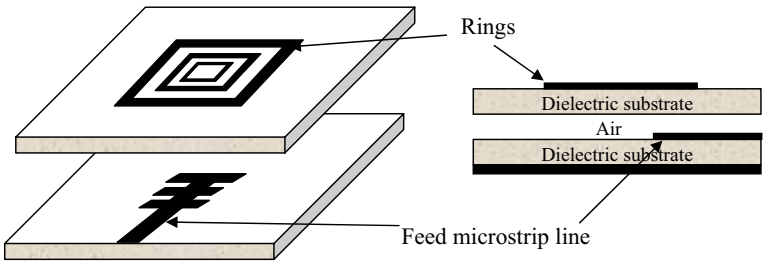

Figure 2. Schematic of the new feed scheme for the triband antenna

Table I Geometric parameters of single band antennas for various bands

Parameter	2.4GHz	3.5GHz	5.78GHz
Ring dimension (mm)	23.7	16.8	10.4
Width of feed strip	1.6	1.6	1.7
Length of feed strip (mm)	11.4	7.6	9.8

Table I1 Gain of the triband antenna obtained using ADS simulations

Frequency (GHz)	Gain (dBi)
2.44	5.44
3.5	5.27
5.78	6.52

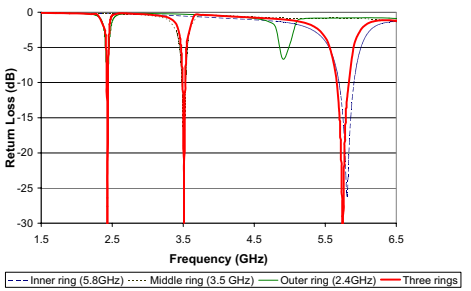

Figure 3 The simulated return loss characteristics of the three single band antennas along with that of the tri-band antenna.

The tri-band antenna has been fabricated and characterized using a vector network analyzer. The measured S11 is shown in Figure 4. These results verify that the resonant frequencies of these antennas differ only marginally compared to simulations. The shift may be due to the infinite ground used in simulations and/or slight inaccuracies in assembling two layers of dielectric substrates. The radiation pattern taken in the anechoic chamber is given here. Here we have taken the co and cross polarization patterns in the E- and H- planes of the antenna. The E-plane is aligned with the length of the feed strip. The radiation patterns are plotted at the three resonant frequencies and are given in figure 5.

Conclusions: In this work we proposed a new feed mechanism for ring type microstrip antennas. It has been observed that the combination of the three rings does not affect the resonant frequencies of the individual rings. Only a slight change in the feeding structure was required for combined multiple rings. Furthermore, the harmonics of the lower resonant rings are filtered out by the feeding arrangement. Due to the unique feed arrangement, the antenna also showed a cross polarization level better than -20dB. The tri-band antenna also shows acceptable radiation characteristics and has a gain of above 5dBi. This prototype antenna is designed to operate in the ISM and WiMAX frequency bands. It may however be pointed out that this feed scheme may be easily adapted for other situations that require multi-band operations. We suspect this may be the first systematic approach to realize

conformal multiband antennas. The limits on the relative bands are currently being investigated.

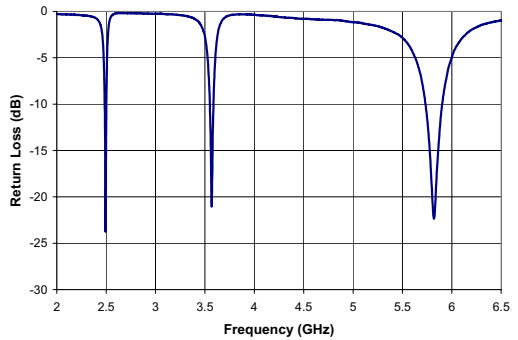

Figure 4 The measured return loss characteristics of the tri-band antenna.

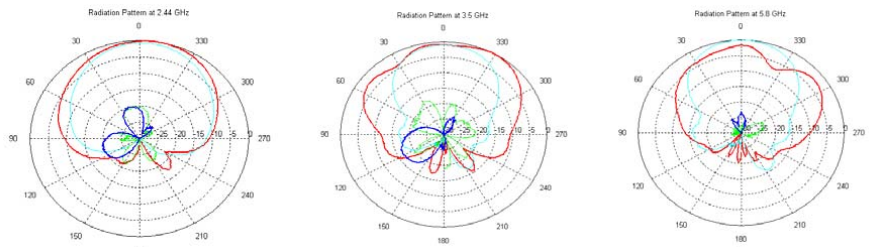

Figure 5 Measured radiation patterns of the triband antenna. H-plane co-pol., E-plane co-pol., E-plane cross pol., H-plane Cross pol.

References

[1] C.T.P. Song, P.S. Hall, H. Ghafouri-Shiraz, "Multiband multiple ring monopole antennas," IEEE Trans. Antennas Propagation, vol. 51, No. 4, pp. 722-729, 2003.

[2] G. Mayhew-Ridgers, J.W. Odondaal and J. Joubert, "New feeding mechanism for annular-ring microstrip antenna", Electronics Letters, vol.36, pp.605-606, 2000.

[3] P.M. Bafrooei, L. Shafai, "Characteristics of single- and double-layer microstrip square-ring antennas," IEEE Trans. Antennas Propagation, vol. 47, No. 10, pp. 1633 – 1639, 1999.

[4] R. Garg, V.S. Reddy, "Edge feeding of microstrip ring antennas," IEEE Trans. Antennas Propagation, vol. 51, No. 8, pp. 1941 – 1946, 2003.

[5] A. Bhattacharyya, R. Garg, "A microstrip array of concentric annular rings," ," IEEE Trans. Antennas Propagation, vol. 33, No. 6, pp. 655-659, 1985.

[6] J.-S. Chen, "Triple-frequency annular-ring slot antennas fed by CPW and microstrip line, IEEE Antennas and Propagation Society International Symposium, 2003.

Proceedings of APSYM2006, Dec. 14-16., Dept. of Electronics, CUSAT, India.

RESEARCH SESSION II

MICROSTRIP ANTENNAS II

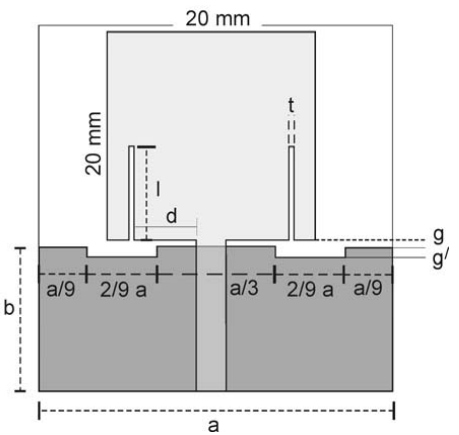

December 14, Thursday
(3.00 p.m. - 4.00 p.m)

RESEARCH SESSION II
MICROSTRIP ANTENNAS II

Chair: Prof. S.N. Sinha

IIT, Roorkee.

Proceedings of APSYM2006, Dec. 14-16., Dept. of Electronics, CUSAT, India.

A Novel Axially Symmetric Electromagnetic Band Gap (EBG) Structure for the Performance Enhancement of Printed Antennas

Manish Jain and Sachendra N Sinha
Department of Electronics & Computer Engineering
Indian Institute of Technology Roorkee, Roorkee-247667

***Abstract*—A novel electromagnetic band-gap (EBG) structure having a cross-like shape is investigated. This structure has an extremely compact size. Several application examples have been considered which include the reduction of mutual coupling between printed antenna elements, replacement of the PEC ground plane with an EBG ground plane for a low profile wire antenna design, and to achieve uni-directional radiation from a slot antenna by backing them with an EBG surface, instead of the conducting reflector.**

I. INTRODUCTION

In recent years, there has been a growing interest in utilizing electromagnetic band-gap (EBG) structures in the electromagnetic and antenna community. The EBG terminology has been suggested in [1] based on the photonic band-gap (PBG) phenomena in optics that are realized by periodical structures. These Electromagnetic band gap (EBG) [2] structures provide frequency bands (so-called band gaps or stop bands) in which waves cannot propagate in the materials. This paper focuses on a novel cross-like EBG structure. Compared to other EBG structures such as dielectric rods and holes, this structure has a winning feature of compactness which is important in communication antenna applications. Its band-gap features are revealed in two ways: the suppression of surface-wave propagation and the in-phase reflection coefficient. The feature of surface-wave suppression helps to improve antenna's performance, such as, increasing the antenna gain and reducing back radiation [3]. Meanwhile, the in-phase reflection feature leads to low profile antenna designs [4], [5].

II. CROSS-LIKE EBG STRUCTURE

The schematic of the proposed cross-like EBG structure is shown in Fig. 1. Gray parts represent the metallic periodic structure which is etched on a dielectric substrate. The patch is connected to the solid lower ground plane by a metal plated via.

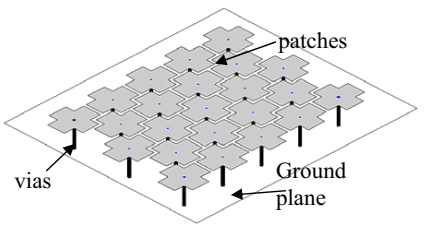

Fig. 1. Three dimensional view of the proposed EBG structure

For the measurement of band gap, the configuration shown in Fig. 2 was simulated on IE3D. The array was built on a 1.27mm thick substrate with the relative permittivity of 10.5. The dimensions of the EBG surface are shown in Fig. 3 and the computed transmission coefficient (S_{21}) is shown in Fig. 4. A distinctive stop band is observed with the central frequency of 5.45 GHz. The frequency range with S_{21} below -30 dB extends from 4.5 to 6.4 GHz.

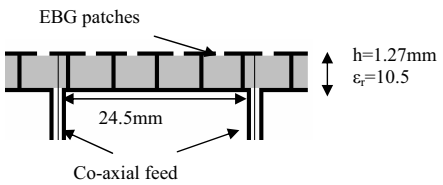

Fig. 2 Measurement of bandgap

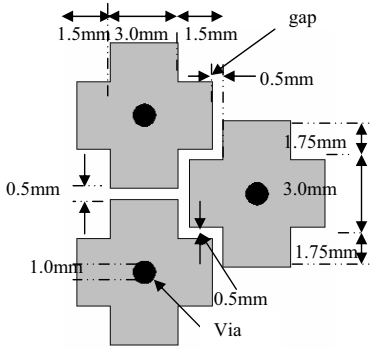

Fig. 3. Three elements of EBG

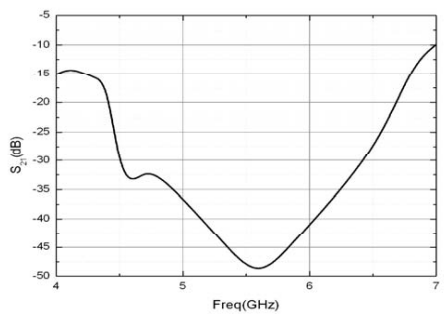

Fig. 4. Band gap calculation using the setup shown in Fig. 2

III. APPLICATIONS

A. Mutual Coupling Reduction: In order to demonstrate the capability of the proposed EBG structure to reduce the mutual coupling between patch antennas, five columns of cross-like EBG patches were inserted between the E-plane coupled patch antennas, as shown in Fig. 5. The patch antennas were designed at a resonant frequency of 4.86 GHz with dimensions 9.4 mm x 7 mm and the distance between the centers of the antennas was 30 mm ($0.5\lambda_{4.86}$ GHz). The resonant frequency 4.86 GHz falls inside the EBG band gap so that the surface waves are suppressed. The simulated mutual coupling results are shown in Fig. 6. Without the EBG structure, the antennas

show a strong mutual coupling of -16.65 dB. When the EBG structure is employed, a 13.14 dB mutual coupling reduction is achieved at 4.86 GHz, which proves that the surface wave is suppressed.

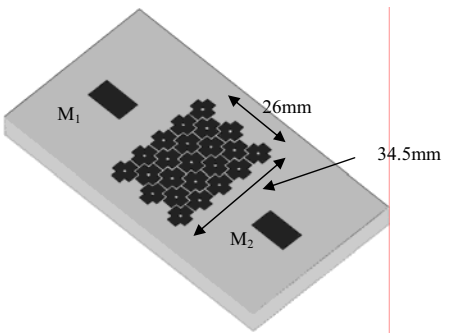

Fig. 5. Microstrip antennas separated by the EBG structure

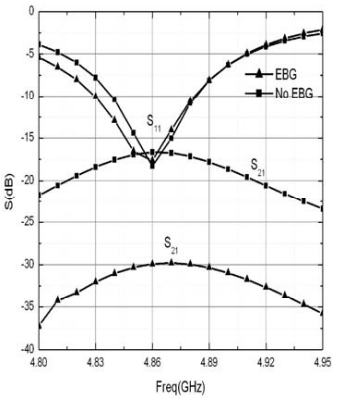

Fig. 6. Return Loss and mutual coupling of E-plane coupled antennas

B. Low profile wire antenna design: This application utilizes the reflection phase feature of EBG surfaces; when plane waves normally illuminate an EBG structure, the phase of the reflected field changes continuously from 180˚ to -180˚ versus frequency. The operating frequency for this experiment was chosen to be 5.27 GHz. A dipole of length 0.45 λ and radius 0.003λ was placed 0.083λ above the EBG ground plane of dimensions 1λ x1λ. The EBG ground plane has been fabricated on a grounded substrate of thickness 0.022λ, thus making the overall height of the dipole 0.105λ. For comparison, same dipole 0.105λ above a PEC ground plane and in free space has been considered.

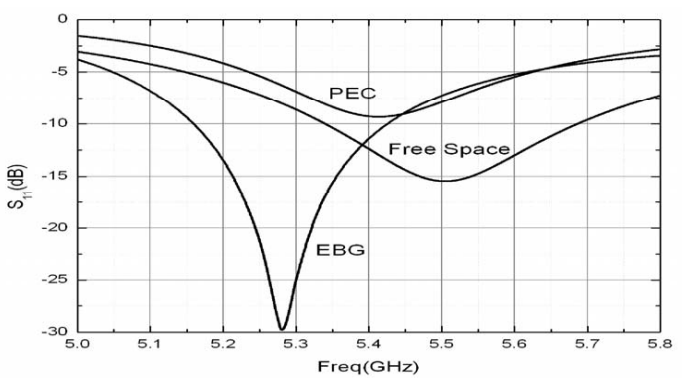

Fig. 7. Return Loss of the dipole antenna over the PEC, Free space and EBG ground planes

Fig. 7 compares the return loss of the dipole antenna over a PEC, in free space, and above an EBG ground plane. The input impedance is matched to a 50-Ω line. With the PEC surface as the ground plane, the return loss of the dipole is only -9.32 dB. This is because the PEC surface has a 180 reflection phase, so that the direction of the image current is opposite to that of the original dipole. For the case when the dipole is placed in free space, it has a return loss of -15.46dB. The best return loss of -29.85 dB is achieved by the dipole antenna over the EBG ground plane. The radiation patterns showed an improvement of 5 dB in front-to-back ratio in the case of EBG ground plane as compared to PEC ground plane. Thus, a considerable reduction in the antenna profile can be obtained.

VI. CONCLUSION

In this paper, a novel cross-like EBG structure has been investigated. The simulated results of the EBG structure show a band gap from 4.5 GHz to 6.4 GHz. It has been demonstrated that the proposed structure can be used for mutual coupling reduction between patch antennas and the reduction of antenna profile. For the later case, the example of a dipole over a ground plane has been considered. Similar reduction in the profile of a cavity-backed slot antenna has been achieved with the use of the EBG surface, although the results are not included here for the sake of brevity.

References

[1] Y. Rahmat-Samii and H. Mosallaei, "Electromagnetic band-gap structures: Classification, characterization and applications," in *Proc. Inst. Elect. Eng.-ICAP Symp.*, Apr. 2001, pp. 560–564.

[2] A. R. Weily, L. Horvath, K. P. Esselle, B. C. Sanders and T. S. Bird, "A Planar Resonator Antenna Based on a Woodpile EBG Material", *IEEE Transactions On Antennas And Propagation,* vol. 53, No. 1, pp. 216-223, January 2005.

[3] Y. Rahmat-Samii and F. Yang, "Microstrip Antenna Integrated with Electromagnetic band-gap (EBG) structures: A Low mutual coupling design for array applications", *IEEE Trans. on Antennas and Propagation,* vol. 51, No. 10, pp. 2936-2946, October 2003.

[4] Z. Li and Y. Rahmat-Samii, "PBG, PMC and PEC surface for antenna applications: A comparative study," in *Proc. IEEE AP-S Dig.*, July 2000, pp. 674–677.

[5] F. Yang and Y. Rahmat-Samii, "Reflection phase Characterizations of an EBG Ground Plane for Low Profile Wire Antenna Applications", *IEEE Trans. on Antennas and Propagation.*, vol. 51, No. 10, pp. 2691-2703, October. 2003.

COMPACT STACKED C-SLOT MICROSTRIP ANTENNA IN SUSPENDED CONFIGURATION

Ravi M.Yadahalli [(1)], R. M. Vani[(2)], K. Usha Kiran[(1)], P. V. Hunagund [(1)] & S. F. Farida[

[1]Department of Applied Electronics, Gulbarga University, Gulbarga, Karnataka.
[2]University Science Instrumentation Center, Gulbarga University, Gulbarga, Karnataka.
[3]Department of Electrical and Engineering, Salt Lake, Community College,
UTAH-84130, USA.
E-mail: prabhakar_hunagund@yahoo.co.in

Abstract: *Antenna miniaturization plays a vital role in the design of modern personal wireless systems. In this paper, a compact stacked microstrip patch antenna (MSA) with embedded with C shaped slot on the lower (driven) patch is proposed and studied to miniature the size & enhance the bandwidth at the same time. Earlier experimental work utilizing dual C shaped slot have achieved a bandwidth of 5.4% and a frequency reduction of 15%. However, the proposed antenna resonates at 3.368 GHz, which is lower than that of the conventional stacked MSA (5.75 GHz) i.e., a frequency reduction of 41.42% is obtained. Also the antenna has a bandwidth of 7.4% centered on 3.368 GHz with a gain of 6.76 dBi.*

NTRODUCTION

Although a microstrip antenna has several practical advantages, like low profile and ightweight, a single patch antenna has low gain and a narrow bandwidth. It is well known hat a multilayer structure is a useful method to improve these problems. By stacking a arasitic patch on a fed patch, an antenna with high gain or wide bandwidth can be realized 1]. These stacked configurations, though provide high gain and wide bandwidth, have xcessive size for the wireless personal applications. Additional effort is needed to reduce ctual geometries to obtain miniaturized designs. Several minimization techniques have been eported to reduce the size of the planar antennas. These techniques can be classified in 1) use f high permittivity substrate; 2) use of magnetic substrates; 3) increase electrical length; 4) hort circuits; 5) superstrates and 6) combination of them [2]. Although significant work has een done to reduce the size of planar antennas, little attention has been given to size eduction of stacked microstrip antennas.

Consequently, our work focuses on developing antenna geometry small enough to be asily accommodated in mobile communication terminals and devices. The miniaturized ntenna presented here consists of two stacked, air-filled, square patches resonating at two lightly different frequencies, fed by a strategically positioned coaxial probe. This design is chieved by cutting a C-shaped slot in the lower patch (driven patch). All the antennas have een simulated using IE3D simulation software [3]. For the simulation of all the antennas, an nfinite ground plane has been assumed.

It has been reported that small dual-C slot printed antenna achieves a 15% reduction n resonant frequency and has 10 dB return loss bandwidth of 5.4% [4]. The proposed

antenna, incorporating a strategically placed C-slot on the driven element, provides more reduction in frequency in comparison with small dual C-slot printed antenna and has more bandwidth & gain, when compared to it.

ANTENNA DESIGN

The patch geometry is presented in Fig.1. The antenna consists of two square conductors with dimensions L_1 x W_1 and L_2 x W_2 etched on substrates of dielectric constant ε_{r1} & ε_{r2} ($\varepsilon_{r1} = \varepsilon_{r2}$) and thickness d_1 and d_2. Substrate 1 is backed with a ground plane. The lower patch is embedded with a suitably placed C-shaped slot and is driven by a coaxial feed of radius r_0, located at a distance x away from the center of the lower patch. This feed is attached to a connector through an opening in the ground plane.

There are thus nine variables for optimization L_1, W_1, L_2, W_2, ε_r, d_1, d_2, r_0 and x. Here, we wish to examine the size reduction and dependence of the antenna bandwidth & gain on the choice of the distance d_2, d_1 and recording the optimum solution as a function of this choice. Hence, seven variables remain same for each optimization

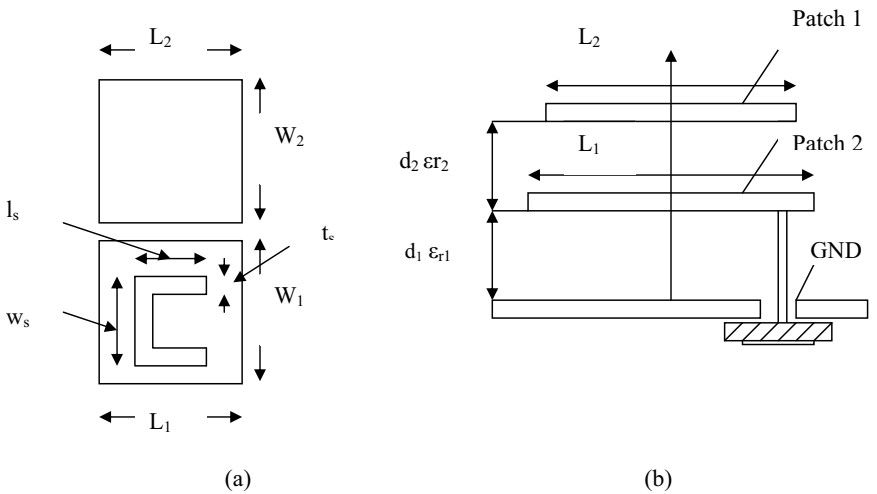

Fig. 1: Geometry of the compact stacked square microstrip antenna with a C- type slot ($h = 1.59$ *mm*, $\varepsilon_{r1} = \varepsilon_{r2} = 4.3$, $d_1 = 1$ *mm*, $d_2 = 1$ *mm*, $L_1 = W_1 = 24.5$ *mm*, $L_2 = W_2 = 25$ *mm*, $l_s = 22.25$ *mm*, $w_s = 21$ *mm* & $t_s = 1$ *mm*) (a) Top view, (b) Side view

EXPERIMENTAL RESULTS

Our experiment began with conventional stacked patch antenna consisting of two square patches of different dimensions, fabricated in glass epoxy substrate with $\varepsilon_r = 4.3$. This yields a resonant frequency of approximately 5.75 GHz and bandwidth of 900 MHz. The thickness of the substrates h chosen in the above experiment is 1.59 *mm*. Later a C-shaped slot is introduced in the lower patch of the stacked microstrip antenna as shown in the Fig.1 and when the antenna is excited, it resonated at a frequency of 2.579 GHz, which is lower

than that of the conventional stacked microstrip antenna. However, the bandwidth of the antenna decreases to 1.94%. To improve upon the bandwidth of this antenna, an air gap d_1=1 *mm* is introduced between the two layers and is varied by 2 *mm* & 3 *mm*. By optimizing the air gap d_1, an antenna with broadband and higher gain as shown in Table 1 is obtained.

Further, an air gap d_2 is introduced between ground and lower substrate in addition to air gap d_1=1 *mm*. As a result, both the fed and parasitic patches are in suspended configuration. Initially the air gap d_1 is kept 1 *mm* and corresponding measured bandwidth is 7.4%. With an increase in d_1 from 1 *mm* to 3 *mm*, the coupling decreases and hence, the bandwidth decreases from 7.4% to 6.24%. However, the gain increases with an increase in the air gap d_1. i.e., it increase from 6.76 dBi to 7.48 dBi and by increasing d_1 further, the gain of the antenna can be increased. Therefore, depending upon the wide BW or high gain requirement, the air gap d_1 between the bottom patch and ground plane can be chosen accordingly.

As noted from Table I, a variation in d_1 between the lower patch and ground can affect the performance of the antenna in different extents. For our proposed antenna, the measured resonant frequency is 3.368 GHz and hence, the corresponding bandwidth is 7.4%, while the gain is enhanced to 6.76 dBi. This is shown in the Return loss Characteristics of Fig.2. The measured bandwidth of the proposed antenna is slightly decreased but there is an increase in the gain.

The proposed antenna present radiation pattern which remains in the broadside direction throughout the bandwidth. The radiation patterns show an acceptably low value of cross polarization and hence this type of antenna is useful in mobile communication devices.

Table 1: Simulation results of compact stacked c-slot microstrip antenna in suspended configuration.

Antennas	Resonant frequency (GHz)	Return Loss (dB)	Band width (%)	Gain (dBi)
Conventional Stacked antenna	5.75	-29.28	15.65	-11.35
Stacked MSA with C-slot (d_2=d_1 = 0 *mm*)	2.579	-11.54	1.94	1.1
Stacked MSA with C-slot (d_2=1 *mm*, d_1=0 *mm*)	2.737	-34.03	9.13	3.5
Stacked MSA with C-slot (d_2=2 *mm*, d_1=0 *mm*)	2.737	-17.87	6.21	3.94
Stacked MSA with C-slot (d_2=3 *mm*, d_1=0 *mm*)	2.737	-15.36	5.12	4.26
Stacked MSA with C-slot (d_2= 1 *mm*, d_1= 1 *mm*)	3.368	-21.4	7.4	6.76
Stacked MSA with C-slot (d_2= 1 *mm*, d_1= 2 *mm*)	3.526	-19.25	7.09	7.3
Stacked MSA with C-slot (d_2= 1 *mm*, d_1= 3 *mm*)	3.526	-15.9	6.24	7.48

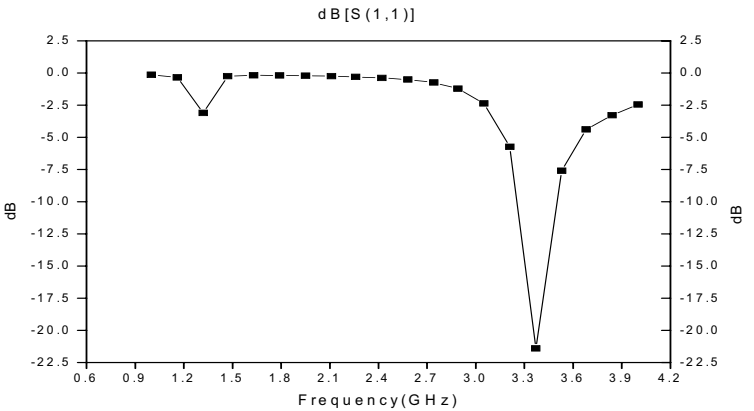

Fig. 2: Return loss characteristics of the proposed antenna

CONCULSIONS

The proposed antenna provides a frequency reduction of 41.42 %, which is more than that provided by the small dual printed antenna C-slot. Also it provides wider BW of 7.4% and higher gain of 6.76 dBi in comparison to small dual printed antenna C-slot.

REFERENCES

[1] Girish Kumar, K.P.Ray, *Broadband Microstrip Antenna,* Norwood, MA, Artech House, INC., 2003.
[2] D.M.Pozar and D.H.Schaubert, *Microstrip Antennas Design,* Piscataway, NJ: IEEE Press, 1995.
[3] IE3D v 11.09, Zeland software, Inc, Fremont, CA.
[4] H.K. Kan and D.Pavlickovski, "*small dual-C slot printed antenna*", Electronics Letters, vol. 39, no.7, pp. 593-594, April 2003.

5GHz WLAN band notched square monopole antenna for UWB systems

M. Gopikrishna, Deepti Das Krishna, Anupam R. Chandran and C. K. Aanandar
Dept. of Electronics, Cochin University of Science and Technology, Cochin., India- 682022,
anand@cusat.ac.in

Abstract: *An ultra wide band (UWB) antenna with band notch characteristics is presented. The proposed antenna is a planar square monopole with a modified ground plane and two narrow slits etched symmetrically with respect to the feed point. The design exhibits a 2:1 VSWR bandwidth from 3 to11 GHz in which the 5.15-5.825 GHz IEEE802.11a and HIPERLAN/2 band has been notched. The radiation patterns are omni directional with a reduced gain in the notched band.*

Introduction: Ultra Wide Band (UWB) systems transmit and receive information coded ultra short electromagnetic pulses with very low power levels. This scheme of wireless transmission occupies a bandwidth of more than 25% of a centre frequency or more than 1.5 GHz and is one of the most promising solutions for future communications systems due to its high data rate and excellent immunity to multipath interference. There are mainly three types of UWB systems specified by Federal Communications Commission (FCC) with different technical standards and operation restriction; vehicular radar systems, communication and measurement systems and imaging systems, to be contained between 3.1 –10.6 GHz. To avoid this extremely wide operating bandwidth from hampering any existing electronic systems, the emission limit is to remain within -43.3 dBm/MHz [1]. In general, there are two ways to limit the radiated power density to conform to the standard mask set by FCC, either by designing the antenna as a filter to suppress the unwanted radiation in a specific band or by selecting a source pulse meeting the specified emission limit. In the present work, we adopted the former technique to design an UWB antenna that will notch out the IEEE802.11a and HIPERLAN/2 (5150-5350/ 5725-5825 MHz) bands from its spectrum of operation. Many researchers have come out with different methods for realizing frequency notch; using parasitic patches [2, 3], using a fractal slot in the ground plane [4] or by incorporating slot type split ring resonators [5] in the antenna. The proposed technique utilizes two narrow slits of approximately $\lambda_g/4$ in length to get the required notch, which makes the design very simple.

Antenna Design: Details of the proposed UWB antenna is shown in Figure 1. The structure consists of a monopole excited by a microstrip feed line. Here, the lower edge of the band is determined by the overall length of the element and the upper edge by the feed gap. Matching in the overall band is obtained by modifying the ground as shown. Two perpendicular slits are symmetrically cut along the lower edge of the square patch to produce high impedance giving a frequency notch. A detailed parametric study by varying the length of the slit (l), distance of the slit from the feed (d) and slit width (t) is carried out in Ansoft HFSS and the results are shown in Figure 2. It shows that the notched frequency can be tuned by varying l, width of the rejection band by varying d and the VSWR by t.

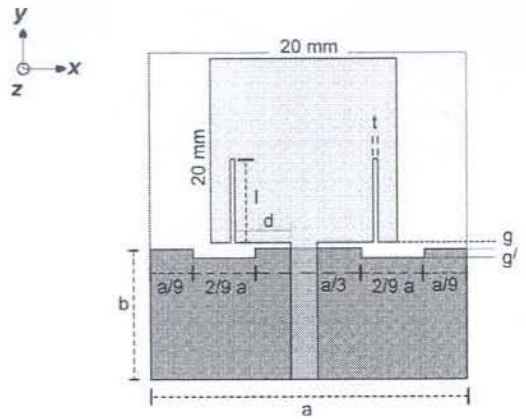

Figure 1 Geometry of the proposed antenna.

The optimized design parameters for getting ultra wideband performance with a rejection band centered at 5.5 GHz are l, d, t, a, b, g, g/ = 10 mm, 6.35 mm, 0.3 mm, 34 mm, 13 mm, 0.5 mm, 1.1 mm. The prototype was realized on RTDuroid 5870 substrate having dielectric constant 2.33 and thickness 0.8 mm.

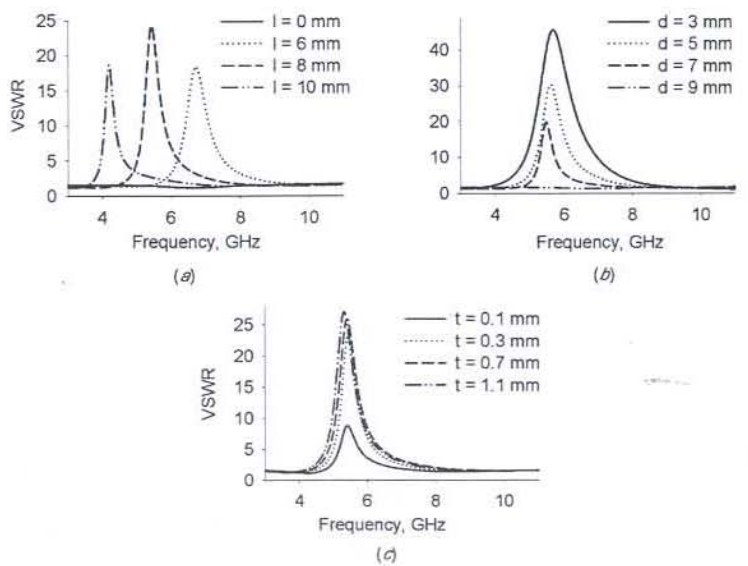

Figure 2 Simulated VSWR plots (a) variation with slot length (l), d = 6.35 mm, t = 0.3 mm (b) variation with distance of the slot (d) l = 10 mm, t = 0.3 mm (c) variation with slot width (t), l = 10 mm, d = 6.35 mm.

Experimental results: VSWR and radiation measurements of the proposed antenna were performed using HP 8510C VNA. The plot given in Figure 3 indicates a 2:1 VSWR bandwidth from 3 to 11 GHz with a notch at 5.5 GH. The band notch at 5.5 GHz can be attributed to the narrow slits functioning as a shorted transmission line having an electrical length of approximately $\lambda_g/4$ at 5.5 GHz, offering infinite impedance at the feed location. Even though a single slit gives the required band notch, use of symmetric slits provides undistorted radiation patterns at all frequencies.

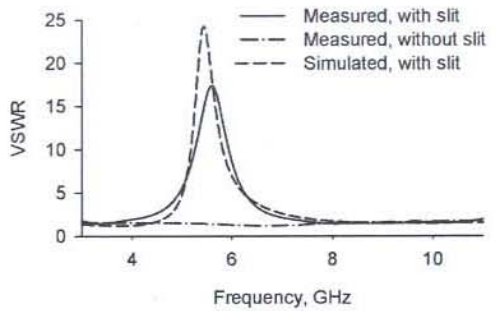

Figure 3 Measured and Simulated VSWR plots for optimized design parameters.

The radiation patterns of the antenna in the principal planes at different frequencies are shown in Figure 4. Nearly omni directional patterns are obtained over the entire frequency range. It is found that the radiated power at 5.5 GHz is much less compared to the rest of the band.

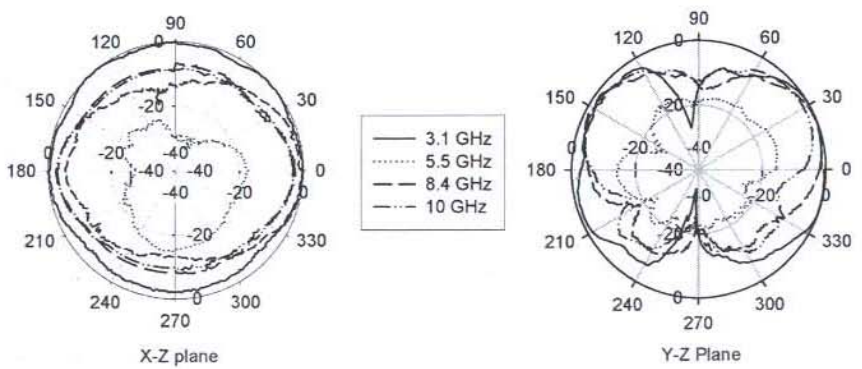

Figure 4 Radiation patterns of the proposed antenna at different frequencies.

Figure 5 shows the measured gain of the antenna and establishes that the antenna ceases its radiation in the rejection band while maintaining an appreciable gain at other frequencies.

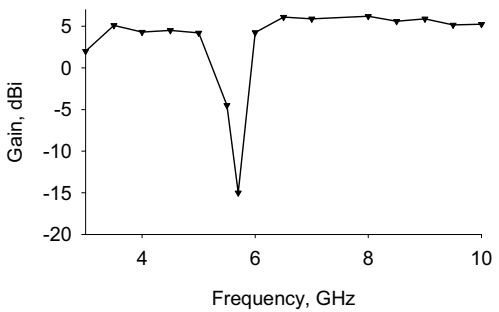

Figure 5 Measured gain of the proposed antenna.

Conclusion: The design, fabrication and testing of a square monopole UWB antenna with band notch at 5.5GHz is presented. Simple in its design, the proposed antenna allows a band rejection by introducing perpendicular slits, symmetrically cut along the edge of the square patch. The notch frequency and the bandwidth can be tuned by varying slit parameters. The antenna with its omni directional radiation characteristics and appreciable gain can be suitably adapted to cater to the needs of any UWB application.

Acknowledgements: M. Gopikrishna acknowledges the University Grants Commission, India for funding this work; Deepti Das Krishna acknowledges Dept. of Science and Technology, Govt. of India for providing financial assistance.

Reference:

[1] Lin, C.C., Kan, Y.C., Kuo, L.C., Chuang, H.R., 'A planar triangular monopole antenna for UWB communications', IEEE Microwave and Wireless Components Letters, Vol. 15, No. 10, October 2005

[2] Kim, K.H., Cho, Y.J., Hwang, S.H. and Park, S.O., 'Band notched UWB planar monopole antenna with two parasitic patches', Electronic letters, Vol. 41, No. 14, July 2005

[3] Kim, K.H., Cho, Y.J., Hwang, S.H. and Park, S.O., 'A band rejected UWB planar monopole antenna with a split ring shaped parasitic patch', APMC 2005 proceedings

[4] Lui, W.J., Cheng, C.H. and Zhu, H.B., 'Compact frequency notched ultra wide band fractal printed slot antenna', IEEE Microwave and Wireless Components Letters, Vol. 16, No. 4, April 2006

[5] Kim, J., Cho, C.S. and Lee, J.W., '5.2 GHz notched ultra wide band antenna using slot-type SRR', Electronic Letters, Vol. 42, No. 6, March 2006

Modified U-slot loaded Rectangular Microstrip Antennas

Amit A. Deshmukh[1] and G. Kumar[1]
(1) Department of Electrical Engineering, I. I. T. Bombay, Powai, Mumbai, India
Email: amitdeshmukh76@yahoo.com, gkumar@ee.iitb.ac.in

Abstract: The broadband and compact rectangular microstrip antennas using modified U-shaped slots like, F-slot, Pi-slot and T-slot, are proposed. Also the compact and broadband rectangular ring microstrip antenna using half U-slot is proposed.

Introduction: Microstrip antenna (MSA) has several advantages like, low profile planar configuration, but has smaller VSWR bandwidth (BW) and larger patch size in 300 – 1000 MHz frequency band. Several techniques like placing a shorting post or cutting a slot inside the MSA to realize the compact MSA and multi-resonator gap-coupled and stacked configurations to realize the broader BW have been reported [1]. By cutting a resonant U-slot inside the rectangular MSA (RMSA), the BW has been increased [2]. The U-slot resonance frequency is largely governed by its inner slot length [3]. In this paper, by modifying the outer U-slot length, the broadband and compact RMSAs using F-slot, Pi-slot and T-slot, are proposed. Also the compact and broadband rectangular ring MSA using half U-slot is proposed. The slotted RMSAs are fabricated on glass epoxy substrate ($\varepsilon_r = 4.3$, h = 0.159 cm, and tan $\delta = 0.02$) and are suspended above the ground plane with an air gap Δ. These MSAs were first analyzed using IE3D software followed by experimental verifications [4].

F-slot RMSA: The F-slot RMSA is shown in Fig. 1(a, b). The vertical U-slot length is increased without changing its inner slot length. This reduces TM_{10} mode resonance frequency of the patch. For the optimized F-slot RMSA with $\Delta = 1.7$ cm, the simulated and measured input impedance and VSWR plots are shown in Fig. 1(c). The simulated BW is 113 MHz (13.4%), and the measured BW is 106 MHz (12.8%). This BW is smaller as compared to that given by U-slot RMSA, which is due to its reduced frequency. The radiation pattern at 843 MHz as shown in Fig. 2(a) is in the broadside direction with cross-polarization level less than 8 dB as compared to that of the co-polar level. However, as the F-slot is un-symmetrical with respect to the feed point axis, the cross-polarization level increases towards the higher frequencies. The gain is more than 8 dBi over the VSWR BW as shown in Fig. 2(b).

Pi and T-slot RMSAs: The asymmetry of F-slot RMSA is removed by extending the outer slot length on both sides of feed point axis, giving Pi-slot RMSA as shown in Fig. 2(c). For the three values of vertical slot length (L_s), the input impedance plots are shown in Fig. 2(d). The L_s alters the patch resonance frequency, which changes the radiation resistance and hence the loop size. For $L_s = 6$ cm and $\Delta = 1.7$ cm**,** the simulated and measured BW's are 149 MHz (16.8%) and 142 MHz (16.1%), respectively. Due to symmetrical Pi-slot, the cross-polar level has been reduced. However, F-slot has larger reduction in the resonance frequency. By employing the even mode symmetry of Pi-slot RMSA, a compact T-slot

RMSA is proposed as shown in Fig. 2(e). T-slot RMSA is optimized with Δ = 2.3 cm. The simulated and measured BW's are 133 MHz (15.4%) and 134 MHz (15.6%), respectively.

Broadband Rectangular ring MSA: Rectangular ring MSA is obtained by cutting a slot in the center of RMSA. Its BW has been increased by cutting a half U-slot as shown in Fig. 3(a). For the optimized MSA with Δ = 2.5 cm, the input impedance and VSWR plots are shown in Fig. 3(b). Since the ring MSA is compact in size it requires a larger air gap for the loop to be within VSWR = 2 circle. The simulated and measured BWs are 125 MHz (14.7%) and 127 MHz (14.9%), respectively. The radiation pattern is in the broadside direction with a cross-polar level less than 10 dB as compared to the co-polar level with peak gain of 8 dBi, as shown in Fig. 3(c, d).

Conclusions: The broadband and compact RMSAs using modified U-shaped slots like F-slot, Pi-slot and T-slot are proposed. They give broader BW with a broadside radiation pattern. The BW of the compact rectangular ring MSA is increased by cutting a half U-slot.

References

[1] G. Kumar and K. P. Ray, 'Broadband Microstrip Antennas', Artech House, USA, 2003

[2] K. L. Wong, 'Compact and Broadband Microstrip Antennas', John Wiley and Sons, Inc., New York, 2002

[3] A. A. Deshmukh and G. Kumar, 'Compact Broadband U-slot loaded Rectangular Microstrip Antennas', *Microw. Opt. Technol. Lett.*, Vol. 46, No. 6, pp. 556 – 559, 2005

[4] IE3D 7.1, Zeland Software Inc., Fremont, CA, USA, 2000

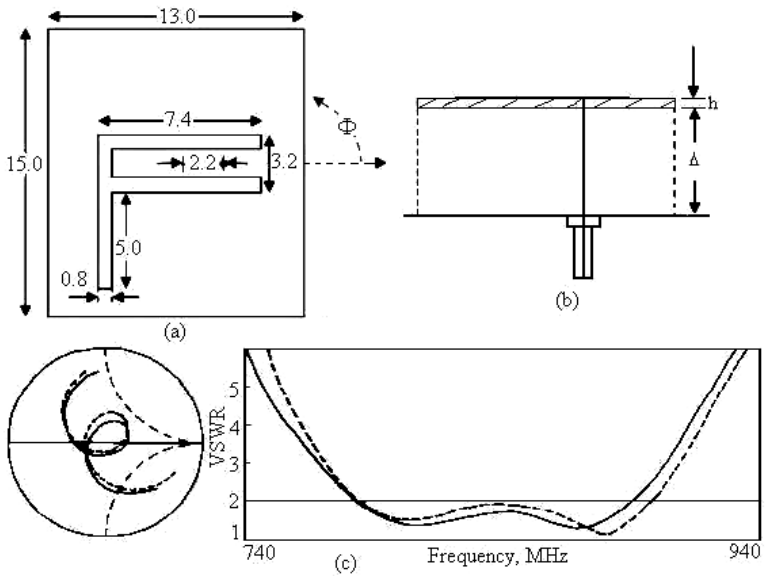

Fig 1 F-slot RMSA, (a) top and (b) side views, and its (c) input impedance and VSWR plots, (- - -) simulated, (——) measured

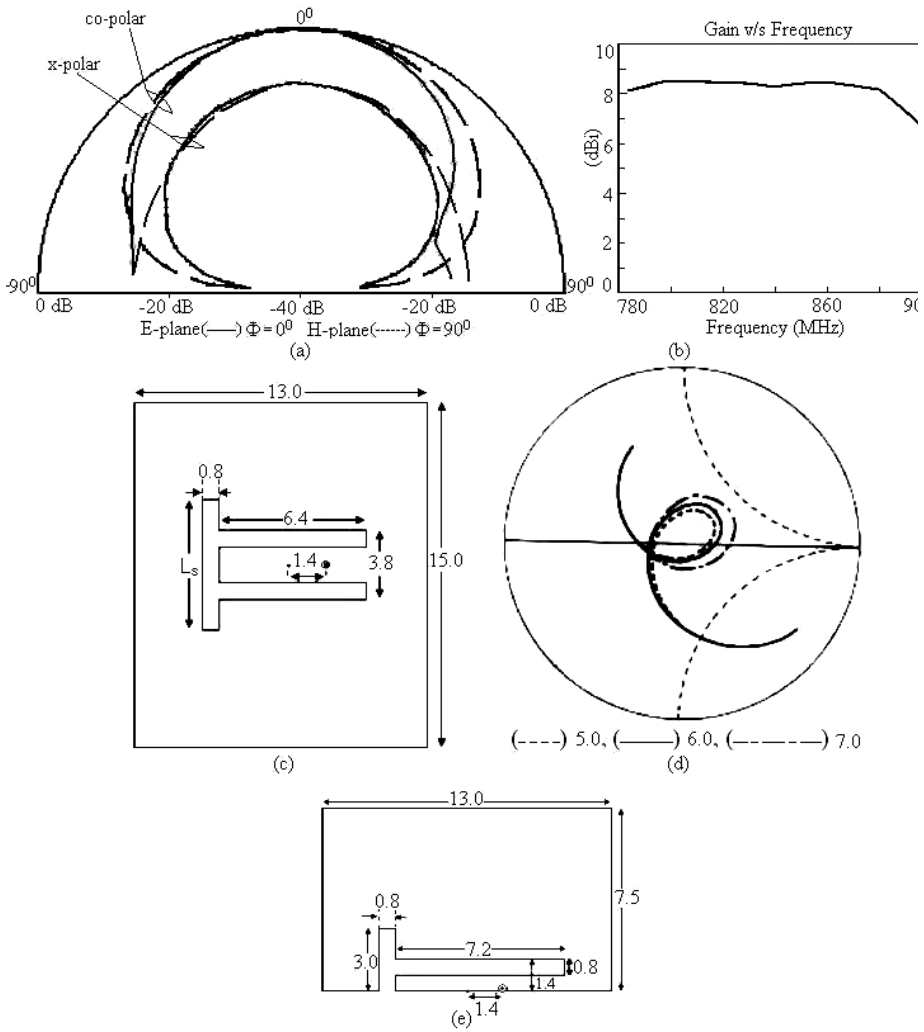

Fig. 2 (a) Radiation pattern at 843 MHz for F-slot RMSA, its (b) gain variation against frequency, (c) Pi-slot RMSA, (d) input impedance plots for different values of L_s and (e) compact T-slot RMSA

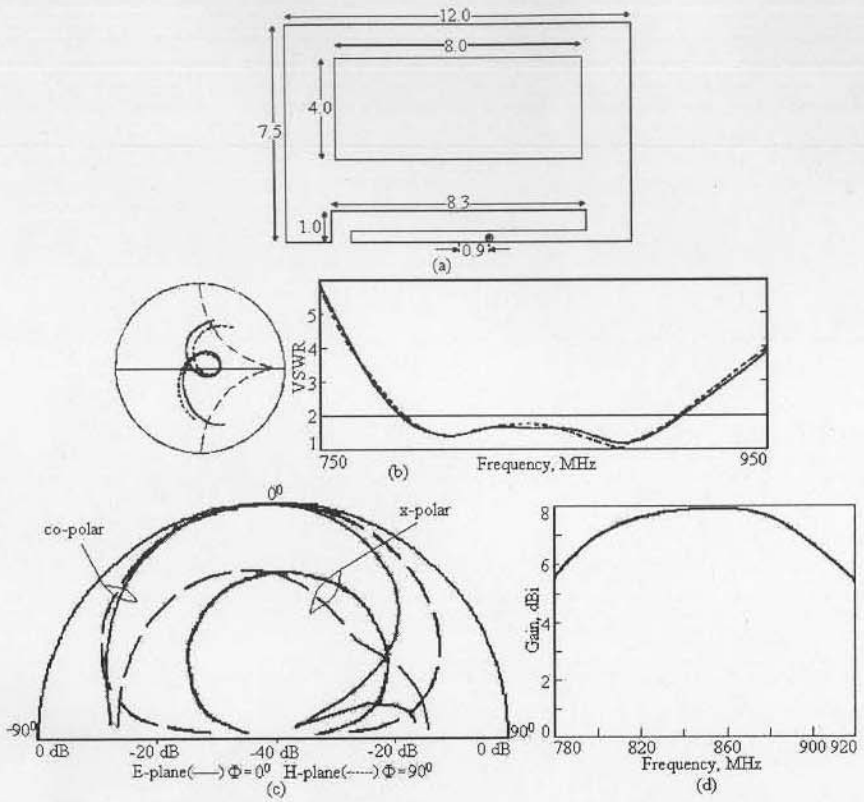

Fig. 3 (a) Half U-slot cut rectangular ring MSA, (b) input impedance and VSWR plots, (- - -) simulated, (—) measured; (c) radiation pattern at 850 MHz and its (d) gain variation against frequency

Electronically Switchable Compact Microstrip Antenna with Triangular Slots for Dual port operation

Deepti Das Krishna, M. Gopikrishna, C.K Aanandan , P. Mohanan & K. Vasudevan,
Department of Electronics, Cochin University of Science and Technology,
Cochin, India – 682022, anand@cusat.ac.in

Abstract *Design of an Electronically Switchable Microstrip Antenna for dual port operation, suitable for GSM and WLAN band, is proposed. The antenna is an electromagnetically excited square patch with triangular slots whose characteristics can be changed by shunting the slots using PIN diode switches. It exhibits a dual frequency dual polarized operation at 1.8GHz and 2.4GHz when the switch is OFF and a dual linear polarization at 2.4GHz when the switch is ON. The two ports have an isolation of more than 30dB.*

Introduction: In land mobile communication system, performance is deteriorated as a result of multi-path propagation. Multi-path effects can be reduced by polarization diversity or by using dual linearly polarized antennas [1-2]. Frequency re-use or dual-polarized antennas, such as [3-5], have widespread application in satellite and wireless communication. We propose the design of a microstrip antenna which can be electronically switched between dual frequency dual polarized operation or dual band linearly polarized operation.

Antenna Design Details: The prototype of the proposed antenna operating in the 1.8 GHz and 2.4 GHz is depicted in Fig. 1.

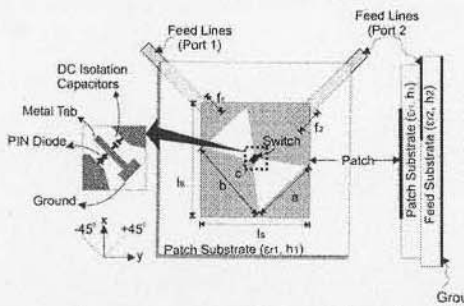

Figure 1. Geometry of the proposed antenna (ls = 25mm, a = 15mm, b = 18.6mm, c =2.4mm, $f_1 = f_2 = 3.7$mm, $\varepsilon_{r1} = 4.36$, $\varepsilon_{r2} = 3.1$, $h_1 = 1.6$mm, $h_2 = 1.6$ mm) with PIN diode and DC isolation capacitors.

A square patch with two triangular slots symmetric with respect to the patch diagonals, is electromagnetically coupled to two 50 ohm feed lines. A PIN diode is connected across the slots along with a DC isolation capacitor as shown in the figure. The diode can be switched ON or OFF by applying DC voltage. When the diode is in the ON state it behaves as a short circuit and the RF signal is guided through it. In the OFF state, it behaves as an open circuit.

Results: When the diode is in the OFF state, it is observed that the antenna exhibits dual band orthogonal polarization at 1.8GHz (port 2) and 2.4GHz (port 1). When diode is in ON state, it exhibits dual linear polarizations at 2.4GHz. The return loss of

the antenna and isolation between the ports, for different diode states, are plotted against frequency in Fig. 2(i) & 2(ii). Simulation results, obtained using the IE3D™ software, agree well with the measured results. Isolation better than 30dB is obtained between the ports.

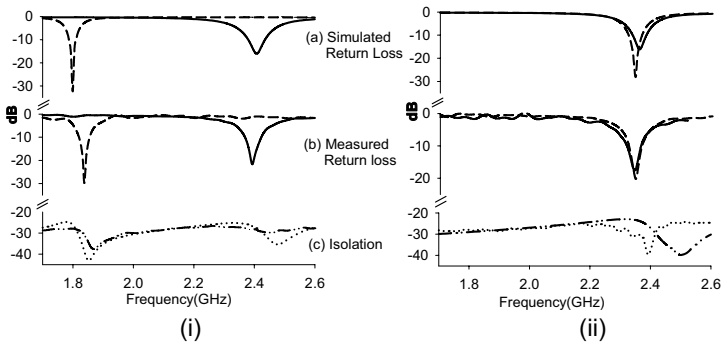

Figure 2. Return Loss and isolation between the ports, when the switch is (i) ON and (ii) OFF.
——— Port 1 – – – Port 2. Isolation ····· Measured — · · Simulated

The transmission characteristics of the antenna (S_{21}), for different diode states, are shown in Fig. 3. The S_{21} plot of a simple square patch antenna, of the same size is also shown for comparison. The plots indicate that the gain of the antenna is comparable under different switching state of the diode. A slight reduction in gain is observed at 1.8GHz.

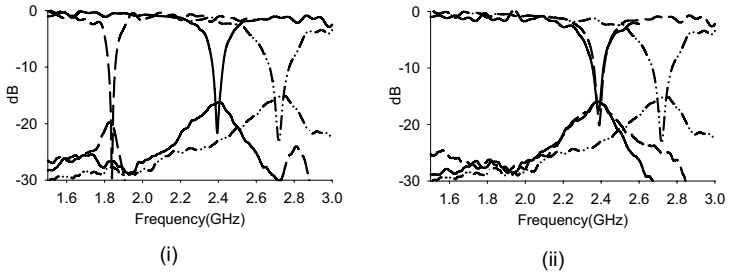

Figure 3. Reflection (S_{11}) and Transmitted (S_{21}) characteristics when the switch is (i) OFF and (ii) ON
– – – Port 1 ——— Port 2 — · · Square patch of same size

It can also be observed that the proposed antenna operates at a much lower frequency compared to a square patch of the same size. For the same resonant frequency (1.8GHz), an unslotted patch has a side dimension of 40mm where as the proposed antenna size is only 25mm. Hence, a size reduction of 61% is achieved. This is achieved by means of reactive loading in the form of slots on the surface of the patch. Such loading increases the surface current path and the electrical length of the element leading to reduction in resonant frequency.

The radiation patterns measured in the E and H planes are plotted in Fig. 4. The radiation from the antenna is obtained along the +/-45^0 planes, i.e. along the

diagonals of the square patch. The cross-polarization level for the antenna remains below -20 dB in the E and H plane.

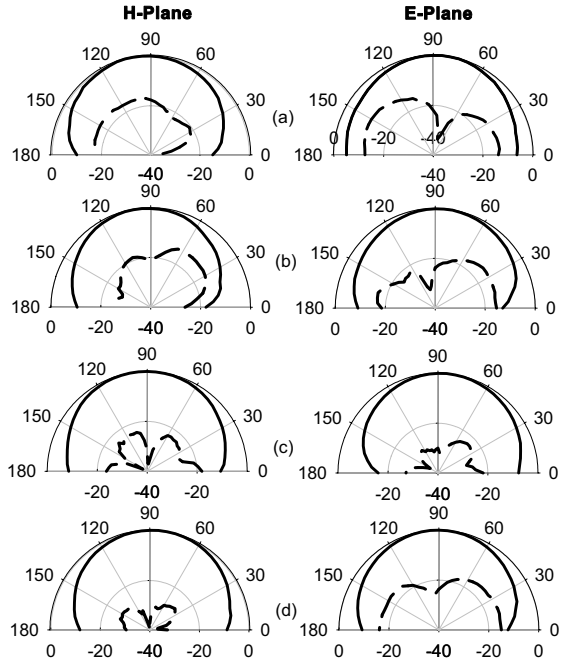

Figure 4. Radiation pattern at (a) port1 and (b) port 2 when the switch is OFF, (c) port 1 and (d) port 2 when the switch is ON. ——— Co-polar — — Cross-polar

Conclusion: Design of a dual port square patch with triangular slots shunted by a PIN diode switch, as an electronically switchable antenna is reported. According to the switching state of the PIN diode, the antenna operates as a dual frequency dual polarization antenna at 1.8GHz and 2.4GHz or as a dual linearly polarized antenna at 2.4GHz. The two ports are giving linearly polarized radiation along +/-45^0 with isolation better than 30dB between them. The cross polarization levels are lower than 20 dB at both the ports. A reduction in patch size ≈ 60% is obtained compared to the square patch operating at the same frequency with out significant reduction in gain.

Acknowledgement: Deepti Das Krishna acknowledges Dept. of Science and Technology, Govt. of India for funding this work. M. Gopikrishna acknowledges the University Grants Commission for providing research fellowship.

References

1. COLBUM, J.S., SAMII Y.R., JENSEN M.A., POTTIE G.J., 'Evaluation of Personal Communications Dual-Antenna Handset Diversity Performance', IEEE Trans. Antennas Prop., 1998, Vo1.47, pp.737- 746.
2. HONG, S.H., LEE, Y.S., CHOI, M.S. and YOON, Y.J., 'Polarization Diversity with Directional Antennas for Indoor Environments', Proc. Int. conf. on IEEE Antennas and Propag. Society, JULY 1999, pp-785-788.
3. DAS KRISHNA D., GOPIKRISHNA M., AANANDAN C.K., MOHANAN P., VASUDEVAN K., 'Compact Dual-Polarized Square Microstrip Antenna with Triangular Slots for Wireless Communication', Electronics Letters, Aug 2006, Vol. 42. No.16.
4. KARODE, S.L., FUSCO V.F., 'Dual Polarised Microstrip Patch Antenna Using Feedforward Isolation Enhancement for Simultaneous Transmit Receive applications', Conference Publication No. 461, IEE, 1999.
5. CHOI D.H., CHO Y. J., PARK S. O., 'Dual-band and dual polarized antenna', Electronics Letters, Jan 2006, Vol. 42, No. 2.

Proceedings of APSYM2006, Dec. 14-16., Dept. of Electronics, CUSAT, India.

RESEARCH SESSION III

MICROWAVE MATERIALS

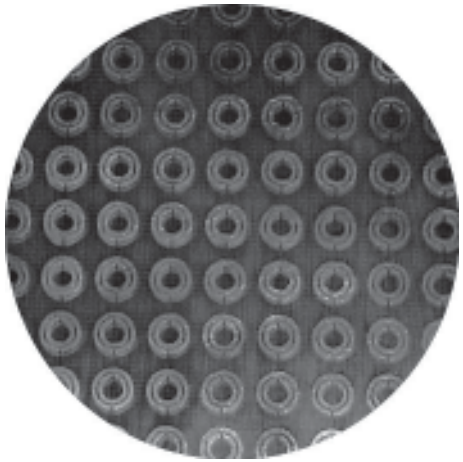

December 14, Thursday

(4.00 p.m.- 5.30 p.m.)

RESEARCH SESSION III

MICROWAVE MATERIALS

Chair: Dr. M.T. Sebastian
RRL, Trivandrum.

LOW–LOSS CERAMIC FOR DR SUPPORT APPLICATION

H. SREEMOOLANADHAN, J. REVATHY*, R. RATHEESH*, and V. CHANDRASEKARAN

Advanced Materials & Ceramics Division, MMG/ PCM, Vikram Sarabhai Space Centre (ISRO), Thiruvananthapuram-695022

*Centre for Materials for Electronics Technology (CMET), Thrissur-680771

Abstract :– *DRs are used in many microwave devices like filters, oscillators etc. operating in the fundamental $TE_{01\delta}$ mode. A low-εr and low-loss support material is often used to mount the DRs on. A promising candidate material, indialite, has been indigenously developed as a support material. Phase pure indialite obtained by calcining high-purity oxides at 1375°C. Fully dense ceramics have been obtained by firing at ~1420°C for 2h with 3wt.% of Y_2O_3 as sintering aid. Dielectric measurements showed εr~3.9, tanδ ~7.5×10^{-5} and temperature coefficient of frequency –22ppm°C at 11GHz. Superior dielectric properties combined with higher thermal shock resistance suggest that indialite may be a good microwave substrate material compared with Al_2O_3.*

INTRODUCTION

Dielectric resonators (DR) are versatile passive components for many microwave devices used in Cellular Telephones and Space communication systems[1,2]. The operation frequency and performance of a circuit using DR strongly depend on the environment of the latter because of the evanescent field. Due to this reason, DRs are centrally mounted inside an enclosure. The support on which DRs are mounted must have low εr to avoid confinement of e.m. wave, low dielectric loss (tanδ) to minimise e.m. wave loss and low thermal expansion to minimise 'tuning' effect. Polymeric materials like PTFE, polystryrofoam etc. are best candidates for ordinary applications. On the other hand if the DR enclosure is in a warm environment, care must be taken that outside heat neither damages the support nor affect the DR frequency. In such cases, ceramics are far superior to polymers. Ceramics like quartz, forsterite, cordierite etc. have been used by many industries for such applications.

Cordierite ($Mg_2Al_4Si_5O_{18}$) is one of the earliest known ceramics and widely used in high-temperature kiln insulation and mechanical filter in hot-gas exhausts. These applications took advantage of high thermal shock resistance and strength of this ceramic. Only in late 80s, the usefulness of this material for electronic and microwave applications was recognized. Recently, IBM published a report showing the advantage of synthetic cordierite over Al-alloy for use in hard discs. Indialite is high-temperature phase of $Mg_2Al_4Si_5O_{18}$ and melts at 1470°C. Many researchers have proved that it is extremely difficult to get high density without proper additives. This paper presents the processing technology to develop fully dense indialite (α-cordierite) ceramics and their microwave dielectric properties.

EXPERIMENTAL

High purity (> 99.9% pure) oxides were used as raw materials for preparing the ceramics. Solid-state synthesis route was used because it is simple and straightforward. MgO, Al_2O_3 and SiO_2 were mixed in 2:2:5 ratio by ball-milling in propanol (AR grade) medium for 15h to get a homogenous slurry. The slurry was dried into powder and was calcined in alumina crucible at 1375°C for 4h in air inside a programmable controlled furnace. A sample of the calcined powder was used for X-ray diffraction analysis to confirm phase formation. The calcined powder was then ball-milled in toughened zirconia bowls using zirconia balls for 10h in propanol. The slurry was dried at

<80°C with intermediate pulverising. Powder was divided into different batches for sintering experiments using different additives. Additives were added to respective batches, mixed with 1% PVA solution and then dried. These were compacted in ∅14mm, ∅18mm and ∅28mm dies under a pressure of 100 MPa. Sintering experiments were performed in the range 1400–1460°C and dwelling hours of 2–6h. Bulk densities of the sintered ceramics were measured by Archimedes method. Phase analysis was again done by XRD using powdered samples.

Microwave dielectric properties were tested in 5–20 GHz using rod resonator method. The εr was evaluated from the frequency of TE_{011} mode under the end-shorted condition. The loss factor(tanδ) was evaluated as inverse of the Qu of the $TE_{01\delta}$ mode inside a silver-coated cavity. Samples were mounted on thin PTFE support and coupled to a 50Ω stripline. The temperature coefficient was estimated by plotting the variation of TE_{011} mode (to avoid any effect of cavity) with temperature in the range 25–75°C.

RESULTS & DISCUSSION

$Mg_2Al_4Si_5O_{18}$ formation could be completed at 1375°C in 4h. XRD patterns obtained after calcinations as well as sintering were identical and is shown in figure. Computer-aided search and match was performed on XRD patterns, which showed more or less good agreement with Indialite $Mg_2Al_4Si_5O_{18}$ (no. 01-08-1540) and $Mg_2Al_{3.96}Si_{5.04}O_{18}$ (no. 01-075-1439). Both the above compositions possess hexagonal primitive unit cell, symmetry and nearly same lattice parameters and theoretical densities (2.51g/cm^3 and 2.52g/cm^3 respectively). No trace of any other phase could be detected.

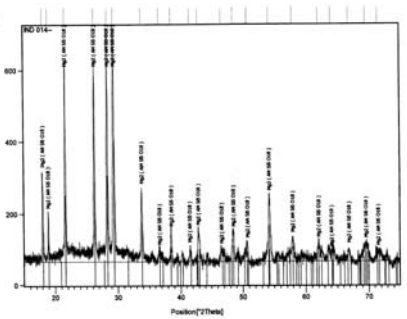

The ceramics did not show good densification during final firing or sintering, when sintered without any additive. Maximum bulk density of 2.11g/cm^3 (84% of TD) only could be achieved even after heating at 1460°C for 6h. Many researchers have reported that it is very difficult to obtain dense indialite in pure form. So, they invariably used additives like TiO_2, CeO_2 and other lanthanides[3–6]. So, before going into the final optimisation of sintering, a set of sintering experiments has been performed using different additives. Only 0.5wt.% of additive was added to respective batch and then ground into fine powder before compaction. Thin discs of ∅10mm×2mm were prepared and sintered at 1420–1445°C for 4h. Most of the additives improved the density as shown in **Table 1**. The maximum density was obtained with Y_2O_3. Hence we further performed optimisation experiments using Y_2O_3 as additive and >98% densities were obtained by sintering the compacts with 3wt.% Y_2O_3 at 1415°C for 2h. Subsequently annealing at 1100°C for 10h was given to promote chemical homogeneity.

Table 1. Comparison of densification effects of various additives (0.5wt.%) on $Mg_2Al_4Si_5O_{18}$ ceramics (TD=2.51g/cm^3).

Sample	Sintering Temperature	Density (% TD)
Pure	1445	79.9
,,	1465	84.0
La	1440	93.7
Ce	1445	93.7
Nd	1440	94.6
Sm	1440	95.3
Gd	1440	96.3
Tb	1445	92.3
Dy	1445	90.4
Yb	1445	73.9
Y	1440	97.1
In	1445	81.9

Proceedings of APSYM2006, Dec. 14-16., Dept. of Electronics, CUSAT, India.

MICROWAVE PROPERTIES

Since the specimens are low–εr materials, the confinement of e.m. energy is less compared to conventional resonator materials. That is, the evanescent wave region around the ceramics is more compared to conventional DRs. Hence the coupling probes had to be kept considerably away from the specimens to avoid any tuning effect. Additionally, identification of TE_{011} mode itself was difficult. Generally, in the case of conventional DRs, the least perturbed mode among the two lowest resonances could be unambiguously identified as TE_{011}. But, in the present case, the methodology had to be slightly modified. Instead of looking at the two fundamental modes, the span was further increased to about 5GHz and about 5 different modes were examined simultaneously. In this condition, the top end-shorting plate was slightly tilted to introduce a gap and the TE_{011} could be easily identified. Now, the span around this mode was reduced and the coupling probes were moved away from the specimen till the frequency became unaffected. This frequency was used for the calculation of εr. The dielectric properties of the samples at microwave frequency were measured using three different dimensions (∅12mm, ∅15mm and ∅24mm). The TE_{011} modes were in the range 11–15GHz and the calculated εr was 3.9 ± 0.2.

The loss factor (tanδ) obtained using TE_{011} mode was found to be only 3.152×10^{-4}at 13GHz. It is well-known that this includes radiation loss as well as the conduction loss at the end-shorting plates. Hence, Qu^{-1}= tanδ were obtained from $TE_{01\delta}$ resonances inside a silver-coated cavity. Initially, the cavity modes along with the PTFE support in position were memorized. Then the specimens were mounted. The fundamental mode of resonance of the specimen was identified from the spectrum of resonances. A little tuning was required whenever the fundamental mode appeared near a cavity mode to separate the former. The unloaded Q values were >11,000 at 10.95 GHz an all cases and the frequency-normalised Q showed a maximum value of 164THz corresponding to a tanδ of 6.39×10^{-5}. The εr and tanδ values are superior to or matching with previous reports[3,7]. The temperature coefficient of frequency was measured in the range 25 to 85°C. The obtained values were in the range –17ppm/°C to –27ppm/°C. This is in accordance with previous data[4]. **Table 2** summarises the microwave dielectric properties of indialite specimens in the present study.

Table 2. Microwave dielectric properties of Indialite ceramics

Dielectric constant (εr)	3.9 ± 0.2
Unloaded Q (Qu)	13,000 ± 2,000
Frequency	10.96 GHz ± 25 MHz
Loss factor (tanδ × 10^{-5})	7.5 ± 1.25
Temperature coefficient of frequency (τf) ppm/°C	–22 ± 5.0

Finally, the performance of a standard DR (TransTech™) inside test cavity were compared using imported support (made of μ–cordierite), present indialite and PTFE. The data are given in **Table 3**. It may be noted that a slightly better value of loss factor obtained on imported support could be due to the greater shift in frequency brought about by larger dimension. However, a similar PTFE gave higher loss for the standard sample. The lesser perturbation in frequency by PTFE is due to lower εr and smaller size. Thus, it can be understood that the indialite material of the present study proves to be equally good as the imported ceramic.

Table 3. Q-values of TRANSTECH 8719 DR obtained using different supports

The DR, ∅ 10mm×4.5mm has an εr=30, Qu~17,000 @ 5.600 GHz corresponding to a tanδ of 5.332×10^{-5}

	Imported	Indialite	PTFE
Dimensions– D, L (mm)	9.0, 4.0	12.2, 6.5	8.0, 4.0
Dielectric constant (εr) of the support	4.5	3.9	2.2
Frequency (GHz)	5.528 938	5.506 875	5.606 875
Perturbation (MHz)	-71.062	-93.125	+6.875
Unloaded Q factor	15,030	14,960	14,640
Loss factor ($\times10^{-5}$)	6.653	6.684	6.831

CONCLUSION

Phase pure indialite could be obtained using a stoichiometric mixture of high-purity oxides by calcining at 1375°C. About 3wt.% of Y_2O_3 can act as sintering aid to get fully dense ceramic below 1420°C. Indialite, with dielectric constant of 3.9, loss factor of 7.5×10^{-5} and temperature coefficient of frequency –22ppm/°C at 11GHz, is a very good support material for DR circuits. It can be a promising candidate for microwave substrate material compared to alumina because of lower εr and higher thermal shock resistance.

ACKNOWLEDGEMENT

Authors are grateful to Dr. P. Mohanan, Dept. of Electronics CUSAT for fruitful discussion and suggestion. Authors wish to acknowledge RF Division of VSSC for valuable inputs with respect to application. Support given by the Metallography section of MMG in characterising the samples is gratefully acknowledged. This project was financially supported by ISRO under the Indigenisation of Space Materials programme.

REFERENCES

1. S. Lundquist, M. Mississian, M. Yu and D. Smith, "*Application of high power output multiplexers for communication satellites*", Proc. Amer. Inst. Aeronautics and Astronautics, **AIAA 2000**, 1191-1199.
2. I. M. Reaney and D. Iddles, "*Microwave dielectric ceramics for resonators and filters in mobile phone network*", J. Am. Ceram. Soc., **89(7)**, July 2006, 2063-72.
3. T. Okamura and T.Kishino, "*Dielectric properties of rare-earth added cordierite at microwave and millimetre wave frequencies*", *Jpn. J. Appl. Phys.*, **vol. 37**, Part 1 No.9B, (1998), 5364-66.
4. J. M. Wu and H-L Huang, "*Effect of crystallisation on microwave dielectric properties of stoichiometric cordierite glasses containing B_2O_3 and P_2O_5*", J. Mater. Res., **vol. 15(1)**, (Jan 2000), 222-27.
5. Lg. Trumbulovic, Z. Acimovic, S. Panic and Lg. Andric, "*Synthesis and characterisation of cordierite from kaolin and talc for casting applications*", FME Trans., **31**, (2003), 43-47.
6. Z. M. Shi, K. M. Liang and S. R. Gu, "*Effect of CeO_2 on phase transformation towards cordierite in MgO-Al_2O_3-SiO_2 system*", Mater. Lett., **vol. 51**, (2001), 68-72.
7. A. Nakayama, A Fukuura and M. Nishimura, "*Millimeterwave measurement of complex permittivity using dielectric rod resonator excited by NRD Guide*", IEEE Trans. Microwave Theory and Tech., **MTT vol-51(1)**, (Jan 2003), 170-77.

Thermal Analysis Using the Dielectric Constant - A New Thermal Analysis Tool

S.B. Kumar[1*], G. M. B. Parkes[2], P. A. Barnes[2], M.J.N. Sibley[3] and G. Bond[4]

[1]System in Package Devices, Philips Research,
5656 AE Eindhoven, The Netherlands
[2]Dept. of Chemical and Biological Sciences
University of Huddersfield, HD1 3DH, U. K.
[3]School of Computing and Engineering
University of Huddersfield, HD1 3DH, U. K.
[4]Centre for Materials Research, University of Central Lancashire
PR1 3HE, U. K.

Abstract: In this paper, the development of equipment for a novel form of thermal analysis is described. The novelty of this new technique lies in the fact that the sample is heated using microwaves while pseudo-simultaneous measurements of its dielectric properties at microwave frequencies are used as the thermal analysis parameters. Physical and chemical processes, such as solid-solid phase changes, dehydrations and decompositions etc can be clearly revealed in different materials as they are heated, as seen by the changes their dielectric constant-temperature profiles. The values of the dielectric constants are calculated employing the cavity perturbation technique and the measurements are done using a Network Analyser (NWA).

roduction: Microwave heating finds extensive application in consumer, commercial, ustrial, scientific and medical fields [1,2]. The use of microwaves can be attributed to the nificant advantages they have over conventional methods of heating, namely high etration depth (and hence more uniform heating), instant heating (i.e. no thermal lag) and entially high heating rate. Microwave heating is related to the dielectric properties of the mple [3]. In general, the more lossy the material, the greater will be its heating rate. asuring dielectric parameters simultaneously with heating, especially at elevated peratures, is of great importance in materials processing as the loss factor, and hence the mple's ability to convert microwave energy to thermal energy can vary widely with peratur and may change dramatically as the sample undergoes chemical or physical cesses on heating. In addition to providing information on the variation of the loss factor h temperature, the technique can be used as new type of Thermal Analysis to investigate se transitions, chemical changes such as dehydration, decomposition and melting and to dict possible thermal run away. The earlier, related technique of Microwave Thermal alysis (MWTA) [4], which measures the thermal energy and temperature effects found in rowave heating, is developing rapidly as it complements conventional thermal analysis hods such as Differential Scanning Calorimetery (DSC). We report here the development a significantly modified form of MWTA, Microwave Dielectric Thermal Analysis

(MDTA), which now incorporates the pseudo-simultaneous measurement of dielectric, rather than thermal parameters, as a function of temperature. The main advantage of MDTA is that the changes in dielectric constant on heating are now measured and can be used throw light not only on the sample's changing ability to heat in a microwave field but also to reveal the fundamental dielectric properties associated with the chemical or physical changes occurring in the sample. In this paper, development of an instrument for MDTA is described, which heats the samples using microwaves and measures dielectric parameters at microwave frequencies using the cavity perturbation technique [5].

Theory of MW heating: Total current density induced in a material when an alternating electric field, $E_0 e^{j\omega t}$ applied is given by Maxwell's equation

$$\nabla x H = J = \sigma E + j\omega\varepsilon_0\varepsilon^{/} E \quad (1)$$

$$J = j\omega\varepsilon_0\left(\varepsilon^{/} - \frac{j\sigma}{\omega\varepsilon_0}\right)E = j\omega\varepsilon_0\varepsilon^{*}_{eff} E \quad (2)$$

where $\varepsilon^{*}_{eff} = \varepsilon^{/} - j\varepsilon_{eff}^{//}$, is the complex relative permittivity. The real part, generally called the dielectric constant, represents the stored energy and the imaginary term accounts for the loss in the material.

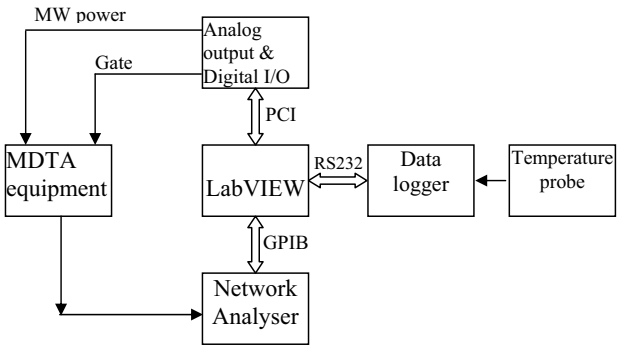

Figure 1. Schematic of the system

Experimental: A schematic diagram of the complete MDTA set-up along with associated instruments and controlling software is shown in figure 1. The function of the equipment is to generate the required microwave power at 2.45 GHz and feed it to the sample chamber for heating. The microwave source applies the power via a three-stub tuner and an iris. The stub tuner is used to modify the electric field so as to get the maximum field strength at the sample position. Tuning is monitored by an e-field probe inserted into the waveguide. The instrument controls the microwave source module and the mechanical gates fitted to the sample chamber. The maximum power output of the magnetron is 1 kW at 2.45 GHz. The output power is controlled by the computer via an ADC (0-10V). The dominant TE_{10} mode is propagated by a waveguide to the sample. A four-port sample chamber in the MDTA equipment facilitates two functions: heating the sample in required mode (constant power, linear heating etc) and measuring the dielectric parameters at pre-set time or temperature intervals. As simultaneous operation of heating and dielectric measurement is not possible, two sets of computer-controlled mechanical gates isolate the heating and measuring sections from each other during measurement and heating respectively.

Proceedings of APSYM2006, Dec. 14-16., Dept. of Electronics, CUSAT, India.

Experimental results: In the present study, three different types of thermally induced processes are reported to illustrate the use of MDTA. Figures 2a and 2b show variations of the dielectric parameters of two materials (SiC and AgI) with temperature. From figure 2a, it can be seen that dielectric constant of SiC slowly and steadily decrease with temperature and the values at room temperature are found to match those measured (ε_r^{*} = 9.01- j*0.58 at 20 ^{0}C) using standard rectangular cavity and the cavity perturbation method. While the SiC shows a steady change in dielectric properties with temperature, the AgI trace shows different behaviour. It can be seen that here the dielectric constant initially does not change significantly until 110 ^{0}C and thereafter it sharply increases until 142 ^{0}C. This region (110 ^{0}C -142 ^{0}C) corresponds to well-known phase transition in AgI. Using MDTA, the phase transition temperature (T_c) is taken at centre of the transition region, i.e. 126 ^{0}C. However, this phase change temperature found using microwave heating appears to be lower than conventional DSC values and this is consistent with the 'microwave effect', which has been reported elsewhere [6]. Figure 2b shows the imaginary part of the complex permittivity ($\varepsilon_r^{//}$) of these two samples measured as a function of temperature and it clearly reveals the changes in the materials. The variation of the value of $\varepsilon_r^{//}$ for SiC with temperature shows a slow but steady decrease with temperature. However, for AgI, it initially decreases slowly but then starts to increase from 110 ^{0}C until 142 ^{0}C, the temperature region which corresponds to the phase transition in the material.

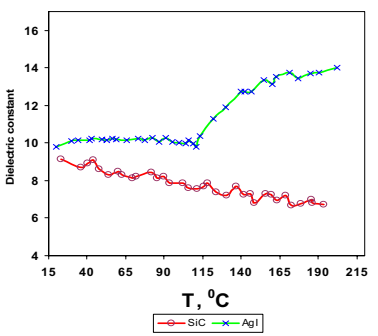

Fig 2a. Dielectric constant of SiC and AgI

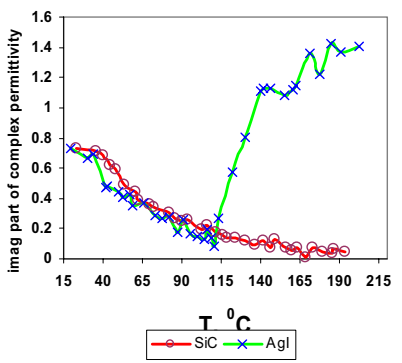

Fig 2b. Dielectric loss of SiC and AgI

The dehydration of materials using MDTA is illustrated by analysing zinc acetate and copper sulphate pentahydrate. Figures 3a & 3b show the dielectric parameters/temperature profiles for these materials, along with those for SiC, which is used for comparison. From figure 3a, it can be seen that the dielectric constant corresponding of zinc acetate initially falls slightly until it reaches 93 ^{0}C and then increases rapidly, reaching a maximum at 113 ^{0}C. This temperature region corresponds to dehydration in the sample and dehydration temperature can be taken as 103 ^{0}C. Conventional DSC thermal analysis of this sample shows dehydration at 106 ^{0}C. In this case, MDTA and the DSC give very similar results.

Copper sulphate has an interesting dehydration mechanism which is generally held to occur in three stages, at approximately 104 ^{0}C, 128 ^{0}C and 243 ^{0}C, depending on the zexperimental conditions used. From the corresponding curve in figure 3a, it can seen that the dielectric constant starts to increase from 88 ^{0}C until 97 ^{0}C, then gives a plateau until 122 ^{0}C, after which it decreases considerably. The mid points of the changes are at ca. 98 ^{0}C and

130 ^{0}C respectively and these correspond reasonably well with the results obtained using conventional DSC.

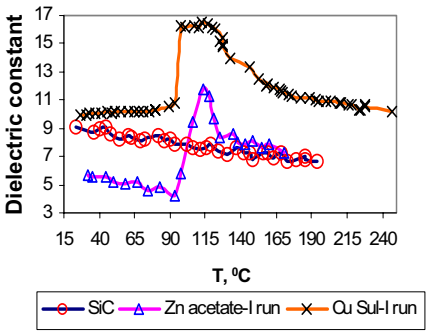

Figure 3a. Dielectric constant of SiC, Zinc acetate and copper sulphate

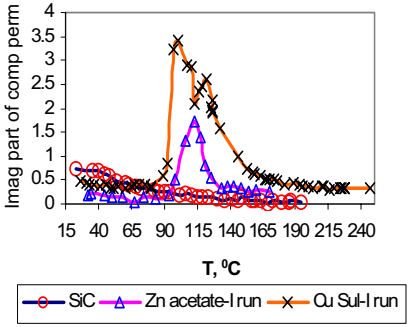

Fig 3b. Dielectric loss of SiC, Zinc acetate and copper sulphate

The variation of $\varepsilon_r^{//}$ for the different samples is shown in figure 3b. For zinc acetate, $\varepsilon_r^{//}$ increases greatly as it is heated between 93 ^{0}C and 113 ^{0}C but thereafter, it decreases rapidly. However, if the same sample is heated for a second time (i.e. after dehydration) sample, it is seen that there is no dramatic change in $\varepsilon_r^{//}$ which clearly reveals the material has been completely dehydrated irreversibly in the first run, as one would expect. The results for copper sulphate (figure 3b) now clearly differentiate the first two, low temperature, dehydration processes while those for zinc acetate are entirely consistent with the irreversible dehydration discussed above. For both of these samples, the reasonably good correspondence of the MDTA and DSC results suggests there is no significant microwave effect in these materials, in contrast to the MDTA of AgI.

MDTA is at an early stage of its development in comparison with conventional thermal analysis methods. However, the results complement the more traditional TA methods and provide a new insight to the changes occurring in materials as they are heated.

Acknowledgements: Authors would like to gratefully acknowledge the financial support from Engineering and Physical Science Research Council (EPSRC) of the UK (Grant reference no. GR/R38460/01).

References:

[1] John M. Osepchuk, "A history of microwave heating applications", IEEE Trans. MTT, Vol. MTT-32, No. 9, pp. 1200-1224, September 1984.
[2] A. C. Metaxas and R. J. Meredith, "Industrial Microwave Heating", IEE Power Series 4, Peter Peregrinus Ltd., London.
[3] Camelia Gabriel et al, "Dielectric parameters relevant to microwave dielectric heating", Chemical Society Review, vol. 27, pp. 213-223, 1998.
[4] G.M.B. Parkes et al, "Qualitative and quantitative aspects of microwave thermal analysis", Thermochimica Acta, Vol. 356, pp. 85-96, 2000.
[5] K. T. Mathew and U. Raveendranath, Sensors Update II, Germany, 2001.
[6] G. R. Robb et al, ''Temperature-resolved, *in-situ* X-ray diffraction of silver iodide under microwave heating'', Phys Chem Comm **5**, 135 (2002).

Effect of silane coating on the dielectric and mechanical properties of ceramic filled PTFE based substrates

K.P.Murali[a], S.Rajesh[a], V.Priyadarsini[a], S.N.Potty[a], R.Ratheesh[a]* and P.Mohanan[b]

a) Microwave Materials Division, Centre for Materials for Electronics Technology (C-MET), Department of Information Technology, Government of India, Athani P.O. Thrissur, Kerala, India -680 771, ratheeshr@yahoo.com
b) Department of Electronics, Cochin University of Science & Technology, Kochi 22, India

Abstract

A systematic study on the effect of silane coating on the dielectric and mechanical properties of fused quartz filled PTFE substrates has been carried out. The composite substrates are prepared through a proprietary process by which silane coated and uncoated fused quartz are incorporated in the PTFE matrix. Filler loading in the polymer matrix is varied from 0 to 70 weight percentage to obtain optimum dimensional stability with better dielectric properties. The filler distribution and filler matrix interface are studied using Scanning Electron Microscopy. The microwave dielectric properties of the composite substrates are measured using X-band waveguide cavity perturbation technique. UTM studies have been carried out to find out the tensile strength and elongation of the hot pressed composite

Introduction

Fluoropolymer based dielectric materials provide excellent electrical, thermal and mechanical properties while used as circuit materials for microwave applications. PTFE based materials with tailored dielectric properties are the most commonly used substrates and are fabricated either by incorporating ceramic fillers or woven glass in the polymer matrix [1, 2]. The selection of ceramic fillers depends mainly on the end properties of the composite substrate. Some of the commonly used fillers are fused quartz, titania, strontium titanate etc.

Often, the processing of these composite substrates is very critical owing to its heterogeneous nature. Processing of these composite systems has to be designed in such a way that the particulate filler are uniformly distributed through out the polymer matrix with minimum porosity [3]. Another major draw back of the composite substrate is the high moisture absorption of the particulate ceramic filler. Since water has high permittivity and loss tangent, even a small amount of water can have detrimental effects on laminate material's performance. To preclude the hydrophilic nature of the filler, usually silane coating is employed. The hydrophobic coating over the particulate filler helps in improving ductility, copper bond strength and reduces water absorption [4]. It has been reported that unexpectedly good results are noticed while silane coating is employed on fillers used for the fabrication of PTFE based composites [5]

In the present study, low loss and low dielectric microwave substrates have been fabricated by incorporating silane coated and/or uncoated fused quartz and microfiber glass in the PTFE matrix through a proprietary process. The substrate materials thus obtained were characterized to ascertain the effect of silane coating on the dielectric and mechanical properties.

Experimental

The raw materials used were 50 micron PTFE powder (H71 grade) supplied by M/S Hindustan Fluoro Carbon, India, Fused quartz supplied by M/S Saint Gobain, France (99.9% purity) and chopped microfiber glass from M/S Binani Glass, India. Phenyl trimethoxy silane procured from M/s Sigma Aldrich, USA was used as silane coating agent. Also di(propylene) glycol obtained from M/S Merck, Germany was used as lubricant to enhance the efficiency of mixing.

Silane coating was carried out as explained in Ref.4. The pH of water was adjusted to 3 using acetic acid. 63 parts of this acidified water was added to 100 parts of the fused silica filler. Vigorous agitation was given for the concentrated slurry in a mixer. After one hour of mixing, phenyltrimethoxy silane was added drop wise and continued mixing for about 10 minutes. The volume of the PTMS was calculated to obtain 1wt% silane coating over the filler. Then the mixture was transferred to a glass container and dried at 120°C.

A proprietary process comprising of sigma mixing, extrusion, calendering followed by hot pressing/thermolamination called as SMECH process has been employed to fabricate nearly isotropic, pore free PTFE laminate with excellent dimensional stability. Composites filled with silane coated and uncoated fused quartz were prepared through SMECH process by keeping all other process parameters constant. The density of the PTFE composites was found out by dimensional method. M/S Philips make SEM was employed to study the filler distribution and the matrix filler interface. The water absorption in the silane coated and uncoated samples were carried out as per IPC-TM-650 2.6.2.1.

The dielectric constant and dissipation factor of the composite samples were measured up to 13MHz using Hewlett-Packard 4192A model impedance analyzer. High frequency dielectric measurements were carried out using X-band waveguide cavity perturbation technique. Ultimate tensile strength of the samples was measured using Shimadzu make (model AGS–1000G) UTM. The measurement parameters were conform to ASTM-D638.

Results & Discussion

The particle size analysis shows that the fused silica filler (Saint Goban, France) has a wide particle size distribution ranging from 1 to 100 microns with major portion occupying 5 to 25 microns. Although small particle diameter exhibits narrow particle size distribution, the greater interparticle attraction forces and friction leads to poor packing fraction in composites whereas wider particle size distribution leads to better packing fractions [6]. In order to study effect of particle size distribution on the packing fraction, 5 μ fused quartz (M/s Chettinad quartz products, India) with narrow particle size distribution was loaded in the PTFE matrix. It was found that the loading of the particulate filler beyond 58 wt% in the PTFE matrix was rather difficult using fillers having narrow particle size distribution Whereas, we could load up to 60 wt. % of filler with excellent dimensional stability in the case of fused silica filler having wider particle size distribution (5 to 50 microns).

From the SEM picture (Fig.1), it can be seen that the distribution of filler is more uniform in composites fabricated with silane coated filler. This is due to the improved flow-properties of the

Proceedings of APSYM2006, Dec. 14-16., Dept. of Electronics, CUSAT, India.

coated filler during processing. In addition, better matrix filler interface is also seen for the samples prepared with silane coated filler.

a) b)

Figure. 1 SEM micrograph of cross section of a) PTFE/fused quartz (silane coated) composite b) PTFE/Fused quartz (uncoated) composite

Water absorption of coated and uncoated filler loaded (60wt%) composites has been studied as per IPC-TM-650 2.6.2.1. Water absorption obtained for silane coated sample is 0.125% where as that for uncoated sample is 0.45%. It can be seen that water absorption of silane coated sample is comparatively less than that of uncoated one. This result shows that surface modification of particulate filler has got profound influence in controlling the water absorption characteristics of composite substrates.

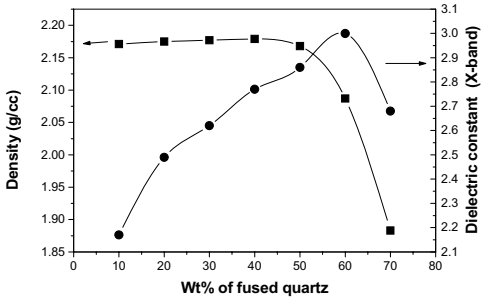

Figure 2. Variation of density and dielectric constant with respect to fused quartz loading

The composite system in the present study comprises of PTFE, fused quartz and microfibre glass having permittivities 2.1, 3.78 and 6.26 respectively. Variation of density and dielectric constant with respect to wt% of silane coated fused quartz is shown in Fig 2. As expected, the permittivity of PTFE composite increases with respect to an increase in filler loading since there are more polarizable ions in the polymer matrix. The density also shows the same trend. However, the density drastically decreases beyond a filler loading level of 60 wt% due to the formation of porosity since there is not sufficient polymer to encapsulate the fillers. Present study shows that through the process methodology employed, it is possible to load PTFE matrix up to 60wt% to obtain a dimensionally stable substrate.

Same experimental procedure has been employed to fabricate PTFE composites filled with uncoated fused quartz. Interestingly, we could load only up to a filler percentage of 58 wt% in the case of uncoated samples. It is found that the density of these samples are less compared to samples filled with same weight % silane coated filler. Although silane coated composites have better density than uncoated ones, their permittivities are observed to be less than that of later. This infers that the silane coating on ceramic filler slightly reduces the effective dielectric constant due to the obscuring of effective polarizability of the particulate fillers.

Ultimate tensile strength (UTS) of coated and uncoated samples is given in Table 1. It can be seen that the sample prepared using silane coated filler has better strength and more ductility than that of uncoated ones. The increase in tensile strength of silane coated sample can be attributed to a better matrix - filler interface where as enhanced rheology is responsible for the improved ductility.

Table 1. Comparison of mechanical properties

Sl. No.	Wt.% of Filler	UTS of PTFE composites (MPa)		Elongation at break (%)	
		Coated filler	Uncoated filler	Coated filler	Uncoated filler
1	58	5.60	4.81	10.2	6.8
2	60	5.56	3.57	9.9	5.3

Conclusion

Dimensionally stable low permittivity and low loss fused quartz filled PTFE substrates have been prepared through SMECH process. Phenyl trimethoxy silane (PTMS) has been used as a precursor for surface modification of fused quartz fillers. Silane coating helps in precluding moisture absorption there by providing better matrix-filler interface which in turn improves the mechanical properties. Further, silane coating also improves the rheological properties leading to better distribution of the filler in the polymer matrix. Present study shows that up to 60 wt% silane coated fused quartz can be loaded in the PTFE matrix with optimum dielectric and mechanical properties.

Reference

[1] David N. Light and James R. Wilcox, "ProcessConsiderations in the fabrication of Fluoropolymer printed circuit boards", IEEE transa. on Compo. and Pack. Techno. 18, 1, 118 – 126, 1995.
[2] Bob Daigle, "Printed circuit board material and desing consideration for wireless application", IEEE Electronic components and technology conference, 354 – 357, 1996.
[3] Arthur David J., Swei. Gwo S., "Ceramic filled fluoro polymeric composite material" US Patent No. 5024871, 1991.
[4] Yung-Chih Chen, Hsueh-chen Lin, Yu-Der Lee, "The effect of filler content and size on the properties of PTFE/SiO_2 composites", J. Poly. Res., 10, 247 – 258, 2003.
[5] Arthur David J., Swei. Gwo S., "Electrical substrate material" US Patent No. 5149590, 1992.
[6] Horn, III, Allen F., "Fouoropolymeric electrical substrate material exhibiting low thermal coefficient of dielectric constant" US Patent No. 5358775, 1994.

EFFECT OF ZnO ADDITION ON THE MICROWAVE DIELECTRIC PROPERTIES OF $CeTiTaO_6$ DIELECTRIC RESONATORS

H. Padma Kumar , Shyla Joseph , J.K. Thomas [b], M.R. Varma [c] and Sam Solomon
Dielectric Materials Research Laboratory, Department of Physics, St.John's College, Anchal, Kollam District, Kerala, India, Pin- 691306, [b] Electronic Materials Research Laboratory, Department of Physics, Mar Ivanios College, Nalanchira, Thiruvananthapuram , Pin-695015, [c] Regional Research Laboratory, Thiruvananthapuram- 695019 , E mail: samdmrl@yahoo.com

Abstract

$CeTiTaO_6$ ceramics, doped with ZnO, were prepared in the solid state ceramic route. The cylindrical samples were sintered at temperatures between 1360-1450^{0}C. The densities were measured using Archimedes method. Samples were characterized by X-ray diffraction and scanning electron microscopic methods. Microwave dielectric properties of the cylindrical samples were measured using the network analyzer. Small doping of ZnO reduced the sintering temperature and increased the dielectric constant (ε_r). The variation of temperature coefficient of resonant frequency (τ_f) also decreases on small doping and increases on higher doping concentrations. Considerable grain growth is also observed on doped samples.

1. Introduction

Ceramic materials with better dielectric characteristics are of increasing importance as the field of solid-state electronics continue to expand rapidly. The main factor is the reliability of the components used in the electronic equipments. It was Richtmyer in 1939 who first proposed that a piece of dielectric material can act as a resonator [1]. For a ceramic material to be used as good dielectric resonator it must have high permittivity (ε_r >20), high unloaded quality factor (Q_u>1000) and a small temperature coefficient of resonant frequency ($\tau_f \leq \pm$20ppm/°C). Rather, their cost of production is low in comparison with other high frequency devices and they are characterized by light weight and compactness. Hence they can be effectively used in microwave appliances to resonate at the frequency of the carrier signal and to allow that signal to be efficiently separated from other signals in the microwave band [2]. A large number of ceramic dielectric materials have been developed over the years satisfying these conditions [3-6].

$LnTiNbO_6$ were prepared by modified Czochralski growth and its characterization were reported by Qi et al and they also reported its crystal growth by laser heated pedestal growth technique. Lanthanide based titanium niobates and tantalates having good dielectric resonator properties were reported by Surendran etal and Sebastian et al [9-10]. Lanthanide based titanium tantalates though possess good dielectric resonator properties, they require high processing temperature to get optimum dielectric properties (Temperature >1575°C). Suitable dopants were generally used to reduce the sintering temperature and also to improve the dielectric properties of different systems.

ZnO, WO_3 and CuO have being used as dopant on $MgTiO_3$–$CaTiO_3$ systems and it's microwave dielectric properties were studied by Cheng-Liang Huang et al [11-12]. Various glass additives are used as a dopant and its influence on the microstructure, phase, sintering and microwave dielectric properties of $Ba(Mg_{1/2}Ta_{2/3})O_3$ system were investigated by

Surendran et al.[13] The effect of sintering time on the microwave dielectric properties and crystal structure of Y_2BaZnO_5 ceramic was investigated by Yoshida et al [14]. Doping effects on the dielectric properties of cerium oxide as a ceramic dielectric resonator was studied by Santha et al [15,16,17]. The choice of dopant is an important factor in determining the sintering and dielectric behavior of ceramics.

2. Experimental

Polycrystalline samples of $LnTiTaO_6$ (Ln = Nd and Ce) ceramic materials were prepared from powders of analar Pr_6O_{11}, Sm_2O_3, Dy_2O_3, TiO_2 (CDH, 99.9%) and Ta_2O_5 (NFC, India) by the conventional solid state ceramic route. The chemicals were weighed in stoichiometric ratios and mixed thoroughly in acetone medium in an agate mortar. The samples were dried and calcined at 1200 ^oC for 5 hours in electrically heated furnace. A definite mass of calcined powder was mixed with 1 weight percent Zinc Oxide and ground well. To this 5 % polyvinyl alcohol was added as a binder and again ground well and dried. The powder was then pressed in the form of a cylindrical pellet at 100 MPa pressure using a hydraulic press. In a similar way pellets were made with 2,3 and 4 weight percent doping. The sintered samples were polished well and the density was measured using Archimedes method. Polished samples were thermally etched at a temperature 50^oC below the sintering temperature and used for Scanning Electron Microscopy (SEM) (Hitachi S 2400). Powdered samples were used for X-ray diffraction studies using Cu K_α (Philips Expert Pro) radiation. The dielectric properties of the samples were measured in the microwave frequency range using the network analyzer (Agilent 8753 ET) and the variation of resonant frequency with temperature was measured with the help of Keithly 2000 multimeter attached with Keithley 2001 model TC scanner. The entire data acquisition process was controlled by a software 'Integrated Microwave Materials Characterisation Tool' (IMMACT). The specimen was placed at the center of a cylindrical cavity whose size is 3-4 times greater than it. The microwave was coupled to the specimen through E-field probes and $TE_{01\delta}$ mode of resonance whose quality factor is intimately related to the dielectric loss, was identified. The dielectric constant (ε_r) and the unloaded quality factor (Q_u) were then calculated using the computer interfaced network analyzer. The coefficient of thermal variation of resonant frequency (τ_f) was also measured over a range of temperature 30-70^oC.

3. Results and discussion

The pure $CeTiTaO_6$ ceramics was sintered at 1450 °C. The doping of ZnO reduced the sintering temperature by more than 100°C. The density is greater than 95 % of the theoretical density for all the samples. Figure 1 shows the variation of the sintering temperature with respect to the percentage of doping of ZnO.

The XRD patterns of pure $CeTiTaO_6$ ceramics and typical 4 % ZnO doped samples are shown in figure 2. It is evident from the XRD patterns that there is no considerable phase change for the doped sample when compared with the XRD pattern of pure sample. Secondary phases of $Zn_{0.17}Ta_{0.33}Ti_{0.5}O_2$ (JCPDS 39-292) and Ce_2O_3 (JCPDS 49-1458) can be observed in the 4 % ZnO doped sample of $CeTiTaO_6$. The presences of these minor secondary phases is one of the reasons for the lowering of sintering temperature. The microwave dielectric properties of zinc oxide doped samples of $CeTiTaO_6$ are given in tables 1. Figure 3 shows the variation of microwave dielectric properties of $CeTiTaO_6$ with various doping concentrations of ZnO. Doping of ZnO increases the dielectric constant (ε_r) for all the samples while the variation of temperature coefficient of resonant frequency increases on doping concentrations up to 3% and decreases for 4 wt% doping

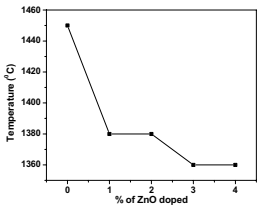

Fig. 1 Variation of sintering temperature of $CeTiTaO_6$ with ZnO doping

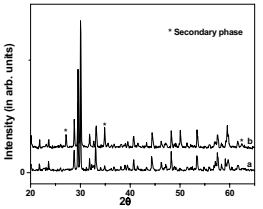

Fig.2 XRD patterns of (a) Pure $CeTiTaO_6$ (b) 4% ZnO doped $CeTiTaO_6$ ceramics

Table 1. Microwave dielectric properties of ZnO doped $CeTiTaO_6$ ceramics

Percentage of ZnO	Frequency (GHz)	Q_u x f (GHz)	Dielectric constant (ε_r)	τ_f (ppm/K)
0	4.688	9700	41.09	70
1	4.702	8539	41.29	55
2	4.684	6918	41.48	53
3	4.887	5811	41.86	49
4	4.622	8966	42.59	55

.

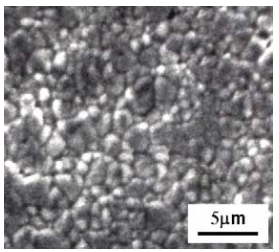

Figure 4a. SEM image of sintered pellet of pure $CeTiTaO_6$

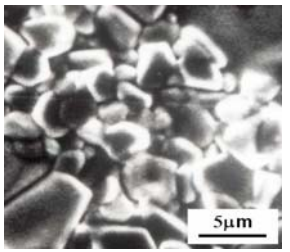

Figure 4b SEM image of sintered pellet of 4 % ZnO doped $CeTiTaO_6$

The SEM images of the sintered samples of pure and typical 4 % ZnO doped $CeTiTaO_6$ ceramics are shown in figures 4a and 4b respectively. It is evident from the SEM images that the samples are well sintered. Considerable grain growth is observed in the image of the doped sample which may be another reason for the variation in the properties of these ceramics.

4. Conclusion

High temperature processing requirements of $CeTiTaO_6$ ceramics can be reduced by ZnO doping with improvement in the microwave dielectric properties. The reduction in sintering temperature is due to the formation of small amount of secondary phases, even then the major phase remains as $CeTiTaO_6$ itself. $CeTiTaO_6$ with 2 % and 3 % ZnO doping is found to have increased dielectric constant and deceased variation of temperature coefficient of resonant frequency while compared with pure $CeTiTaO_6$.

Acknowledgements

We are grateful to Dr. M. T. Sebastian for his help in microwave measurements. The authors Sam Solomon and H. Padma Kumar are thankful to Kerala State Council for Science, Technology and Environment (KSCSTE) for financial assistance

5. References

[1] R.D. Richtmyer, "Dielectric Resonators", J. Appl. Phys, Vol 10, No 6, pp391-398 1939
[2] R. J. Cava, "Dielectric materials for applications in microwave communications", J. Mater. Chem, Vol 11, pp54-62, 2001.
[3] S. Nomura, K. Toyama and K. Kaneta "Mixture Behavior and Microwave Dielectric Properties in the Low-fired TiO_2-CuO System", Jpn. J. Appl. Phys, Vol 21, No 10, pp L624-L626, 1982
[4] G. Wolfram and H.E. Goebel, "Existence range, structural and dielectric properties of $Zr_xTi_ySn_zO_4$ ceramics (x+y+z=2) "Mater. Res. Bull, Vol 16, No 11, pp1455-1463, 1981
[5] H. Sreemoolanathan, M.T. Sebastian, P. Mohanan, "High permittivity and low loss ceramics in the BaO-SrO-Nb_2O_5 system", Mater. Res. Bull, Vol 30, No 6), pp 653-658, 1995
[6] M.T. Sebastian, J. Mater. Sci. Mater. Electron, "New low loss microwave dielectric ceramics in the BaO-TiO_2-$Nb_2O_5Ta_2O_5$ system", Vol 10, No 7, pp 475-478, 1999
[7] X. Qi, H.G. Gallagher, T.P.J. Han and B. Henderson, "Modified czochralski growth and characterization of $ReTiNbO_6$ crystals", J. Cryst. Growth, Vol 180, pp73-80, 1997
[8] X. Qi, R. Illingworth, H. G. Gallagher, T.P.J. Han and B. Henderson, "Potential laser gain media with stoichiometric formula $ReTinbO_6$", J. Cryst. Growth, Vol 160, pp111-118, 1996
[9] K.P. Surendran, Sam Solomon, M.R. Varma, P. Mohanan and M.T. Sebastian, "Microwave dielectric properties of $RETiTaO_6$ (RE = La, Ce, Pr, Nd, Sm, Eu, Gd, Tb, Dy, Ho, Y, Er, Yb, Al, and In) ceramics", J. Mater. Res, Vol 17, No 10, pp2561-2566, 2002
[10] M.T. Sebastian, S. Solomon, R. Ratheesh, J. George, P. Mohanan, "Preparation, Characterization, and Microwave Properties of $RETiNbO_6$ (RE = Ce, Pr, Nd, Sm, Eu, Gd, Tb, Dy, Y, and Yb) Dielectric Ceramics", J. Am. Ceram. Soc, Vol 84 No 7, pp1487-1489, 2001
[11] Cheng-Liang Huang, Chung-Long Pan, Shen-Jiunn Shium, "Liquid phase sintering of $MgTiO_3$–$CaTiO_3$ microwave dielectric ceramics" Materials, Chemistry and Physics, Vol 78, No 1, pp111-115, 2002
[12] Cheng-Liang Huang, Ming-Hung Weng, "Liquid phase sintering of (Zr,Sn)TiO_4 microwave dielectric ceramics", Mater. Res. Bull, Vol 35 No 11 pp1881-1888, 2000
[13] K.P. Surendran, P. Mohanan, M.T. Sebastian, "The effect of glass additives on the microwave dielectric properties of $Ba(Mg_{1/3}Ta_{2/3})O_3$ ceramics", J. Solid state chemistry, Vol 177, No 11, pp4031-4036, 2004
[14] Akinori Yoshida, Hirotaka Ogawa, Akinori Kan, Takashi Kondo, "Sintering time dependence of microwave dielectric properties and crystal structure in Y_2BaZnO_5 ceramic", J. Eur. Ceram. Soc, Vol 25, No 12, pp2897-2900, 2005
[15] N. Santha, M.T. Sebastian, P. Mohanan, Neil McN. Alford, K Sarma, R.C. Pullar, S. Kamba, Alexej Pashkin, Polina Samukhina and Jan Petzelt. "Effect of doping on the dielectric properties of CeO_2 in the microwave and far-infrared frequency range", J. Am. Ceram. Soc, Vol 87, pp1233-7, 2004
[16] S. Solomon, N. Santha, I.N. Jawahar, H. Sreemoolanathan, M.T. Sebastian, P. Mohanan, "Tailoring the microwave dielectric properties of $BaRE_2Ti_4O_{12}$ and $BaRE_2Ti_5O_{14}$ ceramics by compositional variations" J. Mater. Sci: Materials in Electronics, Vol 11, No 8, pp595-602, 2000
[17] Sam Solomon, James T. Joseph, H. Padma kumar., Jijimon K. Thomas, "Effect of ZnO doping on the microwave dielectric properties of $LnTiNbO_6$ (Ln = Sm or Dy) ceramics" Mat.Lett, Vol 60, pp2814-2817, 2006

Proceedings of APSYM2006, Dec. 14-16., Dept. of Electronics, CUSAT, India.

EFFECT OF DOPANTS ON THE LOW TEMPERATURE MICROWAVE DIELECTRIC PROPERTIES OF $BA(ZN_{1/3}TA_{2/3})O_3$ CERAMICS

Manoj Raama Varma
Regional Research Laboratory, CSIR, Trivandrum – 695 019 India
Email: manojraamavarma@yahoo.co.uk

Abstract

$Ba(Zn_{1/3}Ta_{2/3})O_3$ has been prepared with different dopants that gave best microwave dielectric properties at room temperature. Effects of different dopants on the low temperature microwave dielectric properties BZT were investigated. With decrease in temperature, loss tangent was found to decrease marginally and then increase at temperatures lower than 100 K. Increase in loss factor at lower temperatures were found to be less for dopants with smaller ionic radii. Dielectric constant was found to be almost independent of temperature. Temperature coefficient of resonant frequency slowly decreased from a positive value to negative value when temperature was lowered. Temperature at which τ_f becomes zero was found to vary for different dopants. There is a temperature stable region for tanδ, ε_r and τ_f which varies for different dopants.

Introduction

Effect of different dopants on microwave dielectric properties as well as the mechanism by which different dopants improve the microwave dielectric properties of BZT varies from dopant to dopant. The cryogenic behaviour of dielectric properties of single crystals has generated a lot of interest as a tool which can throw light into the intrinsic dielectric loss factor of crystals[1]. In an ideal crystal the main reason for dielectric loss at microwave frequency is due to the interaction of the microwave field with the lattice vibration. Hence the quality factor increases at cryogenic temperature. The intrinsic Q factor of a low loss material is limited by the loss tangent of the dielectric which in turn depends on the unharmonicity terms in the potential energy when pair of atoms is at a mean separation[1,2].

Microwave dielectric properties of $Ba(Sn,Mg,Ta)O_3$, $Ba(Zr,Zn,Ta)O_3$ and (Zr,Sn)TiO_4 at cryogenic temperatures down to 20 K were studied by Wakino[3,4]. They observed that tanδ of all materials decreased up to 100K and then showed an increase. Dielectric loss tangents of these materials increased proportionately to the temperature and their third harmonic distortion levels showed a strong correlation with dielectric loss tangents. In addition unannealed BMT may contain a large number of point defects like oxygen vacancies which also decrease the quality factor at cryogenic temperatures.. Stein[5] et al. studied the dielectric properties of BMT at cryogenic temperatures and observed that the dielectric loss of BMT increases with decrease of temperature due to the presence of paramagnetic impurities. The present investigation aims at studying the low temperature microwave dielectric properties of BZT.

Experimental

BZT has been synthesized in pure and doped forms as described elsewhere[6]. Microwave dielectric property measurement as function of temperature was done using a microwave setup with a cryogenic attachment. The cryogenic system is a commercial cryo-cooler (APD-204S) in which cooling is performed by means of a thermodynamic close cycle of helium gas. The dielectric resonator was mounted on the cold head of the cryocooler taking utmost care to establish good thermal contact between the cavity and the cryocooler using indium foil. The chamber was evacuated to pressure less than 10^{-5} mbar in order to reduce the convection losses. Radiation losses are minimized using a thermal shield maintained at 77K by attaching to the cryostat first stage. Microwave was coupled to the DR using low loss microwave cables to the resonator through two opposite loop probes. The DR was excited with microwave sweep oscillator HP8350B and the resonant frequency and Q-value of TE_{011} modes was measured using the full bandwidth at half power point method by scalar network analyzer (HP8757D). The DR was cooled down to 20 K and the temperature was then raised in steps. A temperature controller (Lake Shore 331S) was used to control temperature by a PID regulator using a Si diode sensor and a heater fixed on the cold finger. A second Si-sensor was attached to the top of the cavity. It was allowed to warm up sufficiently slowly to keep the resonator in thermal equilibrium. At each temperature point, the resonant frequency (f), 3-dB bandwidth (Δf) and insertion loss (IL) were recorded. using a personal computer and an IEEE 488 data bus linking the sweep oscillator, scalar network analyzer and the temperature controller. A visual programming language HP VEE 7.0 was employed for controlling instruments, developing the data interface, creating a customized data display and data collection and storing the data into a data base for evaluation of the unloaded Q-value. The unloaded Q-value of the resonator was obtained, using the relation, $Q_0 = Q_L\,[1\text{-}10^{-(IL/20)}]^{-1}$, where Q_L (=f / Δf) is the measured loaded Q-value.

Results and discussion

Fig.1 show the variation of tanδ with temperature for undoped BZT and BZT doped with 0.5 mol % dopants. Dopants used for 0.5 mol% dopant addition were Ti, Mn, Sb and In which gave excellent microwave dielectric properties in the earlier investigation. For undoped and doped BZT, it can be seen that the tanδ marginally decreases as the temperature is decreased. When the temperature is below 100K, increase in tanδ become drastic. Increase in tanδ is found to be maximum for undoped BZT. For doped BZT, increase in tanδ is found depend on ionic radius of the dopant. Dopant with smallest ionic radius is Ti which has minimum increase in tanδ at lower temperatures. As the ionic radius increases, increase in tanδ also increases and is maximum for In which has the highest ionic radii. Same trends can be seen in Fig.2 which shows the variation of tanδ with temperature for undoped BZT and BZT doped with 1.0 mol % dopants. Here too, the increase in tanδ at lower temperatures is found to be maximum for undoped BZT increases with ionic radius of the dopant. Loss factor increase is minimum for doped BZT with Zr, which has minimum ionic radius among the dopants and the loss factor increase is found to be maximum for Ce which has highest ionic radii. Variation of tanδ with temperature is similar to the observation of Wakino[22] and Stain[23] described before and could be due to the large number of point defects like oxygen vacancies[22] or

due to the presence of paramagnetic impurities which decrease the quality factor at cryogenic temperatures.

Fig.3 and Fig.4 show variation of dielectric constant with temperature for undoped BZT and doped BZT with 0.5 mol% and 1 mol % dopants. From figures it can be seen that the dielectric permittivity varies with the dopant but remains almost constant over the temperature range. The dependence of dielectric permittivity on ionic radii is similar to that of loss tangent. Hence it can be seen that dielectric constant is temperature stable. Fig.5 and Fig.6 show variation of temperature coefficient of resonant frequency with temperature. It can be seen that temperature coefficient of resonant frequency decreases with temperature and become zero at a particular temperature and then changes to a negative value on further cooling. There is temperature stable for τ_f which varies for different dopants as shown in figures. Temperature at which τ_f becomes zero is found to be different for different dopants and is given in table-1 from which no specific trends with respect to ionic radius could be obtained. Reduction in τ_f could be due to the small reduction in dielectric constant which reduces τ_ε and there by affects τ_f . But this effect may not be prominent enough to change sign of τ_f and then move it in negative direction. Hence a weak phase transformation is expected to cause this effect. However more studies are needed to understand the mechanism behind the variation of τ_f at cryogenic temperatures.

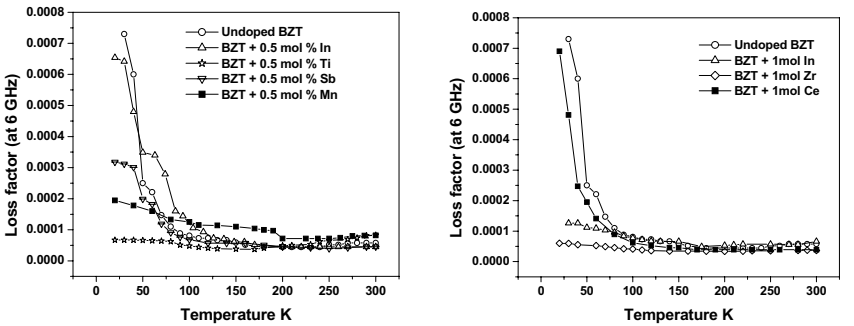

Figure-1 & 2 Variation of loss factor with temperature for 0.5 and 1 mol% dopant addition

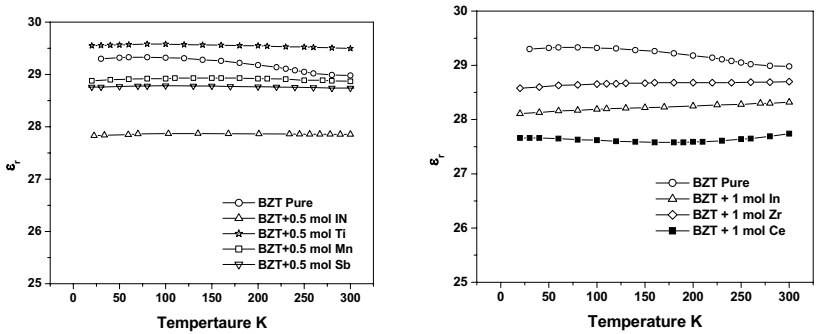

Figure-3& 4 Variation of dielectric constant with temperature for 0.5 mol% and 1 mol% dopant addition

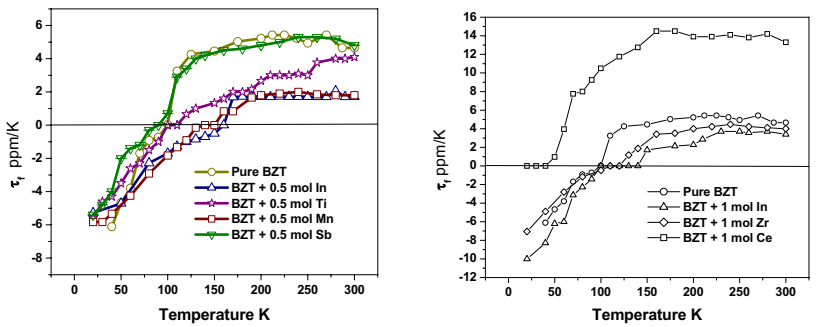

Figure-5 &6 Variation of temperature coefficient of resonant frequency with temperature for 0.5 mol% and 1 mol % dopant addition

References

1. V. Gurevich and A. K. Tagantsev, Sov. Phys.JETP. 64, 142, 1986.
2. V. B. Braginsky, V. S. Ilchenko and K. S. Bagdassarov, Phys. Lett. 120,300 1987.
3. K. Wakino, M. Murata and H. Tamura, J. Am. Ceram. Soc. 69, 34, 1986.
4. K. Wakino and H. Tamura, Ceram. Trans. 15 , 305, 1990.
5. S. R. Stein, Proceedings of the 29th Annual Frequency Control Symposium, (Electronic Industries Association, Washington, D.C.), 321 , 1975.
6. M. R. Varma, R. Reghunandan and M. T. Sebastian, Jpn. J. Appl. Phys. 44, 298, 2005.

Proceedings of APSYM2006, Dec. 14-16., Dept. of Electronics, CUSAT, India.

Low Temperature Synthesis of $BiNbO_4$ for Microwave dielectric resonator application

H. Muthurajan[1], HH Kumar[1], DK Kharat[1], V Ravi[2,*]
[1]Armament Research & Development Establishment, Pune-411 021, India
[2]Physical and Materials Chemistry Division, National Chemical Laboratory, Pune 411008
E-mail address: r.venkat@ncl.res.in (V. Ravi)

Abstract

The requirements of ceramic dielectric resonators used at microwave frequencies are high dielectric constant (ε_r > 100), large quality factor (Q >10,000) and low temperature coefficient of resonant frequency (τ_f). But many dielectric resonator ceramics have higher sintering temperatures (above 1350^{0}C) and are too high to use the low melting-point silver and copper electrode. Bismuth-based dielectric ceramics were well known as low-fired materials and had been investigated for various applications. $BiNbO_4$ is one among the promising material with low sintering temperature for microwave dielectric resonator. This material has good quality factors, especially considering low cost and simplicity of the materials compared with complex perovskites. Here we report our work on low temperature synthesis of $BiNbO_4$ by co-precipitation method. This method is not reported for the preparation of $BiNbO_4$ in the literature. The details about synthesis procedure and characterization are presented in this paper.

1. Introduction

Communication at microwave frequencies has lead to the proliferation of commercial wireless technologies such as cellular phones and global positioning systems. The requirement of ceramic dielectric resonators used at microwave frequencies are high dielectric constant, a high Q value(reciprocal of dielectric loss) and a low temperature coefficient of resonant frequency [1-5] . Most of the known commercial microwave dielectrics such as $Sn_xZr_{1-x}TiO_4$ and $Ba(Mg,Ta)O_3$ are can be sintered only at very high temperatures (>1400˚ C). The so-called passive integration for miniaturization is performed using multiplayer ceramic technology whereby green ceramic tapes of different materials corresponding to different passive functions are laminated and co-fired at low temperatures. Therefore it is necessary to develop microwave dielectric materials that can be sintered at temperatures lower than the melting point of internal metal conductor such as Cu or Ag. Recently, $BiNbO_4$ was reported to be promising microwave dielectric material with relatively lower melting point [1-5]. The reported values for $BiNbO_4$ are the temperature coefficient of resonant frequency ~50 ppm/˚C, the dielectric constant ~ 45, and Q=14,000 [1-5].

Generally traditional solid state method is used for the preparation of oxides and its drawbacks are well documented in the literature. The wet-chemical techniques such as combustion, alkoxide sol-gel and coprecipitation were found to produce these oxides with several advantages namely, nanosized particles (hence high surface area), high reactivity and very good homogeneity in composition. Sometimes metastable phases also formed by these methods. Recently citrate gel method was reported to prepare nanocrystalline $BiNbO_4$ powders [1]. Co-precipitation is one of the more successful techniques for synthesizing ultrafine ceramic powders having narrow particle size distribution [6-13].

The purpose of this study was to prepare ultrafine $BiNbO_4$ powders using co-precipitation technique from simple water-soluble inorganic salts. This process can avoid complex steps such as refluxing of alkoxides, resulting in less time consumption compared to other techniques. The only drawback of this method is that all the cations should have similar solubility product.

2. Experimental

For preparing $BiNbO_4$ compound, niobium (V) oxide, bismuth (III) nitrate, bismuth oxide and ammonium hydroxide were used as starting materials and they were of AR grade (Loba cheme). For the preparation of $BiNbO_4$ by coprecipitation, stoichiometric amount of $Bi(NO_3)_3.5H_2O$ was dissolved in minimum amount of dilute HNO_3 to avoid precipitation of Bi ions and required quantity of Nb_2O_5 was dissolved in minimum amount of HF after heating in hot water bath for 5 hours and both are mixed together. An excess ammonium hydroxide is added by dropwise with constant stirring to the above solution mixture until pH > 9 at room temperature to ensure complete precipitation. After precipitation, it is filtered and washed several times with distilled water to remove the anions and dried in an oven at 100˚C for 12 hrs. The oven-dried precursor was calcined at various temperatures ranging from 200 to 800˚ C for 12 hours to get phase pure samples. For comparison, the samples are also prepared by the conventional ceramic method. Bismuth oxide (Bi_2O_3) and niobium oxide (Nb_2O_5) are taken in stoichiometric ratio and mixed, ground several times and heated at 800˚ C for 12 hours. To ensure completion of reaction, the powders were reground after first cycle of calcination and heated few times at this temperature. The XRD (Rigaku miniflex X-ray Diffractometer) was employed to characterize these powders. The powder X-ray pattern were recorded for all the samples calcined at various temperatures by using Cu-K_α. For lattice parameter and interplanar distance (d) calculation, the samples were scanned in the 2θ range of 10 – 80^o for a period of 5s in the step scan mode. Silicon was used as an internal standard. The standard least squares method was used to determine the lattice parameters.

3. Results and Discussion

Fig 1 shows XRD pattern of the co-precipitated powders calcined at different temperatures ranging from 200 to 400˚ C for 6 hours. At 200˚ C the peaks corresponding to bismuth oxide (45-1344) and niobium oxide (43-1042) were seen in XRD. It can be observed that the incipient product phase begins to form at temperatures as low as at 400˚ C. The complete phase formation occurs at 600˚ as observed from Fig.3. It is the lowest temperature reported for the formation of $BiNbO_4$ phase. These powders are highly crystalline as compared to that prepared by ceramic method supported by the strong intense XRD peaks. The crystal structure is orthorhombic and all the d-lines pattern match with reported values (JCPDS- 16-295). The calculated lattice parameters by least square fit are a = 4.981 Å b= 11.713 and c = 5.673 Å. Fig.3 illustrates the XRD for samples prepared by the solid state method and calcined at different temperatures. At lower temperatures, the XRD peaks corresponding to individual oxides are observed and the product phase begins to form only at 600˚ C. The XRD shows the reaction is incomplete as the individual oxides also present along with the product. However, all the peaks corresponding to the phase formation is complete only at 800˚ C (fig.4) For compassion, ideal XRD pattern of $BiNbO_4$ was also shown in that figure. The average

Proceedings of APSYM2006, Dec. 14-16., Dept. of Electronics, CUSAT, India.

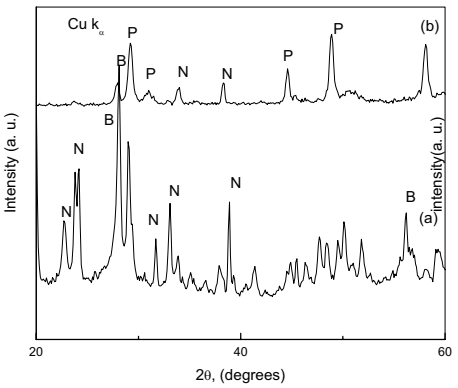

Fig. 1. XRD of $BiNbO_4$ precursor powder calcined at (a) 200 ˚C (b) 400˚C. The alaphabet 'B' correspond to Bi_2O_3, 'N' to Nb_2O_5 and 'P' to product phases.

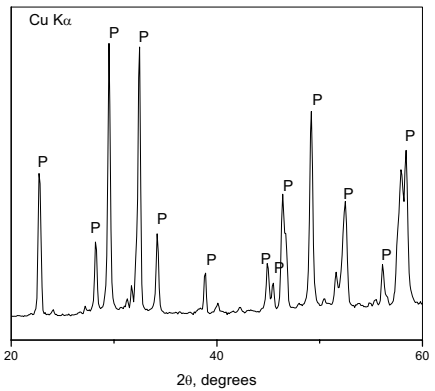

Fig. 2. XRD of $BiNbO_4$ powder calcined at 600˚C

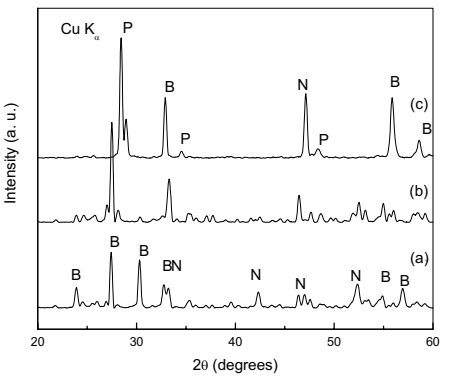

Fig. 3. XRD of $BiNbO_4$ powder (prepared by the solid state method) calcined at (a) 200˚C (b) 400 ˚C and (c) 600˚C. The alaphabet 'B' correspond to Bi_2O_3 and 'N' to Nb_2O_5 and 'P' to

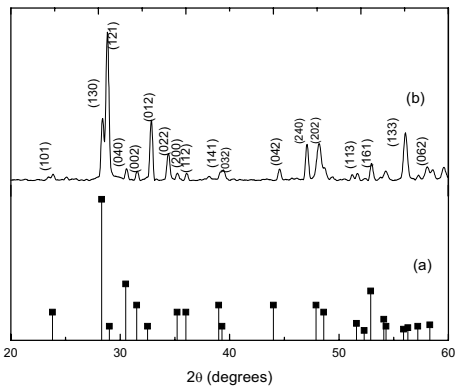

Fig. 4. XRD of $BiNbO_4$ powder (a) ideal case and (a) calcined at 800˚C prepared by the solid state method

particle size for the coprecipitated powders (calcined at 600˚ C for 6 hours) calculated from Scherrer's formula ($t = K\lambda/B\cos\theta_B$) where t is the average size of the particles, assuming particles are spherical, K=0.9, λ is the wavelength of X-ray radiation, B is the full width at half maximum of the diffracted peak and θ_B is the angle of diffraction) were ranging from 50 nm. The measured dielectric constant was 43 for $BiNbO_4$ prepared by co-precipitation method.

4. Conclusions

A simple co-precipitation method was used to prepare ultrafine particles of $BiNbO_4$. This method has advantage of forming this phase at much lower temperature as compared to samples prepared by traditional solid-state method.

References:

[1] N.Wang, M..Y.Zhao, Z.W.Yin and W.Li, "Low-temperature synthesis of β-BiNbO4 powder by citrate sol–gel method", Mater.Lett, Vol 57 No.24-25, pp4009-4013, 2003

[2] H.Kagato, T.Inoue, J.Kato, I.Kameyama, "Low-Fire Bismuth-Based Dielectric Ceramics for Microwave Use", Jpn. J. Appl. Phys. Vol. 31, pp.3152-3155, 1992

[3] W. Choi, K.Y. Kim, M.R. Moon and K.S. Bae, "Effects of Nd2O3 on the miacrowave dielectric properties of BiNbO4 ceramics", J. Mater. Res., Vol. 13, pp. 2945-2949, 1998.

[4] M. A. Subramanian and J. C. Calabrese, "Crystal structure of the low temperature form of bismuth niobium oxide [α-$BiNbO_4$]", Mater.Res.Bull Vol. 28, No. 6, pp. 523-529, 1993.

[5] N.Wang, M.Y.Zhao, Z.W.Yin and W.Li, "Effects of complex substitution of La and Nd for Bi on the microwave dielectric properties of $BiNbO_4$ ceramics", Mater. Res. Bull, Vol. 39, No. 3, pp. 439-448 , 2004.

[6] S.R. Dhage, V. Ravi and S.K. Date, "Preparation of microwave dielectric, $Sn_{0.2}Zr_{0.8}TiO_4$", Bull. Mater. Sci., Vol. 26, No. 2, pp. 215-216, 2003.

[7] S. P. Gaikwad, S. B. Dhesphande, Y. Khollam, V. Samuel and V. Ravi, "Coprecipitation method for the preparation of nanocrystalline ferroelectric $CaBi_2Ta_2O_9$", Mater. Lett Vol. 58, No.27-28, pp. 3474-3476, 2004.

[8] S.P.Gaikwad, H.S.Potdar, V.Samuel and V.Ravi, "Co-precipitation method for the preparation of fine ferroelectric $BaBi_2Nb_2O_9$", Ceram. Inter. Vol 31, No. 3, pp. 379-381, 2005.

[9] V. Ravi, "A coprecipitation technique to prepare SrNb2O6", Mater. Character., Vol. 55, No. 1, pp. 92-95, 2005

[10] V. Ravi and S. C. Navale, "A co-precipitation technique to prepare $CaNb_2O_6$", Ceram. Inter. Vol 32, No 4, pp. 475-477, 2006

[11] V. Samuel, A. B. Gaikwad and V. Ravi, "A coprecipitation technique to prepare $NaNbO_3$ and $NaTaO_3$", Bull. Mater. Sci, Vol. 29, No. 2, pp.123-126, 2006

[12] S. C. Navale, A. B. Gaikwad and V. Ravi, "Synthesis of MgNb2O6 by coprecipitation", Mater. Res. Bull, Vol. 41, No. 7, pp. 1353-1356 , 2006

[13] S. C. Navale, A. B. Gaikwad and V. Ravi, "A coprecipitation technique to prepare $LiTaO_3$ powders" Mater. Lett Vol 60 No.8 pp. 1047-1048, 2006

The effect of filler content on the dielectric properties of PTFE/ZAT composites

Sherin Thomas[a], P. Mohanan[b], M. T. Sebastian[a]

[a]Materials and Minerals Division, Regional Research Laboratory,Trivandrum
[b]Department of Electronics, Cochin University of Science and Technology, Cochin.

Abstract

$0.83ZnAl_2O_4$-$0.17TiO_2$ (ZAT)/PTFE composites were synthesized by powder processing method. The effect of different volume fraction of ZAT (0 – 0.6) on the dielectric properties of the composites were investigated at 1 MHz and 7 GHz. The dielectric properties (dielectric constant and dielectric loss) were found to increase with the ZAT content. The experimental results were compared with that of the theoretical values predicted using Lichtenecker, Maxwell-Garnet, Jayasundere, Poon-Shin formulae. They were found to agree well with the predicted values for low filler content.

1. Introduction

The recent developments in electronics and circuit assembly technology demands low dielectric constant materials for the packaging of RF, microwave and optical products [1]. These substrate materials must possess low dielectric constant for increasing the signal propagation speed, low dielectric loss, good frequency with temperature in a wide spectral range and good mechanical strength [2]. Polytetrafluoroethylene (PTFE) has been widely used in packaging and substrate applications due to its low dielectric constant ($\varepsilon_r \approx 2$) and excellent physical and chemical properties. But the applications are limited due to the high coefficient of thermal expansion and poor thermal and mechanical strength. One way to improve their property is to form a ceramic-polymer composite consisting of ceramic particles in a polymer matrix. Many studies were conducted in ceramic-polymer composite materials for various applications in packaging and substrate industries [1-5].

Earlier studies [6] reveal that $0.83ZnAl_2O_4$-$0.17TiO_2$ (ZAT) ceramics possess good thermal stability and microwave dielectric properties. The dielectric constant of ZAT is 12 and the dielectric loss is less than 0.001 at 5 GHz. Thus the addition of proper volume fraction of ZAT as a filler into the polymer matrix can improve its property to certain extent. The dielectric property of the composite depends on the volume fraction, size and shape of the filler and also on other factors such as preparation method, interface and interaction between the filler and the polymer [4]. The effective dielectric properties (ε_r and $\tan\delta$) of the composite are estimated using classical mixing formulae such as Maxwell-Garnet equation, Lichtenecker, Jayasundere, Poon-Shin formulae and the experimental results were compared [2,7].

2. Experimental

The $0.83ZnAl_2O_4$-$0.17TiO_2$ (ZAT) ceramics were prepared by the conventional solid state ceramic route. ZAT/PTFE (Hindustan Fluorocarbons, Hyderabad, India) composites were prepared by powder processing method. The powdered ZAT was mixed with acrylic acid solution for 1h and dried. This will provide an active surface for binding with polymer since acrylic acid is a well-known polymerizing agent. Different volume fractions (0 to 0.6) of treated ceramics and PTFE powders were dispersed in ethyl alcohol using ultrasonic mixer for about 1 h. Then a dry powder mixture was obtained by removing the solvent at 70°C under stirring. The homogenously mixed PTFE/ZAT powders

were then compacted under uniaxial pressure of 50 MPa for 1 minute. The cylindrical and rectangular pellets thus obtained were kept at 310°C for 2hrs.

The thin pellets with diameter 14 mm and thickness 1 mm were electroded by uniformly coating with silver paste on both sides in the form of ceramic capacitors. The low frequency dielectric properties were measured by LCR meter (Hioki 3532-50). HP 8510 Vector Network Analyzer was used to characterize the composite materials at microwave frequencies. For this purpose rectangular samples of dimensions (40x2x1 mm^3) were made and the dielectric properties were measured using cavity perturbation technique [8,9].

3. Results and Discussion

Fig. 1(a) and (b) shows the variation of dielectric constant and dielectric loss with volume fraction of ZAT at 1 MHz and 7 GHz respectively. It is seen that both the dielectric constant and loss increases with the amount of ZAT. PTFE has a dielectric constant of nearly 2. The increase in the dielectric constant of the composite is due to the comparatively high dielectric constant of the ZAT filler (ε_r = 12). The dielectric properties of the ZAT/PTFE composite are largely influenced by several factors such as air gap, water content and interface phase between the ZAT and the PTFE. A comparative study of the Fig. 1 (a) and (b) shows that the dielectric loss increases in the microwave frequency (7 GHz) as compared to that at low frequency (1 MHz). As volume fraction of the filler increases the density of the composite is lowered due to the air gap and weak binding. This will lead more air and water content inside the composite. At low frequency, the polar liquid dielectric material (ie. water) has both electronic polarization and dipolar orientational polarization. At microwave frequency range the large dielectric loss is due to the dipole relaxation of water [2] and also the increase of interface phase between ZAT and PTFE. These losses are increased with the increase in the amount of ZAT filler.

The prediction of the effective dielectric constant of the composite from the dielectric constant of the components and the volume fraction of the filler is a very important factor for engineering applications. The following equations are used to calculate the effective dielectric constant of the composites with low filler content:

(1) Lichtenecker Equation
$$ln\varepsilon_{eff} = f\,ln\varepsilon_i + (1-f)ln\varepsilon_m$$

(2) Maxwell – Garnet Equation
$$\frac{\varepsilon_{eff}-\varepsilon_m}{\varepsilon_{eff}+2\varepsilon_m} = f\frac{\varepsilon_i-\varepsilon_m}{\varepsilon_i+2\varepsilon_m}$$

(3) Poon – Shin Equation
$$\varepsilon_{eff} = \varepsilon_m\left[1+\frac{f\left(\varepsilon_i/\varepsilon_m - 1\right)}{f+\frac{1}{3}(1-f)\left[\varepsilon_i/\varepsilon_m\,(1-f)+f+2\right]}\right]$$

(4) Jayasundere Equation
$$\varepsilon_{eff} = \frac{\varepsilon_m(1-f)+\varepsilon_i f\left[\frac{3\varepsilon_m}{\varepsilon_i+2\varepsilon_m}\right]\left[\frac{1+3f(\varepsilon_i-\varepsilon_m)}{\varepsilon_i+2\varepsilon_m}\right]}{1-f+f\left[\frac{3\varepsilon_m}{\varepsilon_i+2\varepsilon_m}\right]\left[\frac{1+3f(\varepsilon_i-\varepsilon_m)}{\varepsilon_i+2\varepsilon_m}\right]}$$

where ε_{eff} is the effective dielectric constant of the ceramic/polymer composite, ε_i

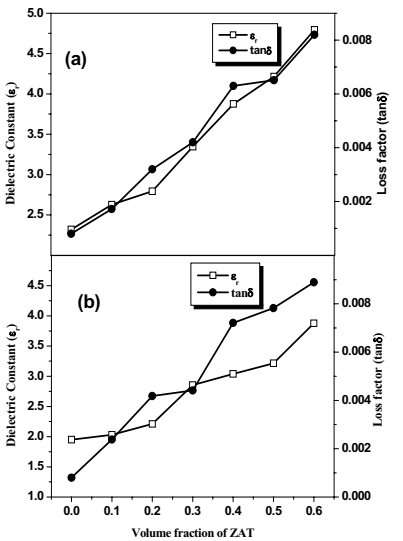

Figure 1. Variation of dielectric constant and tanδ of PTFE/ZAT composite (a) at 1MHz (b) at 7 GHz

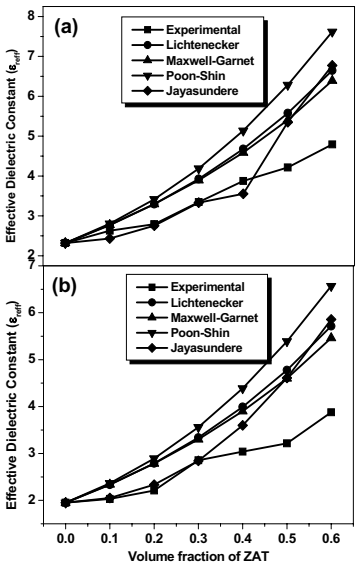

Figure 2. Comparison of experimental and theoretical dielectric constants of PTFE/ZAT composites (a) at 1 MHz (b) at 7 GHz

is the dielectric constant of the filler, ε_m is the dielectric constant of the matrix and f is the volume fraction of the filler.

Fig. 2 (a) and (b) shows the comparison between the experimental and the theoretical values of dielectric constant obtained from the above equations at 1 MHz and 7 GHz respectively. The results show that the experimental values are in good agreement with the theoretical value predicted using Jayasundere equation for low filler content (upto 0.3 volume fraction) and beyond that the deviation increases. This is due to the fact that the dielectric constant is largely influenced by the homogeneity of the component distribution. Also the mixing formulas are based on the assumption of low filler content and they fail for dense mixtures.

4. Conclusion

The ZAT/PTFE composites are prepared by the powder processing technique. The dielectric properties of the composites are studied at 1 MHz and 7 GHz. It is seen that as the amount of ZAT increases the dielectric constant and dielectric loss also increases. The experimental effective dielectric constant is in good agreement with that predicted using Jayasundere equation.

REFERENCES

[1] T. Vo Hung and F. G. Shi, "Towards model-based engineering of optoelectronic packaging materials: dielectric constant modeling", Microelectronics Journal, Vol. 33, pp. 409-415, 2002.

[2] Y. M. Wang D. C. Jia, and Y. Zhou, "Preparation and properties of $Ba_2Ti_9O_{20}$/PTFE microwave dielectric composites. *Piezoelectrics and Accoustooptics*, Vol. 24, pp. 225-229, 2002.

[3] Y-C. Chen, H-C Lin and Y-D Lee, "Effect of filler content and size on properties of PTFE/SiO_2 composites", *J. Polym. Res.*, Vol. 10, pp. 247-258, 2003.

[4] Z-M. Dang, Y-H. Zhang and S-C. Tjong, "Dependence of dielectric behavior on the physical property of fillers in the polymer-matrix composites", Synth. Met. Vol. 146, pp. 79-84, 2004.

[5] G. Subodh, C. Pavithran, P. Mohanan and M. T. Sebastian, "PTFE/$Sr_2Ce_2Ti_5O_{16}$ Polymer ceramic composites for electronic packaging applications", J. Eur. Ceram. Soc. (In Press).

[6] K. P. Surendran, N. Santha, P. Mohanan and M. T. Sebastian, "Temperature stable low loss ceramic dielectric in (1-x)$ZnAl_2O_4$-xTiO_2 system for microwave substrate applications", Eur. Phys. J. B, Vol. 41, pp. 301-306, 2004.

[7] L. Jylha, J. Honkamo, H. Jantunen and A. Sihvola, "Microstructure-based numerical modeling method for effective permittivity of ceramic/polymer composites", J. App. Phys., Vol. 97, pp. 104104, 2005.

[8] Prakash, A., Vaid, T. K. and Mansingh, A., Measurement of dielectric parameters at microwave frequencies by cavity perturbation technique. *IEEE Trans. Micro. Theory Techniques.,* Vol. 27, pp. 791- 794, 1979.

[9] Chen, L., Ong, C. K. and Tan, B. T. G., Amendment of cavity perturbation method for permittivity measurement of extremely low loss dielectrics., *IEEE Trans. Instrum. Meas.* Vol. 48, pp. 1031-1037, 1999.

Dielectric ring resonator band pass filter for 2.4 GHz WLAN frequencies

Jaimon Yohannan and K. T. Mathew

Microwave Tomography and Materials Research Lab., Department of Electronics, Cochin University of Science & Technology, Cochin, Kerala, India, PIN-682022.
Email jaimonyohannan@yahoo.com

Abstract: *A Microwave band pass filter using ring resonator is designed, fabricated and tested. Band pass filter characteristics are studied by measuring the return loss and transmission characteristics of the microstrip line fed dielectric ring resonator. S-parameters, electric field and magnetic field distributions are computed using FEM method and compared with measured results. The measured values agree with predicted values obtained using FEM. Centered at 2404 MHz the dielectric ring resonator filter shows a measured 3-dB band width of 20.6 MHz.*

Introduction: Dielectric resonator filters present a number of advantages such as low loss, high temperature stability, compactness etc. But one main drawback is that a number of spurious resonances appear. To avoid these resonances, a specific cavity and coupling window configuration must be used [1]. With the advance development of improved dielectric materials and the rapid expansion of cellular and satellite communications, dielectric resonator filters have been the source of much research. The dielectric resonator is the basic unit of a ceramic cavity filter. At the resonant frequency most of the electromagnetic energy is stored within the dielectric resonator. The most important characteristics of a dielectric resonator include: its field patterns, Q factor, resonant frequency and spurious free band width [2]. These factors are dependent on the dielectric materials used, the resonator's shape and the resonant mode used. The filters that are currently being used in wireless base stations can be divided into two main categories, coaxial cavity resonator filters and dielectric resonator filters [3-6]. While co-axial cavity filters have limited quality factor (Q) values, they offer the lowest cost design and are still being widely employed, particularly in wide bandwidth applications. With increased demands for high performance wireless systems, dielectric resonators are emerging as the baseline design for wireless base stations [7].

Filters composed of dielectric resonators give excellent in-band performance, but have poor spurious characteristics due to their crowded mode spectrum. The first step in obtaining a filter with good spurious performance is to optimally design the resonator dimensions to give a well spaced mode spectrum. Kobayashi and Miura presented mode charts specifically for these purpose and suggested the introduction of a concentric hole in $TE_{10\delta}$ mode DR to markedly improve spurious performance [8]. In this paper we propose a dielectric ring resonator loaded microstripline band pass filter with spurious response. The coupling between the resonant modes of dielectric ring resonator and a microstripline are studied. The band pass filter is evaluated by experiment and simulation studies.

Design of filter: The filter comprises a dielectric ring resonator, mounted over glass-epoxy substrate. Figure 1 (A) shows two perpendicular microstriplines etched on a rectangular glass

epoxy sheet mounted inside an aluminium cavity with SMA connection. Figure 2(A) shows the schematic diagram of dielectric ring resonator couple to the input/output microstriplines, which is loaded inside the rectangular aluminium cavity. The ring DR is excited by an input coupling probe, a microstripline (3 mm x 60 mm) of 50 ohms impedance. The filtered signal is extracted by an out put coupling microstrip line (3mm x 60 mm) which is designed perpendicular to the input microstrip line. The whole system is enclosed within a rectangular aluminium box of dimensions length = 82 mm, breadth = 82 mm and height = 25 mm.

The dimensions of the dielectric ring resonator are as follows: height = 10 mm, outer diameter = 20 mm and inner diameter = 12.5 mm, with a relative dielectric constant $\varepsilon_r = 69$. Dielectric ring resonator is formed by sintering a dielectric powder material. The resonance frequency of the ring resonator is determined by height, outer and inner diameters, and dielectric constant of the material. The S-parameters are measured with Agilent 8714 ET network analyzer. The E-field and H-field patterns are computed and optimized using Ansoft HFSS software.

Results and Discussion: Figure 1 (B) shows E-field pattern of the microstripline mounted inside the aluminium cavity, (C) shows H-field pattern distribution showing the high intensity at the input feed and low intensity at the output microstrip line. Figure 2(A) shows the dielectric ring resonator coupled to the microstrip line, loaded inside the aluminium cavity. If a high frequency signal at a frequency outside of the pass band of the dielectric resonator is applied, it is basically reflected and sent back from the input terminal without exciting the basic resonance mode in the dielectric resonator. It follows therefore that the frequency characteristics of the dielectric resonator filter is basically a band pass characteristics of the dielectric resonator as shown in figure 2. However low order modes such as the $HE_{11\delta}$ mode, $EH_{11\delta}$ mode or TE_{mnp} modes are present in the dielectric resonator in addition to the $TE_{01\delta}$ mode.

Figure 2 (B) shows E-field pattern of the microstripline fed dielectric ring resonator mounted inside the aluminium cavity, figure 2 (C) shows H-field pattern distribution showing the high intensity at the input feed and low intensity at the output microstrip line. At the resonant frequency of the DR, the magnetic field equals the electric field and electromagnetic waves can be transmitted with minimal loss. Only at a resonant frequency electromagnetic fields can sustain in the DR. The resonant frequencies of the dominant and spurious modes of a DR are important in the design of a DR filter. Figure 3 (A) shows the calculated return loss and transmission characteristics using Ansoft HFSS software. Figure 3 (B) shows the measured return loss (S_{11}) and transmission characteristics (S_{12}) of the band pass filter adopting fundamental $TE_{01\delta}$ mode of the ring dielectric resonator. It is observed that the resonant peak corresponds to the 2404 MHz frequency with a 3 dB bandwidth of 20.6 MHz. The rejection level is larger than 30 dB from 2460 MHz. Simulation results agree with measured results. Some discrepancy between them can still be observed, which can be attributed to the unexpected tolerance of fabrication.

Conclusions: A band pass filter employing a dielectric ring resonator is designed and fabricated and tested. The filter performances were evaluated through finite element analysis method and measurements using network analyzer. Resonant frequencies of the lower order modes were predicted. The simulated electric and magnetic field distributions of the microstripline and ring dielectric resonators were obtained. Centered at 2404 MHz the fabricated dielectric ring resonator filter shows a measured 3-dB band width of 20.6 MHz. Therefore the band pass dielectric ring filter can operate in the 2.4 WLAN frequency range.

Acknowledgements:
This work was sponsored by the Council of Scientific and Industrial research, Human Resource Group, Ministry of HRD, New Delhi, India. The authors thankfully acknowledge the financial support extended for the research.

Reference:

[1] I. C. Hunter, “Theory and design of microwave filters”, IEE, Stevenage, UK, 2001.
[2] I. C. Hunter, L. Billonet, B. Jarry, and P. Guillion, “Microwave filters-applications and technology", IEEE Trans. Microwave Theory Tech., Vol.50 pp. 794-805, Mar. 2002.
[3] S. J. Fiedziuzko, I. C. Hunter, T. Itoh, Y. Kobayashi, T. Nishikawa, S. N. Stitzer, and K. Wakino, "Dielectric materials, devices and circuits", IEEE Trans. Microwave Theory Tech., Vol. 50 pp. 706-720 March 2002.
[4] J. F. Liang and W. D. Blair, High - Q TE_{01} mode DR filters for PCS wireless base stations, "IEEE Trans. Microwave Theory Tech., Vol. 46, pp. 24930-2500, Dec. 1998.
[5] R. R. Mansour et al., Quasi dual-mode resonators, "IEEE Trans. Microwave Theory Tech., Vol. 48, pp. 2476 - 2482, Dec. 2000.
[6] R. R. Mansour, IEEE Microwave Magazine, pp. 68-74, March, 2004.
[7] Y. Kobayashi and M. Miura, “Optimum design of shielded dielectric rod and ring resonator for obtaining the best mode separation” IEEE MTT-S, Int. Microwave Symp. Dig., pp. 184-186, 1984.
[8] J. Hattori, T. Wada, H. Kubo and Y. Ishikawa, "2 GHz band quadruple mode dielectric resonator filters for cellular base stations”, IEEE MTT-S Int. Microwave Symposium Dig., Philadelphia, PA, 2003.

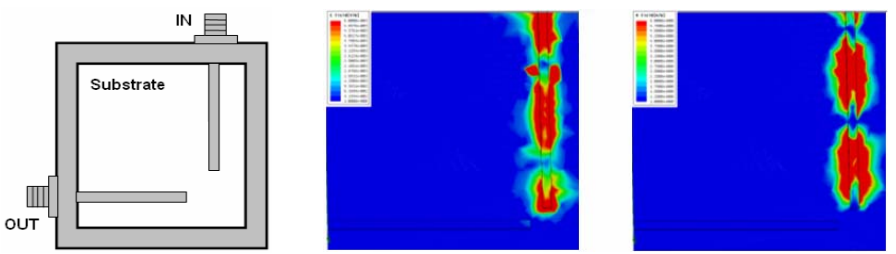

(A) (B) electric field (C) magnetic field

Fig.1. (A) Top view of the microstripline coupled rectangular aluminium cavity, (B) E-field pattern of the microstripline mounted inside the aluminium cavity. (C) H-field pattern distribution showing the high intensity at the input feed and low intensity at the output microstripline (Simulated using Ansoft HFSS).

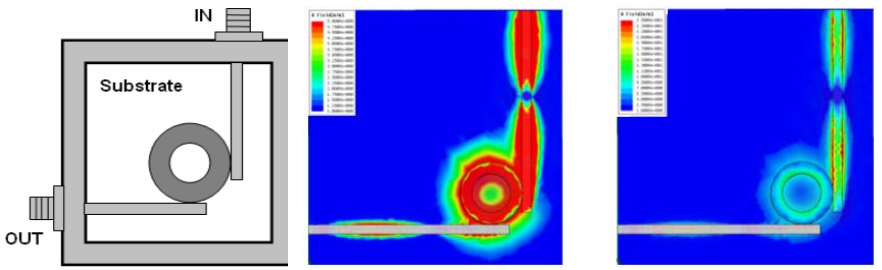

(A) (B) electric field (C) magnetic field

Figure 2. (A) Top view of the microstripline coupled dielectric ring resonator loaded rectangular aluminium cavity, (B) E-field pattern of the microstripline fed dielectric ring resonator mounted inside the aluminium cavity. (C) H-field pattern distribution showing the high intensity at the input feed and low intensity at the output microstripline (Simulated using Ansoft HFSS).

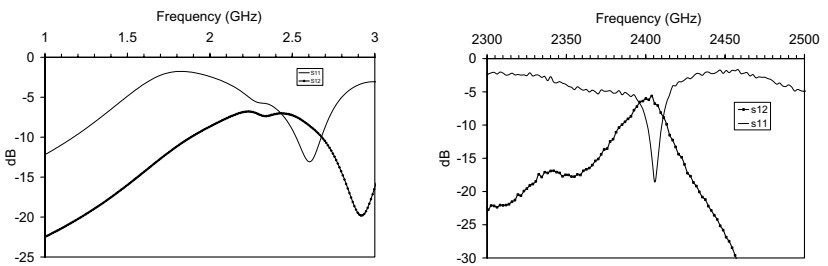

(A) (B)

Figure 3 (A) shows the simulated return loss and transmission characteristics using FEM method. (B) shows the measured return loss (S_{11}) and transmission characteristic (S_{12}) of the band pass filter.

Microwave Studies of Beta Tricalcium Phosphate Bioceramics for Medical Applications

Robin Augustine and K.T. Mathew

Microwave Tomography and Materials Research Laboratory, Department of Electronics,
Cochin University of Science and Technology,
Cochin-682022, India
Phone-91-484-2576418, Fax-91-484-2575800, e-mail: ktm@cusat.ac.in

Abstract— Beta tricalcium phosphate bio ceramics are known for their better biocompatibility and good bioresorption characteristics. Since they are biomaterials they have good interactions with microwave frequencies. β-TCP powder and pellets are prepared and is prepared and studied at the S-band microwave frequencies. Dielectric parameters such as dielectric constant, dielectric loss, conductivity and S-parameters are evaluated. This study is meant for measuring the rate of bioabsorption through microwave imaging.

Keywords- Bioceramics; beta tricalcium phosphate (b-TCP); dielectric properties, osteoconductivity; Microwave absorption

I. INTRODUCTION

In recent years the use of Ca-P materials for bone substitution, augmentation and repair has gained clinical acceptance in many areas of orthopedics and dentistry. Dental applications include fillers for periodontal bony defects, alveolar ridge augmentation, immediate tooth root replacement, coatings for dental implants and maxillofacial reconstruction. Medical applications include ear implants, spine fusion, repair of bony defects and coatings for orthopedic metal implant. Beta tricalcium phosphate ($Ca_3(PO_4)_2$, b-TCP) is found to be more biocompatible than hydroxy apatite bioeramics[1]. b-TCP was prepared by heating an intimate mixture of stoichiometric amounts of dicalcium phosphate anhydrous (DCPA) and Calcium Carbonate (CaCO3) at a temperature of 650 celsius [2].In this paper stress is made on the measurement of dielectric parameters and S-parameters at microwave frequency.

II. THEORY AND EXPERIMENTAL SETUP

Cavity perturbation technique [3] is used for the study of dielectric parameters. In this technique generally rectangular or cylindrical wave-guide resonators are employed. The experimental setup is shown in figure 1. When a dielectric material is introduced into a

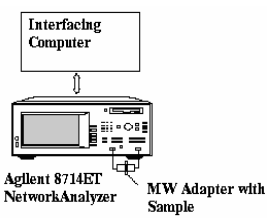

Fig.1: Experimental setup

cavity resonator at the position of maximum electric field, the resonant frequencies of the cavity are perturbed. The contribution of magnetic field for the perturbation is minimum at this position. So from the measurement of the perturbation due to the sample, the dielectric parameters can be determined. For permittivity measurements b-TCP samples in the form of a cylindrical pellet of thickness 3mm and diameter 10mm is used. For this the powder is pressed in to pellet, under a pressure 1 ton/inch^2. Then the pellet is sintered at 1000°C for 6 hours. When the pellet is inserted into cavity the field inside is perturbed.

The field perturbation inside the cavity is given by Kupfer et al [4].

$$-\frac{d\Omega}{\Omega} \approx \frac{(\bar{\varepsilon}_r - 1)\int_{V_s} E \cdot E_0^* \, dV}{2\int_{V_c} |E_0|^2 \, dV} \qquad (1)$$

where $d\Omega$ is the complex frequency shift. V_c and V_s are the volumes of the cavity and sample respectively. E and E_0 are the perturbed and unperturbed fields in the cavity. $\bar{\varepsilon}_r$ is the relative complex permittivity of the sample material. Complex frequency shift is related to the quality factor, Q as

$$\frac{d\Omega}{\Omega} \approx \frac{d\omega}{\omega} + \frac{j}{2}\left[\frac{1}{Q_s} - \frac{1}{Q_0}\right] \qquad (2)$$

Q_s and Q_o are the quality factors of cavity with and without sample. Quality factor Q is given by Q = f / Δf where f is the resonant frequency and Δf is the corresponding 3dB bandwidth. For small samples we assume that E = E_0 and for dominant TE_{10p} mode in a rectangular wave guide,

$$E_0 = E_{0max} \sin(\pi x/a) \sin(\pi pz/d), \quad p=1,2,\ldots \qquad (3)$$

From equations (1) to (3) the real and imaginary parts of the relative complex permittivity are given by

$$\varepsilon_r' = 1 + \frac{f_o - f_s}{2f_s}\left(\frac{V_c}{V_s}\right) \qquad (4)$$

$$\varepsilon_r'' = \frac{V_c}{4V_s}\left(\frac{Q_o - Q_s}{Q_o Q_s}\right) \qquad (5)$$

The real part of the complex permittivity, ε'_r is generally known as dielectric constant and the imaginary part ε''_r is related to the dielectric loss of the material. The effective conductivity of the medium σ_e is given by $\sigma + \omega\varepsilon''_r$. When the conductivity σ due to free charges is negligibly small (good dielectric) the effective conductivity is due to electric polarization and is reduced to

$$\sigma_e = \omega\varepsilon''_r = 2\pi f \varepsilon_0 \varepsilon''_r \qquad (6)$$

From the measurement of S-parameters, absorption coefficient can be found. Samples in the form of powder are used. Beta tricalcium phosphate (b-TCP) was prepared by heating an intimate mixture of stoichiometric amounts of dicalcium phosphate anhydrous and Calcium Carbonate at a temperature of 650°C. b-TCP powder is filled in a perspex holder of 35 mm x 70 mm which is the inner dimension of the S-band wave guide, is kept between two coaxial to wave guide adapters and tightened. Using the network analyzer, the S-parameters S_{11} and S_{21} are measured. Reflection coefficient R and transmission coefficient T are given as R= $|S_{11}|^2$ and T = $|S_{21}|^2$ .The absorption coefficient A can be obtained from the simple relation A+R+T = 1 [5]. The measurement is repeated for different thicknesses of b-TCP powder and the variation in scattering parameters is studied.

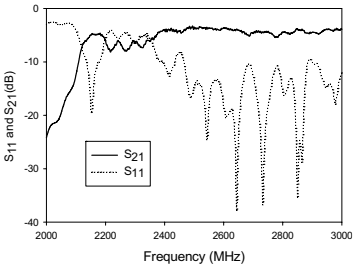

Figure.2
S_{11} and S_{21} graph of perspex holder.

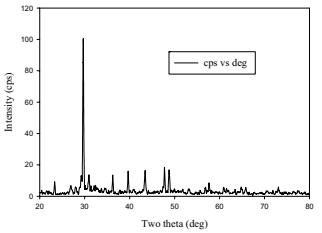

Figure.3

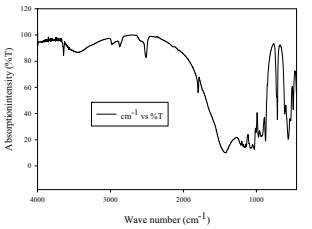

Figure.4

Results and Discussion

The XRD and FTIR of beta TCP are measured (Figure.3&4) and are found to be correlating with that of standard beta TCP [1].

The dielectric parameters of b-TCP are tabulated in Table 1. In the frequency range 2000-3000 MHz, b-TCP shows a variation in dielectric constant from 3.61-3.80. The dielectric constant is less for b-TCP because of its lower polarizability.

The conductivity of dielectric materials in a microwave field depends upon the dielectric loss factor, here as frequency increases the dielectric loss factor increases. The dielectric loss is a direct function of relaxation process, which is due to local motion of polar groups. At high frequencies, the friction between molecular chain increases, which leads to higher dielectric loss. This dielectric loss factor causes the so-called conductivity relaxations. At this relaxation region, polarization acquires a component out of phase with the field and displacement current in phase with the filed, resulting in thermal dissipation of energy, his generates dielectric loss which in turn generates conductivity. In the presence of microwave field the dielectric constant depends on the dipolar polarization as well. The dielectric parameters of b-TCP and human bone marrow falls in the same range [7].The S-parameter of b-TCP HAP has been studied and it is observed that beta tricalcium phosphate is a very good absorber of electromagnetic radiation. The S_{11} and S_{21} characteristics of perspex holder are shown in fig.2. Microwave absorption of b-TCP powder samples of different thickness is shown Fig.5. From the reflection study it

Table 1: Dielectric parameters of b-TCP

Material	Frequency (MHz)	ε_r'	ε_r''	Conductivity σ (S/m)	Skin depth δ_s (m)	$\tan\delta$
Beta Tricalcium Phosphate	2430	3.61	0.195394	2.65×10^{-2}	6.27×10^{-2}	5.41×10^{-2}
	2680	3.75	0.150527	2.24×10^{-2}	6.49×10^{-2}	4.02×10^{-2}
	2970	3.80	0.291094	4.80×10^{-2}	4.22×10^{-2}	7.65×10^{-2}

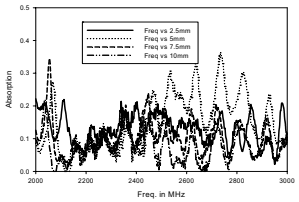

Fig.5 Variation of absorption with thickness and frequency

has been observed that reflection increases with thickness indicating a decrease in the transmitted power. It is also observed that the reflection coefficients of perspex and b-TCP vary with frequency. This may be the reason for fluctuation in the absorption as the frequency varies. b-TCP shows an average increase in absorption of microwave power as the thickness is increased. From S_{11} and S_{21} measurements it is inferred that, b-TCP is a good absorber of electro magnetic wave in the microwave frequency range. This energy may be dissipated in the form of heat. Thus they can be considered for many other applications such as packing and shielding materials.

CONCLUSION

The dielectric properties of b-TCP are studied and variation in absorption characteristics of b-TCP is discussed. This study facilitates the bioabsorption analysis through microwave imaging. And the study reveals that these materials are also probable candidates for EMI shielding

REFERENCES

1. Racquel Z. Le Geros, "Biodegradation and bioresorption pf calcium phosphate ceramics", Review paper, Clinical materials, Vol. 14 (1993), pp. 65-88.
2. Hollinger Jeffrey O, Scott A. Guelcher, "An Introduction to Biomaterials", Biomedical Engineering Series, Vol.2, (21 Dec.2005),pp.212.
3. Uaveendranath, S. Bijukumar and K.T. Mathew,"Broadband co-axial cavity resonator for complex permittivity measurements of liquids", IEEE Trans. on Inst. and Meas., 49,2000,1305-1312
4. K. Kupfer, A.Kraszewski and R. Knochel, "Microwave sensing of moist materials, food and other dielectrics", Sensors update vol. 7,2000,186-209,Wiley VCH, Germany
5. C.Y. Lee et.al, "Electromagnetic interference shielding by using condtive polypyrol and metal compound coated on Fabrics", Poly. For Adv. Tech., 13,2002,577-583
6. Honey John, "Studies on selected conducting polymers for microwave and electrical applications", Ph.D thesis 2003,Cochin University of Science and Technology
7. Gabriel. S, Lau. R.W and Gabriel. C, "The Dielectric Properties of Biological Tissues: II. Measurements in frequency range10Hz to 20GHz", Phys.Med.Biol.,(1996) 41, p.2251-2269.

Dielectric Characterization of Underfill Materials for MMIC Flip-Chip Packaging for Automotive Radar Applications

Deepukumar M Nair[(1)], Micheal Miller [(1)], David Ihms[(1)], David Zimmerman[(1)], and Matthew Walsh[(1)]
(1)Delphi, One Corporate Center, Kokomo, Indiana, USA, 46902,
Email: Deepukumar.m.nair@delphi.com

Abstract: *Millimeter waver radar technology is recently attracting significant research interest due to applications in automotive industry. Such radar systems have stringent microwave performance requirements and automotive applications warrants low-cost and small footprint system solutions. Up-integration of radar functions to a small number of microwave integrated circuits (MMIC) and developing suitable packaging technologies are necessary to meet the conflicting cost-performance trade offs. Flip chip packaging of MMIC has the potential to meet such trade offs. Use of flip chip technology in automotive environment needs use of underfill materials to ensure reliability. However, very little data exist on the microwave properties of underfill materials. This paper reports the results of our investigation on characterizing underfill materials up to 40 GHz.*

Introduction: Traditional applications of millimeter waver radar systems are in military. Commercial applications of millimeter wave radar systems are attracting significant attention in recent years driven by automotive applications. Typical radar applications in automotive arena include adaptive cruise control (ACC), blind spot detection, line departure warning, collision avoidance, and pedestrian detection. Unlike military applications, commercial radar systems need to meet stringent performance requirements as well as lower cost. A high level integration oriented strategy is necessary to meet conflicting performance and cost requirements. Up-integrating functions in to a small number of microwave integrated circuits (MMIC) are a proven method of ensuring high levels of functionality and performance. Interconnect design of microwave/millimeter wave integrated circuits poses several daunting challenges due to the high frequencies of operation and exacting system performance requirements. Harsh operating environment and reliability requirements exasperate the situation in automotive applications. Flip chip packaging as electrical and mechanical interconnection offers very distinct advantages for systems working in millimeter wave frequency ranges. Excellent electrical properties have been demonstrated in radar bands for multi-chip modules[1], extending well into millimeter wave ranges. In addition, flip-chips offer many other advantages such as high port density, short interconnect self-alignment of the die, smaller profile and foot-print as well as high assembly throughput. However, the flip-chip approach also creates significant problems of its own notably in the long-term reliability of packaged devices and systems. One proven technique to ensure reliable operation of flip-chip packaged integrated circuits is to use an inorganic-filled epoxy resin underfill material[2]. A suitably formulated underfill material will act as a buffer medium and mechanical anchor between the flip-chip and substrate. The thermo-mechanical CTE (coefficient of thermal expansion) mismatch of these assembly materials can lead to reliability issues. The presence of the underfill material has a significant effect on the electrical performance of the flip-chip interconnect and the MMIC itself due to the relatively higher values of dielectric constant and

loss tangent of such materials as compared to air[2]. The changes in dielectric properties of the medium in the immediate vicinity of bump interconnect will result in serious problems due to impedance mismatches and excitation of unwanted higher order surface modes in the substrate. Several research groups have investigated flip-chip packaging of MMIC's. Most of that work focused on improving the electrical performance through various design modifications to the transmission lines – on both the substrate and the chip – including bump interconnect geometry[3].Very little has been published on the effect of underfill material on the microwave/millimeter wave performance. Even when this aspect of the design is considered on 'before and after underfill' basis, there was no significant reported effort on the actual dielectric characterization of various underfill materials at frequencies above 10 GHz[4]. The manufacturers of underfill materials typically have not documented dielectric properties of underfills for frequencies greater than 800 MHz. The investigation reported here bridges this gap by studying the very important role of underfill materials reporting the methods employed and results obtained on dielectric characterization; the measurement of dielectric constant and loss tangent of underfill materials up to 40 GHz.

Dielectric Measurements: A microstrip ring resonator technique was used to measure the dielectric properties of candidate underfill materials. The ring resonators were designed and their performance analyzed through full electro-magnetic field simulations using HFSS - High Frequency Structure Simulator (from Ansoft Corporation) by assuming a range of dielectric parameter values. Ground-signal-ground probe structures (250µm) were also included in the test pattern. Excellent agreement between design/simulation and measurement was obtained for this testing. An Agilent network analyzer and Cascade Microtech probe station were used to measure scattering parameters of the resonators. From the resonance data both dielectric constant and loss tangent were extracted. Large, flat and relatively thin (0.5mm) samples of cured underfill, complete with a ground plane, were required for high frequency electrical characterization measurements. These samples were formed by dispensing a candidate underfill into the milled depression, 0.5mm x 6.5cm x 7.6cm, of an aluminum mold, itself measuring 0.3cm x 8cm x 9cm. Aluminum was a good material for underfill adhesion and it also provided the ground plane for the sample. The exposed surface of the underfill was made flat by laying a silver coated alumina substrate on the top of the mold and clamping it tight with four binding clips. The silver surface acted as a release film as it easily separated from the underfill after curing. Open-air curing did not generate a flat surface, and release agent would contaminate the sample's surface. Multiple ring resonators were created on the surface of the molded underfill by screen-printing a thick-film conductive ink and curing. The 4 x 4 array had four different diameter sizes in each column: 1.8, 2.8, 3.8, and 4.8mm. The silver-filled thermosetting conductive ink, Dow Corning PI-2600 conducting ink, was deposited through a 360 mesh stainless steel (15µm dia.) screen having a 5µm emulsion. The ink was then cured at 120 °C for 20 minutes. The PI-2600 generated uniform printed features with a smallest feature dimension of 110µm. The printed rings had a width of 200-220µm, were 10-15µm thick at the center of the conductor feature. The printed microstrip ring had a gap of 113µm at the CPW launch and a gap of 155µm at the ring feedline interface, see Figure 1.

Six underfill materials were characterized for high frequency packaging applications using the ring resonator configuration. The dielectric constant and loss tangent were calculated based on the measured scattering parameters. Four different ring mean diameters were chosen to give four fundamental resonant frequencies from 12-33 GHz. The ring, a 350µm pitch CPW launch, was used followed by a transition to a microstrip feedline.

Proceedings of APSYM2006, Dec. 14-16., Dept. of Electronics, CUSAT, India.

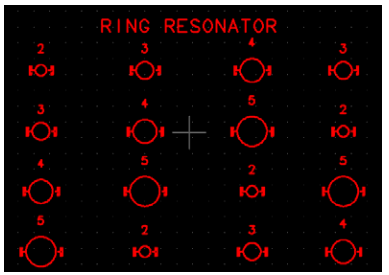

Figure 1: Ring resonators printed on molded underfill epoxy

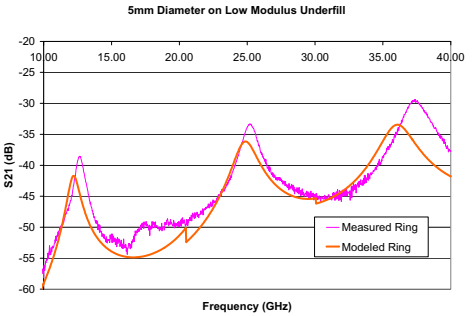

Figure 2: Simulated and measured data

The results for selected underfills and a sample of un-filled epoxy resin are given in Table 1. The data is graphically presented in Figure 2. The thickness and surface roughness of the conductor print measurements were measured from SEM analysis of cross-sections and were used in deriving dielectric parameters.

	n (res mode)	f0 GHz	S21 at f0	BW GHz	Q loaded	Er	Tan D
UF Resin only	1	13.37	-35.22	0.64	20.88	3.04	0.006
No-flow UF	1	13.21	-37.75	0.66	20.09	3.13	0.008
High Tg UF	1	12.70	-39.23	0.64	19.79	3.45	0.010
Low Modulus	1	12.62	-39.35	0.70	18.12	3.50	0.016
Cyanate Ester	1	12.45	-35.18	0.55	22.54	3.61	0.003
Glob Top	1	12.29	-36.66	0.69	17.74	3.73	0.017
UF Resin only	2	26.60	-31.14	1.38	19.26	3.08	0.028
No-flow UF	2	26.47	-33.51	1.31	20.26	3.12	0.025
High Tg UF	2	25.38	-33.77	1.06	23.88	3.45	0.017
Low Modulus	2	25.10	-34.05	1.22	20.63	3.55	0.025
Cyanate Ester	2	24.71	-30.90	1.08	22.88	3.68	0.019
Glob Top	2	24.39	-31.71	1.26	19.45	3.80	0.028
UF Resin only	3	39.68	-26.34	1.77	22.41	3.12	0.026
No-flow UF	3	39.48	-29.22	1.85	21.55	3.16	0.029
High Tg UF	3	37.59	-29.96	1.73	21.72	3.56	0.029
Low Modulus	3	37.38	-29.84	1.79	20.95	3.61	0.031
Cyanate Ester	3	36.51	-26.99	1.71	21.50	3.81	0.029
Glob Top	3	35.98	-27.32	1.90	19.01	3.95	0.036

Table 1: Measured Dielectric Properties of underfill materials

Phase Shifter Flip-chip: The phase shifter device, shown figure 3, uses thin film ferroelectric technology with barium strontium titanate (BST) to achieve a tunable dielectric constant, and is used extensively in the phase array antenna of the radar. The operating frequency of the phase shifter is in the 12-18 GHz band. Silver thick film conductors were printed and fired on a 0.9mm thick substrate in a CPW configuration for test. The center conductor width is 178µm and the gap is 114 µm to allow for a 350µm probe style. A TRL (Thru Reflect Line) calibration and scattering parameter measurement was performed to determine the baseline performance of the flip-chip before underfill and at the endpoints during reliability testing.

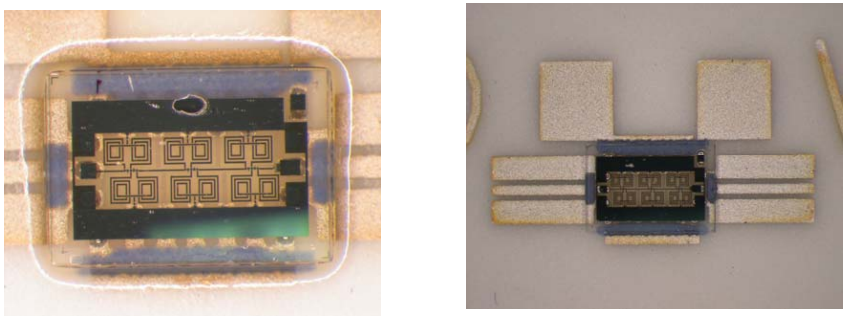

Figure 3 Phase shifter MMIC before and after flip chip packaging with underfill

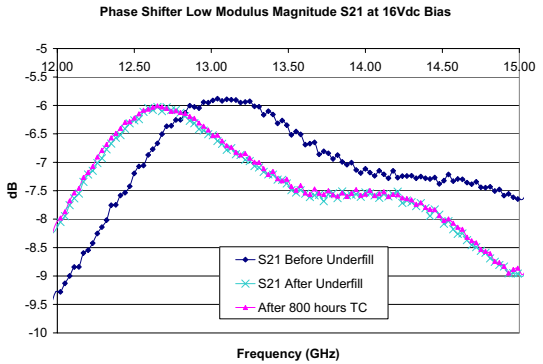

Figure 3: Frequency Shift and Stability of Phase Shifter Flip-chips after 800 cycles of –40/105 °C Temperature Cycling Reliability Testing

Conclusion: Dielectric constant and loss tangent of six underfill materials were measured using microstrip ring resonator technique with a novel molding method. Measured dielectric data is used to select a suitable underfill for flip chip packaging of a phase shifter MMIC. Reliability testing and electrical characterization indicate high-reliability performance with minimum impact due to the presence of underfill material under the chip.

Reference:

[1] K. Boustedt, "GHz flip-chip – an overview," 1998 Electronic Components and Technology Conference, Seattle, WA, pp. 1280-1285.

[2] Z. Feng, W. Zhang, B. Su, K.C. Gupta, and Y.C. Lee, "RF and mechanical characterization of flip-chip interconnects in CPW circuits with underfill," IEEE Trans. Microwave Theory Tech., vol. 6, pp. 2269-2275, Dec. 1998

[3] S. Masuda, H. Kira, and T. Hirose, "110-GHz High-gain Flip-chip InP HEMT Amplifier with Resin Encapsulation on an Organic Substrate," 12th GAAS Symposium, Amsterdam, Netherlands, Oct. 2004, pp. 479-482

[4] E. Öjefors, A. Rydberg, "LTCC and glob top packaging for 24 GHz MMIC with integrated antennas," GigaHertz 2003, Proceedings – 7th Symposium, Issue #8, Session 6, Paper 22, Linköping, Sweden

Proceedings of APSYM2006, Dec. 14-16., Dept. of Electronics, CUSAT, India.

RESEARCH SESSION IV

MICROWAVE ANTENNAS I

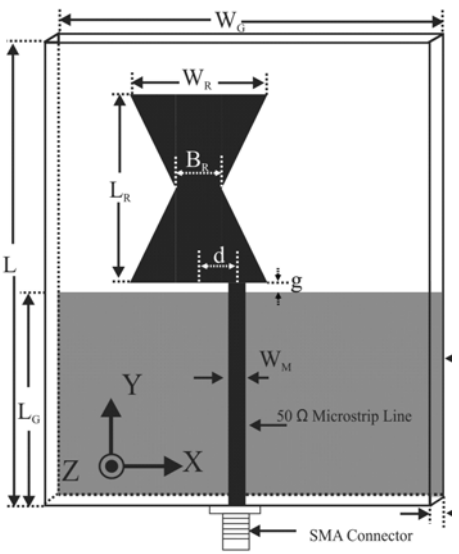

December 15, Friday

(8.30 a.m. -10.00 a.m.)

RESEARCH SESSION IV

MICROWAVE ANTENNAS I

Chair : Prof. Ramesh Garg, IIT Kharagpur

Visakhapatnam – 530 003. *Professor, Dept. of ECE, AU College of Engineering, Visakhapatnam – 530 003.
E-mail :profrrreddy@yahoo.co.in

DESIGN OF FIVE FEED EQUAL HEIGHT WITH TAPERED SECTION ROTMAN LENS FOR MULTIPLE BEAM FORMING AT U.H.F BAND

Satya Bhushan Shukla, P. K. Singhal, Ravi Pratap Singh & P. C. Sharma
Dept. of Electronics
Madhav Institute of Technology & Science,
Gwalior (M. P.)-474005, India
E-mail: pks_65@yahoo.com
and an_satya@rediffmail.com

***Abstract**: Equal height circular lens is the most appropriate choice for multiple beam forming. A modified geometry and design approach for Equal height circular lens has been proposed. An Equal height circular lens at UHF frequency band has been designed and fabricated. The results for the designed lens are in agreement with the design value.*

Introduction: Wide-angle scanning capabilities of Rotman lens [1], [2] are well-established [3]-[6]. Design approach of the Rotman lens is based on geometrical ray optics tracing technique. The Rotman obtained by conventional design approach [1] have unequal height of array contour and feed contour. Feed contour and array contour must have equal heights, as far as possible to couple the maximum power from the feed contour to array contour. P.K. Singhal et al. [7] reported a design approach to equalize the height of array and feed contour.

Lens Design: Figure 1 shows the cross- section of a trifocal Rotman-type lens. One focal point F_0 is located on the central axis and the two others F_1 and F_2 are symmetrically located on either side of a circular focal arc (also called feed contour). Contour I_2 is a straight line and defines the position of the radiating elements. I_1 is the inner contour of the lens (also called the array contour). Two off axis focal points F_1 and F_2 are located on the focal arc at angles $+\beta$ and $-\beta$. It is required that the lens be designed in such a way that outgoing beams make angles $-\alpha$, 0 and $+\alpha$ with the x axis when feeds is placed at F_1, F_0 and F_2 respectively. It may be noted that in this proposed approach the two off axis focal points are located at angles $\pm\beta$ whereas in the approach suggested in [4] these were located at angles $\pm\alpha$. The array contour I_1 is defined by coordinates (X, Y). The position of the radiating elements on the straight-line I_2 is determined by single coordinate N, measured relative to point O_1. Point's O_1 and O lie on the contours I_2 and I_1 respectively and connected by transmission line of length W (0).

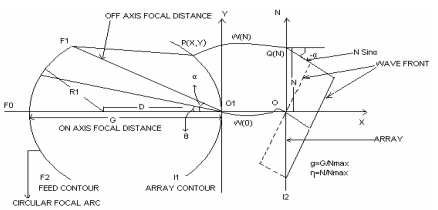

Figure 1: Trifocal Rotman Lens

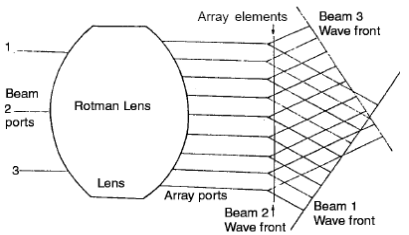

Figure 2: Direction Of Out Going Beam

In Rotman lens, four basic parameters are selected: straight front face, two symmetr off axis focal points and an on axis focal point. Array contours and transmission lines designed in such a way that the outgoing beam makes an angle - α, 0 and α with the axis of lens and terminates normal to their respective wave-front, when feed point is placed at F_1, and F_2 respectively.

The orientation of wave front for each focal point is shown in figure. 2 A ray originat from point F_1 on the feed contour may reach the wave-front through a general point P(X, Y) the array contour, transmission line W(N), point Q(N) and then tracing a straight line at an ar -α. Also the ray may reach the wave front from F_1 to O, transmission line W (0) and termina normal to wave front

DESIGN SPECIFICATION:

This paper describes an example of the design of Equal height circular lens to feed array of microstrip antenna. It is required to the design the lens for the following requirements

Angular coverage = ± 35

Number of antenna elements=7

Number of input beams =5

Central frequency = 800 MHz

The complete structure is assumed to be fabricated in a Microstrip on substrate of thickn 1.6mm and dielectric constant 4.7.

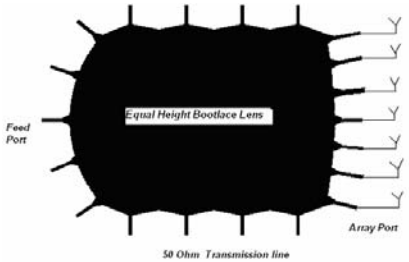

Figure3: Geometry of Lens

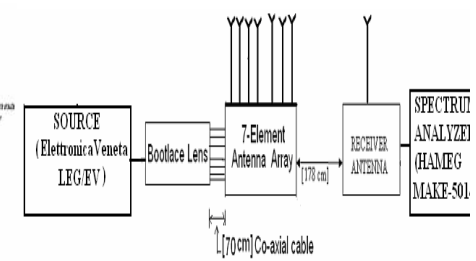

Fig 4:Set-Up for Radiation Pattern Measureme

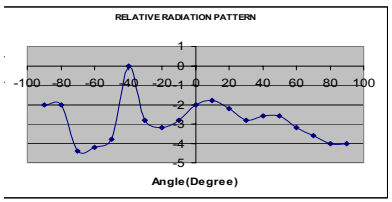

Figure 5.1

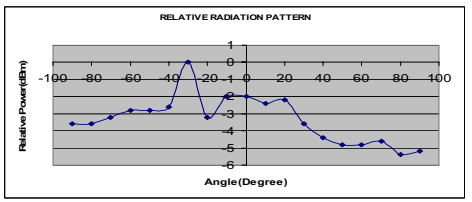

Figure 5.2

Figure 5.3

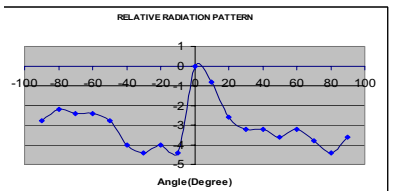

Figure 5.4

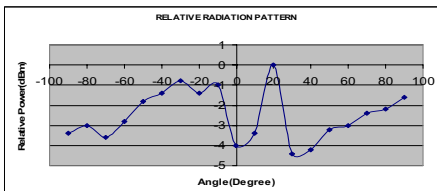

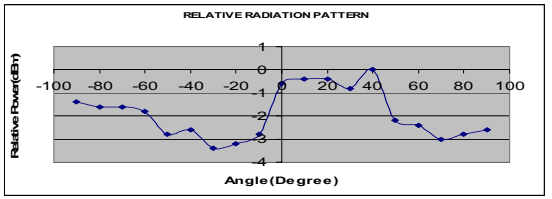

Figure 5.5

Figure 5: RADIATION PATTERN WHEN INPUT AT PORT 1, 2,3,4,5

Input port to Output port	Coupling coefficient (dBm)
1-10	-18.2
1-11	-19.0
1-12	-24.2
1-13	-19.0
1-14	-23.0
1-15	-24.6
1-16	-15.6
2-10	-21.4
2-11	-17.8
2-12	-17.0
2-13	-16.2
2-14	-29.4
2-15	-15.8
2-16	-14.2
3-10	-15.6
3-11	-12.2
3-12	-12.6
3-13	-10.2
3-14	-17.6
3-15	-18.2
3-16	-18.8
4-10	-15.4
4-11	-18.2
4-12	-20.6
4-13	-16.6
4-14	-20.6
4-15	-18.6
4-16	-20.6
5-10	-13.4
5-11	-15.0
5-12	-22.6
5-13	-28.6
5-14	-27.0

Input Port to input Port	Coupling coefficients(dBm)
1-2	-17.4
1-3	-20.0
1-4	-18.2
1-5	-15.8
2-1	-19.4
2-3	-18.2
2-4	-27.8
2-5	-15.4
3-1	-13.4
3-2	-12.6
3-4	-12.4
3-5	-14.8
4-1	-15.4
4-2	-25.8
4-3	-14.8
4-5	-23.4
5-1	-20.6
5-2	-14.6
5-3	-14.0
5-4	-21.0

Table 1.1, 1.2 Coupling from Input Port to Output Port & Input Port

Table 1.3: Direction of outgoing beam

Port No.	Angle (Degree)
1	-38
2	-28
3	0
4	+20
5	+40

RESULTS AND DISCUSSION: Table 1.1&1.2 shows the amplitude coupling from input ports to output ports and input ports to input ports. Figure 4 shows setup for the radiation pattern measurement. Figure 5.1 to 5.5 shows the radiation patterns for input at different feed ports. Table 1.3 shows the direction of the outgoing beams for input at different feed ports. The designed Rootman lens is covering an angular area from +40degree to -38 degree

CONCLUDING REMARKS: Geometry for Equal height circular lens with tapered line section type multiple beams forming lens has been proposed in which design complexities are greatly reduced. Various coupling coefficient and radiation pattern of the designed lens have been determined. The designed Equal height circular lens is covering an angular area from +40 degree to -38 degree.

REFERENCES

[1] W. Rotman and R.F. Turner, "Wide angle microwave lens for line source applications", IEEE Transactions on Antenna and Propagation, Vol. AP-11, pp 623-632, Nov 1963

[2] D. Archer, "Lens Fed multiple-beam arrays", Microwave J. Vol.18, pp 171-195, Sept. 1984.

[3] D. Archer, "Lens Fed multiple-beam arrays", Microwave J.Vol.18, pp 37-42, 1975.

[4] J.P.Shelton, "Focusing characteristics of symmetrically configured bootlace lenses", IEEE Transactions on Antenna and Propagation, Vol. AP-26, pp 513 – 518, July 1978

[5] M.L. Kales and R.M. Brown, "Design consideration for two–dimensional symmetric Equal height circular lenses", IEEE Transactions on Antenna and Propagation, pp 521-528, July 1965

[6] P. C. Sharma, R. D. Gupta, and P. K. Singhal, "Design & Analysis Bootlace Lens for multiple beam forming", IETE Technical Review, Vol.16, No.1 pp 67-73, January-February 1999.

[7] P.K.Singhal, P.C.Sharma and R.D.Gupta, "Rotman Lens with Equal Height of Array and Feed Contours," IEEE Transaction on Antennas and Propagation, Vol.51, No.8, pp 2048-2056, August 2003.

Proceedings of APSYM2006, Dec. 14-16., Dept. of Electronics, CUSAT, India.

Equivalent Circuit Representation of Waveguide Slot Doublet

Priyanka Mondal and Ajay Chakrabarty
Department of Electronics and Electrical Communication Engineering, Indian Institute of Technology, Kharagpur, India, 721302, E.mail: pri.mondal@gmail.com, bassein@ece.iitkgp.ernet.in

Abstract: *In this paper, analysis of an isolated slot doublet in a rectangular waveguide is done using Magnetic Field Integral Equation (MFIE). The equation is solved using Galerkin specialization of Method of Moment (MOM) and reflection and transmission co-efficients are obtained. Equivalent circuit of the waveguide slot doublet is represented on the basis of these co-efficients.*

Introduction: Waveguide slot doublets are widely used as radiating elements of arrays where horizontal polarization and omnidirectional radiation pattern is required. Because of compactness and lightweight these arrays are used in communication systems and beacon radar systems. To design an array with desired radiation pattern characterization of an isolated slot doublet becomes essential. In [1], image theory was applied to analyze the isolated slot doublet. Here, the structure is analyzed directly solving the Magnetic Field Integral Equations for both of the slots.

Analysis Procedure: Waveguide slot doublet consists of two broad wall longitudinal slots of dimension 2L×2W milled at an offset of x_s from the z-axis is shown in Fig.1. The cross-sectional dimension of the waveguide is 2a×2b. The electric field at the slot is assumed to be x-directed and it is assumed that there is no variation of the electric field in the x-direction, i.e. in the direction of the slot width.
The electric field at the slot aperture at y = b is expressed as [2]:

$$\vec{E}_1 = \hat{u}_x \sum_{p=1}^{M} E_{1p} e_{1p} \tag{1}$$

Where e_{1p} is defined as:

$$e_{1p}(x', y', z') = \sin\left\{\frac{p\pi}{2L}(z'+L)\right\}\delta(y'-b) \quad \text{for} \quad \begin{matrix} L \le z' \le L \\ x_s - W \le x' \le x_s + W \end{matrix}$$

$$= 0 \qquad \text{elsewhere} \tag{2}$$

The electric field at the slot aperture at y = -b is expressed as:

$$\vec{E}_2 = \hat{u}_x \sum_{p=1}^{M} E_{2p} e_{2p} \tag{3}$$

Where e_{2p} is defined as:

$$e_{2p}(x', y', z') = \sin\left\{\frac{p\pi}{2L}(z'+L)\right\}\delta(y'+b) \quad \text{for} \quad \begin{matrix} L \le z' \le L \\ x_s - W \le x' \le x_s + W \end{matrix}$$

$$= 0 \qquad \text{elsewhere} \tag{4}$$

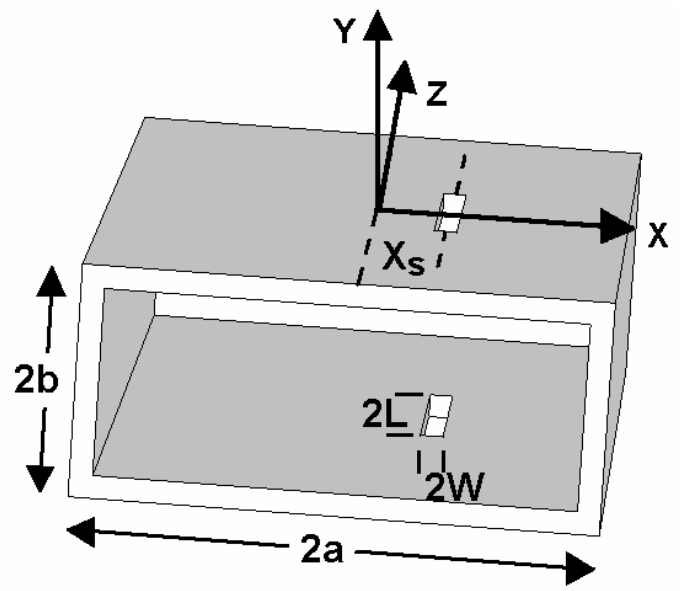

Fig. 1 Isolated slot doublet in a rectangular waveguide and co-ordinate system.

From the continuity of tangential magnetic field at y = b and y = -b,

$$H_{z1}^{inc} + H_{z11}^{\text{int}} + H_{z12}^{\text{int}} = H_{z1}^{ext} \tag{5}$$

$$H_{z2}^{inc} + H_{z22}^{\text{int}} + H_{z21}^{\text{int}} = H_{z2}^{ext} \tag{6}$$

where, $H_{z1}^{inc}, H_{z2}^{inc}$ are the incident magnetic fields at the aperture plane at y = b and -b. $H_{z11}^{\text{int}}, H_{z22}^{\text{int}}$ are internally scattered magnetic field due to self aperture field and $H_{z21}^{\text{int}}, H_{z12}^{\text{int}}$ are due to mutual interaction. $H_{z1}^{ext}, H_{z2}^{ext}$ are the externally scattered magnetic fields at the slot aperture.

Plane wave spectral approach is used to determine the magnetic field at the slot, due to the electric field existing at the slot aperture. Internally scattered magnetic field is obtained solving the Helmholtz equation.

To determine the electric field distribution at the aperture, it is necessary to determine the basis function co-efficient E_p.

Using Galerkin specialization of Method of Moment the testing functions can be written as

$$w_{1q}(x,y,z) = \sin\left\{\frac{q\pi}{2L}(z+L)\right\}\delta(y-b) \qquad x_s - W \le x \le x_s + W, -L \le z \le L$$
$$= 0 \qquad \text{elsewhere} \tag{7}$$

$$w_{2q}(x,y,z) = \sin\left\{\frac{q\pi}{2L}(z+L)\right\}\delta(y+b) \qquad x_s - W \le x \le x_s + W, -L \le z \le L$$
$$= 0 \qquad \text{elsewhere} \tag{8}$$

Following the procedure of Method of Moment we obtain,

$$E_{1p} = \left\{I - \left[L_1^{ext} - L_{11}^{\text{int}}\right]^{-1}\left[L_{21}^{\text{int}}\right]\left[L_2^{ext} - L_{22}^{\text{int}}\right]^{-1}\left[L_{21}^{\text{int}}\right]\right\}^{-1}$$
$$\times\left\{\left[L_1^{ext} - L_{11}^{\text{int}}\right]^{-1} L_1^{inc} + \left[L_1^{ext} - L_{11}^{\text{int}}\right]^{-1}\left[L_{12}^{\text{int}}\right]\left[L_2^{ext} - L_{22}^{\text{int}}\right]^{-1} L_2^{inc}\right\} \tag{9}$$

$$E_{2p} = \left[L_2^{ext} - L_{22}^{\text{int}}\right]^{-1}\left[L_2^{inc} + L_{12}^{\text{int}} E_{1p}\right] \tag{10}$$

Now, the reflection and transmission co-efficients at the aperture plane of the slot can be written as:

$$\Gamma = \frac{\pi^2 W}{4a^3 bk\eta\beta^2}\sin\left(\frac{\pi x_s}{2a}\right)\sin c\left(\frac{\pi W}{2a}\right)\sum_{p=1}^{M}\left(E_{1p} - E_{2p}\right)\frac{S(p)}{1+S^2(p)}\begin{Bmatrix}\cos\beta L & p\,odd\\ j\sin\beta L & p\,even\end{Bmatrix} \tag{11}$$

$$T = 1 + \frac{\pi^2 W}{4a^3 bk\eta\beta^2}\sin\left(\frac{\pi x_s}{2a}\right)\sin c\left(\frac{\pi W}{2a}\right)\sum_{p=1}^{M}\left(E_{1p} - E_{2p}\right)\frac{S(p)}{1+S^2(p)}\begin{Bmatrix}\cos\beta L & p\,odd\\ -j\sin\beta L & p\,even\end{Bmatrix} \tag{12}$$

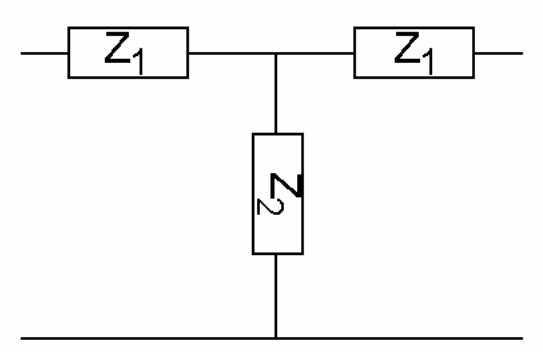

Fig. 2 Equivalent circuit of an isolated slot doublet.

Equivalent Circuit Representation: The isolated slot doublet can be representation by a T-network as shown in Fig.2. If the T-network is terminated by a characteristic impedance of Z_0, then

$$Z_1 = \frac{1+\Gamma-T}{1-\Gamma+T} \qquad \text{and} \qquad Z_2 = \frac{2T}{(1-\Gamma+T)(1-\Gamma-T)} \tag{13}$$

Fig. 3(a) shows the computed field distribution across the slot length for different offsets of the slot doublet. For numerical computation standard X-band waveguide having dimensions 2a = 22.86, 2b = 10.16 mm is used. Slot dimensions are 2W = 1 and 2L = 16 mm. Fig. 3(b) shows the computed shunt conductance as a function of frequency. It is seen that, series impedance Z_1 is negligibly small over the frequency range 8 to 12 GHz. So, the doublet can be represented by shunt admittance.

Conclusion: Analysis of an isolated waveguide slot doublet in a standard rectangular waveguide is presented and it is observed that for standard waveguide the doublet can be represented by shunt admittance. Computed results agree well with the published results.

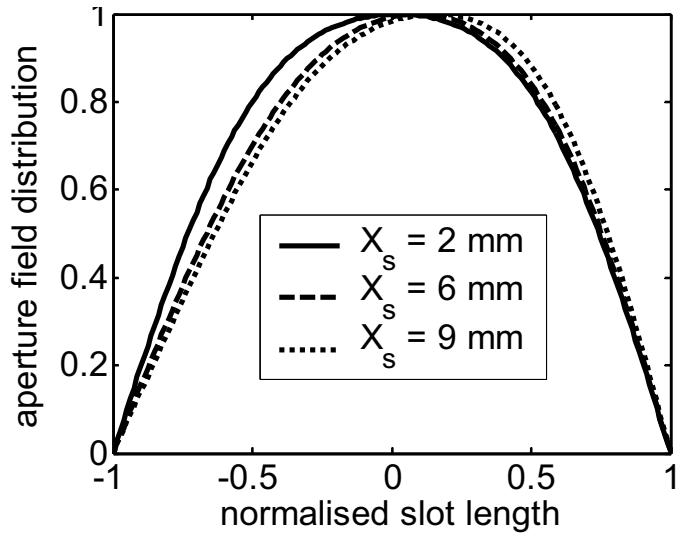

(a)

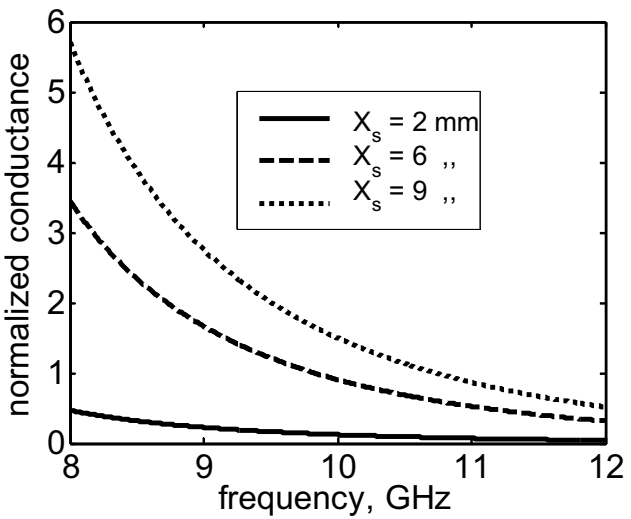

(b)

Fig. 3. Computed normalized (a) aperture field distribution across the slot length and (b) shunt conductance as a function of frequency for different offsets of the slot doublet.

Reference:

[1] J.C. Coetzee and J. Joubert, "Analysis procedure for arrays of waveguide slot doublets based on the full T-network equivalent circuit representation of radiators", IEE Proc.-Microw. Antennas Propag, Vol. 147, No. 3, pp. 173-178, 2000.

[2] S. Gupta, Ph. D. Dissertation, E & ECE Dept., IIT Kharagpur.

Proceedings of APSYM2006, Dec. 14-16., Dept. of Electronics, CUSAT, India.

COMPARISON OF THE NORMALIZED ADMITTANCE AND SUSEPTANCE-CONDUCTANCE FOR LONGITUDINAL SLOT IN RECTANGULAR WAVEGUIDE

Moutusi Mondal[(1)], Priyanka Mondal[(1)],Ajay Chakrabarty[(1)]

Dept of Electronics & Electrical Communication Engineering, IIT-Kharagpur, Pin-721302,
Email:moutusi.etc@gmail.com

Abstract

Computation of the admittance, conductance and suseptance of longitudinal shunt slot in a rectangular waveguide is given here. For theoretical computation the values obtained from Method of Moments (MOM) and simulated data obtained from computer simulation technology (CST) are used.A moment methods with entire basis function is used for solving the electric field in the slot.CST simulation based on finite integration technique (FIT) is also performed. Theoretical results compare very well with simulated results.

I.INTRODUCTION

Planar slotted waveguide antennas are extensively used in radar seeker due to its low profile lightweight and compactness. An analysis of single longitudinal slot in the broad wall of rectangular waveguide is presented. The equivalent shunt admittance of the slot is obtained from moment method solution (MOM) of the field in slot aperture and compares these values with Computer Simulation Technology Microwave Studio (CST). It is fully featured software package for electromagnetic analysis. The solution also provides the resonant frequency (or resonant length) of the slot. The reflection coefficients can be measured quite accurately for comparison with simulated theoretical data and computed data. From the reflection coefficients, we get the normalized admittance and susceptance, etc. We are working for standard waveguide, nonstandard waveguide (both a and b variable) and reduced height waveguide. We are working in Ku-band waveguide in broad wall longitudinal slot.

II. CONDUCTANCE-SUSCEPTANCE CALCULATION WITH THE HELP OF EQUIVALENT SHUNT ADMITTANCE

The scattering of longitudinal slot in broad wall of a rectangular wave-guide is usually modeled by means of equivalent shunt admittance. The reflection coefficients TE10 mode, the slot admittance is obtained as, $Y / Y_0 = -2\Gamma /(1+\Gamma)$

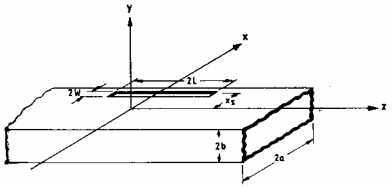

Fig.1. Longitudinal Slot on the Broad Wall of a Rectangular Waveguide

The reflection coefficients measured quite accurately for comparison with simulated data and computed data. The simple shunt model implies that the scattering off the slot is symmetrical, i.e., the back scattering equals to the forward scattering. The co-efficient of basis functions as unknowns which solved by using the method of moments (MOM).The complex reflection or transmission co-efficient are obtained in terms of these complex co-efficient. This is not exactly true for real slots. The resonant length is that length which yields a zero equivalent shunt susceptances. We computed resonant length versus the displacement of the slots for the different offset position. Here the calculation of Γ, was taken from the back scattering and from the forward scattering, respectively. These theoretical values are verified by CST simulation techniques.These electromagnetic simulation based on the finite integration technique (FIT).

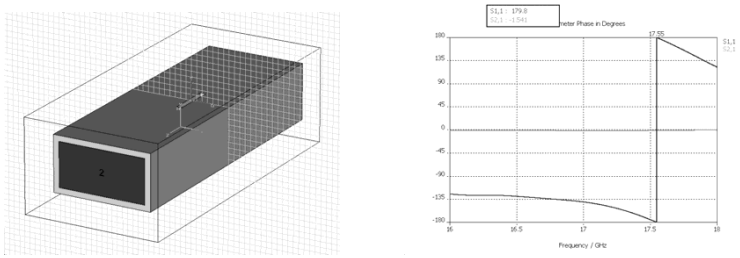

Fig..2. Slotted standard waveguide(offset-2) and reflection coefficient graph from CST.

From the measured or computed reflection coefficients for fundamental TE10 mode the equivalent normalized slot admittances and hence susceptances-conductance can be calculated.

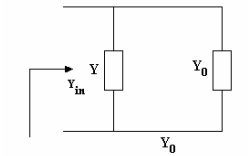

Fig.3. Equivalent circuit of the slot.

From the fig.3. the equivalent shunt admittance of the slot is Y. Considering transmission line model, if transmission line characteristic admittance is Y_0 and and the line is matched terminated, then
$Y_{in} = Y + Y_0$

Now, reflection co-efficient,

$$\Gamma = \frac{Y_0 - Y_{in}}{Y_0 + Y_{in}} = \frac{1 - \bar{Y}_{in}}{1 + \bar{Y}_{in}}$$

where, $\bar{Y}_{in} = \frac{Y_{in}}{Y_0} = 1 + \bar{Y}$

$G + j\,B = -2\Gamma/(1+\Gamma)$

Susceptance and conductance values were checked for different offset around the resonant length a for the different frequencies. For standard waveguide and the reduced waveguide (20%, 40%, 60 the theoretical data and computed data are similar. property of the graphs are quite similar.

III. CASE STUDY

Theoretical results obtained on the basis of theoretical analysis and the computed results obtain from CST Microwave Studio. Ku-band standard waveguide is taken and Waveguide wall thickness 1.015 mm; Slot width = 1 mm. Plots with white background are obtained from analysis and the pl with shaded background are obtained from CST simulation.
Variations of G and B with slot length (around the resonant length) for different offset of the slot 10% reduced width waveguide (Width of the waveguide = 14.22 mm):

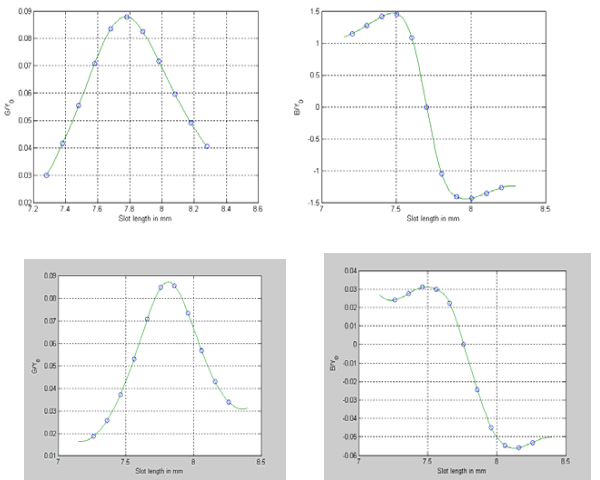

Fig..4. G and B graph for offset-2

Variations of G and B with frequency (around the resonant length) for different offset of the slot on 10% reduced width waveguide (Width of the waveguide = 14.22 mm):

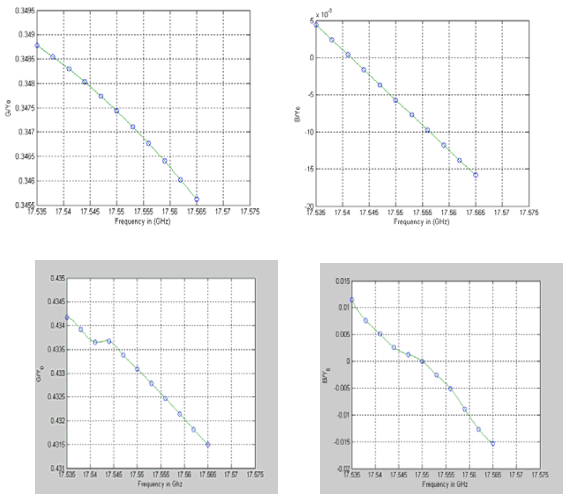

Fig.5. G and B graph for offset-2

IV.CONCLUSION

The method of moments using entire basis functions has been applied to the solution of the field in a longitudinal slot in rectangular wave guide. The measured susceptance-conductance curve is found to be excellent. The basis solution presented here can be used for computing the backward as well as the forward scattered wave amplitudes. The graphs are similar for moment method solution of the field and computed simulation technique.

REFERENCES

[1]. David M.Pozar, Microwave Engineering.
[2]. R.F. Harrington, Field Computation by Moments Methods.
[3]. R.J. Stegen."Longitudinal shunt slot characteristic", Hughes Tech Memo.261, Nov 1971

ANALYSIS OF SLOT EXCITED RECTANGULAR WAVEGUIDE

M. Surendra Kumar (1), B. Sada Siva Rao (2), J. Babu (3), G. Karunakar (4), G.S.N. Raju (5)

(1) Dept. of ECE, Raghu Engineering College, Visakhapatnam.
Email : s_kumarleo@yahoo.co.in
(2) Dept. of ECE, M.V.G.R. College of Engineering, Vizianagaram – 535005
Email : b_sadasivarao@yahoo.co.in
(3) Dept. of ECE, M.V.G.R. College of Engineering, Vizianagaram – 535005
Email : jbabumtech@rediffmail.com
(4) Dept. of ECE, GITAM Engineering College, Visakhapatnam – 530045
Email : karunakargodi@yahoo.co.in
(5) Professor, Dept. of ECE, AU College of Engineering, Visakhapatnam – 530003,
Email : drrajugsn@yahoo.com

ABSTRACT

Slot coupled waveguide junctions are commonly used in various applications. These junctions are used to generate desired polarized fields. The H and E plane T-junctions are analyzed by several Researchers. However, in the present work a slot excited rectangular waveguide is analyzed. The analysis consists of the estimation of self-reaction and discontinuity in modal current. The self-reaction is evaluated from the TE and TM modes.

INTRODUCTION : The basic theory on slot radiators is reported by Watson[1]. Several experiments are conducted by him and the data on coupling and impedance is reported. Several waveguides are coupled by rectangular slots and the theory of coupling was explained by him. A few types of coupling contain shut-series, series-series, series-shunt, shunt-shunt coupling of rectangular waveguides are analysed.

The theory of diffraction by holes is reported by Bethe [2] . However, the holes being small, and they are not used as radiators. Stevenson [3] has developed theory of slots in rectangular waveguides. The analogy with transmission line is developed and established by him. The detailed formulae for reflection and transmission coefficients are derived. Closed form expressions are presented with assumptions on the slots.

Marcuvtz et al. [4] reported a paper on the representation of electric and magnetic fields produced by currents and discontinuities in waveguides. It was shown that the discontinuity can be replaced by equivalent electric and magnetic currents.

Rumsay [5] has developed the concept of the self-reaction in electromagnetic waves. This theory is found to be extremely useful for the analysis of slot coupled waveguides and junctions. In the present work the concept of self-reaction and discontinuity in modal current are made use of for the analysis of slot excited waveguides.

FORMULATIONS

For the purpose of analysis in the guide, the electric field distribution in the aperture plane of the slot can be assumed to be of the form

$$\mathbf{E}_s = \mathbf{a}_x E_o \sin k(L - |z|)\delta(y - 0) \quad (1)$$

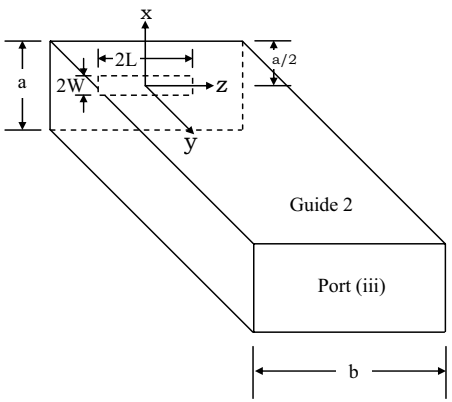

Fig. 1 Longitudinal slot exciting the coupled guide

where $K = 2\pi/\lambda$, λ being the wavelength and E_o is the maximum electric field in the slot, 2L is the slot length and 2W is slot width.

For the coordinate system shown in fig. 1, the variables are related as

$$\mathbf{e}^e = \mathbf{a}_y \times \nabla_t \psi^e \quad (2)$$

$$\mathbf{e}^m = -\nabla_t \psi^m \quad (3)$$

Here ψ^e and ψ^m are the normalized eigen functions for the electric and magnetic fields [6].

The relations between the modal vector functions for the electric and magnetic fields are of the form

$$\mathbf{h}^e_{mn} = \mathbf{a}_y \times \mathbf{e}^e_{mn} \quad (4)$$

$$\mathbf{h}^m_{mn} = \mathbf{a}_y \times \mathbf{e}^m_{mn} \quad (5)$$

The electric field in the aperture plane of the slot can be expressed in terms of modal voltages V^e_{mn} and V^m_{mn} and modal vector functions $\mathbf{e}^e_{mn}$, $\mathbf{e}^m_{mn}$ as

$$\mathbf{E}_s = \sum_m \sum_n \left[V^e_{mn}\, \mathbf{e}^e_{mn} + V^m_{mn}\, \mathbf{e}^m_{mn} \right] \quad (6)$$

But $\mathbf{e}^e_{mn}$ and $\mathbf{e}^m_{mn}$ are orthogonal in nature. The expressions for the modal voltages are obtained from

$$V^e_{mn} = \int_{-W}^{W} \int_{-L}^{L} \mathbf{E}_s \cdot \mathbf{e}^e_{mn}\, dx\, dz \quad (7)$$

$$V^m_{mn} = \int_{-W}^{W} \int_{-L}^{L} \mathbf{E}_s \cdot \mathbf{e}^m_{mn}\, dx\, dz \quad (8)$$

The transverse component of the magnetic field in the guide is of the form

$$\mathbf{H}_t = \sum_m \sum_n \left[(Y_o)^e_{mn}\, V^e_{mn}\, \mathbf{h}^e_{mn} + (Y_o)^m_{mn}\, V^m_{mn}\, \mathbf{h}^m_{mn} \right] e^{-\gamma_{mn} Y} \quad (9)$$

Where $(Y_o)^e_{mn}$ and $(Y_o)^m_{mn}$ are the characteristic admittances of TE and TM modes respectively, $\mathbf{h}^e_{mn}$ and $\mathbf{h}^m_{mn}$ are modal vector functions for transverse component of magnetic field.

From the above equations, the self-reaction is given by

$$\langle a, a \rangle = -\int\int \left[\sum\sum (Y_o)^e_{mn} V^e_{mn}\, \mathbf{h}^e_{mn} + \sum\sum (Y_o)^m_{mn} V^m_{mn}\, \mathbf{h}^m_{mn} \right] . 2\mathbf{E}_s \times \mathbf{a}_y\, ds \quad (10)$$

It can be reduced to the form

$$\langle a, a \rangle = 2\sum\sum (Y_o)^e_{mn} \left(V^e_{mn}\right)^2 + 2\sum\sum (Y_o)^m_{mn} \left(V^m_{mn}\right)^2 \quad (11)$$

Here $(Y_o)^e_{mn} = \dfrac{\gamma_{mn}}{j\omega\mu}$, $(Y_o)^m_{mn} = \dfrac{j\omega \in}{\gamma_{mn}}$ and

$$\gamma_{mn} = \left[\left(\frac{m\pi}{b}\right)^2 + \left(\frac{n\pi}{a}\right)^2 - \left(\frac{2\pi}{\lambda}\right)^2 \right]^{1/2}$$

The discontinuity in modal current, I is found out from the paper reported by Marcuvitz and Schwinger [7].

The admittance loading of the present configuration is given by

$$Y = -\frac{I.I}{\langle a, a \rangle}$$

The normalized admittance, $y_n = \dfrac{Y}{y_{o1}} = g_n + jb_n$

RESULTS

From the equations presented above, the normalized admittance is computed as a function of slot length for the centre frequency of X-band. The results are presented in a tabular form.

Length of the slot	Conductance	Susceptance
0.8	0.00034474541	0.012847405
1.0	0.0018193990	0.029449597
1.2	0.010792075	0.070986211
1.4	0.12158833	0.20779756
1.6	0.25400925	-0.23718566
1.8	0.068729490	-0.16688621
2.0	0.040116452	-0.13163435
2.2	0.031553663	-0.11757274

From the results it is found resonance takes place at a slot length of about 1.5 cm.

REFERENCES

1. W.H. Watson, "Resonant slots," JIEE (London), Vol. 93, Part 3A, pp. 747-777, 1946.
2. H.A. Bethe, "Theory of diffraction by small holes," Phys. Rev., Vol. 66, pp. 163-182, 1944.
3. A.F. Stevenson, "Theory of slots in rectangular waveguides," J. Appl. Phys., Vol. 19, pp. 24-38, January 1948.
4. N. Marcuvitz, "Waveguide Handbook," R.L. Series, Vol. 10, New York, McGraw Hill, 1951.
5. V.H. Rumsey, "The reaction concept in electromagnetic theory," Phys. Rev., Vol. 94. No. 6, pp. 1483, June 15, 1954.
6. R.F. Harrington, "Time-harmonic electromagnetic fields," New York, McGraw Hill, 1961.
7. N. Marcuvitz and J. Schwinger, "On the representation of electric and magnetic fields produced by the currents and discontinuities in waveguides," J. Appl. Phys. Vol. 22, No. 6, pp. 806-819, June 1951.

Proceedings of APSYM2006, Dec. 14-16., Dept. of Electronics, CUSAT, India.

EFFECT OF BROAD DIMENSION OF RECTANGULAR WAVEGUIDE ON THE NORMALIZED CONDUCTANCE OF OPEN SLOT RADIATOR

R. Ramana Reddy (1), G.S.N. Raju (2)

(1) Research Scholar, Dept. of ECE, A.U. College of Engineering, Visakhapatnam – 530003,
Email : profrrreddy@yahoo.co.in
(2) Professor, Dept. of ECE, AU College of Engineering, Visakhapatnam – 530003,
Email : drrajugsn@yahoo.com

ABSTRACT

The rectangular waveguide narrow wall inclined slot radiators are used for the generation of horizontally polarized fields. The analysis of these radiators for their admittance characteristics is carried out by several researchers. However, the characteristics are controlled by basic slot parameters. In the present work, some studies are made to find the behaviour of admittance by waveguide dimension. The variation of normalized conductance and susceptance of a typical slot with the broad wall dimension is presented.

INTRODUCTION : The basic theory of slots in rectangular waveguides is reported by Stevenson [1]. The theory of slots is developed with the following assumptions.

1. The walls of the guide are perfectly conducting and have negligible thickness.
2. The slot is narrow, i.e. the ratio of length to width of the slot is much greater than unity.
3. The penetration of the field into the region behind the face containing the slot is negligible. In other words, problem is treated as if the guide face containing the slot has an infinite perfectly conducting plane on it.
4. The length of the slot is such that it is at resonance.

The well known results of Stevenson for the slot conductance are applicable only at resonance. Closed form expressions on the impedance characteristics of the centred slots are reported by Lewin [2]. The centred slots do radiate and the conductance changes marginally with slot shape.

The effect of slot inclination and its thickness on impedance characteristics are found to be significant and are reported by Oliner [3].

The Oliner work is centred around the slots in the broad wall of a rectangular waveguide. Oliner work assumes that the slot radiates into half space and it has rectangular ends. Slot conductance is determined using variational expressions and susceptance is estimated from the energy storage considerations.

Hsu and Chen [4] applied variational formulae developed by Oliner. The internal reactive energy is included and the admittance properties are studied.

Armstrong et al. [5] reported the design of circularly polarized linear array. The design criteria is based on analytical and empirical data. Perturbation technique is applied for the design of linear antenna array by Murty et al. [6].

Josephson [7] reported the analysis of longitudinal slots in rectangular waveguides. The displaced slots are considered in the analysis.

Elliot et al. [8] reported a paper on the design of small slot arrays. The effect of mutual coupling is also presented.

Most of the works on the slot radiators have one limitation or the other. In the present work an open inclined slot radiator in the narrow wall of rectangular waveguide is considered and the analysis is carried out using the concepts of self-reaction and discontinuity in modal current. The analysis consists of both analytical and computational approaches. The results on admittance characteristics of an inclined slot radiator in a non-standard narrow wall of a waveguide are obtained. It also includes the finite slot of resonant length. The slot of present interest does not protrude into broad wall and hence there are no EMI problems. The variation of normal conductance and susceptance with the dimensions of the broad wall is computed. The double integrals involved are evaluated numerically after testing for convergence.

FORMULATIONS

Consider an inclined slot (fig. 1) in the narrow wall of a rectangular waveguide.

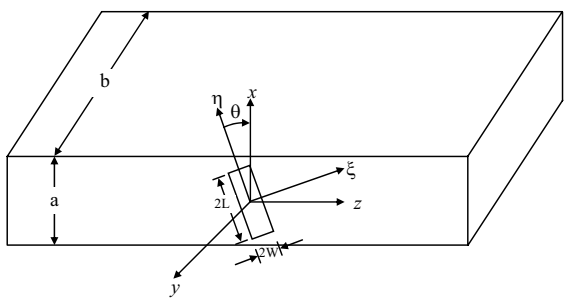

Fig. 1 Geometry of inclined slot

Assuming the electric field distribution in the aperture plane of the slot in the form of

$$\mathbf{E}_{slot}(\xi,\eta,0) = \mathbf{a}_\xi E_o \sin k\left(L - |\eta|\right) \qquad \text{for } |\eta| \le L, |\xi| \le W \tag{1}$$

where $\mathbf{a}_\xi$ is the unit vector along ξ - axis.

The self-reaction <a, a> of the equivalent magnetic current impressed in the slot is given by

$$\langle a, a\rangle = -\iint \mathbf{H}_{tan}(\xi,\eta,0).\mathbf{M}\, ds \tag{2}$$

where $\mathbf{H}_{tan}$ is the tangential component of the magnetic field
$\mathbf{M}$ is the equivalent magnetic current and it is given by

$$\mathbf{M} = -\mathbf{a}_y \times \mathbf{E}_{slot}(\xi,\eta,o) \tag{3}$$

Using the above expressions and plane wave spectrum approach, the expression for the self-reaction is simplified. The real and imaginary parts of self-reaction are given by

$$\langle a, a\rangle_R = A \int_{\phi=0}^{\pi/2}\int_{\alpha=0}^{\pi/2} \left[\frac{\sin(A_1)\sin\phi\cos\alpha}{A_1\sin\phi\cos\alpha}\right]^2 \frac{[\cos(B_1)\sin\phi\cos\alpha - \cos(B_1)]^2}{(1-\sin^2\phi\sin^2\alpha)} \sin\phi\, d\alpha d\phi \tag{4}$$

$$\langle a, a\rangle_I = jA \int_{\phi=0}^{\infty}\int_{\alpha=0}^{\pi/2} \left[\frac{\sin(A_1)\cosh\phi\cos\alpha}{A_1\cosh\phi\cos\alpha}\right]^2 \frac{[\cos(B_1)\cosh\phi\sin\alpha - \cos(B_1)]^2}{(1-\cosh^2\phi\sin^2\alpha)} \cosh\phi\, d\phi d\alpha \tag{5}$$

where $A = \frac{4V_o^2}{\pi^2\eta_o}$, $A_1 = 2\pi W/\lambda$, $B_1 = 2\pi L/\lambda$, $V_o = E_o\, 2W$

The expression for discontinuity in modal current [9] is given by

$$I = jY_{o1}\, 2V_o \sqrt{\left(\frac{2}{ab}\right)} \frac{\pi\sin\theta}{\beta_{o1}\, b}\left[\frac{1}{K^2 - (\beta_{o1}\sin\theta)^2}\frac{\sin(\beta_{o1}\, w\cos\theta)}{(\beta_{o1}\, w\cos\theta)}\right]\left[K\{\cos(\beta_{o1}\, L\cos\theta) - \cos KL\}\right] \tag{6}$$

The equivalent shunt admittance parameter is given by $Y = -\frac{II}{\langle a, a\rangle}$ (7)

and the normalized admittance is given by $y_n = \frac{Y}{Y_{o1}} = g + jb$ (8)

where, $Y_{o1} = \frac{\omega\mu_o}{\beta_{o1}}$, $\beta_{o1} = \left[k^2 - \left(\frac{\pi}{b}\right)^2\right]^{\frac{1}{2}}$

RESULTS AND CONCLUSIONS

Using the expressions (1-8), the computations are carried out to obtain the variation of g and b as a function of the broad dimension of the rectangular waveguide and the results are presented in the following table.

It is found from the results, that the variation of the broad dimension of the guide is effecting the conductance and susceptance as well. The results are obtained for f = 9.375 GHz and a = 1.5 cm, length of slot = 1.48 cm, inclination of the slot = 10^o, width of slot = 0.16 cm. It is also found that for higher dimension of the broad wall, the conductance is small. Similarly, is the case with the susceptance.

Broad Dimension	g	b
2.28600	0.031598680	-0.30238230E-05
2.30000	0.030842304	-0.29514417E-05
2.35000	0.028349370	-0.27128817E-05
2.40000	0.026142433	-0.25016893E-05
2.45000	0.024178002	-0.23137040E-05
2.50000	0.022420764	-0.21455462E-05
2.55000	0.020842060	-0.19944723E-05
2.60000	0.019418087	-0.18582057E-05
2.65000	0.018129051	-0.17348525E-05
2.70000	0.016958315	-0.16228189E-05
2.75000	0.015891787	-0.15207584E-05
2.80000	0.014917463	-0.14275208E-05
2.85000	0.014025111	-0.13421272E-05
2.90000	0.013205774	-0.12637211E-05
2.95000	0.012451841	-0.11915738E-05
3.00000	0.011756567	-0.11250399E-05

REFERENCES

1. A.F. Stevenson, "Theory of slots in rectangular waveguides," Journal of Applied Physics, Vol. 19, pp 24-35, January 1948.
2. L. Lewin, "Some applications on waveguide coupling through medium sized slots," Proc. of IEE, Vol. 107c, No. 12, pp 171-178, September 1960.
3. A.A. Oliner, "Impedance properties of narrow slots in the broad face of rectangular waveguide," IRE Trans. on A&P, AP-5, pp 1-20, January 1957.
4. Powen Hsu and Shin H. Chen, "Admittance and resonant length of inclined slots in the narrow wall of a rectangular waveguide," Trans. on A&P, vol. 37, No. 1, January 1989.
5. M.E. Armstrong and N.G. Alexopoulos, "On the design of a circularly polarized waveguide narrow wall array," IEEE Trans. Antennas and Propagat., pp 244-250, March 1975.
6. P.K. Murty and A. Kumar, "Synthesis of linear arrays," IEEE Trans. Antennas and Propagat., pp 865-869, November 1976.
7. L. Josephson, "Analysis of longitudinal slots in rectangular waveguides," IEEE Trans. A&P, Vol. AP-35, pp 1351-1357, 1987.
8. R.S. Elliot and L.A. Kurtz, "The design of small arrays," IEEE Trans. A&P, Vol. AP-26, pp 214-219, March 1987.
9. N. Marcuvitz and J. Schwinger, "On the representation of electric and magnetic fields produced by the currents and discontinuities in waveguides," J. Appl. Phys., Vol. 22, No. 6, pp 806-819, June 1951.

Low Profile Monopole Antenna on an Artificial Magnetic Conductor

Manish A. Hiranandani[(1)], Alexander B. Yakovlev [(2)], and Ahmed A. Kishk [(2)]*
(1) Mobile Wireless Group, Intel Corporation, Hillsboro, Oregon, United States, 97124,
E.mail:manish.a.hiranandani@intel.com
(2) Center of Applied Electromagnetics Systems Research, The University of Mississippi,
Oxford, Mississippi, United States, 38677
Email id: yakovlev@olemiss.edu, ahmed@olemiss.edu

Abstract: *An artificial magnetic conductor (AMC) is realized by printed slot frequency selective surfaces (FSS) implemented on a grounded dielectric slab. This structure acts as a GO/STOP surfaces for transverse electric (TE) / transverse magnetic (TM) polarization, depending on the direction of a plane wave excitation, thus acting as an artificial hard/soft surface. The realized FSS is proposed for the design of a low-profile monopole antenna. The simulated and experimental results of return loss and radiation pattern are presented, demonstrating the effect of a high impedance surface on scattering and radiation characteristics of a low- profile antenna.*

I. Introduction

Artificial hard and soft surfaces, recently introduced in electromagnetics [1], are characterized by surface anisotropic impedance with GO and STOP characteristics with respect to the propagation of surface waves [2]. Different approaches have been used for the realization of hard and soft surfaces. Traditionally, they are realized by dielectric-filled corrugations initially proposed in the design of corrugated horn antennas [3]. Another common method is to introduce perfect electric conductor (PEC) strips on a dielectric slab of certain thickness [4], [5]. The main characteristics of such strip-loaded surfaces can be modeled by using an ideal model, which represents alternating PEC and PMC strips with vanishing widths [2], [6]-[8]. These anisotropic surfaces are polarization-dependent, such that the hard surface behaves like a PMC for TE-polarized waves and as a PEC for TM-polarized waves propagating along the strips (corrugations) and acts as a GO surface allowing the propagation of surface waves. The soft surface has STOP characteristics for surface waves and behaves like a PEC for TE-polarized waves and as a PMC for TM-polarized waves propagating in the direction transverse to strips (corrugations) [2].

New designs of artificial hard and soft surfaces composed of printed dipole/slot FSS structures on a grounded dielectric slab have been recently presented in [9], [10] (Fig. 1). These FSS structures represent AMC surfaces with anisotropic impedance characteristics controlled by the resonance properties of periodic dipole/slot cells in the presence of a grounded dielectric slab. They are implemented on electrically thin substrate (compare to electrically thick substrates used in strip loaded hard and soft surfaces discussed above), which make them attractive for low profile antenna applications. Based on the idea presented in [9], an artificial magnetic conductor with printed slot FSS is designed. EMPiCASSO commercial software [11] is used for the full-wave analysis of proposed FSS configuration. This printed slot FSS is proposed for the design of a low-profile monopole antenna. The simulated and experimental results of return loss and radiation pattern are presented, which show considerable improvement in the radiation characteristics of the monopole due to the presence of an artificial magnetic conductor.

II. Characteristics of the Printed Slot Frequency Selective Surface

The printed slot FSS structure [9] (as shown in Fig. 1) acts as a hard/soft surface with GO/STOP characteristics for surface waves. With the plane wave incident in the direction of the slots, TM polarization doesn't interact with the structure, thus showing the behavior of the phase of reflection coefficient for a grounded dielectric slab; the TM polarization in this case doesn't "see" the slots and the phase behavior is close to that of a PEC (ground plane with a thin dielectric slab). The TE polarization, on the other hand, strongly interacts with the structure and exhibits high impedance surface behavior (characteristic of artificial magnetic conductors). Thus with the plane wave excitation along the slots, this structure behaves as a hard surface exhibiting PMC behavior for TE polarization, while for TM-polarized plane wave there is no interaction with the slots. In the other case, when the plane wave is incident perpendicular to the slots, the structure exhibits high impedance for TM polarization and low impedance for TE polarization, thus acting as a soft surface. The results for the phase of reflection coefficient versus the angle of incidence θ (0° being normal to the surface) are demonstrated in Figs. 2(a) and 2(b).

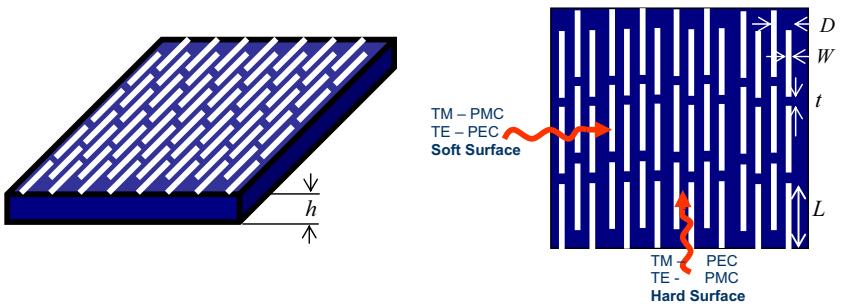

(a) (b)

Fig 1. (a) 3-D view (b) top view of AMC realized by printed slots on a grounded dielectric slab. All dimensions are in mm, $L = 10$, $D = 5.127$, $W = 0.25$, $t = 0.25$, $h = 1$, and $\varepsilon_r = 4$.

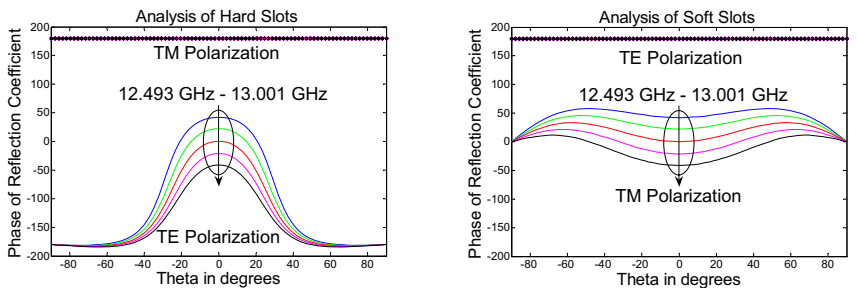

(a) (b)

Fig 2. Phase of the reflection coefficient with respect to angle of incidence (a) Hard slots (b) Soft slots

III. Low-Profile Monopole Antenna: Design and Experiment

Recently, high impedance surfaces (in particular, electromagnetic band-gap (EBG) mushroom-like structures) have been used in low-profile antenna designs in order to suppress surface waves and enhance the antenna radiation [12]. Here, we propose to use the above discussed printed FSS as a high impedance surface to improve the performance of low-profile antennas. A slot FSS, printed on a grounded dielectric slab (RO4003C, Roger's Corporation, $\varepsilon_r = 3.38$, $h = 0.813$), was designed at the frequency of 10 GHz. A quarter-wavelength horizontal monopole (length 9 mm) was used as a radiator placed in a close proximity (1.2 mm) to the slot FSS acting as an artificial magnetic conductor (AMC) at the resonance frequency. The slot FSS consists of an array of 5 x 10 cells of printed slots of dimensions 16 mm × 0.5 mm with the cell size 16.4 mm × 8.19 mm. A prototype of this structure was fabricated and its picture is shown in Fig. 3(a). The simulated and measured return loss of the monopole mounted on an AMC surface compared to a PEC surface is shown in Fig. 3(b). It is clear that the monopole is matched in the case of AMC at approximately 10 GHz (around the resonance frequency of the slot FSS) and is mismatched in the case of PEC (resulting in poor radiation characteristics).

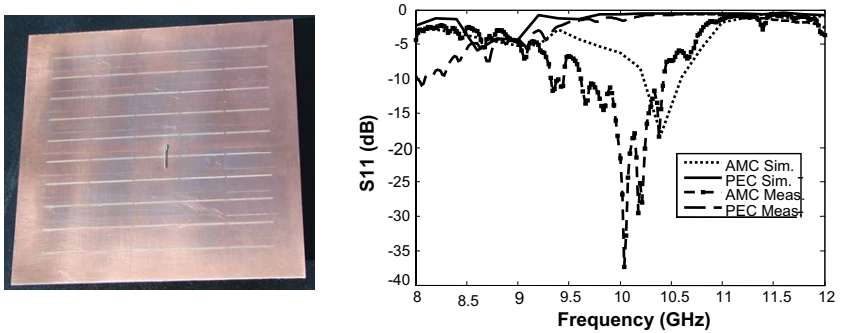

(a) (b)

Fig 3. (a) Picture of the monopole over an AMC (b) Simulated and measured return loss of the prototype

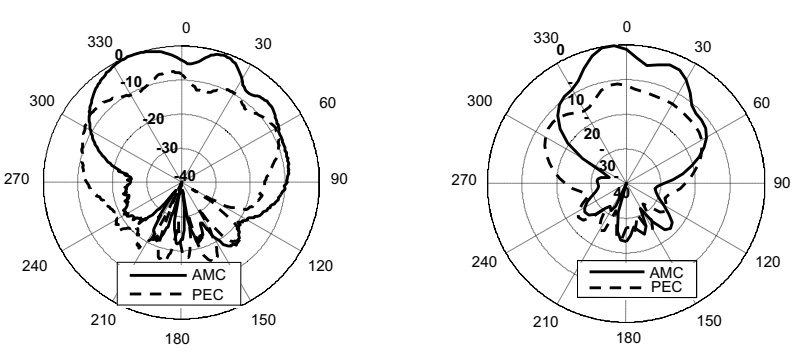

(a) (b)

Fig 4. (a) Simulated radiation pattern and (b) Measured radiation pattern of the designed monopole antenna above an AMC and a PEC surface

The radiation pattern of the monopole mounted on the above designed AMC structure is compared with its patterns over a PEC. The idea was to compare both the patterns to see the effect of the presence of an AMC on the performance of such a low-profile antenna. The simulated and measured E-plane radiation pattern is plotted in Fig. 4(a) and 4(b). When the antenna is mounted on a PEC, its front-side radiation pattern is almost uniform as it radiates the power equally in all directions. Comparing this pattern with the pattern of the same antenna over the AMC shows that the AMC pattern has a power level of 6-10 dB higher than the PEC pattern. This shows that the AMC surface enhances the gain of the horizontal monopole as compared to its inefficient radiation in the presence of the PEC (due to reversed image currents).

V. Conclusion

In this paper, an AMC surface is designed using printed slot FSS which acts as a hard/soft surface for TE/TM polarization depending on the direction of plane wave excitation. The FSS structure with the monopole was designed, fabricated, and measured, showing proper matching and enhancement of radiation for the low-profile antenna.

References

[1] P.-S. Kildal, "Artificially soft and hard surfaces in electromagnetics," *IEEE Trans. Antennas Propagat*., vol. 38, no. 10, pp. 1537-1544, Oct. 1990.

[2] P.-S. Kildal and A. A. Kishk, "EM modeling of surfaces with STOP or GO characteristics – Artificial magnetic conductors and soft and hard surfaces," *Proc. 19th Annual Review of Progress in Applied Computational Electromagnetics*, Monterey, CA, pp. 445-455, Mar. 2003.

[3] P.-S. Kildal, "Definition of artificially soft and hard surfaces for electromagnetic waves," *Electron. Lett.*, vol. 24 , no. 3, pp. 168-170, Feb. 1988.

[4] E. Lier, "Analysis of soft and hard strip-loaded horns using a circular cylindrical model," *IEEE Trans. Antennas Propagat.*, vol. 38, no. 6, pp. 783-793, June 1990.

[5] A. A. Kishk, "Analysis of hard surfaces of cylindrical structures of arbitrarily shaped cross section using asymptotic boundary conditions," *IEEE Trans. Antennas Propagat*., vol. 51, no. 6, pp. 1150-1156, June 2003.

[6] G. Ruvio, P.-S. Kildal, and S. Maci, "Modal propagation in ideal soft and hard surface," *IEEE AP-S Int. Symp*., Columbus, OH, pp. 438-441, June 2003.

[7] V. A. Klymko, A. B. Yakovlev, I. A. Eshrah, A. A. Kishk, and A. W. Glisson, "Dyadic Green's function of an ideal hard surface circular waveguide with application to excitation and scattering problems," *Radio Science*, vol. 40, 2005 (in press).

[8] W. Huang, A. B. Yakovlev, A. A. Kishk, A. W. Glisson, and I. A. Eshrah, "Green's function analysis of an ideal hard surface rectangular waveguide," *Radio Science*, 2005 (accepted).

[9] S. Maci and P.-S. Kildal, "Hard and soft Gangbuster surfaces," *Proc. URSI Int. Symp. Electromagnetic Theory*, Pisa, Italy, pp. 290-292, May 2004.

[10] S. Maci, M. Caiazzo, A. Cucini, and M. Casaletti, "A pole-zero matching method for EBG surfaces composed of a dipole FSS printed on a grounded dielectric slab," *IEEE Trans. Antennas Propagat*., vol. 53, no. 1, pp. 70-81, Jan. 2005.

[11] EMPiCASSO: User's Manual, EMAG Technologies, Inc, 2002.

[12] Yang, F. and Rahmat-Samii, Y.: 'Reflection phase characterizations of the EBG ground plane for low profile wire antenna applications,' *IEEE Trans. Antennas Propagat*., Oct. 2003, vol. 51, no. 10, pp. 2691-2703.

Proceedings of APSYM2006, Dec. 14-16., Dept. of Electronics, CUSAT, India.

INVESTIGATIONS ON A FRACTAL SHAPED APERTURE IN A RECTANGULAR WAVEGUIDE

B. Ghosh, Sachendra N. Sinha, and M. V. Kartikeyan

Dept. of Electronics and Computer Engineering, IIT Roorkee, Uttaranchal, India-247667

Email: basu_iitr@yahoo.co.in , snsecfec@iitr.ernet.in, kartkfec@iitr.ernet.in

Abstract: *In this paper, a new fractal geometry, which is a modification of Devil's staircase fractal, is used as a diaphragm in a rectangular waveguide. The problem of multiple apertures in the transverse cross-section of a waveguide has been formulated in terms of a Magnetic Field Integral Equation (MFIE) using the "Generalized Network Formulation for Aperture Problems" [1]. The MFIE has been solved using the method of moments and the numerical results are compared with those obtained with HFSS, which show a good agreement. The results show that the proposed fractal diaphragm is capable of providing multi-resonance behavior.*

I. INTRODUCTION:

Aperture in the transverse cross-section of a waveguide is a classical problem in electromagnetic theory which has received considerable attention from researchers. The aperture type discontinuity is frequently used in the design of microwave filters, impedance matching networks, transformers, and corrugated structures. In most of these applications, a single resonant or a non-resonant aperture is used. Since fractal geometries offer a multiband behavior [2], it should be possible to obtain multiple resonances with a single fractal shaped diaphragm.

In this paper, we present the results of preliminary investigations on one such fractal diaphragm. The problem has been formulated in terms of an MFIE which is solved using the Method of Moments with rooftop expansion functions. The method is based upon the "Generalized Network Formulation for Aperture Problems" proposed by Harrington [1].

II. FORMULATION OF THE PROBLEM

A. Problem Geometry: The geometry of the fractal aperture considered in this paper is a modification of Devil's staircase fractal [3]. The generation steps of devil's staircase fractal are shown in Fig. 1. It is known that the resonant frequency of a narrow rectangular aperture lies within the operating band of the waveguide, if the aperture dimension parallel to the broad wall is sufficiently large [4]. Along with this consideration and the fact that the wave guide dimension should satisfy $a = 2b$ for largest bandwidth for dominant TE_{10} mode, we have taken an image of the original fractal geometry along the base line and rotated it by 90^0. The resulting geometry of the aperture under consideration is shown in Fig.2 for three iterations.

B. MoM Formulation: The problem configuration is shown in Fig. 3, which consists of N rectangular apertures of arbitrary dimensions in the transverse cross-section of a rectangular waveguide of dimensions $a \times b$. The length and width of the n^{th} aperture are assumed to be L_n and W_n, respectively. The waveguide is excited by TE_{10} mode incident from $z < 0$ region, with the diaphragm placed at $z = 0$. Equivalence principle [1] is used to decouple the

problem into two equivalent problems, one for $z<0$ region and another for $z>0$ region. Enforcing the boundary conditions on the apertures, we obtain an integral equation which is solved by method of moments. A Galerkin procedure is used with rooftop functions and the characteristics of the fractal aperture are studied by evaluating the scattering parameters.

III. NUMERICAL RESULTS:

A general program has been written to compute the electric field distribution on the apertures from which the input reflection coefficient can be found. Firstly, a convergence test was carried out for the number of sub-sections required along x and y directions as well as for the number of waveguide modes for each of the three geometries shown in Fig. 2. The variation of $|S_{11}|$ with frequency for the three iterations of the fractal apertures for a waveguide having cross-sectional dimensions $22.86mm \times 10.16mm$ is shown in Fig. 4. In order to validate the results, the geometry was implemented in Ansoft's HFSS and those results are also shown in Fig. 3 and tabulated in Table I. For the 1st iteration, the resonant frequency is obtained due to the single aperture of Fig. 2(a) which is out of the operating band of the guide. However, for 2nd iteration, an additional resonant frequency appears due to the two apertures of lengths $a/4$ and $3a/4$ and the previous resonant frequency remains unchanged. In the 3rd iteration, the lowest resonant frequency is due to the four additional apertures and the third resonant frequency also shifts downwards. Thus, we obtain three resonances in the pass band of the waveguide.

Table I

Method	1st iteration	2nd iteration		3rd iteration		
	f_1	f_1	f_2	f_1	f_2	f_3
Present Method	14.7	8.45	14.5	7.3	8.5	10.4
HFSS	14.5	8.6	14.7	7.5	8.4	10.5
Difference (%)	1.38	1.74	1.36	2.67	1.19	0.95

IV. CONCLUSION:

From the numerical results, it can be seen that the fractal diaphragm exhibits a multi-resonant behavior with the number of resonant frequencies equal to the number of iterations. This characteristic of the fractal diaphragm can be useful in the design of multiband impedance matching networks and filters.

References

[1] R. F. Harrington and J. R. Mautz, "A generalized network formulation for aperture problems", IEEE Transactions on Antennas and Propagation, vol. 24, No.5, pp. 870-873, 1976.

[2] C. Puente, J. Romeu, R. Pous, and A. Cardama, "On the behavior of the Sierpinski multiband fractal antenna", IEEE Transactions on Antennas and Propagation, vol. 46, No. 4, pp. 517-524, 1998.

[3] H. O. Peitgen, H. Jurgen and D. Saupe, Chaos and Fractals: New frontier of Science, New York, Springer-Verlag, 1992.

[4] R. Yang and A. S. Omar, "Investigation of multiple rectangular aperture irises in rectangular waveguide using TE^{x}_{mn}-modes", IEEE Transactions on Microwave Theory and Techniques, vol. 41, No. 8, pp. 1369-1373, 1993.

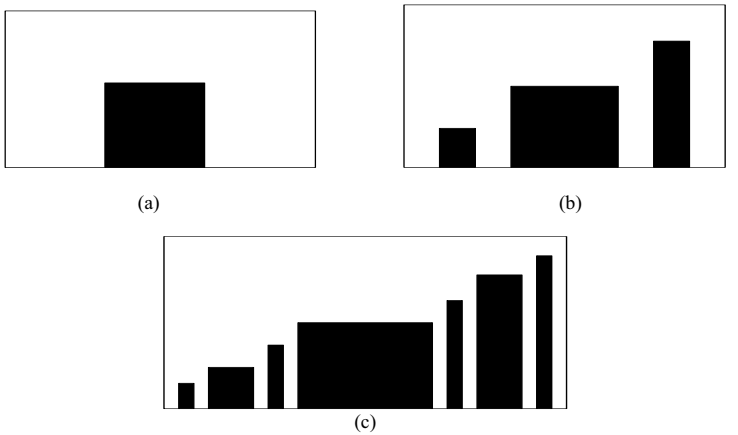

Fig.1. Generation steps for Devil's staircase fractal
(a) 1st iteration (b) 2nd iteration (c) 3rd iteration

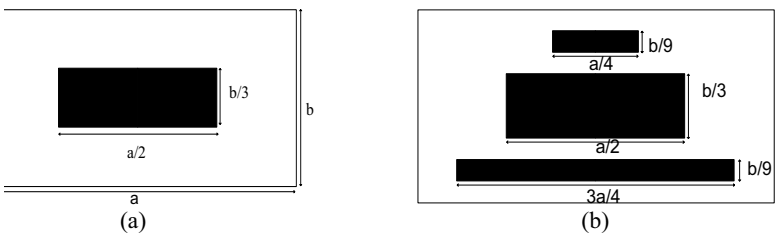

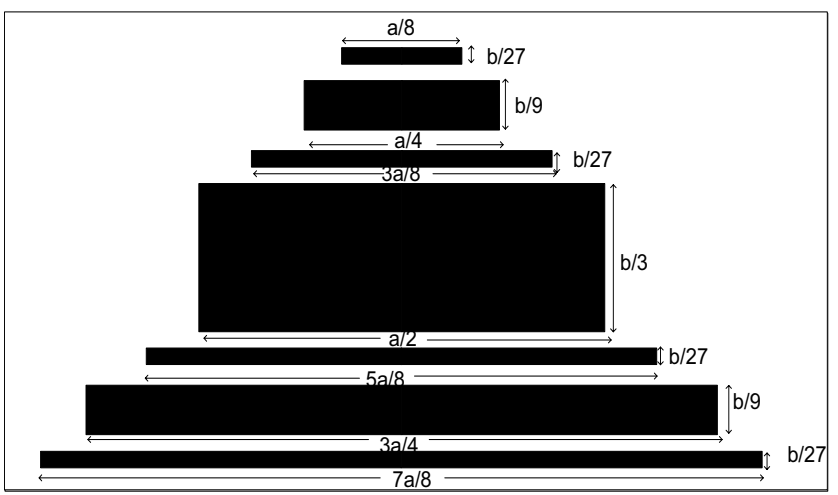

Fig.2. Geometry of the problem (a) 1st iteration (b) 2nd iteration (c) 3rd iteration

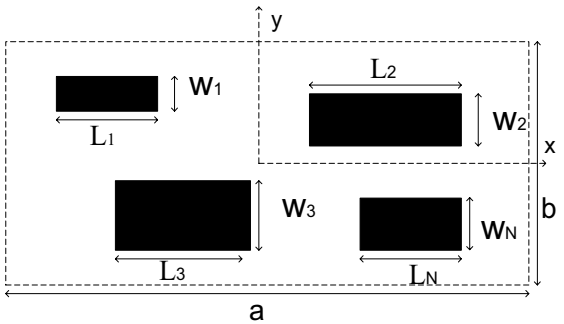

Fig.3. Waveguide diaphragm with multiple apertures

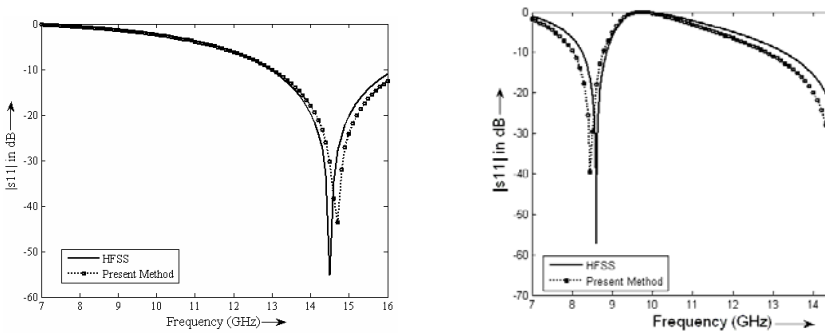

(a) (b)

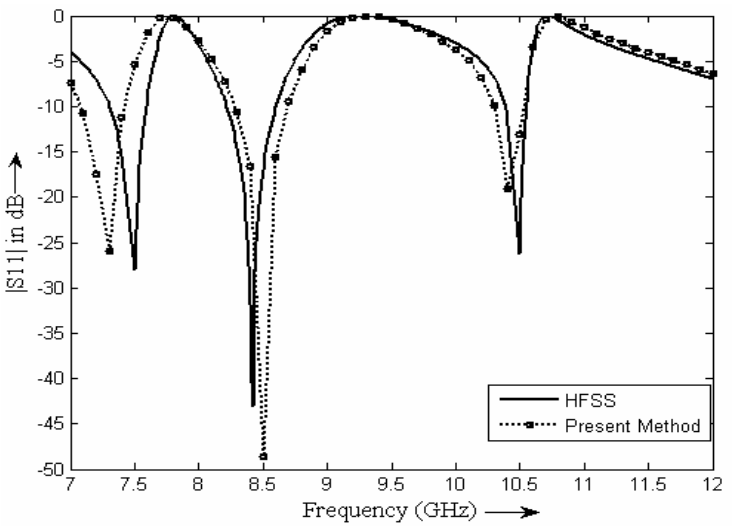

(c)

Fig. 4.Variation of $|S_{11}|$ with frequency (a) 1st iteration (b) 2nd iteration (c) 3rd iteration

Integrated Slotted Wave-guide Antenna Array using Photo-Imageable Thick-Film Techniques for E-Band operations

Manju Henry [(1)], Charles E Free [(1)], B. S. Izqueirdo [(2)], J. C. Batchelor [(2)], and Paul Young [(2)]
(1) Advanced Technology Institute, University of Surrey, Guildford, United Kingdom
E-mail: m.henry@surrey.ac.uk, c.free@surrey.ac.uk
(2) Department of Electronics, University of Kent, Canterbury, United Kingdom

Abstract: *Photoimageable thick-film technology has been used to fabricate an integrated waveguide antenna working around 74GHz. Measured data for the antenna, including return loss, radiation pattern and gain, are presented that demonstrate the potential of this fabrication technology to achieve the resolution and fine line geometries needed for very high frequency millimeter-wave circuits.*

Introduction: The millimeter-wave frequency band is attractive for wireless communication because it offers wide channel bandwidths with consequent high information rates. Also, this frequency band makes it possible to achieve compact designs because of the very short wavelengths. It is very convenient for short-range communication, and as such is employed for position detection and control of mobile robots, where it also provides high angular resolution. The millimeter-wave band is not suitable for long-range communication because of significant attenuation in the atmosphere around 60 GHz due to atmospheric absorption. This is a significant shortcoming where communication is concerned. However, it is widely used for short-range applications, and new technologies are being developed to convert mm-wave signals to optical signals for transmission through optical fibers for long-range communication applications. Despite its large potential, development and application of mm-wave systems have not been promoted because of high production cost. However, photoimageable thick film process is a cost effective process and offers a line resolution comparable to that of etching, and of thin-film, for mm-wave circuit fabrication [1]. In this paper, we show the results for a novel antenna array integrated within a multi-layer ceramic substrate working at 74 GHz, and fabricated using a photoimageable thick-film process. Radiation occurs from an array of narrow slits 30 micron wide located in the upper broad wall of an integrated waveguide, which is 1 mm wide. The position and width of the radiating slits is crucial to obtaining high performance, and thus the antenna serves as a component for demonstrating the potential of the fabrication process.

Structure of the Integrated Antenna: The structure of the antenna is shown in figure 1. The top and bottom walls of the waveguide were formed from printed layers of thick-film conductor. Two narrow sidewalls were formed by first photoimaging trenches in the dielectric, and then filling these trenches with conductor. The radiating slits were photoimaged in the top surface of the conductor. In order to produce good radiation characteristics the slits need to be precisely offset from the axis of the waveguide, so as to interrupt the current flow in the broad wall. Since several slots were used to create an array, axial positioning was also crucial to ensure that the slots radiated in phase [2]. The energy is coupled to the waveguide using a 50 Ω microstrip transmission line with a tapered transition such as was proposed in [3]. A novel side fed H-plane power divider was used to feed the two

4- slot sections of the array [4]. The centre-to-centre slot spacing was λg/2 and the end slot was placed at a distance of λg/4 from the short-circuited end of the waveguide.

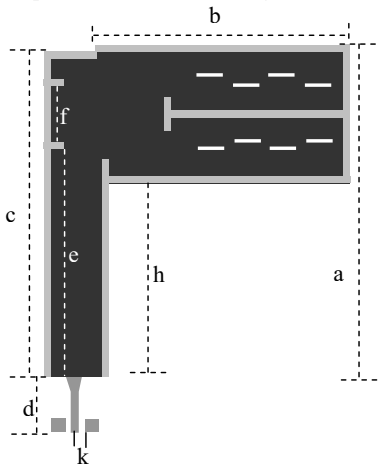

Dimension	Length (mm)
a	5.142
b	4.182
c	4.945
d	1.560
e	3.247
f	1.197
g	4.082
h	2.6485
k	0.1

Figure 1 The structure and dimension of the integrated waveguide antenna array (2X4).

Fabrication Process: The key steps in the fabrication process are summarized in figure 2. Commercially available dielectric and conductor pastes were used in this study. The dielectric had a dielectric relative permittivity of 8. A negative process was used for photoimaging the dielectric and conductor. The pastes were exposed to UV using a Quintel (Q7000) mask aligner, and developed using 1% Na_2CO3 solution. Using this technique it was found to be possible to achieve reasonably fine resolution, with 20 µm gaps and 10 µm lines. Photographs and dimensions of some of the circuits fabricated with fine resolution using the photoimageable thick film printing technique are shown in Figure 3 (a-b). Figure 3 (a) shows a miniature microstrip hybrid ring of diameter 2 mm and width 10 µm and figure 3(b) shows a compact microstrip branch line coupler (4mm X 4mm) having width of 20 µm.

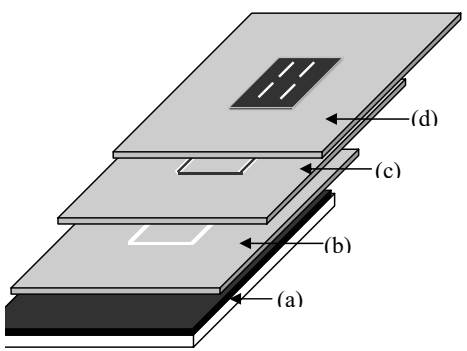

Step a: The ground plane was printed on the top of the supporting alumina substrate and then fired.
Step b: The dielectric layer was printed and the trenches forming the sidewalls of the waveguide were photo-imaged by exposing to UV through a chrome mask.
Step c: Conductor was printed to fill the trenches and hence form the metallic sidewalls of the waveguide.
Step d: the top conductor layer was printed and exposed to form the upper surface of the waveguide, with the radiating slots.

Figure 2 Key fabrication process for substrate integrated antennas.

Figure 3 Micro photographs showing the circuits and dimensions of very fine geometries printed using phtoimageable thick film techniques

Comments on substrate integrated waveguides: The substrate integrated waveguide technology can be utilized for fabrication of different passive components such as filters, multiplexers, antennas and power dividers. One of the advantages of using photoimageable thick film printing techniques for substrate waveguide integration is the feasibility to make continuous vertical waveguide walls, through the use of trenches rather than VIAs. This gives a wider bandwidth, and less loss, when compared to waveguides integrated in LTCC, where the walls are made of VIA fences.

Measurement results:

Novel slotted waveguide antenna array: Results are presented for an integrated waveguide 2x4 antenna array designed for E-band operation (60 GHz – 90 GHz). The geometry of the 2x4 array and the dimensions were shown previously in figure 1. The slots were designed to resonate at a frequency of 74 GHz. The waveguide feed was designed to give a phase difference of 180 degree between the two slotted wave guides in the array. The equivalent slots were positioned on opposite sides of the centerline to produce a further 180 degree phase difference so that the slot pairs are fed in phase. For maximum coupling, two inductive walls were placed in the feeding waveguide separated by a distance f (see figure 1), which was optimized to be 1.2 mm.

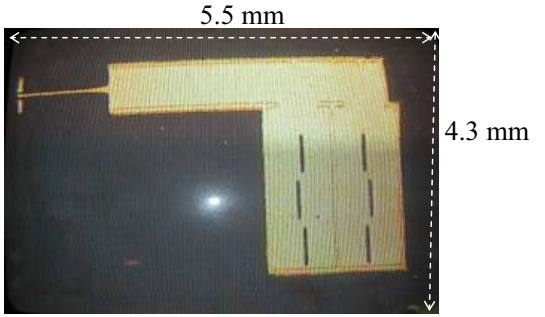

Figure 4 Micro photograph of a typical waveguide integrated antenna array

The measured return loss for the 2x4 array is shown in figure 5 (a), with the azimuthal, copolar and cross polar radiation patterns plotted in figure 5 (b).

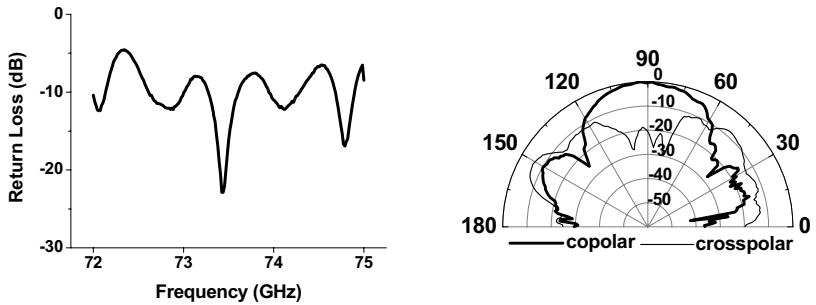

(a) (b)

Figure 5 (a) The return loss (b) copolar and cross polar azimuthal radiation patterns of a 2X4 integrated slotted waveguide antenna array.

Discussion: The integrated antennas gave good results, close to the predicted values. Cross-polarization levels were better than 20dB, with return losses also better than 20dB at the matched frequency. This performance is comparable to that of much larder, non integrated antennas working at these frequencies. There are two principal advantages to using the integration technique that has been discussed: firstly, it enable high antenna performance to be obtained from a relatively small substrate area and, secondly, the use of a waveguide antenna provides isolation between the antenna and surrounding circuitry in a highly integrated multilayer assembly. It has been shown that the photoimageable process is capable of yielding the required dimensional accuracy needed for making very high frequency circuits.

Conclusion: High performance waveguide antennas, working at high mm-wave frequencies, have been successfully integrated into multilayer circuits, fabricated using photoimageable thick-film technology. The results demonstrate a useful mm-wave circuit technique that offers potential for close integration of the antenna with the active circuitry in a mm-wave hybrid receiver sub-assembly.

Acknowledgements: The work was done as a part of a project "Millimeter wave antenna integration into MCM technology", funded by the EPSRC, UK.

References:

[1]K. Wu, D. Deslandes, and Y. Cassivi, "The substrate integrated circuits –a new concept for high frequency electronics and optoelectronics", in Proc. 6th Int. Conf. Telecommunications Modern Satellite, Cable Broadcasting Service (TELSIKS'03), vol. 1, pp. p-III-P-X, Oct 1-3, 2003

[2]W.L. Stutzman and G.A. Thiele, Antenna Theory and Design, Chap. 10, John Wiley & Sons, 1981.

[3]Sehyun Park, Y. Tsunemitsu, J. Hirokawa, M. Ando, "Center feed single layer slotted waveguide array" IEEE Transactions on Antennas and Propagation, volume 54, Issue 5, pp.1474-1480, May 2006.

[4]D. Deslandes and K. Wu, "Integrated microstrip and rectangular waveguide in planar form", IEEE Microwave and Wireless Component letters, vol. 11, no. 2, pp.68-70, Feb 2001.

MICROWAVE MULTI BEAM ANTENNA TECHNOLGY FOR 3-D SURVEILLANCE RADARS

Dr A K Singh, Shubha Elizabeth, P Srinivasa & Preeti Dongaonkar

Electronics and Radar Development Establishment
Defence Research & Development Organisation
C V Raman Nagar, Bangalore – 560 093

Email : singhak62@yahoo.com

Abstract : *A Multi Beam Antenna for long Range 3-D Surveillance Radar is required to generate an ultra low side lobe beam in Azimuth to avoid Jamming and to get better clutter performance and a cosecant squared shaped beam (during transmit) along with stack of simultaneous multiple beams (during receive) in elevation to extend the Radar coverage to high elevation angles. Present paper describes a comprehensive design and development approach towards establishing a very high performance multi beam antenna technology cost effectively meeting stringent electrical, mechanical and environmental requirements.*

Introduction: Multi beam antennas (MBA) is the most critical sub system of 3-D radars where it has become possible to generate three co-ordinates of the object i.e., distance, azimuth and height. A multi beam antenna is one with a capability to form many beams in different directions from a single aperture The antenna is required to form a very low side lobe narrow beam in azimuth (Peak SLL < -35 dB, Average SLL < -50 dB), shaped beam in elevation during transmit for the required coverage and multiple low side lobe beams simultaneously in elevation during receive from a single aperture. The antenna consists of a planar array, a shaped beam former and a multi beam former along with associated electronics and interconnecting cables.

Design and development of high performance multi beam antenna (MBA) system present several challenges to the antenna designer. In the present paper, a design and manufacturing methodology towards realizing the multi beam antenna technology with improved performance with optimum weight and volume has been described.

Design and Development : An over view

A computer aided design approach followed by innovative manufacturing methodologies has been adopted in establishing the core competency in the following critical areas:

[1] Design and development of an ultra low side lobe linear array of 4 m length consisting of 48 triplate dipoles as radiating elements fed by air dielectric stripline

power divider network. A design and manufacturing methodology [1] for achieving an ultra low peak SLL, a good input match and ability to handle a high peak power (more than 15 KW) has been established.

[2] Design and development of high power, compact, light weight shaped beam forming network for generating shaped beam using waveguide corporate power divider network [2]. This innovative design has benefited enormously in improving the performance, reducing the volume and weight as compared to internationally available systems.

[3] Design and development of low weight, high performance multi beam forming network using modified Blass matrix to generate multiple low side lobe beams in elevation [3-4] at pre-fixed elevation angles with no deviation in beam positions with frequency in the required band of operation.

Performance Evaluation & Test Results

All the three core elements of multi beam antenna system have been evaluated rigorously for its performance characteristics. The test results are summarized in the following paragraphs.

1. Ultra Low Side Lobe Planar Array : The 4 meter long linear array uses air-dielectric strip line feed network integrated with 48 triplate dipoles as radiating element. The array has been fabricated using precision machining and EDM wire cutting technologies to achieve the tolerances. Numbers of such linear arrays are used to make a planar array. Photograph of the present planar array is shown in Fig. 1. The array has been tested in Planar Near Field Test Range and the measured radiation pattern at center frequency is shown in Figure 2. The array has shown an excellent performance with a peak SLL better than –40 dB for 300 MHz & better than –35 dB for 600 MHz in S-band with a very good input VSWR.

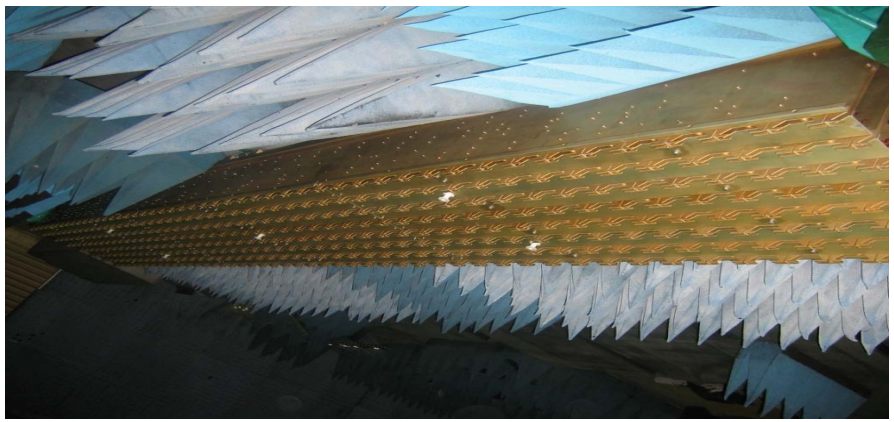

Fig. 1 Photograph of Planar Array

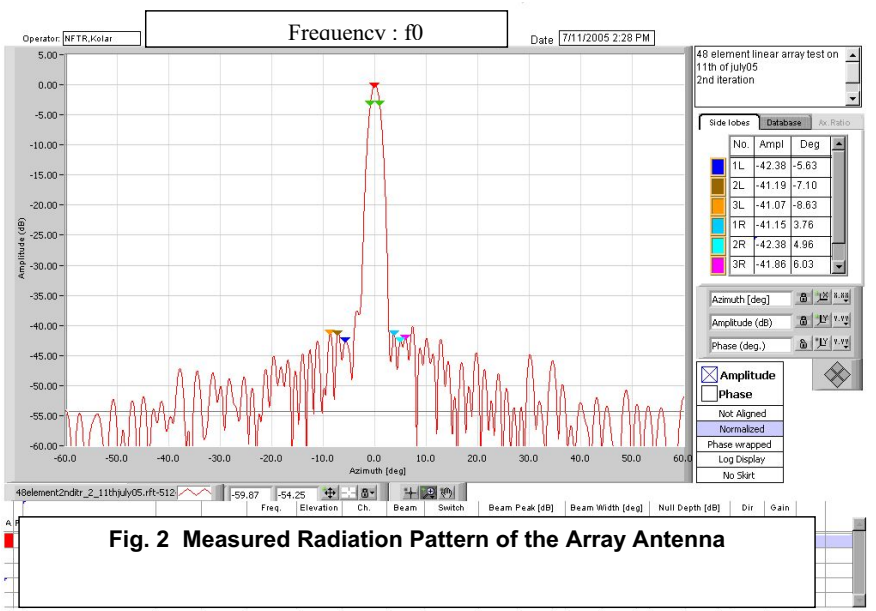

Fig. 2 Measured Radiation Pattern of the Array Antenna

2. High Power Shaped Beam Forming Network

Shaped beam former network (SBFN) generates amplitude and phase which when fed to the planar array forms a cosec-squared pattern in elevation. The compact, light weight, high power shaped beam antenna feed network based on non-standard, reduced height waveguide unequal power divider network, with integrated high power cables has been designed, fabricated and evaluated. Photograph of the SBFN is shown in Fig. 3. The measured test result of the SBFN is shown in Fig. 4. The innovative design technique has improved performance with substantial weight reduction, compared to the imported system.

Fig. 3 SBFN under test

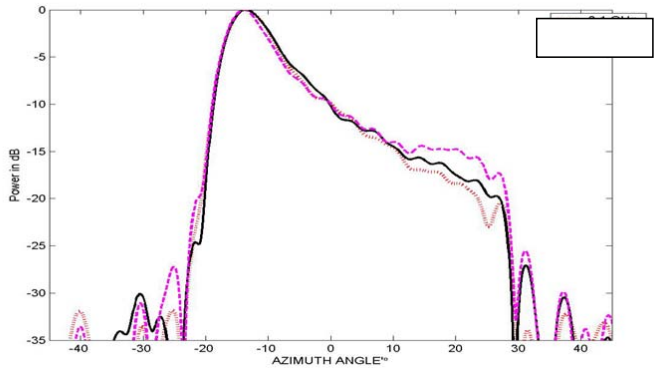

Fig. 4 Measured Pattern of SBFN

3. Modified Blass Multi Beam Forming Network

The receive beam former is designed & developed to generate 7 low side lobe beams of different beam width in pre fixed position in elevation plane during receive. It uses 7 channels of air-line cylindrical directional coupler [3] integrated as a modified Blass matrix [4] with inter connecting true delay lines to form 7 beams at the specific beam pointing location. The photograph of the feed network is shown in Fig. 5. Rigorous evaluation of the feed network has been carried out and the results are shown in Fig. 6. A Peak side lobe level better than –30 dB and beam pointing accuracy less than 0.1 degrees over a band of 600 MHz has been obtained.

Fig. 5 Photograph of Multi Beam Forming Network

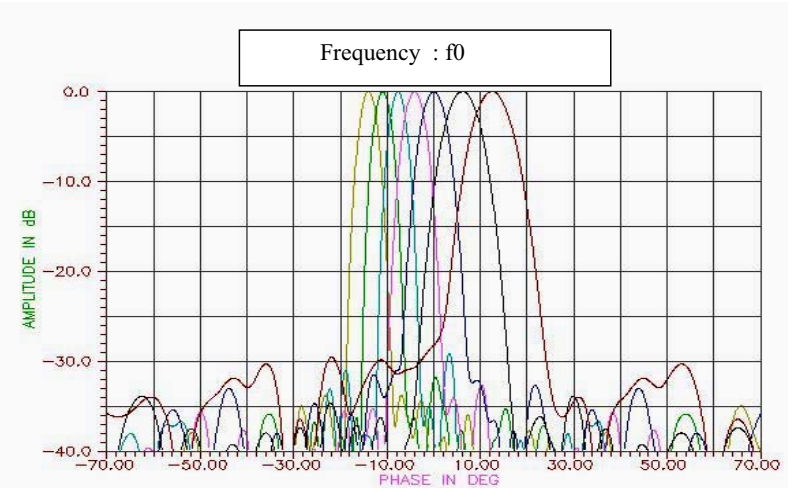

Fig. 6 Measured radiation pattern of 7 beams

Conclusion: The development of indigenous core competency in establishing Multi Beam Antenna Technology has enhanced self-reliance in two innovative ways :

- Self reliance for the country in the field of Multi Beam Antenna Technology fore 3-D radars, which were being sourced from outside the country till recently at a huge cost.
- Computer aided design (CAD) and knowledge aided design (KAD) capabilities to meet the stringent electrical, mechanical and operational requirements of similar radars for various other applications

References

[1] Ms. Preeti Dongaonkar, Ms. Shubha Elizabeth Avirah & Dr. A.K.Singh, “A Computer Aided Approach for Designing Very Low Sidelobe Triplate Dipole Array for Multi Beam Antenna System, “ (Accepted), IEEE Int. Symp. On Microwaves – 2006, Bangalore, India

[2] Shubha Elizabeth, A K Singh & S Christopher, “Tunable compact feeder network for shaped beam antennas of long range 3-D Surveillance Radar,” Proc. PIERS-2005, Hangzhou

[3] A K Singh & S Christopher, “ Characterisation of coupler elements for Blass matrix design for MBA Arrays”, Proc. ELECTRO-2001, Varanasi, pp. 37-52

[4] Design of modified Blass matrix for Multiple Beam Antenna”, ICMARS-2004, Jodhpur

Proceedings of APSYM2006, Dec. 14-16., Dept. of Electronics, CUSAT, India.

RESEARCH SESSION V

MICROWAVE ANTENNAS II

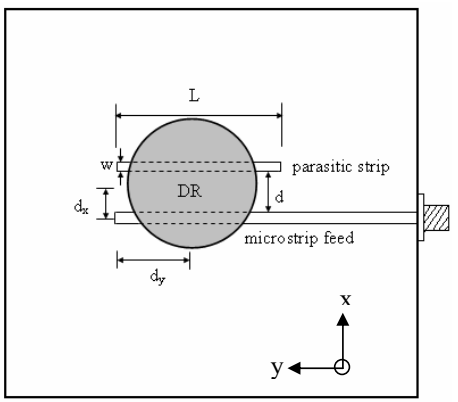

December 15, Friday

(11.00 a.m. -12.00 noon)

RESEARCH SESSION V

MICROWAVE ANTENNAS II

Chair : Prof. T.K. Sarkar, Syracuse University, USA.

Proceedings of APSYM2006, Dec. 14-16., Dept. of Electronics, CUSAT, India.

Electrical Characterization of Polymers and Evaluation of the CP Traveling Wave Antenna Performance

Manju Henry [(1)], *Richard Hopkins* [(1)], *Charles Free* [(1)], *Terho Kutilainen* [(2)] *Yoshihiko Tsujimoto* [(3)],
(1) Advanced Technology Institute, University of Surrey, Guildford, United Kingdom
(m.henry@surrey.ac.uk, r.hopkins@surrey.ac.uk, c.free@surrey.ac.uk)
(2) Aspocomp Technology Oy, Tutkijantie 13, FI 90570, Oulu, Finland.
(3) Advanced Material Division, Marubeni Chemic Corporation, Japan.

Abstract: *The electrical characteristics of polymer materials at millimeter wave frequencies up to 100 GHz are presented. The permittivity and losses in the material are calculated using planar resonant and non-resonant techniques. The performance of a CP traveling wave antenna fabricated on a polymer substrate is also evaluated.*

Introduction: High volume commercial wireless applications at millimeter wave frequency bands demand inexpensive high performance circuit technologies. Polymers are particularly suitable for applications involving conformal and flexible circuit designs. In this paper the microwave characteristics of a new non-fluorinated polyolefin based grafting polymer have been investigated. The new polymer is conventional PCB friendly but with superior high frequency properties. The transmission properties of the material were measured using two alternative test structures, namely meander lines and resonant rings. From the measured transmission data obtained using a network analyzer, both the line loss and the permittivity of the substrate material were obtained. Through calculation, the measured total line loss was separated into individual sources of conductor and dielectric loss, and these percentage loss calculations give a useful insight into the importance of the loss mechanisms in the substrate material. The performance of the material at microwave frequencies was also evaluated through the radiation characteristics of a CP traveling wave antenna designed for 15 GHz.

Measurement Techniques: The test circuits consisted of 50Ω straight and meander Finite Ground Coplanar Waveguide (FGCPW) lines as shown in Figure 1 (a) and a resonant ring structure shown in Fig. 1 (b). The circuits were measured up to 100 GHz using an HP8510C VNA, with the test circuits mounted on a Cascade on-wafer probe station.

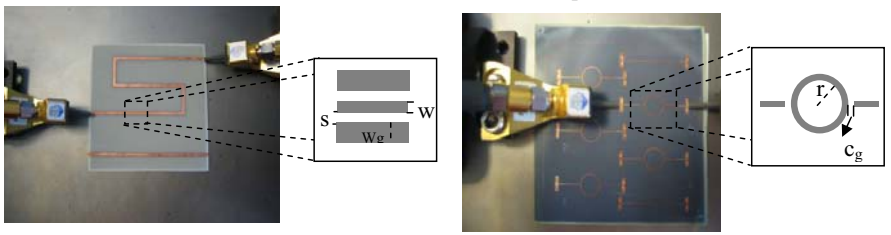

(a) (b)

Figure 1 Test circuits with their dimensions (a) the straight and meander FGCPW lines (b) the ring circuit.

Results:

(A) Relative Permittivity

1) Non resonant FGCPW meander line technique: The effective permittivity was obtained by measuring the difference in transmission phase ($\Delta\phi$) through the two FGCPW lines. The effective permittivity, ε_{eff}, can be obtained from (1) by measuring Δl_p (difference in the physical lengths of the two lines), and $\Delta\phi$ (phase difference) at different frequencies,

$$\Delta\phi = \frac{2\pi f(\Delta l_p)\sqrt{\varepsilon_{eff}}}{c} \qquad (1)$$

where f is the frequency and c is the velocity of light in free space. From ε_{eff} the relative permittivity can be calculated as explained in [1].

2) Resonant ring measurements: It is well known that when the electrical circumference of the ring is an integer number of wavelengths, a resonance will be obtained. Resonances were measured for two different resonant rings with the same radius of 3mm and width of 0.18mm but with different coupling gaps (c_g=0.12mm and 0.07 mm) to ensure that the ring was not too tightly coupled to the feed lines. Using standard microstrip design equations the actual relative permittivity is deduced from

$$f_n = \frac{nc}{2\pi r\sqrt{\varepsilon_{eff}(f)}} \qquad (2)$$

where *n* is the resonance number and *r* is the mean radius. The measured data obtained from the non-resonant FGCPW meander lines and the resonant ring structures are compared in Figure 2 (a). The data obtained from these two independent measurements agrees well, with the difference in the data obtained from two sets of measurements being less than 1.5 %.

(B) Losses

The total loss (α_t) per unit length will be the ratio of the difference in the S_{21} magnitudes of the two FGCPW lines, to the difference in the physical lengths of the lines. The measured total loss in dB/mm for the polymer is shown in Figure 2 (b). A detailed investigation of the surfaces of copper conductor on polymer was performed using a Scanning Electron Microscope (SEM), and from the results the surface loss of the conductors was calculated.

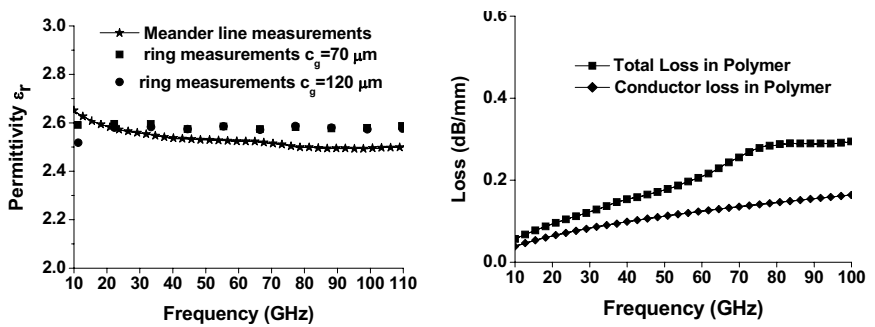

Figure 2 (a) The variation of relative permittivity in polymer with frequency obtained from meander line and resonant ring measurements (b) The total losses and conductor losses in dB/mm in FGCPW lines printed on polymers.

The bulk conductor loss was calculated theoretically from (4) using the loss analysis given in [2]. Note that

$$\alpha_c = \frac{R_s\sqrt{\varepsilon_{eff}}}{480\pi K(k1)K(k1')(1-k_{ab}^{\,2})}\times\left\{\begin{aligned}&\frac{1}{a}\left[\log\left(\frac{8\pi a}{t}\frac{1-k_{ab}}{1+k_{ab}}\frac{1+k_{ac}}{1-k_{ac}}\right)\right]\\&+\frac{1}{b}\left[\log\left(\frac{8\pi b}{t}\frac{1-k_{ab}}{1+k_{ab}}\frac{1-k_{bc}}{1+k_{bc}}\right)+\pi\right]\frac{1-k_{ac}^{\,2}}{1-k_{bc}^{\,2}}\\&+\frac{1}{c}\left[\log\left(\frac{8\pi c}{t}\frac{1+k_{ab}}{1-k_{ab}}\frac{1-k_{bc}}{1+k_{bc}}\right)+\pi\right]\frac{1-k_{ab}^{\,2}}{1-k_{bc}^{\,2}}k_{bc}^{\,2}\end{aligned}\right\} \qquad (3)$$

where K is the complete elliptical integral of first kind, R_s is the surface resistance (calculated from the surface roughness obtained from the SEM data), *t* is the thickness of the conductor, and *a, b, c,* k_{ab}, k_{ac}, k_{bc}, *k1* and k_1' are variables that depend on the FGCPW geometry [2]. The loss data are plotted in Fig 2 (b). Having calculated the conductor loss, the dielectric loss was simply found from the difference between the total loss and the conductor loss. For interest, the total loss is re-plotted as dB/wavelength in Fig 3 (a). It can be seen that the total loss in dB/wavelength decreases with frequency, and becomes almost independent of frequency above 50GHz. This is a significant result because many planar microwave components are a specific fraction of a wavelength long, and the result indicates that the loss per component is almost independent of frequency above 50GHz.

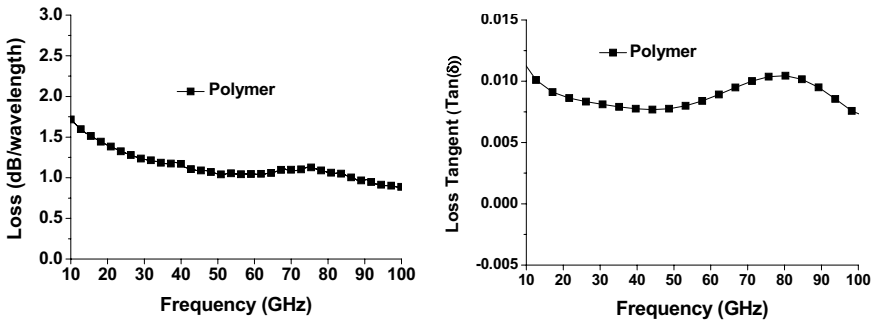

Figure 3 (a) Total loss plotted in dB/wavelength and (b) the loss tangent, for polymers at mm-wave band.

The variation of loss tangent with frequency for the polymer is shown in Figure 3 (b). It should also be noted that the loss tangent curve for polymer plotted in Figure 3 (b) shows Debye relaxation around 80 GHz. At the Debye relaxation frequency (f_τ) the loss tangent reaches the maximum value, which is mainly determined by the permittivity at dc (ε_{r0}), permittivity at infinite frequency ($\varepsilon_{r\infty}$) and τ the relaxation time.

Antenna Design and Measurement Results: A circularly polarized rectangular microstrip antenna array [3] working at 15 GHz was designed on the polymer substrate to evaluate the practical performance of the material. The antenna is shown in Figure 4. The structure is composed of eight planar rectangular radiating patches each with dimension L_p and W_p. L_p is the resonant dimension for the fundamental mode, and W_p is the optimum width to give good radiation from the patch. Each patch is linearly polarized with an annular spacing of $\lambda/8$ between the patches. A circular slot line channel of width W_s runs in the ground plane and

excites the patches successively 45 degree out of phase and will lead to circular polarization. The amount of energy fed into the patches is controlled by setting variable slot line offset for the patches. The antenna shows good return loss and circular polarization at the resonant frequency. We have focused on new materials aspects in this paper, and due to limitations of space we have not shown the CP patterns and return loss, but these have been reported elsewhere [3] for this antenna on other materials and show good performance. The return loss was found to be better than 20dB, with a CP bandwidth around 3% for the polymer material.

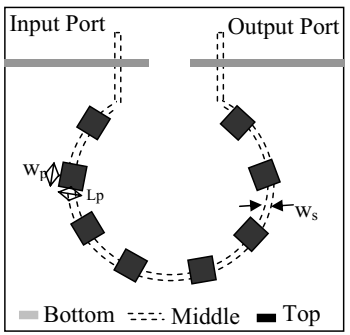

Figure 4 Geometry of the traveling wave feed circularly polarized planar antenna array designed on polymer substrate of permittivity 2.6 and height 0.508mm.

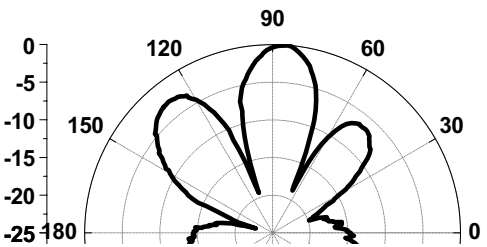

Figure 5 Measured radiation pattern for the traveling wave fed CP antenna array.

Conclusion: This study has shown that modern polymer materials exhibit a good microwave/millimeter wave performance. The excellent agreement between the results from the resonant ring and meander line measurements shows the validity of the latter broadband measurement technique.

References

[1] M. Henry, C. E. Free, Q. Reynolds, S. Malkmus and J. Wood, "In Depth Electrical Characterization of LTCC substrates at Millimeter Wave Frequencies up to 65 GHz", Proceedings of 7th MINT Millimeter-Wave International Symposium (MINT-MIS 2006), 15-17 February 2006, Espoo, Finland, pp. 37-42.

[2] G. Ghione and M. Goano, "The influenze of ground plane width on the ohmic losses of coplanar waveguides with finite lateral ground planes," *IEEE Trans. Microwave Theory & Tech.,* vol. 45, no. 9, pp. 1640-1642, September1997.

[3] K. M. Lum, C. Laohapensaeng, and C. E. Free, "A novel traveling wave feed technique for circularly polarized planar antennas" IEEE Microwave Component Letters, vol 15, no. 3, pp. 180-182, March 2005.

LINEAR ARRAY ANTENNA PATTERN OPTIMISATION USING GENETIC ALGORITHM

Sona O. Kundukulam and K. S. Beenamole
Electronics & Radar Development Establishment
Bangalore

ABSTRACT

A simple Genetic Algorithm (GA) has been implemented for optimizing the radiation pattern of linear array antenna. Validity of the proposed method is established by the comparison of the simulated results using GA with the calculated radiation patterns using standard equations.

INTRODUCTION

In the design of a microwave antenna array, classical optimisation methods do not solve the problem successfully, because they generally find only local minima and maxima, and hence do not find the optimal solution. Combination of Genetic Algorithm and other synthesis methods have already been reported [1,2] for the synthesis of linear arrays. In this paper, a simple GA [3] is applied to directly change the amplitude and phase of each element of the array until the desired radiation pattern is achieved.

A SIMPLE GENETIC ALGORITHM

Genetic Algorithms solve problems in the same way that nature solves the problem of adapting living organisms to the harsh realities of life in a hostile world: evolution. The mechanics of a simple genetic Algorithm are surprisingly simple, involving nothing more complex than copying strings and swapping partial strings. Simplicity of operation and power of effect are two of the main attractions of the genetic algorithm approach.

A simple Genetic Algorithm that yields good results in many practical problems is composed of three operators:

(i) Reproduction

Genes are the basic building blocks of Genetic Algorithms. A gene is a binary encoding of a parameter. A chromosome in a computer algorithm is an array of Genes. Each chromosome has an associated cost function, assigning a relative merit to that chromosome. The chromosomes are ranked from the most-fit to the least-fit, according to their respective cost functions. Unacceptable chromosomes are discardrd, leaving a superior species-subset of the original list.

(ii) Crossover

The operation of crossover is a form of "mating" which combines two chromosomes to produce two new chromosomes. The crossover operation randomly selects a site along the length of the chromosome, and then splits the two chromosomes into two pieces by breaking them at the crossover site. The new chromosomes are then formed by matching the top piece of one chromosome with the bottom piece of the other, as shown in Fig. 1.

(iii) Mutation

The operation of mutation randomly changes the value of a single bit (Fig. 2).

IMPLEMENTATION OF GAIN OPTIMISATION OF SHAPED BEAM PATTERN

In the case of a coded GA, each element of the array is represented by a string of bits where one part of the string corresponds to the amplitude and the other corresponds to the phase. Each element of the array is represented by its amplitude and its phase. This relationship is shown in TABLE 1. The process cycle for the simple GA optimizer developed for antenna design optimization is depicted in Fig. 3. The radiation pattern for four element array is calculated using standard equations [4] and the radiation pattern is sampled to get Q sampling points. The fitness function for these sampled points is defined as Eq. (1) [2]

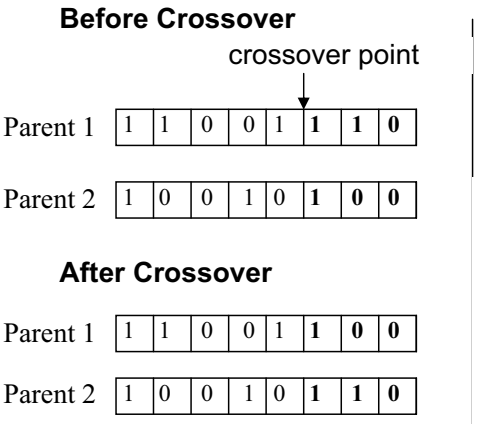

Fig 1 An illustration of single-point crossover

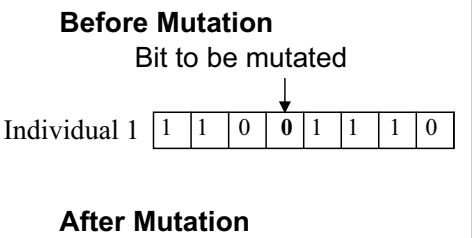

Fig 2 An illustration of the mutation process

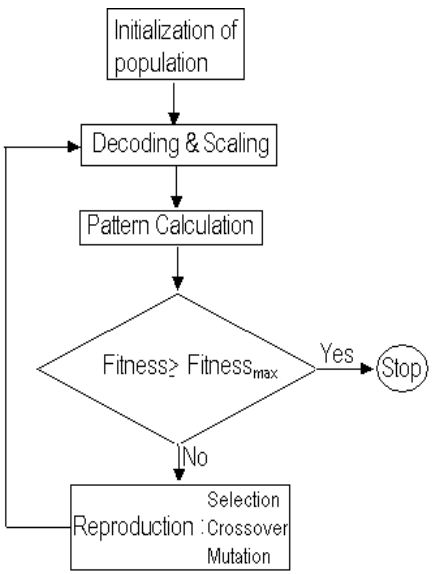

Fig 3 The Genetic Algorithm cycle

$$fitness = \frac{1}{1 + \sum_{i=1}^{Q} P_0 \left| \left(S_{di} - S_{ci} \right) \right|} \quad (1)$$

where P_0 is the penalty constant with the value within (0,1), S_{di} is the desired radiatio value and Sci is the computed value using GA respectively. The fitness value is calc a weighted sum of the individual comparisons for getting more precision in the shape of the pattern.

RESULTS

The Genetic Algorithm was developed for a population of 16 arrays with an inter spacing of d=0.825λ. Fig. 4 shows the desired radiation pattern and the pattern o using GA after 300 generations. Result shows that the optimized pattern is in close a to the desired pattern. The maximum fitness versus generation is plotted in Fig. 5 for trials. The current distribution values listed in Table 2 correspond to the radiatio shown in Fig. 4.

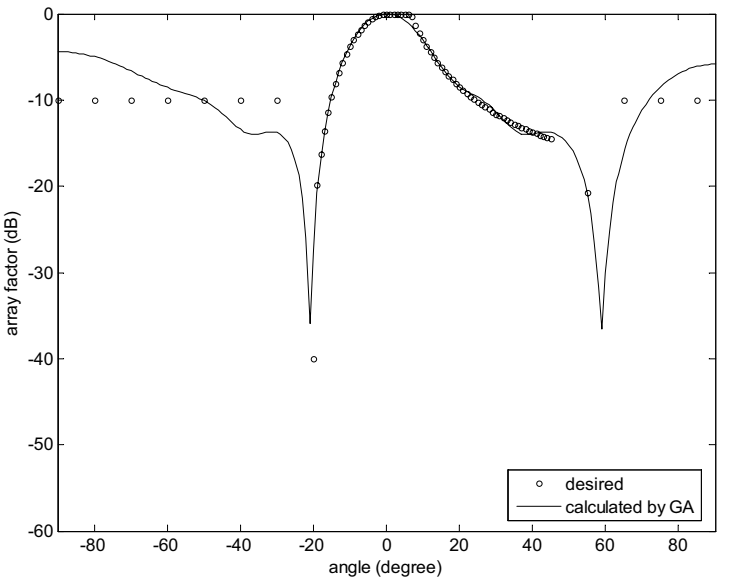

Fig. 4 The calculated and desired radiation patterns for a 4-element array

TABLE 1 The relationships between elements of GAs and arrays

Genetic Parameter	Antenna Array
Gene	Bit chain (string)
Chromosome	One element
Individual	One array
Population	Several arrays

TABLE 2 The optimized amplitude and phase values using GA

Element	Amplitude	Phase (deg.)
1	0.274678	-113.647059
2	0.682403	-84.000000
3	1.000000	-69.882353
4	0.995708	-99.529412

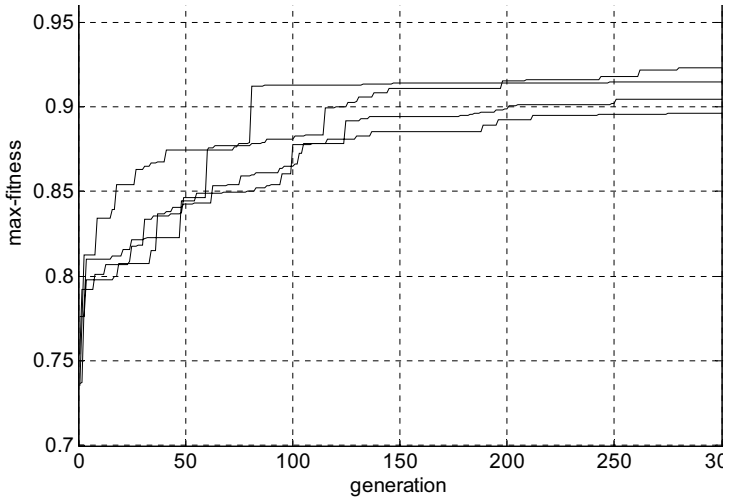

Fig. 5 Variation of fitness with generation for four different runs

CONCLUSION

The Genetic Algorithm is applied to optimize a shaped pattern for a linear array antenna by comparing the desired and calculated patterns. The capacity of simple GA to solve complex synthesis problems has been demonstrated by the results showing the good agreement between the desired and calculated radiation patterns, using GA.

REFERENCES

1. L.L.Wang, D.G. Fang, and W. X. Sheng, "Combination of Genetic Algorithm (GA) and Fast Fourier Transform (FFT) for Synthesis of Arrays", *Micowav. And Opt. Tech. Lett.,* Vol. 37, No.1, April 5, 2003

2. Diogenes Marcano and Filinto Duran, "Synthesis of Antenna Arrays using Genetic Algorithms", *IEEE Antennas and Propogation Magazine*, Vol.42,No.3, June 2000

3. Randy L. Haupt, "An Introduction to Genetic Algorithms for Electromagnetics", *IEEE Antennas and Propagation Magazine,* Vol. 37, No. 2, April 1995

4. C. A. Balanis, "Antenna Theory, Analysis and Design", 3rd ed. New York: Wiley, 2005

Development of Algorithm for Adaptive Antenna Array for satellite Communication

Anindya Kundu, Mainak Mukhopadhyay, Binay Kumar Sarkar, Ajay Chakrabarty
Kalpana Chawla Space Technology Cell (KCSTC)
Dept. of Electronics & Electrical Communication Engineering
Indian Institute of Technology, Kharagpur – 721 302
Email: akundu@ece.iitkgp.ernet.in,

Abstract: *Adaptive array antennas involve processing of signals induced on an array of sensors to steer the antenna beam towards the desired signal and produce null towards interference. Adaptive array have the property of spatial filtering, which makes it possible to receive energy from a particular direction while simultaneously blocking it from another angular direction. The capacity of smart antennas to direct transmit and receive energy toward a desired direction makes them useful for military satellite applications.*

Introduction: Processing signals from different sensors involves amplifying each signal before combining them. The amount of gain of each amplifier dictates the properties of the antenna array. To obtain the best possible cancellation of unwanted interferences, the gains of these amplifiers must be adjusted. For optimal processing, the typical objective is maximizing the output signal-to-noise ratio (SNR). For an array with a specified response in the direction of the desired signal, this is achieved by minimizing the mean output power of the processor subject to specified constraints. In the absence of errors, the beam pattern of the optimized array has the desired response in the signal direction and reduced response in the directions of unwanted interference. Finally we will implement the adaptive processing in a FPGA platform to reduce the processing power required. This FPGA processor will execute the adaptive algorithms to adjust the required weighting on antennas, direction-of-arrival (DOA) estimation methods[2] including performance comparisons, diversity-combining methods to combat the effect of interference in space applications.

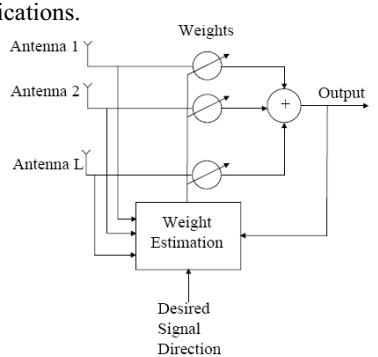

Fig:1 Block Diagram: Adaptive array antenna

A block diagram of a narrowband communication system is shown where signals induced on an antenna array are multiplied by adjustable complex weights and then combined to form the system output. The processor receives array signals, system output, and direction of the desired signal as additional information. The processor calculates the weights to be used for each channel.

Adaptive Beam-forming: The basic requirements of an adaptive Nulling antenna array are that it should provide enough gain margin to the user (or users) to satisfy the link calculations and at the same time suppressing the interfering signals. To achieve this, the elements of the antenna should have enough gain individually and should be physically configured in such a way as to be able simultaneously to point pattern nulls in the direction of interfering sources. To be sure of being able to place independent nulls on as many as N-1 interference sources, a satellite nulling antenna array needs to have at least N independently weighted antenna elements. The algorithm is the most crucial in steering the main beam in the direction of the SOI (signal of interest).

LMS algorithm: This algorithm is based on method of steepest decent. Changes in weight vectors are made along the direction of the estimated gradient vector [1].

Accordingly, $W(j+1) = W(j) + k_s \hat{\nabla}(j)$

Where $W(j)$ = weight vector before adaptation

$W(j+1)$ =weight vector after adaptation

k_s = scalar constant controlling rate of convergence and stability (k_s <0)

$\hat{\nabla}(j)$ =estimated gradient vector of $\bar{\varepsilon^2}$ with respect to W.

Where the difference between the desired response and the output response forms the error signal $\varepsilon(j) = d(j) - W^T X(j)$

W^T =transpose of the weight vector and $W^T X(j)$ is output at j th sampling instant

$$\hat{\nabla}(j) = \nabla[\bar{\varepsilon^2}(j)] = 2 * \varepsilon(j) * \nabla(\varepsilon(j))$$

$$\nabla(\varepsilon(j)) = \nabla[d(j) - W^T X(j)]$$

$$= -X(j)$$

$$\hat{\nabla}(j) = -2 * \varepsilon(j) * X(j)$$

using the gradient estimation formula the weight iteration rule becomes

$$W(j+1) = W(j) - 2k_s \varepsilon(j) X(j)$$

i.e., the next weight vector is obtained by adding to the present weight vector the input vector scaled by the value of the error. The LMS algorithm [1] is directly usable as a weight adaptation formula for digital systems.

The LMS algorithm requires about 2M complex multiplications per iteration, where M is the number of weights (elements) used in the adaptive array. The response of the LMS algorithm is determined by three principal factors: (1) the step-size parameter, (2) the number of weights, and (3) the eigen-value of the correlation matrix of the input data vector. Convergence of the mean of the weight vector to the wiener solution is insured if and only if proportionality constant k_s is set within certain bounds. From the stability

analysis of LMS algorithm we can prove that if $0 \rangle k_s \rangle -\frac{1}{\sum_{i=k-n+1}^{k} d^2(i)}$, then e(k) indeed converging. If we choose k_s too small then algorithm will adopt the change very slowly, and if we chose k_s too big, then error will not converge [1].

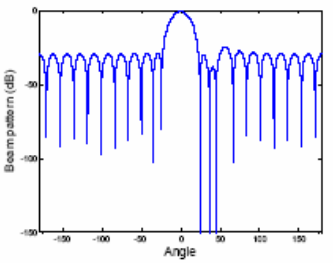

Fig:2

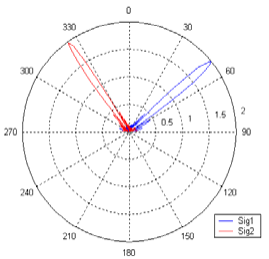

Fig:3

Fig:2 Adaptive Array Antenna Creating Nulls towards the Undesired Signal Directions

Fig:3 Adaptive Antenna Scanning two signal form -35˚and from 55˚.

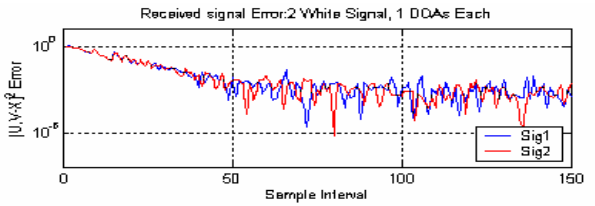

Fig:4 LMS algorithm converging around 46-47 iteration for both signals.

Implementation of Adaptive Algorithm in FPGA platform: Operating a fully adaptive antenna array requires a considerable increase in digital signal processing. Instead of one stream of data coming from a single antenna, adaptive antenna arrays produce multiple data streams, which must be processed. Adaptive array antenna used for beam-forming application, which involves N data streams from N antenna elements. The data stream from each antenna is put through an adaptive finite impulse response (FIR) filter. We will implement the adaptive algorithm in the FPGA based system so that the time required for adaptation reduces. FPGA kit allows a large number of multipliers and accumulators to be configured and interconnected in such a way that it performs certain tasks. This fine gain parallelism allows adaptive beam forming technique to be implemented much more efficiently than on a DSP based application specific integrated circuit for real time application. For real time application of digital beam forming the FPGA has four main processing modules 1. Coefficient update block: updates weights using LMS algorithm 2.input signal delay block: delays input signals according to the no of taps, 3. FIR algorithm block: carries out weight vector multiplications and scalings, 4. Tree adder block: carry out summations. In narrowband applications, the adaptive FIR filters simplify to a single weight vector. In a simple example with four antennas and a

narrowband system (such that the adaptive filters result in a single multiplication) the processing requirements approach one-half billion multiple accumulates (MACs) per second, for a sample rate of 105 mega samples per second. This sample rate is for a single beam and does not include the processing requirements for the adaptive update algorithm. While this level of processing could be achieved by a digital signal processor (DSP), the processing capability of a standard DSP would soon be exhausted if it had to support multiple beams or if the number of antennas was increased to produce finer beams. In this scenario, the processing requirements could easily reach several billion MACs per second[3].

Conclusion: When performing software simulations of adaptive LMS spatial filters, calculations are normally carried out with floating point precision. Unfortunately, the resources required of an FPGA to perform floating point arithmetic is normally too large to be justified, and measures must be taken to account for this. Another concern is the spatial filter tap itself. Numerous techniques have been devised to efficiently calculate the convolution operation when the filter's coefficients are fixed in advance. For an adaptive filter whose coefficients change over time, these methods will not work or need to be modified significantly. First, the issues involved in transitioning to a fixed point algorithm will be detailed. Next, the design of the filter tap will be considered. The reconfigurable filter tap is the most important issue for high performance adaptive filter architecture. Our objective is to create an adaptive filter IP core for use in an embedded PowerPC system. In this hybrid design, the microprocessor is used to handle memory transfers and give inputs to the FIR filter. The filter core performs the convolution and returns the result.

The microprocessor runs the training algorithm in software and updates the filter core when new coefficients are available

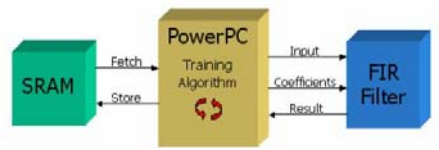

Fig: 5 Adaptive filter block

The benefits of this design are that a complete system prototype can be built quickly by utilizing the high level software(verilog / VHDL) for mundane tasks such as I/O, and also that the training algorithm used can be easily interchanged to evaluate their effectiveness. Of course, performance is slower but this can be overcome by training only at specific intervals (when signal statistics change), or by moving parallelizable sections of the training algorithm into the core as needed.

References:

[1] B. Widrow, P. E. Mantey, L. J. Griffiths & B. B. Goodeb "Adaptive Antenna Systems" (IEEE Proc, December 1967, pp.2143-2159).

[2] B.D.Vanveen and K.M.Buckley, "Beamforming: A versatile approach to spatial filtering"IEEE ASSP Magazine,pp.4-24,April 1988.

[3] Article written by Michael Gay and Isabel Phillips of QinetiQ's Real-Time Embedded Systems http://www.afrlhorizons.com/ETB/ETBriefs/Apr06/5657_400.html

DEVELOPMENT OF LINEAR BLADE ANTENNA ARRAY FOR AIRBORNE IFF APPLICATION

Gaurav Anand, A.K. Singh, T. Balakrishnan
Centre for Airborne Systems, DRDO, Belur, Yemalur post
Bangalore –560037
Email: gauravkumaram@rediffmail.com

Abstract:
This paper describes the design and development of an airborne, lightweight Linear Blade Antenna Array for indigenous Airborne Surveillance system. The antenna aperture dimension has been fixed to 1.12m × 0.2m based on the space available. This gives the antenna aperture gain of 12.5 dB. The antenna configuration is optimized to make it compact and lightweight to meet the platform requirement. The sidelobe level requirement is -24 dB in azimuth plane with a null depth of –20 dB for monopulse application. The antenna needs to have a power handling capability of 5 kW (peak), 50 Watt (avg.) and weight less than 3.5 Kg (with feed network). The theoretical design based on Inverted 'F' antenna technique was carried. The simulation has been carried out in CST Microwave studio and the simulation results are found to be in good agreement with the measured results. The antenna was tested for its VSWR, impedance bandwidth, radiation pattern & gain. A bandwidth of 16% for a return loss of -10 dB was achieved. The sidelobe level in azimuth plane is found to be better than -24 dB.

Keywords IFF, Blade Antenna, Inverted F antenna, monopulse, hybrid ring.

1. Introduction

The Identification Friend or Foe [IFF] system plays a vital role in the air defence syste country. IFF system in civilian sector is called Secondary Surveillance Radar (SSR). T system comprises of Interrogator and a compatible Transponder that is fitted on th aircraft. It operates as per the recommendations of Annexure 10 of Internationa Aviation Organisation (ICAO) and STANAG 4193. The Interrogator transmits pulsed in a specified direction. Aircraft fitted with compatible transponder receives the interro signal and replies back in the form of another coded signal.

The IFF system operates at a frequency of 1030 MHz during transmission and 109 during reception. In order to meet this requirement of dual frequency operation, the has been designed for a center frequency of 1060 MHz with a bandwidth of 85 MHz for VSWR of 1.6:1. The system is required to have two ports viz. Interrogate (INT) and (CNTRL) port to give a SUM pattern and a DIFF pattern from the same aperture.

2. Array Configuration

Based on the available dimension of 1.12m×0.2m, the antenna is designed to consist elements at an inter element spacing of 0.495λ. The antenna array elements are fed with a way azimuth power divider through eight cables of equal length.

3. Radiating Element

Blade antenna based on Inverted F antenna has been selected as the radiating eleme the requirements of small size that in turn satisfies the requirement of light weight, lo and low profile.

An inverted-F antenna is a post loaded antenna fed by a probe. As shown in fig. 1, th of inverted F antenna is the inverted L antenna (ILA), which consists of a short monc a vertical element and a wire horizontal element attached at the end of the monop height of the vertical structure is constrained to a fraction of the wavelength and so it profile structure. The horizontal portion is nearly a quarter wavelength long. The IL inherently low impedance due to its short vertical monopole loaded with a long hor wire at the end. To increase the radiation impedance, another inverted L-shaped el attached at the end of the vertical element and this is called the Inverted F antenna a in fig. 2, which is presently adopted 'Blade Antenna'.

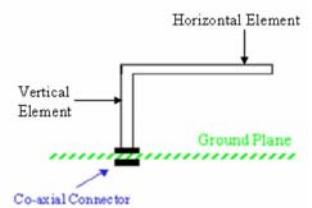

Fig 1: Inverted 'L' Antenna

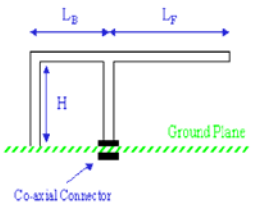

Fig 2: Inverted 'F' Antenna

The parameters of IFA that plays the vital role in determining the antenna characterist

H: is the height of the horizontal element above the ground plane.
L_F: is the horizontal distance from the feed point to the open end of the antenna.
L_B: is the horizontal distance from the feed point to the closed end of the antenna

Here, the desired tuning of the element can be achieved for any frequency, by adjus the short-end & open-end lengths of the element.

The theoretical design for a blade antenna was carried out and simulation has beer CST Microwave Studio to obtain the optimum performance. The simulated blade ant shown in Fig 3. Here, a cylindrical structure of teflon has been placed at the oper support the horizontal element. The return loss at 1.06 GHz is -33.7 dB as shown i The 10 dB return loss bandwidth is around 15%, which is 160 MHz. The simulated a radiation pattern is shown in Fig 5 and is found to be omni-directional. It was found t bottom ground plane of the antenna contributes a lot to the antenna performance. H dimension and shape of the ground plane was optimised for the antenna functionality as aerodynamic point of view because of its intended airborne application.

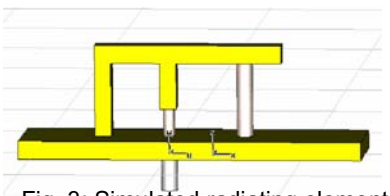

Fig. 3: Simulated radiating element

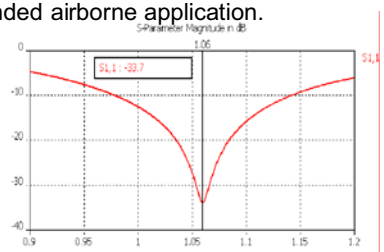

Fig. 4: Simulated Return Loss Pl

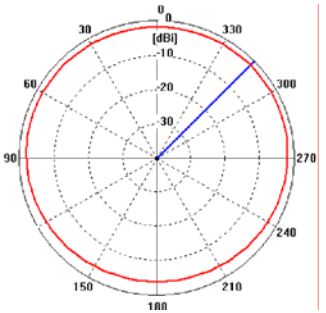

Fig 5: Azimuth Pattern

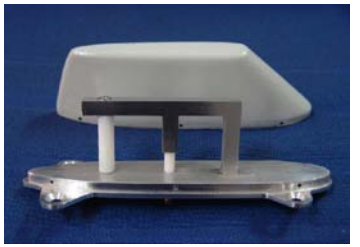

Fig 6: Fabricated Blade Antenna with radome

The fabrication of the blade antenna has been carried out by machining out from a aluminum (Al-6061T651) block of 180mm x 70mm x 38mm. The fabricated antenna radome is shown in Fig. 6. The measured return loss plot and the radiation pattern ar in Fig 7 and 8 respectively.

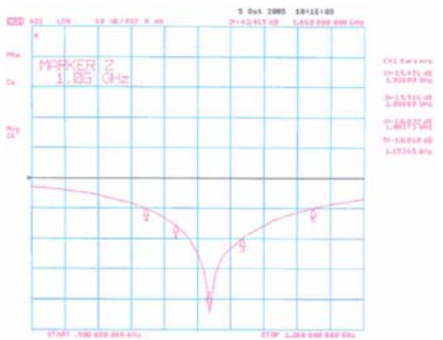

Fig 7: Measured return loss plot

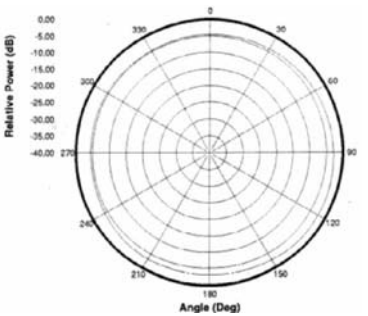

Fig 8: Azimuth Pattern

4. Feed Network

The feed network comprises of two elements namely the azimuth power divider and a ring. The feed network is also called the monopulse comparator. In order to obt required side lobe levels, Taylor distribution for -30dB SLL has been chosen. The the design of 8-way power divider has been done. In order to achieve high accuracy a insertion loss, the individual power divider were realized using microstrip line on a dielectric substrate of ε_r = 2.17 and loss tangent of 0.0019.
As the antenna array is required to have a SUM pattern and a DIFFERENCE pattern, ring has been designed. To make it compact, the hybrid ring was integrated with the power divider and configured on the same substrate and optimized for the ir application and minimum volume. The simulation was carried out to obtain an am balance of ± 0.1 dB and phase imbalance of ±3° over the frequency band as shown in Fig The simulated return loss plot is shown in Fig. 10.

The fabricated monopulse comparator is shown below in Fig 11. The amplitude and p all the eight ports are given below in Table 1. It was observed that the variations in m

amplitude and relative phase at all eight ports are within ±1 dB and ± 3° respectively w.r.t. the design goal.

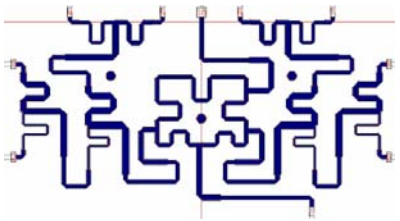

Fig. 9: Simulated Monopulse comparator

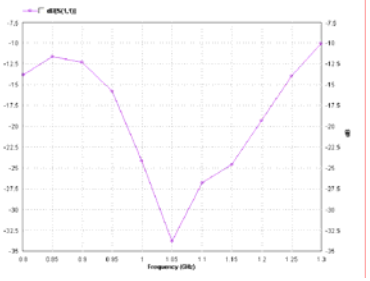

Fig. 10: Simulated Return Loss Plot

Input	Freq. In GHz	Port No 1		Port No 2		Port No 3		Port No 4		Port No 5		Port No 6		Port No 7		Po
		Amp.	Phase	Amp	Phase	Amp.	Phase	Amp.	Phase	Amp.	Phase	Amp.	Phase	Amp.	Phase	An
Σ Port	1.03	-17.3	139.1	-12.6	142.0	-7.92	142.8	-6.66	143.5	-6.59	143.9	8.09	143.9	-12.6	140.2	-17.4
	1.09	-17.4	80.99	-12.7	81..7	-7.87	81.01	-6.60	83.36	-6.48	83.57	7.97	83.40	-12.7	83.54	-17.4
Δ Port	1.03	-17.4	-44.7	-12.6	-48.9	-8.01	-46.5	-6.74	-48.5	-6.61	133.8	-8.02	132.2	-12.5	131.3	-17.3
	1.09	-17.4	-114	-12.7	-113	-7.94	-114	-6.67	-112	-6.60	67.90	-8.07	67.19	-12.7	67.97	-17.5

Table 1: Measured Amplitude and Pha

Fig. 11 Fabricated Monopulse comparator

The measured return loss plot at both Σ and Δ port are shown fig. 12(a) and 12(b).

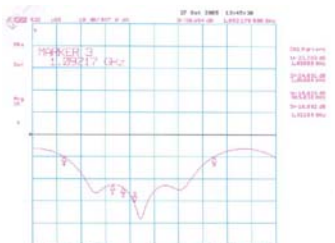

Fig 12(a) Measured return loss at Σ Port

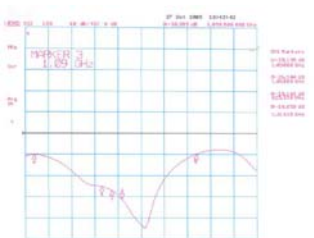

Fig 12(b) Measured return loss at Δ Port

4. Linear Array

The linear array was also simulated & the return loss plot for all the eight elements is shown in Fig 13. In the simulation, all the eight elements of the array were excited with the

coefficients & phase for -30 dB sidelobe level using Taylor's distribution so as to obta & difference pattern as shown in Fig 14.

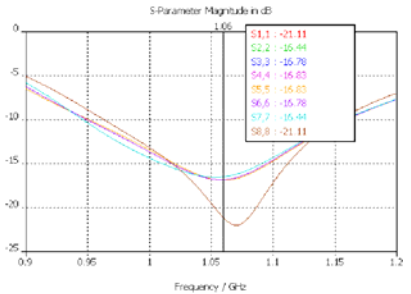

Fig. 13: Simulated Return Loss Plot

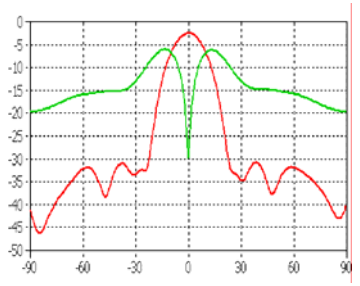

Fig 14: Simulated Sum & Difference Pa

The eight blade antennas with their radomes have been assembled on a 2mm thic sheet of dimension 1.12m×0.2m as shown in Fig 15.

Fig. 15: Linear Blade Antenna Array

All the eight outputs from the fabricated array shown in Fig 13 are connected monopulse comparator through cables of equal length. The weight of the linear array to be 3.1 Kg. The measured return loss plot Σ and Δ port are shown in Fig. 16 and respectively.

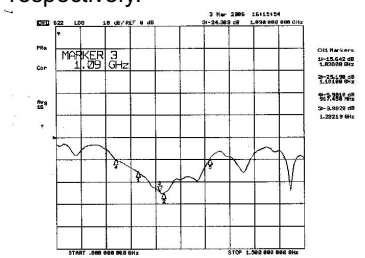

Fig. 16: Measured return loss Σ port

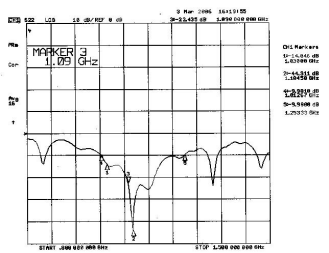

Fig. 17: Measured return loss Δ port

Radiation pattern measurement was carried out in the far field range. The azimuth p shown below in Fig. 18.

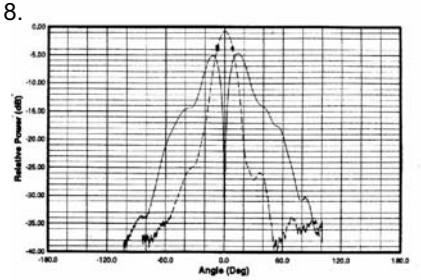

Fig. 18: Measured Azimuth Pattern

5. Conclusion

A linear blade antenna array of dimension 1.12m 0.2m was developed for Airbor application with stringent specification. The blade antenna was designed as an In antenna. A novel approach has been followed towards design of the compact mc comparator. The 3 dB beamwidth for the simulated pattern & measured pattern were be 16.9° & 15.9° respectively. The over all performance of the linear array exceeds the goal.

6. Acknowledgement

The authors gratefully thank Sri. K. Tamilmani, Director, CABS for the encourag provided and for granting permission to publish this work.

7. References

[1] K.R. Venkataramani, S. Vaidyanathan, "Quadraloop antenna for launch ve Proceedings of APSYM-CUSAT, December 1992.
[2] R.C. Fenwick, "A New Class of Electrically Small Antennas" IEEE Trans. Antennas and Propagation, Vol. AP-13, pp. 379-383, May 1965.
[3] Mitsuo Taguchi, Kazumasa Tanaka, "Active Inverted-F Antenna on Side of Conducting Plate" Dept. of Electrical & Electronic Eng. Nagasaki University, Ja
[4] Warren L Stutzman, Gary A. Thiele "Antenna Theory and Design" 2nd edition, Publication, 1998.

EFFECT OF ELEMENT CHARACTERISTIC AND SCAN BLINDNESS ON THE SCANNING PERFORMANCE OF PHASED ARRAY RADAR

Atanu Roy, Saswati Ghosh, Binay kumar sarkar ,Ajay Chakrabarty

Dept of Electronics & Electrical Communication Engineering,IIT-Kharagpur,Pin-721302,
Email:atanu_roy1981@yahoo.co.in

Abstract
A comprehensive study of finite phased arrays of Patch antennas and Vivaldi antennas is presented for missile seeker radar, with emphasis on the active admittance, scan blindness and scanning performance. The search, detect and track a high velocity target at a long distance by missile seeker is becoming more and more difficult as the target RCS becoming smaller due to application of stealth technology. Active phased array as missile seeker due to its potential to offer high power is a possible solution. For smaller array configuration of both patch and vivaldi, VSWR vs. scan angles, Active Admittance vs. scan angles are calculated using MATLAB™ 6.5 showing small variation with scan angles from 0^0 to 45^0.Also the patch and vivaldi array designs have been simulated showing the radiation pattern of single antenna and planar four element array using CST Microwave Studio™, Version 5 in KCSTC, IIT Kharagpur.

Index Terms-Active Admittance, phased array antenna, patch antenna,vivaldi antenna.

I.INTRODUCTION

Electronic scanning meets the growing need for radars to provide longer detection ranges and faster data rates and accommodates increased target densities. With electronic scanning, the radar beams are positioned almost instantaneously and completely without inertia, time lags and vibration of mechanical system.
Phased arrays of printed antennas elements constitute a potentially successful approach to the goal of low cost scanning arrays. Phased arrays may contain hundreds and thousands of elements, and may operate at microwave or millimeter wave frequencies on dielectric substrates. In phased array radar surface wave coupling can lead to scan blindness, where no effective power is transmitted or received by the array. Another point of interest to the array designer is the variation of antenna impedance with scan angle, which is important for impedance matching. The usual kind of array for radar, and the kind with which this paper is concerned, has been that in which the radiating elements are arranged in a periodic lattice in a plane or in a line and are each excited by an individual generator. The phases of the generators are varied linearly from one element to the next to form a beam, which can scan about the broadside direction to the plane or the line. Grating lobes can be avoided in an array antenna if the element spacing is restricted [4] to $d \le \frac{\lambda}{1+\sin(\theta_0)}$,where θ_0 is the scan angle.
Since past forty [1] years there has been good deal of interest in an unusual phenomenon, which occurs in certain of the phased arrays. It

has been observed that the element pattern exhibits a dip or null at an angle closer to broadside than that at which an endfire-grating lobe can exist. Although the possibility of such dip was expected at the latter angle, it was not expected at angles closer to broadside and was somewhat of a surprise.

Therefore the radiation pattern of the phased array is equal to the radiation pattern of its single element (assuming all the elements of the array are identical) multiplied by the array factor i.e. $E_a(\theta) = E_1(\theta) \times A.F$, where $E_1(\theta) =$ field due to single element., and the array is "blind' at those angles for which the element pattern has a null.

II. CORRECTION OF PHASE TO NEUTRALIZE MUTUAL COUPLING EFFECTS

The mutual coupling between the array elements is always present in phased arrays. These coupling effects may produce increased sidelobe levels, main beam squint, filled or shifted nulls, grating lobes, and array blindness at some scan angles. The effect of the mutual coupling between the elements in an array is incorporated in the expression for the active impedance of an antenna. The impedance of an antenna element when placed in an array defines the active impedance. The active impedance turns out to be a sensitive indicator not only of the bandwidth, but also of the scan performance. The more gradual the variation of the active resistance with scan, the slower is the active reactance scan variation and the more gradual is the mismatch scan loss.

The active admittance of the M-th element in an N-element array is given as follows

$$Y_{M_{act}} = Y_{M1}\frac{V_1}{V_M} + Y_{M2}\frac{V_2}{V_M} + \ldots + Y_{MM} + \ldots + Y_{MN}\frac{V_N}{V_M} = \sum_{r=1}^{N} Y_{Mr}\frac{V_r}{V_M}$$

where V_1, V_2, ……., V_N are the driving voltages of the corresponding elements.

From the above equation it is noticed that the active admittance of an element in the array is a complex quantity, which depends on the position of the element in the array. In a phased array, the current on the mn-th element in the antenna array located at (mD_x, nD_y) depends on the active admittance by the following relation

$$I_M = V\, e^{-j(m\phi_x + n\phi_y)} \times Y_{M_{act}}$$

If the active admittance of an element in the array is known, then the phase variation due to the mutual coupling can be estimated.

III. SELECTION OF ANTENNA ELEMENTS AND BEAM STEERING CONCEPT

The performance of different antenna elements has been studied to achieve an antenna system with the following design requirements:

- Coverage of ± 45°
- Operating in the Ku-band

To design an array with the desired specification the performance of different antenna elements [3] have been studied in regards of its scan performance and high frequency performance. The desired features of an antenna element are as follows:

- compact size
- high efficiency
- broad bandwidth
- low sidelobes
- low cross-polarizati

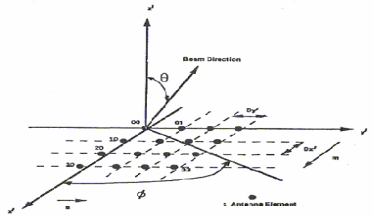

Fig.1.Planar phased array element rectangular grid geometry and beam scanning notation.

Here in the case of patch and vivaldi antenna array respectively we are considering the case of planar 4-element array. If M elements are

initially placed along the x-axis, let us assume that all the elements have identical amplitudes but each succeeding element has a progressive phase lead current excitation relative to the preceding one. An array of identical elements all of identical magnitude and each with a progressive phase is referred as a uniform array. The array factor can be

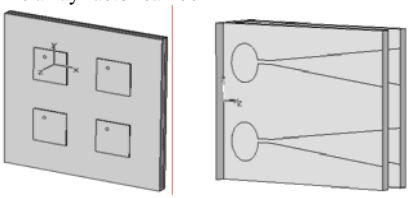

(a) (b)

Fig.2. (a) Planar four element patch antenna array

(b) Planar four vivaldi antenna array

obtained by considering the elements to be point sources. The array factor of the linear array can be written as

$$AF = \sum_{m=1}^{M} I_m e^{j(m-1)(kd_x \sin\theta\cos\phi + \beta_x)}$$

where I_m is the excitation coefficient of each element. The spacing and progressive phase shift between the elements along the x-axis is represented, respectively, by d_x and β_x.And m is the no. of elements in the x-axis. If N such arrays are placed next to each other in the y direction a distance d_y apart and with a progressive phase β_y, a rectangular array will be formed .The array factor of the entire planar array can be written as

$$AF = \sum_{n=1}^{N} I_n \left[\sum_{m=1}^{M} I_m e^{j(m-1)(kd_x \sin\theta\cos\phi + \beta_x)}\right] e^{j(n-1)(kd_y \sin\theta\cos\phi + \beta_y)}$$

where, $\beta_x = -kd_x \sin\theta_0 \cos\phi_0$ ……A

$\beta_y = -kd_y \sin\theta_0 \sin\phi_0$ ……B

Therefore phase can be written as

PHASE= $(m-1)\beta_x + (n-1)\beta_y$ ……..…C

Now while plotting the radiation pattern of the 4 element planar array we will first fix ϕ_0 to a value of 0 degree and vary θ_0 and in the second case we will just do the reverse one i.e. fix theta at a value of 90 degree and vary phi from 0-45 degree in the expression no …C. Therefore we are changing the progressive phase among the elements to steer the main beam in our desired location.

IV. RESULTS AND ANALYSIS

Software simulations of planar four element patch antenna and vivaldi antenna array using CST Microwave Studio [2] along with plotting VSWR vs. scan angle and Active Admittance vs. scan angle using Matlab 6.5 have been done in order to predict the performance of antennas over the scan angle in array configuration at higher frequency (17GHz).

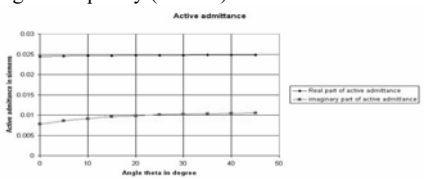

Fig.3.Variation of active admittance of element 1 over scan angle (Planar four element patch array)

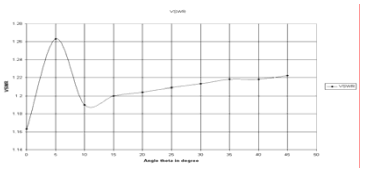

Fig.4.Variation of VSWR of element 1 over scan angle (Planar four element patch array)

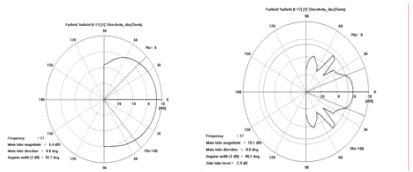

(a) (b)

Fig.5.(a)Radiation pattern of single patch antenna

(b)Radiation pattern of single vivaldi antenna

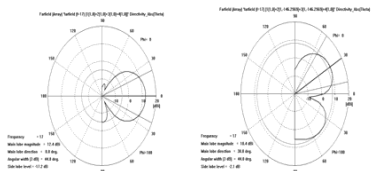

(a) (b)

Fig.6. Scan performance of planar four element patch array

(a) Phi fixed, desired theta direction 0 degree

(b) Phi fixed, desired theta direction 45 degree

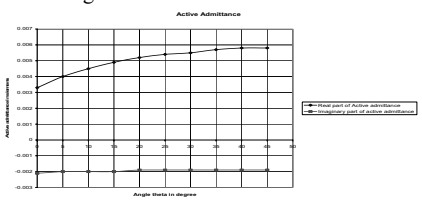

Fig.7.Variation of active admittance of element 1 over scan angle (Planar four element vivaldi array)

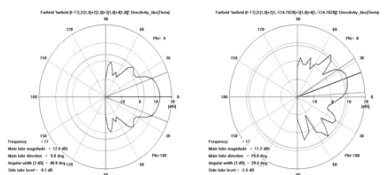

(a) (b)

Fig.8. Scan performance of planar four element vivaldi array

(c) Phi fixed, desired theta direction 0 degree

(d) Phi fixed, desired theta direction 45 degree

VI.CONCLUSION

Patch antennas can be used as phased array radar elements as scan range is more incase of patch array compared to vivaldi array. The above result shows that though the beam was shifting due to change in phase shift between elements, after 20^0 in case of vivaldi array any increase in progressive phaseshift to change the beam direction was not effective in moving the peak of the beam. This is due to narrow beamwidth of the vivaldi notch antenna element (Fig.5b) (i.e higher gain of the Vivaldi notch radiator). Therefore, to increase the scan angle it is required to have low gain antenna elements like microstrip patch in the array so that the radiation pattern is very wide and scanned array factor does not fall outside the element radiation pattern. Active admittance variation and VSWR variation is also less in case of patch array. Also the surface wave excitation and mutual coupling also contribute a lot for scan blindness in phased array antenna.

REFERENCES

[1] G.H.Knittel,A.Hessel and A.A.Oliner,"Element Patern Nulls in Phased Arrays and Their Relation to Guided waves,"Proc.IEEE,Vol.56,pp.1822-1836,November 1968

[2] CST Microwave Studio,Version 5

[3] Joon Shin and Daniel H. Schaubert, "A Parameter Study of Stripline-Fed Vivaldi Notch-Antenna Arrays", IEEE, Trans. Antenna and Propagation, Vol. 47, no. 5, pp. 879-886,May 1999.

[4] Understanding Radar Systems by Simon Kingsley and Shaun Quegan., Sci Tech Publishing, Inc, USA, 1999.

CYLINDRICAL DIELECTRIC RESONATOR ANTENNA WITH A COPLANAR PARASITIC CONDUCTING STRIP

A.V. Praveen Kumar and K.T. Mathew
Microwave Tomography and Materials Research Laboratory
Department of Electronics
Cochin University of Science and Technology, Kochi-682 022, India
Email: ktm@cusat.ac.in

Abstract: *The effect of a conducting parasitic strip, loaded co-planar with a dielectric resonator antenna excited in the broadside radiation mode is presented here. An improvement in the impedance bandwidth from ~7 % to ~17 % (by >50%) is achieved for optimum design parameters. Radiation mode remains broadside, with moderate gain over the band of interest.*

Introduction: Dielectric resonators (DR) have been proved to be highly effective in microwave and millimeter wave applications especially because of their low conduction loss and less bulk [1]. An interesting feature of DR is that certain low-Q modes ($HEM_{11\delta}$, $TM_{11\delta}$, $TE_{01\delta}$, $TM_{01\delta}$ etc) can be excited, which can radiate energy rather than confining it over a particular frequency band [2]. Shape of the resonator is an important parameter that determines the mode of operation. Among various shapes, cylindrical shape is the most popular and is well analyzed in [3] .Mainly two radiating modes of a cylindrical DR have practical application, designated as broadside ($HEM_{11\delta}$, $TM_{11\delta}$, $TE_{01\delta}$) and broadside-null ($TM_{01\delta}$) modes.

Literature [4, 5] shows that loading of metallic objects on the resonator surface can modify the impedance as well as the polarization characteristics. The present design shows how the addition of a parasitic coplanar strip adjacent to the microstrip fed DRA improves the impedance bandwidth. At the optimum strip position and dimensions, dual radiating modes of similar radiation characteristics are excited in close vicinity thereby forming a wide impedance band.

Antenna Structure and measurement: The antenna structure is shown in **Fig.1**. A cylindrical DR of permittivity $\varepsilon_{r1} = 20.8$, diameter $2a = 27.3$ mm and height $h = 8.4$ mm is fed with a 50Ω microstrip transmission line fabricated on a microwave substrate of permittivity $\varepsilon_{r2} = 4$. HP 8510C network analyzer is used for measuring the antenna.

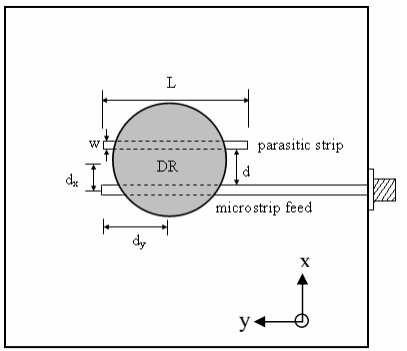

Fig 1: Antenna structure

Results and Discussion: As the initial step, the DR is proximity-coupled to the microstrip line so as to excite the broadside mode at a frequency of 2.605 GHz with a bandwidth (VSWR< 2) of 7.37 % from 2.545 to 2.74 GHz. This is shown by the solid line in **Fig 2**. Now a metallic strip of length *L* and width *w* is adhered at a distance of *d* from the feed as shown in **Fig 1**. It is observed from the measurements made that the strip dimensions and its spacing from the feed affect the impedance bandwidth of the DRA very notably. For optimum design parameters of *L*=45 mm, *w*=2 mm and *d*=12.5 mm, the DRA offers a bandwidth from 2.53 to 3.01 GHz or 17.33 %. The return loss and impedance plots with and without the strip loading are shown in **Fig. 3** and **Fig. 4** respectively.

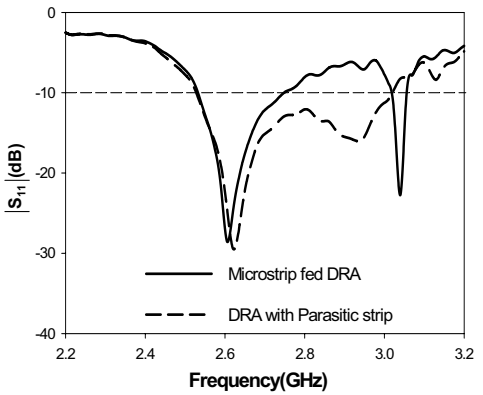

Fig 3: Measured return loss

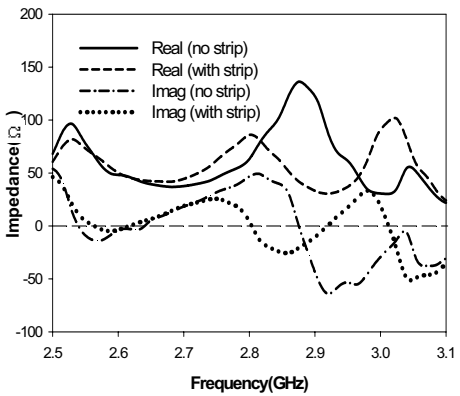

Fig 4: Input impedance

Measured radiation patterns in the two principal planes at the centre frequency of 2.77 GHz are shown in **Fig. 5**. Patterns are broadsided with cross-polar level better than -20dB indicating linear polarization of radiation. Similar characteristics are exhibited at other frequencies also in the operating band. Measured gain is ~5dBi at the centre frequency of 2.77 GHz.

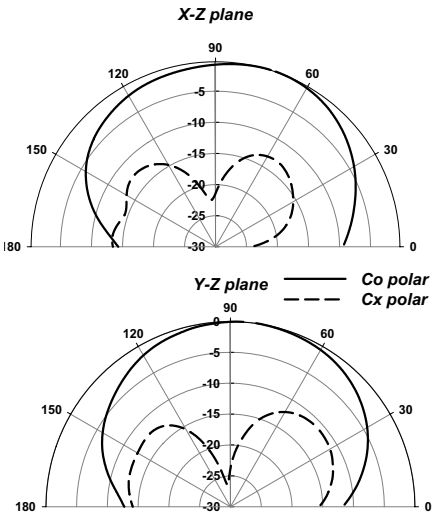

Fig 5: Measured radiation patterns at the centre frequency

Reference:

[1] Petosa A., A. Ittipiboon, Y. M. M Antar, D. Roscoe and M. Cuchaci., "Recent Advances in Dielectric Resonator Antenna Technology", IEEE Antennas and Propagation Magazine Vol. 40, No.3, 35-48, 1998

[2] Mongia R. K. and P. Bhartia, "Dielectric resonator antennas-A review and general design relations for Resonant Frequency and Bandwidth", Inter. J. Microwave and Millimeter-Wave Computer-Aided Engineering. Vol.4, No.3, 230-247, 1994

[3] Long S. A., M. McAllister and L. C. Shen, "The Resonant Cylindrical Dielectric Cavity Antenna", IEEE Transactions on Antennas and Propagation Vol. 31, No. 3, 406-412, 1983

[4] H. K. Ng and K. W. Leung, "Frequency Tuning of the Dielectric Resonator Antenna using a Loading Cap", IEEE Transactions on Antennas and Propagation Vol. 53, No. 3, 1229-1232, 2005

[5] Long R.T., R.J. Dorris, S.A. Long, M.A. Khayat and J.T. Williams, "Use of Parasitic Strip to produce Circular Polarisation and Increased Bandwidth for Cylindrical Dielectric Resonator Antenna", Electronics Letters Vol. 37,No.7 ,406-408,2001

Proceedings of APSYM2006, Dec. 14-16., Dept. of Electronics, CUSAT, India.

RESEARCH SESSION VI

MICROWAVE ANTENNAS III

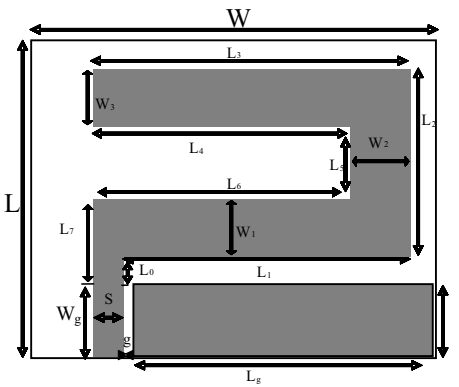

December 15, Friday

(12.00 noon -1.00 p.m.)

RESEARCH SESSION VI

MICROWAVE ANTENNAS III

Chair : Prof. G.S.N. Raju

AU College of Engineering, Visakhapatnam

Proceedings of APSYM2006, Dec. 14-16., Dept. of Electronics, CUSAT, India.

INTEGRATED DIELECTRIC RESONATOR ANTENNAS ON CONDUCTIVE SILICON SUBSTRATE FOR MILLIMETER WAVE APPLICATIONS

P.V. Bijumon[1], A.P. Freundorfer[2] and Y.M. M. Antar[1]*
[1]Department of Electrical and Computer Engineering
Royal Military College of Canada, Kingston, Ontario, Canada - K7K 7B4
E-mail: Bijumon@rmc.ca, antar-y@rmc.ca
[2]Department of Electrical and Computer Engineering
Queens University, Kingston, Ontario, Canada – K7L 3N6
Email: freund@post.queensu.ca

Abstract: *This paper addresses the feasibility of integrating dielectric resonator antennas on conductive silicon substrates. The antenna configuration, which has been chosen, is a high permittivity rectangular dielectric resonator, excited using a monolithic differential launcher. Design parameters were optimized employing Ansoft HFSS. The proposed antenna has a usable impedance bandwidth of 2.23 GHz at 39.56 GHz and 2.4dB gain with 77% radiation efficiency.*

Introduction

With the advancement in silicon technology, significant progress in the frequency integrated circuits (RFICs) has been made, including the demonstration of on chip antenna solutions [1]. The important classes of on-chip antennas investig includes, printed circuit monopoles, dipoles and microstrip patch antennas used for both wireless interconnect and air transmission applications [2-4]. However, the uses o printed planar integrated antennas in broadband wireless applications is limited becaus of their low power, efficiency and directivity performances. This is mainly because o losses involving (i) conductor losses in the antenna as well as substrate and (ii) surface wave effects. Hence efforts were made to improve the antenna performance by using high resistance silicon [1], use of embedded structures [5] and multilayer antenna fabricatio [6]. However, none of these methods could improve the antenna gain and radiation efficiency to the usable range in millimeter wave applications.

Dielectric resonator antennas (DRAs) have been established as a possible replacement of metallic antennas, since they have the inherent property consisting only of non-metal portions to eliminate the conduction loss. In addition, compared to metallic antennas, DRAs offer several other potential advantages like small size, higher radiation efficiency, wider bandwidth and no excitation of surface waves. They also offer the ease of integration with other active or passive MIC components. Hence it is anticipated that, the integration of a high permittivity dielectric resonator in place of the metallic antenna could be a possible solution to reduce the source of the losses on conducting silicon mentioned above. With this in mind, we propose a novel integrated dielectric resonator antenna (IDRA) on conductive silicon substrate. The characteristics

of the proposed IDRA are demonstrated in terms of some simulation results employing Ansoft HFSS. Fabrication and experimental investigations of the antenna are in progress.

Antenna Geometry

The investigated antenna topology is shown in Fig. 1. The radiating element is a high permittivity (ε_{dr} = 55) cubical DR of side L_{DR} = 0.93mm. The excitation mechanism is in the form of a printed dipole launcher, which is fed through a 50Ω co-planar strip line of length L_{CPW} = 1060μm. The dipole excitation is made in a differential mode.

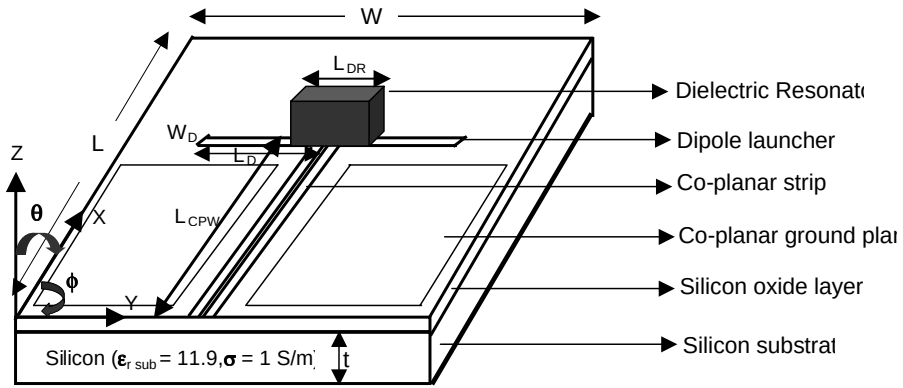

Fig. 1. Geometry of the proposed IDRA.
ε_{dr} = 55, L_{DR} = 0.93, L = 2.25, W = 2, t = 0.25, $\varepsilon_{r\,sub}$ = 11.9, σ = 1S/m, L_{CPW} = 1.06, L_D = 0.785 and W_D = 0.085 (all dimensions in mm)

The dipole has a single arm length, L_D = 785 μm and width, W_D = 85 μm, which is printed on a silicon metal oxide layer of thickness 6.22 μm and ε_r = 4. The length of the dipole and the position of DR on the substrate were optimized to yield maximum coupling of energy between the two. The resultant position of DR is as shown. A thick polymer passivation layer of thickness 4 μm and ε_r = 3.5 provides an isolation between DR and the metal dipole. The whole circuit is fabricated on a silicon substrate of dimensions, length x width, L x W = 2.25mm x 2 mm, thickness t = 250 μm, $\varepsilon_{r\,sub}$ = 11.9 and conductivity σ = 1 S/m.

Results and Discussions

Several challenges are to be met in the design and fabrication of IDRA to operate at millimeter wave frequencies. Effects of various antenna parameters such as launcher dimensions, permittivity of the dielectric resonator, conductivity and thickness of the substrate are examined to obtain an optimum input impedance response needed to yield maximum gain and radiation efficiency. It is observed that the gain and radiation efficiency of IDRA increases with resistivity of the substrates. However, the antenna performance cannot be increased to a maximum on the expense of high resistance silicon as the later is not easily available and is costly. Hence, a value of 100 Ω-cm (conductivity 1 S/m) silicon substrate is a good compromise between cost and performance, and the

characteristics of an IDRA with parameters as mentioned in Fig. 1 are demonstrated. The entire antenna structure is placed on a rectangular copper strip of length = 10mm and width 16mm, which acts like a ground plane. The DR is excited in the lowest order $TE_{11\delta}$ mode, which was confirmed based on the full wave solutions of HFSS.

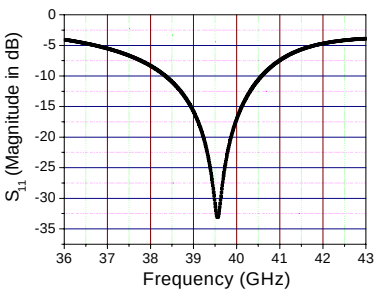

Fig. 2. Variation of S_{11} of the antenna with frequency (parameters as shown in Fig

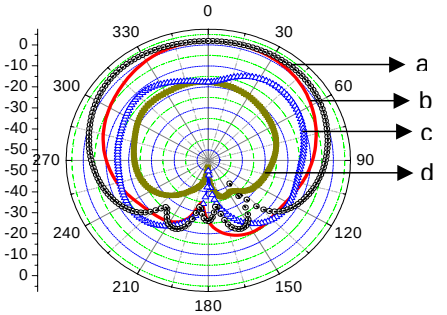

Fig. 3. Radiation pattern of proposed IDRA at 39.56 GHz
a - H plane co-polar, b- E plane co-polar
c - H plane cros-polar, d- E plane cros-polar

Table 1.Comparison of proposed IDRA with previously reported works

Ref.	Application	Antenna type	Substrate Material	Gain	Comments
[2]	Wireless interconnect	Printed dipole	Si 10 Ω-cm	-56 dB @ 18 GHz	High transmission loss
[3]	Air Transmission	Printed monopole	Si 10 Ω-cm	-6.0 dBi @ 40 GHz	Lossy, single-ended antenna, non-uniform radiation pattern
[4]	Air Transmission	Printed dipole	Si 100 Ω-cm	-5 dBi @ 21GHz	Differential antenna Lossy antenna for air transmission
			Si 15 Ω-cm	-8.0dBi @ 21 GHz	
[5]	Air Transmission	Aperture coupled printed patch antenna	Very high resistance Silicon	2.2 dB @ 15 GHz	Very bulky ($V = 124mm^3$) and complicated structure
[6]	Air Transmission	Micromachined inverted F	Low resistance Silicon	-0.7 dBi @ 24 GHz	Very bulky ($V = 36mm^3$) and complicated structure
This Work	Air Transmission	Integrated DRA	Si 100 Ω-cm	2.4 dB @ 39.56 GHz	Differential antenna: Highly compact ($V = 3.27\ mm^3$), excellent gain and radiation performance
			Si 15 Ω-cm	0.96 dB @ 40.10 GHz	

Fig. 2 shows the variation of return loss of IDRA with frequency. The antenna resonates at 39.56 GHz with an acceptable bandwidth (< -10dB) of 2.23 GHz (38.35 -

40.58 GHz). Simulated radiation patterns of IDRA in the elevation and azimuth planes at 39.56 GHz are illustrated in Fig. 3. The angles θ and ϕ are taken as illustrated in Fig. 1. In both the planes, the cross-polar isolation is better than –20dB. The simulated gain of the antenna is 2.4 dB and the resultant radiation efficiency is 77%.

Simulation was also performed on an IDRA on standard silicon of conductivity 6.66 S/m (resistivity 15 Ω-cm). The gain and radiation efficiency decreased drastically to reach 0.96 dB and 28.16 % respectively. However, this is better than reported on any other printed circuit antennas. A comparison between the results reported so far in silicon based integrated antennas are described in Table 1. It is evident that the proposed IDRA has better bandwidth, radiation performance and simpler structure than that of the previously reported antennas and is highly suitable for ultra miniaturization of ICs and for the integration of active devices.

Conclusions

An integrated dielectric resonator antenna on conductive silicon substrate is reported for the first time. Effects of various antenna parameters such as launcher dimensions, permittivity of the dielectric resonator, conductivity and thickness of the substrate on the radiation performance of the antenna are investigated. On silicon substrate of conductivity 1S/m, the antenna has an impedance bandwidth of 2.23 GHz at 39.56 GHz, gain of 2.4 dB and 77% radiation efficiency. On standard silicon substrate, the antenna gain and radiation efficiency decreases to reach 0.96 dB and 28.16 % respectively. These characteristics are far better than any other antenna previously fabricated on silicon substrate of the same resistivity. This IDRA technique is useful for application in wireless communication devices as well as chip-to-chip interconnect.

References

[1] K.O. Kenneth et al. "On-chip Antennas in Silicon ICs and their application" IEEE Trans. on Electron Devices, Vol. 52, No. 7, pp.1312-1323, 2005.

[2] K. Kihong and K.O. Kenneth, "Characteristics of integrated dipole antennas on bulk, SOI and SOS substrates for wireless communication" Proc. of the IEEE Int. Electron Device Technology Conference, pp. 21-23, 1998.

[3] K.Chan et al. "Integrated antennas on Si with over 100GHz performance, fabricated using on optimized proton implantation process", Microwave and Wireless Component Letters, Vol. 13, No. 11, pp. 487 – 489, 2003.

[4] M. Pons, F. Touati and P.Senn, "Study of on-chip integrated antennas using standard silicon technology for short distance communication" Proc. of the Eur. conf. on Wireless Technology, pp. 273 – 276, 2005.

[5] I.K. Itotia and R.F. Drayton, "Aperture coupled patch antenna chip performance on lossy silicon substrates" IEEE Antennas and Propagat. Symp. Vol. 1B, pp. 377-380, 2005.

[6] E. Orjefors, K. Grenier, L. Mazenq, F. Bouchriha, A. Rydberg and R. Plana, "Micromachined inverted F antenna for Integration on low resistivity silicon substrates", IEEE Microwave and Wireless Component Letters, Vol. 15, No. 10 pp. 627-629,2005.

[7] K.M. Luk and K.W. Leung, "Dielectric resonator antennas", Research Studies Press Ltd, Baldock, England, 2003.

Application of Neural Network for solution of partial differential equation in Electromagnetics

Sridhar Pattanaik[1] and R.K Mishra[2]

(1) Department of Electronic Science, Berhampur University, Orissa, India, 760 007, sridhar_pattanaik@yahoo.co.in

(2) Department of Physics (Electronics), Sambalpur University, Burla, India, 768 019

Abstract: *Differential equations is used in different engineering applications like in image processing, Antenna problems control application. There are different methods to solve the differential equation like Analytical and Numerical. Each method has its own advantage and disadvantage. The function approximation properties of neural networks tend to be very attractive as trial solutions for Differential equation for the boundary value problems. Ordinary Differential equation (ODE), Partial Differential equation (PDE) has been solved by Neural Networks [1,2,3]. The Neural network approach is accurate at the same time requires fewer parameters than other methods. The most commonly used are the Multi Layer Perceptron (MLP) and the Radial Basis Functions (RBF) architectures. In this paper the procedure involved in solving partial differential equations (Poisson's equation) using neural network is discussed with example.*

Index Terms—Boundary value problems, engineering problems, neural networks, partial differential equations (PDEs, multilayer perceptron, radial basis function (RBF) Networks.

duction: There are many boundary value problems, which involves partial differential ion. Only of the few can be solved by analytical methods. Generally we depend on the rical methods to solve partial differential equation. Finite difference is the most ion method. In finite difference method the derivative appearing in the equation and the lary condition are replaced by their finite difference approximation. The given equation nged to a difference equation, which is solved by iterative procedure. This process is and gives a good result of boundary value problems.

olution of differential equations in terms of ANNs possesses several attractive features: tely differentiable closed analytic form.

- Superior interpolation properties as compared to well-established methods such as finite elements.
- Small number of parameters.
- Suitability for efficient implementation on parallel computers.
- Implementability on existing specialized hardware (neuroprocessors [3]) a fact that will result to a significant computational speed.

od to solve partial differential equation using ANN:

ion of partial differential equation plays a major role for antenna analysis. The wave ion is a partial differential equation. Every antenna problem needs to satisfy the wave ion. In this section the general method to solve a partial differential equation is ssed and the procedure can extend this method for the complex differential equations.

ANN is being used for solving ordinary and partial differential [1] equation. The trial solution is written as sum of two terms

$$\varphi_t(\vec{x}) = A(\vec{x}) + F(\vec{x}, N(\vec{x}, wt)) \quad (1)$$

The term A(x) contains no adjustable parameters and satisfies the boundary condition. N(x,wt) is a single-output feedforward neural network with parameters 'wt' and input units fed with the input vector x . The second term F is constructed in such a way so as not to contribute to the BC's $\varphi_t(\vec{x})$ must also satisfy them. This term employs a neural network whose weights and biases are to be adjusted in order to deal with the minimization problem. The problem know has been reduced from the original constrained optimization problem to an unconstrained one (which is much easier to handle) due to the choice of the form of the trial solution that satisfies by construction the BC's.

The function F discussed above is different for different differential equations, which may be difficult to construct. This can be avoided by taking the trail solution of the differential equation to be N(x,wt) and the cost function is constructed by taking the error due to the equation and the error due to the boundary and is minimized by training the network.

The cost function construction is much easier, which is the salient feature of the method. This is discussed as an example in the next section.

Illustration

Consider the two-dimensional partial differential equation (Poisson's equation)

$$\frac{\partial^2 \varphi}{\partial x^2} + \frac{\partial^2 \varphi}{\partial y^2} = f(x, y) \quad (2)$$

x ∈ [0,1] , y ∈ [0,1] with *Dirichlet* BC: φ (0,y) = f_0 (y) , φ (1,y) = f_1 (y) , φ (x,0) = g_0 (x), φ (x,1) = g_1 (x)

Here φ_t (x, y) = N (x, y, wt) is taken as the trial solution of the neural network instead of equation (1), 'wt' is the weight to be determined by training.

In this paper two errors are taken into account for the construction of error function one due to the equation and the other due to the boundaries.

The equation error is given by

$$Eq\_error = \left(\frac{\partial^2 \varphi_t(x_i, y_j)}{\partial x^2} + \frac{\partial^2 \varphi_t(x_i, y_j)}{\partial y^2} - f(x_i, y_j) \right)^2 \quad (3)$$

As in the problem there are four boundaries the boundary errors are given by

$$E_{b1} = \left(\varphi_t(0, y_j) - f_0(y_j)\right)^2 \quad (4)$$

$$E_{b2} = \left(\varphi_t(1, y_j) - f_1(y_j)\right)^2 \quad (5)$$

$$E_{b3} = \left(\varphi_t(x_i, 0) - g_0(x_i)\right)^2 \quad (6)$$

$$E_{b4} = \left(\varphi_t(x_i, 1) - g_1(x_i)\right)^2 \quad (7)$$

The cost function for training the network is given by

$$E = Eq\_error + E_{b1} + E_{b2} + E_{b3} + E_{b4} \quad (8)$$

Proceedings of APSYM2006, Dec. 14-16., Dept. of Electronics, CUSAT, India.

Equation (8) is used for updating the weights of the neural network and is discussed more detailed in the next section.

Example

Consider a two-dimensional Poisson's equation

$$\nabla^2 \phi(x, y) = e^{-x}(x - 2 - y^3 + 6y) \quad (9)$$

with x ∈ [0,1] , y ∈ [0,1] with Dirichlet BC: φ (0,y) = y^3 , φ (1,y) = (1 + y^3) e^{-1} , φ (x,0) = x e^{-x},

$$\varphi_a(x, y) = e^{-x}(x + y^3) \quad (10)$$

A feed forward neural network with back-propagation algorithm [4,5] is used to train the network in a sequential way. The number of input units, hidden neurons and output neurons are two, ten and one respectively. The transfer function for the hidden neuron is 1/(1 + exp (-x)) and linear transfer function is used for the output neurons.

For training the network the cost function is determined for the problem according to equation (8).

$$v_{hj}^{k+1} = v_{hj}^{k} - \eta \frac{\partial E^k}{\partial v_{hj}} + \alpha\left(v_{hj}^{k} - v_{hj}^{k-1}\right) \quad (11)$$

$$w_{ih}^{k+1} = w_{ih}^{k} - \eta \frac{\partial E^k}{\partial w_{ih}} + \alpha\left(w_{ih}^{k} - w_{ih}^{k-1}\right) \quad (12)$$

$$\theta_h^{k+1} = \theta_h^{k} - \eta \frac{\partial E^k}{\partial \theta_h} + \alpha\left(\theta_h^{k} - \theta_h^{k-1}\right) \quad (13)$$

Where v_{hj} is the weights from the input to hidden neuron, w_{ih} is the weights from hidden to output and θ_h is the threshold. η, α are the learning rate and momentum respectively. Selection of a value for the *learning rate parameter*, η, has a significant effect on the network performance. Usually, η must be a small number – of the order of 0.05 to 0.25 – to ensure that the network will settle to a solution. A small value of η means that the network will have to make a large number of iterations. It is often possible to increase the size of η as learning proceeds. The value of alpha should be positive but less than 1 and represent the momentum term.

We have taken η = 0.05, α = 0.5 and training tolerance 0.5 × 10^{-3}.

The exact solution of the PDE is $\varphi_a(x, y) = e^{-x}(x + y^3)$ and is compared with the Neural Network output φ_t (x, y) = N (x, y, wt). A graph is plotted between (x, y, error)

Where,

$$error = \varphi_a(x, y) - \varphi_t(x, y) \quad (14)$$

In the neural network method, increasing the number of hidden units can control the accuracy. In this approach time increases linearly with the number of parameters. It must be noted that our experiments have been carried out on a P-III with 192MB RAM.

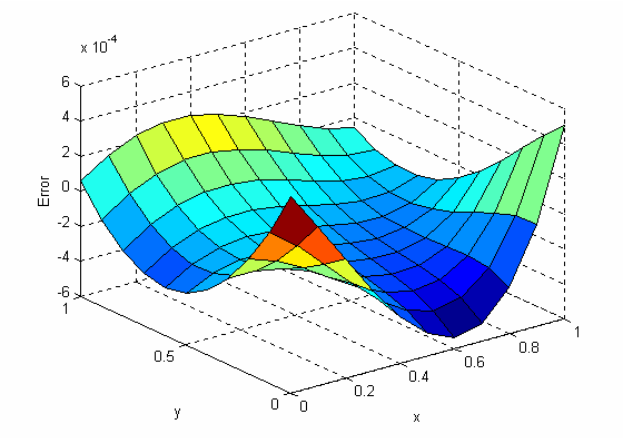

Figure 1 Accuracy of the solution

Conclusion and future research

A method has been discussed for solving differential equations defined on orthogonal box boundaries that relies upon the function approximation capabilities of feedforward neural networks and provides accurate and differentiable solutions in a closed analytic form. This method can be extended to three-dimensional problems. As the dimensionality increases, the number of training points becomes large. This fact becomes a serious problem for methods that consider local functions around each grid point. In the case of the neural method, the number of training parameters remains almost fixed as the problem dimensionality increases. Trials are under way to apply this method for the solution of wave equation and complicated complex differential equations.

Reference:

[1] I. E. Lagaris, A. Likas, and D. I. Fotiadis "Artificial neural networks for solving ordinary and partial differential equations", *IEEE Trans. Neural Networks*, Vol. 9, No. 5, pp. 987–995, Sep. 1998.

[2] Silvia Ferrari and Robert F. Stengel, "Smooth Function Approximation Using Neural Networks", *IEEE Trans. Neural Networks,* Vol. 16, No. 1, pp. 24–28, Jan. 2005 .

[3] R. Yentis and M. E. Zaghoul, "VLSI implementation of locally connected neural network for solving partial differential equations", *IEEE Trans. Circuits Syst. I*, Vol. 43, No. 8, pp. 687–690, 1996.

[4] H. Lee and I. Kang, "Neural algorithms for solving differential equations," J. *Comput. Phys.*, Vol. 91, pp. 110–117, 1990.

[5] S. Haykin, "Neural Networks, A Comprehensive Foundation, Macmillan, New York", 1994.

Novel ANN model for Resonant Frequencies of Regular Patch Antennas

Sridhar Pattanaik[(1)], and Rabindra. K. Mishra[(2)]
(1) Department of Electronic Science, Berhampur University, India 760 007
E.mail: sridhar_pattanaik@yahoo.co.in
(2) Department of Physics (Electronics), Sambalpur University, Burla, India 768 019

***Abstract:** In this paper we propose a single neural network [1], which will be valid for determination of resonant frequencies of both Rectangular and Circular Microstrip Antenna. A single artificial neural network is developed for the same. A two-layer feed forward network with back propagation algorithm is used. Four input units are used and the number of neurons in the hidden and output layers is ten and one respectively. The network designed gives the resonant frequency for rectangular or circular microstrip antenna depending on the value of a parameter termed as antenna type. The resonant frequency of RMA is a function of length 'l' of the patch, dielectric constant 'ε_r' of the dielectric material, and 'w/h' ratio of the structure, where 'w' is the width of the patch and 'h' is the height of the substrate. Similarly the resonant frequency for a CMA is a function of radius 'a' of the patch, dielectric constant 'ε_r' of the dielectric material and height 'h' of the substrate. The network developed takes four inputs [length for RMA or radius for CMA, dielectric constant, h/w for RMA or h for CMA, Antenna type 1 for RMA and 2 for CMA] and gives the resonant frequency as output. The neural network results are found to be in good agreement with the theory and the results are compared.*

Introduction: Artificial neural networks (ANN) have some distinguished characteristics, including the ability to learn from data, to generalize patterns in data and to model nonlinear relationships. Moreover, this technique has already been applied successfully in different branches of microwave design [2] . This prompted us to develop a single ANN model for regular patch (rectangular and circular) patch antenna, which is valid for both the antennas.

The resonant frequency of a rectangular patch antenna [3] of length L, width W and height h, dielectric constant of the dielectric ε_r in its dominant mode is given by.

$$f_r = \frac{c}{2L_{eff}\sqrt{\varepsilon_{reff}}} \tag{1}$$

where

$$\varepsilon_{reff} = \frac{\varepsilon_r + 1}{2} + \frac{\varepsilon_r - 1}{2}\left[1 + 12\frac{h}{W}\right]^{1/2} \tag{2}$$

$$L_{eff} = L + 2\Delta l \tag{3}$$

$$\Delta l = 0.412\,h\frac{\left(\varepsilon_{reff} + 0.3\right)\left(\frac{w}{h} + 0.264\right)}{\left(\varepsilon_{reff} - 0.258\right)\left(\frac{w}{h} + 0.8\right)} \tag{4}$$

L_{eff}: effective patch length (which is a function of L and h)
ε_{eff}: effective dielectric constant considering the fringing field effects (which is also a function of L, h, and ε_r).

Similarly the resonant frequency of a circular patch antenna [4,5,6] of radius a, height h and dielectric constant ε_r is given by

$$f_r = \frac{1.84118c}{2\pi a\left[\varepsilon_{eff}\left\{1+\frac{2h}{\pi\varepsilon_r a}\left(\ln\left(\frac{a}{2h}\right)+(1.44\varepsilon_r+1.77)+\frac{h}{a}(0.268\varepsilon_r+1.65)\right)\right\}\right]^{1/2}} \quad (5)$$

$$\varepsilon_{eff} = \frac{\varepsilon_r+1}{2}+\frac{\varepsilon_r-1}{2}\left(1+\frac{12h}{a\sqrt{\pi}}\right)^{-1/2} \quad (6)$$

Implementation of ANN Model: The class of neural network and/or architecture selected for a particular model implementation is dependent on the problem to be solved. These networks can in theory perform any complex nonlinear mapping. The neural network architecture used in this modeling effort is a multilayered feedforward neural network [1] trained in the supervised mode using Resilient backpropagation algorithm.

In Resilient backpropagation (Rprop) training algorithm only the sign of the derivative is used to determine the direction of the weight update; the magnitude of the derivative has no effect on the weight update. The size of the weight change is determined by a separate update value. The update value for each weight and bias is increased by a factor delta_inc whenever the derivative of the performance function with respect to that weight has the same sign for two successive iterations. The update value is decreased by a factor delta_dec whenever the derivative with respect that weight changes sign from the previous iteration. If the derivative is zero, then the update value remains the same. Whenever the weights are oscillating the weight change will be reduced. If the weight continues to change in the same direction for several iterations, then the magnitude of the weight change will be increased.

The network developed takes four inputs [length for RMA or radius for CMA, effective dielectric constant, h/w for RMA or h for CMA, Antenna type 1 for RMA and 2 for CMA] and gives the resonant frequency as output.

The number of neurons in the hidden and output layers is ten and one respectively. The network designed gives the resonant frequency for rectangular or circular microstrip antenna depending on the value of a parameter termed as antenna type. Sigmoidal transfer function is used for the hidden neuron and linear transfer function is used for the output neurons. We have taken delta_inc = 1.2 and delta_dec = 0.9

Results and Discussion: The network is trained for the RMA in the range of $5mm \le L \le 50mm$, $2 \le \varepsilon_r \le 10$, $0.5mm \le h \le 3mm$ and for the CMA in the range $2mm \le a \le 10mm$, $2 \le \varepsilon_r \le 10$, $1mm \le h \le 3mm$. Two data files namely RMA and CMA are generated and then merged into one. The data file contains five columns namely [length for RMA or radius for CMA, effective dielectric constant, h/w for RMA or h for CMA, Antenna type 1 for RMA and 2 for CMA, resonant frequency] and are normalized. Then one third of the rows of the data files selected in random for training. The network is trained for tolerance 0.1 x 10^{-3} and the network is tested for its success. The neural network result is found to be in good agreement with the theory and the results are compared.

Proceedings of APSYM2006, Dec. 14-16., Dept. of Electronics, CUSAT, India.

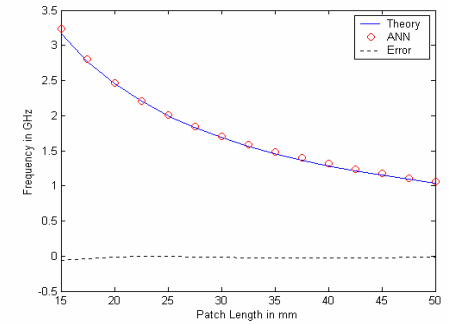

Figure 1 Comparison of the Theory and ANN output for Rectangular Microstrip Antenna

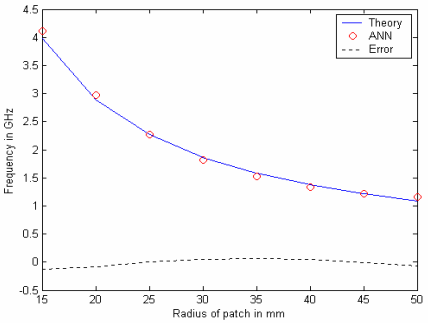

Figure 2 Comparison of the theory and ANN output for Circular Microstrip Antenna

Conclusion: A desirable design method will be both fast and accurate. As of now such a technique does not exist. This paper tries Artificial Neural Network (ANN) to achieve this goal from user's perspective. By this we mean that the model development stage may take a large time, but once the model is developed, the user will get result in much less time compared to other existing models. This work will involve two stages. The first stage consists of development of the networks. This is the model development stage. It takes long computation time, since it involves the training of the networks. Once the last network is trained and weights are determined, the model development is complete and it is handed over to the user. This is the second stage, where the clients use the developed model. In this stage, the time required will be much less than the available commercials models. In this paper for the first time a neural network is present which is valid for both rectangular and circular patch antenna, which is the salient feature of the network.

Reference:

[1] S. Haykin, Neural Networks, A Comprehensive Foundation, Macmillan, New York, 1994.

[2] Qi-Jun Zhang, Kuldip C. Gupta, Vijay K. Devabhaktuni, "Artificial Neural Networks for RF and Microwave Design—From Theory to Practice" IEEE Transactions on Microwave Theory and Techniques, vol. 51, no. 4, April 2003

[3] R. K. Mishra and A. Patnaik, "Neural network-based CAD model for the design of square-patch antennas," IEEE Trans. on Antennas and Prop., vol. 46, no. 12, pp. 1890-1891, 1998.

[4] R. K. Mishra and A. Patnaik, "Design of circular microstrip antenna using neural network," Inst. Electron. Telecomm. (IETE) Eng. J. Res., vol. 44, nos. 1-2, pp. 35 – 39, Jan. – Apr., 1995.

[5] K. Guney, "Resonant frequency of electrically-thick circular Microstrip antenna," Int. J. Electronics, vol. 77, pp. 377-386, 1994.

[6] Wollf and N. Knoppik, "Rectangular and circular microstrip disk capacitors and resonators," IEEE Trans. Microwave Theory Tech., vol. MTT - 22, pp. 857 – 864, Oct. 1974.

COMPACT ASYMMETRIC COPLANAR STRIP FED MULTI-BAND ANTENNA FOR WIRELESS APPLICATIONS

Deepu.V, Rohith K Raj, Manoj Joseph, Suma M.N,
C.K Anandan,K.Vasudevan and P.Mohanan
Centre for Research in Electromagnetics and Antennas, Department of Electronics,
Cochin University of Science and Technology, Cochin, India.

Abstract: A compact asymmetric coplanar strip fed monopole antenna for multi-band applications is presented. The antenna exhibits three resonances around 1.8 GHz, 2.4 GHz and 5.6 GHz covering the DCS/PCS/UMTS IEEE802.11b/g/IEEE802.11a/ HIPERLAN2 bands. The multi-band characteristic of the antenna is due to the various meandered current paths excited on the radiating structure. The antenna has an overall dimension of only 28 x 30 mm^2 when printed on a substrate of dielectric constant 4.4

Introduction: Recent advances in wireless technologies has revolutionized the field of information technology by making high speed internet and data transfer "wire free" via mobile gadgets. This has created demand for compact antennas with multiple bands which indeed has paved way for the design of various types of antennas such as monopole antennas, patch antennas, PIFAs [1]-[5] etc. These antennas are commonly excited by a probe feed or a microstrip feed with a large ground plane and has a double layer structure Uniplanar feeding techniques gained attention due to advantages like single metallic layer structure and easy integration to MMICs. Coplanar waveguide feed is the widely used uniplanar feeding technique and several antennas with this feeding mechanism [6]-[7] have been reported. In this paper a compact multi band monopole antenna is presented. Emphasis is given both in the design of the antenna feed and the radiating structure. Asymmetric coplanar strip (ACS) feeding is employed in this design so that a simplified single layer feed structure is obtained. A meandered inverted C is chosen as the radiating structure so as to excite lower frequencies within a smaller area.

.

Description of Antenna geometry:

The geometry of the proposed multiband antenna is shown in Fig.1.The antenna comprises of a compact ACS feed and an inverted C patch top loaded monopole. The C patch is used to effectively bring down the resonant frequency keeping the antenna dimensions within the desired specifications. The feeding arrangement comprises of a signal strip of width S and length Wg separated from the ground plane of length Lg and width Wg by a gap g selected using standard design equations [8]. The radiating structure comprises of two vertical strips of dimensions L_7 x S, L_2 x W_2 and two horizontal strips L_1 x W_1 and L_3 x W_3.The length of the individual strips are selected to obtain resonances at the desired frequencies. The width of the strips is adjusted to obtain the required bandwidth. The width of the vertical strip (L_0 x S) is set as that of the signal strip for design convenience. The optimum dimensions of the strips and the ground plane are obtained after the exhaustive simulation studies. The antenna has an overall dimension of 28 x 30 mm^2 including the ground plane when constructed on an FR4

substrate having dielectric constant 4.4 and thickness 1.6 mm. The uniplanar antenna can be easily printed on the single side of a substrate.

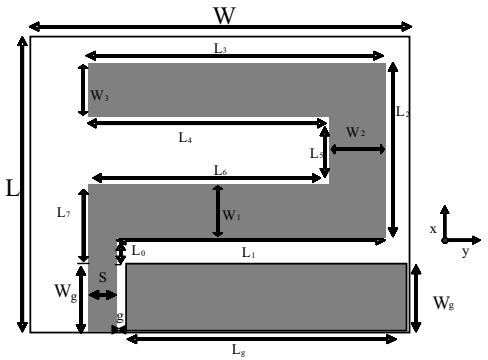

Fig. 2 Geometry of the proposed multi band antenna
Lg=22.5 mm, Wg=7 mm, S=3 mm, g=0.5 mm Lo=3.4.mm, L_1=21.5mm, W_1=6.5 mm, L_2=17.6 mm, W_2=7 mm, L_3=26 mm, W_3=6.25 mm, L_4 = 19 mm, L5=4.85 mm, L_6=16.5mm, L=28 mm, W=30mm

Experimental Results and Discussion

The measured return loss characteristics of the prototype antenna printed on FR4 substrate (εr=4.4 and thickness 1.6 mm) using PNA 8362B network analyzer is shown in Fig.2.The experimental results and the simulation results obtained from Ansoft HFSS are shown in figure 2.

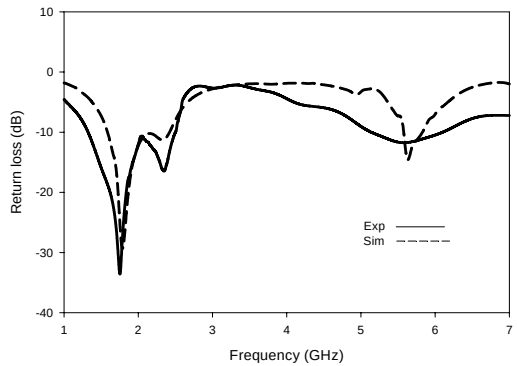

Fig. 2 Experimental and simulated return loss characteristics of the proposed antenna.

The experimental curve obtained shows that antenna has three resonances at 1.74 GHz, 2.34 GHz and 5.58 GHz respectively. The first two bands coalesce to give a wide bandwidth of 62 % (1.32 GHz to 2.50 GHz, 1188 MHz) while the third band has a bandwidth of 17 % (5.13 GHz to 6.08 GHz, 960 MHz). The influence of different parameters on antenna performance is also studied.

From the parametric analysis the various resonant paths of the antenna can be calculated as follows. The first resonance is due to the outer length of the radiating structure and the total meandered length is found to be nearly equal to half of the dielectric wavelength excited in the radiating structure. The second resonance is due to the inner length of the radiating structure. The resonant length is found to be nearly equal to half of the dielectric wavelength excited in the radiating structure. The third resonance is due to the strips L_1 x W_1 and the resonant length is found to be nearly equal to the half of dielectric wavelength excited in the strip.

The experimental E plane and H plane patterns of the antenna for the three resonant frequencies are shown in Fig.3.The antenna exhibits good radiation characteristics. Also it is found that the antenna is polarized along the X axis.

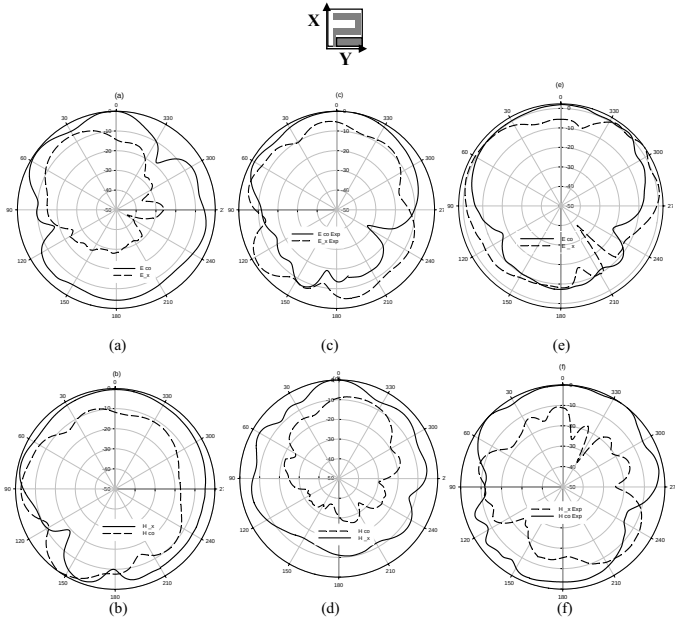

Fig.3 .Radiation patterns of the antenna (a) E plane pattern at 1.74 GHz. (b) H plane pattern at 1.74 GHz. (c) E plane pattern at 2.34 GHz. (d) H plane pattern at 2.34 GHz. (e) E plane pattern at 5.56 GHz. (f) H plane pattern at 5.56 GHz

The simulated and experimental gain of the antenna in the two bands is shown in figures 4(a) and 4(b) .The antenna has an average gain of 2.4 dBi in the first band and 2 dBi in the second band.

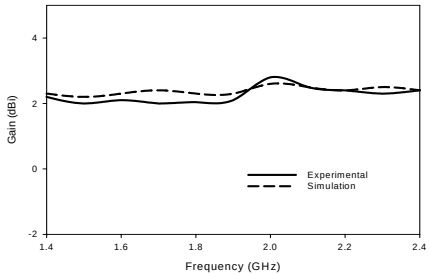

Figure 4(a) Measured and simulated gain of the antenna in the first band

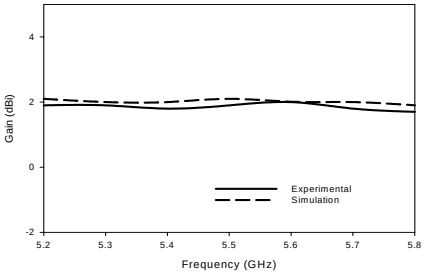

Figure 4(b) Measured and simulated gain of the antenna in the second band

Conclusion

A compact multi band antenna for DCS/PCS/UMTS/IEEE802.11b/g / IEEE802.11a/ HIPERLAN2 applications is presented and discussed. Compactness is achieved by using a compact feed and a meandered radiating structure. The design can be effectively used for constructing compact antennas for wireless gadgets.

Acknowledgement

The authors are grateful to Defence Research and Development Organization (DRDO), Govt. of India, UGC, Govt. of India, and Kerala State Council for Science Technology and Environment (KSCSTE) for providing financial assistance.

References

[1] Yen-Liang Kuo And Kin-Lu Wong , "Printed double –T monopole antenna for 2.4/5.2 GHz dual-band operations", *IEEE Trans. Antennas Propagat.,* vol. no. 51,no.9, pp. 2187-2192, September 2003.

[2] Jen-Yea Jan and Liang-chih Tseng, "Small planar monopole antenna with a shorted parasitic inverted-L wire for wireless communications in the 2.4-,5.2-, and 5.8- Ghz bands," *IEEE Trans. Antennas Propagat.,*vol. 52, no.7, July 2004.

[3] C.-Y.Huang and P.-Y. Chiu, "Dual –band monopole antenna with a shorted parasitic element", *IEE Electron. Lett.,* vol. 41, no.21, Oct. 2005.

[4] J.-S.Row and S.-W. Wu, "Monopolar square patch antennas with wideband operation", *IEE Electron. Lett.* vol.42, no.3, february. 2006.

[5] P.Nepa,G Manara A.A.Serra and G. Nenna, "Multiband PIFA for WLAn applications",IEEE Antennas and prop lett .,Vol.4,2005

[6] Horng-Dean Chen and Hong-Twu Chen, "A CPW fed dual frequency monopole antenna", *IEEE Trans. Antennas Propagat.,* vol. 52, no. 4, April 2004.

[7] W.C.Liu and C.-F.Hsu, "Dual-band CPW-fed Y-shaped monopole antenna for PCS/WLAN application" *IEE Electron. Lett.,* vol. 41, no.7, March. 2005.

[8] Ramesh Garg,Prakash Bhartia and Inder Bahl,Microstrip antenna design hand book, 1st ed. MA Artech House, 2001,pp.794-795

Analysis of phase variation due to varying length and loading of dipoles

Abdulla. P[(1)] and A. Chakrabarty[(1)]

(1) Department of Electronics & Electrical Communication Engineering, Indian Institute of Technology, Kharagpur, India. 721 302 Email: abdulla@ece.iitkgp.ernet.in

Abstract: *A theoretical method – Method of Moments is used to compute the phase of reflected wave from wire antennas by varying the length of wire, the position of loading and the length of load arm. This can be used as a scattering element in a reflectearray antenna to obtain the desired phase .*

Introduction: A good amount of work has already been performed by other researchers on wire antennas [1, 2, 3]. However, to obtain accurate solution for the phase of the reflected wave, the current on the wire must be solved for, subject to the boundary condition on the wire surface. This approach gives rise to an integral equation, which can be solved using Method of Moments (MOM). In this paper, a MOM based numerical technique has been presented for the accurate evaluation of the phase of the current on the wire antennas at different configurations. Studies have been performed on the variation of the magnitude and phase of current due to the variation in the length of the wire. Next, studies have been extended for loaded antenna of same length with various positions and length of the load arm. Loading position need to change from center to top. Both the cases are analysed separately and the variations of phase are plotted. The plotted result are verified by the commercial electromagnetic WIPL D software [4]. These computed graphs can be used as a ready reference for the design of reflecting element to obtain the desired phase in the relfectarray antenna.

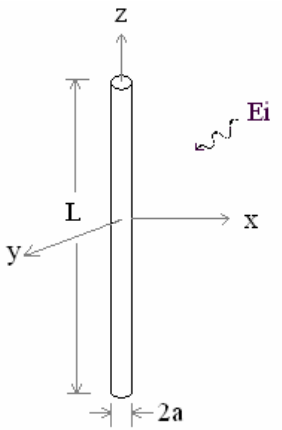

Figure.1.Straight wire subject to incident illumination

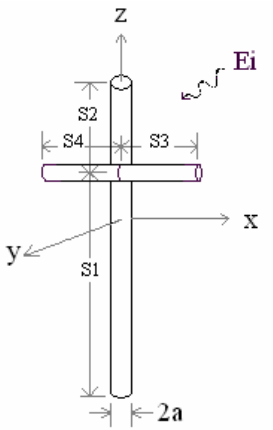

Figure 2.Loaded wire subject to incident illumination

1) Unloaded wire antenna.

Consider a plane wave incident upon a wire as illustrated in figure 1.The wire radius is assumed to be much smaller than the length L and the wave length λ. For a perfectly conducting wire, the surface current, J_S has $\hat{z}$ and $\hat{\phi}$ components in the cylindrical coordinate system. The assumption that the $\hat{\phi}$ component of J_S is very small is true for thin wire condition ($a<<\lambda$). Therefore, J_S can be written as follows

$$\vec{J}_S = \hat{z}J_z = \hat{z}\frac{I_Z(z')}{2\pi a} \qquad \ldots \qquad (1)$$

Here $I_z(z')$ is assumed to be an equivalent filament line–source current located on the surface of the wire i.e. at a radial distance $\rho = a$ from the z-axis. The only significant component of current on the wire is then the axial component, which can be expressed in terms of the net current $Iz(z)$ at any point z along the wire. The current distribution will then be modeled as an infinitely thin sheet of current forming tube of radius a, with the density of current independent of circumferential position on the tube. The z component of the field scattered by the wire is given by the following expression [5].

$$\int_{-L/2}^{L/2} Iz(z')\left(\frac{e^{-jkR}}{4\pi R^5}\right)[(1+jkR)(2R^2-3a^2)+(kaR)^2]dz' = -j\omega\varepsilon Ez^i(z)(\rho=a) \qquad (2)$$

Where $Ez^i(z)$ is the z component of impressed electric field at the wire surface, $Iz(z')$ is surface current density, and R is the distance from the source point to the observation point .If the observation point is on the axis of wire, ρ=0, then

$$R = \sqrt{a^2+(z-z')^2} \qquad (3)$$

The electric field intensity is the sum of the impressed and scattered intensities:

$$E = E^i + E^s \qquad (4)$$

Thus,

$$E^i = -E^s \qquad (5)$$

The solution of equation (2) is obtained by Method of Moments and numerical integration. Figure.3 compares the reflection phase against length of wire in wavelength with the WIPL-D simulation result, in the case of a plane wave incident at an angle of incidence 30^0 .The radius of wire is taken as 0.003λ. The phase is calculated at the center point of dipole. It can be see that by varying the length of dipole from 0.2 to 1λ, 160^0 phase change is possible.

Proceedings of APSYM2006, Dec. 14-16., Dept. of Electronics, CUSAT, India.

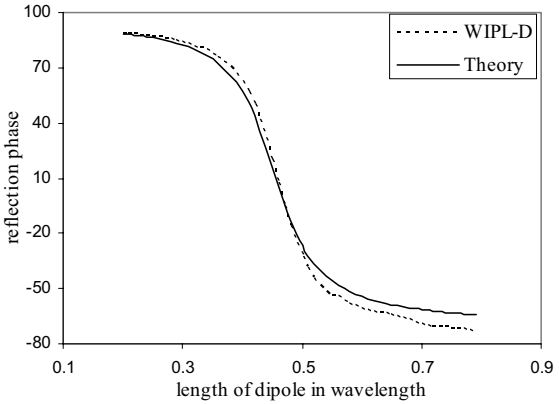

Figure.3 comparing reflection phase using WIPL-D and present theory

2) Loaded wire antenna

A phase varying element of crossed arm is connected across the wire as illustrated in figure 2. The analysis is done for both varying the length of arm and varying the position of arm separately. To evaluate the current distribution and the reflected phase along the wire elements, it is required to solve for the electric field components along the elements. The scattered electric field on a conducting wire due to the current distribution on the same wire is given in equation (2). Considering all elements are perfectly conducting wire of same radius a ($a<<\lambda$), the tangential component of total electric field on the surface of the wire can be taken as zero. The surfaces of the main elements are defined as S1 and S2 and that of the cross arms are S3 and S4. The total field contains the components of incident, E^i, scattered, E^s, fields respetively. The total tangential field components on each element are written as follows.

$$E_{tS1} = E^i_{\ z} + E^s_{\ zS1S1} + E^s_{\ zS1S2} - E^s_{\ yS1S3} + E^s_{\ yS1S4} = 0 \qquad (6)$$

$$E_{tS2} = E^i_{\ z} + E^s_{\ zS2S1} + E^s_{\ zS2S2} - E^s_{\ yS2S3} + E^s_{\ yS2S4} = 0 \qquad (7)$$

$$E_{tS3} = E^s_{\ yS3S1} + E^s_{\ yS3S2} + E^s_{\ zS3S4} + E^s_{\ zS3S3} = 0 \qquad (8)$$

$$E_{tS4} = -E^s_{\ yS4S1} - E^s_{\ yS4S2} + E^s_{\ zS4S4} + E^s_{\ zS4S3} = 0 \qquad (9)$$

The component of scattered electric field $E^s_{\ z}$ is given in equation (1) and $E^s_{\ y}$ is simplified as [6, 7]

$$E^S_{\ y} = -\frac{j\eta}{4\pi k}\int_{-L/2}^{L/2} Iz(z')\left(\frac{e^{-jkR}}{R^5}\right)[(y-y')(z-z')(3+3jkR-k^2R^2)]dz' \qquad (10)$$

A moment method solution with numerical technique was implemented to obtain the reflected phase of the wires in all configurations using pulse basis function. Equation (2) is solved to calculate the reflected phase of the unloaded wire, and equations (6)-(9) are solved for loaded wire.

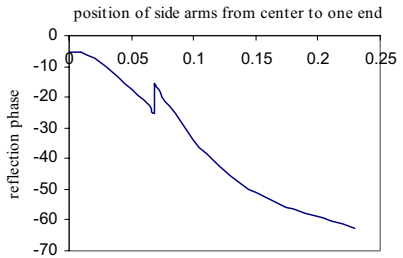

Figure.4. moving the side arms from center to one end.

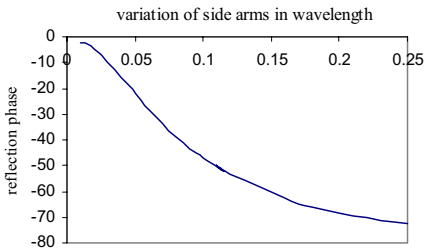

Figure 5. varying the length of side arms in wavelength

For the loaded wire, keeping total length (S1+S2) of wire 0.47 times wavelength, the reflection phase is calculated by varying the position/length of loaded arms. In position variation it needs to change the loading position from center to end. The length of side arms are selected as S3=S4=0.1 λ and the phase is calculated by solving the equations (6)-(9) and (2) using MOM and numerical techniques. Figure 4. illustrates the plot of calculated reflection phase of wire antenna against moving the side arms together from center to top. In second case, values of S1 and S2 are selected as 0.37 λ and 0.1 λ respectively. Both side arms length are varying in unison. Figure 5 illustrates calculated graph of reflection phase against change in length of side arms by keeping the loading position unchanged. Both the ways an additional 60^0 phase change is possible.

Conclusion

Method of moments (MOM) based numerical technique has been presented for the accurate evaluation of the phase of the current for different configurations of wire antenna and the calculated graphs are plotted. The above computed graphs can be used as a ready reference for the design of reflecting elements in reflectarray antenna.

Reference:

[1] R.F. Harrington "Field computation by Moment methods", R.E. Krieger publishing Company, Malabar, Florida.

[2] K.K. Mei, "On the integral equation of thin wire antenna", IEEE Transaction On Antennas and Propagation, vol. 13, issue 3, may 1965 pp 374-378.

[3] Richmond J.H.,"Digital Computer Solutions of the Rigorous Equations for Scattering Problems", Proceedings of IEEE, vol. 53, pp.796-804, August 1965.

[4] WIPL-D user's manual Pro 5.0, 2004.

[5] C.A. Balanis "Antenna Theory Analysis and Design", John wiley & Sons Inc.

[6] S.Ghosh, A.Chakrabarty, S.Sanyal, "Loaded Wire Antenna as EMI sensors", Progress in Eletcromagnetic Resesrch, PIER 54, page 19-36,2005

[7] C.A Balanis, "Advanced Engineering Electromagnetics", John Wiley & Sons Inc.

Proceedings of APSYM2006, Dec. 14-16., Dept. of Electronics, CUSAT, India.

DUAL FREQUENCY HEXAGONAL DIELECTRIC RESONATOR ANTENNA FOR DCT AND WLAN APPLICATIONS

*V. Hamsakutty and K. T. Mathew**
Microwave Tomography and Materials Research Laboratory, Department of Electronics,
Cochin University of Science and Technology, Kochi-682 022, India.
Phone-91-484-2576418, Fax-91-484-2575800, e-mail: ktm@cusat.ac.in
**Author for correspondence*

Abstract **:** A simple dielectric resonator antenna (DRA) with hexagonal geometry for dual frequency operation is investigated. The feed of excitation used is a simple 50Ω microstrip transmission line to provide a broadband and conical radiation patterns. The experiments and simulations were employed to investigate the proposed antenna, and a good agreement between them was obtained. The proposed antenna offers dual frequencies at 1.926 GHz and 2.451GHz with the first band covering the digital cordless telephones (DCT: 1.88 to 1.92 GHz) and the second band covering the wireless local area networks band (WLAN: 2.4 to 2.484 GHz). The radiation patterns measured in the first band are found to be broad sided and that in second band are conical shaped. The measured average gain is 6.1dBi and 5.4 dBi in the first and second operating bands respectively.

Introduction

Dielectric resonator antennas (DRAs) have received extensive attentions, for they offer high radiation efficiency of more than 98% since there is little or no loss due to the absence of metals, lightweight, small size, low loss and ease of excitation [1]. A variety of excitation methods are investigated such as coaxial probe, microstrip-transmission line an aperture coupled microstrip transmission line [2, 3] etc. Various geometries of DRAs are available; these include cylindrical, half- cylindrical, spherical, rectangular, triangular [4-5] etc. Double or multi- frequency operations have gained wide attention in wireless communications [6-8]. But in all cases, multiple frequencies are obtained by using more than one element or more than one feed or additional structure, which may cause design complexity.

In this paper, we propose a hexagonal shaped dielectric resonator antenna (HDRA). The HDRA is fed with a microstrip line as feed and with suitable adjustment on the HDR position, the antenna excite dual frequency suitable for DCT and WLAN applications. The modes of excitation are the broad side $HE_{11\delta}$ mode and broadside null (conical pattern) $HE_{12\delta}$ mode of the HDRA. The input impedance, radiation patterns and gain of the antenna are measured and discussed.

Antenna Design

The geometry of the proposed DR is shown in **Fig.1 (a)**. It consists of a DR of permittivity ε_{r1} = 69 with hexagonal geometry, side length a = 14.4 mm and height h = 11 mm is fed with a 50Ω microstrip transmission line of length 100 mm and width 3mm, mounted on a ground plane microwave substrate of permittivity ε_{r2} = 4 and size 140mm x 110mm x 1.64 mm. The feed position is optimised experimentally as (x_o, y_o) = (13mm, 8mm)

for the desired dual frequency operation, where x_o and y_o are defined respectively as the vertical and horizontal distances from the stripline end to the DR as shown in **Fig.1 (b)**. The DRA is excited at the $HE_{11\delta}$ mode (broad side) at the first frequency and $HE_{12\delta}$ mode (broad side null) at the second frequency. The experimental and simulated results are verified in terms of impedance and radiation pattern, a good agreement is observed. The detailed results follow in the next section.

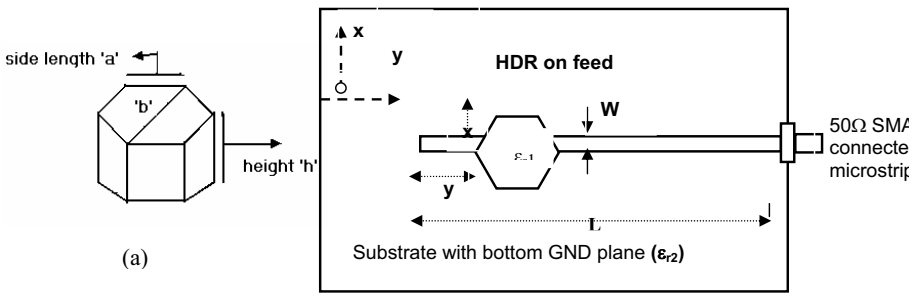

Fig.1: Geometry of the Antenna (a) Hexagonal DR (b) DRA (Top view)

Results and discussion

To verify the above results, an HP 8510C Vector Network Analyzer is used for the antenna measurements. Return loss $|S_{11}|$ for the optimized feed position for the required dual frequency operation is x_o=13mm and y_o=8mm. The measured and simulated, using Ansoft high frequency structure simulator (HFSS), return loss at this position is shown in **Fig. 2 .**

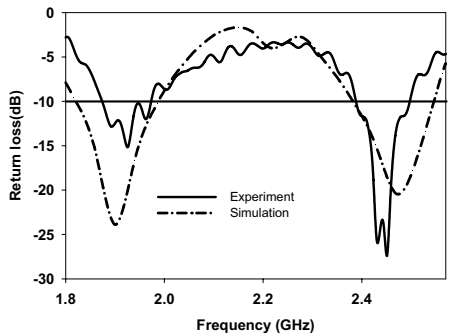

Fig. 2: Return Loss of the DRA

It is found that a good agreement between the measurement and simulation is obtained. It is noted that experimentally the return loss is minimum at 1.926 GHz and 2.451 GHz. The antenna has a 2:1 SWR bandwidth of 5.2 % ranging from 1.875 GHz to 1.975 GHz that includes digital cordless telephone bands and 4.2 % ranging from 2.395 to 2.5 GHz that includes the 2.45 GHz WLAN band of 2.4 to 2.485 GHz. There is an error of 1.35% and 0.78% in the resonant frequencies of measured and simulated results of the lower and upper

frequency bands. The first frequency band also covers almost all frequencies for personal communication band (PCS: 1.85-1.99GHz).

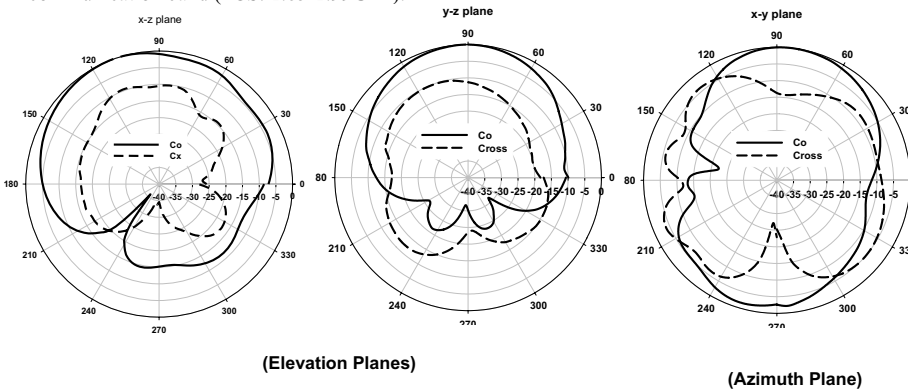

Fig. 3 Radiation patterns measured at 1.926 GHz

Measured radiation patterns at 1.926 GHz and 2.45 GHz are shown in **Figs.3** and **4** respectively and are found to be linearly polarized. It is found from **Fig. 3** that the patterns at the lower band are broad with good cross-polar level whereas the pattern of **Fig. 4** shows conical shaped radiation at the upper band. Radiation patterns at other frequencies in the band are also seen to have similar characteristics. Conical patterns find application in vehicular communications.

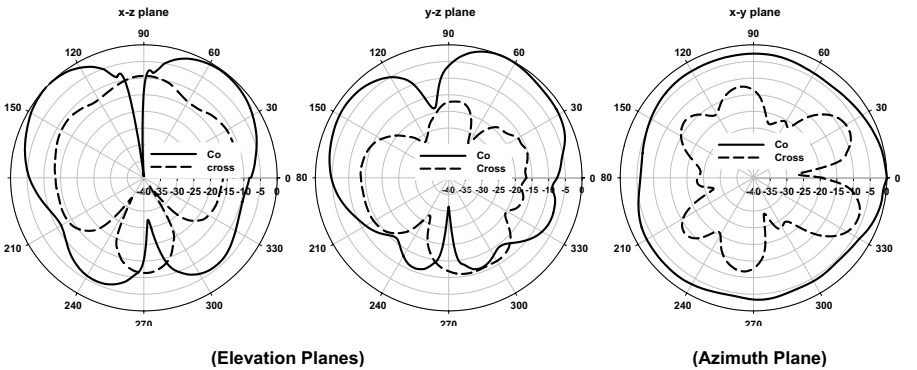

Fig. 4 Radiation patterns measured at 2.45 GHz

Measured gains are shown in **Fig. 5(a) and (b)**. It is noted that the antenna offers an average gain of 6.1 dBi and 5.4dBi respectively in the elevation plane.

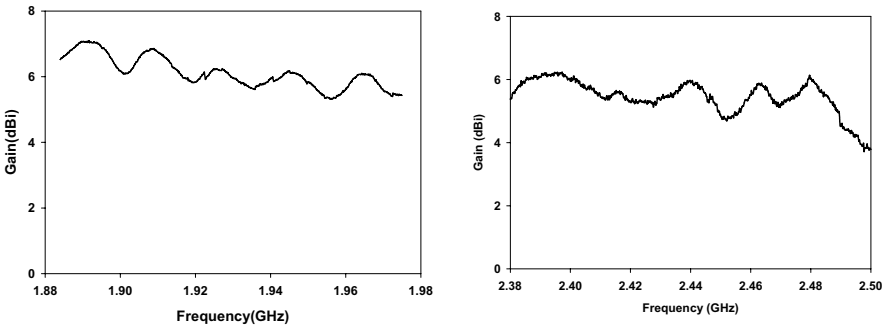

Fig. 5 Measured antenna gain in the boresight direction

Conclusion

A hexagonal dielectric resonator antenna fed with a microstrip transmission line has been presented and discussed. All the characteristics of the antenna are studied. The antenna offers dual band operation covering DCT and WLAN.

References

[1] S. A Long, M. W. Mcallister, and L. C. Shen, "The resonant cylindrical dielectric cavity antenna", IEEE Trans on Antennas and Propagation, Vol. AP31, No. 3,pp. 406-412, 1983.

[2] R.A karenburg and S.A. Long, "Microstrip transmission line excitation of dielectric resonator antenna, Electronic letters", vol.24, No. 18, pp. 1156-1157, 1988.

[3] J.T. St. Martin, Y.M.M. Antar, A.A. Kishk, A. Ittipiboon, and m. Cuhaci, Dielectric resonator antenna using aperture coupling" Electronic letters, Vol. 26, No. 4, pp. 2015-2016, 1990.

[4] R. K. Mongia and P. Bhartia, "Dielectric resonator antennas – A review and general design relations for resonant frequency and bandwidth", International journal of Microwaves and Millimeter wave computer Aided Engineering, Vol. 4, No. 3, pp. 230-247, 1994.

[5] H.Y.Lo, K.W.Leung, K.M. Luk, and E.K.N. Yung, "Low profile equilateral- triangular dielectric resonator antenna of very high permittivity", IEE Electronics letters, Vol.35 No. 25, pp. 2164-2166, 1999.

[6] Tayeb A. Denidni, and Qinjiang Rao, "Hybrid Dielectric Resonator Antennas With Radiating Slot for Dual-Frequency Operation", IEEE Antennas and wireless propagation letters, Vol. 3, pp. 321-323, 2004.

[7] Y. Sung, C. S. Ahn, and Y.-S. Kim, "Microstripline fed dual frequency dielectric resonator antenna, Microwave and optical technology letters", Vol. 42, No. 5, pp. 388-390, 2004

[8] Qinjiang Rao, Tayeb A. Denidni, and abdel R. sebak, "Hybrid Resonator Antenna suitable for wireless communication applications at 1.9 and 2.45GHz", IEEE Antennas and wireless propagation letters, Vol. 4, 2005, pp. 341-343.

MOS CAPACITOR LOADED ACTIVE MICROSTRIP ANTENNA

A. K. Gautam and B. R. Vishvakarma
Department of Electronics Engineering, Institute of Technology,
Banaras Hindu University, Varanasi 221 005 E-mail: brvish@bhu.ac.in

Abstract: A new technique for designing the frequency agile microstrip antenna is presented. The frequency agility is achieved by symmetrical loading of two identical MOS capacitors at the radiating edge of the patch, in which the operating frequency of the rectangular microstrip antenna is electronically controlled by the bias voltage of MOS capacitors. Theoretical model for the antenna is developed using modal cavity model approach and results are also simulated with MOM based simulator. The tuning range is found to be 1.527 GHz (61.09%), which is much better than earlier reported data and the unloaded patch radiator. Antenna shows consistant return loss and radiation pattern for the entire tunable frequency range.

I. INTRODUCTION

Microstrip antenna has numerous inherent advantages such as low profile, light weight, easy fabrication and suitability of mass production. It has also been found suitable in satellite communications, radars, missiles, high-speed space vehicles and other strategic defence equipments, due to compatibility with planar solid-state devices in addition to diversified applications. One of the major disadvantages of microstrip antenna is narrow bandwidth. However, in some applications such as, frequency agile radio or radar systems, a narrow band but tunable antenna element can be used instead of wide band antenna. Several techniques have been proposed to enhance the bandwidth [1-5]. In previous paper, Gautam and Vishvakarma [6] proposed a frequency agile microstrip antenna symmetrically loaded with tunnel diodes and they obtained frequency agility of 55.92 MHz (6.67%). While in this paper the bias dependent MOS capacitor is used to enhance the bandwidth of the microstrip antenna. A typical schematic of the proposed frequency agile active microstrip antenna is shown in Fig.1. As is evident, two identical MOS capacitor are used and symmetrically positioned at the radiating edge of the patch. The resulting structure has been accurately modeled and simulated. The equivalent circuit of MOS capacitor consists of a bias dependent depletion-layer capacitance C_d. Thus, the effective capacitance is varies with the bias voltage. With the change of bias voltage, the capacitance introduced at the radiating edge changes, resulting into change in the electrical length of the patch and hence its resonant frequency. So, the resonance of the microstrip antenna is electronically controlled by the bias of MOS capacitor. The details of entire investigations are given in the following sections.

II. ANALYSIS OF MOS CAPACITOR LOADED ACTIVE MICROSTRIP ANTENNA

The equivalent circuit of the proposed MOS capacitor loaded active microstrip antenna is shown in figure 2. In which the MOS capacitor and fringing capacitance are parallel with R, L, and, C of the patch. Thus the total capacitance will be

$$C_{total} = 2\,C_{mos} + C_s + C \qquad (1)$$

where, C_s is its fringing capacitance and is given as

$$C_s = \frac{0.01668}{\omega}\ \frac{\Delta l}{h}\ \frac{W}{\lambda}\ \varepsilon_e \qquad (F) \tag{2}$$

where, C_{mos} is CMOS capacitance and is given as

$$C_{mos} = \left[\left\{\frac{C_0}{\left[1+\frac{2V_g C_0^2}{\varepsilon q N_a}\right]^{\frac{1}{2}}}\right\} A\right] \qquad (F) \tag{3}$$

The input impedance of the MOS capacitor loaded active microstrip antenna can be calculated as

$$Z_{in} = \frac{\omega^2 L^2 R + j\omega RL(R-\omega^2 C_{total} RL)}{\omega^2 L^2 + (R-\omega^2 C_{total} RL)} \tag{4}$$

The reflection coefficient (ρ) can be calculated as

$$\rho = \left|\frac{Z_{in}-Z_0}{Z_{in}+Z_0}\right| \tag{5}$$

where, Z_0 is impedance of the coaxial feed (50 Ω).

The return loss of the antenna is given by

$$RL = 10\log\frac{1}{\rho^2} \tag{6}$$

and the resonance frequency is given by

$$f_r = \frac{1}{2\pi\sqrt{L(2C_{mos}+C_s+C)}} \tag{7}$$

III. RADIATION PATTERN

The radiation pattern for MOS capacitor loaded active microstrip antenna can be calculated as [7]

$$E(\varphi) = \frac{jk_0 WVe^{-jk_0 r}}{\pi r}\cos(kh\cos\theta)\ \frac{\sin\left(\frac{k_0 W}{2}\sin\varphi\sin\theta\right)}{\frac{k_0 W}{2}\sin(\varphi)\sin\theta}\ \cos\left(\frac{k_0 l}{2}\sin\theta\sin\varphi\right)\ \cos\varphi$$

$$0\le\varphi\le\pi/2 \tag{8}$$

IV. DISCUSSION OF RESULTS

The value of the MOS capacitor of MIS diode and operating frequency for MOS capacitor loaded active microstrip antenna were calculated as a function of bias voltage using Eqs. (4) and (16), respectively. The data thus obtained are shown in Figs. 3-4. From Fig.3, it is found

Proceedings of APSYM2006, Dec. 14-16., Dept. of Electronics, CUSAT, India.

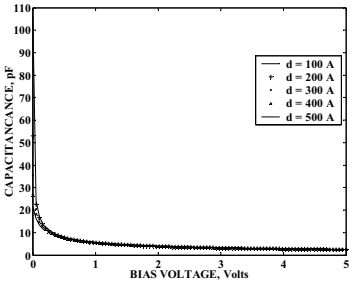

Fig. 3 Variation of MOS Capacitor of MIS diode as function of bias voltage for various insulator thicknesses.

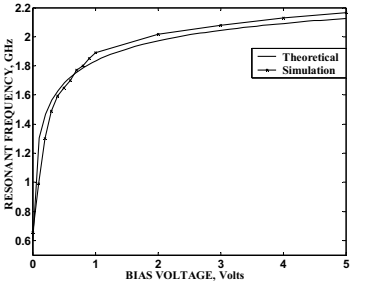

Fig. 4 Variation of Resonance frequency as function of Bias Voltage.

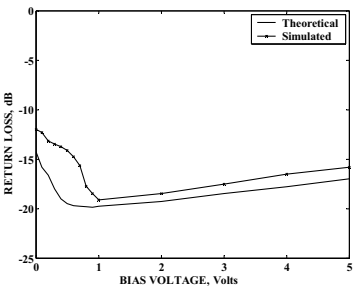

Fig. 5 Variation of return loss as function of bias voltage.

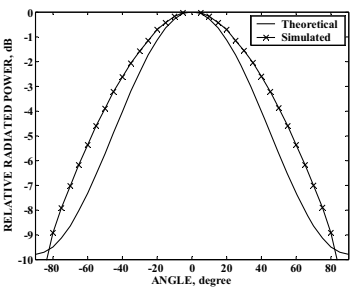

Fig. 6 Radiation pattern for MOS capacitor loaded active microstrip antenna

Design Parameters	
MOS capacitor structure : $Au-Si_3N_4-Si$ (n +0.0005 Ω cm)	Acceptor concentration: 1.45×10^{22} m^{-3}
	Gate bias voltage (V_g) :0-5 Volts
Area A of cross-section : 1.6×10^{-8} m^2	Substrate material used : RT-Duriod 5880
Thickness of oxide layers : 100 to 500 Å	Relative dielectric constant ε_r : 2.35
ε_r of (Si_3N_4) material :7.5	Thickness of substrate material : 1.5784 mm
ε_r of semiconductor material :11.9	Length : 39.14 mm
	Widths : 50.00 mm

Table: Design specification for frequency agile active microstrip antenna.

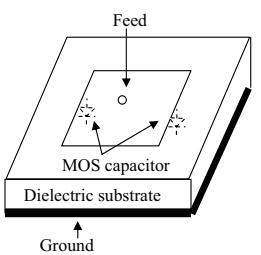

Fig. 1 Schematic of MOS capacitor loaded active microstrip antenna.

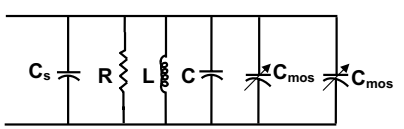

Fig. 2 Equivalent circuit of MOS capacitor loaded active microstrip antenna

that the value of MOS capacitor decreases with bias voltage for all the five insulator thicknesses. A larger variation in capacitance is found near zero volt while very small at higher bias voltages. The antenna is simulated in IE3D(Zeland software, USA). The theoretical and simulated response of antenna for various bias voltages of MOS capacitor are a relatively in good agreement. The range of frequency achievable for operation is 1.527 GHz (i.e., varies from 0.5986 GHz to 2.1259 GHz), which is much better than earlier reported data [6] and the unloaded patch radiator. The range of obtainable operating frequency band is 61.09%. It is also observed from Fig. 4 that the variation in resonance frequency with bias voltage is faster near zeo bias voltage which becomes steady towards higher values of bias voltage. This is because of the fact that change in frequency is soley governed by the MOS capacitance (Eqn. (3)). It is evidently clear that the proposed MOS capacitor loaded active microstrip antenna can be operated with varying tuning capabilities at microwave range by controlling the bias voltage of the device integrated with the patch. The theoretical and simulation results for return loss of proposed frequency agile active microstrip antenna as a function bias voltages are shown in Fig 5. It is observed that the return loss remains well below the -10 dB range (varies from -19.85 dB to -14.3 dB). The radiation pattern of the antenna is shown in Fig. 6. Which is invariant with the bias voltage of MOS capacitor.

REFERENCES

1 J A Navarro, K A Hummer and K. Chang, "*Active Integrated Antenna Elements*", Microwave Journal (USA), pp 115-126, 1991.

2 D H Schaubert, F G Farrar, A R Sindoris, and S T Hayes, "*Microstrip Antennas with Frequency Agility and Polarization Diversity*", IEEE Trans Antennas Propag (USA), AP-27**,** pp. 118, 1981.

3 Waterhouse R B & Shuley N B, "Frequency agile microstrip rectangular patches using varactor diode", in *IEEE Antenna and propagation Society International Symposium Digest*, held in conjunction with URSI Radio Science Meeting and Nuclear EMP Meeting, 4 pp 2188, 1994.

4 J Lin and T Itoh, "*Active integrated antennas*", IEEE Trans on Microw Theory Tech (USA), 42, pp 2186, 1994.

5 M C Pan and K L Wong, "*A broadband active equilateral-triangular microstrip antenna*", Microw Opt Technol Lett (USA), 22, pp 387, 1981.

6 A K Gautam and B R Vishvakarma, "*Frequency agile microstrip antenna using symmetrically loaded tunnel diodes*", Microw Opt Technol Lett (USA), Vol-48, no. 9, pp 1807-1810, 2006.

7 K R Carver and J W Mink, "*Microstrip antenna technology*", IEEE Trans Antennas Propag (USA), 29, 2, 1981.

CREMA SOFT – MICROWAVE MEASUREMENT AUTOMATION SOFTWARE

Deepthi K.V., Shameena V.A.,Gijo Augustin ,Binu Paul,C.K Aanandan, K.Vasudevan and P Mohanan

Centre for Research in ElectroMagnetics and Antennas
Department of Electronic, Cochin University of Science and Technology
Cochin - 22, Kerala. Email : drmohan@cusat.ac.in

This article introduces a novel, user friendly, Graphical User Interface (GUI) for the automation of microwave measurements using HP8510c Vector Network Analyzer. The Matlab® based package developed at Center for Research in Electromagnetics and Antennas (CREMA), supports automated calibration of the analyzer, Antenna measurements and microwave material measurements

INTRODUCTION

An accurate Measurement setup plays a victual role in any research and development organization. A simple, user friendly, Matlab® based package – 'CREMA SOFT*'* is introduced for the automation and visualization of microwave measurements using HP8510C vector network analyzer(VNA) . It integrates automated calibration, measurement and visualization in a user friendly environment. CREMA SOFT is equipped with S parameter, Radiation Pattern, Polarization pattern, Gain and Near field measurement capabilities. The package also facilitates Microwave material characterization, based on Hakki, Khanna and cavity perturbation methods. Automatic calibration of the analyzer for S_{11}, S_{21}, Full two port and RCS is also incorporated within the CREMA SOFT. Network analyzer front panel control operations like HOLD, CONTINUE, LOCAL and INTENSITY ON/OFF can be performed directly with the push button options provided in the main window. It can also estimates the resonant frequencies and specified impedance bandwidths within the specified measurement band for the device under study.

DESCRIPTION OF CREMA SOFT PACKAGE

Graphical User Interface (GUI) module exhibits the user friendliness of the underlying source code of software package. Complete automation of the reflection and radiation characteristics measurements is incorporated in CREMA SOFT. Onece loaded, it offers four panels for the user to interact

(1) *Calibration* (2) *Antenna Measurements* (3) Material *Measurements* and (4) Instrument

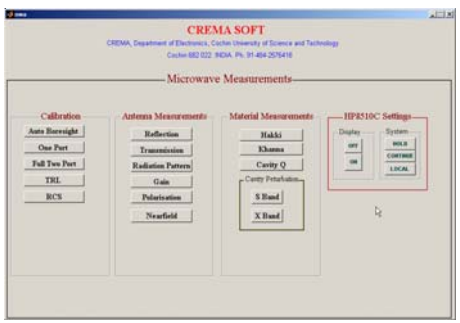

Fig 1 : The title window of CREMA SOFT

Settings. The title window of CREMA SOFT is shown in Fig.1

1. *Calibration* :The calibration panel accessible to the user from the title window facilitates various calibration options like Auto boresight, One Port, Full Two Port, TRL and RCS. The ***AutoBoresight*** option prompts to enter start frequency, stop frequency, Number of points with in the specified band and maximum size for the test antenna [Fig.2].

HP8510C VNA has the gating feature which gives user the flexibility to selectively filter time domain reflection or transmission time domain responses. In reflection measurements, the effects of unwanted mismatches can be eliminated while in transmission measurements the responses of multiple transmission pathscan be removed. CREMA SOFT calculates the gate span from the size of the antenna, turns the gate ON and automatically position the AUT in the bore sight direction based on the measured field strength comparison.

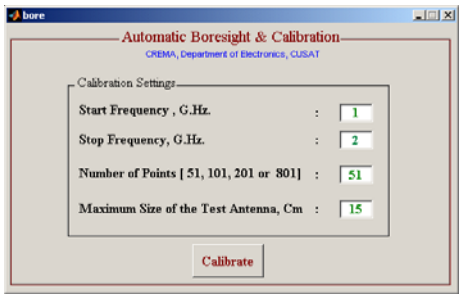

Fig 2: Automatic Boresight and Calibration window

One port calibration option under calibration is suitable to calibrate either port 1 or Port 2 of the network analyzer for reflection measurements. CREMA SOFT prompts to connect appropriate calibration standards (open, short and matched load). ***Full two port*** option facilitates calibration of both ports of the VNA while TRL calibrates the system with TRL standards. In RCS calibration [Fig 3] the chamber is calibrated in the specified band, prior to the measurements. In all the cases user has to enter the start frequency, Stop frequency, number of points and maximum size of the antenna

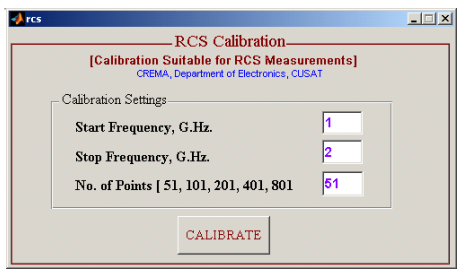

Fig 3: RCS calibration window

2. *Antenna Measurements*

The antenna measurements panel facilitates various antenna measurements. This includes ***Reflection***, ***Transmission***, ***Radiation Pattern***, ***Gain***, ***and Polarization*** *and* ***near field*** Measurements.Prior to any antenna measurements, the Network analyzer should be calibrated in the desired band with a suitable number of points. We can perform reflection measurement on either Port 1 or Port 2 of the Network Analyzer by accessing '*reflection measurement'* button provided in the antenna measurement panel of CREMA SOFT. The package displays a plot of the measured Return loss for various frequency points in the band of measurement [Fig 4]

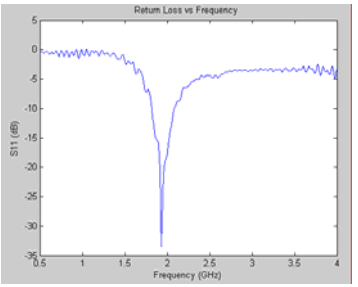

Fig 4: Plot of Return loss using CREMA-SOFT

softwares like Microsoft exel, Systat Sigmaplot etc. Similarly, transmission measurements can be performed by activating the Transmission button in the main window. One of the important features of CREMA SOFT is its fully automated antenna pattern measurement capability with a resolution of up to 1° step angle [Fig 5]. User will be prompted to enter ***start angle***, ***stop angle***, ***step angle*** and ***file name*** in the antenna pattern measurement window. Prier to the measurement, the system should be calibrated either manually or using the ***autoboresight calibration*** from the calibration panel of crema soft. While measuring ,the package provides a real time plot of radiation pattern at the center frequency. This provides the user an idea of radiations around the antenna while the pattern measurement is in progress. Each row of the radiation pattern data file contains both magnitude (p) and phase data (θ) of the radiation for each step angle in '.csv' format [Table 1]. CREMA SOFT utilizes gain comparison method in order to determine gain of an antenna. Fig 6 shows the gain measurement window. In the gain measurement windowthe used is prompted for the band of the gain measurement, number of points, maximum size of the test antenna, standard antenna type and the file name for data storage . The gain of the test antenna is compared with the gain of the standard antenna available in the database of CREMA SOFT. The output file gives the gain of the test antenna for each frequency point in the band of measurement in a '*.csv'* file format.

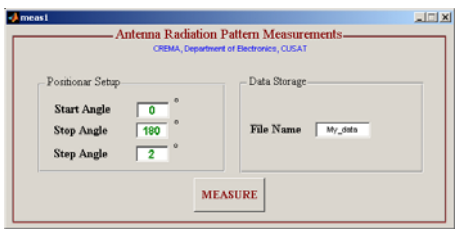

Fig 5: Radiation pattern measurement window

Angle	f_1	f_2	..	f_n	f_1
$A(\theta_1)$	$P[f_1]$	$P[f_2]$	..	$P[f_n]$	$[f_1]$
$A(\theta_2)$	$P[f_1]$	$P[f_2]$	..	$P[f_n]$	$[f_1]$
..	..	..	..	..	..
$A(\theta_n)$	$P[f_1]$	$P[f_2]$	..	$P[f_n]$	$[f_1]$

Table 1 : Radiation Pattern file

Polarization pattern measurement window [Fig.7] prompts for the band of measurement and file name to store the measured data. The system will give a real time plot of the polarization pattern at the center frequency while the pattern measurement in progress which helps the user to

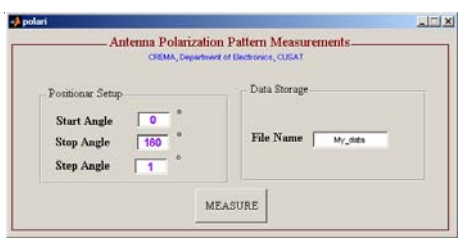

Fig 7: Polarization measurement window

Fig 8: Near field measurement window

visualize the polarization ellipse of the antenna. The Near field measurement window of CREMA SOFT is shown in Fig 8. User can specify the scanning area in X scanner and Y scanner panel with a step size as small as 0.01mm. The software stores raw near field data, its FFT and the 2D polar Data which can be processed further. The 2D polar and 3D polar radiation patterns can be easily obtained through the corresponding buttons [Fig 9].

3. Material Measurements

The material measurement capabilities include Hakki, Khanna, Cavity Q and Cavity perturbation technique. [3-6]

Selecting ***Hakki*** from the front panel allows the user to calculate dielectric constant of the Dielectric Resonator (DR) using Hakki Coleman method. For the measurement, DR is placed between two plates and two probes connected to VNA excites the DR. Dielectric constant of a sample with length, L and diameter, d can be found using the following relation,

$$å_r = 1 + (c / ð d f_r)^2 [á(kk)^2 + â^2]$$

where,

$$â = ð d f_r / c[(c/2f_rL)^2 - 1]^2$$

$$á(kk) = (â-1)/0.2 + 1 ; f_r = c/ ë_0$$

and f_r is the resonating frequency.

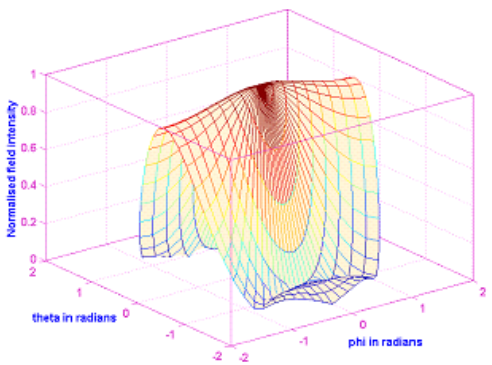

Fig.9: 3D polar plot of radiation pattern using the near field data in CREMA SOFT

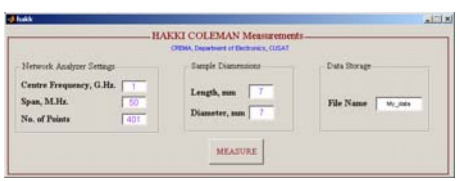

Fig 10: Hakki Coleman Measurement window

Fig.10 shows the Hakki Coleman measurement window. User has to enter the band of measurement, sample dimensions and the file name to store the measured data.

Another capability included in this package for material measurements is ***Khanna method***. Selecting Khanna

from the front panel, Q of the sample can be calculated using the relation $Q = f_0 / (f_2 - f_1)$ where f_0 is the resonating frequency and f_2 and f_1 are the frequencies corresponding to a value of mag[2/(1+mag^2)]^{½} where 'mag' is the gain in dB corresponding to f_0. The resonant frequencies and the Q values get stored in the specified file

Fig 11 Cavity perturbation measurement window of CREMA SOFT

CREMA SOFT facilitates cavity perturbation technique to determine the dielectric constant and Q of the sample. User can specify upto five resonant frequencies and the corresponding Q values of cavity in the cavity perturbation window of CREMA SOFT [Fig 11]. The software detects the maximum perturbation at these resonat frequencies(f_s)on loading the sample inside the cavity and computes both the real and imaginary parts of dielectric constant using the following relations,

$$\text{Real } (å_r) = 1 + (f_0 - f_s)\, V_c / 2f_s V_s$$

$$\text{Imag}(å_r) = Vc(Q_0 - Q_s) / 4V_s(Q_0 + Q_s)$$

f_0 is the resonant frequency of the air filled cavity, V_c and V_s are the volumes of cavity and sample respectively, Q_0 and Q_s are the quality factor of the air filled cavity and that of the sample loaded cavity.

4. Instrument (HP8510c) Settings:

The package enables user to perform certain commonly used operations like HOLD, CONTINUE, LOCAL, ON / OFF of the intensity of the Vector Network Analyzer. It is recommended that the source should be kept in the HOLD mode and intensity of the CRT in the off position during the intervals between measurements. The software gives a better flexibility for the user in this regard. Agilent provides the modern Plug and Play USB/ GPIB interface (Agilent 8535) which provides and easy interface with Laptops.

CONCLUSION

A simple Matlab based measurement automation package has been introduced in this article. Matlab[7]provides highly effective and efficient solution for instrument control, versatility and ease of programming. Superior savings in time and effort in the data acquisition process made the work a successful one. Moreover, the user is privilaged to modify or improve the features by editing the highly modular source code.

REFERENCES:

1. HP8510C Network analyzer system operating and programming manual, Hewlett Packard, USA.
2. Martin, W., *"Computation of antenna radiation pattern from near-field measurements"*, IEEE Transactions on Antennas and Propagation, Vol 15, Issue 2, March – 1967, pp.316-318
3. B.W. Hakki, and P.D. Coleman, *" A dielectric resonator method of measuring inductive capacities in the millimeter range"*, IRE Transactions on Microwave Theory and Techniques, July 1960.
4. APS Khanna and Y. Garault, *" Determination of Loaded, Unloaded and External Quality factors of Dielectric Resonator coupled to a microstip line"*, IEEE Transactions on Microwave the3ory and Techniques, Vol. 31, No.3, March 1983.
5. R.A. Waldron, M.A. , A. Inst.P., *"Perturbation Theory of Resonat Cavities"*, The Institution of Electrical Engineers, No. 373E, Apr. 1960.
6. Data acquisition techniques using PCs, Howard Austerliz
7. http://www.mathworks.com

Proceedings of APSYM2006, Dec. 14-16., Dept. of Electronics, CUSAT, India.

RESEARCH SESSION VII
MICROSTRIP ANTENNAS III

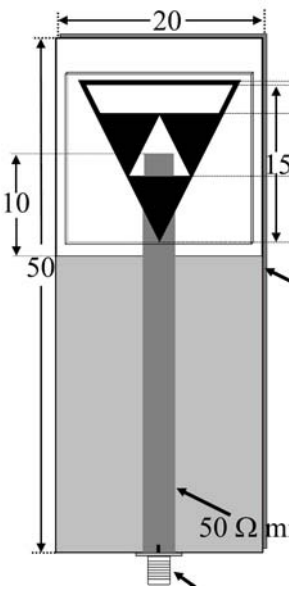

December 15, Friday

(4.00 p.m. - 6.00 p.m.)

RESEARCH SESSION VII

MICROSTRIP ANTENNAS III

Chair: Prof. C.S. Sridhar, Principal, SBMS Institute of Technology, Bangalore

Broadband Equilateral Triangular Microstrip Antennas

Amit A. Deshmukh[1] and G. Kumar[1]
(1) Department of Electrical Engineering, I. I. T. Bombay, Powai, Mumbai, India
Email: amitdeshmukh76@yahoo.com, gkumar@ee.iitb.ac.in

Abstract: Broadband and compact equilateral traingular microstrip antennas using variations of U-slot, V-slot and pair of rectangular slots cut inside the patch, are proposed. They give broader bandwidth with a broadside radiation pattern.

Introduction: Microstrip antenna (MSA) is a low profile planar configuration but has lower operating bandwidth (BW) and larger patch size in 300 – 1000 MHz frequency band. Several techniques have been reported for compact and broadband MSAs [1]. For the same patch size, the BW of MSA is increased by cutting a resonant slot [2]. In this paper, several broadband and compact variations of equilateral traingular microstrip antenna (ETMSA) using U-slot, V-slot and pair of rectangular slots cut inside the patch, are proposed. These ETMSAs were fabicated on glass epoxy substrate (ε_r = 4.3, h = 0.159 cm, and tan δ = 0.02) and are suspended above the ground plane with an air gap Δ. They were first analyzed using IE3D software followed by experimental verifications [3].

Variations of U-slot loaded ETMSA: ETMSA with a U-slot is shown in Fig. 1(a). The broader BW is due to the coupling between the patch (TM_{10}) and U-slot modes. The ETMSA is designed to operate at around 900 MHz. The U-slot is cut with respect to the centroid of ETMSA. The slot dimensions were selected to have two frequencies close to each other. For optimized MSA with Δ = 2.2 cm, the simulated and measured BW's are 166 MHz (17.9%) and 171 MHz (18.6%), respectively.

By using the even mode symmetry of U-slot ETMSA, a half U-slot cut half ETMSA (HETMSA) is proposed, as shown in Fig. 1(b). The slot is quarter wave in length. The MSA optimized with Δ = 2.2 cm, has simulated and measured BW's of 111 MHz (12.3%) and 118 MHz (13.1%), respectively, as shown in Fig. 1(c). The radiation pattern is in the broadside direction with cross-polar level less than 10 dB as compared to the co-polar level with a gain of more than 6 dBi over the BW, as shown in Fig. 2(a, b).

Variations of V-slot loaded ETMSA: A variation of U-slot, the V-slot cut ETMSA is shown in Fig. 2(c). The MSA is optimized with Δ = 2.2 cm. The simulated BW is 176 MHz (18.9%) and the measured BW is 209 MHz (22.2%). The radiation pattern is in the broadside direction with a cross-polar level less than 15 dB as compared to the co-polar level. A compact HETMSA with half V-slot is shown in Fig. 2(d). The slot angle is decreased to optimized the loop inside the VSWR = 2 circle. The MSA optimized with Δ = 2.3 cm, has the simulated and measured BW's of 140 MHz (15.3%) and 144 MHz (15.7%), respectively, as shown in Fig. 2(e). The radiation pattern is in the broadside direction with a cross-polarization level less than 10 dB as compared to the co-polar level with the peak gain of 7.7 dBi.

Pair of rectangular slots cut ETMSA: ETMSA with a pair of rectangular slots is shown i Fig. 3(a). The slots are quarter wave in length. The patch is optimized for Δ = 1.9 cm. Th simulated and measured input impedance and VSWR plots are shown in Fig. 3(b). Th simulated and measured BW's are 170 MHz (17.7%) and 167 MHz (17.4%), respectively The radiation pattern at 961 MHz and gain variation with frequency are shown in Fig. 3(c, d) The pattern is in the broadside with peak gain of 8.1 dBi.

Conclusions: Various broadband and compact ETMSAs using U-slot, V-slot and pair o rectangular slots are proposed. For same substrate thickness, ETMSA with pair of rectangula slots has larger BW as compared to the U and V-slot cut ETMSAs. The BW of compac HETMSA is increased by cutting half U or V-slot.

References

[1] G. Kumar and K. P. Ray, 'Broadband Microstrip Antennas', Artech House, USA 2003

[2] K. L. Wong, 'Compact and Broadband Microstrip Antennas', John Wiley and Sons Inc., New York, 2002

[3] IE3D 7.1, Zeland Software Inc., Fremont, CA, USA, 2000

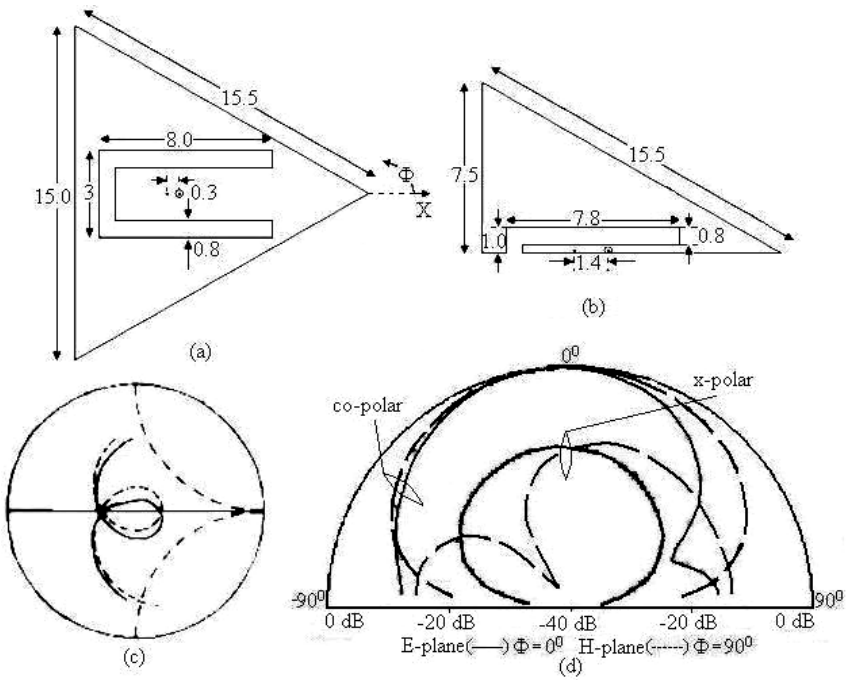

Fig.1 ETMSA with (a) U-slot and (b) half U-slot, (c) input impedance and VSWR plots for half U-slot HETMSA, (- - -) simulated, (——) measured

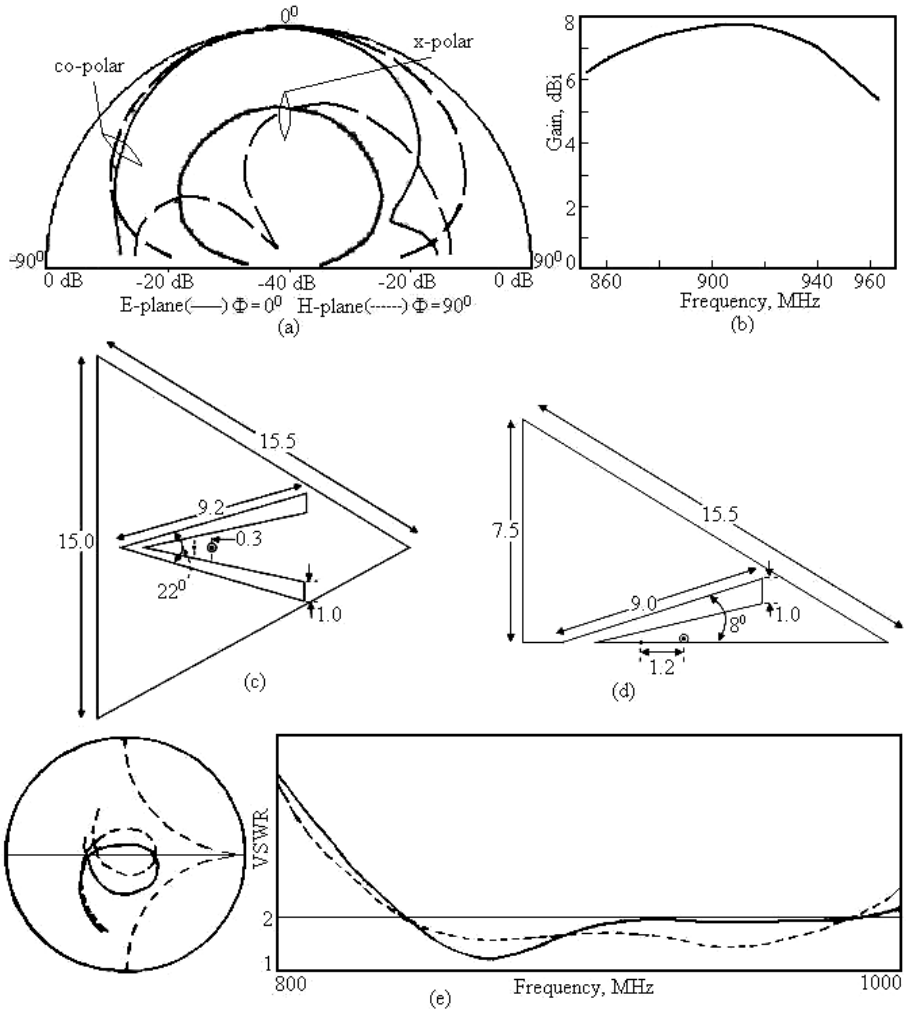

Fig. 2 (a) Radiation pattern at 902 MHz for half U-slot cut HETMSA, its (b) gain variation against frequency, ETMSA with (c) V-slot and (d) half V-slot, and (e) input impedance and VSWR plots for half V-slot HETMSA, (- - -) simulated, (——) measured

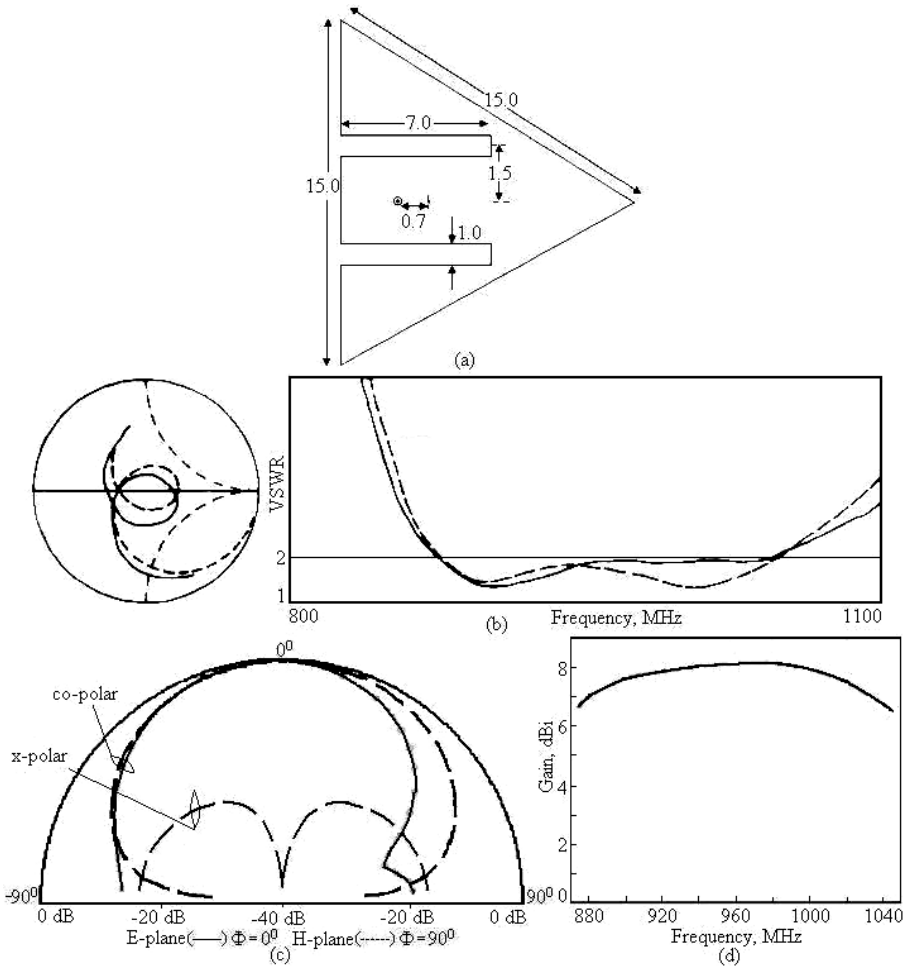

Fig. 3 (a) Pair of rectangular slots cut ETMSA, (b) input impedance and VSWR plots, (- - -) simulated, (——) measured; (c) radiation pattern at 960 MHz and its (d) gain variation against frequency

PLUS SHAPE FRACTAL ANTENNA

Animesh Kushwaha, P.K. Singhal and Shafali Kapur
Department of Electronics & CSE
Madhav Institute of Technology and Science
Gwalior – 474 005, INDIA
E-Mail: animesh_kushwaha@yahoo.com & pks_65@yahoo.com
Fax: (+91) – 751 – 2364648

ABSTRACT:
This paper outlines a multiband antenna design based on fractal concepts. Fractal antennas show multiband behavior due to self – similarity in their structure. The proposed antenna is simulated using the method of moment based commercial software (IE3D) and results for return loss, radiation patterns and gain are presented.

Introduction:
Fractal antennas are new member in the family of antennas [1]. Fractals are the structures that preserve their shape at different scales. Cohen [2] was first to develop an antenna element using the concept of fractal. The fractal concept can be used to reduce the antenna size or it can be used to achieve multiple bands [3-5]. In the present work a plus shape patch is taken as a base shape and in first iteration four other plus shape patches of the order 1/3 of base shape are placed touching the base shape. Similarly next iterations can be performed but here results of simulation studies only for base shape and first iteration is presented because for next iterations shape of geometry becomes complicated.

Design:
For base shape a plus shaped patch is taken as shown in figure 1(a). For first iteration four plus shapes of the order 1/3 of base shape are placed touching the base shape as shown in figure 1(b). Same procedure can be repeated for next iterations. For each iteration plus shapes of the order of $(1/3)^n$ of base shape are taken, where n is the number of iterations. This geometry is simulated assuming a dielectric substrate having a dielectric constant ε_r =4.4 and height of substrate is 4 mm. In our simulation a=c=45 mm and b=d=15 mm. Dimensions for first iteration can be calculated as

$$e = g = (1/3)a = (1/3)c \text{ and}$$
$$f = h = (1/3)b = (1/3)d$$

which gives e=g=15 mm and f=h=5 mm respectively. Probe Feed is used as a feed line with probe radius 0.5-mm and length of probe is equal to the substrate thickness.

Results and Discussion:
The proposed design has been simulated using Zealand's simulation package [6]. The resonant frequencies for which minimum return loss occurs for various bands for base shape and first iteration are given in Table 1. Figure 2(a) shows the variation of return loss with frequency for base shape. Similar result for first iteration is shown in figure 2(b). It is observed that for first iteration three bands occurs in the frequency range 8-16 GHz, while for base shape only one band is achieved. These results clearly show as the number of iterations are increased multibands are achieved. Radiation patterns at different bands for first iteration are shown in figure 3(a), 3(b) and 3(c) respectively. These radiation patterns clearly show that

the antenna radiates almost like an omni directional antenna. Figure 4 shows the gain vs. frequency plot for first iteration.

Geometry	Resonant Frequency		
	F_{r1}	F_{r2}	F_{r3}
Base shape	_	13 GHz	_
First iteration	11.8 GHz	13 GHz	13.8 GHz

Table 1: Table for frequencies at which minimum return loss occur

CONCLUSION:

A new design of fractal antenna has been proposed. This antenna is multiband and gives three bands in the frequency range 8-16 GHz. The multiband behavior of the antenna, together with the shape of patterns suggest a possible application of this antenna to land vehicles linked to ground base station that might require the operation of several communication systems in a single antenna. As usually in mobile communication systems, no polarization restrictions have been considered.

ACKNOWLEDGEMENT:

The authors thankfully acknowledge the authorities of Madhav Institute of Technology & Science, Gwalior.

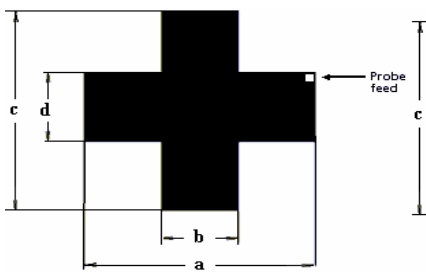

FIGURE 1(a): Geometry for base shape

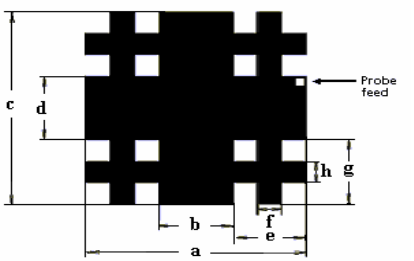

FIGURE 1(b): Geometry for first iteration

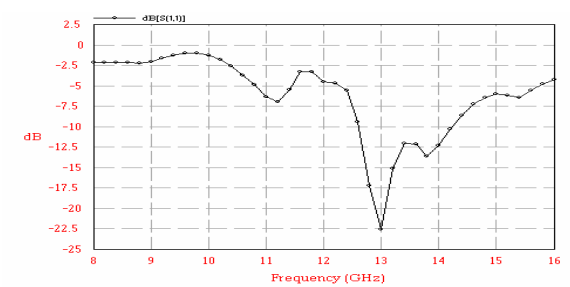

Figure 2(a): Graph for return loss vs. frequency for base shape

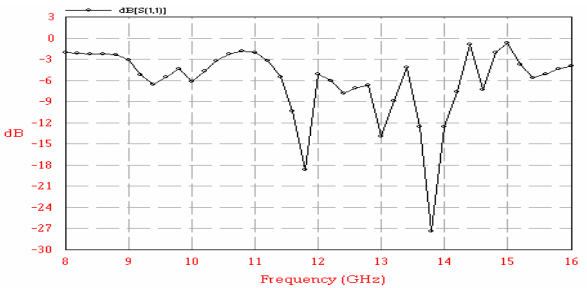

Figure 2(b): Graph for return loss vs. frequency for first iteration

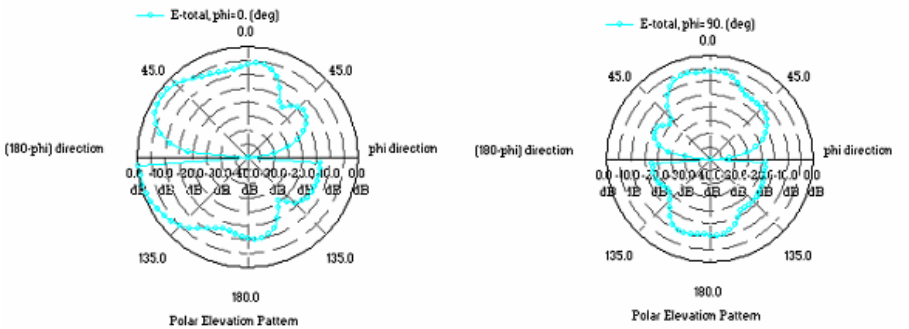

Figure 3(a): Radiation patterns at 11.8 GHz

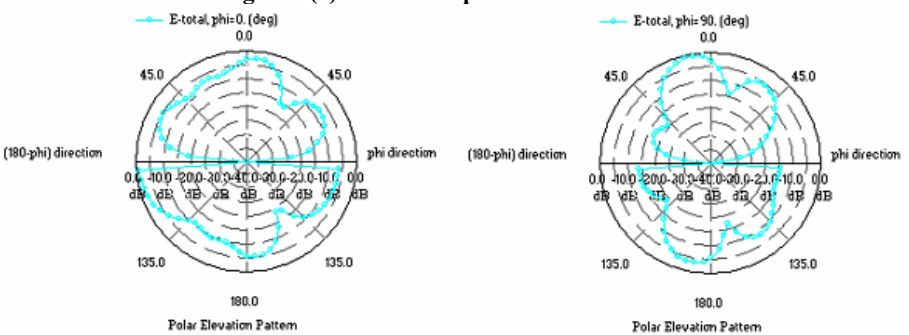

Figure 3(b): Radiation patterns at 13 GHz

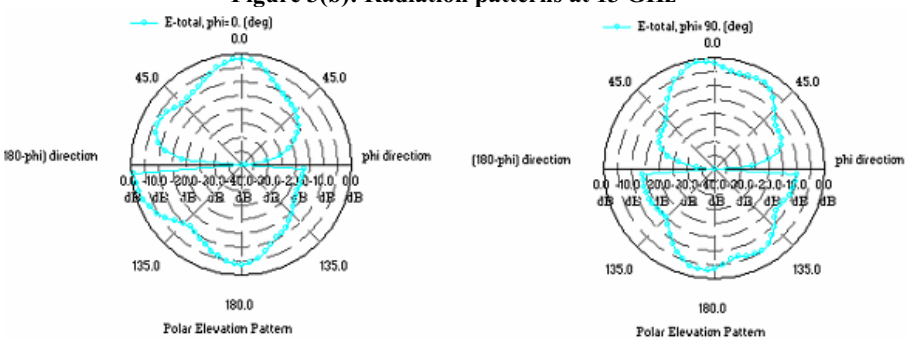

Figure 3(c): Radiation patterns at 13.8 GHz

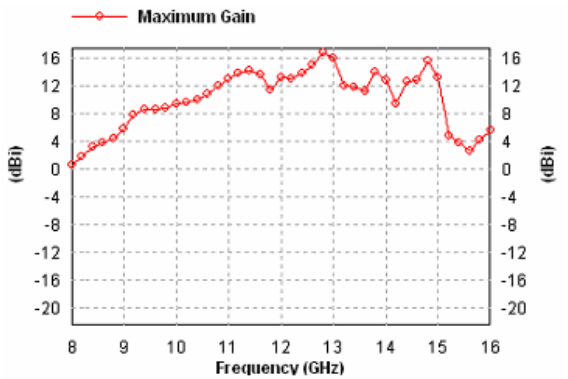

Figure 4: Gain vs. frequency plot

REFERENCES

[1] D.H. Werner and S.Ganguly, An overview of fractal antenna engineering research. *IEE antennas and Propagation society, Volume 45, No. 1, Pages 38-57, Feb 2003.*

[2] N.Cohen, Fractal antenna application in wireless telecommunication. *Proceedings of Electronics Industries Forum of New England, 1997, pp. 43-49.*

[3] Deschamps, G.A, Microstrip Microwave antenna. *3rd USAF Symposium on antennas 1953.*

[4] Steven R Best, The significance of self-similar fractal geometry in determining the multiband behavior of the Sierpinski gasket antenna. *IEEE antennas and wireless propagation magazine. vol.1, No. 1, Jan 2002, pp22-25.*

[5] John P.Gianvittorio and Yahaya Rahamat-Samii, Fractal antennas: A novel antenna miniaturization technique, and application. *IEEE antennas and propagation magazine, vol. 44, No1, Feb.2002, pp 20-36.*

[6] IE3D Software Release 8 and developed by M/S Zeland Software, Inc.

Proceedings of APSYM2006, Dec. 14-16., Dept. of Electronics, CUSAT, India.

New printed log-periodic dipole array

Dhyanendra Parashar, Deepak Sharma and P. K. Singhal
Dept. of Electronics, CSE & IT
Madhav Institute of Technology & Science, Gwalior (India)
E mail: er_dp23@ yahoo.com

Abstract *A 6-element printed log-periodic dipole array antenna is designed in the frequency range of 7.5 to 15GHz.The return loss, radiation pattern and directivity has been determined using electro magnetic simulator(Zeland's Integral equation based IE3D 8.21). The Present antenna operates from 7.5 GHz to 15 GHz with a percentage bandwidth of 75. The radiation pattern is found to be very broad and can be used for communication purposes.*

Introduction

Log-periodic dipole array was first reported in [1]. Lot of experimental and theoretical work has been reported in [2-4]. The log-periodic dipole array is a frequency independent antenna. The present work describes the design and analysis of microstrip log-periodic dipole array. The analysis of the designed geometry has been carried out using IE3D software [5].

Antenna configuration

The log-periodic dipole array (LPDA), which is printed on one side of a low cost dielectric substrate, is designed, as shown in Fig. 1. The array elements are connected through a microstrip. The design procedure of this log-periodic dipole array is similar to that presented by Carrel [2]. Design of log periodic dipole array antenna depends upon various parameters such as geometric ratio (τ), width (σ) and angle (α) as given in [6].

Where,

$$\alpha = 2\tan^{-1}[(1-\tau)/4\sigma)]$$

Designing Parameters in the frequency rage between 7.5 GHz to 15 GHz are given below

$$\tau = 0.865 \text{ and } \sigma = 0.157$$

$$\text{Then, } \alpha = 2\tan^{-1}[(1-\tau)/4\sigma] = 24.26^0$$

Where $\tau = l_2/l_1$ and the spacing factor $\sigma = (R_2 - R_1)/2l_2$

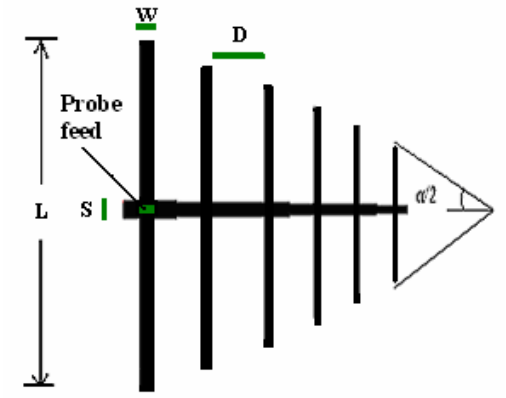

Fig.1 Configuration of printed LPDA

All the parameters, required for the design calculated as per [6], and are given in table-1

Table-1

Frequency (GHz)	Length of the dipole L (mm)	Spacing D (mm)	spacing (s) between the poles of each dipole S (mm)	Width of dipole W (mm)
F_1=7.5	L_1= 19.01	D_1 = 5.97	S_1 = 0.865	W_1 = 0.20
F_2=8.67	L_2= 16.44	D_2 =5.16	S_2 = 0.75	W_2 = 0.173
F_3=10.024	L_3= 14.22	D_3 = 4.47	S_3 = 0.65	W_3 = 0.15
F_4=11.59	L_4= 12.30	D_4 = 3.86	S_4 = 0.56	W_4 = 0.13
F_5=13.397	L_5= 10.64	D_5 = 3.34	S_5 = 0.484	W_5 = 0.112
F_6=15.487	L_6= 9.21	D_6 = 0.00	S_6 = 0.419	W_6 = 0.097

Traditionally matching microstrip of constant width is used. Here it is periodically varied as given in table-1.

Results and discussion

LPDA prototype was designed on substrate having thickness 1.6mm and ϵ_r=2.56. The simulated VSWR of the LPDA is shown in Fig. 2, fig.3 shows the radiation pattern and directivity is shown in Fig.4.

Conclusion

The proposed LPDA operates satisfactorily from the 7.5 to15GHz band. Antenna is considered on low cost substrate which can be easily designed and can be used

for various applications. These LPDAs offer the advantages of compact si: lightweight, and low cost.

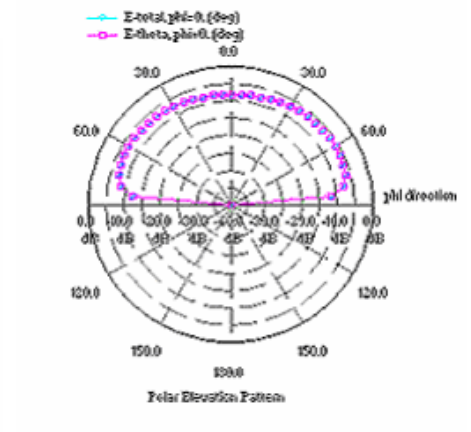

Fig.3 Polar plot

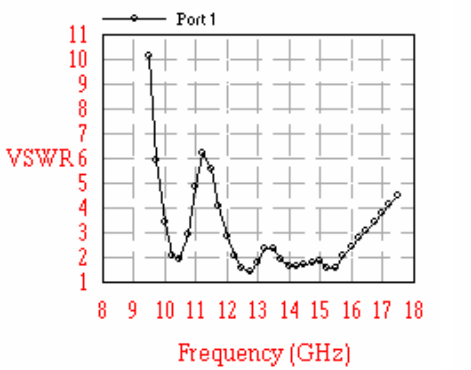

Fig.2VSWR against Frequency

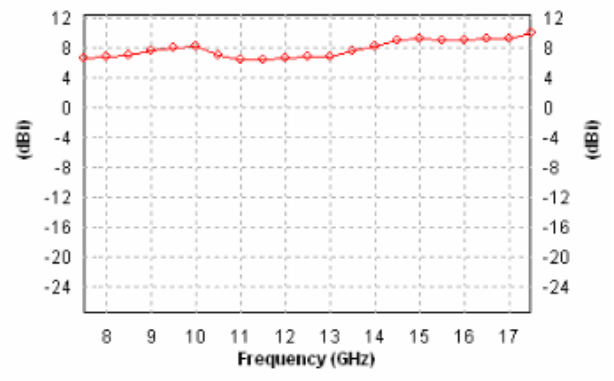

Fig.4 Directivity Vs frequency

References

[1] D. Isbell, "Log periodic dipole arrays," IEEE transactions on Antenna a Propagation, volume 8, Issue 3, pp. 260-267, May 1960.

[2] R. Carrel, 'The design of log-periodic dipole antenna," IRE Internatio convention record, volume 9, part 1, pp. 61-75, Mar 1961.

[3] C. Donn, J. Lew, and J. Scherer, "Microstrip log-periodic dipole array," IE antenna and propagation Society International symposium, volume 23, pp.70 712, Jun 1985.

[4] O. Ergul, and L. Gurel, "Log-periodic antenna design using electromagne simulations," IEEE Antenna and propagation Society International symposiu volume1, pp. 245 – 248, 22-27 June 2003

[5] IE3D Software Release 8.21 version and developed by M/S Zeland Softwa Inc.

[6] Rhodes, "The Log-Periodic Dipole Array," QST, November. 1973.

COMPACT BROADBAND RECTANGULAR MICROSTRIP ANTENNA WITH OPEN END MEANDERING SLOTS IN THE GROUND PLANE

K. Usha Kiran[(1)], R. M. Vani[(2)], Ravi M. Y.[(1)],P. V. Hunagund [(1)] and S. F. Farida[(3)]

[1]Department of Applied Electronics, Gulbarga University, Gulbarga, Karnataka.

[2]University Science Instrumentation Center, Gulbarga University, Gulbarga, Karnataka.

[3]Department of Electrical and Engineering, Salt Lake, Community College, UTAH-84130, USA.

E-mail: prabhakar_hunagund@yahoo.co.in

Abstract: *In this paper, a compact broadband rectangular microstrip antenna with open end meandering slots in the ground plane is presented. Three identical narrow open end meandering slots were embedded in the antenna's ground plane parallel to the rectangular patch's radiating edge. Experimental study is carried out by varying the length of open end slots. Using open end meandering slots in the ground plane the resonant frequency of the antenna is greatly lowered with large enhancement in the bandwidth. With the proposed design a broad bandwidth of 40% is achieved with an extreme reduction of 82.9% in the antenna size when compared to rectangular microstrip antenna without slots.*

INTRODUCTION

Modern communication devices and applications such as mobile cellular handsets, cordless phones, blue tooth devices and WLAN's call for an extreme compact antennas covering a wide operational bandwidth. In the literature, meandering technique (using narrow slots) when applied to the ground plane of the microstrip antenna was proved to be one of effective method in reducing the size of the microstrip antenna and enhancement of bandwidth [1]. However, the obtained bandwidth in this case is comparatively very less when met with the requirements of the above said applications. Further enhancement in the antenna bandwidth and size reduction was very much in need. Many combinations of radiating patch and the ground plane slots were configured and analyzed to achieve extreme compact and broadband antennas. T. W. Chiou *et al* [2] introduced slots in the ground plane that helped to enhance operational bandwidth of a terminal antenna at the upper end of the invested frequency band. Recently broadening of the lower operational frequency band was achieved using two open end slots in the ground plane under the radiating element (inverted F-type patch) [3]. It was found that the use of two parallel open end slots in the ground plane decrease the resonant frequency of the ground plane and enhance the bandwidth of the lower operational frequency band. The obtained bandwidth is 50% for –6 dB return loss in this case.

In this paper, we present a compact broadband rectangular microstrip antenna with open end meandering slots in the ground plane. Three identical narrow open end slots were embedded in the antenna's ground plane. These slots are aligned with an equal spacing of $L/4$ parallel to the rectangular patch's radiating edge. Experimental study was carried out for different open end slot lengths. Using three open end meandering slots the resonant frequency is greatly lowered with large enhancement in the bandwidth. With the proposed design a broad bandwidth 40% (-10 dB return loss) is achieved with extreme reduction of 82.9% in the

antenna size. The obtained antenna bandwidth and size reduction are more when compared to R. Hossa *et al* [3].

ANTENNA DASIGN

First, a reference antenna (RA) i.e., a rectangular microstrip antenna of patch size (L, W) = (11.33, 15.24) *mm* is designed for operating frequency of 6 GHz (ε_r = 4.4 and h = 1.6 *mm*) for TM_{10} mode [4]. This rectangular patch in turn is fed by a 50Ω center fed microstrip line feed of dimensions (L_{f50}, W_{f50}) = (6.187, 3.060) *mm,* through a quarter wave transformer having (L_t, W_t) = (4.922, 0.500) *mm* as shown in Fig. 1(a) [5-6]. Here the microstrip line feed is used to excite the patch as the planar feed makes the structure suitable for integration with associated microwave circuitry.

Later three identical narrow open end slots were embedded in the antenna's ground plane that are aligned with an equal spacing of L/4 parallel to the radiating edge of the rectangular patch as shown in Fig. 1(b). The embedded open end slots are narrow (Ws = 1 *mm*) and have a slot length of Ls + Lo. Ls and Lo are the slot lengths inside and outside the projection image of the radiating patch in the ground plane respectively. The slot length Lo for the prototypes is fixed to be 11.2 *mm* (as the groundplane size is taken to be 38x38*mm*) while the slot length Ls is varied for different slot lengths. As the reduction in the resonant frequency is more significant for longer slot lengths [1], hence a detail study was carried out for the longer slot lengths 'Ls' i.e., from 12*mm* to 13.5mm by an interval of 0.5*mm*. However, for the reference antenna (RA) Ls = Lo = 0.

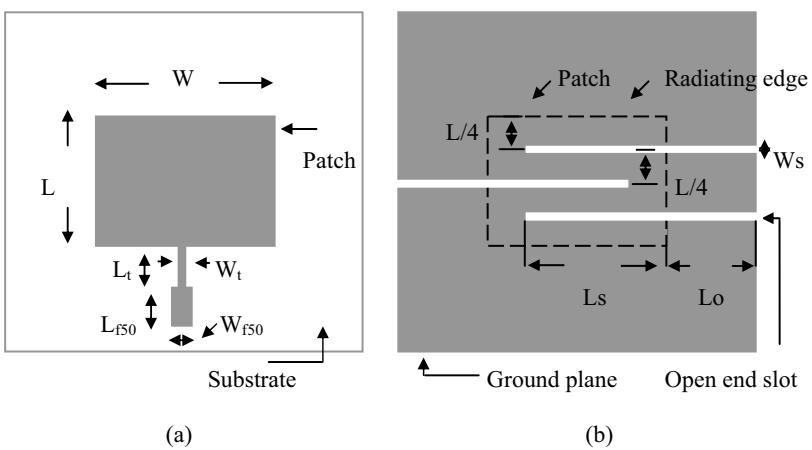

Fig. 1: Geometry of rectangular microstrip antenna with open end meandering slots in the ground plane. (a) Top view, (b) Rear view.

EXPERIMENTAL RESULTS

The prototype antennas with the proposed geometry have been fabricated and measured experimentally using Vector Network Analyzer (Rohde and Schwarz, Germany make ZVK model). The obtained results are tabulated in Table 1.

Table 1: Measured results of rectangular microstrip antenna with open end meandering slots in the ground plane.

Lo (*mm*)	*Ls* (*mm*)	f_r (GHz)	Return loss (dB)	Band width (MHz, %)	Reduction in size (%)
0	0	5.987	–18.50	275, 4.5	-
11.2	12	f_1 = 1.12	– 14.82	71.5, 6.3	82.2
		f_2 = 1.33	– 18.59	184, 13.8	78.8
		f_3 = 2.05	– 10.61	60, 2.9	67.5
11.2	12.5	1.11	–17.11	318, 28.6	82.4
11.2	13	1.09	–23.06	424, 38.6	82.6
11.2	13.5	1.08	–30.13	430, 40	82.9

From the Table 1, the reference antenna with out any slots is resonating for 5.987 GHz. A bandwidth of 4.5% (–10dB return-loss) is obtained. As the meandering slot length, Ls increases from 0 to 12mm, it is seen from the table that the antenna resonates for three frequencies f_1, f_2 and f_3 having great lowering in their resonance frequencies when compared to RA. It is also seen that f_1 and f_2 have more bandwidth when compared to RA. But f_3 has reduction in the bandwidth which is less than RA.

Later, when Ls increases from 12*mm* to 12.5*mm*, f_3 disappears and the frequencies f_1 and f_2 further lowers and their bands merge with each other. Here, the antenna gives a size reduction of 82.4%. It is also found that the bandwidth of the antenna in increased greatly due to merging of the two frequencies bands of f_1 and f_2. From the table, a measured bandwidth of 28.6% is achieved which is 6.35 times the bandwidth of RA.

Again when the slot length Ls is further increases to 13mm, the resonance frequency slit lowers further slightly and resonates at a frequency f_r = 1.09 GHz giving a size reduction of 82.6%. The bandwidth is also found to be further increased to 38.6%.

Later as the slot length increases to 13.5mm, Ls = 0.88W, the resonance frequency lowers slit slightly and resonates at a frequency which is 0.183 times the resonant frequency of RA giving a size reduction of 82.9%. Moreover, from the table it is seen that the bandwidth of the antenna is further increased to 40%, which is 8.88 times the RA. At this optimized slot length an optimum bandwidth has been achieved. For the further increase in the slot length the bandwidth decreases. The variation of the return loss with the frequency when Ls = 13.5mm is as shown in Fig. 2. The coplanar radiation pattern of H-plane and E-plane are taken for this antenna for the slot length 13.5mm. E-plane was found to smoother than H-plane. A gain of 5.2dB is obtained.

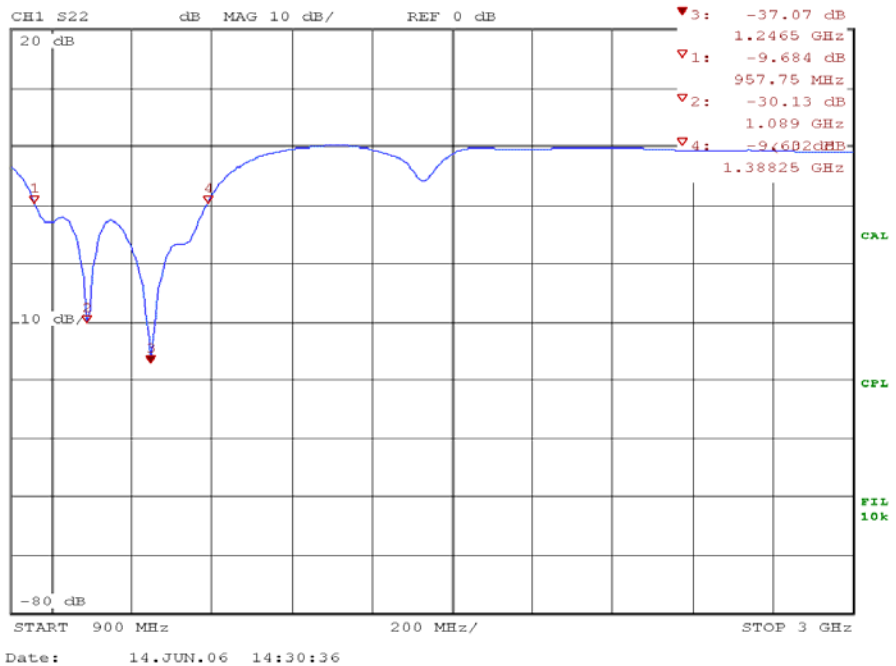

Fig. 2: Variation of return loss with frequency for rectangular microstrip antenna with open end meandering slots in the ground plane when *Ls* = 13.5*mm*.

CONCULSIONS

Compact broadband rectangular microstrip antenna with open end meandering slots in the ground plane is designed, fabricated and studied in detail. It is found that by inserting open end meandering slots in the ground plane, the resonance frequency of the antenna is significantly lowered. And at the same time there is enhancement in the bandwidth. With the proposed design an extreme reduction of 82.9% in the antenna size is obtained with a wide bandwidth of 40%, which is 8.88 times the rectangular microstrip antenna without any slots.

REFERENCES

[1]. J. S. Kuo and K. L. Wong, "A compact microstrip antenna with meandering slots in the ground plane," *Microwave Opt. Technol. Lett.,* vol. 29, pp. 95–97, 2001.

[2]. T. W. Chiou and K. L. Wong, "Design of compact microstrip antennas with a slotted ground plane", *IEEE APS. Int. Symp. Dig.*, pp. 732-735, 2001.

[3]. R. Hossa, A. Byndas and M. E. Bialkowski, "Improvement of compact terminal antenna performance by incorporating open-end slots in the ground plane", *IEEE Microwave and wireless comments letts.* vol. 14, June 2004.

[4]. J. I. Bhal and P. Bharatia, *Microstrip antennas*, Artech House, Dednam, MA, 1980

[5]. Da M. Pozar, *Microwave Engineering*, Wesley publishing company, Inc., 1990.

[6]. K. C. Gupta, *Microwaves*, Wiley Eastern LTd., New Delhi, 1976.

SINGLE FEED DUAL-FREQUENCY BROAD-BAND EQUILATERAL TRIANGULAR MICROSTRIP ANTENNA

G M Pushpanjali, R B Konda, S K Satnoor, S N Mulgi and P V Hunagund
Department of PG Studies and Research in Applied Electronics,
Gulbarga University, Gulbarga (Karnataka) 585 106, India.
E-mail: pushpa_metri@yahoo.co.in

Abstract: *Single feed two-element conventional equilateral triangular microstrip antenna (TCETMA) is designed for X-band frequency gives an impedance bandwidth of 480 MHz. The resonant frequency of this antenna shifts towards the extreme ends of X-band by using a common parasitic element between the driven elements of TCETMA. Using a slot at the center of driven elements the antenna operates at dual bands. The impedance bandwidth of this antenna is found to be 500 MHz. If the slot is placed at the center of parasitic element, the impedance bandwidth increases to 680 MHz. Further the impedance bandwidth increases to 760 MHz by inserting a slot at the center of driven and parasitic elements. These wide and dual band operations of antenna may find application in microwave communication systems. Details of antenna design are described and experimental results are discussed.*

ntroduction: Microstrip antennas (MSAs) have limited applications due to their narrow npedance bandwidth i.e. 1 to 2% [1]. Various techniques are available in the literature to nhance the impedance bandwidth of MSAs made of different types. One of the most ttractive features of the equilateral triangular type microstrip antenna is that, the area ecessary for the patch becomes about half as large as that of a nearly square microstrip ntenna [2]. Dual band antennas with small physical size and good performance are an ncoming challenge to meet the needs of integration, cost and efficiency of the emerging ireless world [3]. In synthetic aperture radar (SAR), a dual-frequency printed circuit ntenna can be used to avoid the use of a separate array for each band for reduced weight nd surface [4]. Dual frequency antennas are useful where integration of two services is equired where two bands cooperate. In view of this an effort is made to enhance the npedance bandwidth of the antennas and to operate in dual-frequency band. The proposed ntennas are designed on commercially available glass-epoxy substrate of thickness h=1.66 m and dielectric constant ε_r = 4.2. First the TCETMA is constructed by using corporate eed technique.

The gap-coupled slot in driven elements equilateral triangular microstrip antenna GSD-ETMA) is constructed by inserting a slot at the center of the driven elements coupled ith a parasitic element in the form of gap-coupled to the two driven elements. The dimension f the slot used in the radiating element is usually taken in terms of λ_0. The length of the slot s taken as $\lambda_0/5$ and width is $\lambda_0/32$, where λ_0 is the free space wavelength in cm. This slot is onsidered as wide slot as its width is comparable to its length [1]. The wide slots are more

effective in enhancing the impedance bandwidth of MSAs.The gap-coupled slot in parasitic element equilateral triangular microstrip antenna (GSP-ETMA) is constructed by inserting a slot at the center of the parasitic element only. The gap-coupled slot in driven and parasitic elements equilateral triangular microstrip antenna (GSDP-ETMA) is constructed by inserting a slot at in both the driven and parasitic elements at their center.

Description of antenna geometry: Fig.1 shows the geometry of TCETMA. The two-elements in this figure is kept at a distance of $3\lambda_0/4$ from their center. The distance between the radiating patch and parasitic element is selected as $3\lambda_0/4$ to add the radiated power in free space by the two radiating elements [5]. The antenna is fed by corporate feed technique. This feed arrangement consists of quarter wave transformer, microstrip bend, two-way power divider and matching transformers for better impedance matching [6]. At the tip of the 50 Ω microstrip line feed a SMA connector is used for feeding the microwave power.

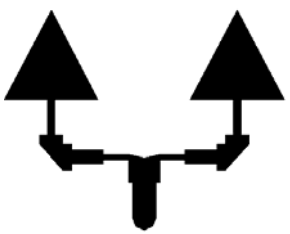

Fig.1 Geometry of TCETMA

Fig.2 Geometry of GSD-ETMA

Fig.3 Geometry of GSP-ETMA

Fig.4 Geometry of GSDP-ETMA

The geometry of GSD-ETMA is shown in figure 2. The gap between the radiating and parasitic element is taken [7] as 0.025 λ_g, where λ_g is the operating wavelength in cm [1]. Fig.3 shows the geometry of GSP-ETMA. The geometry of GSDP-ETMA is as shown in Fig.4.

Experimental results: The impedance bandwidth over return loss less than -10 dB for the proposed antennas is measured for X-band frequencies. The measurement is taken on vector network analyzer E8362B. The variation of return loss versus frequency of TCETMA is shown in Fig. 5. From this graph the impedance bandwidth is calculated using the formula

$$BW = [(f_2 - f_1)/f_c] \times 100\ \%$$

where, f_H and f_L are the higher and lower cut-off frequency of the band respectively when its return loss becomes -10 dB and f_c is the center frequency of this band.

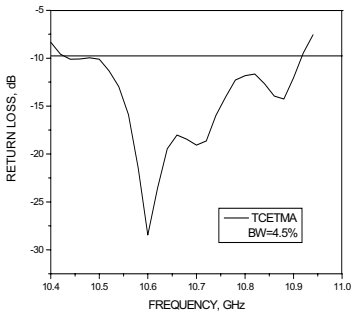

Fig 5: Variation of return loss verses frequency of TCETMA.

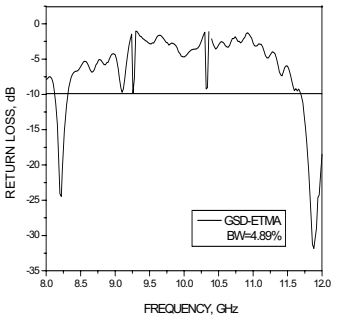

Fig 6: Variation of return loss verses frequency of GSD-ETMA.

The experimental impedance bandwidth of this antenna is found to be 480 MHz i.e. 4.5%. The variation of return loss versus frequency of GSD-ETMA is shown in Fig. 6. From this figure the impedance bandwidth is found to be 500 MHz i.e. 4.89 % which is 1.09 times more when compared to impedance bandwidth of TCETMA and the antenna operates at two bands of frequencies.

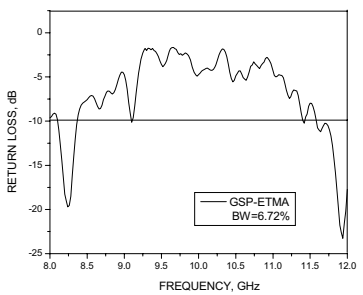

Fig 7: Variation of return loss verses frequency of GSP-ETMA.

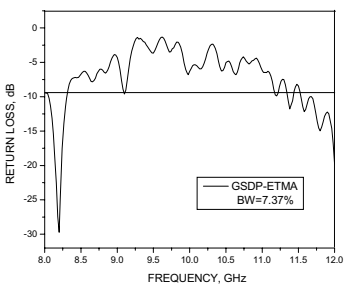

Fig 8: Variation of return loss verses frequency of GSDP-ETMA.

The increase in bandwidth and shift in the resonant frequency at the extremity of the X-band is due to the use of slot and parasitic element in this antenna. The variation of return loss versus frequency of GSP-ETMA is shown in Fig. 7. From this figure the impedance bandwidth is found to be 680 MHz i.e. 6.72 %, which is 1.37 times more than GSD-ETMA. Fig.8 shows the impedance bandwidth curve of GSDP-ETMA and its impedance bandwidth is found to be 760 MHz i.e. 7.37 % that is 1.1 times more than the GSP-ETMA. Hence it is clear that the use of optimum slots in the driven and parasitic elements is quite effective in enhancing the impedance bandwidth and makes the antenna operate at dual-band of frequencies.

Conclusion: From the detailed experimental study it is found that, the proposed antennas such as GSD-ETMA, GSP-ETMA and GSDP-ETMA are quite capable of enhancing the impedance bandwidth when compared to TCETMA. These antennas can also operate in the dual-frequency band. This shows the superiority of gap-coupled technique and use of parasitic element with slot over TCETMA in controlling the resonant frequency of the antenna. Such broadband and dual-band antennas may find applications in wireless communication systems.

Acknowledgement: The authors would like to acknowledge there thanks to Sri D.Govind Rao, Scientist, LRDE, Bangalore, LRDE, for providing measurement facilities and useful discussions.

References:

[1] Bahl I J and Bhartia P, Microstrip Slot Antennas, *Microstrip Antennas*, Dedham, MA: Artech House, 1981.

[2] Suzuki Y, Miyano N and Chiba T, "Circularly polarized radiation from singly fed equilateral-triangular microstrip antenna", *IEEE. Proc.,* vol.134, no.2, pp. 194-197, April 1987.

[3] George F. Tsachtsiris, Constantine F.Soras, P. Karaboikis and Vassilios T. Makios, "Analysis of a modified sierpinski gasket monopole antenna printed on dual band wireless debices", *IEEE, Trans. Antennas Propagat.,* vol. 52, no.10, pp. 2571-2574, October 2004.

[4] M.A.Matin, B.S.Sharif and C.C.Tsimenidis, "Dual-frequency microstrip antenna with V slot", ….. pp.184.

[5] Constantine A Balanis, *Antenna Theory Analysis and Design,* John Wiley & Sons Inc., New York, 1982.

[6] Kai Fong Lee and Wei Chen, *Advances in Microstrip and Printed Antennas,* Wiley-Interscience Publication, John Wiley & Sons, INC. New York, 1997.

[7] Mulgi S N, Vani R M, Hunagund P V and Hadalgi P M, "A compact broadband gap-coupled Microstrip antenna", *Indian J Radio & Space Phys*, vol. 33, pp. 139-141, April 2004.

BROADBAND DESIGN OF SLOT-LOADED RECTANGULAR MICROSTRIP ARRAY ANTENNA

R B Konda, G M Pushpanjali, S K Satnoor, S N Mulgi and P V Hunagund
Department of PG Studies and Research in Applied Electronics,
Gulbarga University, Gulbarga - 585 106, Karnataka, India.
E.mail: rbkonda@yahoo.com

Abstract: *The slot microstrip antennas have advantages over conventional microstrip antenna for enhancing the impedance bandwidth. In this presentation an experimental effort is made to enhance the impedance bandwidth of two-element rectangular microstrip array antenna by inserting different optimum slot configuration in the radiating patches. The results show the wide and multiband operation of the antenna operating at 15-30 GHz. These wideband and multi-band operation of the antennas may find applications in microwave communication systems. The design concepts of antenna are described and experimental results are presented and discussed.*

Introduction: Microstrip antennas (MSAs) are increasingly finding applications in microwave communication systems as they are found to be lightweight, planar configuration and inexpensive to fabricate. However, they possess the intrinsic limitations as the narrow impedance bandwidth nearly 1 to 2% [1]. Various techniques are available in the literature for broadening the impedance bandwidth of MSAs [2-4]. As the slot loading technique is simple and strait forward in enhancing the impedance bandwidth of MSAs compared to other techniques available in the literature. Hence an effort is made to enhance the impedance bandwidth of the two-element rectangular microstrip array antenna by using optimum slots with proper dimensions in terms of operating wavelength λ_0 in the radiating patches, where λ_0 is the free space wavelength in cm. In this presentation a comparative experimental study is made by inserting circular, square ring, pair of longitudinal and I-shaped slots in the radiating element of microstrip array antenna to see their impedance bandwidth. The antennas are designed and fabricated on low cost glass epoxy substrate of thickness h=1.66 mm and permittivity ε_r = 4.2. The artwork of these antennas is designed by using computer software AutoCAD 2000 and fabricated using photolithography process.

Description of antenna geometry: The geometry of circular slot microstrip array antenna (CSMAA) is as shown in Fig 1. The two radiating elements shown in this figure are kept at a distance of $3\lambda_0/4$ in order to add the radiated power in free space by the individual element [5]. The circular slots are placed at the center of the radiating elements. The feed arrangement consists of matching transformer, quarter wave transformer, microstrip bends and two-way power divider for better impedance matching between feed and radiating elements and

maintaining uniform TE_{10} mode [6]. At the tip of microstrip line feed a 50 Ω SMA connector is used for feeding the microwave power.

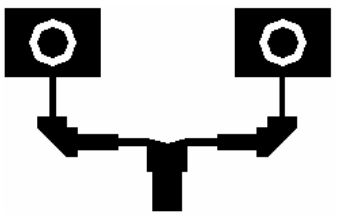

Fig.1 Geometry of CSMAA.

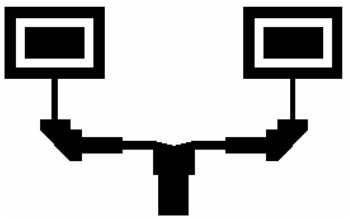

Fig.2 Geometry of SRSMAA.

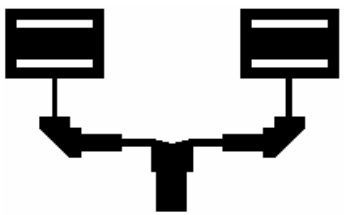

Fig.3 Geometry of PLSMAA.

Fig.4 Geometry of ISMAA.

The geometry of square ring slot microstrip array antenna (SRSMAA) is as shown in Fig. 2. In this figure a square ring slot of width $\lambda_0/32$ parallel to radiating and non-radiating edges kept at a distance of 1mm from the edge. Figure 3 shows the geometry of pair of longitudinal slot microstrip array antenna (PLSMAA). The pair of slots is placed parallel to the radiating edges kept at a distance of 1mm from the edge. The length of the slot is taken as $\lambda_0/4$ and width of the slot is taken as $\lambda_0/32$. This slot is considered as wide slot as its width is comparable to the length. The wide slot is selected, as it is more effective in enhancing the impedance bandwidth when compared to narrow slot [1]. The PLSMAA is modified in to I-shaped slot microstrip array antenna (ISMAA) by placing a transverse slot at the center of PLSMAA, which forms a shape of 'I' as shown in Fig. 4.

Experimental results: The return loss of the designed antennas is measured on vector Network Analyzer. The variation of return loss versus frequency of CSMAA is shown in Fig. 5. From this graph the impedance bandwidth is determined by using the equation

$$BW = [(f_2 - f_1)/f_c] \times 100\ \%$$

where, f_1 and f_2 are the lower and upper cut-off frequencies of CSMAA , respectively when its return loss becomes –10 dB, and f_c is the center frequency between f_1 and f_2.

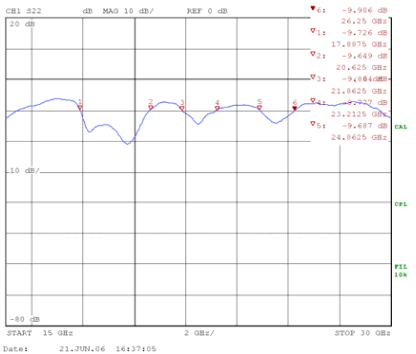

Fig 5 : Variation of return loss verses frequency of CSMAA .

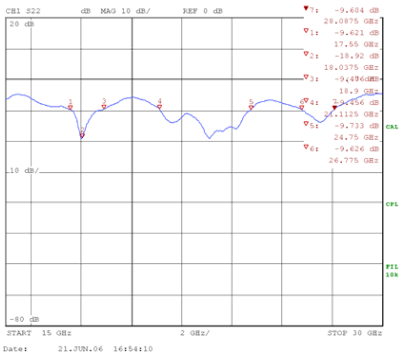

Fig 6 : Variation of return loss verses frequency of SRSMAA.

The slot that couples energy from the strip line to the patch can be either resonant or non-resonant. If it is resonant, it provides another resonance in addition to the patch resonance [7]. Thus from the graph, it is observed that, the antenna operates for three band of frequencies. The total bandwidth of this antenna is found to be 25.65%. Fig. 6 shows the graph of return loss versus frequency of SRSMAA. The total bandwidth of this antenna is found to be 28.05% which is 1.1 times more than that of the CSMAA.

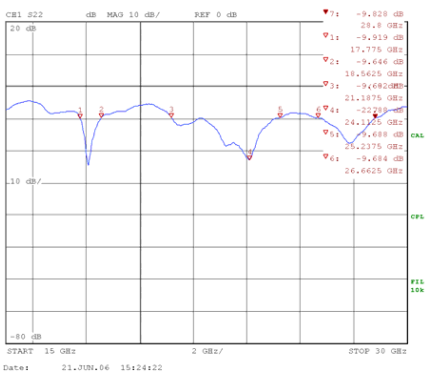

Fig 7 : Variation of return loss verses frequency of PLSMAA.

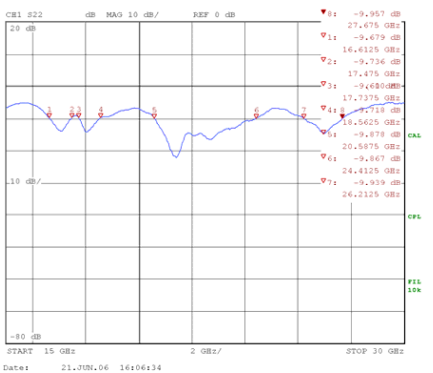

Fig 8 : Variation of return loss verses frequency of ISMAA.

The variation of return loss versus frequency of PLSMAA is as shown in Fig. 7, which is resonating for three band of frequency. The total impedance bandwidth is found to be 29.48%, which is 1.05 times more than SRSMAA. In ISMAA the center slot that is parallel to the length of the patch adds another resonance causes wide impedance bandwidth as shown

in the Fig. 8. The total magnitude of impedance bandwidth is 32.04 %, which is 1.09 times more than the impedance bandwidth of PLSMAA.

Conclusion: From the above experimental study it is quite clear that the impedance bandwidth of the antenna can be enhanced considerably by inserting a slot in the radiating elements. In this study the impedance bandwidth is enhanced from 25.65% to 32.04 % by inserting different optimum slots in the radiating elements. This shows the predominant effect of slot in enhancing the impedance bandwidth. Further it is amply clear from the experimental study that by the insertion of slots the antenna operates at multiband of frequencies. Thus the wideband and multi-frequency operation of these antennas may find application in microwave communication systems.

Acknowledgement: The authors would like to thank the authorities of Department of Science & Technology (DST), Govt. of India, New Delhi, for sanctioning the FIST project to the Dept. of Applied Electronics, Gulbarga University, Gulbarga.

References:

[1] Bhal I J and Bhartia P, Microstrip Slot Antennas, *Microstrip Antennas*, Dedham, MA: Artech House, 1981.

[2] Pozar D M, "Microstrip antenna aperture-coupled to a microstripline," *Elect. Lett.,* vol.21, no.2, pp.49-50, Jan. 1985.

[3] Quing Song & Xue-Xia Zhang "A study on wide band gap-coupled microstrip antenna array" *IEEE, Trans. Antennas Propagat.,* vol.43, pp.313-317, March 1995.

[4] Saeed I.Latif, Lotfollah Shafai and Satish Kumar Sharama, "Bandwidth Enhancement and Size Reduction of Microstrip Slot Antennas," *IEEE, Trans. Antennas Propagat.,* vol. 53, pp. 994-1003, March 2005.

[5] Constantine A Balanis, *Antenna Theory Analysis and Design*, John Wiley & Sons Inc., New York, 1982.

[6] Kai Fong Lee and wei chen, *Advances in Microstrip and Printed Antennas*, John Wiley & Sons, INC. New York 1997.

[7] Jeen-Sheen Row, "Dual frequency triangular planar inverted-f antenna", *IEEE, Trans. Antennas Propagat.*, vol. 53, pp. 874-876, Feb. 2005.

Proceedings of APSYM2006, Dec. 14-16., Dept. of Electronics, CUSAT, India.

DESIGN AND ANALYSIS OF ASCENDANT TAPERED MEANDER LINE ANTENNA

Pankaj Singh Tomar & P.K. Singhal
Dept. of Electronics, CSE & IT
Madhav Institute of Technology & Science, Gwalior (India) - 474005
E mail: pankaj_tomar7@yahoo.com & pks_65 @ yahoo.com

Abstract: *The meander line antenna (MLA) subjects to reduce the physical dimension of the overall antenna size while still maintain the required electric length to achieve different resonant frequencies for global system mobile (GSM), personal communication system (PCS), digital communication system (DCS), microwave sensor and radar application. The novel design of meander line antenna provides a wide band and characteristics with 50 Ω input impedance.*

Introduction: Small antennas for mobile handset applications are very attractive recently due to the increasing demand of wireless communication devices. In addition, an idea of integration antennas inside System-In-a-Package (SIP) is currently receiving much attention to further reduce the size and lower manufacturing cost. The size of the MLA is small, of the orders of wavelength. The features of MLA consisting of one wire have been shown in [1]-[4]. The MLA has a feature that its input impedance can be easily matched by the use of impedance step-up and balance mode impedance loading. A compact meander-type slot antenna with non-uniform slot line widths to yield lower operating frequency has also been reported [5]. In another study, dual-frequency antenna has been designed by using a tapered meander slot antenna with a short-ended microstrip line feed and fabricated on a high permittivity substrate [6]. However, these designs are not suitable for the applications of SIP because of their large dimensions. Moreover, high dielectric constant can possibly produce small size antennas, but the idea cannot be applied in SIP applications as thin and low dielectric constant substrates are usually used in such applications. The MLA with multi-frequency capabilities exhibits high gain, ultra-wide bandwidth, multiple polarizations, increased directivity control, reduced power needs, inherent 50 Ohm impedance and improved efficiency in a surprisingly small package (compact in size).

The MLA (Meander Line Antenna) is a new type of radiating element, made from a combination of a loop antenna and frequency tuning meander lines. The electrical length of the MLA is made up mostly by the delay characteristic of the meander line rather than the length of the radiating structure itself. MLAs can be designed to exhibit broadband capabilities that allow Operation on several frequency bands.

If number of turns of tapered meander line increases operating frequency reduced. As the frequency increases, the operating modes have not only wider bandwidth but also better return loss values [7]. Meander antenna or meander pattern, is an antenna with the wire folded and forth where resonance is found in a much more compact structure than can otherwise be obtained. In all three cases the radiation resistance, bandwidth and efficiency reduces as size is decreased, and tuning becomes increasingly critical.

Design: The antenna is constructed by making tapered meander line antenna in a perfectly conducting plane supported by a dielectric substrate of 1.6 mm thickness and relative dielectric constant 4.52, fig.1 shows the top view of antenna and design parameters. The dimensions of major parts of the antenna are listed in table 1. Spacing between the parallel slots is 1 mm the width of slot is 1 mm and 3 mm.

Table 1 (all dimensions in mm)

A	B	C	D	E	F	G	H	I
3	4	8	9	10	11	12	1	1

Simulation and Results: The resonant properties of an antenna have been simulated using the method of moment based commercial software (IE3D) [8]. IE3D is a full-wave, method of moments based electromagnetic simulator solving the current distribution on 3D and multilayer structures of general shape. Simulation results are shown in figure 2 and figure 3 which shows return loss, efficiency v/s frequency respectively. Band width of meander line antenna can be significantly increased if substrate with lower dielectric constant is used.

Probe Feed is used as a feed line of 50 Ω with probe radius 0.4 mm and length of probe is equal to the substrate thickness.

Conclusion: We proposed a multi band ascendant tapered meander line antenna for frequencies 5.7 GHz, 6 GHz, 6.6 GHz & 8.9 GHz operation. Antenna has high radiation and antenna efficiency.

Acknowledgement: Authors thankfully acknowledge the all authorities of Madhav Institute of Technology & Science Gwalior (M.P.) - 474005 INDIA.

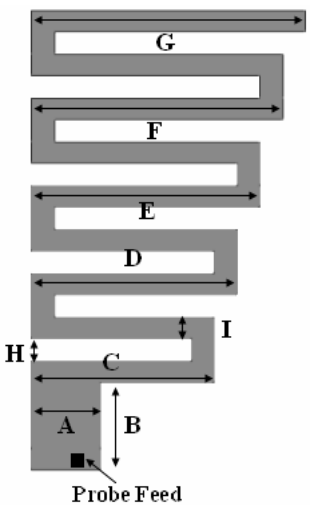

Fig.1: Proposed Geometry

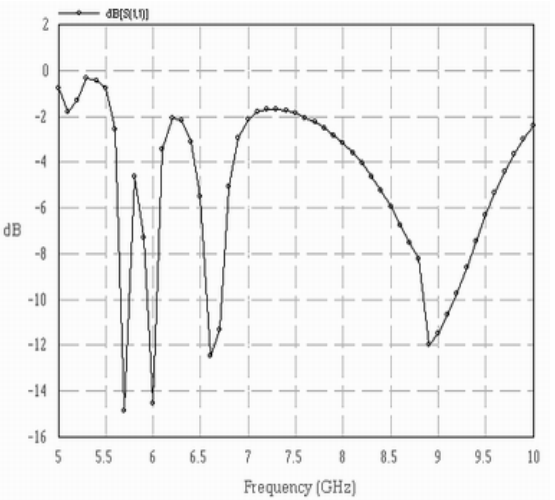

Fig.2: Return Loss v/s Frequency

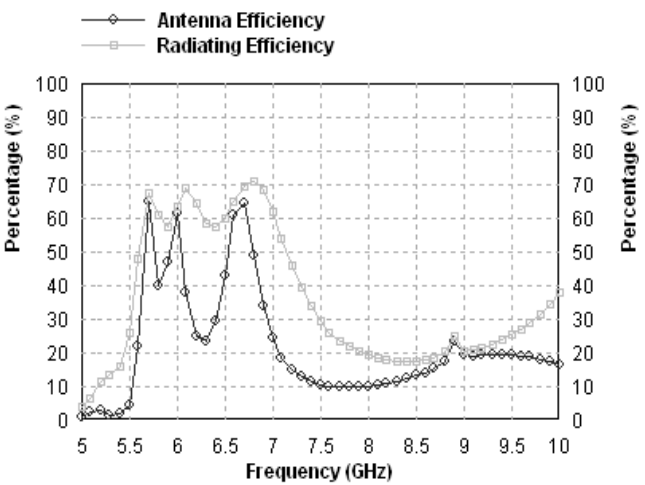

Fig.3: Efficiency v/s Frequency

References:

[1] T. J. Warnagiris and T. J. Minardo, "Performance of a meandered line as electrically small transmitting antenna," *IEEE Trans. Antennas Propagation*, vol. 46, no. 12, pp.1797–1876, Dec. 1998.

[2] M. Ali and S.S. Stuchly, "A meander-line bow-tie antenna," *IEEE AP-S International Symposium*, pp.1566–1569, July 1996.

[3] H. Nakano and H. Takagi et al, "Shorting Ratios of Modified Dipole Antenna," *IEEE Trans. on Antennas and Propagation*, vol.AP-32, no.4, pp.385-386, April1984

[4] G.Marrocco, "Gain-optimized self-resonant meander line antennas for RFID applications," *IEEE Antennas Wireless Propagat. Lett.*, vol. 2, pp. 302–305, 2003.

[5] J. Kim, J Yook, W. Song, J. Yoon, J. Park, and H. Park, "Compact meander-type slot antennas," *IEEE Antenna and Propagation Symp Proceedings*, pp 724-726, 2001.

[6] C M. Allen, A Z. Elsherbeni, C E. Smith, C P. Huang, and K. Lee, "Tapped Meander Slot Antenna for Dual Band Personal Wireless Communication Systems," *Microwave and Optical Technology Letters*, vol. 36, No. 5, pp 381-385, March, 2003.

[7] Elsherbeni, A.Z.; Huang, C.-W.P.; Smith, C.E., "Wide band meander line antenna for wireless communication systems Antennas and Propagation for Wireless Communications," 2000 IEEE-APS Conference on 6-8 Nov. 2000 Page(s):17-20.

[8] IE3D Software Release 8.21 version and developed by M/S Zeland Software, Inc.

Proceedings of APSYM2006, Dec. 14-16., Dept. of Electronics, CUSAT, India.

DESIGN AND DEVELOPMENT OF THE FEED FOR PARABOLIC REFLECTOR TRACKING ANTENNA DEPLOYED IN RADIO THEODOLITE

Tapas K. Bhuiya, K.R. Tuckley
SAMEER, IIT Campus, Powai, Mumbai-76, E-mail: tapask2001@yahoo.co.in

ABSTRACT

The microstrip patch antenna is very popular because of it's low profile, conformal, low cost, ease of fabrication and can be deployed for a wide variety of applications. However, microstrip antennas inherently have narrow bandwidth which is the main drawback. In order to enhance the bandwidth, the air gap is introduced between the substrate and ground plane. In this paper, a 2×2 rectangular microstrip antenna with an air gap is presented and proposed as a feed for parabolic reflector antenna particularly in balloon tracking in the Radio Theodolite system. It has several advantages over the horn or wire dipole as a feed due to their light weight, simple low cost structure and ability of integrating with microwave circuit. The impedance bandwidth for VSWR<2:1 in case of without air gap is around 2.2% whereas it is 4% with an air gap of 2 mm which meets the requirement of Radio Theodolite.

I INTRODUCTION

The microstrip patch is a suitable candidate as an antenna in the field of wireless communication, RF sensors and radar system because of it's simple low cost structure. There was rapid advancement in last two decades. However the development is restricted by it's narrow band property. There are several methods of bandwidth enhancement such as aperture coupling, stacked elements, coplanar parasitic elements, introduction of air substrate etc. Here, we have presented 2×2 rectangular microstrip antenna with an air gap introduced between the substrate and ground plane and proposed as a feed for parabolic reflector tracking antenna. An air gap reduces the effective dielectric constant and increases the thickness of the microstrip configuration, as a result bandwidth increases. The antenna is developed at 1.68 GHz with a substrate of relatively high dielectric constant ε_r =3.2 and thickness h=3.18 mm.

The 2×2 microstrip antenna is proposed as a feed for the parabolic reflector tracking antenna. Fig.2 shows the developed feed for the tracking antenna. The feed is placed normal to the axis of the parabolic disc inside a cylindrical radome along the axis of the parabola at a distance 0.77 m from the vertex. The elements are symmetrically displaced from the bore sight axis. The displacement decides the scanning angle of the tracking antenna. The elements are kept independent to allow the beam scanning in two orthogonal direction. The tracking technique uses the simultaneous lobe comparison method. The antenna system is proposed to be deployed in the Radio Theodolite at 1.68 GHz.

Radio Theodolite is a receiver that receives the signal sent by Radiosonde (a balloon borne transmitter). It receives the information regarding the humidity, temperature and pressure of the atmosphere. The Theodolite also tracks the radiosonde signal with suitable tracking mechanism like sequential or simultaneous lobbing. The gain of the antenna system is 31 dB at 1.68 GHz. F/D for this parabolic disc is 0.37. The bandwidth required for the antenna system is more than 40 MHz which was one of the main objective in the development. Fig. 1 shows the antenna system for Radio Theodolite.

Fig.1 Parabolic reflector tracking antenna in Radio Theodolite system

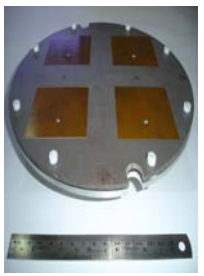

Fig. 2 Photograph of the developed feed for the antenna shown left

II RECTANGULAR MICROSTRIP PATCH ANTENNA

This consist of a rectangular radiating patch on one side of a dielectric substrate which has a ground plane normally on the other side. In this design, the air gap is introduced between the substrate and ground plane to get the required bandwidth as discussed in the next section.

The rectangular microstrip patch can be thought as a transmission line along the length L of the patch antenna as shown in Fig.3. The width and length of the patch in the fundamental mode (TM_{10}) is given by

$$W = \frac{c}{2 \cdot f_0}\left(\frac{\varepsilon_r + 1}{2}\right)^{-\frac{1}{2}} \tag{1}$$

$$L = \frac{c}{2 \cdot f_0 \sqrt{\varepsilon_{re}}} - 2 \cdot \Delta l \tag{2}$$

respectively, where c is the velocity of light, f_0 is the desired resonant frequency of the patch, ε_r is the dielectric constant of the substrate, ε_{re} is the effective dielectric constant of the substrate and is given by [1]

$$\varepsilon_{re} = \frac{\varepsilon_r + 1}{2} + \frac{\varepsilon_r - 1}{2}\left(1 + \frac{10 \cdot h}{W}\right)^{-\frac{1}{2}} \tag{3}$$

and normalized line extension [2] is

$$\frac{\Delta l}{h} = 0.412 \cdot \frac{(\varepsilon_{re} + 0.300) \cdot (\frac{W}{h} + 0.264)}{(\varepsilon_{re} - 0.258) \cdot (\frac{W}{h} + 0.813)} \tag{4}$$

Input impedance at the feed point for a microstrip antenna is an essential parameter; it should be accurately known so as to provide a good match between the coaxial to antenna. Assuming no variation of input impedance along W, the input impedance varies from zero in the center to the edge resistance approximately as

$$R_i = R_e \cdot \sin^2 \frac{\pi \cdot x}{L} \qquad for\ 0 \le x \le L/2 \tag{5}$$

where R_i is the input resistance, R_e is the input resistance at the edge, and x is the distance from the center of the patch to the feeding point. The value R_e of normally varies from170 to 200 Ω.

Proceedings of APSYM2006, Dec. 14-16., Dept. of Electronics, CUSAT, India.

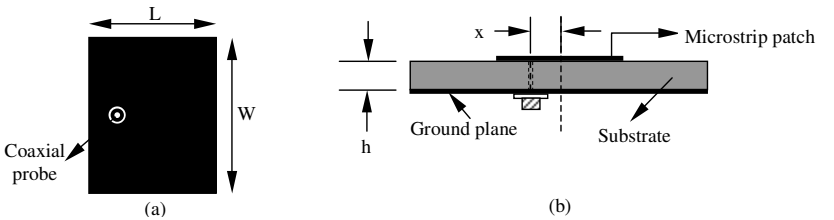

Fig.3 Rectangular Microstrip Patch Antenna (a) Top view (b) Side view

III BANDWIDTH ENHANCEMENT

It is well known that the decrease in dielectric constant, increase in substrate thickness implies an increase in percentage bandwidth in microstrip antenna. Therefore an air gap between the substrate and ground plane results a decrease in dielectric constant and an increase in substrate thickness. Hence the bandwidth increases. Additionally, the resonant frequency can be tuned externally by means of adjustable screw between the substrate and ground plate(Fig.4). The formula for resonant frequency in T_{nm} mode is given by [3]

$$f_{nm}(\Delta) = f(0) \cdot \sqrt{\frac{\varepsilon}{\varepsilon_{eff}}} \tag{6}$$

where $f_{nm}(0)$ is the resonant frequency when there is no gap and ε_{eff} is effective permittivity of the composite structure shown in Fig.4:

$$\varepsilon_{eff} = \frac{\varepsilon\ (\Delta + h)}{(h + \varepsilon_r \cdot \Delta)} \tag{7}$$

It is noted that, as the air gap width Δ increases, ε_{eff} decreases and resonant frequency increases.

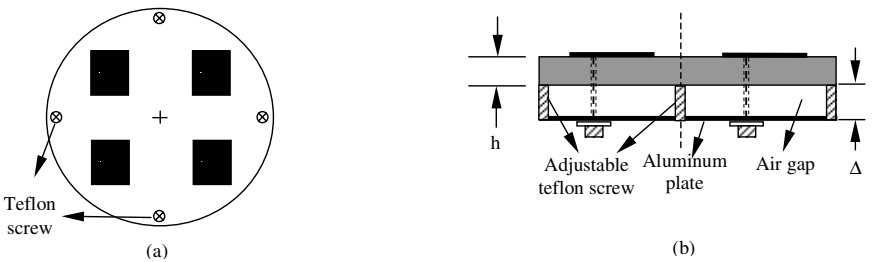

Fig.4 2×2 microstrip antenna with air gap, proposed feed for parabolic reflector tracking antenna (a) Top view (b) Side view

2×2 rectangular microstrip antenna is printed on a common substrate of dielectric constant ε_r =3.2 and thickness h=3.18 mm. The shape of the antenna is made circular as it is to be fitted on a circular radome of diameter of 23 cm. The antenna is stacked with another aluminum circular plate (ground plane) of same diameter keeping some air gap to get the larger bandwidth. The gap between the substrate and plate is variable by adjustable screw to tune the desired frequency. The space in the ground plate can be used for microwave circuits such as LNA, hybrid ring, attenuator etc. It reduces the cable losses, as a results, noise figure of the system improves.

IV MEASUREMENTS AND RESULTS

Fig. 5 shows the impedance characteristics of an element in the array. 2×2 rectangular microstrip antenna is printed on a common substrate of dielectric constant ε_r=3.2 and thickness *h=3.18* mm. The impedance bandwidth for VSWR<2:1 in case of without air gap is shown in Fig.5(a). The VSWR 2:1 circles in the smith chart indicates the bandwidth around 37 MHz (2.2 %) whereas it is 66 MHz (4%) in case of an air gap of 2 mm shown in Fig 5(b) which meets the requirement of the Radio Theodolite system.

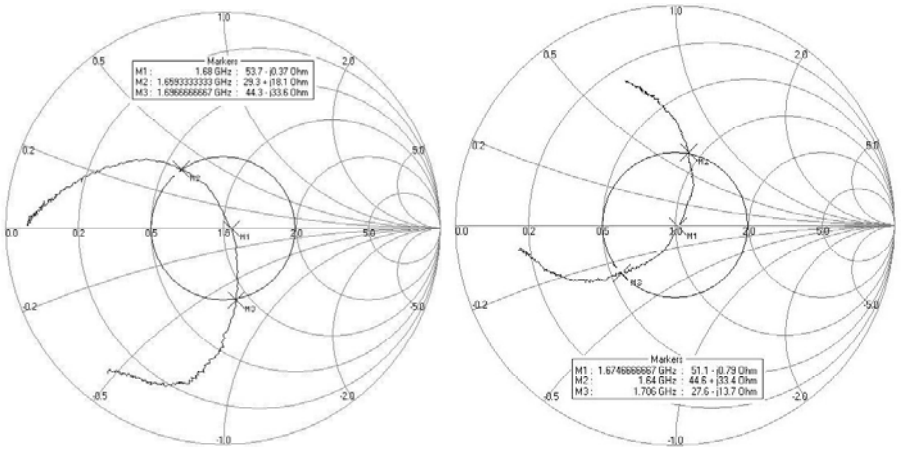

(a) (b)

Fig. 5 Input impedance of an element in the array (a) without air gap (b) with air gap Δ=2 mm

V CONCLUSIONS

A 2×2 rectangular microstrip antenna is proposed as a feed for parabolic reflector tracking antenna in Radio Theodolite system. It has certain advantages as a feed over the conventional horn or wire dipole with balun such as light weight, simple, low cost and integrity with microwave circuit. The bandwidth enhancement of the microstrip antenna is obtained introducing an air gap between the substrate and ground plane. We have achieved 4% impedance bandwidth for VSWR<2:1 with an air gap of 2 mm whereas it is 2.2 % in case of without air gap.

REFERENCE

[1] Scheider, M.V., "Microstrip Dispersion",*Proc. IEEE*, Vol.60, No.1, pp.144-146, Jan.1972
[2] Hammerstad, E.O., "Equations for Microstrip Circuit Design", *5th Europeon Microwave conf.*, pp. 268-272, 1975
[3] Lee, K.F., Ho, K.Y., and Dahele, J.S., "Circular-disk microstrip antenna with an air gap", *IEEE Trans*, AP-32, pp. 880-884,1984.
[4] Bahl, I. J., and P. Bhartia, *Microstrip Antennas*, Artech House, Dedham, MA, 1980
[5] J. R. James and P.S. Hall, *Hand book of Microstrip Antennas*, Peter Peregrinus Ltd., 1989.
[6] Thomas A. Milligan, "*Modern Antenna Design*" Mc Graw Hill

COMPACT DRUM SHAPED MONOPOLE ANTENNA FOR NEW GENERATION MOBILE APPLICATIONS

Bybi P.C, Jitha B, Gijo Augustin, Binu Paul, C.K Aanandan, K. Vasudevan and P.Mohanan

Center for research in Electromagnetics and antennas (CREMA), Dept.of Electronics, CUSAT,
Cochin., India, 682022,

ABSTRACT: *A wideband drum shaped monopole antenna having a 2:1 VSWR bandwidth greater than 80% (1456-3477 MHz) is presented. The wide bandwidth along with omni directional pattern and moderate gain makes it suitable for existing and modern mobile applications.*

INTRODUCTION

Wideband antennas are gaining prominence and becoming very attractive in modern wireless and mobile communication systems. These antennas avoid multiple band designs [1, 2] of narrow band elements and hence are simpler. One of the most popular antenna employed in wireless and mobile communication systems is the monopole antenna because of simple structure and powerful merits such as wide impedance bandwidth, omni-directional radiation pattern and moderate gain.

In this paper we report a wide band printed drum monopole, fed by a microstrip line. The parameters which affect the operation of the antenna are analyzed both numerically and experimentally.

ANTENNA DESIGN

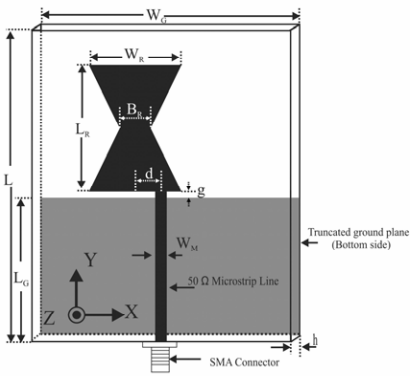

Fig. 1 Geometry and optimized dimensions of the proposed antenna
[L =81, W_G = 67, L_G=35.5, W_M =3, W_R = 24, L_R =33, B_R = 8, d = 6.5, g =1.5, h=1.6 (units in mm) ε_r =4.2]

Fig. 1 presents the geometry of the proposed drum shaped monopole antenna for wide band operation. The antenna is designed to cover the present day requirement of the communication channels with VSWR of 2:1 over the designated frequency range. The radiating drum shaped monopole with parameters W_R = 24mm, L_R= 33mm and B_R= 8mm and the 50Ω microstrip feedline of width W_M of 3mm are etched a substrate of thickness 1.6mm and relative permittivity 4.2. The truncated ground plane of length L_G =35.5mm and width W_G =67mm below the microstrip feed line is etched on the other side of the substrate. The offset distance (d) of the patch relative to the feed strip and the feed gap (g) between the ground plane and the radiating patch are optimized for wideband performance.

EXPERIMENTAL RESULTS

The impedance characteristics of the antenna were simulated using the Ansoft HFSS^{TM} V10. Based on the variation of d from 0 to 9.75mm the return loss characteristics are analyzed (Fig.2.a). The -10dB bandwidth changes significantly with varying offset distance'd' [3]. The optimized offset distance is found to be d =6.5mm.The simulated return loss curves with different feed gap 'g' [4] are plotted in Fig.2.b. It is observed that the performance of the antenna changes with varying feed gap 'g'. The optimized feed gap for maximum bandwidth is found to be g =1.5mm.

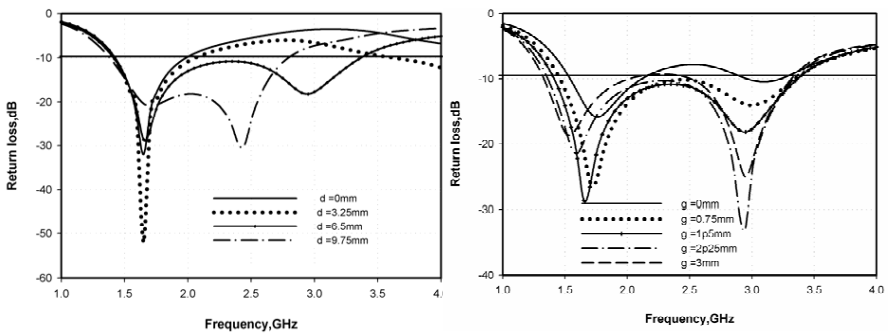

(a) (b)

Fig. 2.a. Simulated return loss for different offset distance d [L =81, W_G = 67, L_G =35.5, W_M =3, W_R = 24, L_R =33, B_R = 8, g =1.5, h=1.6 (units in mm) ε_r =4.2]
Fig. 2. b Simulated return loss for different feed gap g [L =81, W_G = 67, L_G =35.5, W_M =3, W_R = 24, L_R =33, B_R = 8, d =6.5, h=1.6 (units in mm) ε_r =4.2]

It has been shown in the simulation that by selecting the proper offset distance d and feed gap h, much enhanced impedance bandwidth can be achieved for the proposed antenna. The strong electromagnetic coupling between the ground plane and the patch is responsible for the enhanced bandwidth.

The prototype of the drum monopole antenna with optimal design, ie d= 6.5mm and g = 1.5mm was fabricated and measured. The measurement was performed using Agilent E8362B PNA series network analyzer. Fig.3 shows the simulated and measured return loss curves. The measured return loss agrees well with the simulation. The measured bandwidth of -10dB is from 1.46 to 3.48GHz, and in simulation from1.45 to 3.35GHz. The measurement confirms the wideband characteristic of the proposed drum shaped monopole antenna, as predicted in the simulation.

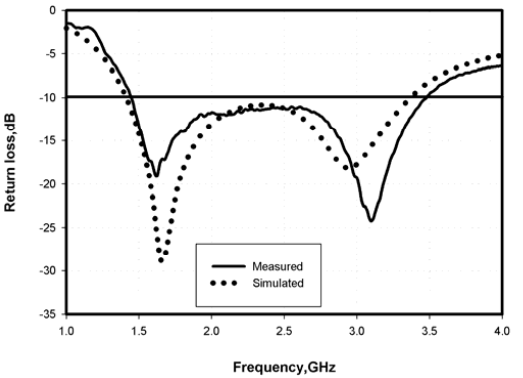

Fig. 3 Simulated and measured return loss curves for the proposed antenna[L =81, WG = 67, L_G =35.5 W_M =3, W_R = 24, L_R =33, B_R = 8, d = 6.5, g =1.5, h=1.6 (units in mm)ε_r =4.2]

Fig.4 shows the measured radiation patterns in the X-Z and Y-Z planes at 1.8, 2.4 an GHz respectively. The antenna offers nearly similar radiation pattern throughout the except at the higher band edge. The pattern is found to be omni directional along the plane and figure of eight shape in the Y-Z plane. The antenna is linearly polarized alon Y direction along the entire band. The measured antenna gain, is shown in fig.5.

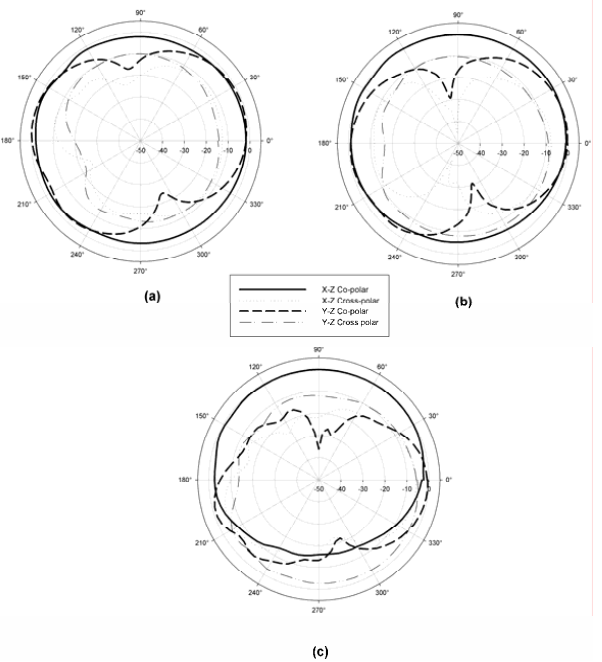

Fig. 4 Measured radiation pattern of the proposed antenna at (a) 1.8 GHz (b) 2.4 GHz (c) 3.4 GHz [L =81, W_G = 67, L_G =35.5, W_M =3, W_R = 24, L_R =33, B_R = 8, d = 6.5, g =1.5, h=1.6 (units in mm)ε_r =4.2]

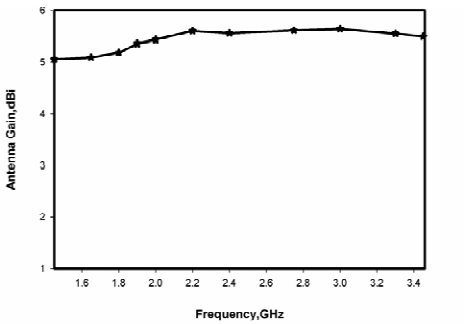

Fig. 5 Measured Gain of the proposed antenna [L =81, W_G = 67, L_G =35.5, W_M =3, W_R = 24, L_R =33, B_R = 8, d = 6.5, g =1.5, h=1.6 (units in mm) ε_r =4.2]

CONCLUSION

A wide band drum shaped antenna fed by microstrip feed line capable of serving the needs of new generation mobile applications has been proposed and successfully implemented. It has been shown that the operating bandwidth of the antenna heavily dependent on the feed gap and the offset distance due to the impedance matching. Wide impedance bandwidth and omni-directional patterns with moderate gain are the striking features of the design.

REFERENCES

1. Y.D. Lin and P.L. Chi, Tapered Bent Folded Monopole for Dual-Band Wireless local Area Network (WLAN) Systems, *IEEE Antennas and Wireless Lett 4* (2005), 355-357.
2. J. W. Wu, C. R. Lin and J. H. Lu, A Planar Meander-Line Antenna for Tripple Band Operation of Mobile Handsets, *Microwave Opt Technol Lett* 41 (2004), 380-386.
3. H. D. Chen, J. S. Chen and J. N. Li,Ultra-Wideband Square-Slot Antenna, *Microwave Opt Technol Lett* 48 (2006), 500-502.
4. J. Liang, C. C. Chiau, X. Chen and C. G. Parini, Printed circular disc monopole antenna for ultra-wideband applications, Electronics Lett 40 (2004), No.20

COMPACT MULTIBAND ANTENNA FOR WIRELESS ACCESS POINT

Gijo Augustin, Shynu S.V., P. Mohanan, C.K. Aanandan and K Vasudevan

Centre for **R**esearch in **E**lectro**M**agnetics and **A**ntennas (CREMA)
Department of Electronics,
Cochin University of Science and Technology
Cochin - 22, Kerala, India.
Ph : +914842576418, Fax: +914842575800. E-mail : gijoaugustin@cusat.ac.in

Abstract: A multiband antenna which can cater both the 2.4 GHz (2400MHz - 2485 MHz) and 5.8 GHz (5725MHz - 5825 MHz) Wireless LAN bands is presented. Experimental analysis using Agilent E8362B PNA, shows a 2:1 VSWR bandwidth of upto 23.1% and 19% for 2.4 GHz and 5.8 GHz respectively.The antenna is simulated using Ansoft's HFSS v10, which shows good agreement with simulated results. Measured radiation patterns are observed to be nearly omnidirectional which is suitable for applications like wireless access point.

I INTRODUCTION

Wirelss communication has evolved exponential growth during the last decade, leading to the development of highly integrated communication devices which incorporate latest communication protocols like Wireless LAN and Bluetooth. A wireless access point facilitates communication between PCs, Laptops, Wireless routers and other such communication devices. To fulfil the requirements of modern handheld communication devices ,development of a compact, multiband antenna with omnidirectional radiation proporties and moderate gain is of prime interest.Many techniques have been used to develp antennas [1,2,3] which fulfill the needs of modern communication systems.Printed monopole antennas are a good choice for the short range communication devices becaue of their low cost, light weight and easy fabrication.As per IEEE recommendation, the 2.4 GHz WLAN occupies a spectrum from 2400 MHz – 2485 MHz whereas the 5.8 GHz Hyperlan occupies the 5725MHz - 5825 MHzThe present scenario in the wireless communication systems indicates a shift of operating frequency from the 2.4 GHz band to the 5.8 GHz band for various reasons. Hence a single, compact antenna supporting both these WLAN bands is of great significance.

In this manuscript we propose a dualband antenna capable of serving the needs of Wireless Access Point. Various antenna parameters are optimized using Ansoft HFSS™ v10 to meet the design goals at both frequency bands of interest. The prototype of the proposed and antenna is constructed and tested. Details of the simulated and measured antenna characterestics are presented and discussed.

2.ANTENNA GEOMETRY

Fig.1 shows the proposed geometry of the multiband, triangular patch loaded

monopole antenna. It is constructed on a substrate with dielectric constant, ε_r = 4.4 and thickness, h = 1.6 mm. The proposed antenna consists of a of a triangular patch on layer 1, excited by the planar strip monopole on layer 2. Note that the ground plane of diamension 30 x 25 mm is printed on the back surface of layer 1. A 50 microstrip line with truncated ground plane etched on layer 2 serves as the feed and radiating monopole. The overall size of the antenna including the feeding mechanisum is (25 x 50 x 3.2) while the ground plane diamension is (30 x 25) mm. The monopole provides resonance at higher band while the loaded triangular patch resonates at the lower band. The position of the triangular patch is optimized experimently for optimum impedance matching.

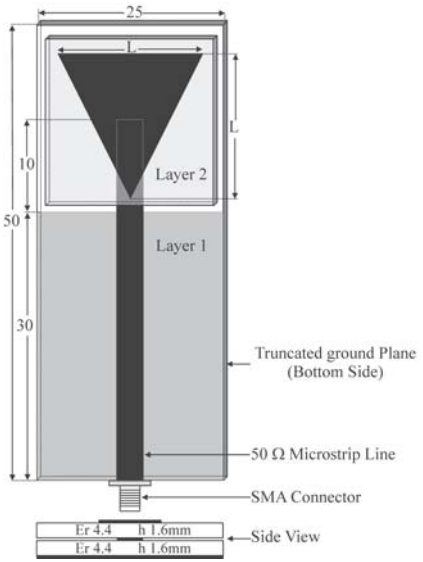

Fig. 1 Geometry of the proposed Antenna

3.Experimental Results and Discussion

The proposed antenna is simulated using commercial electromagnetic solver- Ansoft HFSS and a prototype of the same is constructed and tested. Fig. 2 depicts the experimental results along with the simulated results for the antenna diamension L = 20. A good agreement between simulated and

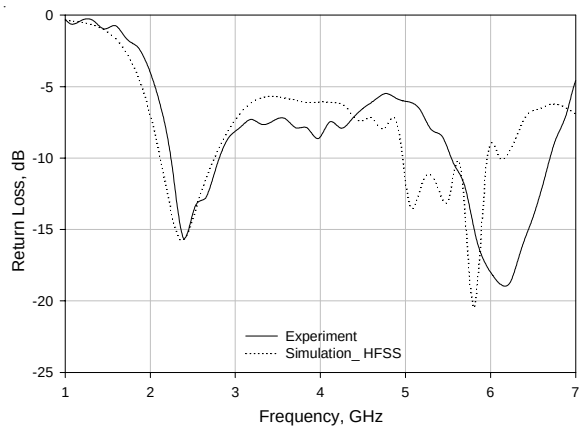

Fig. 2 Measured and Simulated Reflection characteristics of the proposed Antenna

experimental results are observerd. It is evident from the plot that the first band corresponds to (2.23 - 2.81) GHz while the second resonance include (5.54 - 6.71) GHz. It is clearly seen that the antenna can provide % bandwidth of 23.1% in the lower band and

19 % in the 5.8 GHz band. Considering the bandwidth specifications of 2.4 /5.8 GHZ WLAN operating band, the antenna found to be a good candidate.

In the proposed structure, the strip monopole provides the higher resonance. The experimental study for different values of the monopole legth is provided in Fig 3 with all other paramenters including the ground dimensions a constant.

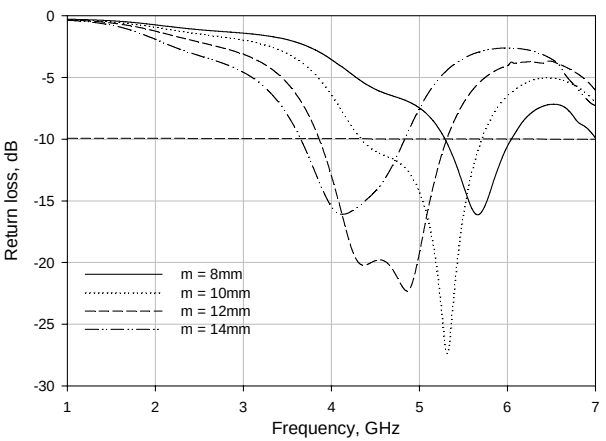

Fig. 3 Tunning of second resonant frequency by varying the parameter 'L'

The triangular patch is prototyped for different dimensions of L, keeping all other parameters constant and effect of patch diamension 'L' are studied. Fig 3. shows the typical return losses for the cases of L = 15,20,25. It is evident form the plot that the first resonance of the antenna can be tunned by varying the diamension 'L' and keeping

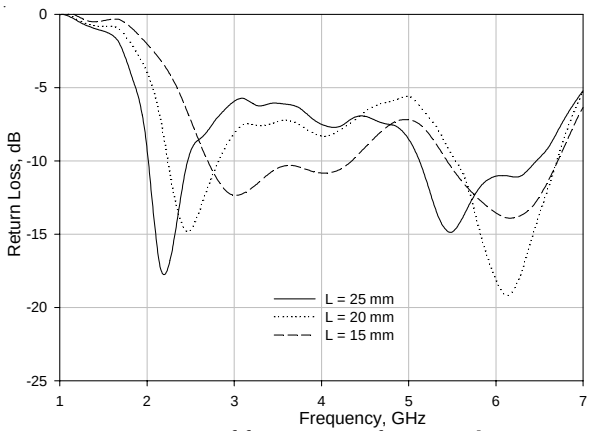

Fig. 4 Tunning of first resonant frequency by varying the parameter 'L'

all other parameters constant.

Simulated current density plots of the proposed antenna is shown in figure 5. It

is clear from the figure that at 2.4 GHz the triangular patch is more excited while at 5.8 GHz the monopole is excited more.

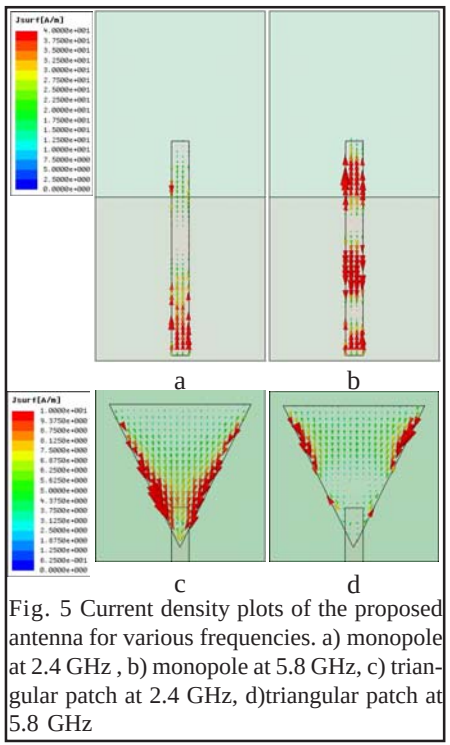

Fig. 5 Current density plots of the proposed antenna for various frequencies. a) monopole at 2.4 GHz , b) monopole at 5.8 GHz, c) triangular patch at 2.4 GHz, d)triangular patch at 5.8 GHz

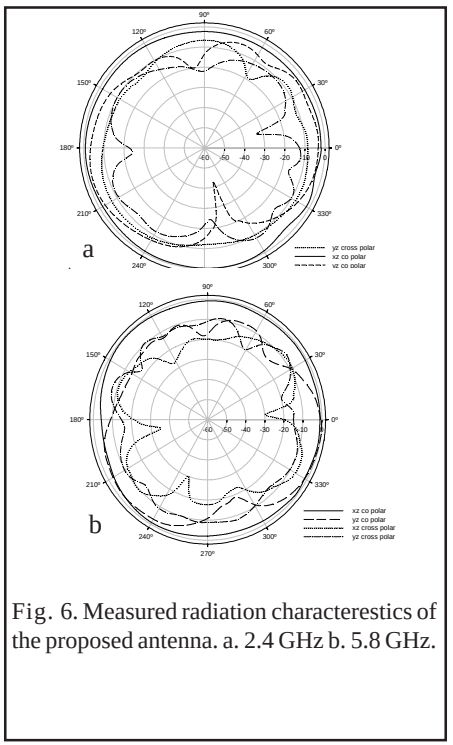

Fig. 6. Measured radiation characterestics of the proposed antenna. a. 2.4 GHz b. 5.8 GHz.

Fig 6. shows the measured nearly omnidirectional radiation patters at 2.4 GHz and 5.2 GHz respectively. The gain of the antenna is also measured using gain comparison method. It has an average gain of 2.2 dBi and 3.3 dBi in the 2.4 GHz and 5.8 GHz bands,respectively.

4. Concludsion.

A compact dual band, triangular patch loaded monopole antenna is presented. Various antenna parameters are studied and optimized for 2.4/5.8 WLAN bands. The antenna offers omnidirectonal radiation characteristics with moderate gain suitable for the use in wireless access points.

5. Reference.

[1] Lin, C.-C.; Kuo, L.-C.; Chuang, H.-R., *"A Horizontally Polarized Omnidirectional Printed Antenna for WLAN Applications"*, IEEE Transactions on Antennas and Propagation, Vol:54, No.11, November 2006

[2] Feng-Wei Yao and Shun-shi Zhong, *"Broadband and High-gain microstrip slot antenna"*, Microwave and optical technology Letters, Vol. 48, No.11, November 2006.

[3] G. Augustin, S.V. Shynu, P.Mohanan, C.K. Aanandan and K Vasudevan, *"compact dual band antenna for wireless access point"*, IEE Electronics Letters, Vol.42, No.9, April 2006

Proceedings of APSYM2006, Dec. 14-16., Dept. of Electronics, CUSAT, India.

THE DESIGN OF NOVEL CROWN CIRCULAR FRACTAL ANTENNA

Raj Kumar, J. P. Shinde[1] and P. Malathi[2]

Department of Electronics Engg.
Defence Institute of Advance Technology, Girinagar, Pune – 411 025, India
raj34_shivani@yahoo.co.in

ABSTRACT

This paper presents the novel crown shaped circular fractal antenna. The new proposed antenna introduces the self-similarity in fractal antenna based on nearly circular – triangular geometry. This crown shaped antenna has been designed on substrate of dielectric constant ε_r = 4.3 and thickness 1.53mm. The antenna has been fabricated and tested. It has been observed that antenna is radiating at multiple resonant frequencies. The resonant frequency for the solid conventional nearly circular patch of dimension a/b=0.98 with a = 40 mm is 1.44GHz. This resonant frequency is shifted to 0.938GHz.by application of fractal geometry in antenna which indicates the physical size reduction of antenna. The simulated and experimental results of the nearly circular triangular antenna are in good agreement. This nearly circular fractal geometry has been studied with two interactions.

1. INTRODUCTION

Microstrip antennas are commonly used in a broad range of applications such as GSM 900, GSM1800, UMTS and PCs. This is primarily due to their simplicity of fabrication, ease of production, low manufacturing cost and light in weight. Nowadays, the size of electronics systems has decreased drastically, whereas their functionality has increased. The antennas have not experienced the same evolution. The antenna size with respect to the wavelength is the parameter that will have influence on the radiation characteristics. For efficient radiation, the size should be of the order of half a wavelength or larger. But as antenna size reduces, the bandwidth, gain, efficiency and polarization purity of antenna deteriorate [1-3].

Micro strip antenna with fractal geometry is right choice for miniaturization, operation of antenna at several resonant frequencies broad band coverage. Because of this, there has been a lot of interest in fractal geometry in antennas. The multi-band properties of these antennas have been investigated by N.Cohen [5] and others [6-8]. The circular polarization with multi band in Fractal antenna has not been in much research progress. The generation of circular polarization with multi band properties and compact size is much more advantageous in comparison to linear polarization. The circular polarized antennas transmits and receive in all planes and give a higher probability of link because it transmit and receive in all planes. In this paper, the new geometry of fractal antenna has been studied for circular polarization. This new antenna provides multiband, compact size and bandwidth improvement at higher resonance.

2. DESIGN EXPRESSIONS:

The resonant frequency of conventional microstrip circular patch can be calculated using the following expressions [9] as given below,

$$f_r = \frac{C\,\alpha_{nm}}{2\pi r_{eff}\sqrt{\varepsilon_r}} \qquad \text{where } \alpha_{nm} = 1.841 \qquad (1)$$

$r_{eff} = r_o[1+2h/2r_o\varepsilon_r\{\ln(r_o/2h)+(1.41\varepsilon_r+1.77)+h/r_o(0.268\varepsilon_r+1.65)\}]^{1/2}$ (2)

where 'r_o' is physical radius of patch, and 'r_{eff} ' is the effective radius of patch. This above expression can also be used to calculate the resonant frequency of fractal antenna of given geometry as shown in Fig.1. It is seen that effect of fractal geometry with several iterations is not affecting the antenna properties, except the shift in the frequency because of removal of metallization.

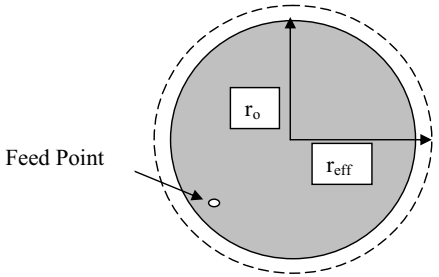

Fig.1, Solid circular patch.

3. DESIGN OF CIRCULAR FRACTAL ANTENNA

Nearly circular solid microstrip antenna has been designed on substrate ε_r= 4.3 and h=1.53 mm. The dimension of solid circular patch been taken as, b/a= 0.98, where a = 40 mm. This solid patch has been fed with single feed position at 45° and 1 mm inside from circumference as shown in Fig. 1. For fractal antenna, nearly equilateral triangle in first iteration is subtracted from this nearly circular patch. In second iteration, the nearly circular solid patch is constructed inside the first subtracted triangle and a triangle has been subtracted from small second nearly circular patch. Like this, n^{th} iteration can be repeated for this geometry. This geometry of antennas has self-similarity. Here, the antenna has been designed with 2^{nd} iteration. The crown circular fractal antenna has been simulated with the same feed position as of nearly solid circular patch antenna by FDTD source code. The fractal antennas has been constructed with 2^{nd} iteration since higher order iteration do not have much effect on antenna properties.

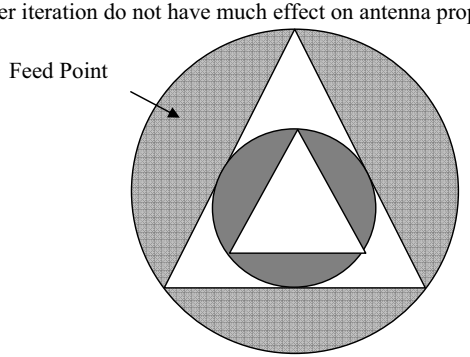

Fig. 2, Crown Shaped Circular Fractal Antenna

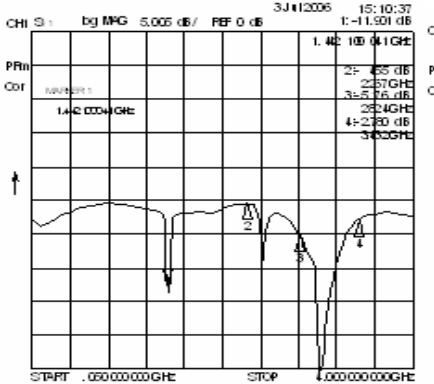

Fig. 3, Return loss of solid Circular Microstrip Patch Antenna

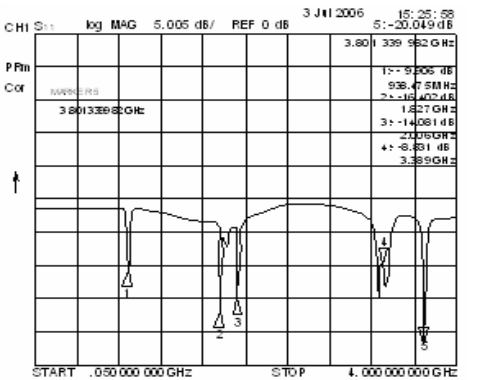

Fig. 4, Return Loss of Crown Shaped Fractal Antenna

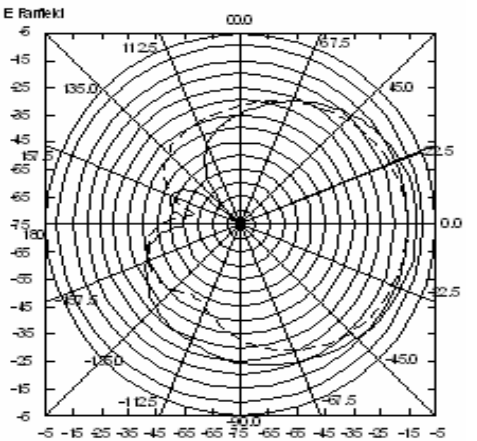

Fig. 5, Simulated Radiation pattern of Crown shaped Fractal Antenna At 0.938 and 1.87 GHz

4. SIMULATION AND EXPERIMENTAL RESULTS

The nearly solid circular patch antenna and crown circular fractal antenna has been simulated with feed position at 45° and 1 mm inside the circumference. Both antenna has been designed and fabricated. The simulated centre frequency of solid circular patch has been observed at 1.48 GHz and experimental center frequency is 1.44GHz. as shown in Fig. 3. The shift in the frequency in comparison to the simulated resonant frequency is due to fabrication and the manufacture tolerance of the substrate dielectric constant. Similarly, the crown circular fractal shaped antenna has been tested and the experimental result in the form of return loss is shown in Fig. 4. It is observed from Fig. 3 and Fig. 4 that the first resonant frequency of the circular shaped fractal antenna has been shifted to 0.938GHz. The frequency is shifted to the lower side by 0.502GHz in comparison to solid near circular patch antenna. This indicated the size reduction of the antenna by 58%. It is also observed from Fig. 4, the higher mode of crown circular fractal patch provides the circular polarization with improved bandwidth at higher resonance. This figure also indicated that antenna resonating at multi-band. The simulated radiation of antenna is shown in Fig.5. The study of this new antenna requires further improvement..

4. CONCLUSIONS

The crown circular shaped fractal antenna has been designed and tested. The simulated results are in good agreement with experimental results . It has been predicted by applying the fractal properties to microstrip antenna, the size has been reduced at first resonant frequency around 58% and higher order mode provide the circular polarization with improved bandwidth. This crown circular shape fractal antenna has the privilege of size reduction, multi band and circular polarization and useful for Mobile Communication and military applications where RCS of antenna is an important parameter.

ACKNOWLEDGEMENT

Author is grateful to Vice Chancellor, DIAT(Deemed University) Pune, Prof. P. Ramchandra Rao for constant encouragement and permit to publish this work. The author is also thankful to Head of the Department of Electronics Engineering for valuable suggestion.

REFERENCES

1. M.Pozar,"Microstrip antennas "Proceedings of IEEE Vol.80.pp 79-91, Jan 1999.
2. R. Garg, "Progress in Microstrip antennas "IETE Technical review, Vol .18 No.2, pp 85-98, March-June 2001
3. A. Hinderson, J. R. James and C.M.Hall, "Bandwidth extension techniques in printed conformal antenna ", Military Microwaves, MM86, pp 329-334, 1986
4. P. C. Sharma and K.C.Gupta, "Analysis and optimized design of single feed circularly polarized Microstrip antennas ", IEEE transactions on AP, Vol.AP-31, pp 949-955, 1983
5. N. Cohen, "Fractal antenna application in wireless telecommunications ", Proceedings of Professional Program Electronics Industry Forum, pp 43-49, 1997.
6. C. Puente et.al, "Fractal multiband antenna based on the Sirpinski gasket" IEE Electron.Lett, Vol.32, and No: 1, pp 1-2 June 1996.
7. D.H.Werner, R.L.Haunt and P.L.Werner, "Fractal Antenna Engineering: The theory and Design of fractal antenna arrays." IEEE AP,Magazine, 41,5, Oct.1999, pp. 37-59.
8. D.H.Werner, and P.L.Werner" Frequency –Independent Features of self-similar fracta antenna, Radio Science,31(6):1331-43,Nov.-Dec.-1996.
9. S.K. Verma & Nasimuddin,"Simple &accurate expression for directivity of circular micr strip antenna", Journal of Microwaves & Optoelectronics, Vol.2, No.6, Dec.2002

Proceedings of APSYM2006, Dec. 14-16., Dept. of Electronics, CUSAT, India.

RESEARCH SESSION VIII

MICROWAVE DEVICES I

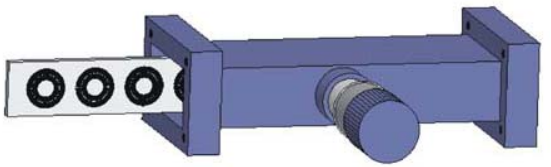

December 16, Saturday

(12 Noon - 1:00 p.m.)

RESEARCH SESSION VIII

MICROWAVE DEVICES I

Chair :Dr. D. Srinivasan, Formerly Director of NPOL, Cochin

Proceedings of APSYM2006, Dec. 14-16., Dept. of Electronics, CUSAT, India.

HIGH-PERFORMANCE COMPACT, WIDE-BAND BANDPASS FILTERS FOR MICROWAVE CIRCUIT APPLICATIONS

Subrata Sanyal[(1)] *and Mrinal Kanti Mandal*[(2)]

Department of Electronics and Electrical Communication Engineering,
Indian Institute of Technology Kharagpur,
Kharagpur-721302, West Bengal.
ssanyal@ece.iitkgp.ernet.in [(1)],
mkmandal@ece.iitkgp.ernet.in [(2)]

Abstract— Here, two quarter wavelength microstrip stubs with a shorted slot line are used to design compact wideband bandpass filters (BPF). Wideband characteristics are obtained using broadside-coupling between the stubs and the slot line. The 3-dB fractional bandwidth (FBW) is varied by varying the coupled line widths. The filter has the advantages of compactness, wide bandwidth, low insertion loss (IL) and ease of fabrication. The prototype fabricated filter of FBW 69.4% show a maximum IL less than 1.0 dB over 64 % of the passband. The basic BPF occupying area is less than $0.18\lambda_g \times 0.20\lambda_g$, where λ_g is the guided wavelength at the midband frequency. Good agreement between measurements and simulations are obtained.

1. INTRODUCTION

High performance, low cost, low insertion loss, compact wide-band BPF is highly desirable for the next generation wireless and satellite communication system. For this purpose, parallel coupled microstrip line (PCML) filters are most popular for their simple design procedure [1, 2]. At the expense of implementation area, filter performance improves in a straightforward manner with increasing filter order. Some other popular versions of the coupled-line filters are using hairpin and open-loop resonators. Different shapes were proposed to improve filter performance and simultaneously to obtain compactness. The design procedures for all the filters uses classical filter theory and are based on either edge-coupled or end-coupled resonators. Wideband coupled-lines BPF having 3-dB fractional bandwidth (FBW) greater than 20% becomes difficult to fabricate due to the close line spacings required to enhance the coupling of the first and last coupled stages.

In [3], ground plane aperture technique was proposed for enhanced coupling to design a multi-pole compact BPF having 60% 3-dB fractional bandwidth (FBW). In [4], this idea of enhanced coupling by etching a slot in the ground plane was extended to design a parallel line wideband BPF having FBW up to 30% with spurious band suppressions. All these BPFs had gradual cutoff. Filters using strong coupling produced by broad-side coupled lines have inherently wideband characteristics. Broadside coupling has some additional advantages that cannot be obtained by its edge-coupled counterparts. A broadside-coupled single section filter can produce multi-pole stopband or low IL multi-pole passband. For examples, in [5] a wideband microstrip BPF was designed using broadside-coupled half-wavelength microstrip lines. However, the upper stopband width was less than its passband width. In our previous attempt, a compact BPF having high FBW of 95-115% was designed for ultra wideband communication in microstrip line using broadside slot coupling at the crossings [6]. Here, broadside coupling has been used between microstrip and slot lines. The slot line is etched in the ground plane of the microstrip line and is therefore a single substrate structure, unlike [5].

II. FILTER DESIGN

The basic BPF section is shown in Fig. 1. Open ended circular slot of inner radius R_i and outer radius R_O is etched in the ground plane. This slot of width W_S is coupled to two microstrip stubs, each of width W_m and length L_m. The separation between the stubs is g_{m1} at the open end and g_{m2} at the feed end. The gap width g_s in slot line is initially made equal to g_{m1}. The coupling between the slot and microstrip line is dominantly magnetic. The pass band center frequency is determined by the coupled microstrip line length, L_m. It is quarter wavelength at the passband centre frequency. The full wave simulation software, IE3D® has been used for simulations. Average current distributions at the passband centre frequency and at the upper stopband center frequency are shown in Fig. 2. Current minima exist at the two microstrip line ends. When a current minimum occurs near the coupled line feed point P_1, power transfer is stopped, thus producing a stopband. At the upper stop band center frequency the coupled line lengths, L_m is equal to half-wavelength. The BPF characteristics are insensitive to small variations in slot line length. Decreasing the stub lengths L_m by increasing g_{m2} shifts the BPF passband towards higher frequency side. Slight increase in g_{m1} with respect to g_s initially decreases the IL.

The FBW can be varied by varying the line impedances. Decreasing the line width decreases the FBW. The simulated scattering parameters for different coupling widths are shown in Fig. 3. In each case, slot width is kept equal to coupled microstrip line width. The higher cutoff frequency can be increased by decreasing the inner radius, R_i whilst the lower cutoff frequency by decreasing the outer radius, R_o.

In the next step, a LPF section is cascaded to improve the stop band characteristics. The LPF used is a U-shaped structure comprising of two shunt stubs of lengths θ_s and characteristic impedance Z_s separated by a narrow width line segment of lengths θ_m and characteristic impedance Z_m (see Fig. 4). Its transmission response is given by

$$S_{21} = \frac{2}{A + \frac{B}{Z_0} + CZ_0 + D}$$

$A = D = \cos\theta_m - Z_m Y_s \sin\theta_m \tan\theta_s$, $B = jZ_m \sin\theta_m$ and

$C = j\left[Y_m \sin\theta_m + 2Y_s \cos\theta_m \tan\theta_s - Z_m Y_s^2 \sin\theta_m \tan^2\theta_s\right]$

where, Y_s and Y_m are the characteristic admittances of the shunt stubs and the connecting narrow-width line segment. The rejection band can be controlled by varying the LPF dimensions. Two examples are shown in Fig. 5. In each case BPF to LPF separation, S is fixed at 1.0 mm. The separation value was optimized by the full wave simulation software. In the first example, a deeper rejection just after the BPF passband was obtained, while in the second example, the 22 dB stop band extends up to 15 GHz.

III. FABRICATION AND MEASUREMENTS

A prototype BPF was designed having FBW 69.4% and center frequency 3.253 GHz. The substrate used was 0.381mm thick RT/duroid® 5880 having dielectric constant, ϵ_r = 2.2. Shown in Fig. 6 are the simulated and measured S-parameters of this filter. Measurements have been carried out using a HP 8510C vector network analyzer. The measured IL is less than 1.0 dB from 2.364 to 3.807 GHz. The filters have no undesired pass band below the main passband with DC is completely blocked. On the upper side, 30 dB stopband extends from 5.248 to 9.142 GHz. The measured and simulated group delays are compared in Fig. 7. Maximum passband group delay variation obtained is 0.9 nS. A photograph of the fabricated BPF is shown in Fig. 4.

Proceedings of APSYM2006, Dec. 14-16., Dept. of Electronics, CUSAT, India.

S. Sanyal et al.

IV. CONCLUSION

Broadside coupling between microstrip line and slotline is used to design compact, wideband BPF. A single section BPF can produce good rejection characteristics. The rejection performance can be further improved by cascading a LPF. The BPF has a number of advantages; a maximum IL of 1.2 dB over 70.4% of the pass band; single section skirt attenuation rate greater than 30 dB/ GHz on the both sides of the passband. Total rectangular occupying area is less than $0.31\lambda_g \times 0.14\lambda_g$ when the LPF section is included; otherwise it is less than $0.18\lambda_g \times 0.20\lambda_g$. The filter is easy to fabricate as no via or holes are required. The present BPF has the least occupying area compared to other reported compact wideband BPFs [4-6]. It has higher FBW than those reported in [1-5]. Also, FBW can be varied between 44% and 76%.

REFERENCES

[1] Matthaei, G. L., Young, L. and Jones, E. M. T., "Microwave filters, impedance-matching network, and coupling structures", Artech House, Norwood, MA, 1980.

[2] J.-S. Hong and M. J. Lancaster, *Microstrip Filters for RF/Microwave Applications*. New York: Wiley, 2001.

[3] L. Zhu, H. Bu and K. Wu, "Broadband and compact multi-pole microstrip bandpass filters using ground plane aperture technique," *IEE Proc.-Microw. Antenna Propag.*, *Vol*. l49, No. 1, pp. 71-77, Feb. 2002.

[4] M. C. V.-Ahumada, J. Martel and F. Medina, "Parallel coupled microstrip filters with ground-plane aperture for spurious band suppression and enhanced coupling," *IEEE Trans. Microw. Theory Tech.*, vol. 52, no. 3, pp. 1082–1086, March, 2004.

[5] M. Tran and C. Nguyen, "Modified broadside-coupled microstrip lines for MIC and MMIC applications and a new class of broadside-coupled band-pass filters," *IEEE Trans. Microw. Theory Tech.*, vol. 41, no. 8, pp. 1335–1342, Aug. 1993.

[6] M. K. Mandal and S. Sanyal, "Compact Wideband Bandpass Filter," *IEEE Microw. Wireless Compon. Lett.*, vol. 16, no. 1, pp. 46-48, Jan. 2006.

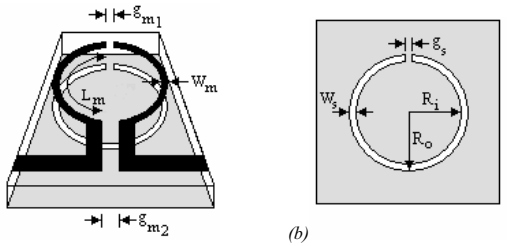

Fig. 1. The basic BPF: (a) complete filter structure black (white) portion represents the microstrip (etched slot) and (b) ground plane structure.

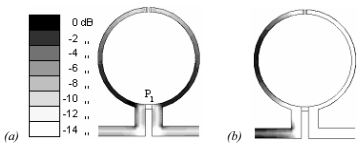

Fig. 2. Microstripline average current distributions at (a) passband and (b) stopband centre frequencies. Maximum values of average currents are 42.6 and 41.1 amp/m for (a) and (b) respectively.

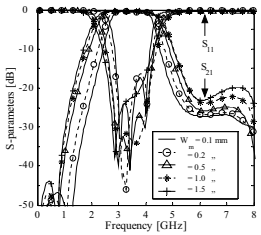

Fig. 3. Simulated S-parameters for different widths; in each case $W_m = W_s$, Mean radius = 5.75 mm.

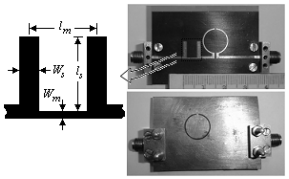

Fig. 4. Photograph of the BPF.

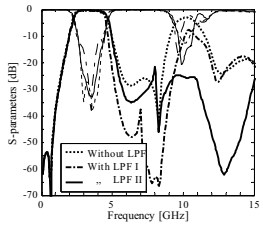

Fig. 5. Dependence of overall rejection performance on LPF dimensions; in each case BPF dimensions are R_i = 5.5, R_o = 6.0, W = 0.5, g_{m1} = 0.6, g_{m2} = 0.8, g_s = 0.4 and S = 1.0 mm. LPF I : l_m = 6.0, W_m = 0.5 and l_s = 6.0, W_s = 1.5 mm; LPF II: l_m = 6.0, W_m = 0.5 and l_s = 4.0, W_s = 1.5 mm. The same substrate RT/duroid 5880 was used.

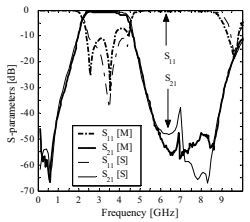

Fig. 6. Measured and simulated S-parameters of the BPF in Fig. 4. LPF I of Fig. 5 was used.

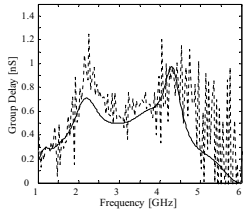

Fig. 7. Measured and simulated group delay of the BPF of Fig. 4. Dotted: measured, solid: simulated.

COMPUTER –AIDED DESIGN OF MICROSTRIP MONOPULSE COMPARATOR

V. Senthil Kumar, V.V.Srinivasan, V.K. Lakshmeesha, S. Pal
Communication Systems Group, ISRO Satellite Centre
Airport Road, Bangalore-560 017.INDIA
senthil@isac.gov.in

Abstract: *High performance microstrip monopulse comparator at S-Band has been developed for ground station tracking antenna application. Construction of eight-port comparator with four rat-race hybrids has been developed and experimentally tested & implemented in a Ground station. Microstrip monopulse comparator has been developed in .0 – .3 GHz frequency range. The grou nd station antenna utilizes diplexer network to perform transmit and receive operations simultaneously. The measured insertion loss is about 0. dB, return loss is better than 30 dB and isolation is better than 30 dB over the required frequency range. Excellent amplitude & phase balance response along with good isolation between error ports are obtained.*

Introduction

The driving parameters in the design of satellite receive terminals are G/T (Gain to Noise Temperature), the weight and size of the antenna system. For a given noise temperature of the receiver, the G/T requirements can be met by increasing the gain of the reflector and / or by reducing the noise temperature of the antenna feed system. Feed system noise temperature is dictated by losses in the feed and transmission lines connecting the feed to receiver LNA (Low Noise amplifier). Losses can be reduced by proper design of feed system using low loss waveguide components. The monopulse tracking system requires a sum signal and error/difference signals in two orthogonal planes (viz. X and Y or azimuth and elevation) one of the compact ways of realising this is to use four radiating elements and feeding them using a monopulse comparator. This paper describes the low loss microstrip comparator network. Monopulse comparator is an eight-port network with one sum channel and three difference ports (Azimuth, Elevation and Diagonal difference) from four equal amplitude and phase input ports. This paper discusses the specifications, design challenges, EM (Electro Magnetic) simulation and measured test results.

Description

The monopulse tracking system requires azimuth and elevation difference signals and a sum signal from four equal amplitude and phase signals. From radiation efficiency and tracking performance point of view, it is essential that the comparator networks are low insertion loss, minimum amplitude and phase imbalance, and high isolation between the output ports. Rat-race hybrid is the basic building block in the monopulse comparator assembly. Three or four hybrids can be used to construct the comparator. Three-hybrid configuration has less hardware requirement and more flexibility of phasing. Both the configurations (3 Hybrids, 4 Hybrids) give the same sum pattern and differed in difference pattern. Four-hybrid configuration is selected due to its better difference pattern characteristics. Figure shows the block diagram of such arrangement. The azimuth and elevation error signals are connected to servo system and the diagonal error port is not used and it is terminated with 50 ohms load. The sum port is connected with Diplexer network without any transmission lines to avoid any further insertion loss. Microstrip configuration is selected due to its size & weight.

Rat-Race Hybrid

Rat-race hybrid is a four-port network in which a signal incident on any one of the ports gets divided between two output ports with the remaining port being isolated. Rat race hybrid consists of a ring . 5 wavelengths in circumference having four arms separated by 60° angular rotations. This has a common input arm, there are two output arms spaced one-quarter wavelength away and a fourth terminated arm spaced a quarter wavelength away from one of the output arm and three quarters of a wavelength from the other output arm. Theory and its theoretical S-parameters are given in [2].

Circuit Simulation

A rat-race circuit element has been designed and simulated in commercially available LINMIC software [] for its S-parameters. The ring impedance and ci rcumference have been optimised to get better S-parameters at 2.0-2.3 GHz frequency band. After finalising a retrace element, using mitered bends and microstrip straight lines the comparator network has been modelled and simulated. Importance has been given in optimising the amplitude and phase imbalance at the frequency band of 2.2 - 2.3GHz (Tracking band). Amplitude balance at 2.02 – 2.2 band is not that critical since this ba nd is used only to obtain sum pattern for transmission mode. The simulated return loss of the sum port is better than 30db. Amplitude and phase imbalance is negligible in simulation. The optimised comparator layout is shown in figure 2.

Fabrication & Testing

The optimised network has been fabricated on a .6 mm thick Teflon Fibre Glass (TFG) microwave substrate using PCB etching method. The complete network is plated with solder for 5 microns thickness to provide the environmental protection. Accuracy of the PCB fabrication is 0 microns. The assembled com parator network has been tested in Microwave Network Analyser (HP 850C). The electrical characteristics (retu rn loss, insertion loss, amplitude and phase imbalance, and isolation response) have been verified for the required frequency range of 2.20 to 2.30 GHz. The measured insertion loss of the network is about 0.2 dB. Return loss response is better than 30 dB and is shown in figure 3. The amplitude and phase imbalances are ± 0. dB and ±2° respectively. The isolation between sum port and difference port is better than 30 dB over the required bandwidth. Measured return loss, isolation, amplitude & phase balance characteristics of comparator at 2.25 GHz are given in Table. The phase values provided are with respect to Port A.

Table. Return loss, Isolation, amplitude & phase response of the comparator

Port identification	Return loss (dB)
Sum port	-36.3
Azimuth Difference	-37
Elevation Difference	-34.6
	Isolation (dB)
Sum to AZ. Difference	40
Sum to EL. Difference	-36
Az. Difference to El. Difference	-47

Input	Output	Amplitude (dB)	Phase (degrees)
Sum	A	-6.8	0
	B	-6.7	-0.7
	C	-6.7	-0.9
	D	-6.23	-.6
Az. Diff	A	-6.26	0
	B	-6.3	0.3
	C	-6.27	-80.4
	D	-6.8	-80.9
El. Diff	A	-6.26	0
	B	-6.24	-78
	C	-6.22	.6
	D	-6.30	-79.2

Conclusion

The microstrip comparator constructed of four hybrids has been designed and developed at S-band (2.0 –2.3 GHz). The measured results are very good and meet all the required specifications. Additionally the measured performance matches close to the simulated results. The comparator assembly has been integrated with the radiating elements to construct the tracking feed system and is used to illuminate the 0 met er Cassegrain reflector system. The comparator assembly with four radiating elements is used to track & receive the signals from low earth orbiting satellites. Null depth of 35 dB and better was achieved in the two tracking error channels across the frequency band of 2.2 to 2.3 GHz. Radiation patterns (sum and difference patterns) of feed at 2.25 GHz is shown in figure4. Auto track performance of the S-band Ground station is very good reflecting the superior performance provided by the monopulse comparator.

References

. "LINMIC circuit simulator software", Janson microwave, Germany.
2. Harlan Howe, "Stripline Circuit Design", Artech House, 974.

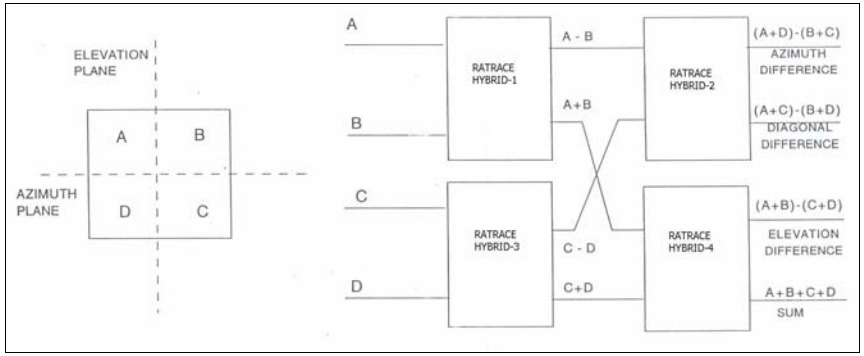

Figure : Block Diagram of Monopulse comparator net work

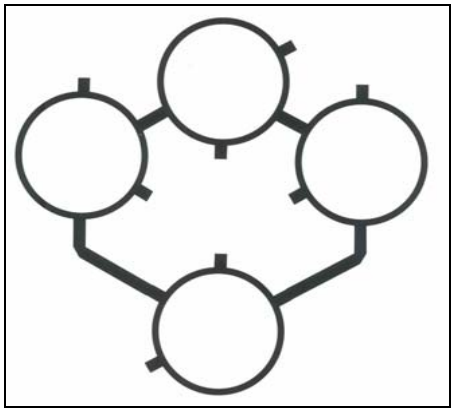

Figure 2: Schematic of microstrip comparator

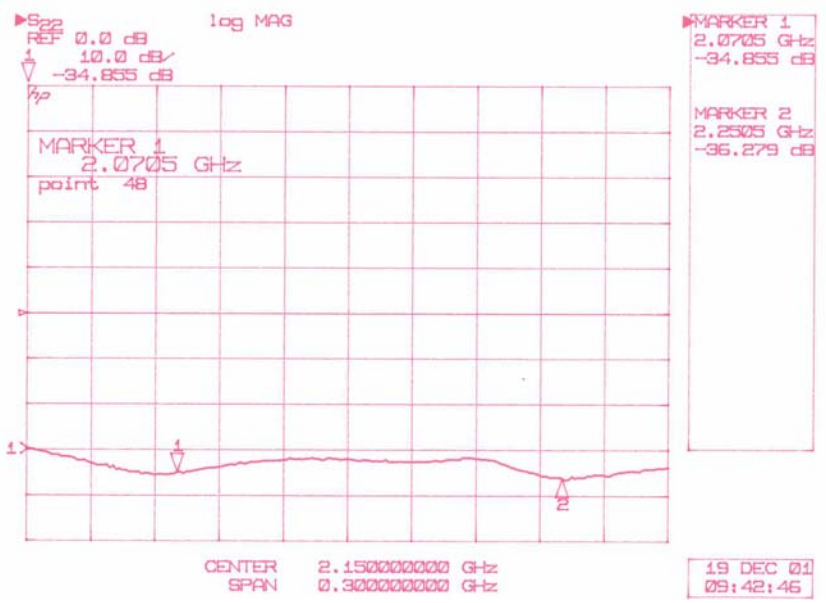

Figure 3: Return loss response of sum port in microstrip comparator

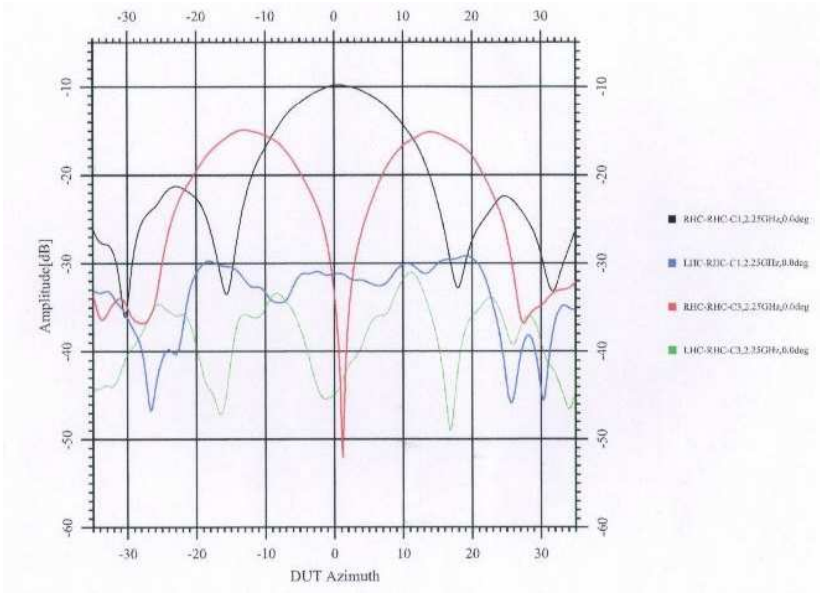

Figure 4: Sum and difference patterns of the feed

SIMULATION & ANALYSIS OF SOLID STATE IFF TRANSMITTER FOR AIRBORNE APPLICATIONS

S. Rajes, AK Singh, D. Saravanan, T. Balakrishnan
Centre for Airborne Systems (CABS)
Defence Research & Development Organisation
Bangalore-37, India
Telephone: 080-25225556, Fax: 080 – 25222326
E: mail: tamil_saravana@yahoo.com

Abstract:

This paper presents brief overview of the simulation and analysis of an L–band IFF transmitter airborne applications that provides a peak power of 2.5 kW and average power of 25W. At the sa time, it complies with the severe constraints on size, volume, weight, power consumption and the dissipation as required in the airborne environment. This transmitter development is done us modular approach. The transmitter designed at the center frequency of 1030 MHz as per IC standard to cater for civil and military applications. It requires to switch its output between th Interrogate (Σ) and Control (Ω) channel for Receiver Sidelobe Suppression (RSLS). The ma parameters of the transmitter such as peak power, average power has been analysed and link bu analysis done to ensure that the required output power is obtained considering the losses induce each component. The entire simulation & analysis is carried out in AWR microwave office & VS The mode pulses generation is carried out in MATLAB platform. The simulated time and spec domain response for the various interrogation modes at the key points are presented. The output p power variation with temperature is also presented.

Key words: IFF, SPDT, RSLS, Solid state.

1. INTRODUCTION

The IFF (Identification Friend or Foe) also called Secondary Surveillance Radar (SS instantly comprehends whether the target is an enemy or a friend and mostly works in tan with the primary radar. The SSR system operates as per the International Civil Aviati Organisation (ICAO) standards. IFF radar system is constituted by two subsystems i.e Interrogator and a Transponder. The airborne interrogator transmits coded signal i specified direction. Aircraft fitted with compatible transponder receives the interrogatic signal and reply back in the form of another coded signal. These coded replies are rece by the interrogator and processed for identification. It is capable of differentiating betwe friendly and enemy targets, picked up by the primary radar by comparing the respo received from the interrogated target with its own database. Additional target details such height, range and azimuth is also available. In addition, it can extract the target status communication failure, emergency and hijack based on the reply received from interrogat in mode 3/A. The Interrogator comprises of Antenna, Transmitter, Receiver and Sig Processor. The design of a solid state transmitter is being presented. The major sub mo of the Tx are RF source, Solid-state pulse amplifier & high power SPDT switch. Mode puls from the mode pulse generator is applied to the pulse power amplifier and then fed to SPDT switch to obtain the output power on Interrogate & Control channel. The blo diagram is shown in Fig.1. The IFF operates basically in four Mk-X modes viz. 1, 2, 3/A a C. The interrogation signal format for the Mk-X mode (shown in Fig. 2) comprises of thre

pulses with duration of 0.8 ± 0µs each and the mode identification is decided by the puls separation between P1 and P3. The pulse P2 is used for RSLS.

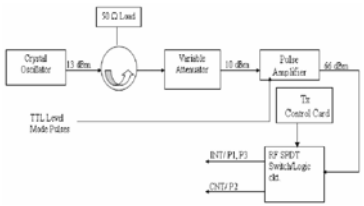

Figure 1 Transmitter Block Diagrar

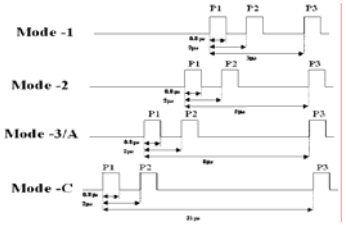

Figure 2 Mk X Mode Signal Forma

2. MODELLING AND SIMULATION

Simulation of the IFF transmitter has been carried out in AWR using Visual Syste Simulator (VSS). The VSS schematic block of entire transmitter chain comprising of mc pulse generator, RF source block, on-off modulator, pulse power amplifier and a high po RF SPDT switch is shown below in Figure 3. The insertion loss of all the components plumbing loss is simulated by equivalent attenuation.

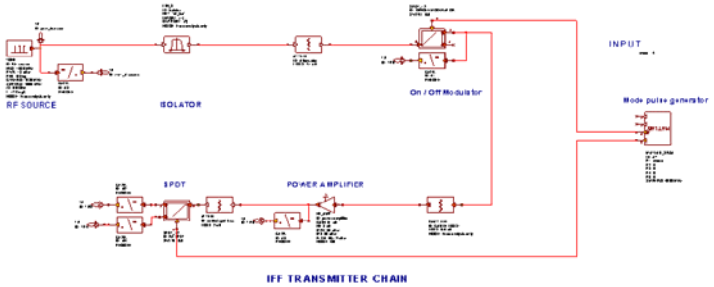

Figure 3 VSS Schematic of Transmitter Ch

Transmitter description

RF Source Block

The RF source block shown below in Fig-4 consists of a continuous wave oscillator, isol and variable attenuator. This attenuator has been used to regulate the desired RF powe at the input of the pulse amplifier, which is 10 dBm in this case. The isolator is used protect the oscillator from reflected power.The power spectrum at the crystal oscillator ou is shown in Fig-5.

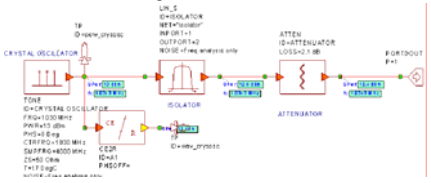

Figure 4 RF Source Bloc

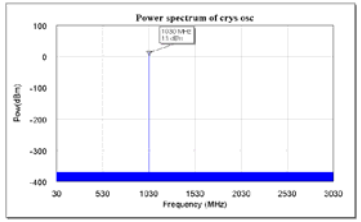

Figure 5 Power spectrum of Crystal oscilla

Mode Pulse Generator and On-Off Modulator

A Matlab module (Matlab_SRC4) is incorporated into the VSS system as shown in the Fig This Matlab code has been developed to generate TTL level mode control pulses determines the mode of operation of the interrogator. The time interval between the th pulses is as per the ICAO standards. Simulation was carried out for different modes operation and the time response of one of the modes is shown below in Fig-7.

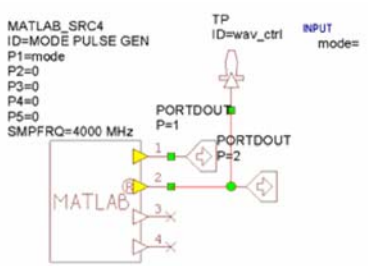

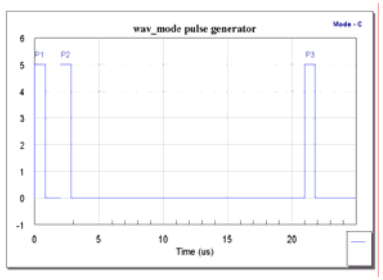

Figure 6 Mode Pulse Generator

Figure 7 Time domain wave form for Mc

The CW output from the crystal oscillator is fed to an on-off modulator which gets th modulating signal from mode pulse generator. The modulated signal for Mode C is shown Fig. 8. The sub-system model of the power amplifier from VSS is integrated with the swit as shown in Fig. 9.

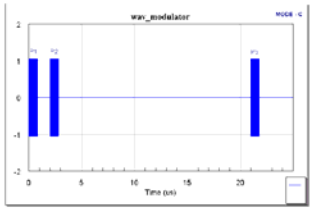

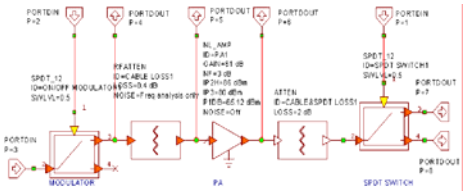

Figure 8 Modulator o/p in time domain for Mode

Fig 9 Pulse Amplifier with Switch

Power Amplifier and RF SPDT Switch

The pulse power amplifier is the most crucial component of the transmitter and has b modeled and analysed in VSS as an independent entity. In order to achieve an overall ga 56 dB so as to obtain the amplifier output of 66 dBm, the power amplifier design is carri out in the cascaded configuration. It has got three stages of amplification. The first stage buffer amplifier that accepts the 1030 MHz signal from the Tone generator of 0 dBm a gives an output of 30 dBm. This signal is then applied to the pre-amplifier stage with a g of 17 dB. This 47 dBm output from the pre-amplifier stage is applied to the driver amplifi stage. The driver amplifier is configured with two parallel paths, each having a gain of 10 thus providing 54 dBm output to provide the final stage that is the power amplifier. Th stage is realised with the four amplifiers having gain of 10dB each and operating in paral

The output of 60 dBm obtained at each amplifier is combined to get the desired outp 66dBm. The schematic of the Pulse Power amplifier configuration modeled in VSS is sl in Fig. 10.

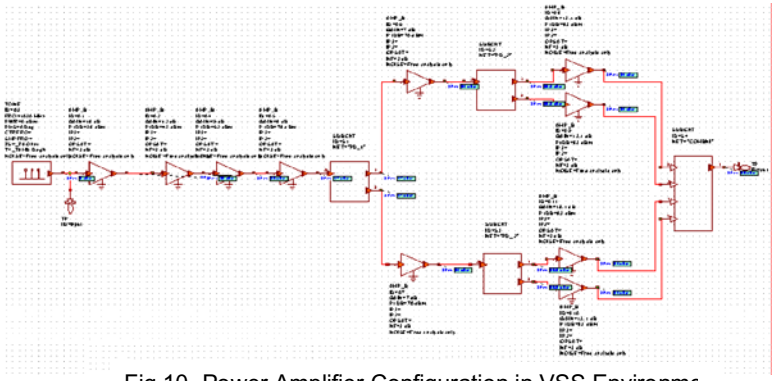

Fig 10. Power Amplifier Configuration in VSS Environme

The output of the power amplifier in time domain and frequency domain is depicted in Fi and 12 respectively.

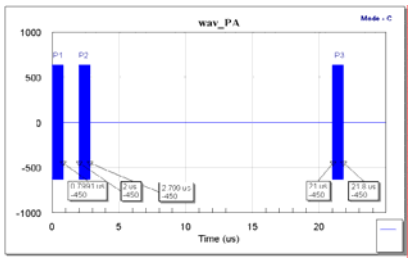

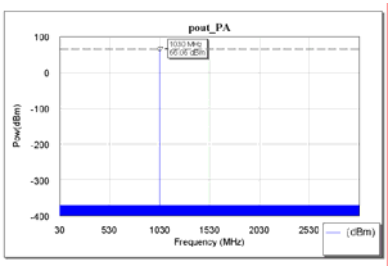

Figure 11 Amplifier output in time domain Figure 12 Amplifier output in frequency don

The amplified signal from the power amplifier is fed to a RF SPDT switch that channelis into INT (P1, P3) and CNT (P2) signal on two different ports. The high power RF SI switch has a switching speed of 100 nsec (max.). The time domain waveform a interrogate port and control port for mode C is shown in Fig. 13.

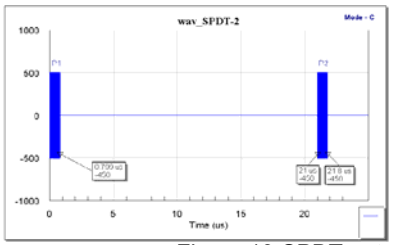

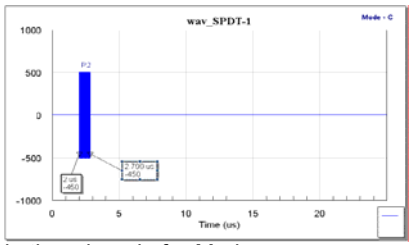

Figure 13 SPDT output in time domain for Mode

3. POWER AMPLIFIER ANALYSIS:

An approach to study on the selection of Power amplifier (PA) has been done. The crit parameters of an amplifier are:

P1dB (1 dB compression point) – defined as the output power level where the gain is reduced by 1dB from its small signal gain.

P_{sat} (Saturation point) – defined as the point where any increase in input power does produce a corresponding increase in output power.

Output power versus input power:

The power amplifier is made to operate very close to saturation region to achieve h efficiency and relatively stable output power. It is found that the output powers of 65. 66.06 & 66.22 dBm is obtained for input power of 8, 10 & 12 dBm respectively. Th resultant plot is shown in Fig-14.

Harmonics:

The fundamental, 2nd and 3rd harmonics power output is found to be 65.92 dBm, 22dBm an 14.5dBm respectively for an input power of 10dBm as shown in Fig. 15. The variation o 2dBm in input power has a negligible effect on these levels.

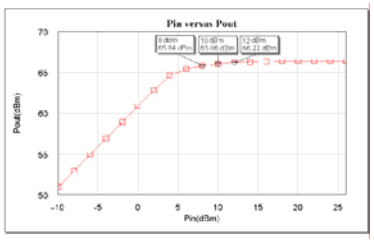

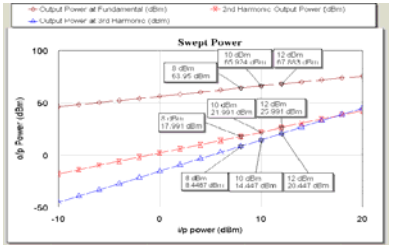

Figure 14. Input power versus Output power Fig-15: Harmonic response

Effect of frequency variation and Temperature variation

Simulation was carried out to observe the effect of variation in the frequency of the inpu the amplifier by ± 0.2 MHz. The effect at the output of the amplifier is shown in Fig. 16. T study on the stability of the output of IFF-TX over the ambient temperature range of -20°C to +55°C has been carried out. The resultant plot is shown in fig 17.

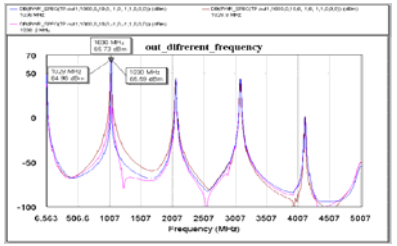

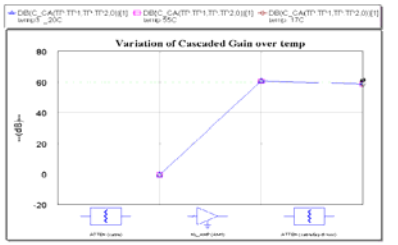

Figure 16. Effect of input frequency variation Figure 17. Cascaded outpu

CONCLUSION

This report gives the end-to-end simulation of IFF transmitter with the time domain frequency domain response at the key points. Power level is not affected over the d range of operation under the required operational conditions. For the RF input p variations of ± 2dB, the variation at the output of the power amplifier is ± 250W, whicl within acceptable limits. The simulation enables to validate design parameters of transr Simulation Results are in good agreement with the desired results.

ACKNOWLEDGEMENT

The authors thankfully acknowledge the support from K.Tamilmani, Director, CABS for encouragement and grant of permission for publishing this work.

REFERENCES

[1] Michael C. Stevens “Secondary Surveillance Radar” Artech house Boston, Lon 1988.
[2] Aeronautical telecommunications, Annex 10 to the convention on International C Aviation, Vol. IV. Third Edition July 2002.
[3] P Sreenivasulu, ”Design and development of 1KW solid state power amplifier T/R switch for VHF band T/R module IRSI-2005, 497-502.
[4] J.Dhar,” Design and development of C band Pulsed power amplifier for T/R mod of radar imaging satellite. IRSI-2005, 749-753.
[5] Applied Wave Research, Micro Wave Office, Visual System Simulator manu version - 7.

EXPLORATION OF HIGH POWER IMPATT DIODES WITH 4H-SiC FOR MM-WAVE APPLICATIONS

S.R. Pattanaik[1], S.K. Swain[2], J. Pradhan[2] and G.N. Dash[2]
[1]Department of Electronics and Telecommunication, KIST, Bhubaneswar, Orissa, INDIA
[2]P.G. Department of Physics, Sambalpur University, Jyoti Vihar, Sambalpur 768 019, INDIA

The prospect of 4H-SiC material for being used as a base material for high power IMPATT diodes is explored following a computer simulation method. Different device properties like negative conductance, mean square noise voltage per bandwidth and noise measure are computed using a small signal model for mm-wave applications around the atmospheric window frequencies like 35, 94 and140 GHz. The device properties for application in short distance communications around a frequency of 60 GHz are also explored.

INTRODUCTION

Ever since its evolution, IMPact Avalanche Transit Time (IMPATT) diodes have been accepted as power devices for millimeter wave applications. Several works on IMPATT diode have confirmed that the underlying base material properties play important roles in determining the performances of the device. Some favourable material properties for IMPATT diode operation are high saturation drift velocity, high breakdown voltage and high thermal stability. 4H-SiC with a high value of thermal conductivity possesses all such properties and thus makes itself suitable for being used as a base material for IMPATT diode. Though many researchers have already reported many experimental and theoretical works on SiC IMPATT [1-4], still then there are a lot to explore about the SiC IMPATT diode. So in this present work, we have tried to explore the device properties of 4H-SiC IMPATT diode using a small signal model for mm-wave applications around 35, 60, 94 and140 GHz. The power performance and noise behavior of the diode is determined. As expected some advantages over traditional Si double drift region IMPATT diodes are found.

DESIGN CONSIDERATION

Double drift region (DDR) structure of IMPATT diode is mostly used for realization of high power mm-waves. The structure has the doping distribution of the form n^+npp^+. A one dimensional schematic diagram of the DDR IMPATT diode structure is shown in figure 1. The n^+ and p^+ regions of the diode are heavily doped with each having a doping concentration of 1.0×10^{26} m^{-3}. Each n and p regions has a moderate doping concentration of 3.5×10^{23} m^{-3}. The n^+ and p^+ regions are generally used for ohmic contacts and their widths are considered to be negligible. The width of the n-region and p-region are determined with the help of a standard formula as follow.

$$W_{n,p} = \frac{v_{sn,sp}}{2f} \qquad (1)$$

Where $W_{n,p}$ is the width of n-region or p-region, $v_{sn,sp}$ is the saturated drift velocity of the electrons or holes and f is the frequency of operation. The total active region width is considered to be the sum of the n region and p region. These values of doping concentrations and diode active region width are taken for optimum conversion efficiency and operation at corresponding frequency. The net doping concentration at any space point is determined by using the exponential and error function profiles. Material parameters like carrier ionization

rate, saturation drift velocity, mobility, permittivity etc used for the simulation purpose are obtained from the research reports [5].

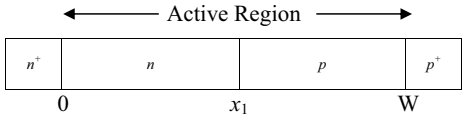

Figure 1: A 1-D schematic diagram of the proposed DDR IMPATT diode.

METHODOLOGY

The computer simulation method consists of DC analysis, small signal analysis and noise analysis. The equations involved in these analyses are nonlinear in nature and thus their solution involves complexity. So we have first considered the diode to be consisting of small space points. The diode active layer width is divided into several number of space points with a space step of 1 nm. The DC analysis is done by solving simultaneously three important device equations namely Poisson's equation, the carrier continuity equation and the space charge equation using a double iterative DC simulation program. The DC electric field profiles, carrier current profiles, breakdown voltage etc are obtained from this analysis.

The high frequency analysis of the diode is carried out using a small signal simulation method developed by our group. The small signal model takes into account the contribution from each space point and effectively determines the device parameters such as negative conductance ($-G$), susceptance (B) and negative resistance ($-Z_R$) of the diode. The variations of these values with frequency are also computed with the help of a double iterative computer program.

The fundamental process involved in the IMPATT diode operation leads to noise generation in the device. So noise is an important aspect of the present study and the noise characteristics of the diode structure are computed using a generalized noise simulation program. The noise characteristics like mean square noise voltage per bandwidth ($\langle v^2 \rangle$/df) and noise measure (NM) of the device are computed from this analysis.

The details of the computer simulation method are presented elsewhere [1,6,7].

RESULTS AND DISCUSSIONS

The potential of 4H-SiC for millimeter wave applications for operation around are explored using the simulation method describe above. The results thus obtained are presented in Table 1 and Table 2. Table 1 provides information about the breakdown voltage, power density and efficiency while Table 2 reveals the noise properties of the IMPATT diodes under consideration. It can be seen from Table 1 that the IMPATT diode exhibits higher value of breakdown voltage for lower frequency. This is due to the fact that the active width of the diode decreases with increase in frequency of operation. Further, for all frequencies of interest, the values of breakdown voltage for 4H-SiC IMPATT diode are 9-10 times higher than those for the Si IMPATT diodes. This in turn provides high values of power density for 4H-SiC IMPATT diode as compared to the values of power density for Si IMPATT diodes. It can also be seen from Table 1that similar trend is also reflected in the computation of efficiency of the diode.

The noise properties like mean square noise voltage per bandwidth and noise measure are presented in Table 2. Table 2 reveals that the 4H-SiC IMPATT diodes are noisier as compared to Si IMPATT diodes. This is because the power generation mechanism in IMPATT diode is such that it generates more noise when we go for more power output. This has been explained in our earlier report [1]. However, IMPATT diodes are meant for high

power and high frequency applications and thus 4H-SiC is a good candidate for IMPATT applications around the frequencies 35, 60, 94 and 140 GHz.

Table 1: MM wave properties of Si and 4H-SiC IMPATT diodes at 35, 60, 94 and 140 GHz.

Frequency (GHz)	Breakdown Voltage (V)		Power Density (W/m^2)		Efficiency (%)	
	Si	4H-SiC	Si	4H-SiC	Si	4H-SiC
35	45.2	441	1.04×10^{8}	7.72×10^{8}	8.6	15.3
60	33.0	293	2.59×10^{8}	1.79×10^{9}	8.4	15.2
94	23.1	221	8.09×10^{8}	2.92×10^{9}	7.4	12.9
140	15.3	156	8.72×10^{8}	4.79×10^{9}	8.2	11.6

Table 2: Noise properties of Si and 4H-SiC IMPATT diodes at 35, 60, 94 and 140 GHz.

Frequency (GHz)	Mean square noise voltage per bandwidth (V^2s)		Noise Measure (dB)	
	Si	4H-SiC	Si	4H-SiC
35	3.0×10^{-15}	5.82×10^{-14}	30.0	33.1
60	8.1×10^{-16}	2.41×10^{-15}	26.1	32.2
94	5.0×10^{-16}	5.51×10^{-15}	24.9	31.3
140	1.10×10^{-16}	1.99×10^{-15}	22.8	30.7

CONCLUSION

A systematic and thorough study of 4H-SiC IMPATT diode reveals its potential in terms of power performance and noise behaviour. The devices properties obtained around the frequencies of interest i.e. 35, 60, 94 and 140 GHz are strongly in favour of 4H-SiC for being used as a base material for mm-wave applications in comparison to conventional Si IMPATT diodes. Some care is also required for reducing noise from 4H-SiC IMPATT diode.

ACKNOWLEDGEMENT

Sri S.R. Pattanaik wishes to acknowledge CSIR, New Delhi for its support.

REFERENCES

1. S.R. Pattanaik, G.N. Dash and J.K. Mishra, 2005 *Semicond. Sci. Technol.* 20 p. 299
2. Yuan L, Cooper J A, Melloch M R Jr and Webb K J 2001 *IEEE Electron Devices Lett.* 22 p. 266
3. Yuan L, Melloch M R Jr, Cooper J A andWebb K J 2000 *Proc. IEEE/Cornell Conference on High Performance Devices* p. 158
4. Zhao J H, Gruzinskis V, Luo Y, Weiner M, Pan M, Shiktorov P and Starikov E 2000 *Semicond. Sci. Technol.* 15 p.1093
5. Electronic archive: New Semiconductor Materials, Characteristics and Properties [online], Available: http://www.ioffe.ru/SVA/NSM/Semicond/SiC/
6. G.N. Dash and S.P. Pati, 1992 *Semicond. Sci. Technol.*, 15 p.222
7. G.N. Dash, J.K. Mishra and A.K. Panda, 1996 *Solid-State Electronics* 39 p.1473

Proceedings of APSYM2006, Dec. 14-16., Dept. of Electronics, CUSAT, India.

BAND REJECTION CHARACTERISTICS OF A WAVEGUIDE WITH SRR ARRAY INSERTS

B .Jitha,C S Nimisha,C K Aanandan,P Mohanan,K V Vasudevan
Center for Research in Electromagnetics and Antennas (CREMA)
CUSAT-Cochin India-682022

ABSTRACT

This paper presents a study of the band rejection properties of a waveguide inserted with a Split Ring Resonator (SRR) array along its axis. The width of the stop band can be adjusted by suitably positioning the SRR array in the waveguide when used in its second resonance.

Key words: Band reject filter; split-ring-resonator; negative permeability.

INTRODUCTION

The SRR introduced by Pendry [1], which exhibits negative values of permeability, have received much attention due to their interesting characteristics and compact size. It has been shown that split-ring resonators (SRRs) due to its high Q are extensively used to develop structures which filter certain frequency bands or suppress spurious harmonics [2–3]. In the simplest representation, the SRR can be thought of as an LC resonator. When a time-harmonic magnetic field is applied along the ring axis, an electromotive force appears around the SRRs. Since the electrical size of the SRR is small, the induced current lines pass from one ring to the other through the capacitive gap between them in the form of field-displacement current lines. Magnetic resonance is induced by the split at the rings and by the gap between inner and outer rings. Parameters such as split width, gap between the rings, and the metal width affect the resonant frequency. Study of transmission characteristics of an SRR array inserted in a waveguide by Hrabar *et .al,* showed that the signal propagation is inhibited in a small frequency band in the wave guide pass band [4]. This has been interpreted as due to the characteristic of periodic medium exhibiting a negative permeability near the resonant frequency of the SRR. In this paper, we propose the use of an SRR array for the design of a waveguide band-rejection filter with adjustable bandwidth. A single layer of an edge-coupled split-ring resonator (EC-SRR) etched on a dielectric is used for this purpose, whose position with respect to the waveguide axis determines the width of the stop band. This property is observed for the array when used in its second resonance. Waveguide filters are used at high frequencies where very low insertion loss and high power handling is the requirement. They find applications in the field of avionics, satellite communication, and so forth.

DESIGN OF SRR ARRAY

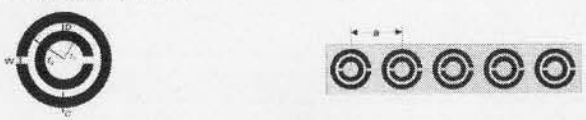

(a) (b)

Figure 1(a). Schematic drawing of an SRR unit cell. **(b)** SRR array with period *a*

The SRR array is fabricated on a single-sided FR4 substrate with dielectric constant $\varepsilon_r = 4.36$ and thickness h = 1.6 mm using the conventional photolithographic technique. Two types of SRR arrays are considered, SRR1 with resonant frequency 9.5GHz (*r1=.6mm,r2=1.8mm,c=.5mm,d=.2mm and w=.6mm*) and SRR2 with 4GHz(r1=1.6mm,r2=2.7mm,c=.9mm,d=.2mm and w=1mm). A time varying magnetic field, polarized perpendicular to the plane of SRR will induce circulating currents according to Faraday's law. Because of the split gap in the SRR, this circulating current will result to build up a charge across gap with energy stored as capacitance. For frequencies below resonance currents in the SRRs can keep up with the driving force produced by externally varying magnetic field and a positive response is achieved. However, as the frequency of the external magnetic field is increased the currents can no longer keep up and eventually begin to lag, resulting in an out-of-phase or negative response.

The general formula connecting permeability and frequency of an SRR array has the form

$$\mu_{eff} = 1 - F\omega^2 / (\omega^2 - \omega^2_{0m} + j\omega\zeta)$$

Where $F = \pi(r_1/a)^2$ represents the fractional area occupied by the SRR
ω_{0m} is the magnetic resonance frequency tunable in the GHz range.
$\zeta = 2a/(r_1\mu_0)$ is the damping factor due to metal losses

The effective magnetic permeability presents a highly resonating peak at the resonant frequency f_0 ,It is at this point the magnetic permeability becomes highly negative , being less negative as frequency is increased. At the point at which magnetic permeability equals zero is known as magnetic plasma frequency. Therefore the range in which the magnetic permeability is negative is $\omega_{0m} < \omega < \omega_{pm,.}$

Where $\omega_{pm} = \omega_{0m} / \sqrt{1-F}$ is the magnetic plasma frequency.

FILTER DESIGN

An X-band waveguide is used for the design of the filter. The SRR array is inserted in the wave guide along its axis. At the center line of the waveguide, i.e, at x=11.5mm, the H field lines are exactly perpendicular to the plane containing SRR array producing maximum interaction. The X-band waveguide is excited in the TE_{10} mode with an SRR array insert is simulated using Ansoft HFSS™ v10 . The transmission coefficient S21 as the SRR array is moved towards the waveguide wall is given in figure2.

Figure 2(a) shows the results for SRR1 where resonant frequency lies in the x-band. It can be seen that as the array is moved towards the wall, attenuation decreases. A different result is obtained for SRR2 whose second resonance lies in the x-band. The width of the stop band varies with the distance x of the SRR array along the x-direction. The stop band is very narrow when the strip is near the waveguide wall and reaches a maximum value when the structure is placed at the center of the waveguide, as is evident from Figure 2(b). Here, x = 0 corresponds to the rings in contact with the narrow wall of the waveguide. Use of second resonance allows better tuning than the first resonance at the same frequency with less number of SRRs.

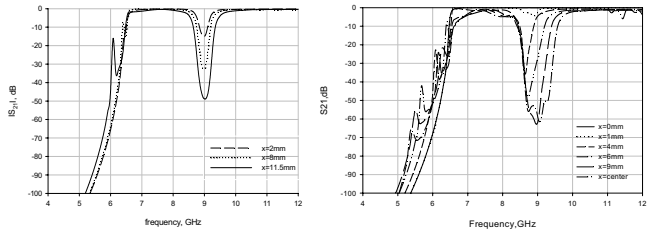

(a) (b)

Figure 2.Transmission spectra of SRR loaded waveguide at different position along x-axi obtained by simulation;
(a) SRR1 (r_1=*0.6mm, r_2=1.3 mm, c=.5 mm, D=.2 mm and w=.6 mm, N=12*)
(b) SRR2 (r_1=*1.6mm, r_2=2.7 mm, c=.9 mm, D=.2 mm and w=1 mm, N=5*)

FILTER FABRICATION

The model of the waveguide filter and its cross-sectional view are shown in fig 3(a). and fig 3(b) respectively.FR4 substrate is used as the holding arms of the SRR array which minimizes the insertion losses and a screw-gauge is connected externally to vary the position of the array.

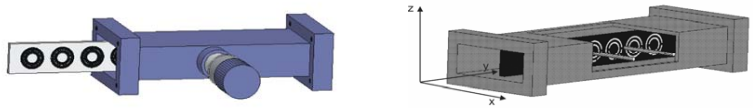

Fig 3(a) Model of the waveguide filter (b) Cross-sectional view

The X-band waveguide excited in the TE_{10} mode with two coaxial-to-rectangular waveguide transitions as input and output. An HP 8510C Network Analyzer is used to measure the transmission coefficient $|S_{21}|$.

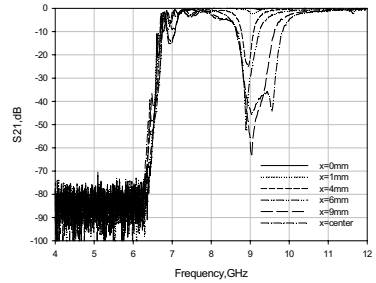

Figure 4. Experimental result of transmission spectra of SRR2 loaded waveguide at different position along x-axis

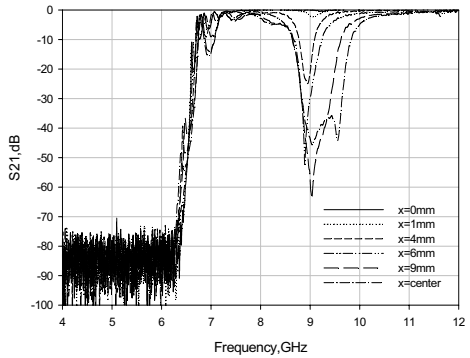

Figure 4. Experimental result of transmission spectra of SRR2 loaded waveguide at different position along x-axis

It can be seen that for values of x>5mm , the stop band width varies with an attenuation above 40dB. An absorption dip is observed in the waveguide pass band at 8.5 GHz, which is extendable up to 9.5GHz.

CONCLUSIONS

Construction of waveguide band reject filter in the X-band by loading a split-ring-resonator (SRR) array having is reported .The width of the rejection band can be controlled by adjusting the position of the array inside the waveguide. A maximum band rejection up to 1 GHz is possible with an attenuation ~ 50 dB.

REFERENCES

1. J.B. Pendry, A.J. Holden, D.J. Robbins, and W.J. Stewart, Magnetism from conductors and enhanced nonlinear phenomena, IEEE Trans Microwave Theory Tech 47 (1999), 2075–2084.
2. F. Falcone, T. Lopetegi, J.D. Baena, R. Marques, F. Martin, and M. Sorolla, Effective negative-_ stopband microstrip lines based on complementary split-ring resonators, IEEE Microwave Wireless Compon Lett 14 (2004), 280–282.
3. J.D. Baena, J. Bonache, F. Martin, R. Marques, F. Falcone, T. Lopetegi, M.A.G. Laso, J. Garcia Garcia, I. Gil, M. Flores Portillo, and M. Sorolla, Equivalent-circuit models for split-ring resonators and complementary split-ring resonators coupled to planar transmission lines, IEEE Trans Microwave Theory Tech 53 (2005), 1451–1461.
4. S. Hrabar, J. Bartolic, and Z. Sipus, Waveguide miniaturization using uniaxial negative permeability metamaterial, IEEE Trans Antennas Propagat 53 (2005), 110–119.

Proceedings of APSYM2006, Dec. 14-16., Dept. of Electronics, CUSAT, India.

RESEARCH SESSION IX

MICROWAVE DEVICES II

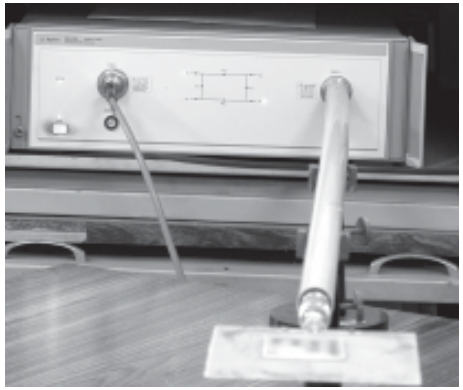

December 16, Saturday

(2.00 p.m. - 3.00 p.m.)

RESEARCH SESSION IX

MICROWAVE DEVICES II

Chair :Prof.M.C.ChandraMouly,M.I.C. College of Technology., Vijayavada

Proceedings of APSYM2006, Dec. 14-16., Dept. of Electronics, CUSAT, India.

DESIGN OF HIGH POWER LOW LOSS COMPACT SHAPED BEAM FEED NETWORK FOR SHORT RANGE 3D SURVEILLANCE RADAR

Preeti Dongaonkar, Shubha Elizabeth Avirah and Anil Kumar Singh
Electronics & Radar Development Establishment
Defense Research & Development Organisation
C. V. Raman Nagar, Bangalore, India

Abstract: *Present paper deals with design and development of a compact feeder network based on air dielectric stripline with phase gradient coaxial cables to get the required amplitude and phase distribution for shaped beam pattern with 20^0 coverage. The design of sixteen way feed network of unsymmetrical topology with T-junctions and modified hybrid rings power dividers to get low sidelobe level outside the shaped region which is mandatory for radar antennas is elaborated. The design has been optimized using EM CAD tools to get less than $\pm$ 0.2 dB ripple in shaped region and a side lobe less than –25dB across a bandwidth ±150MHz (9%) in S Band.*

I. Introduction: Generally, 3-D radar systems uses a shaped antenna pattern to cover the given elevation region [1]. In this paper we discuss a feed network based on air dielectric stripline with phase gradient coaxial cables to get the required amplitude and phase distribution for shaped beam pattern. While synthesizing a shaped beam pattern with phase alone synthesis, to get a low side lobe outside the shaped beam region large amplitude taper is required from less number of elements. For large amplitude taper distribution or when the numbers of antenna elements are less, the power division ratio to be handled by a single power divider in a corporate feed network is quite large. This leads to individual power divider modules with less impedance bandwidth. This drawback of the common corporate feed network is overcome by using sixteen way feed network of unsymmetrical topology with T-junctions and modified hybrid rings power dividers. This design methodology gives low sidelobe level outside the shaped region, which is mandatory for radar antennas.

II. Design Of Air Dielectric Stripline Feed Network: High power feed network, which will give the suitable amplitude distribution, is achieved through a 16 way in phase corporate network with unequal power division at each level. Air dielectric is chosen so that losses are less and power-handling capability is high. Teflon bushes are placed at appropriate places to support the central conductor. These Teflon supports are specially designed to give good mechanical strength at the same time no adverse effect in the electrical performance of power divider. Design of power divider with a very high taper is very difficult because of the high power division ratio of more than 10 dB between two ports. Usually when the number of elements 'N' is a power of two ($N=2^n$, n is an integer) like 16,32,64 etc, at every stage two way power divider can be used which can be connected as shown in Figure1a. Due to symmetry of this topology it is very easy to achieve equal phase at all the ports of the feed network. But this conventional topology is

suitable only for uniform distribution or distribution with less taper. If this topology is used for 40 dB Taylor Distribution power division ratios become too high to realize.

So a different topology as shown in Fig 1 has been chosen. Though achieving equal phase for all the ports is difficult because of asymmetry of this topology, power division ratios are lesser. In this case T-junction power divider is used as the basic unit for power division. Still at some places in the feed network, power division ratios are difficult to realize with T-junction power divider, as the width becomes very narrow to fabricate. This problem is overcome by designing a novel modified Hybrid Ring wherever very high power division ratio is required in the feed network .A layout of modified Hybrid Ring is shown in Fig 2.

As the present antenna is used for Surveillance Radar it is designed to handle 15 KW peak and 400 W average power. Corporate feed network is designed in Stripline with air dielectric so that high power can be handled with low loss. PTFE supports are used at various places to maintain a constant gap between top and bottom plate of stripline feed. These supports are specially designed to give good mechanical strength at the same time have no adverse effect on the electrical performance of power divider.

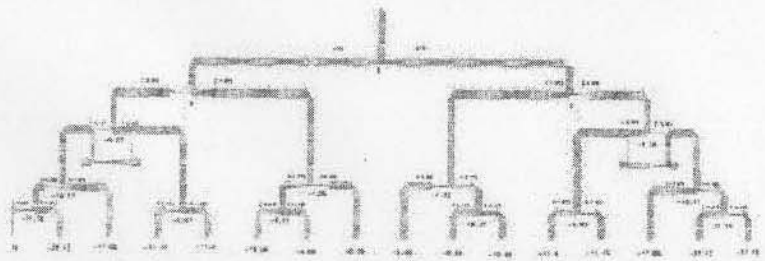

Fig 1 Power Divider with Modified Topology

III. Analysis Of Stripline Feed Network: As low sidelobe level antenna has, amplitude distribution with very high taper across array elements its side lobe level is very sensitive to amplitude and phase errors. So amplitude distribution has to be very close to required value and there should be no phase difference across all the ports of the feed network. To meet these requirement feed network is initially designed in a 2-D Circuit Simulator Advanced Design System version 1.5, and then it is imported and analyzed in 3-D Electromagnetic Simulator CST Microwave Studio version 5.0. Design iterations were carried out to get required amplitude distribution and zero phase difference in CST Microwave Studio. ADS is used for initial design as it is much faster than CST but results were optimized in CST because

1) Being a 3-D electromagnetic simulator it is more accurate as the structure can be accurately modeled and analyzed.
2) PTFE supports along with fixing metal screws cannot be modeled in ADS but it can be correctly modeled, analyzed and optimized in CST MWS.

Proceedings of APSYM2006, Dec. 14-16., Dept. of Electronics, CUSAT, India.

PTFE supports used to maintain a constant gap of 8 mm between top and bottom plate of stripline air dielectric feed, affect the performance of feed network. When individual power dividers are analyzed in CST MWS with PTFE supports, it is observed that supports do not have much effect on amplitude distribution, but they do change the phase between the two ports considerably. Design iterations are carried out to bring the phase difference to zero. Another effect is that these PTFE Supports shift the response to lower frequencies. Hence design optimization is done to get the desired response for the required band of operation.

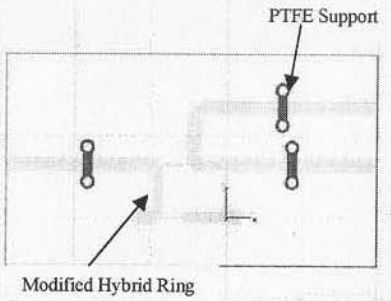

Fig 2. Modified Hybrid Ring

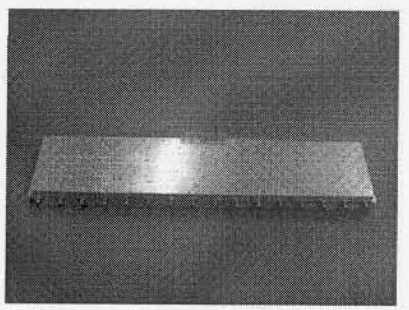

Fig 3. Sixteen way Feed network

IV. Fabrication: Fabrication of the Feed network is the most critical. The amplitude distribution has to be maintained with the least rms error possible to have a ripple free shaped region. Hence the air dielectric complex contoured Power Divider network needs to be fabricated using 0.8 mm thick brass having multiple sharp corners with power divider line width varying from 1 mm to 12 mm. Further this power divider needs to be placed between two ground planes (two aluminum plates of thickness 1.2 mm and dimension 1000 mm × 200 mm) separated by 8 mm and has to be supported by number of aluminum / PTFE bushes. As uniform gap of 8 mm between the two ground planes is essential, no. of specifically designed PTFE bushes are used at various places for the power divider to meet stringent electrical specifications. The mechanical tolerances for sharp corners < 0.2 mm and for other dimensions < 10 micron has been aimed. Phase distribution to generate the shaped beam is achieved through medium power coaxial cables with in built phase trimmer of 10^0. The advantage of this generic design using phase gradient cables with inherent phase trimmer is that any beam shape can be obtained with phase alone synthesis and slight errors in the antenna fabrication which leads to different antenna elements can be over come to a certain extent.

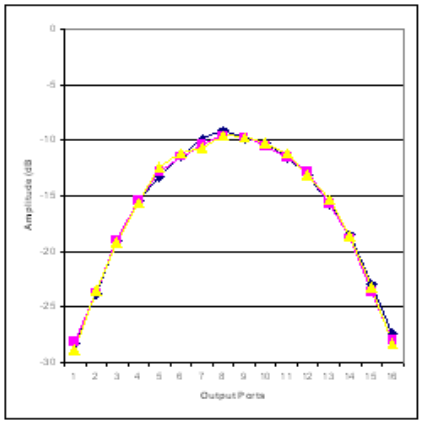

Fig 4. Amplitude Distribution Across 16 ports at f_0, f_0 GHz ± 150 MHz

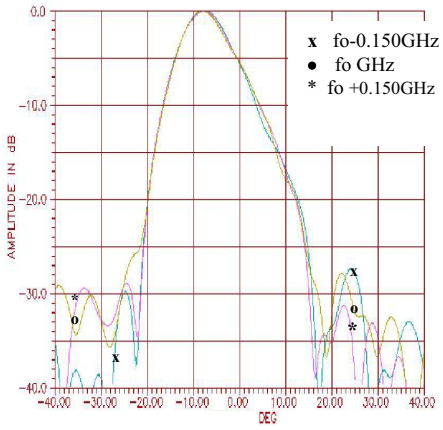

Fig 5. Simulated Shaped Antenna Pattern with measured amplitude and phase.

V. Results & Conclusion: The amplitude distribution of the feed network at f_0, $f_0 \pm 150$ MHz is shown in Fig 4.The simulated pattern from amplitude and phase distribution is shown in Fig 5. The pattern shows a ripple of ± 0.2 dB, which is much within the specified limits. The feed network is very compact, weighing about 2.5 kg and can handle a power of 15KW or more. This type of feed network is very useful for light weight short range 3-D surveillance radar systems.

VI. References:

[1] Merrill L. Skolnik, *Introduction to Radar Systems, Chapter 2, 3 rd Edition,* Tata McGraw-Hill.

[2] Bharathi Bhat & Shiban K. Koul, *Stripline Like Transmission Lines for Microwave Integrated Circuits,* John Wiley & Sons.

DESIGN OF ADAPTIVE EQUILIZER FOR SPECTRUM MANAGEMENT AND CHANNEL EQUILIZATION

Moutusi Mondal(1), Mainak Mukhopadhayya(1) ,Ajay Chakrabarty(1)

Dept of Electronics & Electrical Communication Engineering,IIT-Kharagpur,Pin-721302,
Email:moutusi.etc@gmail.com

Abstract

In digital communication system, the basis form consists of a transmitter channel, and receiver connected together. The function of transmitter is to convert a message signal generated by digital sources into a waveform suitable for transmission over the channel. In communication system, the present channel distortion, which is not known priorities the channel distortion results in inter symbol interference (ISI) and additive noise as much possible. The solution of the ISI problem is to design a receiver that employs a means for compensating or reducing the ISI in the received signal.

I.INTRODUCTION

From the definition of the equalizer we have:

$H_e(e^{j\omega}) = [\ H_c(e^{j\omega})]^{-1}$

Equalization with filters uses filters to compensate the distorted pulses. The equalizer based on algorithm for automatically adjusting the equalizer coefficients to optimize a specified performance index and to adaptively compensate for time variations in the channel characteristics are called *adaptive equalizers*.

There are two modes that adaptive equalizer works:

- *decision mode*
- *training mode*

Adaptive equalizer assume channel is time varying channel and try to design equalizer filter whose filter coefficients are varying with time according to change of channel. Transversal filter are actually FIR discrete time filter.

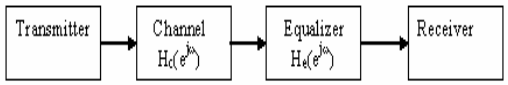

Fig.1.Basic communication system with equilizer

II.TRANSVERSAL FILTER

A tapped delay line filter or finite duration impulse response (FIR) filter, the transversal filter consists of three basis elements as

1. a unit-delay elements,2.a multiplier,3.an adder

The number of delay elements used in the filter determines the finite duration of its impulse response. The delay elements are each identified by the unit delay operator Z^{-1}.when the Z^{-1} operates on the input u(n),the resulting output is u(n-1).the multiplier in the filter is to multiply the tap input by a filter coefficients referred to as a *tap weight*. A multiplier connected to the k-th tap input u (n-k) produces ω_k^* u (n-k), where ω_k is the respective tap

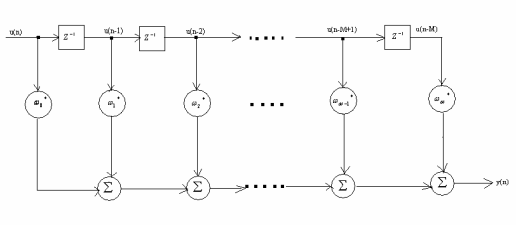

Fig.2.Transversal Filter

III.LEAST MEAN SQUARE ADAPTATION ALGORITHMN

Consider a transversal filter with tap inputs *u*(n), *u*(n-1), ….., *u*(n-M+1) and a Corresponding set of tap weights *w*0 (n), *w*1(n)… *w*M-1(n). The tap inputs represent Samples drawn from a wide-sense stationary stochastic process of zero mean and Correlation matrix **R**.

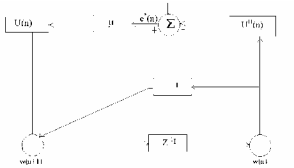

Fig.3.Signal flow graph representation of LMS algorithm

The desired response at the filter output is denoted by **d**(n). By comparing this estimate The desired response *d* (n), we produce an estimation error denoted by *e* (n).

e (n) = *d*(n) - **d**(n)

= *d* (n) –**W**H(n)**u**(n)

From this we have,

1. Filter output:

y (n) = **u**H(n) **w** (n).

2. Estimation error or error signal:

e (n) = *d* (n) – *y* (n).

3. Tap-weight adaptation:

W (n+1) = **w** (n) + μ**u** (n) e*(n).

At each iteration or time update, this algorithm requires knowledge of the most recent Values: **u** (n), *d* (n), and **w** (n).

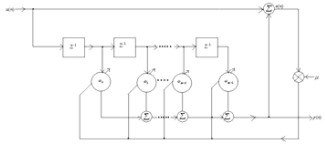

Fig.4.Linear Transversal Filter in Training Mode

Typically, adaptive equalizers used in digital communication require an initial training period, during which a known data sequence is transmitted. Thereby making it possible for adjustment to be made to the equalizer coefficients in accordance with adaptive filtering algorithm employed in the equalizer design.

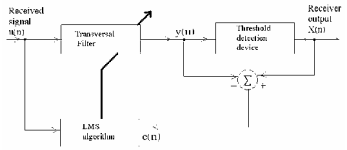

Fig.5.Linear Transversal Filter in Decision Directed mode

IV.CASE STUDY

• The degree of adaptive filter is 11.
• The impulse response of the channel is a raised cosine function;

$h_n = (\frac{1}{2})[1+\sin(2\pi(n-2)/w)]$, n=1,2,3

0 otherwise

• The signal applied to this channel consists of a Bernoulli sequence taking Values 1 or 0 with probability 0.7 each.
• The additive noise is Gaussian noise with zero mean, and variance $\sigma_2 = 0.002$.
• The step size parameter of the adaptation algorithm (the filter) is $\mu_1 = 0.06$ for the training mode and $\mu_2 = 0.0005$ for decision mode directed mode.
• The adaptive filter is working on training mode for the first 1000 samples.
• The adaptive filter is working in decision directed mode for the samples between 1000 samples and 5000 samples.
• The equalized signal is passed through a slicer; the slicer is actually a quantizer. The rule of quantization is that it quantizes the signal to 1 when the signal is greater than 0.5 and quantizes to 0 when the signal is less than 0.5.

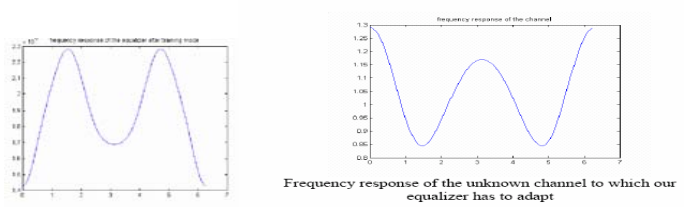

Frequency response of the unknown channel to which our equalizer has to adapt

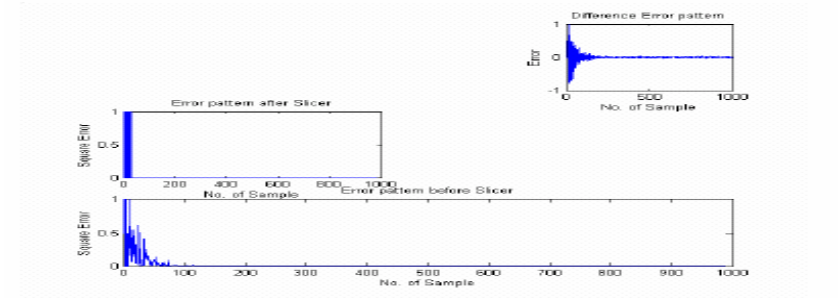

Fig.5.Different stage of the system after training mode

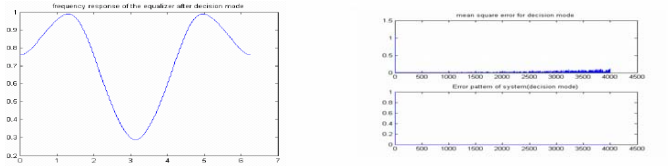

Fig.6.Different stage of the system of decission mode

V.CONCLUSION

Adaptive Equalizers are the most important device to encounter unpredictable channel behavior for communication system and must be augmented for any telecom device carefully especially for rural area where distance between base station and receiver may be huge, corresponds to a long distance channel of highly unpredictable behavior for faithful transmission.

REFERENCES

[1]Simon Haykin, Adaptive Filter Theory, Communications Research Laboratory, McMaster University, Hamilton, Ontario, Canada
[2]T. K. Sarkar, M. C. Wicks, M Salazar-Palama, and R. J. Bonneau, *Smart Antenna*, IEEE Press.
[3]M. A. Halim, Adaptive Array Measurements in Communication, John-Wiley.

PERFORMANCE ENHANCEMENT OF MICROSTRIP LOW PASS FILTER BY APPLICATION OF DEFECTED GROUND STRUCTURE

Susanta Kumar Parui, and Santanu Das
Dept. of Electronics and Telecommunication Engineering
Bengal Engineering and Science University, Shibpur
Howrah-711103, India, Phone 91 033 26684561-63
E-mail: arkapv@yahoo.com & santanumdas@yahoo.com
Institute website: www.becs.ac.in

Abstract:. In this paper, we have proposed a scheme for enhancement of the performance of a stepped impedance, ladder type lowpass filter by incorporating Defected ground structure (DGS). The DGS cell consists of two rectangular slots connected by a thin slot symmetrically under the microstrip line. The slowwave characteristic of DGS microstrip line has been utilized here to obtain sharp, wide and deep lowpass characteristics of the proposed structure. The structure has been simulated by full-wave MOM based IE3D software and compared the result with experimental measurement by vector network analyzer.

Key words: DGS, microstrip, lowpass filter

I. INTRODUCTION

In recent age, defected ground structure (DGS) for planar transmission lines has drawn a wide interest because of their extensive applicability in antenna and microwave circuits [1]-[3]. DGS etched in the metallic ground plane of microstrip line, are attractive to obtain deep stop band and unwanted frequency rejection characteristic and compact design. Various shapes of DGS cells, such as rectangular, square, circular and dumbbell have appeared in the literature. D. Ahn et al. reported the design of a lowpass filter using microstrip DGS for the first time [1]. One-dimensional periodic DGS was studied by Kim et al [2] and showed lowpass characteristic. Since DGS have an inherent resonance property, many of them have been applied to design of filter circuit. In this paper, we have designed a conventional 5^{th} order, stepped Impedance, L-C Ladder type lowpass filter with cutoff frequency 5 GHz [4]. We have incorporated DGS cells under input and output feed line to enhance the performance of the filter.

II. DESIGN OF DGS

We have designed DGS cell consist of two rectangular slots of length 4.4 mm and width 4 mm are connected by a thin transverse rectangular slot of width 0.4 mm and length 2.0 mm symmetrically under 50 ohm microstrip line, assuming the substrate with thickness 0.79 mm and dielectric constant of 3.2 as shown in Fig.1(a). Here we put different number of DGS cells with separation of 5.5 mm under microstrip line to study lowpass filtering characteristics. Simulated result shows 3-cell structure provides better sharpness and wider stop-band characteristics compare to 1-cell or 2-cell structure as shown in Fig. 1(b). The frequency response of DGS can be tuned by adjusting the width of transverse rectangular slot or by changing area of each rectangular slot.

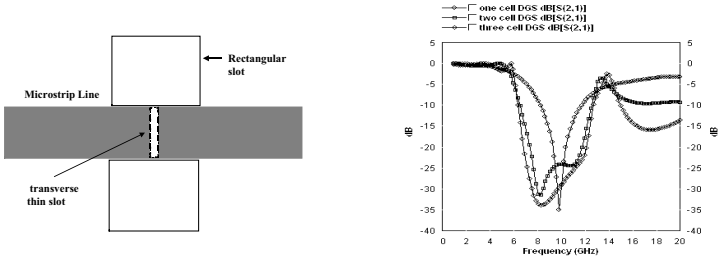

(a) (b)

Fig. 1: (a) Layout of Microstrip line with DGS cells (b) Plot of Frequency response of S_{21}

III. SLOWWAVE CHARACTERISTICS OF DGS

From classical definition, the value of effective dielectric constant of microstrip lies between air dielectric constant and substrate dielectric constant. But the effective dielectric constant of the microstrip with DGS is greater than substrate dielectric constant. It increases towards the edge of stopband. It can change either with the number of DGS cells or with the dimension of each DGS cell. The slow-wave factor of the microstrip line is defined by square roots of effective dielectric constant. So, the slow-wave factor at passband varies with the dimension of DGS cell and maximum value is achieved at the edge of stopband.

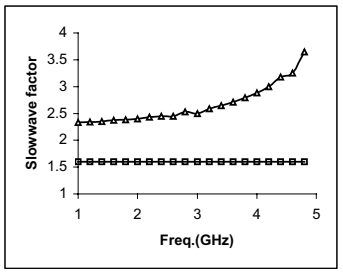

Fig. 2: Slowwave Factor vs frequency plot with/without DGS line

The plots in Fig. 2 show that the slow-wave factor of microstrip line with 3 cells DGS has been increased towards edge of stopband whereas it is almost constant with frequency for line without DGS.

IV. DESIGN OF LOWPASS FILTER

We have designed a conventional 5th order, stepped Impedance, L-C Ladder type lowpass filter, which use a cascaded structure of alternative high and low impedance transmission lines. The high-impedance lines act as series inductors and low impedance lines act as shunt capacitors. A layout of such microstrip filter is illustrated in Fig. 3(a). The circuit has been designed on a substrate with thickness 0.792 mm and dielectric constant of 3.2. Input lines have width (W) of 1.92 mm assuming 50 Ohm external feeding lines. Other design

parameters are L= 4.69 mm, W1 =5 mm, L1 =3 mm, W2= 0.5 mm, L2 = 3.75 mm, W3 =6.0 mm, L3 = 4.042 mm, W4 =W2, L4 =L2, W5=W1, L5=L1.

The performance of the filter has been obtained by full-wave MOM based IE3D simulation. The simulated scattering parameters are plotted in Fig. 3(b). Plots show the cut off frequency has been obtained at 5 GHz and achieved center stopband at 10 GHz and 15 dB rejection bandwidth of 8.5 GHz. We achieved the sharpness factor of 8 dB/GHz at lower transition edge.

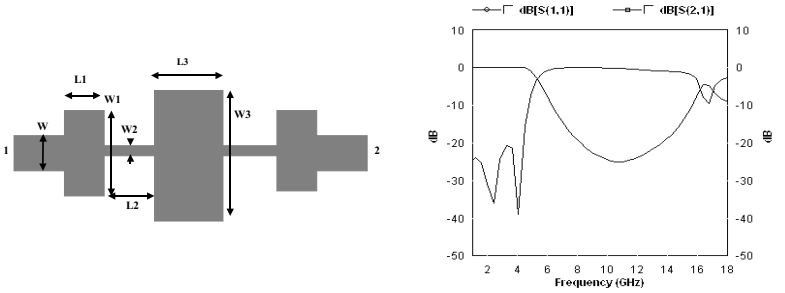

(a) (b)

Fig. 3: (a) Layout of lowpass filter and (b) Simulated S-parameter plot of he filter

The circuit has been fabricated by chemical etching method on Arlon make PTFE substrate PCB. The experimental measurement has been carried out by Agilant make vector network analyzer of model N5230A. The measurement result for magnitude (dB) of S11 and S21 has been shown in Fig. 4(a) and phase characteristics of S21 in Fig. 4(b). The stopband center frequency has been accurately measured at 8.8 GHz from phase plots of S21. The 15 dB rejection bandwidth of 8.1 GHz and 3dB cutoff frequency of 4.5 GHz is measured from magnitude plots of S21. The calculated sharpness is given by 7 dB/GHz. The measured results almost comply with the simulation. The small inaccuracy has been obtained due to fabrication tolerances.

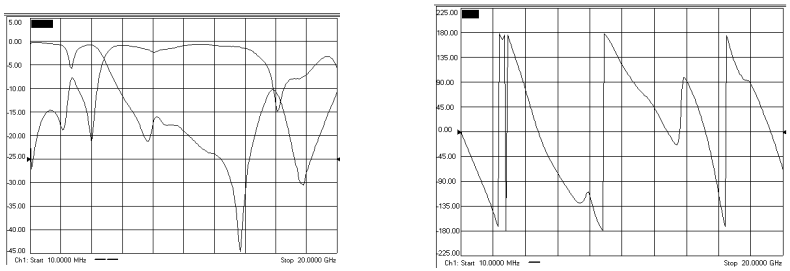

(a) (b)

Fig. 4: Measured S-parameters: (a) Magnitude Plot of S11 and S21 & (b) Phase Plot of S21

V. FILTER INTEGRATED WITH DGS

We have etched two DGS cells under input and out put feed line as shown in Fig. 5. The dimension of DGS has been mentioned earlier.

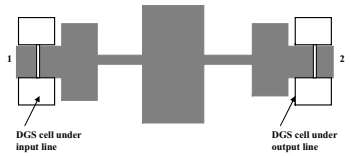

Fig. 5: Layout of proposed scheme for filter integrated with DGS

The simulated results in Fig. 6(a) show that sharpness factor at lower cutoff has been improved from 8 dB/GHz to 40 dB/GHz and the 20dB rejection-bandwidth increases from 40% to 70%. Maximum stop band attenuation of 38 dB is achieved instead of 24 dB without DGS. The measured result has been shown in Fig. 6(b). The calculated sharpness factor from measurement plot has been given by 45 dB/GHz.

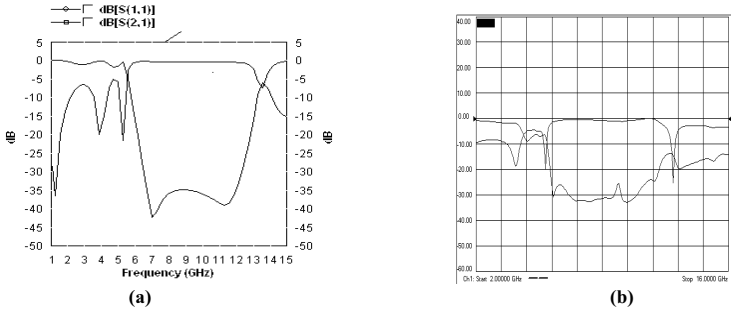

(a)

(b)

Fig. 6: S-parameter of filter with DGS (a) Simulated Magnitude plot and (b) Measured magnitude Plot

VI. CONCLUSION

We have proposed a scheme to incorporate DGS cells under input and output feed lines of stepped Impedance, ladder type low pass filter to enhance the performance. The proposed DGS cell consists of two rectangular slots connected by a thin slot symmetrically under the microstrip line. We have achieved wide bandwidth, high sharpness and deep stopband attenuation. The pass-band ripple is maintained at a low value. Finally the structure is simple to design, easy to fabricate and take no additional fabrication space for such improvement.

REFERENCE

[1] C.S.Kim, J.S.Park, D.Ahn and J.B. Lim, "A novel one dimensional periodc defected ground structure for planar circuits," IEEE Microwave and Guided wave Letters, Vol. 10, No. 4, pp. 131-133, 2000.
[2] D. Ahn, J.S.Park, C.S.Kim, J.Kim, Y Qian andT. Itoh, "A design of the lowpass filter using the novel microstrip defected ground structure," IEEE Trans. On MTTs, Vol. 49, no.1, pp. 86-93, 2001.
[3] Liu H.W., Li Z.F., Sun X.W. and Mao J.F., "An improved 1-D periodic defected ground structure for microstrip line," IEEE Microwave and Wireless Comp. Letter, Vol. 14, no. 4, pp. 180-182, 2004.
[4] Jia-Shen G. Hong and M.J. Lancaster, "Microstrip filters for RF/microwave applications," John Willey & Sons, Inc. 2001.

An Integrated Design for FPGA based GPS Receiver Interface

Meena D[1], Taniza Roy[1], L G M Prakasam[1], Karthik K. S.[2]
[1]ERD, LRDE, C.V.Raman Nagar, Bangalore,India,560093, dmeenasatish@rediffmaill.com
[2] Department of Electronics & Communication, K. L. E. C.E.T, Belgaum

Abstract: *This paper emphasizes on the design methodology behind the formulation of a generic FPGA based GPS receiver interface library module in a most commonly used Simulink environment. This module builds a link between GPS receiver and the system, which uses information. The module integrated with Simulink environment will directly generate the code for a FPGA circuitry residing on a target board. The user friendly GUI associated with the component eases the configuration of the module. In addition the other required inputs have to be fed as real time signals for the proper functioning of the hardware. The GPS receiver considered here is expected to work on Trimble Standard Interface protocol. The performance of the design module has been enhanced with a communication controller supporting RS232 communication for TSIP protocol implementation. The configuration and communication parameters are stored in core memory of FPGA to provide the versatility, which can be accessed from any system. Thus the work highlights the entire implementation aspects considered the integrated design approach for this generic library module. The integrated environment of the model makes the component more flexible, user friendly and reliable for any FPGA based real time applications with GPS receivers.*

I. Introduction: The main focus of the paper is to discuss briefly the design of a generic library component, which helps to interface GPS receiver to various systems. Unlike the other methods, this design provides the complete solutions using digital methods without any additional hardware requirements using FPGAs. A serial communication controller implemented by using digital methods eases the interface design. This generic GPS interface library component can be tuned to synchronize any GPS receiver, which works on TSIP protocol. The entire design is developed using VHDL and System Generator models of Xilinx and integrated with Mat lab Simulink environment.

II. Design architecture: The library component integrated with the Simulink environment acts like a media for communications between data processor and GPS receiver. The GPS receivers offer two full-duplex serial ports and a 1-PPS open-collector timing output for the time reference. TSIP protocol communication is based on dual RS-232 data ports (Ref Fig.1).

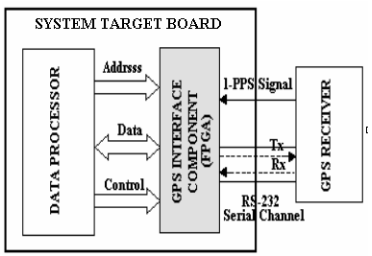

Fig. 1:Interface Block diagram

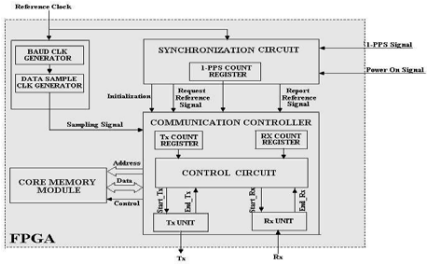

Fig. 2: FPGA Architecture of the design.

From a reference clock, the required baud rate clocks are generated and configured for the RS-232 serial communication. The primary output of the GPS unit is time-tagged position at an approximate interval of one second. Other available information includes satellite status and diagnostics of receiver operational status etc, depending upon the protocol. The entire design is placed as generic library in Simulink so that user can access this module easily. The interactive GUI of the component provides the facility to alter the baud rate parameter along with necessary information pertain to it. The paper describes integrated library model with interactive GUI followed with the detailed design of the FPGA based interface.

2.1 Integrated library component: This is accomplished through following two steps. Firstly basic VHDL based models are ported as the System Generator models of Xilinx. This establishes a link between Simulink environment to FPGA based development environment. Secondly these models have been integrated to form a library component in the normal Matlab Simulink environment. The underlined fact of this component is that the FPGA based GPS interface module has been brought to a commonly used environment to have more flexibility in the usage. In addition, like other Simulink models this model also can be used for any real time applications by providing necessary inputs. This component has been developed as a part of new Radar application library of Simulink (Ref. Fig. 3). The generic nature of the component makes it suitable for any other systems interface with GPS receivers.

2.1.1 Interactive component GUI: A separate block parameter GUI has been provided along with the component. It provides the flexibility for the user to select suitable baud rate to establish communication with GPS receiver (Ref. Fig. 4). The selection of the component itself will provide the first level information regarding component. Additional detailed information is provided through GUI control and also from Simulink environment to enhance the usage of the component (Ref. Fig. 5 & 6).

2.2 FPGA based interface model: The design consists of various modules for Configuration of communication parameters, Baud and Data sampling clock generation, Transmission, Reception and Protocol generation (Ref. Fig 2).

The Interface design module uses TSIP protocol for the communication with the GPS receiver. So a serial communication controller, which supports RS-232 communication requires configuration of various communication parameters. A reference clock is used as the reference to generate the baud clock based on the baud rate selection. For the proper transmission and reception of data packets further a data-sampling clock is derived from the above clock. This clock will ensure sufficient number of samples for each data bit in a packet both during transmission and reception.

The data to be transmitted are expected to store in core memory in prior. This transmission module reads the parallel data from the memory and converts in to serial format. Further this data is formulated with start and stop bit based on the communication parameters stored in memory. In addition this module also caters the transmission of data bits at the data sampling clock intervals through the Tx port of serial communication channel. This module receives the data through the Rx port of serial communication channel. Further actual data is segregated from the received data by considering start and stop bits. This also includes conversion of serially received data to parallel format for further processing.

The bit oriented TSIP (Triple Standard Interface Protocol) Protocol follows a specific format for the communication with the GPS receivers. Each packet includes an identification code that identifies the meaning and format of the data that follows. Each packet begins and ends with control characters. Specific data packets with different packet ids are sent between GPS receiver and the data processor based on the requirement. In this interface module GPS receiver is initially configured with mode of operation, I/O port specification, port

characteristics and filter control packets. Once the initialization is completed request packets are sent from the data processor to the GPS receiver in synchronization with the signals generated from the control circuitry. Each request packet expects report packet with specific packet ids as per the standard TSIP protocol [1], [2].

3. Design implementation and Results: The model from the Simulink environment can be directly used as a System Generator model to realize the GPS interface (Ref. Fig. 3). Model expects the required inputs in the proper format for the hardware realization of the module. Like any other System Generator model, these will generates code for Xilinx FPGA, which can be downloaded to target systems. Through the GUI control user can configure the communication controller baud rate (Ref. Fig. 4). Other communication controller parameters such as start bit and end bits are chosen to be of 1 bit in the design. In order to ensure proper transmission and reception of data bits in a packet minimum of 16 data samples are considered for the data validation.

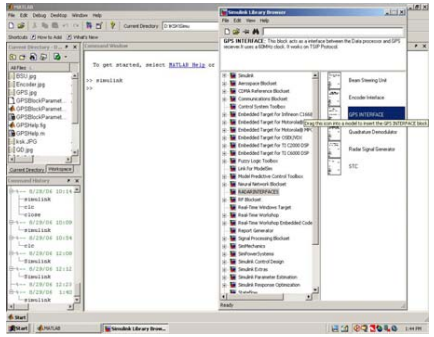

Fig. 3: GPS interface library component in Simulink.

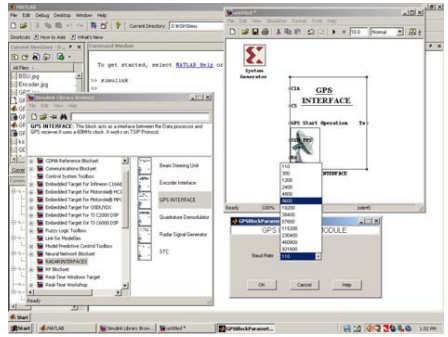

Fig. 4: GUI for the GPS interface component.

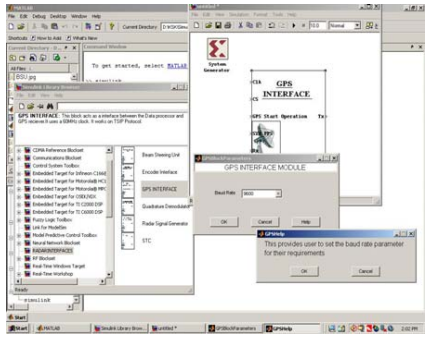

Fig. 5: Component help with GUI.

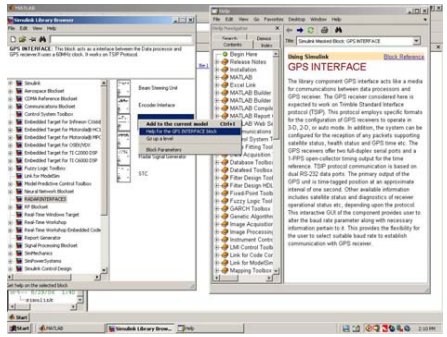

Fig. 6: Information from Simulink environment.

Fig. 4 shows the information provided through GUI control (Help button). Fig. 5. Shows the documentation available for the component with the generic Simulink environment

Based on the control circuit signal initialization, GPS receiver is configured for TSIP protocol format. Then periodically request packets are sent from the data processor by taking 1 PPS signal received from the GPS receiver as the reference. The request packets include Health Status request, Time request and UTC-GPS time offset [1] .In response to this request packets GPS receiver sends respective report packets for Health status, Time, and UTC-GPS time offset [1]. The communication controller module will be in the receiving mode based on the

report reference signal. A time out facility is provided for the reception of report packets. In case of failure in the reception of data packets in the time specified again request packets are sent to the GPS receiver. The Time report packet provides the current GPS time of week and the week number (10 data bytes). The data processor will utilize the offset report packet (43 bytes) [1] for the UTC time derivation. Received packets are extracted in the parallel format by the communication controller module and relevant values are stored in the core memory. These values will be read by the data processor for further computations.

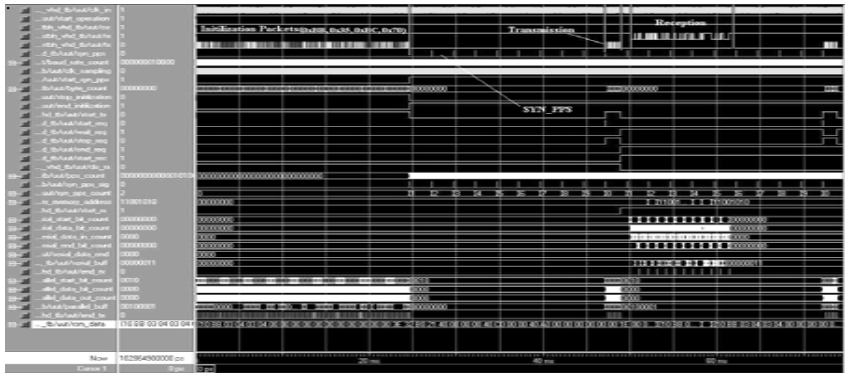

Fig. 7: TSIP implementation simulation results (Initialization, Transmission, and Reception packets)

The entire interface module has been implemented on a single Xinix FPGA chip, which provides a lot of programmability and compatibility. This module is tested for timing and logic and validated with simulation results by using ModelSim simulation software. Simulation results are validated as per requirements of TSIP implementation. Fig. 7 shows the complete simulation of the module consists of initialization of GPS receiver, Transmission of request packets, and reception of report packets in ModelSim environment

4. Conclusion: This generic interface component in the Simulink environment can be configured for any real time GPS receiver interface with out altering the programming level aspects. Additionally this module can be utilized with variations in the configuration parameters stored in core memory module in support of TSIP protocol. This configuration process can be made independent of the platform of the external system with suitable device drivers. But the configuration process expects the exact knowledge of parameter allocation tables and its order of storage.

In the design implementation, proper care has been taken to avoid effects of propagation delays by using separate concurrent processes for transmission and reception modules. In addition this module uses the Intellectual Property (IP) core elements during implementation phase to reduce the propagation delays. These customized cores deliver high levels of performance and area efficiency. It resulted in the efficient implementation of the interface logic by using less percentage of FPGA resources. The generic nature of the integrated design makes it available for FPGA based real time applications.

References

[1] ACE II GPS System Design Manual, Trimble Navigation Limited, Part No. 39538-00.
[2] LG SK8MRS V1.1- 232. System Designer Reference Manual. Part No: 34149- 01.
[3] Radio Technical Commission for Maritime Services, "*RTCM Recommended Standards for Differential NAVSTAR GPS Service:* RTCM, Washington, Jan-1990.

Hairpin Bandpass Filter with Wide Upper Stopband

Priyanka Mondal and Ajay Chakrabarty
Department of Electronics and Electrical Communication Engineering, Indian Institute of Technology, Kharagpur, India, 721302, E.mail: pri.mondal@gmail.com, bassein@ece.iitkgp.ernet.in

Abstract: *In this paper, slot line hairpin resonators are used to design bandpass filter and a T-shaped microstrip feed line is proposed for excitation of the filter. This feeding structure produces frequency dependent external coupling which is utilized to obtain wide upper stopband of the filter. A fabricated three-pole filter having centre frequency (f_0) of 900 MHz shows 30 dB upper stopband at least up to 6.6f_0, while implementing area of the filter is less than 0.65λ_g × 0.31λ_g, λ_g being the guided wavelength at f_0.*

Introduction: Bandpass filters (BPF) with good in-band as well as out-of-band performances are highly desirable for wireless communication systems. There are several approaches reported in literature to improve the out-of-band rejection performance. In [1], integration of a bandstop filter was proposed to suppress the second harmonic. T-shaped microstrip feed line was proposed to suppress harmonics of a shorted slotline resonator BPF [2]. Here, the same feeding technique is used to widen upper stopband of a slot line hairpin (SLH) resonator BPF.

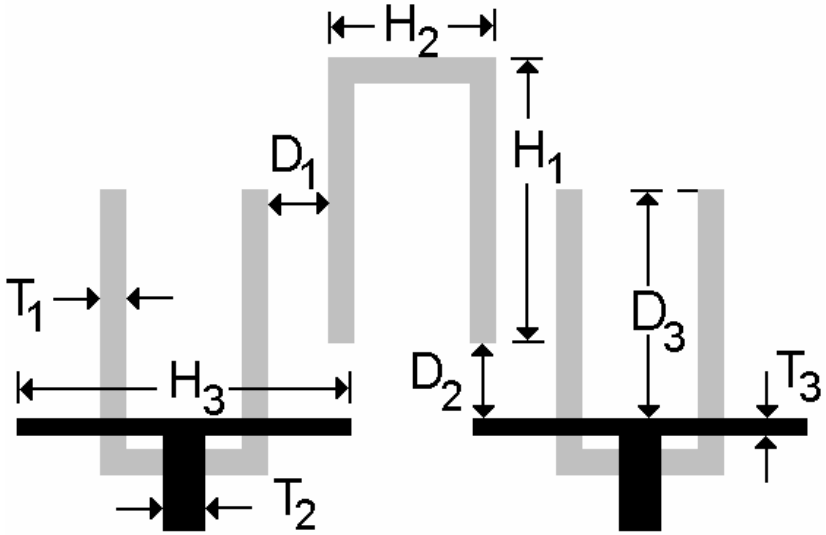

Fig.1 Layout of the BPF: Black region represents the upper side metallization and grey region represents the etched slot on the ground plane.

Designing harmonic suppressed BPF: Fig.1 shows the proposed filter layout. The 50 ohm microstrip feed line (T_2) is modified by attaching a stub of length H_3 and width T_3. The feed line is placed centrally relative to the SLH and hence only odd harmonics are excited. Even harmonics are not excited due to their sinusoidal electric field distribution and that the feed line crosses the SLH at the point of electric field minima. Now, the line length H_3 is varied to control the external coupling to the odd harmonics. It is seen that, when $H_3 \approx 0.19\ \lambda_g$, λ_g being the guided wavelength at passband centre frequency (f_0), coupling to the fifth resonant mode is minimal. However, the third resonant mode is excited. If H_3 is increased to $0.28\ \lambda_g$, coupling to the third resonant mode is minimized but it increases for the fifth resonant mode. Finally, both the harmonics are suppressed when $H_3 \approx 0.25\ \lambda_g$ and a wide stopband is obtained.

Conventional approach of coupled-line filter design [3] is used to design the BPF. The filter has the following specifications: fractional bandwidth (FBW) = 17.3% at f_0 = 900 MHz. A three-pole Chebyshev lowpass prototype with passband ripple of 0.1 dB is chosen. So, required external quality factors are $Q_{e1} = Q_{e2} = 5.96$ and mutual couplings are $M_{2,1} = M_{3,2} = 0.16$. To compensate the loading effect due to feed line, H_1 for the input and output resonators is shorter than the middle resonator. Q_e is obtained adjusting D_3 and T_3.

Fabrication and Measurements: The filter is fabricated on the same FR4 substrate and corresponding measured and simulated s-parameters are shown in Fig. 2. Measurements have been done using a HP8510C® vector network analyzer. Measured 3 dB cut-off frequencies of the filter are 824.6 and 983.2 MHz. Maximum passband insertion loss is less than 1.86 dB

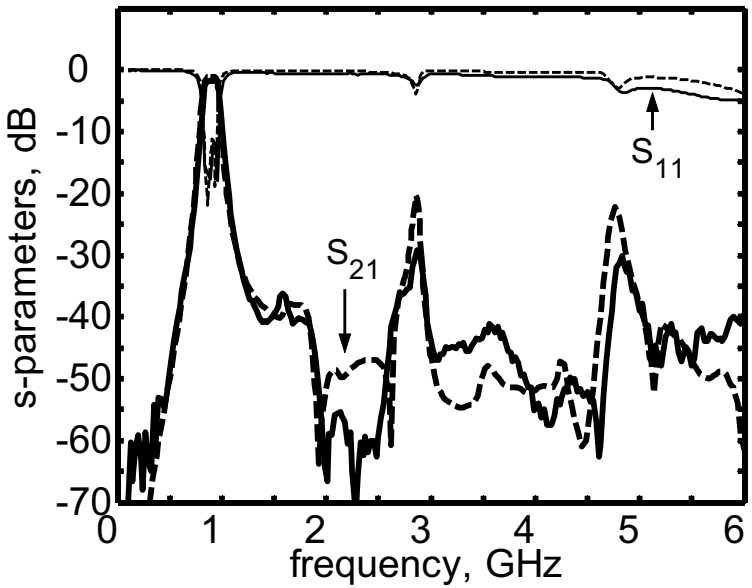

Fig.2 Measured (solid line) and simulated (dashed line) s-parameters of the filter.

and minimum return loss is better than 11.8 dB. DC is completely blocked and 29 dB upper stopband extends at least up to 6 GHz.

Conclusions: In this paper, a T-shaped microstrip feed line is proposed for harmonics suppression of a slot line hairpin bandpass filter. Rectangular implementing area of the three-pole filter is less than $0.65\lambda_g \times 0.31\lambda_g$. The proposed structure is easy to fabricate as no via hole or air-bridge is required.

Reference:

[1] W.–H. Tu, and K. Chang, "Compact second harmonic-suppressed bandstop and bandpass filters using open stubs", IEEE Transaction on Microwave Theory and Technique, Vol. 54, No. 6, pp. 2497-2502, 2006.

[2] Priyanka Mondal and Ajay Chakrabarty, "Compact Wideband Bandpass Filters with Wide Upper Stopband", to be published in IEEE Microwave and Wireless Components Letters.

[3] J.-S. Hong, and M.J. Lancaster, "Microstrip Filters for RF/ Microwave Applications", John Wiley, New York, 2001.

Proceedings of APSYM2006, Dec. 14-16., Dept. of Electronics, CUSAT, India.

INVITED TALKS

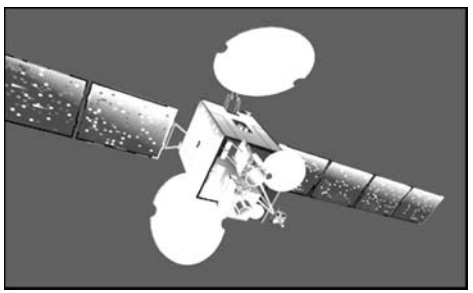

Proceedings of APSYM2006, Dec. 14-16., Dept. of Electronics, CUSAT, India.

Who Was James Clerk Maxwell and What Is/Was His Electromagnetic Theory?

Tapan K. Sarkar
Department of Electrical Engineering, Syracuse University, Syracuse, New York 13244-1240, USA, tksarkar@syr.edu

SUMMARY: First, a brief overview [1] will be presented of some of the interesting developments in electricity, magnetism and optics till the time of Maxwell. This will create the scenario in which Maxwell came in. Then we will do a review of the contributions of Maxwell's work.

Next, the contribution of one of the greatest scientist – James Clerk Maxwell – will be presented as his name is synonymous with the development of modern physics. He laid the basic foundation for electricity, magnetism, and optics. The theory on electromagnetism is one of the few theories where the equations have not changed since its original conception, whereas their interpretations have gone through revolutionary changes at least twice. He introduced the terms "curl", "convergence" and "gradient". Nowadays, the convergence is replaced by its negative, which is called "divergence", and the other two are still in the standard mathematical literature. The first revolution was by Hertz and Heaviside and the second by Larmor. Maxwell's work on electromagnetic theory was only a very small part of his research. In his hands electricity first became a mathematically exact science and the same might be said of other larger parts of Physics. In whatever area he worked, he brought new innovation. He published five books and approximately 100 papers. *Maxwell can be considered as one of the world's greatest scientists even if he had never worked on electricity and magnetism*. His influence is everywhere, which surprisingly is quite unknown to most scientists and engineers! The talk will describe some of that research including for example, the ophthalmoscope and the Maxwell's yellow spot test for macular degeneration, the three colors used in color television, as inventor of the concept of ensemble averaging and the developer of the concept of entropy which was expounded by Leo Szilard and others as information theory. He took the first color photograph, laid the basic foundation on the choice of three primary colors in characterizing any color, and developed accessories for color blind people, which are still used today, and I wonder how many people are aware of that? He developed general laws of Optical instruments and even developed a theory on the composition of Saturn's rings. He created a standard for electrical resistance. He also wrote the first paper on negative feed back which was the cornerstone of Norbert Wiener's work on cybernetics. He elevated the system of dimensional analysis to a science and surprisingly also wrote the method of solving the loop currents as the ratio of determinants, to name a few. He developed a coherent set of units of measurement of electricity and magnetism, which became misleadingly known as the Gaussian system [1].

Even though Maxwell has influenced development in many areas of physical sciences and had started a revolution in the way physicists look at the world, he is not very well known, unfortunately, outside some selected scientific communities. The reasons for that will also be described.

The worst part is even the electromagnetic practitioners who espouse on his theory are seldom aware of his genius!

Reference:

[1] Tapan K. Sarkar, Robert J. Mailloux, Magdalena Salazar-Palma and Dipak L. Sengupta, *History of Wireless*, John Wiley & Sons, Inc., 2006.

ACHIEVEMENTS OF THE EUROPEAN NETWORK ACE

Per Ingvarson
Saab Ericsson Space AB, SE-40515 Gothenburg, Sweden
E-mail: per.ingvarson@space.se

European Commission
Information Society and Media

***Abstract**: In order to improve the European research, the European commission has created a new tool in the 6th framework program called Network of Excellence. ACE, Antenna Centre of Excellence, is such a network. Starting 1 January 2004, it has a duration of 4 years and 51 participants from 17 European countries. 323 researchers and 130 PhD students are involved.*

The activities focus on mm-wave and integrated antennas, wideband and multiband antennas, small and smart antennas, active and passive planar and conformal arrays, software, testing, education and dissemination in the antenna area.

BACKGROUND

The new antenna technologies: In the past, antennas have had simple coaxial or wave connections to the radio equipment, with the exception of large and very expensive military radar The emerging technology contains:

- active antennas, i.e. array antennas with amplifiers connected to each radiator
- integrated antennas, i.e. the active circuits are directly integrated in the radiator
- adaptive antennas, i.e. antennas that can change their antenna pattern adaptively
- diversity, i.e. the antenna can produce two or more independent links
- digital beamforming, i.e. the signals to/from each element are digitised before combination
- multiband and ultra-wideband antennas
- interaction with close environment, e g human body

This increasing antenna capability is a necessary response to the greater demands of the user and increasing congestion of the frequency spectrum. Whilst active microwave circuits and digital hardware become cheaper and thus a smaller proportion of the equipment cost, the new, more capable antennas are of increasing value, due to the fact that much of the system performance is determined by the antenna.

European antenna research: European Universities produce much excellent antenna research. However, the work is split between many relatively small institutions with limited co-operation. Also the collaboration with industry and the users is, in many cases, inadequate, partly due to geographical separation. The result is research duplication, results without applications, and a less than optimal output.

The European Commission is a major source for funding of European research. In order to increase the efficiency of European research, the Commission has created, in the European Community 6th Framework Programme a new "tool" called "Network of Excellence".

The creation of ACE: The "Antenna Centre of Excellence" (ACE) was proposed from members of the European COST 284 action in antennas. (COST is for "European Cooperation in the field of Scientific and Technical Research"). It was awarded a first contract for 2004-5, and we have now a second contract for 2006-7.

OBJECTIVES

The main purpose of ACE is to increase the efficiency and relevance of antenna research in Europe. It is also an objective to increase the inter-European cooperation, and to be a platform for global cooperation.

A careful preliminary investigation of the research structure has shown a number of application oriented research areas that need to be developed. These are dealt with in the so-called *vertical activities*. For these, coupling to the applications is established by involvement of industry and institutes and also by involving universities with relevant system activities.

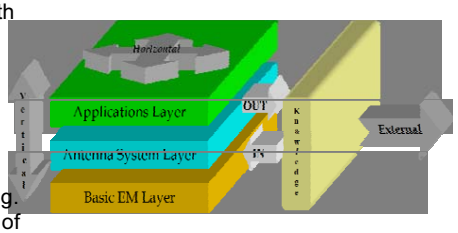

ACE structuring approach

ACE also includes transversal or *horizontal activities* dealing with software and testing. The main objective is the integration of knowledge from different application areas, thereby avoiding duplication. A virtual centre of excellence (VCE) serves as a knowledge base and communications centre. It is also an objective to integrate the higher level education on antennas in Europe and to make dissemination more efficient.

ACE aims to bridge the gap between systems and electromagnetic experts. This is done by incorporating the system aspects of MIMO and smart antennas, by including a strong group of experts in the smart antenna systems activity.

SCOPE

ACE deals with the antenna function of radio systems. This includes the electromagnetic interface from conductors to free space radiated waves, beam-forming functions, whether they are analog or digital, adaptive systems to change the beam pattern, and other antenna-related signal processing. The radiative coupling to the close surroundings and scattering environment, are also included.

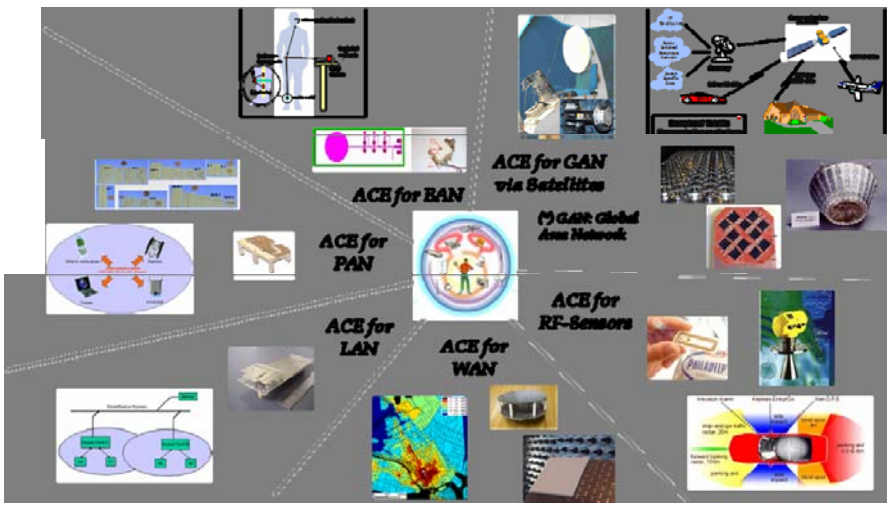

Scope of ACE. BAN, PAN, LAN, WAN and GAN stands for Body, Personal, Local, Wide and Global Area Network

Proceedings of APSYM2006, Dec. 14-16., Dept. of Electronics, CUSAT, India.

VERTICAL ACTIVITIES

MM-&sub-mm waves/Integrated antennas: Millimetre wave and Integrated antennas form two distinct topics, which nevertheless have some common features. The millimetre wave band extends from 30GHz to 300 GHz. Integrated antennas are those in which some, or all, of the radio frequency front end is integrated with the antenna or vice versa. The work includes review of the state of the art in millimetre wave and integrated antennas, as well as of software, test facilities, materials, manufacturing processes.

Small terminals and smart antenna systems: The activity aims to structure research on antennas for mobile phones and their system integration, and evaluate methods for characterization. Major activities include evaluation of fundamental limits for small antennas, integration of antennas and methods. A benchmarking campaign with a “golden device” has been performed.

Wideband and multiband antennas: The activity aims at structuring research on multiband and wideband radiators and reflectors. Specifically, various wideband/multiband/UWB radiators are studied, polarisation and frequency selective reflectors and suitable software is investigated, and a common test facility for surface penetrating radar antennas has been created.

Planar and conformal arrays: The activity aims to structure research on the architecture, synthesis, analysis, beamforming networks and conformal application of array antennas.
Focus is on generic simulation of complete and novel active phased arrays, on reflectarrays and conformal arrays.

Smart antenna systems: The activity aims to coordinate the research on smart antenna systems to foster their development in next generation wireless and mobile communication. Major study objects are reconfigurable multiple antenna transceivers, reconfigurable multiple antenna terminals, smart antenna system level strategies including cross-layer approaches, context aware MIMO network optimisation and smart antenna deployment. MIMO channel modelling, measurement methologies for smart antennas and array technologies for UWB systems and for laptops are also covered.

HORIZONTAL ACTIVITIES

Coordination with wireless applications: In order to certify the relevance of the research, the needs are defined by dedicated meetings with users, manufacturers and agencies, and from literature and conferences.

Antenna software initiative: Many universities produce good antenna software, which is only used within that university. The objective of ACE is to make more software available. Major activities include: common data file formats (EDI), interfaces for combining different codes, benchmark structures, integration of software.

Antenna measurement techniques: The purpose is to facilitate the consolidation and expansion of European expertise in research and development of antenna measurements. Major activities are mapping of available test facilities, comparison of selected test facilities with common reference antennas, sharing of test facilities and best practice recommendations.

Virtual centre of excellence (VCE): An antenna Virtual Centre of Excellence (VCE) has been created. It offers remote services inside the EACN network (private section), by supporting network activities, knowledge sharing, meetings, project management, contractual aspects, etc. It also offers services outside the Network (public section), by creating an ACE Community.

The VCE home page is www.antennasvce.org which is linked, as part of the European Commission Information Society Technology, to the ACE home page www.ist-ace.org

Training and education: The objective is to make much better use of the good educatio material and good teachers already available Europe. ACE has created a European Schoo Antennas (ESoA), giving about 12 courses p year, ACE also creates a virtual laboratory allow use of educational software on the w (VALab).

Dissemination and knowledge transfer management: The knowledge within ACE is disseminated to the scientific community, to users and to industry. There are special ACE sessi and invited papers at most of the maj conferences, and we create a new Europ international antenna conference, EuCAP. T first EuCAP took place in Nice in Novembe 2006. The following ones, for 2007 and 2008, a being planned.

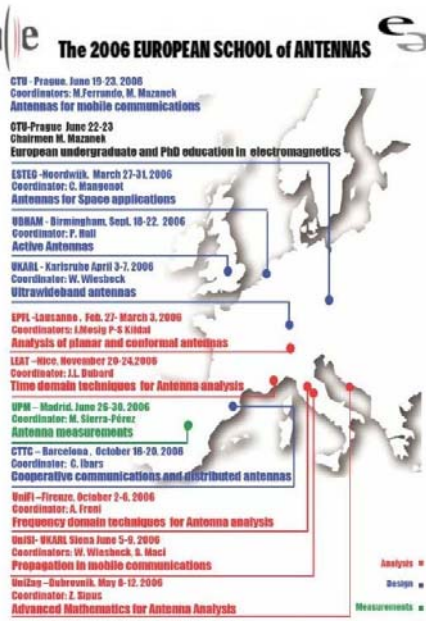

ORGANIZATION

ACE has 51 participants from 17 Europea countries. 323 researchers and 130 PhD stud are involved. Most of the participants a universities, but many are companies a institutes.

The major decisions are taken by the Governing Board, in which each participant has one vote. It meets at least once a year and is chaired by the Network Coordinator. The technical work is lead b the Executive Board, chaired by the Technical Coordinator. The work is divided into 12 activities Each activity has an activity leader, who is also part of the Executive Board. The activities are divide into work packages, with work package leaders. There are 35 work packages in total. A Scientific Council of outstanding international experts helps ACE to reach its goals.

CONTACTS

Contact points:
Network Co-ordinator: Bruno Casali, IDS, b.casali@ids-spa.it
Technical Co-ordinator: Per Ingvarson, Saab Ericsson Space, per.ingvarson@space.se
Vice Technical Co-ordinator: Juan R Mosig, EPFL, Juan.Mosig@epfl.ch
Technical Secretary: Peter Balling, ASC, pballing@asc-consult.com

CONCLUSION

ACE will harmonize the antenna research in Europe. Horizontal activities will make reuse of tools an technologies possible, and vertical activities will assess the relevance of the research. ACE will al increase the interactions between the antenna research and engineers within Europe, and it will be contact point for international cooperation, thus also giving increased possibilities for worldwid interactions.

Antennas are the key elements in the new wireless world. They will interact more with othe components in the systems. ACE will combine systems and electromagnetic knowledge, and fo research to relevant areas.

ACE has been well received by the antenna community, and given good marks by the Europe Commission. ACE will continue after the funding by EC, the creation of a European Association Antennas and Propagation (EurAAP) and thus to have a lasting impact on European antenna resea EurAAP is open to global cooperation with other organisations in the antenna field.

Global Navigation Satellite System (GNSS)

(A vast system of systems providing global positioning, navigation & timing information to scores of user community)

Dr. S Pal, Outstanding Scientist
Programme Director, Satellite Navigation Program
Chairman, GAGAN Project Management Board
Deputy Director, Digital & Communication Area
ISRO Satellite Centre, Bangalore-17

ABSTRACT

Global Navigation Satellite System (GNSS) is a vast system of systems, providing global positioning, navigation and timing information to scores of users in oceans, land, air and even in space. The present talk traces the history of navigation, evolution of navigation satellites, the three present constellations and a world scenario in this direction. The talk also dwells upon Indian efforts in the area of Navigation Satellites and its future plans.

Proceedings of APSYM2006, Dec. 14-16., Dept. of Electronics, CUSAT, India.

About Solar Panels and Printed Antennas

Fred E. Gardiol[(1)], Stefano Vaccaro[(2)], and Juan R. Mosig[(1)]
(1) LEMA-EPFL Station 11, CH-1015, Lausanne, Switzerland,
E.mail: fred.gardiol@hispeed.ch, juan.mosig@epfl.ch, http://itopwww.epfl.ch/LEMA
(2) JAST Antenna Systems SA, PSE-EPFL, CH-1015, Lausanne, Switzerland
E.mail: stefano.vaccaro@jast.ch, http://www.jast.ch/

Abstract: *By depositing photovoltaic solar cells on top of printed antennas (patch or slot antennas), one can use the same surface twice. This hybrid approach presents a particular interest for space applications, but can also prove valuable for many other autonomous microwave systems. Original developments made at the Laboratory of Electromagnetism and Acoustics (LEMA) and at the JAST Company, with the sponsorship of the European Space Agency (ESA) are reviewed.*

Introduction: When microwave transmitters, receivers or relays are to be installed in remote locations, providing the electrical power required for their operation may present some difficulties. It may be difficult — when not downright impossible — to draw a power line, generators need fuel and maintenance, dry cells must be replaced, and batteries have to be recharged from time to time. The most interesting approach is then to use a renewable energy source, such as solar energy collected by photovoltaic cells. In the remotest locations, in particular in space, solar panels are currently being used to feed a variety of satellites.

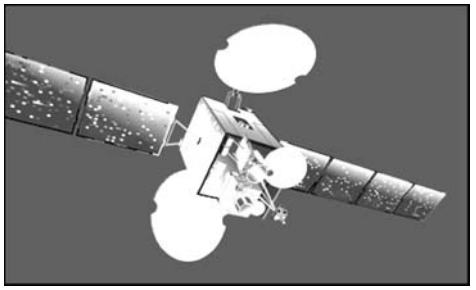

The solar panels and the antennas of the satellite shown in the figure require considerable surfaces, and must be deployed separately when the satellite reaches its orbit. It would be very interesting, both in terms of reliability and weight, to regroup these elements upon a single surface — using printed antennas arrays. One could simply place solar cells and antennas next to one another, but it would be far better, if at all possible, to combine them, for instance to deposit or glue the solar cells on top of the antennas, saving considerable "real estate" [1, 2]. This approach was developed at LEMA, and several prototypes were built. In 1999 ESA selected LEMA as prime contractor for the realization of an Advanced SOLar ANTenna (ASOLANT). Within six years, the project met all the requirements of ESA, from the feasibility study, through the first prototypes, all the way to the industrial realization, by the society RUAG (formerly HTS) based in Zürich, Switzerland. The antenna was space-qualified and inserted into a small satellite, launched from Plesetsk on 27th of October, 2005.

Some basic requirements must be satisfied when one wishes to combine an antenna with solar panels. The solar cells must of course be placed on top, where they can collect the sunlight (transparent antennas have not been designed as yet…). Antennas must more or less be realized on flat surfaces, so that printed antennas are generally selected. Furthermore, the antenna performance must not be dramatically perturbed by the presence of the solar cells on top of them — this limits somewhat the choice and the organization of the assembly.

The first prototypes, called SOLANT (SOLar ANTennas) were realized with the SSFIP structure originally developed by Mr. J.-F. Zürcher at LEMA [3]. This multilayer structure provides broadband performance and is relatively insensitive to perturbations. The near field in the vicinity of the antenna surface was visualized by the modulated scatterer technique [4], which indicates where conductors may be placed without perturbing the operation of the antenna. At the Microtechnique Institute of Neuchâtel University the group of Professor Arvind Shah deposited amorphous silicon solar cells on patch antennas [1].

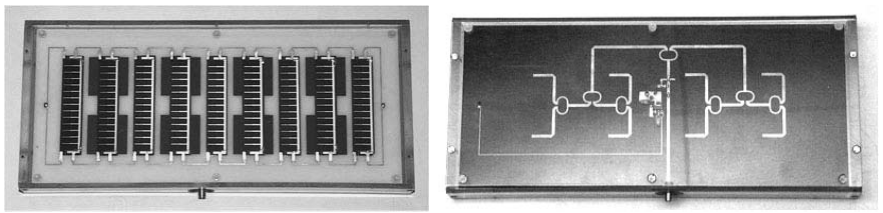

The SOLANT 4 prototype (front and back, 1999), shown here, is a a 4□2 linearly polarized broadside subarray working at 4 GHz, with an MMIC amplifier integrated on the back side — this is an autonomous design, because the electronics on the back side are powered by the 9 solar cells, which provide 100 mW at 5 V. The gain is 13 dBi for the passive antenna, and it reaches 30 dBi with the MMIC amplifier. A good antenna match and a wide bandwidth were achieved, and the effects of the cells on the antenna were controlled by a careful design: solar cells must not be placed too close to the radiating edges, because the presence of the connecting conductors would perturb the radiation from the array. This requirement limits the surface available for the panels, and thus the collected power, when patch antennas are used. The overall thickness of the complete assembly is 8 mm.

In the present design, the microstrip circuit on the backside feeds all the patches with the same amplitude and phase, so that the main lobe is pointed perpendicularly to the plane of the antenna. To modify the antenna pattern, different line lengths would provide different phases, while an unequal power distribution can be obtained with asymmetric power splitters. With the help of electronically tunable phase shifters, one can also steer the main beam.

For optimal power collection, the solar cells should always face the sun, while the antenna beam must be pointed towards the counter station in the communications link. The two directions coincide only in some particular locations, and some compromises must be made elsewhere. This is a drawback of solar antennas, which either reduces the performances — for the solar cells and/or the antenna — or actually restricts their use to particular geometrical conditions. Steering the beam in a phased array may somewhat improve the situation. ESA announced the SOLANT concept at the Salon du Bourget in Paris, in 2001.

Further developments showed that solar cells could cover a much larger part of the available surface when slot antennas are used, providing thus a more efficient operation [5]. In addition, solar cells can then be deposited or glued directly on the ground plane of the slot antennas, which presents a definite advantage for their practical realization. On the minus side, slot antennas have a somewhat narrower frequency bandwidth than SSFIP antennas, but this does not significantly affect their usefulness. Several antennas were designed using this approach, also using amorphous silicon cells. Measurements showed that the presence of the cells did not significantly modify the radiation pattern of the antennas.

In space applications, the surfaces available are severely limited, so that the highest possible efficiency is mandatory. For this reason, the more efficient GaAs cells replaced the amorphous silicon cells, and commercial space-qualified devices were selected. The antennas were then called “Advanced” SOLar ANTennas, i.e. ASOLANT.

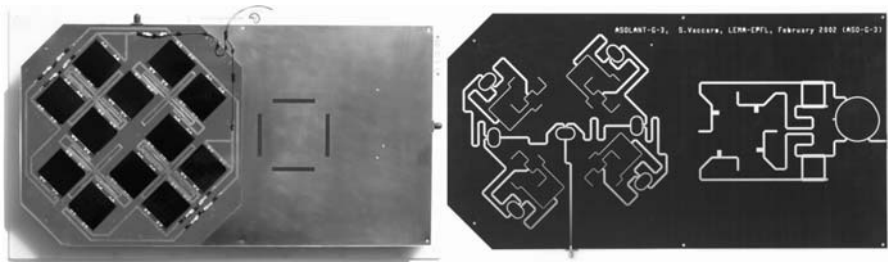

The above figure shows the two sides (front and back) of the A-SOLANT-G-3 design, which is a wideband (19%) circularly polarized transmit/receive antenna system, with enhanced directivity. Four radiating cross-slots with an elaborate feed network provide the circular polarization. The twelve standard GaAs solar cells modules deliver 4.29 watts. Galileo Avionica in Italy performed the space-qualified integration of the cells, and the cost of a single panel reached 35’000 euros (space is expensive!). To prevent back radiation from the slots, a metallic reflector is placed at 3 cm from the back of the antenna.

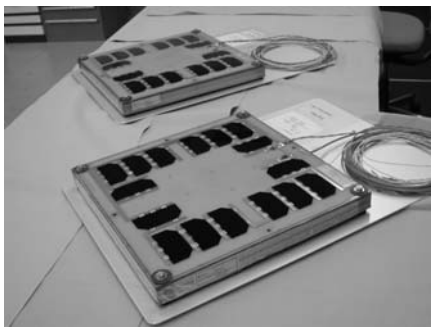

An in-flight experiment to validate ASOLANT antennas **in space** is in progress. Two different antennas were designed and manufactured (shown in the above figure), one for GPS reception and the other one for S-Band beacon transmission. Both units use slot aperture radiators embedded in identical mechanical structures. The GPS antenna generates an omnidirectional radiation pattern with right-handed circular polarization, fulfilling NavStar

specifications. The S-Band Beacon antenna is based on a four element circularly polarized array providing 6 dBi of gain. Two identical solar panels form the upper layer of the antenna structure, making use of GaAs solar cells arranged in two strings. The two panels provide a peak power of 10 Watts each. The antennas were launched, fixed to a COSMOS payload adapter, on the 27th of October, 2005 and are still in operation ten months later [7].

Back to earth: the concept of hybrid solar antennas is also of interest for terrestrial applications, to design roof tiles for the simultaneous power generation and reception of satellite TV, isolated base stations for mobile telephones, burglar alarms, sea buoys, and other systems. Low cost devices can be realized, making use of flexible technologies — with the antennas cut on solar cell foil. Recently developed is a circularly polarized 6□1 antenna phased array with a 15° beam tilt, with an integrated MMIC amplifier. Six solar cell modules deliver 821 mW (122 mA @ 7 V).

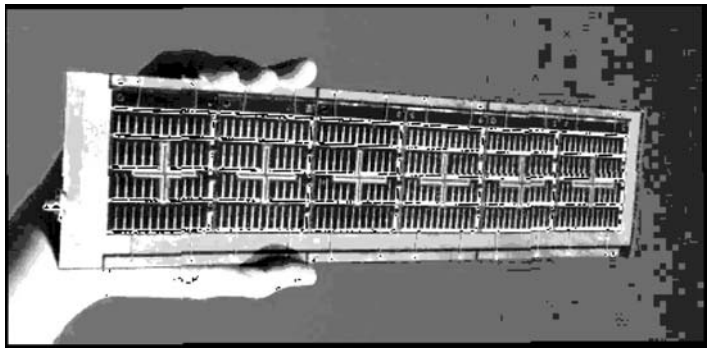

Acknowledgements:
This research was partially supported by the European Space Agency (ESA-ESTEC) under contract AO/1-3543/99/NL/SB. More on the website: http://itop.epfl.ch/LEMA/Asolant/

Reference:

[1] M. Tanaka, Y. Suzuki, K. Araki, R. Suzuki, "Microstrip antennas with solar cells for microsatellites," Electronics Letters, Vol. 31, No. 4, pp. 263-266, 1996.
[2] S. Vaccaro, P. Torres, J.R. Mosig, A. Shah, J-F. Zürcher, A.K. Skrivervik, F. Gardiol, P. de Maagt, L. Gerlach, "Integrated solar panel antennas," Electronics Letters, vol. 36, no. 5, pp. 390-391, 2000.
[3] J.-F. Zürcher, F. Gardiol, "Broadband Patch Antennas," Norwood, MA, USA: Artech House, 1995.
[4] J.-C. Bolomey, F. Gardiol, "Engineering Applications of the Modulated Scatterer Technique," Norwood, MA, USA: Artech House, 2001.
[5] S. Vaccaro, J.R. Mosig, P. de Maagt, "Two advanced solar antenna 'SOLANT' designs for satellite and terrestrial communications," IEEE Transactions on Antennas and Propagation, vol. 51, No. 8, pp. 2028-2034, 2003.
[6] S. Vaccaro, J.R. Mosig, P. de Maagt, "Patch and slot antennas integrating high efficiency GaAs solar cells for space applications," Journées Internationales de Nice sur les antennas (JINA'02), Nice, 12-14 November 2002, vol. II, pp. 117-120, 2002.
[7] S. Vaccaro, C. Pereira, J. R. Mosig, P. de Maagt, "Flight models of advanced solar antennas 'ASOLANT', submitted for publication.

Proceedings of APSYM2006, Dec. 14-16., Dept. of Electronics, CUSAT, India.

DIELECTRIC RESONATOR ANTENNA FOR WIRELESS AND OTHER APPLICATIONS

Yahia M. M. Antar
Canada Research Chair in Electromagnetic Engineering
Department of Electrical and Computer Engineering
Royal Military College of Canada, Kingston, Ontario, K7K 7B4, Canada.
E-mail: antar-y@rmc.ca

Abstract: *Dielectric resonator antennas (DRA's) have recently emerged as new alternative in wireless devices, with many advantages compared to conventional metallic antennas. Considerable amount of research, dealing with aspects such as analyzing their resonant modes, radiation characteristics and various feeding schemes, has demonstrated that, these "new" radiators could offer new and attractive features in antenna design. In order to effectively make use of the advantages of these radiators, it is essential to provide means for easy fabrication and integration with new types of microwave circuitry. A brief review of the topic is presented in this article. Also some novel designs and new directions of reserach in this field are described.*

I. Introduction

Pioneering investigations with dielectric resonator as a radiator date back to1983 [1]. Since then, several groups of researchers all over the world have been active in this area of research and have made remarkable advances during last two decades. The main goals have been to explore efficient feeding techniques, methods to obtain wide and ultra wide impedance bandwidth, high gain, new geometrical shapes for improved features, etc. Indeed, from the very beginning of the DRA research, it has been regarded as a variant of the planar radiator like a microstrip patch, but compared to microstrip it is more advantageous in many aspects and also there are some disadvantages too. Some new efforts have also been made to integrate microstrip patches with a DRA to acheive better performances. As has been demonstrated, DRAs offer a high degree of flexibility and versatility over a wide frequency range, allowing for the designer to suit many requirements. Many new elements and arrays with attractive characteristics for wireless and other applications have been implemented, and a description of some of these are included in the literature [2].

Even after so many new developments and achievements, practical design and implementation of these DRAs are still challenging in many cases. In recent years, more focus has been given to enhance antenna bandwidth and gain which are more relevant to the requirement of modern wireless applications. Many new techniques have been explored, most of them apply various composite and hybrid type structures [3]-[9]. Further, due to the mature technology of microwave integrated circuit (MIC) and monolithic microwave integrated circuit (MMIC) on silicon, on-chip DRAs [10] have received a great deal of attention because they can reduce the size, weight and cost of many transmit and receive systems. All these aspects are discussed in the limited scope of the article.

II. Various Geometries of DRAs

One of the attracting features of a DRA is that it can assume any one of a number of shapes. Moreover the mode of operation and performance of a DRA can be varied by selecting a DR with desired structure. Hence a number of DRA geometries have been experimented. The first systematic, theoretical and experimental study was made on cylindrical disk DRA geometry. Later geometries [11-15] such as split cylinder, sectored cylinder, cylindrical rings, metallised DRAs, triangular, rectangular, notched rectangular DRA, chamfered DRA conical, elliptical, spherical, hemispherical, spherical cap, tetrahedral, perforated DRA, stepped DRAs and hybrid DRAs have been reported (see few such geometries shown in Fig. 1).

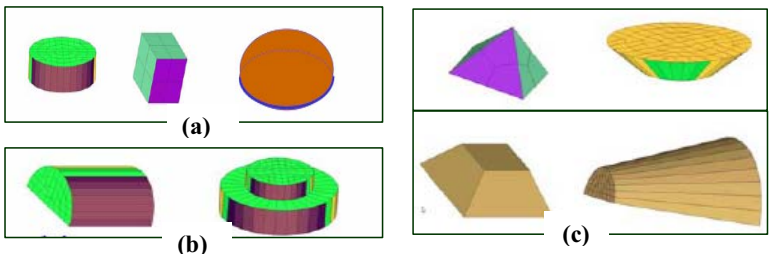

Fig.1 Various shapes of DRAs explored (a) Basic shapes, (BW = 5-10%) (b) combination of basic shapes, (BW = 15-20%) (c) arbitrary shapes, (BW = 30-40%)

III. Broadband DRAs for wireless communications

The important and most common methods adopted for the fabrication of wide band DRAs can be broadly classified as (a) single element methods (b) multiple DRAs and (c) hybrid antennas. Few examples of single element geometries developed to yield broadband characteristics are shown in Fig. 1 (b) and Fig. 1 (c). Yet another novel geometry (shaped DRA), which attracted recent attention is shown in Fig. 2. The geometry is an inverted L-shaped cylindrical DRA, which is examined [9] for wireless applications covering four wireless bands as labelled in Fig. 3. About 40 % impedance bandwidth with 8 dBi peak gain is demonstrated.

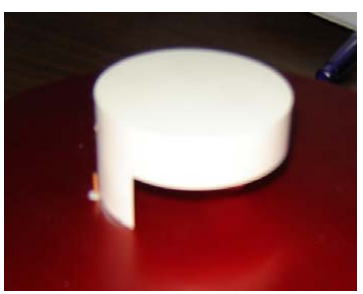

Fig.2. Shaped DRA: DCS-WLAN bands

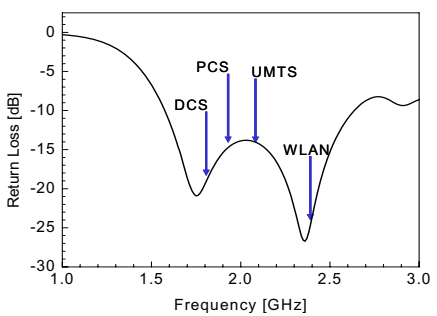

Fig.3. Return loss characteriscs of shaped DRA with possible bands of operation

Multiple DRAs:

One example of multiple DRA [4] is shown in Fig. 4, where a monopole type radiation pattern is generated using a compact four-element cylindrical DRA. It has been explored with $HEM_{11\delta}$ mode to radiate over nearly 30 % matching bandwidth as demonstrated in Fig. 5.

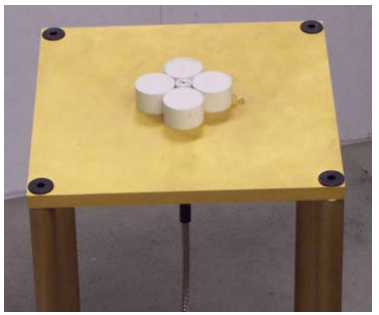

Fig.4. Four-element composite cylindrical DRA

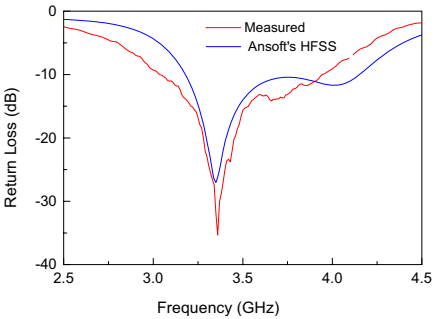

Fig.5. Variation of S11 with frequency of ultra-wide band four-element DRA

Hybrid configurations:

Mainly two types of DRA based hybrid antenna structures are reported. They are (i) DRA-loaded microstrip patch antennas and (ii) DRA-loaded monopole antennas. The reports shows that, the bandwidth performance of microstrip antenna can be improved to reach about 24% by loading with a DRA [16].

One of the recent technique developed to have an ultra wide band hybrid antenna [6] is shown in Fig. 6. Here a dielectric ring resonator surrounds a monopole antenna. Both are centered at the same axis and the monopole acts as a quarter-wave length radiator as well as a feed for DRA. The DRA is designed to excite in the dominant $TM_{01\delta}$ mode, which has a circular symmetric field distribution similar to that of monopole. An ultra-wide bandwidth has been achieved with monopole-type radiation pattern over the entire bandwidth. Here both the monopole and the DRA resonate along with an intermediate resonance and cause the wide matching bandwidth (see Fig. 7).

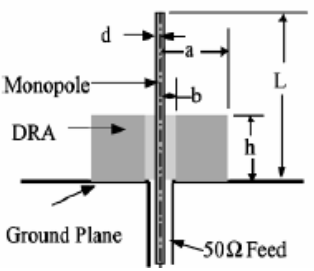

Fig. 6. Cross-sectional view of Monopole-fed hybrid DRA

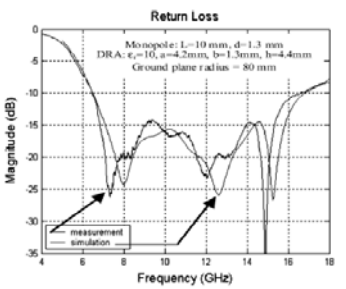

Fig. 7. Wide band characteristics of monopole-fed DRA

IV. High Gain Planar Antennas

An aperture-coupled dielectric resonator fed by a microstrip line as the feed system, and a substrate-superstrate resonance geometry with $\varepsilon_{r2} >> 1$ has been investigated recently [17] for high gain applications (see Figs. 8-11). By proper choice of the parameters ε_{r1}, ε_{r2}, h_1 and h_2, the radiated power is maximized with negligible power losses to the higher order surface wave modes and therefore resulting in a gain enhancement and radiation efficiency improvement of the antenna. The gain has been measured over a wide range of frequencies (Fig 10) and the value was found to be as high as 18 dB. The radiation pattern of the antenna in the *E*-and *H*-planes are shown in Fig. 11.

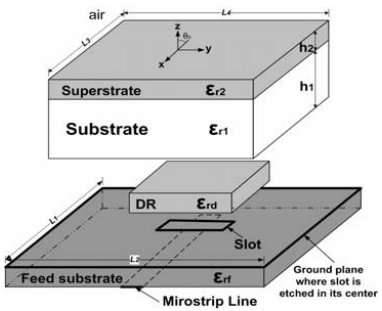

Fig. 8 Geometry of high gain planar DRA $\varepsilon_{rd} = 10$, $\varepsilon_{r1} = 1$, $\varepsilon r_2 = 25$, $h_1 = 8.57$ mm, $h_2 = 0.85$ mm, $L_3 = L_4 = 55$mm, $L_1 = L_2 = 85$mm

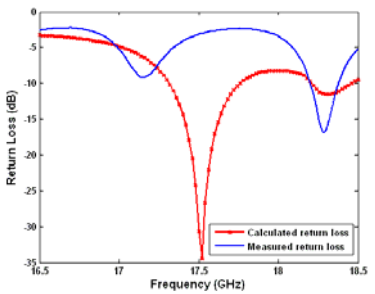

Fig. 9 Return loss plot of high gain planar DRA

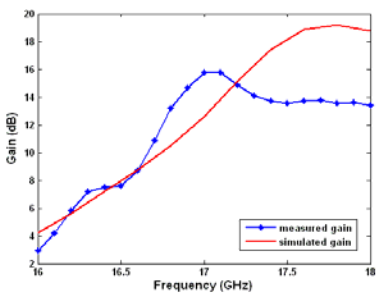

Fig. 10 Simulated and measured gain of DRA described in Fig. 8.

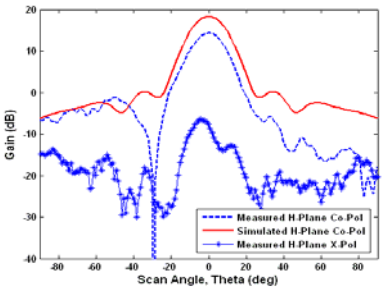

Fig. 11 Simulated and measured E and H-plane radiation patterns of DRA described in Fig. 8.

V. Integrated DRAs

Over the past few years, integrated antennas have received a great deal of attention because they can reduce the size, weight and cost of many transmit and receive systems. However, several performance factors of the antennas, such as gain, efficiency, bandwidth, operational range etc. deteriorate due to the high permittivity, conductor losses and surface wave effects generated by the substrate material. The integration of a high permittivity dielectric resonator in place of the metallic antenna could be a possible

solution to reduce the source of some of the losses on conducting silicon since they are devoid of any conductor loss and surface wave effects. Moreover, the high permittivity of the DR forces the electromagnetic field to concentrate more on its surface and hence reduces the extend of fields fringing towards the conducting silicon substrate. With this view, recently we have designed [18] an integrated dielectric resonator antenna excited using differential dipole launcher for 40 GHz applications. The reported antenna on high resistance silicon (resistivity = 100 Ω-cm) has a gain of 2.4 dB and 77% radiation efficiency. More recently, a new high gain on-chip dielectric resonator antenna for 60 GHz radio wireless systems was designed [19]. The DRA launcher is an open circuit co-planar waveguide fabricated on conductive silicon substrate. The growth of DR on the silicon surface was performed by a novel, ultra-low temperature sol-gel composite hydrothermal process. A rectangular integrated dielectric resonator antenna fabricated on conductive silicon (resistivity = 10 Ω-cm) to operate in the fundamental $TE_{11\delta}$ mode has an impedance bandwidth of 1897 MHz at 59.56 GHz and 3.2 dB gain with 54 % radiation efficiency, whereas for the same antenna on high resistance silicon (resistivity = 100 Ω-cm), the transmission gain increased to 5.3 dB and radiation efficiency reached 89%.

VI. Conclusions

In this article, some of the recent developments in the design and fabrication of dielectric resonator antennas are decsribed. A brief review of the novel geometries, and hybrid DRAs for ultra-wide band operations, planar DRAs for high gain operations and on-chip DRAs on conductive silicon for millimeterwave applications are discussed. This will open a scope for further investigations with some new results.

References

[1] S. A. Long and M. W. McAllister, and L. C. Shen, "The resonant cylindrical cavity antenna" IEEE Trans. Antennas and Propagat., Vol. 31, pp.406-412, 1983.

[2] K. M. Luk and K. W. Leung, "*Dielectric Resonator Antennas*", Ed. J. R. James (Resrach Studies Press Ltd. Baldock, Hertfordshire, U. K.), 2003.

[3] A. A. Kishk, "Experimental study of broadband embedded dielectric resonator antennas excited by a narrow slot," IEEE Antennas and Wireless Propagat. Lett., Vol. 4, pp.79-81, 2005.

[4] D. Guha and Y. M. M. Antar, "Four-element cylindrical dielectric resonator antenna for wideband monopole-like radiation," IEEE Trans. Antennas and Propagat., Vol. 54, No. 9, pp. 2657-2662, Sept. 2006.

[5] M. Lapierre, Y. M. M Antar, A. Ittipiboon and A. Petosa, "Ultra wideband monopole/dielectric resonator antenna," IEEE Microwave and Wireless Components Lett., Vol. 15, no. 1, pp. 7 – 9, Jan. 2005.

[6] A Ittipiboon, A. Petosa, S. Thirakoune, D. Lee, M. Lapierre and Y. M. M. Antar, "Ultra wideband antenna," US Patent No. 6,940,463 B2, Sept. 2005.

[7] D. Guha, Y. M. M. Antar, A. Ittiboon, A. Petosa, and D. Lee "Improved design guidelines for the ultra wideband monopole-dielectric resonator antenna," IEEE Antennas and Wireless Propagat. Lett., Vol. 5, pp. 373-376, Dec. 2006.

[8] D. Guha and Y. M. M. Antar, "New half-hemispherical dielectric resonator antenna for broadband monopole-type radiation," IEEE Trans. Antennas and Propagat. (to appear in Dec. 2006).

[9] L. C. Y. Chu, D. Guha and Y. M. M. Antar, " Air gap loaded ultra wideband dielectric resonator antenna for commercial wireless bands" Int. Sym. Antenna Technology and Applied Electromagnetics & Canadian Radio Sciences (URSI/CNC) Montreal, July, 2006.

[10] D.B. Rutledge, D.P. Neikirk and D.P. Kasilingam *"Integrated circuit antennas"* in Infrared and Millimeter-waves, K.J. Button, ed; Chapt. 1, Vol. 10, New York: Academic 1983, pp. 25.

[11] A. A. Kishk, Y. Yin and A. W. Glisson, "Conical dielectric resonator antennas for wide-band applications" IEEE Trans. Antennas and Propagat. Vol. AP-50, No.4, pp. 469-474, 2002.

[12] A.A. Kishk, Microwave and Opt.Technol. Lett. Vol. 37, No.6, pp. 454, 2003.

[13] A.A. Kishk, **"**Wide-band truncated tetrahedron dielectric resonator antenna excited by a coaxial probe", IEEE Trans. on Antennas and Propagat. Vol. 51, No.10, pp. 2913-2917, 2003**.**

[14] A.Petosa, A.ittipiboon and S.Thirakoune, **"**Perforated dielectric resonator antennas", IEE Electron. Lett., Vol. 38, No.24, pp.1493-1495, 2002.

[15] R.Chair, A.A. Kishk. L.F. Lee and C.E. Smith, **"**Wideband flipped staired pyramid dielectric resonator antennas", IEE Electron. Lett., Vol. 40, No.10, pp. 581-582, 2004.

[16] E.K.N. Yung, W.S.S. Lee and K.M. Luk, Microwave and Opt. Technol. Lett., Vol. 7, No. 2, pp. 55, 1994.

[17] A. M. Etrugh, "High gain planar Antennas", Masters thesis, Queens University, Kingston, Ontario, Canada, 2005.

[18] P.V.Bijumon, A.P.Freundorfer and Y.M.M. Antar, "Integrated dielectric resonatorantennas on conductive silicon substrate for millimeter wave applications" Proc. of Antennas and Propagation Symposium, Kochi, India, Dec. 14-16, 2006.

[19] P.V.Bijumon, A.P.Freundorfer, M.Sayer and Y.M.M. Antar, "High gain on-chip Dielectric resonator antennas using silicon technology for millimeter wave wireless links" (submitted to Canadian conf. on Computer and Electrical Engineering, VB, Canada, April, 2007).

Proceedings of APSYM2006, Dec. 14-16., Dept. of Electronics, CUSAT, India.

The European School of Antennas

Stefano Maci[(1)]*, Anja Skrivervik** [(2)]*,*
(1) University of Siena, Department of Information Engineering, Siena, 53100, Italy, *macis@dii.unisi.it*
(2) LEMA, EPFL-STI-ITOP Station 11 CH1015 Lausanne Switzerland, *anja.skrivervik@epfl.ch*

Abstract: *The European School of Antennas (ESoA) is a new model of geographically distributed school with the objective to reinforce the European training and research in wireless applications. ESoA feasibility has been successfully proved in the FP6 Network of Excellence "ACE - Antenna Centre of Excellence", using a highly qualified integrated set of advanced post-graduate courses, distributed in the most accredited European research centres on antennas. The general objectives of the School are: 1. reinforcing the European excellence in the systems air interface with emphasis on antenna components; 2. creating an effective speciality formative offer to complete individual PhD curricula of European students; 3. increasing the ties in wireless research and development between Universities and Industries on a European scale; 4. facilitating the interchange of ideas among early stage researchers and trainers as well as among young researchers, thus increasing the future mobility and synergy.*

Introduction: In the last few years, Europe is loosing the leading role in the wireless systems and antennas that was occupied some years ago thanks to the GSM success. One of the motivation is probably due to the fact that the explosion of research and technology development has not been accompanied by an equivalent increase of post graduated level educational activity. Many Universities are changing their curricula in view of delivering new Bachelor-Master degrees at the horizon 2006-2007, motivated by the wish to adapt to new European rules as codified by the Bologna declaration. The countries which have already changed their University organization have concentrated the resources on undergraduate level, without adequately restructuring the PhD. For lack of financial resources, the PhD courses organized by the various Universities are often concerned with transverse subjects, in order to group students of different scientific formation. If on one side this can enrich the interdisciplinary knowledge, it also leads to a lack of specialized training offer. We moreover assist to a diminishing of the education background in the electromagnetic area, mostly due to the increasing teaching of communication standards and computer languages. This imposes to recover the basic educational background at the PhD stage, resuming the necessary advanced knowledge to do research and enforcing the process of training of the engineer specialized in antennas. The previous aspects, accompanied by the demand of exchange of research information and by the needs of high-level scientific qualification, motivated the constitution of the proposed model of a geographically distributed European School of Antennas (ESoA).

Institution	Acronym	
Univ. degli Studi di Siena	UNISI	IT
Univ. degli Studi di Firenze	UNIFI	IT
Kungliga Tekniska Högskolan	KTH	SE
Danmarks Tekniske Universitet	DTU	DK
Helsinki Univ. of Tecnology	TKK	FI
Univ. De Marnes La Vallee	UMLV	FR
Inst. National des Scie. Appl. de Rennes	IETR	FR
Univ. degli Studi di Roma "La Sapienza"	SAPIENZA	IT
Politecnico di Torino	POLITO	IT
Univ. Politecnica de Catalunya	UPC	ES
Univ. Politecnica de Madrid	UPM	ES
Univ. Politecnica de Valencia	UPV	ES
Chalmers Tekniska Högskola	CHALMERS	SE
Ecole Polytechnique Fed. de Lausanne	EPFL	CH
Netherlands Org. for Appl. Scientific Res.	TNO	NL
Univ. de Nice Sophia Antipolis	UNSA	FR
IMST GmbH	IMST	D
Ingegneria dei Sistemi	IDS	IT
Univ. of Naple "Federico II"	UNINA	IT
Univ. of Karlsrhue	UNIKARL	D
Czech Technical University	CTU	RO
Univ. of Zagreb	UNIZAG	HR
Univ. of Birmingham	UNIBHAM	UK
Centre Tecnologic de Telecom. de Catalunya	CTTC	ES

Table 1: Institutions belonging to ESoA

The European School of Antennas, a new model of geographically distributes school: Th European School of Antennas is a coordinated and integrated conglomerate of post-graduate courses distributed in the most accredited European research centers on antennas and wireless systems. Th initiative started in 2004 from a group of institutions composed by Universities and industria research centers of 12 different European countries belonging to a Network of Excellence of the sixt framework program called "Antenna Center of Excellence" [1]. Presently the group has been enlarge up to date to the 24 institutions listed in Table 1.

#	Name	Location and period	Host insti-tutions	Co-ordinators	Main Teachers	Total trainers and % from the host instit.	Students and % from the host country
1	High Frequency techniques and Traveling-Wave Antennas	Siena, February 21–23 Rome, February 23-26	UNISI Sapienza	S. Maci F. Frezza	S. Maci, F. Frezza, P. Pathak, A. Toccafondi, G. Manara, M. Albani, A. Galli	15 80%	34, 91%
2	Phased Arrays and Reflectarrays	The Hague, April 11-15, 2005	TNO	G. Gerini	H. Legay, C. Renard, J. Johasson, L.Pettersson, G. Vecchi, G. Gerini, A. Neto, S. Maci, J. Encinar, M. Gillard	12, 16%	27, 55%
3	Artificial EBG surfaces and metamaterials	Gothenburg, April 18-22, 2005	Chalmers	P.-S. Kildal	P.-S. Kildal, S. Maci, S. Tretyakov, K. Mahdjoubi	7, 42%	21 24%
4	Design and analysis of large reflector antennas and lens antennas	Copenhagen, May 9-13, 2005	TICRA	H. H. Viskum	H. H. Viskum, M. Lumholt, S. B. Sorensen, S. Maci, P-S. Kildal R. Sauleau	7 57%	11 18%
5	Microwave and millimeter wave antenna design	Rennes, May 16-20, 2005	IETR	K. Mahdjoubi	K. Mahdjoubi, J.-M. Laheurte, M. Grzeskowiak, M. Himdi, M. Drissi, O. Lafond, R. Sauleau	11 81%	13 54%
6	Antenna measurements at millimetre and submillimetre wavelengths	Helsinki, May 23-27, 2005	TKK	A. Räisänen	A. Räisänen, A. Lehto, J. Ala-Laurinaho J. Mallat J Häkli, T Koskinen A Lönnqvist, V Viikari	8, 100%	14 79%
7	Compact antennas	Barcelona, June 6-10, 2005	UPC	L. Jofre	L. Jofre, J. M. Rius, A. Skrivervik, D. Manteuffel, W. Simon, S. Blanch	6 50%	33 21%
8	Antenna measurements	Madrid, June 20-24, 2005	UPM	M. Sierra	M. Sierra, O. Breinbjerg, P.-S. Kildal, A. Räisänen, L. Foged, M. Calvo Ramon, L. de Haro Ariet, J. L. Besada Sanmartin,	10 60%	24 50%
9	MIMO Communication System and Antennas	Stockholm, Sept. 5-9, 2005	KTH	B. Lindmark	B. Lindmark, P. Vainakinen, C. Icheln,P. Suvikunnas, P. Zetterberg, E. Larsson, M. Bengtsson, C. Anton	12 50%	19 58%
10	Antennas for news systems of mobile communications	Valencia, Sept. 14-17, 2005	UPV	M. Ferrando	M. Ferrando, A. Valero, L. Jofre,A. Cardama, S. Blanch,M. Sierra Perez,L. de Haro Ariet, M. Sierra-Castaner	9 22%	24 70%
11	Computational EM for antenna analysis	Torino, Sept. 19-23, 2005	POLITO	G. Vecchi	G. Vecchi, R. Graglia, A. Freni, S. Maci, R. Loison, R. Mittra	6 33%	23 65%
12	Analysis of planar and conformal antennas	Lausanne Febr. 27- March 3, 2006	EPFL	J. Mosig P.-S. Kildal	J. Mosig, P.-S. Kildal, A. R. Djordjevic, Z. Sipus, G.Vandenbosch, P. Persson, S. Raffaelli	7 14%	27 25%
13	Antennas for Space Applications	Noordwijk March 27-31 2006	ESA/ ESTEC	M. Sabbadini	C. Mangenot, M. Sabbadini, P. de Maagt, L. Salghetti Drioli, J.S. Prowald, J. Sandberg, P.M: Besso, A. Guidoni, H.H Viskum, N.Rando C. Buck	12 67%	26 43%
14	Ultra Wideband Antennas	Karlsruhe, April. 3-7 2006	UKARL	W. Wiesbeck,	W. Wiesbeck, W. Sörgel, C. Sturm, F. Jondral, M. Eisenacher, L. Jofre, J. Romeu, A.Neto	8 62%	22 18%
15	Advanced Mathematics for Antenna Analysis	Dubrovnik, May 8-12, 2006	UNIZAG	Z. Sipus S. Maci	S. Maci, Z. Sipus, A. Freni, G. Vecchi, J. Bartolic	5 40%	22 25%
16	Propagation in mobile communication	Siena May 5-9, 2006	UNISI	W. Wiesbeck, S. Maci	W. Wiesbeck, S. Maci, S. Knozer, T. Funken, M. albani	5 40%	22 23%
17	Antennas for mobile communication	Prague June 19 -23, 2006	CTU	M. Ferrando M. Mazanek	M. Ferrando,M. Mazanek L. Jofre, ...	11 27%	17 71%
18	Antenna measurements	Madrid, June 26-30, 2006	UPM	M. Sierra	M. Sierra, O. Breinbjerg, P.-S. Kildal, A. Räisänen, L. Foged, M. Calvo Ramon, L. de Haro Ariet, J. L. Besada Sanmartin,	11 55%	28 68%

TABLE 2 Summary of the ESoA course in the period Jan 2005-August 2006

Table 2 presents the courses done in the period Jan 2005/August 2006, with statistics of students and teachers. The overall number of students registered to the courses was 407, with an average of 23 students per course. The major part of the students have followed one course; some students have followed more than one up to four courses. Due to the economic facilities of the institutions belonging to ACE, about the 70% of the students came from the ACE institutions. However, European students external to ACE have had exclusive access to 5 grants for each course to cover entirely their mobility and fee expenses. An average of 50% of the students came from the host country. Concerning with the teachers we had 162 among teachers and assistants, 50% belonging to the institution hosting the course. These data confirm the international character of the school.

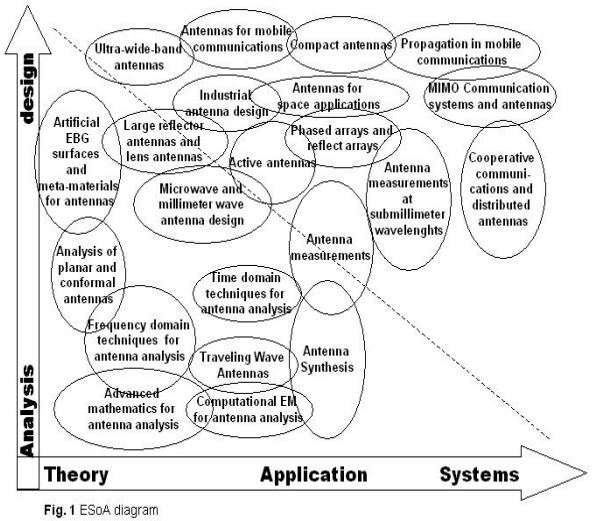

Fig. 1 ESoA diagram

Content of the courses: an overall view of the ESoA courses, comprising courses will be given in 2007, is given in the diagram in Fig. 1, where the position of the courses is related to their content. The diagram presents a vertical axis that ranges from analysis to the design and a horizontal axis ranging from theory to wireless systems through application. Broadly speaking, the diagram could be divided in two parts from a bisector diagonal from the upper-left to the lower-right corner. The courses positioned in the lower part (analysis and theory) are more devoted to students interested in basic research (like academic PhD students) and the ones in the upper part (design, application and systems) are more appealing for industrial PhD students and post-graduate students oriented toward the industrial applications. Small overlapping of topics can occur and serve to guarantee a uniform continuity to this unitary framework. The courses of theory and analysis (lower/left part of the diagram) have the main objective to give to the PhD students the advanced concept on the analysis method for antenna and electromagnetic scattering problems and the basic and advanced knowledge for developing software tools for antenna modeling. These courses synthesize all the modern computational techniques based on integral equations (method of moments), and on differential equations (finite difference time domain and finite element methods), as well as on the high-frequency and hybrid techniques based on asymptotic methods. The basic methodologies are completed by a course about antenna synthesis and optimization and by two courses about measurements techniques, which provide the techniques from microwave to submillimeter wave frequencies. The courses in the upper/right part of the diagram are more concerned with antenna design and wireless systems. These course provide to the students design methods inside the application framework (upper/right corner) of radio wireless fixed and mobile communications, radar, remote sensing, aeronautics and space, transport, security, with special emphasis on a) System for mobile communications and propagation channels in urban environment b) MIMO systems c) Cooperative communications d) Space systems of communications . The courses on antenna design (upper/left corner) advanced issues on the classical antenna typologies like reflector antennas and feed-horns, lens antennas, phased array antennas, planar and conformal antennas, traveling wave antennas. Furthermore, they include the emerging antenna technology as a matter of research with special emphasis on i) Active and integrated antennas, ii) Multibeam and adaptive antennas iii)

Antenna with digital beamforming, iv) Ultrawideband antennas v) EBG and metamaterial antennas, vi) Compact antennas vii) Fractal antennas.

Format of the courses: Each course extends for one week; this format allows the students to organize their mobility without sacrificing their research activity at home, and leaving open the possibility to extend their stay in the host institution – assumed excellent in the specific area – to complete their research training. The courses should be held during 5 days, with possible home-assignments for extra-credits. The typical format of one course consists on 5 hours of lectures on the morning, and 3-4 hours of other activities in the afternoon These activities will be concerned with exercises, reading of key papers on topical subjects, laboratory experiments (when available), panel discussions and student presentations. The total structure thus consist on about 25 hours of lectures and 15-20 hours of other activities. The lectures will be provided by people from the host Universities and from speakers from the other team members. Participation of key-note speakers from industries and Universities external to the group is also foreseen. All the speakers have been already identified and they are presented in Appendix A. Each course, which foresees a written assessment test, provides to the students from 3 to 4 ECTS credits, depending on the quantity of additional home assignments.

WEB support: The school is supported by a dedicated WEB site [2], which is a special section of the "Virtual Center of Excellence" (VCE) [3], the official WEB site of ACE. The relevant items are: a) Centralizing and facilitating as much as possible the on line registration of the students; b) Organizing and making publicity and dissemination actions; c) Collecting the electronic material to support the school (namely: i - Electronic forms of the speaker presentations, ii- Homework, iii- Evaluation forms, iv- Notes and reference to textbooks, v- Output of the exams); d) Collecting the progress report ad final documentation e) Updating the list of the grants for the students; f) Showing the availability of research positions in the EM research area within Europe; g) Creating and updating of the Virtual Antenna Laboratory (VALab) with the purpose to render available the free-ware educational software or software developed by the partners [4].

Concluding remarks: The European School of Antennas constitutes a new geographical distributed post-graduate school model, successfully experimented in 2005 and 2006. The school will continue till the end of 2009 under financial support of a Marie Curie Action project.

Reference

[1] "Network of Excellence contract FP6-IST 508009 and FP6-IST 026957, acronym ACE (Antenna Center of Excellence)
[2] VCE section of EsoA: htpp://www.antennasvce.org/education/ESoA/view
[3] Virtual Center of Excellence (VCE), ACE web site: htpp://www.antennasvce.org
[4] VCE section VALab: web site htpp//valab.det.unifi.it/new/valab

Modeling of planar multilayered structures comprising finite dielectric bodies.

Francisco J. Nuñez Calvo[(1)], Juan R. Mosig [(2)], and Anja K. Skrivervik[(2)]
(1) SPEAG, Zeughausstrasse 43, CH-8004 Zurich, Switzerland, E.mail: nunez@speag.com
(2) LEMA, Ecole Polytechnique Fédérale de Lausanne, Station 11, CH-1015 Lausanne, anja.skrivervik@epfl.ch

Abstract: *This paper presents a method to model finite dielectric bodies embedded in multilayered media. The method used is based on the mixed potentials integral equation technique, where the finite dielectric bodies are represented by equivalent electric and magnetic currents. Examples of an antenna and a dielectric resonator are presented .*

Introduction

This paper presents a general model for the electromagnetic analysis of arbitrary shaped conductors and dielectric bodies embedded in stratified media. The problem is set in term of electric/magnetic field integral equations, which are translated into mixed potential integral equations and solved using the Method of Moments. The dielectric bodies are modeled by electric and magnetic surface currents, using the equivalence theorem.
The method presented here is based on the general theory clarifying the use of vector and scalar potentials in multilayered structures including oblique current sources [1]. The so called "C" formulation of this theory was extended to include dielectric bodies of finite dimensions, by the means of the equivalence theorem [2].

Theory

The general problem we want to resolve is depicted in figure 1. It consists of a set of metallic shapes and dielectric bodies embedded in a multilayered dielectric structure, and illuminated by an incident electromagnetic field $\mathbf{E_i}$, $\mathbf{H_i}$.
The total field in this problem can be decomposed as :

$$\mathbf{E}_{tot} = \underbrace{\left(\mathbf{E}_i^{out} + \mathbf{E}_i^{in}\right)}_{\text{incident wave}} + \underbrace{\left(\mathbf{E}_s^{out} + \mathbf{E}_s^{in}\right)}_{\text{scattered wave}} \quad ; \quad \mathbf{H}_{tot} = \underbrace{\left(\mathbf{H}_i^{out} + \mathbf{H}_i^{in}\right)}_{\text{incident wave}} + \underbrace{\left(\mathbf{H}_s^{out} + \mathbf{H}_s^{in}\right)}_{\text{scattered wave}}$$

where $\mathbf{E}_i^{out}$ and $\mathbf{E}_i^{in}$ are the incident electric field placed inside and outside any dielectric body, and $\mathbf{E}_s^{out}$ and $\mathbf{E}_s^{in}$ are the scattered fields generated in the external and internal volume with respect to the dielectric bodies. The application of the principle of equivalence [2] to this problem leads us to the substitution of the dielectric bodies by equivalent magnetic and electric scattered currents, $\mathbf{M}_s$ and $\mathbf{J}_s$, that reproduce the external/internal scattered field in our objects. We apply then the boundary conditions on the metallic surfaces and the surfaces of the dielectric bodies, and we obtain, along the classical formulation of the conducting surfaces the following mixed potential integral equation system on the surfaces of the embedded dielectric bodies :

$$\hat{\mathbf{n}} \times \left[\mathbf{E}_i^{out} - \mathbf{E}_i^{in}\right] = j \int_{S_e} \left(\bar{\bar{\mathbf{K}}}_A^{out} + \bar{\bar{\mathbf{K}}}_A^{in}\right) \cdot \mathbf{J} dS' - j \int_{S_e} \nabla \left(K_\phi^{v,out} + K_\phi^{v,in}\right) \nabla \cdot \mathbf{J} dS' + \int_{S_e} \nabla \left(\bar{\bar{\mathbf{G}}}_{EM}^{out} + \bar{\bar{\mathbf{G}}}_{EM}^{in}\right) \nabla \cdot \mathbf{M} dS'$$

$$\hat{\mathbf{n}}\times\left[\mathbf{H}_i^{out}-\mathbf{H}_i^{in}\right]=j\int_{S_e}\left(\bar{\bar{\mathbf{K}}}_F^{out}+\bar{\bar{\mathbf{K}}}_F^{in}\right)\cdot\mathbf{M}dS'-j\int_{S_e}\nabla\left(K_\phi^{w,out}+K_\phi^{w,in}\right)\nabla\cdot\mathbf{M}dS'+\int_{Se}\nabla\left(\bar{\bar{\mathbf{G}}}_{HJ}^{out}+\bar{\bar{\mathbf{G}}}_{HJ}^{in}\right)\nabla\cdot\mathbf{J}dS'$$

where the dyads $\bar{\bar{\mathbf{K}}}_A^{in,out}$, $\bar{\bar{\mathbf{K}}}_F^{in,out}$ are the magnetic and electric vector potentials, $K_\phi^{v,(in,out)}$ and $K_\phi^{w,(in,out)}$ are the electric and magnetic scalar potentials inside or outside the dielectric bodies. $\bar{\bar{\mathbf{G}}}_{EM}^{in,out}$ and $\bar{\bar{\mathbf{G}}}_{HJ}^{in}$ are the electric and magnetic field Green's functions for magnetic respectively electric current sources. S_e are the surfaces of the dielectric bodies

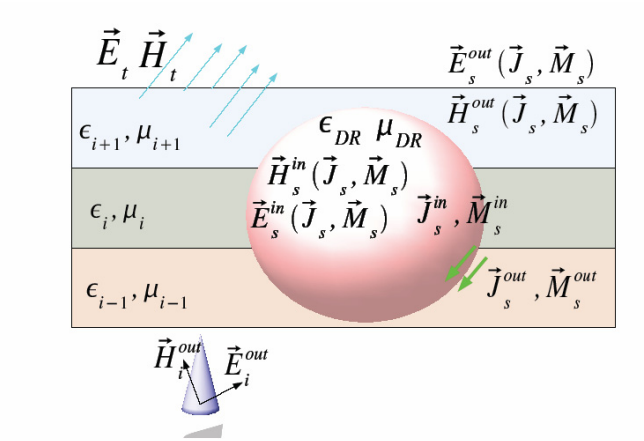

Figure 1 : General structure (conductors omitted for the sake of clarity).

The Green's functions shown above have to obey following rules : $\bar{\bar{\mathbf{K}}}_*^{in}=\bar{\bar{0}}$ when source and observer are outside any dielectric object. $\bar{\bar{\mathbf{K}}}_*^{out}=\bar{\bar{0}}$ when source and observer are inside any dielectric object. If the observer is inside (resp. outside) a dielectric body while the source is outside (resp. inside) this specific body, all the Green's functions are set to 0. If the source and the observer are placed on the surface of a dielectric body, by continuity we use $\bar{\bar{\mathbf{K}}}_*^{in}+\bar{\bar{\mathbf{K}}}_*^{out}$ in the integrands of the integral equations.

These integral equations and the classical one defined on the conductors embedded in a stratified medium are solved using a Method of Moments, where RWG basis functions and a Galerkin testing scheme are used. It has to be noted that in order to obtain a solution which is efficient in the point of view of computing time, an accurate and fast procedure to evaluate the MoM matrix terms by the integration of the corresponding Green's functions was introduced. It is based on a pre computation of all the relevant Green's functions, followed by an efficient interpolation. This is performed by removing the quasi static terms of the Green's function in the spectral domain [3], and then interpolating a continuous and smooth function in the spatial domain.

Results

The first example is a high dielectric resonator coupled to a microstrip line via a slot. The structure was proposed by J. Chen et al in 2001 [4]. The geometry of the structure is depicted

in figure 2, and its input impedance is shown in figure 3. Our results are compared to the simulated and measured result of [4], and the agreement is very good. The small discrepancies between the results of the two simulation methods and the measurement are certainly due to the tolerances in the definition of the permittivity of the dielectric resonator.

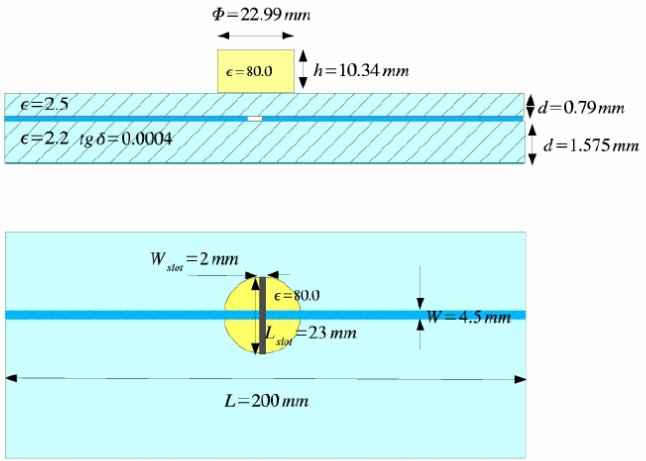

Figure 2: Dielectric resonator

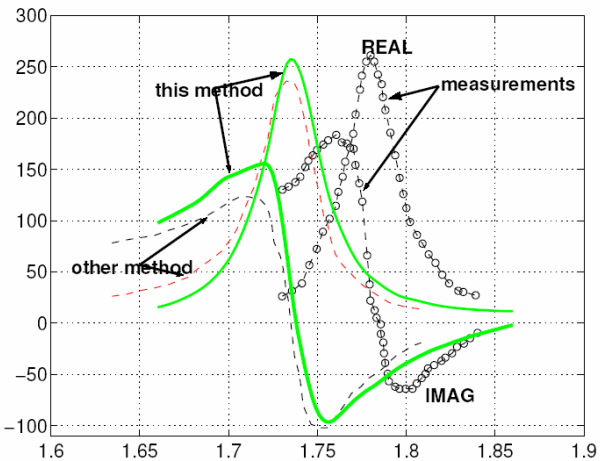

Figure 3 : Real and imaginary parts of the input impedance of the dielectric resonator of figure 2. Our method compared to the simulations and measurements of [4].

The second example is a very broad band antenna called TAROS proposed by the Middle East Technical University at Ankara [5], and is a good test for a simulation tool, as it is quite complex to model : It includes curved conductive surfaces and finite dielectric bodies over a microstrip structure. The antenna was built in our lab, and is depicted in figure 4. Its

reflection coefficient is shown in figure 5. Again, we see a very good agreement between simulation and measurement.

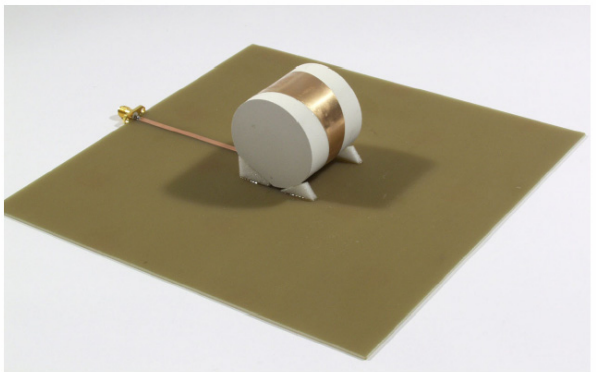

Figure 4 : Photograph of realized TAROS antenna.

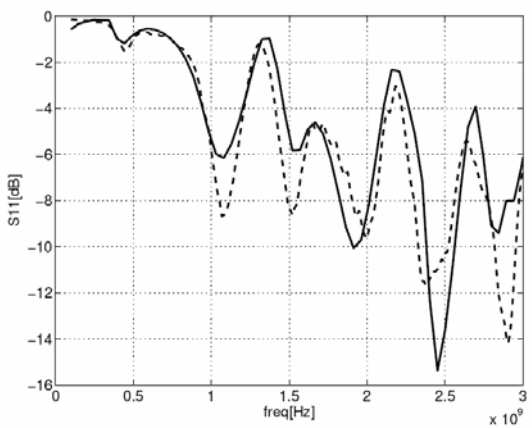

Figure 5 : Simulated (solid line) and measured (dashed line) reflection coefficient of the realized TAROS antenna.

References

[1] K.A. Michalski and D. Zheng, "Electromagnetic scattering and radiation by surfaces of arbirary shape in layered media, part I : Theory", IEEE Trans. on Antennas and Propagation, Vol. 38, pp. 335-344, 1990.
[2] C.A. Balanis, "Antenna theory, analysis ans design", John Wiley, 1988.
[3] J.Van Bladel, "Singular Electromagnetic fields", Oxford University Press, 1991.
[4] J. Chen, A. A. Kishk and A.W: Glisson, "Application of a new MPIE formulation to the analysis of a dielectric resonator embedded in a multilayered medium coupled to a microstrip circuit", IEEE Trans. on Microwave Theory Tech., Vol. 49, pp. 263-279, 2001.
[5] Çağlar Yardım, "Design and Construction of Annular Sector Radiating Line(Anserlin) and Microstrip Helix Radiating Line (Misherlin) and Tapered Rolling Strip (TAROS) Antennas ", Ms. Sc Thesis, Middle East Technical University, Ankara, ref. 062117110523 , 2001.

Proceedings of APSYM2006, Dec. 14-16., Dept. of Electronics, CUSAT, India.

Advanced Substrate Technologies for Millimetre-Wave Interconnections and Antennas

Charles Free
Advanced Technology Institute
University of Surrey
Guildford, Surrey GU2 7XH, UK
C.Free@surrey.ac.uk

Abstract The paper will give an overview of the properties of modern substrates that are available for millimetre-wave circuits and antennas. Included are details of the fabrication processes, together with an assessment of the fabrication errors associated with the different processes, and their influence on practical circuits. Since precise knowledge of substrate parameters is essential for accurate circuit design at very high frequencies, the paper includes a discussion of the characterization techniques that are available for millimetre-wave frequencies.

Introduction: The rapid expansion of commercial wireless communication systems into the microwave spectrum has generated a need for low-cost circuit materials, giving good high frequency performance. Associated with this is the need for manufacturing processes that can combine low production costs with the relatively high circuit quality needed for microwave applications. Circuits and processes based on ceramic substrate technology have traditionally met the requirements of the microwave designer. However, whilst this technology may offer very high performance, it tends to be expensive.

A recent derivative of the traditional ceramic technology is LTCC (low temperature co-fired ceramic). Whilst this technology has a relatively well developed infrastructure for low frequency applications, it is still a relatively recent innovation for microwave work. Recent studies [1,2] have shown that LTCC technology can offer the required materials quality at frequencies up to 100GHz. An additional advantage of LTCC is that, because it is essentially a multi-layer technology, it offers the circuit designer the opportunity to design in three dimensions. So the designer can take advantage, for example, of broad-wall coupling in filters and couplers, which leads to higher quality components. Also, a multilayer approach enables the designer to achieve a high degree of circuit integrated, with buried passives, and close coupling to integrated antennas.

A more recent development at millimetre-wave frequencies is the use of polymer substrates. These substrates can be handled in a similar way to traditional PCB, with the polymers coated with copper, and then photo-patterned using normal etching techniques. The manufacturers of these materials also claim some success in laminating the polymers, so as to form an alternative to LTCC.

Materials requirements: The key requirements for materials used for microwave and millimetre-wave planar circuits are:
CONDUCTORS: low bulk resistance, good surface finish, fine line geometries
DIELECTRICS: small loss tangent, well defined and stable permittivity.

The general procedure for measuring the performance of the materials is to first determine the loss tangent and dielectric constant (relative permittivity) of the dielectric,

using a resonant cavity technique. Then dielectric is patterned with conductor, to form a microstrip or coplanar transmission line, and from the transmission line measurements the conductor loss can be deduced.

Dielectric measurement: The traditional method for measuring the microwave properties of dielectrics is to use a waveguide resonant cavity. The resonant frequency, f_O, and Q-factor of the cavity are first measured with the cavity empty, and then re-measured with a sample of the dielectric material in the cavity. From the changes in resonant frequency and Q-factor, the properties of the dielectric can be deduced. One of the problems encountered with this technique for modern dielectrics, is that the changes in f_O and Q are small, because the materials are low-loss, and significant errors can arise because of the need to dismantle the cavity to insert the dielectric sample. A technique to overcome this problem is to use a cavity with a slit, as shown schematically in figure 1.

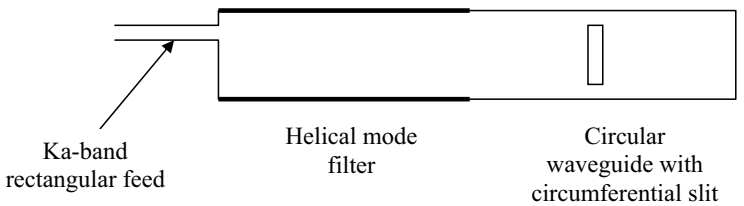

Figure 1 System for dielectric measurements at mm-wave frequencies

Using circular waveguide cavities enables to user to take advantage of the low loss properties of the TE_{01} mode, giving high Q-factors and sensitive measurements. With this type of measurement it is usually necessary to include a mode filter, such as a helical waveguide section, to suppress the unwanted modes. It should be noted that a circumferential slit will not interrupt the current flow of the TE_{01} mode. Figure 1 depicts the situation in which the circular resonant cavity has a circumferential slit. The slit enables the sample to be inserted into the cavity without the need for dismantling, and providing the slit does not interrupt the current flow in the waveguide walls it will have minimum effect on performance. The circular waveguide technique, with the slit for inserting the sample has proved a reliable method, giving accurate, repeatable results up to 40GHz; examples of results for typical modern substrate materials are given in Figure 2.

The data shown in Figure 2 provides a useful comparison of the potential of three substrate technologies for millimetre-wave applications. As expected, alumina shows the lowest loss, but printed dielectric and LTCC also provide very good values of loss

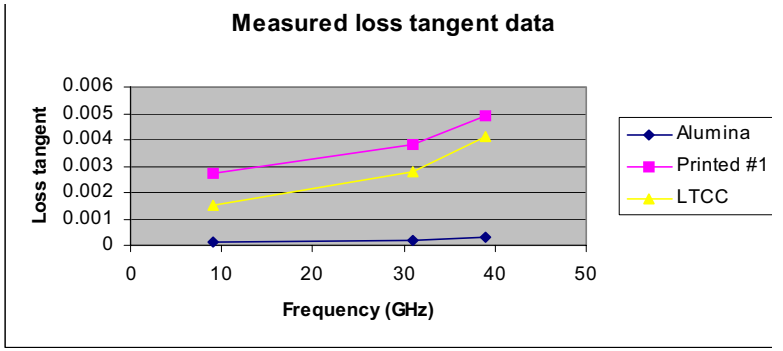

Figure 2 Data from circular cavity measurement technique

Fabrication technologies: The microwave designer has a range of substrate technologies to choose from:

(1) Alumina: using thin or thick film techniques for conductor patterning, alumina provides a high quality substrate, with well established characteristics; it tends to be expensive, but can provide very high performance, especially if the conductors are photo-patterned

(2) Photoimageable thick-film: by including a UV-sensitive photo-vehicle within the printed pastes, this technology combines the low-cost advantages of thick-film with the high line/space resolution that can be obtained from photo-patterning

(3) LTCC: a well-established technology at lower frequencies, LTCC materials are now available with excellent characteristics for use up to 100GHz; the technology offers two particular advantages. These are: (i) the ability to make multilayer circuits, with opportunities for 3-D microwave design, and close integration of the antenna into a transceiver package, and (ii) low-cost, due to the parallel processing of the individual layers, and the single firing stage.

(4) Polymer: recent advances in polymer technology have produces substrates with good microwave performance, that can patterned easily with etchable copper conductors, and which have the potential for lamination. Also, they provide flexibility in the substrate, which can be an advantage when designing planar antennas.

Characterization of planar interconnections: The resonant ring structure is a well known test pattern for characterising planar interconnections. However, it has three main disadvantages for use at millimetre-wave frequencies: (i) it can only provide data at a series of discrete and harmonically related frequencies; (ii) it is difficult to compensate for the errors associated with the coupling gaps; (iii) it is difficult to produce in a coplanar format, which is the preferred interconnection format for mm-wave application. An alternative to the resonant ring is the 'meander line' structure, shown in Figure 3.

The essence of the meander line measurement is that the transmission characteristics of two lines are different lengths are measured, and from this data the loss/mm and the effective dielectric constant can be deduced [1]. The advantages of the method are that there are no loading errors, and broadband measurements are possible.

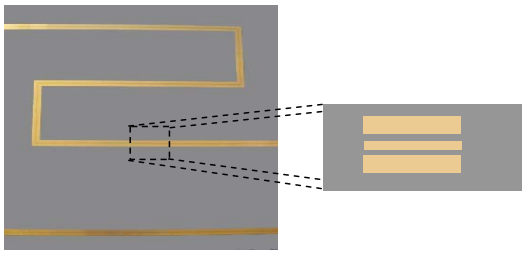

Figure 3 Test structure for broadband measurements on coplanar lines

Reduction in surface losses: At millimetre-wave frequencies approaching 100GHz, surface losses can become the dominant source of loss in planar interconnections. Recent work [2] using the test structure shown in Figure 3 has shown that significant benefit can accrue by flash-etching (or chemical polishing) the conductors as the final stage in the production process. Typical results are shown in Figure 4.

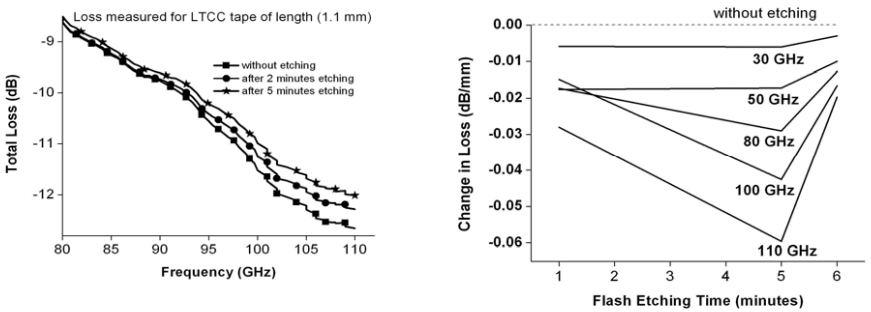

Figure 4 Effects of chemical polishing on interconnection loss

The results presented in figure 4 give a clear indication of the benefits of chemical polishing, particularly at the higher mm-wave frequencies. Moreover, the technique is simple and does not detract from the benefits of low cost fabrication processes, such as thick-film and LTCC.

Conclusions: Two useful techniques have been established through practical measurements: (1) the use of the low loss TE_{01} mode in circular waveguide for mm-wave dielectric measurements; (2) the use of chemical polishing to reduce surface losses at high mm-wave frequencies.

References

1. Free, C. 'Techniques for Assessing the Performance of Circuit Materials at Microwave and Millimetre-Wave Frequencies', Proc Materials Research Society Symposium, Boston, USA, Nov 2003

2. Henry, M., Free, C. 'Characterization of LTCC Substrates at Millimetre-Wave Frequencies up to 110GHz' Proc. 7th Millimetere-Wave International Symposium, Espoo, Finland 2006.

Proceedings of APSYM2006, Dec. 14-16., Dept. of Electronics, CUSAT, India.

Requirements of Microwave Tubes and Future Trends

S.N. JOSHI
Central Electronics Engineering Research Institute, Pilani (Rajasthan)

Microwave Tubes still play an important role, in spite of competitive incursion from solid-state devices. This is particularly true for devices in high power and high frequency regime of the rf spectrum. These devices have significant applications in strategic, communication, scientific, industrial and bio-medical sectors which includes radar, electronic warfare (ECM and ECCM), missile guidance and tracking, remote sensing, high power microwave weaponry, material processing and sintering, plasma heating, particle accelerators, domestic heating including cooking industrial heating, hypothermia etc. The ADSS programme of Department of Atomic Energy and India's participation in International ITER project for fusion application has further strengthened the country's requirement in respect of these devices. The ADSS programme requires very high average power ($\triangle$ 1 MW) devices based on slow wave interaction at low frequencies and ITER Project requires 1.0 MW CW rf power at very high frequencies (120 to 170 GHz). The space sector in the country requires very efficient (> 65%), long life (> 15 years) and reliable devices meeting the stringent environmental conditions. On the other hand for electronic warfare devices, having extremely large band width (2-3 octave) are required. For plasma heating and particle accelerators, again large average power is required.

The advancement in the area of Microwave Tubes for attaining very high power up to very high frequencies has been possible due to availability of advanced CAD tools, advent of new materials, high energy magnets, high current density cathodes etc. New cooling concepts and growth in fabrication technology has further paved the way for the advancements.

Recently an exercise has been undertaken in the country for assessing the requirement of these devices for the coming 10 years and beyond that. For this, all concerned agencies (developers, users, production and academic) were approached for evolving a position paper in the area of Microwave Tubes. An overwhelming response was received, indicating huge requirement of these devices in foreseeable future. The list included space qualified and broadband Traveling-wave Tubes, high average and pulse power klystrons, miniature klystrons, pulse power magnetrons, gyrotrons, high power ($\triangle$ 1 MW) Tetrodes, Thyratrons etc.

Though the requirement of conventional (-based on slow wave phenomenon) tubes would remain in the foreseeable future, however, efforts are being made in the country for further enhancing their performance capabilities by adding new concepts. These include devices like Gyrotrons and Gyro TWTs (-based on the fast-wave phenomenon), Microwave Power Modules that are combination of vacuum and semiconductor technologies, vacuum microelectronic devices based on fabrication of rf structures using semiconductor technologies like MEMs and LIGA and developing field

emitters. Multi-beam technology is another important area, which uses multi-beam electron gun in place of a single electron gun. This improves the efficiency and lowers the operating voltage. Technology has very important role in development of these sophisticated devices particularly for attaining high average powers to a tune of 1 MW or more. As regard very high frequency devices in THz range, it would be possible only with the amalgamation of vacuum and semiconductor technologies taking advantage of both of them.

As on today, only limited agencies are involved in the design and development of these devices and Bharat Electronics in Bangalore is the only production agency. Efforts are also being made by an agency in private sector named Pilani Electron Tubes and Devices Private Limited, Sangrur. However, they are at present only developing non-microwave Tubes. To meet the futuristic demands of the country, these Centers would have to be strengthened both in manpower and infrastructure.

Use of Computational Methods in Teaching Electromagnetics

Ramesh Garg
Department of Electronics and Electrical Communication Engineering
Indian Institute of Technology Kharagpur,
India – 721302
garg@ece.iitkgp.ernet.in

Abstract: *In this paper, we propose the use of computational methods to make teaching and learning of electromagnetics as a memorable experience. The source codes developed for the purpose should help improve basic concepts, and analytical capability. A few case studies are presented.*

Introduction: The best way to learn a computer language is to start writing a computer programme. Similarly, the best way to learn any subject is to start solving the related problems. If the subject of electromagnetics is taught like this, it may be better understood. The solution methods may be classified as analytical method or computational/ numerical method. The analytical methods in electromagnetics include separation of variables, series expansion, use of Green's function, variational formulation, analysis in spectral domain, etc. to meet the demands of various types of problems. These methods basically solve boundary value problems and require knowledge of vector algebra, vector calculus, integrals, derivatives, series, etc. The vector algebra and calculus are very unpopular with the students. Additionally, a number of concepts like vector potentials, equivalent currents; electric and magnetic polarizabilities, equivalence principle, reaction, etc are introduced to simplify the analytical solution of the problem. The additional topics put a burden on the curriculum and confuse a student in the absence of proper grasp. The device geometry is idealized in shape, size and dielectric loading to arrive at the analytical solution, whereas most of the problems of engineering interest are not confined to these limited configurations. One of the most frustrating aspects of problem solving in electromagnetics is that analytical methods do not lead to systematic and general approach to problem solving. For example, multilayered dielectric configuration can best be handled in spectral domain.

The computational methods do not suffer from the limitations of analytical methods. The popular computational methods are: finite difference method (FDM), finite difference time domain (FDTD) method, finite element method (FEM), method of moments (MoM), boundary integral method (BEM), mode matching, transmission line matrix (TLM) method, etc. The computational methods are general in nature and not specific to a particular problem because the methods have been developed for a particular type of differential or integral equation. The differential equation for electromagnetic problems is of the type $\nabla^2\varphi + k^2\varphi = g$. It is an inhomogeneous wave equation. Setting $k = 0$ gives the Poisson's equation and $g = 0$ also gives Laplace's equation. Maxwell's equations are used as such in FDTD. These differential equations should be put in vector form to make them more general.

The integral equations may be derived either from the differential forms or by using Green's function. In this general framework, the individual problems are addressed through the geometry, boundary conditions and properties of dielectric medium. The analysis based on computational methods therefore becomes general in nature and one can write general software once the computational method has been selected. The use of software besides taking care of hand calculations can address another important difficulty in electromagnetics. This is the problem of visualization. The computed results may be plotted and displayed using colour graphics to make it interesting. Visualization of fields and currents in the device is very useful in developing and clarifying concepts. These softwares may also be used to bridge the gap not covered by analytical methods. For example, the effect of inhomogeneous dielectric loading of a device can only be answered using softwares developed for the purpose.

Elements of Computational Methods: The analysis of a problem using computational methods involves three major steps. These are shown as block schematics in Fig. 1. The first step is to discretize the device geometry in terms of cells so that the dielectric material is homogeneous in each cell and the cell size should be such that the unknown function representing field or current may be assumed to be at most linearly varying in the cell. The discretization of the geometry may be done employing an automatic mesh generator. The governing matrix equations for each cell are now used to obtain the set of simultaneous equations in the next step. The continuity of field components across the cell boundaries eliminates the extra number of equations. The boundary conditions are applied at this stage to remove some of the unknowns. The matrix equation is solved in the last step to obtain the unknown function for the problem. This function may represent potential distribution or charge density distribution for the electrostatic problem, or field distribution H_z or E_z for studying cut-off in a waveguide or current density distribution on a dipole antenna.

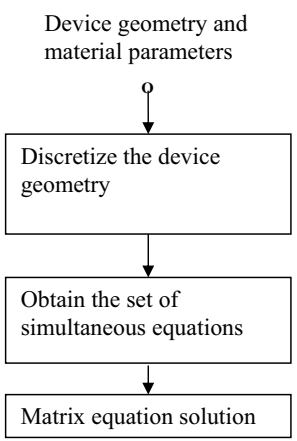

Fig.1: Basic structure of a computational method in electromagnetics

Before the computational methods are introduced, the students need to be assured that these methods are simple, at least at the basic level. By the time the undergraduate students are

ready for the study of electromagnetics they have undergone a course on numerical solution of partial differential equations in which they are taught about the finite difference method (FDM). Therefore, the study of computational methods in electromagnetics may start with FDM. We next present some case studies to put the above ideas in perspective.

Finite Difference Simulations:

- Using FDM as the basis one may attempt a simple problem of potential distribution in say a rectangular trough.
- Next, analytical solution of the above problem may be attempted. The importance of the analytical technique may be emphasized here because the solution is a closed-form solution and free from discretization errors of the FDM.
- Now make the geometry irregular shaped for which analytical solution cannot be obtained. This example emphasizes the importance of computational methods or the limitations of analytical technique.
- The trough may be partially filled with a dielectric and solved using FDM. This problem again cannot be solved analytically in general.
- The other aspects which can be taught easily using FDM include: analysis of microstrip line, etc for the capacitance per unit length and corresponding Z_0 and β. Equi-potential contours about the strip of a microstrip line are plotted in Fig.2.

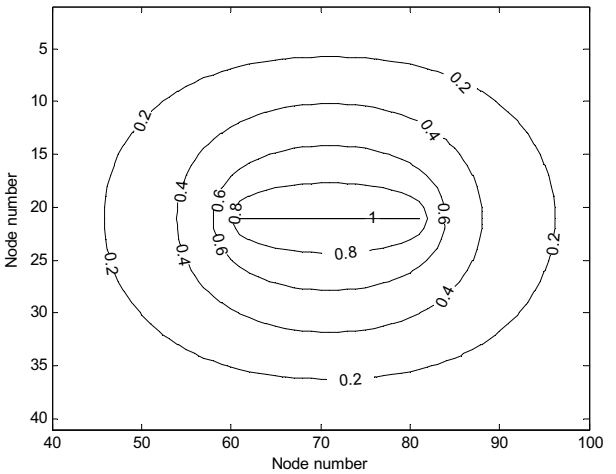

Fig.2: Equi-potential contours about the strip

FDTD Simulations: The propagation aspect is the basis of time varying signals for communications, radar, power lines, etc. This phenomenon is best illustrated in time domain although we have been using time harmonic analysis to convert the problem into frequency domain. The study of propagation of signal in a circuit or transmission line is very instructive and interesting also for the beginners. Therefore, time domain methods like FDTD and TLM are very useful in teaching and learning electromagnetics. The FDTD method is a direct implementation of Maxwell's equations and it produces behaviour of signal as a function of time and space. Fig. 3 shows the snap shot of sine wave in one-D FDTD mesh consisting

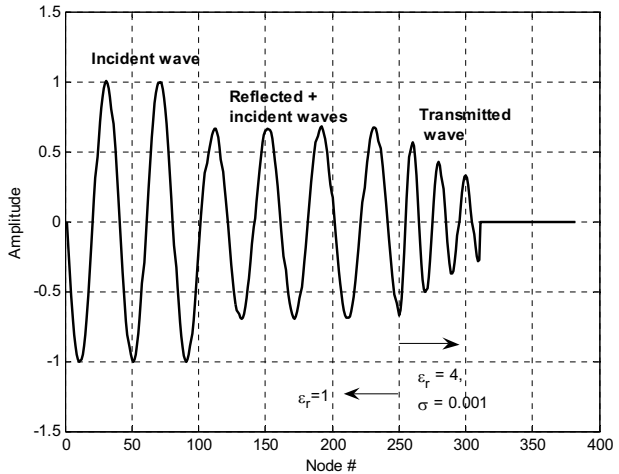

Fig.3: The time snap shot of propagating sine wave at $n = 800\Delta t$, f = 50 MHz.

of air on the left and lossy medium on the right side. One can identify separately the incident wave, reflected+incident portion, and the transmitted portions. Some more simulation studies in FDTD will be presented.

Method of Moments Simulations: The method of moment (MoM) is a useful computational approach which is analytically intensive because it requires the knowledge of Green's function for the problem. Simulation results for a centre-fed dipole are plotted in Fig. 4. Some more MoM simulations will be presented.

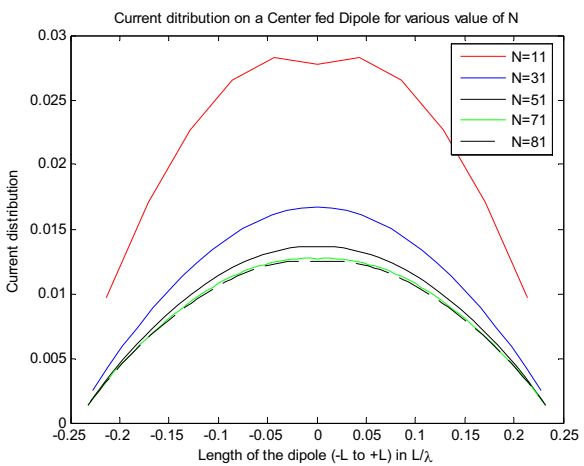

Fig.4: Simulated current distribution on a centre-fed half-wave dipole using pulse expansion and point matching

The Manufacture and Measurement of Microwave Dielectric Ceramics as Combinatorial Libraries

***Robert C. Pullar*[$], Yong Zhang*, Lifeng Chen*, Shoufeng Yang*, Julian R. G. Evans* and Neil McN. Alford*[$]**

[$] Centre for Physical Electronics and Materials (PEM), Faculty of Science, Engineering and the Built Environment (FESBE), London South Bank University, 103 Borough Road, London, SE1 0AA,UK. E-mail: r.c.pullar@lsbu.ac.uk

[*] Department of Materials, Queen Mary, University of London, Mile End Road, London, E1 4NS, UK

PEM is moving to Imperial College, London, in 2007.

Abstract

Dielectric ceramics operating at microwave (GHz) frequencies are used throughout the telecommunications industry, in filters, oscillators, antennas, resonators and other electronic components. They have applications at all levels of the technology, from satellites and base stations to mobile hand-held units, and in the future will be needed for on-board control, collision avoidance and fee collection systems in automobiles. They also have applications in security systems (millimetre wave scanners), sensors and biomedical nanotechnology.

The discovery of new dielectric materials, and the optimization of existing ceramic systems, is limited by the time consuming process of producing and analyzing samples. This innovation cycle can be greatly accelerated by the application of high-throughput combinatorial methods. Combinatorial chemistry is the rapid synthesis and analysis of large numbers of molecules, through many combinations of a relatively small number of starting compounds. This was initiated in the 1960's for the solid-phase synthesis of peptides, by Robert Bruce Merrifield at Rockefeller University [1], who later won the Nobel Prize in Chemistry in 1984 for this work. However, it took until the 1990's for industry to adopt this technique, although it is now essential for the pharmaceutical industry. Each year tens of thousands of new molecules are discovered through automated high-throughput combinatorial searches, in which both sample preparation and analysis is carried out by robots.

Joseph Hanak proposed his 'multiple sample concept' in 1970, in the Journal of Materials Science, as a way around the traditional, slow, manual, laboratory preparation procedures [2], but it took until 1995 for the first combinatorial searches in Materials Science to be carried out by Xiang, Schultz et al [3], on luminescent materials obtained by co-deposition of elements on a silicon substrate. Since then the interest in combinatorial materials science searches has increased greatly, to the extent that there are now conferences on this specific field, and after only 10 years industry is already heavily involved in the development of this technique and the development and automation of measurements suitable for combinatorial searches. However, to date most high-throughput Combinatorial Materials Science uses thin films. The work reported in this paper represents the first attempts to develop a high-throughput combinatorial technique for the manufacture and measurement of bulk ceramic samples.

Applying combinatorial methods offers the opportunity to accelerate the discovery of more efficient microwave dielectrics. High throughput methods have the potential to investigate the effects of a

1 R. B. Merrifield, "Solid Phase peptide Synthesis. I. The synthesis of a tetrapeptide", *J. Am. Chem. Soc.* **85** (1963) 2149-2153.

2 J. J. Hanak, "The multiple sample concept in materials research; synthesis, compositional analysis and testing of entire multi-component systems", *Journal of Materials Science* **5** (1970) 964-971.

3 X.-D. Xiang, X. Sun, G. Briceno, Y. Lou, K.-A. Wang, H. Chang, W. G. Wallace-Freedman, S.-W. Chen and P. G. Schultz, "A Combinatorial Approach to Materials Discovery", *Science* **268** (1995) 1738-1740.

wide range of dopants on the dielectric properties, and to optimize existing systems, encouraging the short innovation cycles that the communications technology industry requires. London South Bank University (LSBU) is currently part of a consortium of London Universities exploring methods of producing and measuring combinatorial libraries of microwave dielectric ceramics. These include polycrystalline bulk ceramic libraries made by the LUSI robot at Queen Mary University (QMU), as well as thin films produced by Pulsed Laser Deposition (PLD, at LSBU), and a hydrothermal method at QMU.

The Functional Oxides Discovery using Combinatorial Methods project (FOXD; http://www.foxd.org) uses high-throughput combinatorial thick-film production and screening techniques, with samples made using thick film technology. The project is a consortium between four London Universities; London South Bank University (LSBU), Queen Mary, University of London (QMUL), Imperial College (IC) and University College London (UCL). The samples are made by the London University Search Instrument (LUSI [4]), a fully automated, high-throughput combinatorial robot that prints samples from oxide suspensions using ink-jet printers, and also sinters the samples in a multi zone furnace at up to 1600 °C [5]. LUSI has the potential capability to produce thousands of different sintered bulk ceramic samples with varying composition in one day, as combinatorial libraries on alumna substrates. The aim is to discover new ceramics with ferroelectric, dielectric, electronic and ionic properties advantageous to industrial users. As LUSI is unique in producing polycrystalline sintered bulk samples, this will allow us to examine bulk properties, sintering, dopants, grain effects, diffusion coefficients, etc.

Left: Fig. 1, the printing bed of LUSI. This can hold 100 alumina substrates, each of which can contain 30 or 40 printed dots (1-2 mm diameter), each of a different composition. The inkjet printer can be seen on the right, and a robot arm moves the samples from printer to furnace to measurement table, all under automation.

Right: Fig. 2, the 4-zone furnace, also part of the LUSI robot.

[4] See http://www.materials.qmul.ac.uk/research/facilities/lusi/index.php for details of the LUSI robot.

[5] J. R. G.Evans, M. J. Edirisinghe, P. V. Coveney and J. Eames, "Combinatorial searches of inorganic materials using the ink-jet printer; science, philosophy and technology", *Journal of the European Ceramic Society* **21** (2001) 2291-2299.

Proceedings of APSYM2006, Dec. 14-16., Dept. of Electronics, CUSAT, India.

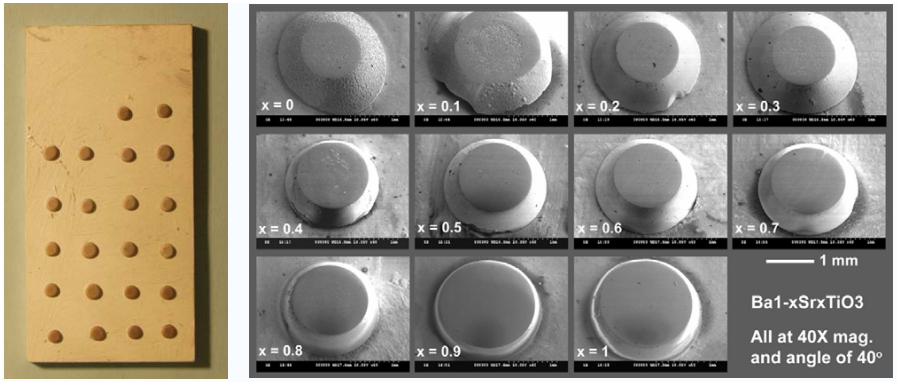

Left: Fig. 3, printed & sintered LUSI $Ba_{1-x}Sr_xTiO_3$ library. 11 pairs of dots (~2mm in diameter) with varying composition from x = 0 - 1 in 0.1 steps.

Right: Fig. 4, SEM images of polished $Ba_{1-x}Sr_xTiO_3$ library, sintered at 1350 °C / 1hr.

In this presentation, the method of sample manufacture by the LUSI robot will be described, and the synthesis of $Ba_xSr_{1-x}TiO_3$ (BST) libraries will be used as a proof of concept to demonstrate that the robot works. The LUSI robot has been demonstrated to be able to automatically print and sinter libraries of bulk ceramic $Ba_{1-x}Sr_xTiO_3$ (BST), for x = 0-1 in steps of 0.1. The samples were prepared from inks consisting of suspensions of $BaTiO_3$ and $SrTiO_3$ nanopowders, stabilised with a dispersant. The samples were printed as arrays of twenty two 2mm diameter dots, two of each composition, on alumina substrates (fig. 3). These were then sintered at 1350 and 1400 °C / 1hr by LUSI. SEM showed the samples to be well sintered, with a large 20 μm grain size for pure $BaTiO_3$ decreasing rapidly for increasing x values (fig. 4). EDXA and XRD confirmed the compositional gradient throughout the libraries (figs. 5 & 6). The permittivity and Curie point values of these libraries have been measured between 100Hz-1MHz, confirming the compositional and functional gradient, and providing expected values for T_c and ε_r in well sintered BST samples. Fig. 7 shows permittivity measured at room temperature using the parallel plate capacitor technique at 100 Hz, with the expected values being 300 for $SrTiO_3$ and several thousand for $BaTiO_3$. The non-linear section around x = 0.3 - 0.4 is due to peaks and troughs around the phase transition at the Curie point (T_c) for these samples, which is near room temperature for x = 0.4 (fig. 8). This also demonstrates that such small samples can be measured – not a trivial matter, and developing methods to rapidly analyse hundreds or thousands of samples is as important as their manufacture in combinatorial synthesis. With this in mind, their microwave dielectric properties have been assessed using an Evanescent Microwave Probe (EMP), a scanning microscope able to measure dielectric loss (or Q), relative permittivity (ε_r) and topography simultaneously over a 2D area.

Finally, other systems made by the LUSI robot will be looked at and their results discussed. These include other dielectric perovskite systems, as well as ionic conductors for use as fuel cells, based on lanthanum-strontium-manganese-cobalt perovskites investigated at IC. I will also briefly talk about the AI search and predictive software that has been developed at UCL for use with the LUSI robot. For a useful large-scale combinatorial search, a database must e created which records all data generated throughout the project. In addition to building a useful reference library, 'data mining' techniques are being used to discover new and interesting materials for analysis. Once possible search areas have been determined, LUSI can be 'steered' to produce materials in the search area. These materials can then analysed and the cycle repeated to discover materials with optimal properties.

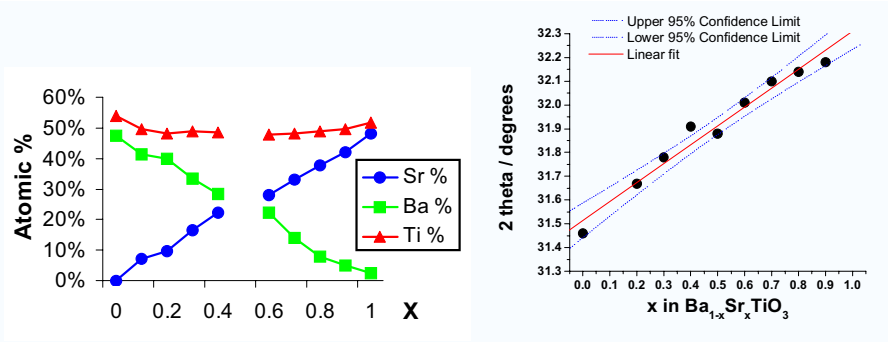

Left: Fig. 5, Atomic% values for Ti, Ba and Sr with x from EDXA of an uncoated $Ba_{1-x}Sr_xTiO_3$ array. The x = 0.5 sample was missing from this library.

Right: Fig. 6, plot of variation in XRD 100% peak position vs. x for $Ba_{1-x}Sr_xTiO_3$ array (both x = 0.1 and 1 were missing from this library).

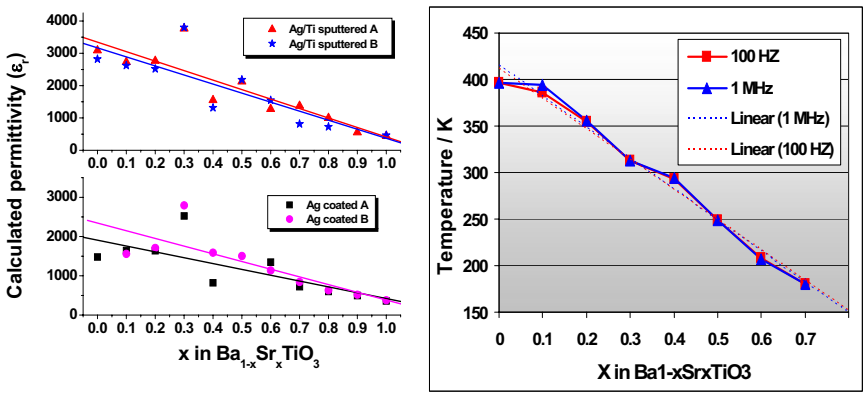

Left: Fig. 7, change in permittivity with composition for Ag/Ti deposited samples fired to 1350 °C, and Ag paste coated samples fired to 1400 °C. Each library has two sets of samples, A and B. Lines represent linear fit of the data.

Right: Fig. 8, plot of T_c against temperature for BST library.

Overview
Introduction: What is High-Throughput Combinatorial Materials Science?
Part 1: Manufacture of Combinatorial samples by the LUSI robot
Part 2: Characterisation and properties of BST libraries
Part 3: Other samples from LUSI and Data Mining
Final Summary and Acknowledgements

SMART ANTENNAS FOR MOBILE COMMUNICATIONS

Dr. V.M. Pandharipande
Professor, Dept. Electronics & Communication Engineering
Director, Centre of Excellence in Microwave Engineering
University College of Engineering (Autonomous)
Osmania University, Hyderabad – 500 007
Vijaympande@yahoo.com

The adoption of smart antenna techniques in wireless communication systems is expected to have a significant impact on efficient use of the spectrum, the minimization of the cost of establishing new wireless networks, the optimization of service quality, and realization of transparent operation across multi technology wireless networks. The smart antenna features need to be considered early in the design phase of future systems (top-down compatibility), second, a realistic performance evaluation of smart antenna technique needs to be performed according to the critical parameters associated with future system requirements (bottom up feasibility).

Smart antenna systems consist of multiple antenna elements at the transmitting and / or receiving side of the communication link, whose signals are processed adaptively in order to exploit the spatial dimension of the mobile radio channel. Depending on whether the processing is performed at the transmitter, receiver, or both ends of the communication link, the smart antenna technique is defined as

- multiple input single output (MISO)
- single input multiple output (SIMO) or
- multiple input multiple output (MIMO)

Exploitation of the spatial dimension can increase the capacity of wireless network by improving link quality through the mitigation of a number of impairments of mobile communications, such as multi path fading and co-channel interference and by increasing the data rate through the simultaneous transmission of multiple streams by different antennas.

Critical Issues ---

- The design and development of advanced smart antenna processing algorithms that allow adoption to varying propagation and network conditions and robustness against network impairments.

- The design and development of innovative smart antenna strategies for optimization of performance at the system level and transparent operation across different wireless systems and platforms.

- Realistic performance evaluation of the proposed algorithms and strategies based on the formulation of accurate channel and interference models, and the introduction of suitable performance metrics and simulation methodologies.

- Analysis of the implementation, complexity and cost efficiency issues involved in realization of the proposed smart antenna techniques for future generation wireless systems.

Multipath Propagation, defined as the creation of multipath signal paths between the transmitter and receiver due to the reflection of the transmitted signal by physical obstacles is one of the major problems of mobile communications.

The **delay spread** and resulting intersymbol interference due to multiple signal paths arriving at the receiver at different times have a critical impact an communication link quality.

Co-channel interference is a major limiting factor on the capacity of the wireless systems, resulting from the reuse of the available network resources (eg. Frequency, time) by a number of users.

Benefits of Smart Antennas ---

(1) **Increased range / coverage –** The array or beam forming gain is the average increase in signal power at the receiver due to coherent combination of the signals received at all antenna elements. It is proportional to the number of receive antennas and also allows for lower battery life.

(2) **Lower power requirements and cost reduction** – optimizing transmission toward the wanted user (transmit beam forming gain) achieves lower power consumption and amplifier costs.

(3) **Improved Link quality / reliability**:-

Diversity gain is obtained by receiving independent replicas of the signal through independently fading signal components.

(4) **Increased spectral efficiency** – Precise control of the transmitted and received power and exploitation of the knowledge of training sequence and / or other properties of the received signal (eg. constant envelope, finite alphabet, cyclostationarity) allows for interference reduction / mitigation and increased number of users sharing the same available resources (eg. time, frequency codes) and / or reuse of these resources by users served by the same base station / access point.

Increased data rate and therefore increased spectral efficiency can be achieved by exploiting the spatial multiplexing gain, that is the possibility to simultaneously transmit multiple data streams, exploiting the multiple independent dimensions, the so called spatial signatures or MIMO channel eigenmodes.

Tradionally, smart antenna systems have been designed focusing on maximization of one of the above mentioned gains (beam forming, diversity, and multiplexing gains).

In the multi user case, where the base station communicates with multiple users who share the available resources (frequency, time, codes etc.) the design of smart antenna transceivers is more challenging, as it aims to optimize the impact of interference and heavily depends on the specifics of the multiple access scheme employed.

Performance metrics for the characterization of smart antenna transceivers are the mean square error, SINR, bit error rate, achievable throughout, required transmitter power and channel capacity. Transmission schemes & receivers are designed to optimize one of these criteria.

Next generation wireless systems require signal processing techniques capable of operating in a wide variety of scenarios with respect to propagation, traffic, interference, user mobility, antenna configuration, radio access technology an channel state information (CSI) reliability.

Proceedings of APSYM2006, Dec. 14-16., Dept. of Electronics, CUSAT, India.

SPECIAL EUROPEAN ACE SESSION

Proceedings of APSYM2006, Dec. 14-16., Dept. of Electronics, CUSAT, India.

Overview of the European Research structure within the EC frameworks

B.Casali[1]
(1) IDS Ingegneria dei Sistemi, 1019 Via Livornese, 56010 Pisa, Italy, E-mail: b.casali@ids-spa.it

Abstract: *The European Research Area (ERA) is the final objective of the political views on research in Europe. The Framework Programmes (FPs) are the operational structures that support the implementation of ERA, since 1984.*
The current FP6 and the future FP7 are reviewed together with the funding instruments available. FPs mechanisms for international collaboration are presented.

I. The European Research Area

The ***European Research Area (ERA)*** is a strategic objective of the European Union that combines three complementary concepts:

- a restructuring of the European research fabric, in particular by improved coordination of national research activities and policies;
- the creation of an "internal market" in research, an area of free movement of knowledge, researchers and technology;
- the development of a European research policy, at national and EU levels.

By ERA, the European research will be as familiar as those of the single market or the single currency are today.

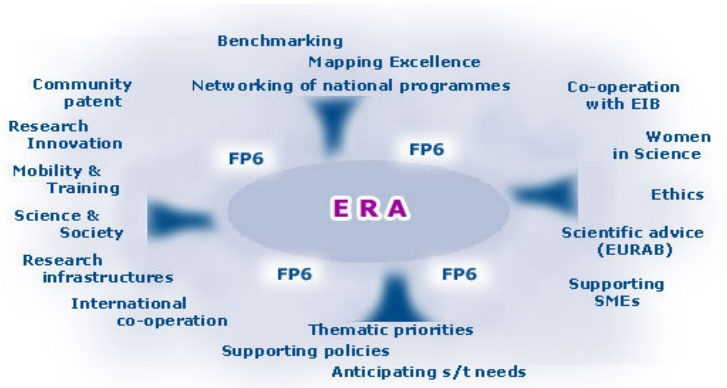

Fig. 1 Activities to promote the European Research Area

In order to create the European Research Area, the EU stimulates and supports programme coordination and joint activities conducted at national or regional level, as well as among European organisations, and thus helps to develop the common knowledge base necessary for the coherent development of policies.

II. The EU Framework Programmes

The ***Framework Programmes (FPs)***, represent the infrastructure created to implement the ERA. Since1984, the Framework Programmes have been strategically planned and coordinated within four multiannual frames, the purpose of which is to set out the priority areas to be covered during the life of the programme.

Following the grouping of Community research activities under the First Framework Programme (1984-87), the main aim of the Second Framework Programme (1987-91) was to develop the technologies of the future, in particular in the area of information technology and electronics, and materials and industrial technologies.

Whilst the Third Framework Programme (1990-94) broadly followed the same lines as its predecessors, an increased emphasis was placed on activities relating to the dissemination of research findings, life sciences and technologies and the training and mobility of researchers. For the period 1994-1998, all Community RTD activities were covered under the Fourth Framework Programme, largely influenced by the RTD provisions introduced by the Maastricht Treaty.

The Fifth Framework Programme (FP5) sets out the priorities for the European Union's RTD activities for the period 1998-2002. Like its predecessor, FP5 covers research, technological development and demonstration activities.

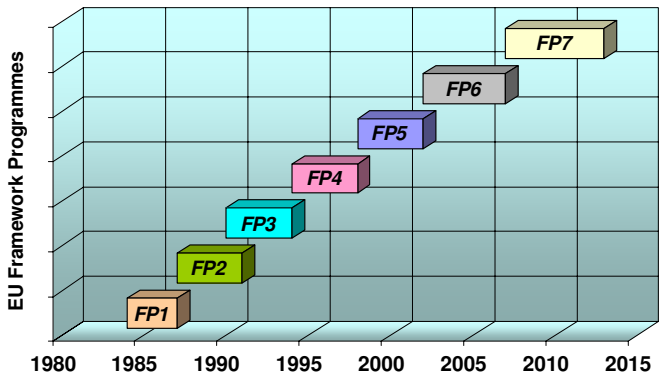

Fig. 2 EU Framework Programmes since 1984

The Framework Programmes are proposed by the European Commission and adopted by Council and the European Parliament following a co-decision procedure.

III. The Sixth Framework Programme (FP6)

The current FP is the Sixth Framework programme (FP6), which started in 2002 and will be running up to the end of 2006. In FP6, a number of thematic priorities (and selected topics within the overall priorities) have been identified, as detailed in the following figure.

Fig. 3 The Sixth Framework programme

With a budget of 17.5 billion euros for the years 2002 – 2006, FP6 represents about 4 to 5 percent of the overall expenditure on RTD in EU Member States.

IV. The Seventh Framework Programme (FP7)

FP7 will be fully operational as of 1 January 2007 and will expire in 2013. It has been structured in Research Themes and Objective Categories, as detailed in the following figure.

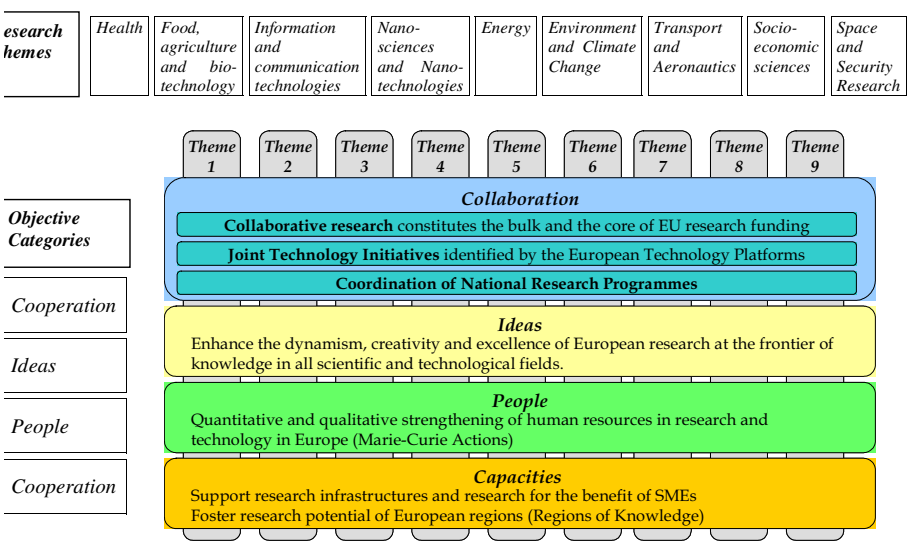

Fig. 4 The Seventh Framework Programme

With a budget of 50.5 billion euros for the years 2007 - 2013 it will double the budget per year available for EU funded research in the next 6 years.

V. The Funding Instruments

In EU FPs, the distribution of the funding is implemented by the following instruments:

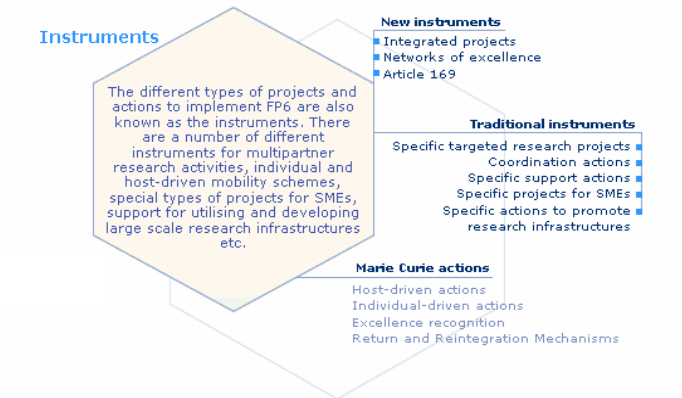

Fig. 5 The FPs Funding Instruments

where:

- *Integrated Projects* are instruments to support objective-driven research, where the primary deliverable is knowledge.
- *Networks of Excellence* are instrument for strengthening excellence by tackling the fragmentation of European research.
- *Specific Targeted Research Projects* are shared-cost RTD projects.
- *Coordination Actions* are actions to concertate research across Europe.
- *Specific projects for SMEs* are specific support for Small Medium Enterprises.
- *Marie Curie actions* fund the Improving Human Resources.
- *Specific Support Actions* are accompanying funding for big projects.

As an example, the Antenna Centre of Excellence (ACE) is a FP6 NoE focused on the antenna research for radio systems and sensors.
ACE is a pan-European effort involving 51 top level European Organisations (323 researchers and 130 PhD) for a 4 years duration (2004-2007) and with a total budget of 10.5 MEuro. ACE has links with outstanding international experts worldwide, in USA, Japan, etc.

VI. Conclusions

The *EU Framework Programmes* are the organizational and financial pillars for the creation of the *European Research Area,* since 1984.
The recent political agreements and the resulted boost in the *EU Framework Programmes* budgets open new horizons for the international collaboration and create new synergies among European centers and towards worldwide research.

ACE 2 Activities on Small antennas

Marta Martínez-Vázquez [(1)], Raquel Serrano[(2)], Jan Carlsson[(3)], Anja K. Skrivervik[(4)]
[(1)]IMST GmbH, Carl-Friedrich-Gauß-Str. 2, D-47475 Kamp-Lintfort, Germany, martinez@imst.de
[(2)]Universitat Politecnica de Catalunya, Jordi Gerona 31, Barcelona, Spain, raquel.serrano@tsc.upc.edu
[(3)]Chalmers Tekniska Högskola AB,Horsalvägen 11, S-41296 Gothenburg, jan.carlsson@sp.se
[(4)]LEMA, Ecole Polytechnique Fédérale de Lausanne, Station 11, CH-1015 Lausanne, anja.skrivervik@epfl.ch

Abstract:
This paper presents the work carried out in the ACE Network of Excellence regarding small antennas. Three aspects are covered in three projects : Small antenna technologies, small terminal antenna technologies and benchmarking of small terminal antennas measurement facilities. The aim is to identify the newest trends in antenna design and measurement for personal communications devices, and suggest novel solutions and design methodologies for various applications.

Introduction

The Networks of Excellence were introduced in the 6th Framework Program of the European Union as a new instrument to integrate and structure research activities around Europe, to increase the relevance of their results by avoiding overlapping [1]. Among them, the Antenna Centre of Excellence (ACE, 2004-2005) was created, complementing the activities of the COST 284 action: "Innovative Antennas for Emerging Terrestrial & Space-based Applications" [2]. ACE 2 (2006-2007) follows up the work started in ACE, to try to achieve a durable structuring.

This paper gives an overview of the activities carried out within the ACE 2 (Antenna Centre of Excellence) Network of Excellence, regarding antenna technologies for small terminals and their applications. The aim is to carry on with the work initiated in the first ACE, where new applications had already been identified. The work is subdivides into three work packages : Small antenna technologies, small terminal antenna technologies and benchmarking of small terminal antennas measurement facilities.

Small antenna technologies : future trends

The growth in the number of wireless systems over the past decade has been coupled with the ever-decreasing size of the RF systems. A modern mobile terminal is not only physically small but also required to operate well across a large number of wireless standards. The evolution of an important number of communication applications which require mobility such as RFID and sensing systems enforces the use of devices with an energy efficiency that allows reducing costs and size. All these new applications imply new requirements on the device that connects the terminal to free-space; namely the antenna. No longer can large, single-band, externally mounted antennas be considered. The future, therefore, lies in small, internally mounted, antennas that are able to work well across a large bandwidth. Neither the radiation mechanism nor the design of small antennas in modern applications such as Ultra Wide Band, MIMO systems and sensor networks, can be understood with traditional radiation theories for small antennas. New antenna requirements entail new modeling tools

and new design technologies. Since the compactness of the RF transmitter and receiver is increasing, the effects of integrating the antennas with the active element are studied. The newest trends in compact small antenna design have to be rapidly detected. The aim of our work is to optimize the existing design methodologies, and make use of the possibilities offered by new methodologies applied to small antennas.

A large number of downsizing solutions for small antennas can be found in literature. Some of the techniques applied to reduce antenna size are folding configurations, surface etching, shorting walls or pins, or utilizing high dielectric constant materials. However, there is difficulty in obtaining good electrical performance (bandwidth, efficiency, gain) when reducing size. And each of these miniaturization techniques will affect differently the performances. These techniques and their effects are well known and have been summarized in different publications [4, 5].

- The use of parasitic resonators to obtain a double resonant behavior
- Slit etching as a way of increasing the electrical path while maintaining physical size.
- Short-circuiting walls to utilize the half-size reduction factor.
- Dielectric loading, especially in packaged applications, for further size reduction at the cost of lower efficiency.

These downsizing solutions are however not sufficient when the new applications (UWB, MIMO, RF-ID) are considered, as the quality of these devices require additional criteria : UWB systems for instance asks from antennas a very large frequency band, but also a very short impulse response, a phase centre which remains fixed over the entire frequency band and a high radiation efficiency. An important indicator of the quality of a MIMO system is the channel capacity. This capacity depends on many factors, namely the number of transmit antennas and their spacing, the number of receive antennas and their spacing and the multipath environment and, in particular the spread of direction of arrival angles. As result the antenna is getting more and more interrelated with the system parameters (RF active parameters and channel parameters) what leads to the recommendation of considering the antenna as a central part of the system, designing its parameters in the context of the full system optimization. All these solutions put in distress the actual analytical modeling techniques, basically formulated for a single port quasi-resonant stand-alone antenna. A deep approach to the requirements, modeling and design techniques for the future small antennas must be carried out, which implies an special effort. An intense ongoing research work is being done in this direction.

Small terminal antenna technologies

The first focus of this activity is to keep on with the identification of the emerging needs, trends and standards that may be deployed in the near future. This will be accompanied by a follow-up of the review of novel applications, technologies and materials. On-going research lines concerning mobile communications terminals will be analyzed and evaluated, to ascertain if they are leading to relevant results with possible application to future terminals.

The problem of the integration of the antenna into the terminal will also be addressed, to gain new insight on the coupling mechanisms between the radiating element and the surrounding devices. Indeed, the assessment of the integration of small antennas into the terminal has to be done as a whole, that means taking into account other components, such as PCB, battery, plastic case, etc. This will include, for example, a study of the integration of receive/transmit amplifiers within the antenna, for direct optimization of the noise temperature on receive mode, and of the radiated power efficiency on transmit mode. This should enable much better receiver sensitivity and longer battery life. The aim is to produce a set of recommendations

for the integration of small antennas into user terminals, which could help enhance the efficiency of the antennas when combined with the communications devices. This is especially important in applications such as HAC (Hearing aid Compatible) phones, as near-field effects must be taken into account.

To be able to accurately assess the problem of the integration of small antennas into user terminals, the latest technologies and design methodologies will be reviewed, in order to optimize them. This includes traditional antenna design methodologies, but also new trends such as the analysis of the characteristic modes on the chassis of the handset.

Antenna design is very much connected with antenna analysis tools both in the frequency domain and in the time domain. The design and development of antennas for mobile terminals relies mostly on the expertise and know-how of the designers. Although important efforts have been focused on developing automated design procedures, either based on genetic algorithms or other random optimizers, in-depth knowledge of the physics involved on radiation mechanisms is always necessary to provide a reliable solution. Therefore, the integration of the right analysis procedures and design tools is also a key issue in this activity. Thus, as analysis of new tools for antenna design will be carried out, and their performance will be tested with a comparison of simulation results obtained with different simulation tools. A judicious combination of both semi-analytical optimization methods based on the radiating modes of the antenna and random optimization procedures can also lead to new design strategies and tools.

Benchmarking of small terminal antennas measurement facilities

Benchmarking of test facilities is a work package included in the small terminals and smart antennas activity within ACE – Antenna Centre of Excellence [1]. Among the main objectives of the work package are the definition of test cases for the characterization of terminal antennas and the comparison of results from measurements performed at different antenna test facilities around Europe.

Usually, antennas are characterized by their radiation patterns. This is useful when the lobes are narrow and there is line of sight between the two sides. For the case of terminal antennas, e.g. mobile phone and PDA antennas, the environment varies with time and is complex with several scatterers, so it can only be described statistically. A better way to describe the radiation characteristics of terminal antennas is to use the total radiation efficiency. This includes contributions from losses in the antenna itself, losses in the near-in environment of the antenna and impedance mismatch. When the impedance mismatch is not included, we call the remaining factor the radiation efficiency. The total radiation efficiency is a correct measure of the quality of antennas that are designed for use in a so called uniform multi-path environment, where there is no “line of sight” to the base station and reflected and scattered waves come in with equal probability from all directions in space. Total radiation efficiency can be measured using many different methods, e.g. by measuring the 3D radiation pattern and integrating, using a reverberation chamber [5] or a Wheeler cap [6]. Therefore, a test case that should be used for benchmarking of different test facilities must be constructed so that it can be used in different set-ups and at the same time be configurable so that several test cases can be defined. It is also an advantage if the test case is simple enough to allow numerical simulations with good accuracy for enabling additional comparisons. The developed test fixture fulfils these requirements and can be used for both efficiency and diversity gain measurements.

For the active devices total radiated power (TRP) and total isotropic receiving sensitivity (TIS) are measured. TRP is measured for two test cases: a GSM phone with special software

allowing it to radiate at a constant power level, and a specially developed 1.875 GHz device. Sensitivity is measured for a standard GSM phone, and therefore a base station emulator is needed for these measurements. Both the TRP and the TIS measurements for the GSM phones are done with the phone both in a free space position and in a talk position close to a head phantom. TRP for the 1.785 GHz device is only measured for free space conditions. An overview of the different test cases can be seen in figure 1.

Figure 1 : Benchmarking test antennas

As an example of results that came out of the comparison of the different testing equipment, the total radiation efficiency for a 5.2GHz slota antenna measured at ten facilities is shown in Fig.2. The maximum divaition from mean is of 2.7 dB.

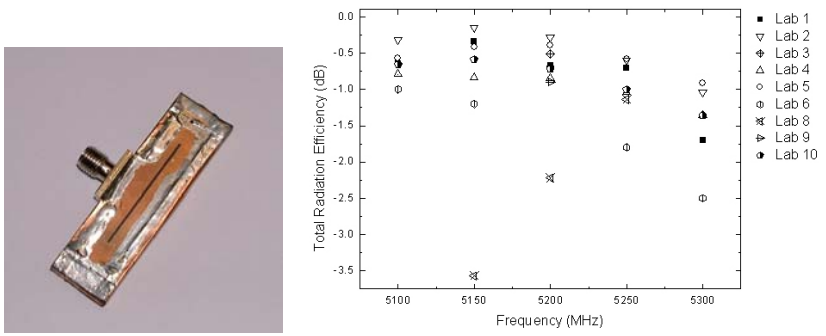

Figure 2 :Benchmark antenna and benchmarking results

References

[1] www.ist-ace.org.
[2] www.cost284.com
[3] A.K. Skrivervik, J-F. Zürcher, O. Staub, J.R. Mosig, "PCS antenna design: the challenge of miniaturization", IEEE Antennas and Propagation Magazine, vol. 43, Issue 4, August 2001, pp. 12-27.
[4] Jofre, L., Cetiner, B.A. and De Flaviis, F. "Miniature Multi-Element Antenna for Wireless Communications". IEEE Trans. Antennas Propagat. Vol. 50. pp 658-669, May, 2002.
[5] Measuring Efficiency of Small Antennas in Reverberation Chambers," IEEE AP-S International Symposium and URSI Science Meeting, Columbus, Ohio, USA, June 22 – 27, 2003.
[6] H.A. Wheeler, "The Radiansphere Around a Small Antenna," Proceedings of the IRE, Vol. 47, August 1959

ASI: the European effort to structure antenna software

Guy A. E. Vandenbosch[(1)], and Raphaël Gillard[(2)]
(1) Department of Electrical Engineering, Katholieke Universiteit Leuven, Kasteelpark Arenberg 10, B-3001 Leuven, Belgium, Email: guy.vandenbosch@esat.kuleuven.be
(2) IETR, INSA, Avenue des buttes de Coësmes, 35043 Rennes, France,
Email: raphael.gillard@insa-rennes.fr

Abstract: *This paper aims at giving an overview of what is going on in the field of structuring antenna software at a European level. In other words, at the end of this paper, the reader should have a good overall idea about what is being done already, who is doing what in this field, and what remains to be done. The paper consists of several sections, where specific aspects of this structuring are briefly described*

Introduction: ACE is a Network of Excellence (NoE) within the 6th framework of the European Union (EU). A NoE provides the means to establish integrated European research communities. ACE stands for 'Antenna Center of Excellence'.
One of the efforts being performed within ACE is the Antenna Software Initiative (ASI). The reason for this is the observation that although for a long time already there has been a strong coordination in fundamental antenna modeling problems in Europe, concerning the actual software itself, the European effort is still scattered. In answer to this problem, within the ACE network in a first step an inventory was made of the software available among all partners of ACE, describing the possibilities and limitations (capabilities to handle complex structures, environments, feeds, active components,...). This was the basis for all further work within the ASI. The result of this inventory can be consulted at the ACE website [1].
Two high level activities have been performed after the inventory phase: 1. benchmarking of existing software codes, and 2. laying the foundations for a European software library.
The pillars on which this library will be built are the following:
1. The Electromagnetic Data Interface (EDI). This activity consists of defining a standardized way of storing electromagnetic data (currents, fields, ...) in files (the so-called Data Dictionaries), and of developing the software routines to do this automatically through a simple routine call [2].
2. A better understanding of the problems encountered during the integration of actual software already available at this moment at a European level [3].
3. Development of modular and hybrid techniques at a European level. The idea is to work out procedures to develop these approaches in a "European" group rather than at the research group level, taking into account different views and the various constraints.
These activities will be explained in more detail in this paper. They have been performed by the partners within the framework of the ASI structure, a structure set up in a democratic way to cope with the most important bottle necks encountered.

ASI structure: The goal of the software integration activity within ACE is by no means to conceive the ultimate all-integrating software package for antenna design. This is not feasible at all, and even questionable. The main idea is to initiate a long-term process for antenna software integration within the European antenna community, to take the first steps in the direction of a European Antenna Software Library. Two major tasks have been performed:

1. A few illustrative cases of antenna software integration have been completed, chosen in such a way that they open possibilities for the European antenna industry. They can be seen a sort of test for a larger scale integration, discovering difficulties and possible solutions.
2. The start of the implementation of the so-called EDI (the Electromagnetic Data Interface). The EDI is the combination of a possible standard for electromagnetic data file formats (consisting of so-called Data Dictionaries for electromagnetic quantities), and corresponding software routines in order to create these formats in a very user-friendly way. The EDI is absolutely necessary for a long-term further efficient integration. It solves a long lasting problem in the antenna community once and for all: the exchange of data.

One of the first tasks was to set up a more dedicated structure. The resulting structure is given in Fig. 1 below. It is set up in view of covering both ACE 1 (2004-2005) and ACE 2 (2006-2007). The structure consists of the WP (Work Package) group on benchmarking, the Working Groups (WGs) and the Special Interest Groups (SIGs). The leading partner is mentioned in between brackets.

- There are 4 working groups covering 4 different basic topologies of industrially important antenna structures (WGs on planar arrays, composite horns, radome structures, conformal structures). Their job is to structure modeling for their specific type of antennas. The working group on planar arrays has been most active. It has delivered most integration activities and the Data Dictionary for meshes and currents. The WG on composite horns has generated the Data Dictionary for Modes.

- The WG on time domain modeling, responsible to structure modeling tools in the time domain, has been mainly focusing on the definition of the Data Dictionary for near fields.

- The SIG on GFs focuses on the concept of the use and exchange of Green's functions, typically used within the Method of Moments. They have been responsible for the definition of the Data Dictionary for Green's functions.

The data dictionaries on far fields and S-parameters have been defined in cooperation with the measurement activity of ACE.

The SIG on the EDI coordinates all ACE activities performed within the framework of the EDI.

Towards a European antenna software library: The ASI was organized around three questions:
1. Exactly what software tools do we have available within Europe?
2. What is the quality of the tools we have?
3. How can we boost the capabilities of the tools by restructuring the European effort?

The first question is answered. A catalogue is available describing the ASI software tools.
Question two is being tackled within the benchmarking WP of ACE, see further in this paper.
The last question is a very strategic one. Boosting the capabilities of software obviously can be done through developing new modelling techniques. However, this is fundamental research, not restructuring, and thus not the task of a NoE. It can also be done through ***integration of existing software***. In our view restructuring of research on antenna software does not mean trying to develop the "ultimate" monolithic software package. There are many reasons for this: 1. Such an effort is not the task of a NoE. Efforts like that are more in line with the strategy of commercial software companies. 2. A monolithic tool is bound to be not very flexible. 3. Such an effort would require much larger investments. 4. It would take a huge continuous effort to manage such a software tool.
Instead, the brainstorming process within ACE 1 has worked out a very specific view on integration. This view involves five pillars.
1. An integrated library of software routines. Each routine performs part of the analysis. The routines are available with the ASI partners, but at this moment they are not integrated.

2. The integration of the library is performed through the development of a common "language", the Electromagnetic Data Interface (EDI), which enables the routines to communicate. In a first phase, file formats are defined for all the important physical quantities, for example: currents, fields, waveguide modes, etc.. The result is a "data dictionary". In a second phase, an Electromagnetic Data Interface library is developed, a set of new routines that writes / reads the physical quantities in a standardized way, according to the data dictionary, to / from files.
3. The exploration of emerging new software capabilities by explicitly using the possibility to combine existing routines from different ASI partners. Within ACE 1, the first integration activities have been implemented. They did not use the EDI yet. Within ACE 2, one of the major tasks will be the implementation of the full EDI in the software codes of all partners.
4. The study of further modelling strategies, now based on the EDI. To that goal the Special Interest Group on Structures and Structuring, the so-called SIG-SaS will have to interact with the group defining and implementing the EDI. It has to ensure that the EDI is developed in line with future needs of the whole antenna modelling community.
5. The dissemination of the existence and capabilities of the EDI to the (European) antenna community. This will be done by presenting it at conferences and in workshops and by organizing courses on it within the European School on Antennas, a result of ACE 1.

The benchmarking working package:
Antenna design definitively relies on the availability of user-friendly and powerful antenna software. The assessment of these software tools is essential for antenna designers. CAD tools must be seen as heavy investments. Only experienced engineers can extract the best performances that these software tools can yield. Even when a freeware CAD tool can be downloaded instantaneously from the web, it is not acceptable to waste a couple of weeks before discovering that it cannot correctly handle the antenna structure to be studied!
Unfortunately, the assessment process is not an easy task due to several factors. First, there are many software packages, both commercial and home-made, with very different features and performances. Even if we limit the investigations to a single analysis method (FDTD for instance), many different tools can be found whose differences could sometimes appear to be very subtle for non-specialists. Indeed, there is no real overview anywhere concerning the actual capabilities of all these codes. None of them can of course be regarded as the universal solution for antenna simulation. When different codes yield different results, there is no way of determining which one has to be preferred. Moreover, it is very likely that the optimal CAD tool for a given job depends on the specific antenna topology under consideration. The recent emergence of new types of algorithms (wavelet-based compression techniques and other fast solvers) has sometimes significantly extended the performances of classical methods. This makes the global vision even more difficult as the traditional references have changed. In most cases, only the people who have developed the software know precisely its actual capabilities. There is another reason why the assessment of software is complex. The needs of the users themselves can vary. Some of them are only interested in the accuracy of results while others are also considering computer requirements (CPU time and memory storage), user-friendly GUI or any other secondary features.
The main objective of this benchmarking work-package is to define a set of benchmarking structures in order to assess the antenna software. As a result, it provides standards for the evaluation of existing and future antenna software. It also improves communication between software developers and antenna designers, by clarifying the actual challenges in antenna modelling (from both the expressed needs and the expected scientific capabilities). Finally, it facilitates the convergence to future research programs in antenna modelling by concentrating the effort on a set of agreed problems.

Conclusion: This paper focuses on the software activities performed within ACE. The main goal is to structure the scattered, very labor intensive efforts that are being spent in this field. It is shown that part of the path that has been chosen has already been finished within ACE 1, but a lot of work still has to be done. A major milestone in the whole integration effort will be the implementation of the EDI in the software of the partners. This will open up a huge range of new possibilities. Only accomplishing this can already be considered as a real success.

References:

[1] www.antennasvce.org
[2] Martinaud J.-P., Frandsen P. E.,. Vandenbosch G. A. E., *The ACE activity on standardized file formats for electromagnetic software,* EuCAP, Nice, France, Nov. 2006.
[3] Volski V. et al., *Overview of the software integration activities within ACE*, EuCAP, Nice, France, Nov. 2006.

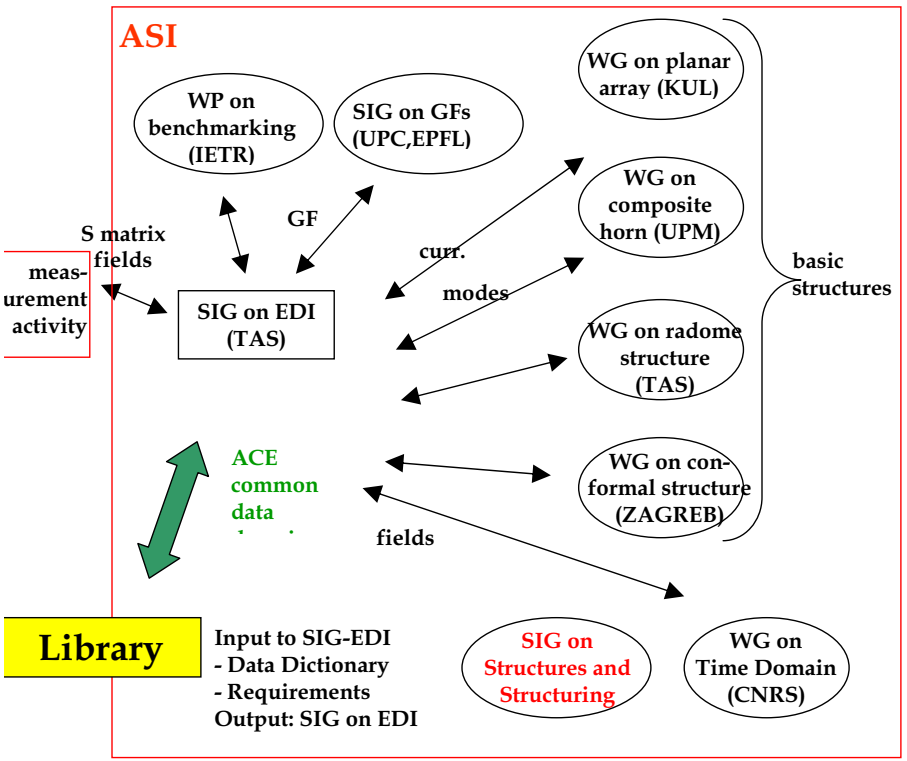

Fig. 1. The ASI structure.

Proceedings of APSYM2006, Dec. 14-16., Dept. of Electronics, CUSAT, India.

Diversity Measurements of a Reconfigurable Antenna with Switched Polarizations and Patterns

J-M. Laheurte, B. Poussot, L. Cirio, M. Goumballe
Université de Marne-La-Vallée, 77454 Marne-La-Vallée, France
laheurte@univ-mlv.fr

Abstract: *A switchable patch antenna is designed to provide polarization and pattern diversities. The performance of the device is predicted using a commercial simulator including a pin diode modelling and an optimisation procedure of the switched loads based on an equivalent flow graph. Measurements of the correlation factor and the diversity gain in an indoor environment are performed using a dedicated platform..*

Introduction: Many recent studies have presented significant research progress on reconfigurable antennas, with switchable radiation characteristics. Various topologies have been proposed with different types of switched components [1-2]. This type of antenna has tremendous potential to improve the performance of future-generation wireless systems developed for dense multipath applications

Our reconfigurable antenna is based on the switched parasitic concept [3]. The antenna system comprises a central patch connected to the receiver, and two adjacent switchable parasitic elements strongly coupled to the central patch (Fig.1). The different switch settings result in different far-field patterns and polarizations invoking different fading in the corresponding channels. The advantage of the system is that it is a simpler and more compact configuration than that of conventional antenna diversity where one receiver is connected to each element or channel. To date, few attempts have been made to characterize switchable antennas in terms of diversity gain in indoor environments and to evaluate the real performance improvement over conventional passive single-port (nondiversity) antennas. To fully characterize the reconfigurable antena, a dedicated measurement setup has been developed to determine the diversity gain (DG) in the specific multipath environment of a lab room. Cumulative distribution functions are calculated for all channels and general conclusions are drawn on the minimum number of channels required for an optimal DG.

Antenna Design: The antenna operating at 5.8 GHz is depicted in Fig.1. The prototype is a three-element parasitic antenna array where aperture-coupled square patch antennas are used as radiating elements. The central patch antenna is printed on top of a 5880 Duroid substrate. It can be excited by one of the two orthogonal crossed slots and feedlines etched on a top and bottom sides of an AR 1000 substrate. DC-bias circuit and slot geometries are depicted on Fig.2. The slot selection results either in an E-plane or H-plane coupling with the adjacent parasitic patches. The selected slot also enforces one of the two linear orthogonal polarizations. The slot selection is performed with a SPDT, consisting of two beam-lead pin diodes metelics MBP-1030 (d1 and d4 on Fig.2), directly connected to the feeding microstrip line below the ground plane. By switching ON a diode while the other is OFF, the antenna can switch between horizontal or vertical polarization states with a single feeding port.

Each of the slot pairs in the parasitic patches is loaded by a switchable stub (pure reactance) through a SPDT (d3-d6 and d2-d5). The stub lengths are adjusted by pin diodes (d7 and d8). The SPDT role is to select a slot parallel to the slot of the central patch to keep the same polarization in the three patches. To keep the same diversity patterns for both polarisations, the gap between adjacent patches is adjusted so that similar E-plane and H-plane couplings are obtained.

The values of the switchable stub lengths must provide a set of patterns with a proper antenna matching for each pattern. To determine these lengths, it is necessary to use the procedure described in [3] based on the equivalent flow graph of the antenna. The S-parameters of the structure and the active element patterns of each radiating patch are first extracted from an electromagnetic simulation (HFSS). The active radiation pattern of an element is defined as the radiation pattern of one radiating element when the other elements of the array are terminated by a reference load [3]. These data are then exported in a dedicated software (Matlab) to calculate the return loss and radiation pattern of the antenna array for any loading reactance. An optimization procedure is finally developed to select the reactive loads (or stub lengths) for the best trade-off between beam direction and return loss. The gap width between the patches is a crucial parameter to reach this trade-off.

All simulations include the effects of the DC-bias circuit and limited ground plane. The diodes states are modelled by electrical equivalent circuits extracted from the S-parameters provided by the manufacturer at 6 GHz (ON state: forward bias current I_F=10 mA OFF state: reverse voltage V_R=-10 volts).

1A **1B**

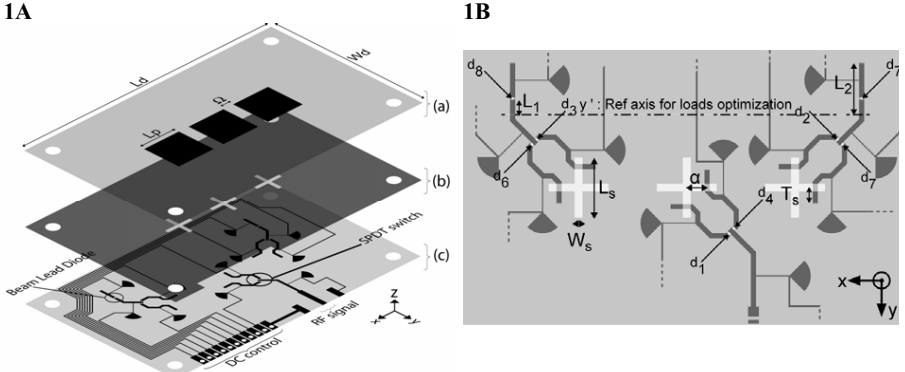

Fig.1A. Antenna layers: (a) Radiating element (b) Coupling elements (c) Active and passive circuit components. Antenna dimensions: L_d = 90 mm, W_d = 55mm, L_p = 12.7mm, $\Omega = 0.07\ \lambda_0$ with f_0 = 5.8 GHz.

Fig.1B. Details of the feeding layer and the biasing layer. Slots: L_S = 9mm, W_S = 1.2mm, α = 3mm. Tuning stub: T_S = 2.5 mm. Line width: L_w = 0.750 mm for Z_0 = 50 Ω.

Measurement platform: The diversity characteristics are evaluated with a dedicated measurement platform. The transmitter consists of a vertically polarized monopole antenna. The immediate vicinity of the transmitting monopole is a rich scattering environment (metal furniture, laboratory tables, measurement equipment) yielding homogenous radiating directions and polarizations. The large dimensions of the room (120 m^2) allows to separate the transmitter and receiver by a distance of approximately 10 meters. Experimental data

gathered throughout the measurement campaigns indicate that this scenario represents a typical indoor propagation environment with a short-term fading respecting a Rayleigh distribution for each diversity branch. The reconfigurable antenna under test (RAUT) is fixed 1.8 m above the ground at the end of a 1.5 m-long plastic arm. The other end of the arm is connected to a computer-controlled stepper motor which allows the rotation of the antenna around a 3m-diameter circle. The biasing of the SPDTs and switchable stubs is electronically controlled by the computer.

The signal is amplified (LNA 28 dB), fed into a spectrum analyser, analog-to-digital converted and transferred to the computer for post-processing. The receiving measurement setup is placed on a trolley which is wheeled around its initial position, usually by 10 to 30 cm only to keep sample values which statistically remain relatively constant . This allows to increase the number of data files and improve the statistical convergence. A 0.5° angular step is small enough to provide a large number of samples (720) for an entire rotation and large enough to avoid redundant information. The operation is repeated until 7000 samples are collected. The RAUT is tested by measuring all eight channels (4 patterns times 2 polarizations) for each arm position. The correlation factor between the channels and the various diversity gains are extracted from the measured data.

Antenna measurement: Measurements of the eight switched patterns (eight channels) are presented in Fig.2 with four switched patterns for each polarization. The patterns are labelled from b1 to b8 in accordance with the diode states indicated in Table 1. L1=2.6mm is the stub length when the diode stub (d7 or d8) is OFF. It results in a -30 Ω reactance at the reference axis position (Fig .1). L2=8.05mm is the stub length when the stub diode (d7 or d8) is ON which results in a 250 Ω reactance at the reference axis position. If Z1 and Z2 are the impedances for each stub, symmetrical reactive loads (Z_1, Z_2) on the parasitic elements give rise to symmetrical patterns. When Z_1 =Z_2=250 Ω , a maximum gain is observed at broadside while Z_1=Z_2=-30 Ω yields a minimum in the same direction. When Z_1=250 Ω and Z_2=-30Ω and inversely, the beam angles are directed toward +/- 45°. Reasonable bandwidths and cross polarization levels are observed for all 8 patterns.

	b1	b2	b3	b4	b5	b6	b7	b8
ON state	d_1,d_2,d_3	d_1,d_2,d_3,d_7	d_1,d_2,d_3,d_8	d_1,d_2,d_3,d_7,d_8	d_4,d_5,d_6	d_4,d_5,d_6,d_7	d_4,d_5,d_6,d_8	d_4,d_5,d_6,d_7,d_8
OFF state	d_4,d_5,d_6,d_7,d_8	d_4,d_5,d_6,d_8	d_4,d_5,d_6,d_7	d_4,d_5,d_6	$d_1,d_2,d_3,$ d_7,d_8	d_1,d_2,d_3,d_8	d_1,d_2,d_3,d_7	d_1,d_2,d_3

Table 1:Diode combinations for all 8 channels

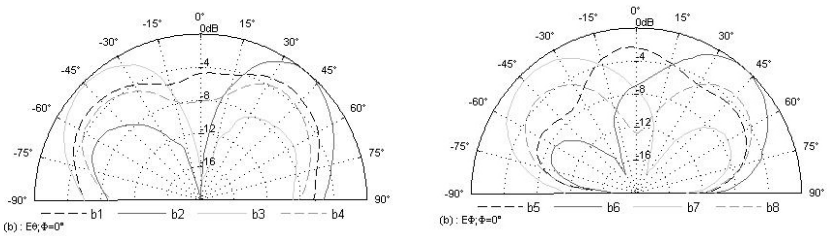

Fig.2. Measured switched patterns for the horizontal (E-plane coupling) and vertical polarization (H-plane coupling)

gathered throughout the measurement campaigns indicate that this scenario represents a typical indoor propagation environment with a short-term fading respecting a Rayleigh distribution for each diversity branch. The reconfigurable antenna under test (RAUT) is fixed 1.8 m above the ground at the end of a 1.5 m-long plastic arm. The other end of the arm is connected to a computer-controlled stepper motor which allows the rotation of the antenna around a 3m-diameter circle. The biasing of the SPDTs and switchable stubs is electronically controlled by the computer.

The signal is amplified (LNA 28 dB), fed into a spectrum analyser, analog-to-digital converted and transferred to the computer for post-processing. The receiving measurement setup is placed on a trolley which is wheeled around its initial position, usually by 10 to 30 cm only to keep sample values which statistically remain relatively constant . This allows to increase the number of data files and improve the statistical convergence. A 0.5° angular step is small enough to provide a large number of samples (720) for an entire rotation and large enough to avoid redundant information. The operation is repeated until 7000 samples are collected. The RAUT is tested by measuring all eight channels (4 patterns times 2 polarizations) for each arm position. The correlation factor between the channels and the various diversity gains are extracted from the measured data.

Antenna measurement: Measurements of the eight switched patterns (eight channels) are presented in Fig.2 with four switched patterns for each polarization. The patterns are labelled from b1 to b8 in accordance with the diode states indicated in Table 1. L1=2.6mm is the stub length when the diode stub (d7 or d8) is OFF. It results in a -30 Ω reactance at the reference axis position (Fig .1). L2=8.05mm is the stub length when the stub diode (d7 or d8) is ON which results in a 250 Ω reactance at the reference axis position. If Z1 and Z2 are the impedances for each stub, symmetrical reactive loads (Z_1, Z_2) on the parasitic elements give rise to symmetrical patterns. When $Z_1 = Z_2 = 250\ \Omega$, a maximum gain is observed at broadside while $Z_1 = Z_2 = -30\ \Omega$ yields a minimum in the same direction. When $Z_1 = 250\ \Omega$ and $Z_2 = -30\ \Omega$ and inversely, the beam angles are directed toward +/- 45°. Reasonable bandwidths and cross polarization levels are observed for all 8 patterns.

	b1	b2	b3	b4	b5	b6	b7	b8
ON state	d_1,d_2,d_3	d_1,d_2,d_3,d_7	d_1,d_2,d_3,d_8	d_1,d_2,d_3,d_7,d_8	d_4,d_5,d_6	d_4,d_5,d_6,d_7	d_4,d_5,d_6,d_8	d_4,d_5,d_6,d_7,d_8
OFF state	d_4,d_5,d_6,d_7,d_8	d_4,d_5,d_6,d_8	d_4,d_5,d_6,d_7	d_4,d_5,d_6	d_1,d_2,d_3,d_7,d_8	d_1,d_2,d_3,d_8	d_1,d_2,d_3,d_7	d_1,d_2,d_3

Table 1:Diode combinations for all 8 channels

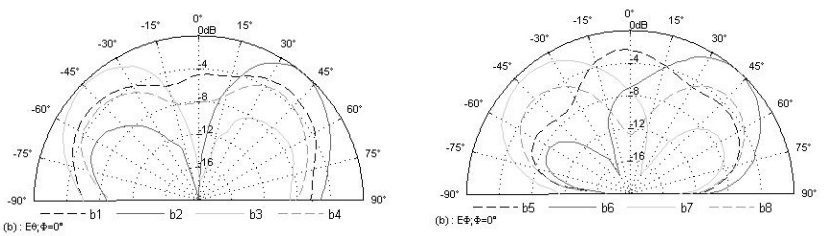

Fig.2. Measured switched patterns for the horizontal (E-plane coupling) and vertical polarization (H-plane coupling)

Diversity measurements: In all measurements, the antenna position was vertical, i.e., the y-axis in Fig.1 was directed toward the ceiling. The diversity gain is defined for a 1% outage probability in the cumulative distribution function (CDF) of the received signal. The CDFs are given in Fig. 3 for all eight channels. Table 2 summarizes the DG performance for several channel combinations When two channels are used, for instance polarization diversity only and pattern diversity only with θ=±45°, measured DGs are DG=7dB and DG=6.7dB respectively.

The 2dB Cross-Polarization Discrimination Ratio (XPR) observed in the room explains that the optimal 10 dB DG is not reached for two channels when polarization diversity is used. In a selection combining scheme and a two-branch configuration, a 10 dB value can only be obtained with an ideal power balance and uncorrelated branches. It can be noticed that a combination of two patterns (θ=±45°) and two polarizations allows a 10 dB DG that is to say a 3 dB improvement compared to the two-channel diversity. Only a slight improvement is observed when the channels corresponding to the broadside patterns are added (10.2dB) while 10.6 dB corresponds to the case including all 8 channels as seen in Fig.3. It must be recall that in a space diversity configuration with two-monopoles separated by a half wavelength, similar performance were reached at the cost of larger overall dimensions.

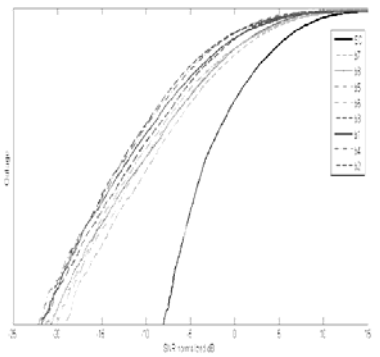

Fig.3. Cumulative distribution function for the 8 channels

NUMBER OF CHANNELS	DIVERSITY GAIN
2 Pattern diversity with θ=±45°	6.7 dB
2 Polarization diversity only	7dB
4 Polarization diversity and pattern diversity with θ=±45°	10 dB
6 Polarization diversity and pattern diversity with θ=±45° and θ=0°	10.2 dB

Reference:

[1] J. Panagamuwa, A. Chauraya and J. C. Vardaxoglou, "Frequency and Beam Reconfigurable Antenna Using Photoconducting Switches", IEEE Transactions on Antennas and Propagation, vol. 54, n°.2, 449-454

[2] C. Jung, M. Lee, G. Li, F. De Flaviis, "Reconfigurable Scan-Beam Single-Arm Spiral Antenna Integrated With RF-MEMS Switches", IEEE Transactions on Antennas and Propagation, vol. 54, n°.2, 455-463, February 2006

[3] L. Petit, L. Dussopt, J.-M. Laheurte, "MEMS-Switched Parasitic-Antenna Array for Radiation Pattern Diversity", IEEE Transactions on Antennas and Propagation, September 2006.

Proceedings of APSYM2006, Dec. 14-16., Dept. of Electronics, CUSAT, India.

AUTHOR INDEX

Proceedings of APSYM2006, Dec. 14-16., Dept. of Electronics, CUSAT, India.

Proceedings of APSYM2006, Dec. 14-16., Dept. of Electronics, CUSAT, India.

CREMA,CUSAT